

MAY 2020

AJNR

VOLUME 41 • PP 737-941

AJNR

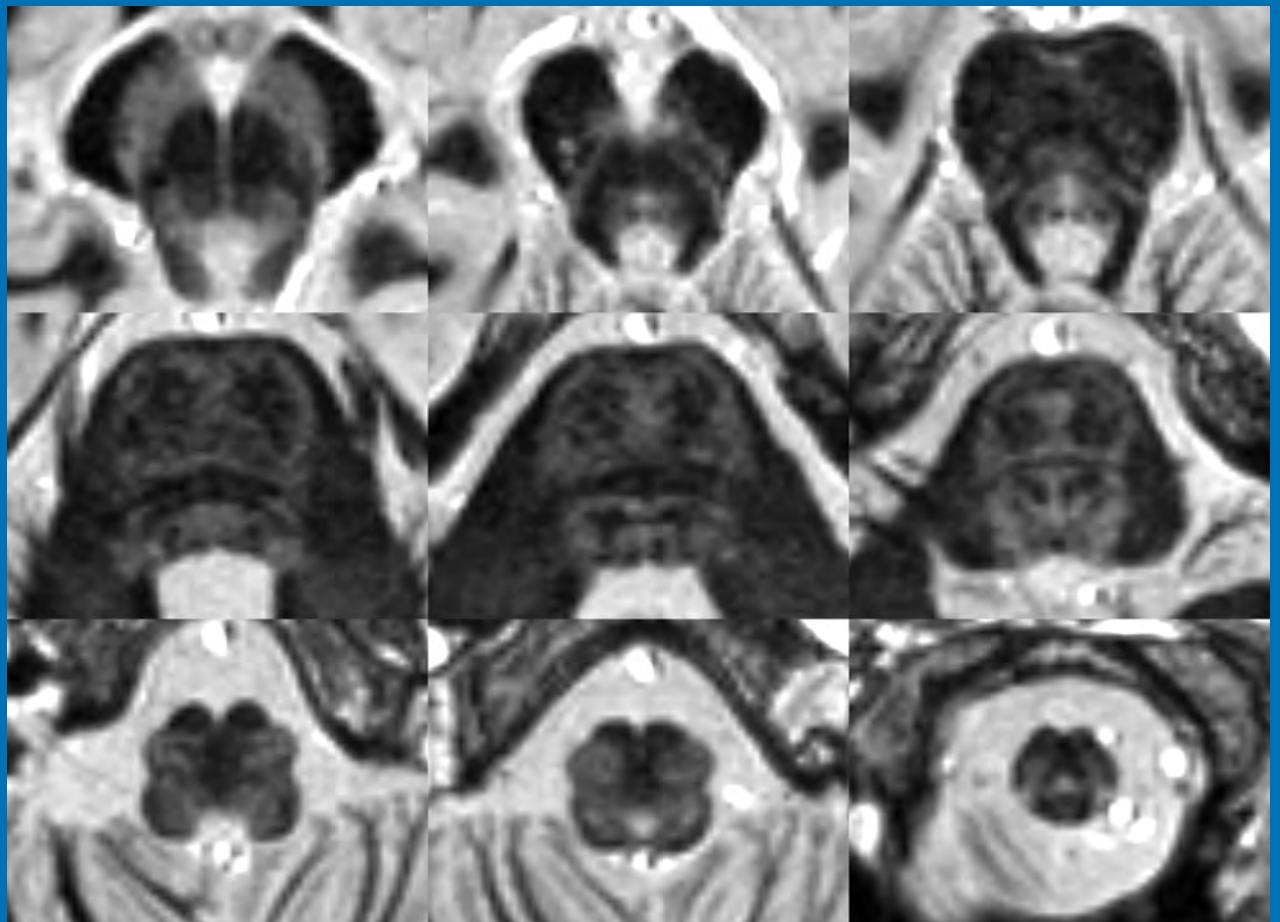
AMERICAN JOURNAL OF NEURORADIOLOGY

MAY 2020
VOLUME 41
NUMBER 5
WWW.AJNR.ORG

THE JOURNAL OF DIAGNOSTIC AND
INTERVENTIONAL NEURORADIOLOGY

Medicare for all: considerations for neuroradiologists
MRI discrimination of brain stem nuclei and pathways
Fast stent retrieval improves recanalization rates of thrombectomy
Tumor response assessment in diffuse intrinsic pontine glioma

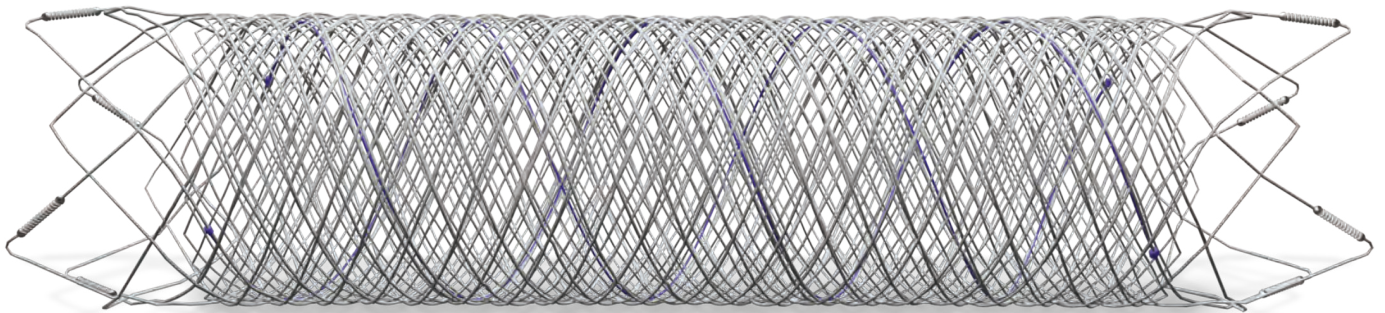
Official Journal ASNR • ASFNR • ASHNR • ASPNR • ASSR



FRED™

Flow Re-Direction
Endoluminal Device

FLOW DIVERSION.



SIMPLIFIED.



MicroVention Worldwide
Innovation Center
35 Enterprise
Aliso Viejo, CA 92656 USA
MicroVention UK Limited
MicroVention Europe S.A.R.L.
MicroVention Deutschland GmbH
Web

PH +1 714.247.8000

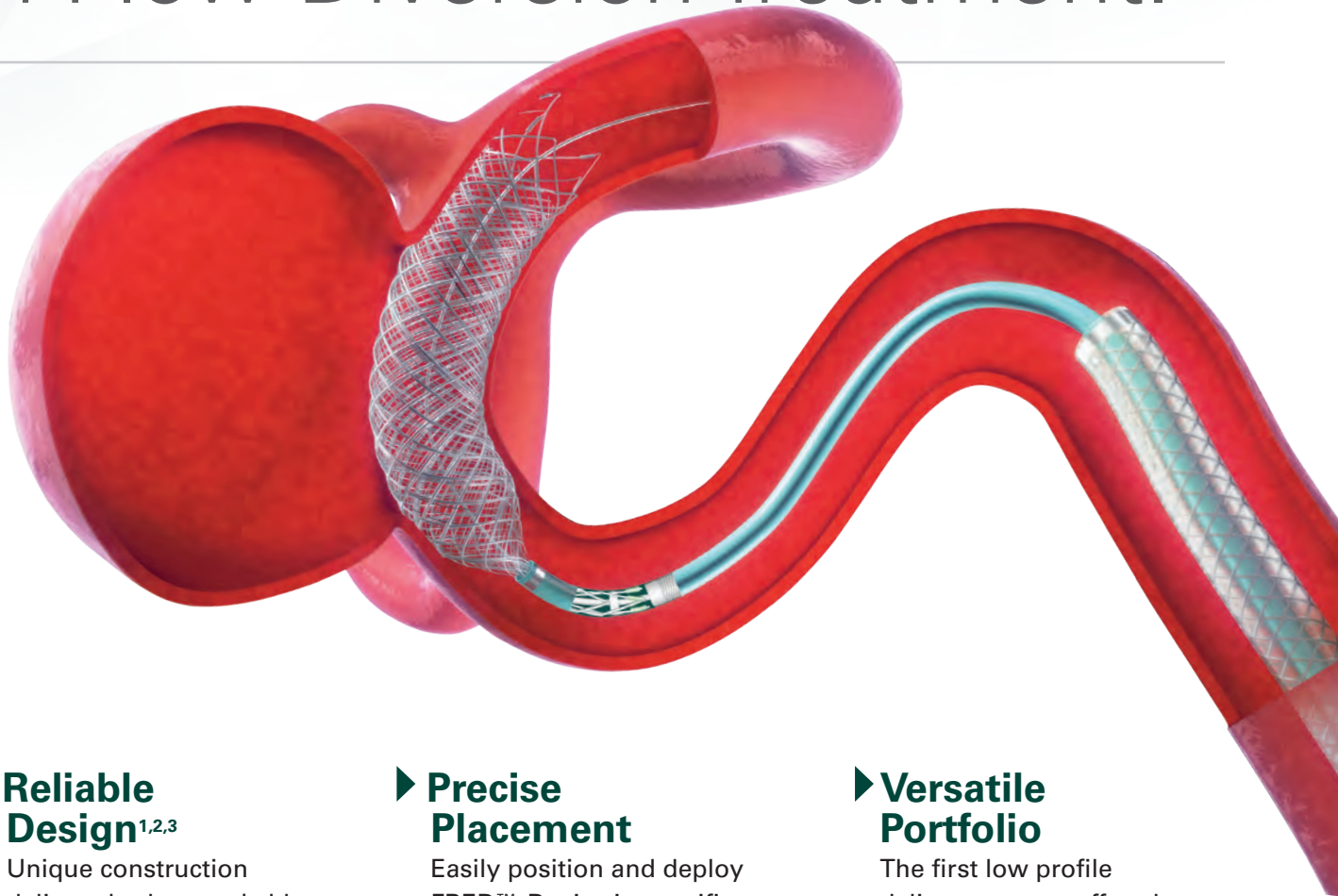
PH +1 44 (0) 191 258 6777

PH +33 (1) 39 21 77 46

PH +49 211 210 798-0

microvention.com

The New Standard of **Ease and Simplicity** in Flow Diversion Treatment.



► **Reliable Design**^{1,2,3}

Unique construction delivers both remarkable ease of use and excellent flow diversion^{1,2,3}

► **Precise Placement**

Easily position and deploy FRED™ Device in specific, targeted locations^{4,5,6}

► **Versatile Portfolio**

The first low profile delivery system offered in combination with large diameter and long length options

References:

1. TR11-211 2. TR13-171 3. TR15-055 4. TR13-192 5. TR15-072 6. TR19-145

The Flow Re-Direction Endoluminal Device (FRED™) System is indicated for use in the internal carotid artery from the petrous segment to the terminus for the endovascular treatment of adult patients (22 years of age or older) with wide-necked (neck width ≥ 4 mm or dome-to-neck ratio < 2) saccular or fusiform intracranial aneurysms arising from a parent vessel with a diameter ≥ 2.0 mm and ≤ 5.0 mm.

Use of the FRED™ System is contraindicated under these circumstances: Patients in whom anticoagulant, anti-platelet therapy, or thrombolytic drugs are contraindicated. Patients with known hypersensitivity to metal such as nickel-titanium and metal jewelry. Patients with anatomy that does not permit passage or deployment of the FRED™ System. Patients with an active bacterial infection. Patients with a pre-existing stent in place at the target aneurysm. Patients in whom the parent vessel size does not fall within the indicated range. Patients who have not received dual anti-platelet agents prior to the procedure. For complete indications, contraindications, potential complications, warnings, precautions, and instructions, see instructions for use (IFU provided in the device).

RX Only: Federal (United States) law restricts this device to sale by or on the order of a physician.

MICROVENTION™ and FRED™ are registered trademarks of MicroVention, Inc. in the United States and other jurisdictions. © 2020 MicroVention, Inc. 04/2020.

EDITOR-IN-CHIEF

Jeffrey S. Ross, MD

Professor of Radiology, Department of Radiology,
Mayo Clinic College of Medicine, Phoenix, AZ

SENIOR EDITORS

Harry J. Cloft, MD, PhD

Professor of Radiology and Neurosurgery,
Department of Radiology, Mayo Clinic College of
Medicine, Rochester, MN

Christopher G. Filippi, MD

Professor and Vice Chair of Biomedical and
Translational Science,
Donald and Barbara Zucker School of Medicine at
Hofstra/Northwell,
Lenox Hill Hospital and Greenwich Village
Healthplex, New York, NY

Thierry A.G.M. Huisman, MD

Radiologist-in-Chief, Texas Children's Hospital,
Houston, TX

Yvonne W. Lui, MD

Associate Professor of Radiology,
Chief of Neuroradiology,
New York University School of Medicine,
New York, NY

C.D. Phillips, MD, FACR

Professor of Radiology, Weill Cornell Medical
College, Director of Head and Neck Imaging,
New York-Presbyterian Hospital, New York, NY

Lubdha M. Shah, MD, MS

Professor of Radiology and Director of Spine
Imaging, University of Utah Department of
Radiology and Imaging Sciences, Salt Lake City, UT

Charles M. Strother, MD

Professor of Radiology, Emeritus, University of
Wisconsin, Madison, WI

STATISTICAL SENIOR EDITOR

Bryan A. Comstock, MS

Senior Biostatistician,
Department of Biostatistics,
University of Washington, Seattle, WA

ARTIFICIAL INTELLIGENCE DEPUTY EDITOR

Peter D. Chang, MD

Assistant Professor-in-Residence,
Departments of Radiological Sciences,
Computer Sciences, and Pathology,
Director, Center for Artificial Intelligence in
Diagnostic Medicine (CAIDM),
University of California, Irvine, Irvine, CA

EDITORIAL BOARD

Ashley H. Aiken, Atlanta, GA

Lea M. Alhilali, Phoenix, AZ

Kubilay Aydin, Istanbul, Turkey

John D. Barr, Dallas, TX

Ari Blitz, Baltimore, MD

Barton F. Branstetter IV, Pittsburgh, PA

Jonathan L. Brisman, Lake Success, NY

Keith Cauley, Danville, PA

James Y. Chen, San Diego, CA

Asim F. Choudhri, Memphis, TN

Daniel Chow, Irvine, CA

J. Matthew Debnam, Houston, TX

Seena Dehkharghani, New York, NY

Yonghong Ding, Rochester, MN

Clifford J. Eskey, Hanover, NH

Saeed Fakhra, Phoenix, AZ

Massimo Filippi, Milan, Italy

Nils D. Forkert, Calgary, Alberta, Canada

Wende N. Gibbs, Phoenix, AZ

Christine M. Glastonbury, San Francisco, CA

John L. Go, Los Angeles, CA

Philipp Göltz, Erlangen, Germany

Allison Grayev, Madison, WI

Brent Griffith, Detroit, MI

Ajay Gupta, New York, NY

Rakesh Kumar Gupta, Haryana, India

Lothi Hacein-Bey, Sacramento, CA

Christopher P. Hess, San Francisco, CA

Andrei Holodny, New York, NY

Benjamin Huang, Chapel Hill, NC

Mahesh V. Jayaraman, Providence, RI

Valerie Jewells, Chapel Hill, NC

Christof Karmonik, Houston, TX

Timothy J. Kaufmann, Rochester, MN

Hillary R. Kelly, Boston, MA

Toshiumi Kinoshita, Akita, Japan

Kenneth F. Layton, Dallas, TX

Alexander Lerner, Los Angeles, CA

Michael Lev, Boston, MA

Karl-Olof Lovblad, Geneva, Switzerland

Franklin A. Marden, Chicago, IL

Joseph C. McGowan, Merion Station, PA

Stephan Meckel, Freiburg, Germany

Christopher J. Moran, St. Louis, MO

Takahisa Mori, Kamakura City, Japan

Suresh Mukherji, Ann Arbor, MI

Alexander J. Nemeth, Chicago, IL

Renato Hoffmann Nunes, Sao Paulo, Brazil

Sasan Partovi, Cleveland, OH

Laurent Pierot, Reims, France

Jay J. Pillai, Baltimore, MD

Whitney B. Pope, Los Angeles, CA

Joana Ramalho, Lisbon, Portugal

Otto Rapalino, Boston, MA

Álex Rovira-Cañellas, Barcelona, Spain

Paul M. Ruggieri, Cleveland, OH

Amit M. Saundane, Atlanta, GA

Maksim Shapiro, New York, NY

Timothy Shepherd, New York, NY

Mark S. Shiroishi, Los Angeles, CA

Bruno P. Soares, Baltimore, MD

Maria Vittoria Spampinato, Charleston, SC

Khin Khin Tha, Sapporo, Hokkaido, Japan

Krishnamoorthy Thamburaj, Hershey, PA

Cheng Hong Toh, Taipei, Taiwan

Aquila S. Turk, Greenville, SC

Anja G. van der Kolk, Utrecht, the Netherlands

Willem Jan van Rooij, Tilburg, Netherlands

Arastoo Vossough, Philadelphia, PA

Elysa Widjaja, Toronto, Ontario, Canada

Max Wintermark, Stanford, CA

Ronald L. Wolf, Philadelphia, PA

Kei Yamada, Kyoto, Japan

Carlos Zamora, Chapel Hill, NC

Vahe M. Zohrabian, New Haven, CT

EDITORIAL FELLOW

Hediyeh Baradaran, Salt Lake City, UT

SPECIAL CONSULTANTS TO THE EDITOR

AJNR Blog Editor

Neil Lall, Denver, CO

Case of the Month Editor

Nicholas Stence, Aurora, CO

Case of the Week Editors

Juan Pablo Cruz, Santiago, Chile

Matylda Machnowska, Toronto, Ontario, Canada

Sapna Rawal, Toronto, Ontario, Canada

Classic Case Editor

Sandy Cheng-Yu Chen, Taipei, Taiwan

Health Care and Socioeconomics Editor

Pina C. Sanelli, New York, NY

Physics Editor

Greg Zaharchuk, Stanford, CA

Podcast Editor

Wende N. Gibbs, Phoenix, AZ

Twitter Editor

Roger Jordan, Houston, TX

Official Journal:

American Society of Neuroradiology

American Society of Functional Neuroradiology

American Society of Head and Neck Radiology

American Society of Pediatric Neuroradiology

American Society of Spine Radiology

Founding Editor

Juan M. Taveras

Editors Emeriti

Mauricio Castillo, Robert I. Grossman,

Michael S. Huckman, Robert M. Quencer

Managing Editor

Karen Halm

Assistant Managing Editor

Laura Wilhelm

Editorial Assistant

Margaret B. Sabato

Executive Director, ASNR

Mary Beth Hepp

AJNR

AMERICAN JOURNAL OF NEURORADIOLOGY

MAY 2020
VOLUME 41
NUMBER 5
WWW.AJNR.ORG

Publication Preview at www.ajnr.org features articles released in advance of print. Visit www.ajnrblog.org to comment on AJNR content and chat with colleagues and AJNR's News Digest at <http://ajnrdigest.org> to read the stories behind the latest research in neuroimaging.

737 **PERSPECTIVES** *A. Gordhan*

REVIEW ARTICLES

 738 **Tyrosine Kinase Inhibitor Therapy for Brain Metastases in Non-Small-Cell Lung Cancer: A Primer for Radiologists** *C. Dodson, et al.* **ADULT BRAIN**

   751 **Advanced Multicompartment Diffusion MRI Models and Their Application in Multiple Sclerosis** *D.A. Lakhani, et al.* **ADULT BRAIN**

LEVEL 1 EBM EXPEDITED PUBLICATION

    758 **Methylphenidate Effects on Cortical Thickness in Children and Adults with Attention-Deficit/Hyperactivity Disorder: A Randomized Clinical Trial** *K.B. Walhovd, et al.* **PEDIATRICS**
ADULT BRAIN

RESEARCH PERSPECTIVES

 766 **Scientific Collaboration across Time and Space: Bibliometric Analysis of the *American Journal of Neuroradiology*, 1980–2018** *V.M. Zohrabian, et al.*

PRACTICE PERSPECTIVES

772 **Medicare for All: Considerations for Neuroradiologists** *T.H. Nguyen, et al.*

GENERAL CONTENTS

   777 **Direct In Vivo MRI Discrimination of Brain Stem Nuclei and Pathways** *T.M. Shepherd, et al.* **ADULT BRAIN**

  785 **Acetazolamide-Loaded Dynamic 7T MR Quantitative Susceptibility Mapping in Major Cerebral Artery Steno-Occlusive Disease: Comparison with PET** *K. Fujimoto, et al.* **ADULT BRAIN**
FUNCTIONAL

  792 **Spatial Resolution and the Magnitude of Infarct Volume Measurement Error in DWI in Acute Ischemic Stroke** *J.M. Ospel, et al.* **ADULT BRAIN**

  798 **Structural Connectivity and Cortical Thickness Alterations in Transient Global Amnesia** *J. Hodel, et al.* **ADULT BRAIN**
FUNCTIONAL

   804 **The Impact of Intracortical Lesions on Volumes of Subcortical Structures in Multiple Sclerosis** *I. Kalinin, et al.* **ADULT BRAIN**

 809 **Aging and the Brain: A Quantitative Study of Clinical CT Images** *K.A. Cauley, et al.* **ADULT BRAIN**

AJNR (Am J Neuroradiol ISSN 0195–6108) is a journal published monthly, owned and published by the American Society of Neuroradiology (ASNR), 800 Enterprise Drive, Suite 205, Oak Brook, IL 60523. Annual dues for the ASNR include approximately 21% for a journal subscription. The journal is printed by Cadmus Journal Services, 5457 Twin Knolls Road, Suite 200, Columbia, MD 21045; Periodicals postage paid at Oak Brook, IL and additional mailing offices. Printed in the U.S.A. POSTMASTER: Please send address changes to American Journal of Neuroradiology, P.O. Box 3000, Denville, NJ 07834, U.S.A. Subscription rates: nonmember \$410 (\$480 foreign) print and online, \$320 online only; institutions \$470 (\$540 foreign) print and basic online, \$935 (\$1000 foreign) print and extended online, \$380 online only (basic), \$825 online only (extended); single copies are \$35 each (\$40 foreign). Indexed by PubMed/MEDLINE, BIOSIS Previews, Current Contents (Clinical Medicine and Life Sciences), EMBASE, Google Scholar, HighWire Press, Q-Sensei, RefSeek, Science Citation Index, SCI Expanded, Meta/CZI, ReadCube, and Semantic Scholar. Copyright © American Society of Neuroradiology.

	815	Prognostic Value of Preoperative MRI Metrics for Diffuse Lower-Grade Glioma Molecular Subtypes <i>P. Darvishi, et al.</i>	ADULT BRAIN
	822	A Critical Assessment of the Golden Hour and the Impact of Procedural Timing in Stroke Thrombectomy <i>A.P. Wessell, et al.</i>	INTERVENTIONAL
	828	Predictors of Cerebral Aneurysm Rupture after Coil Embolization: Single-Center Experience with Recanalized Aneurysms <i>Y. Funakoshi, et al.</i>	INTERVENTIONAL
	836	Signal of Carotid Intraplaque Hemorrhage on MR T1-Weighted Imaging: Association with Acute Cerebral Infarct <i>D. Yang, et al.</i>	EXTRACRANIAL VASCULAR
	844	Distinguishing Recurrent Thyroid Cancer from Residual Nonmalignant Thyroid Tissue Using Multiphasic Multidetector CT <i>J.M. Debnam, et al.</i>	HEAD & NECK
	852	MRI Signal Intensity and Electron Ultrastructure Classification Predict the Long-Term Outcome of Skull Base Chordomas <i>J. Bai, et al.</i>	HEAD & NECK
	859	Inter- and Intrareader Agreement of NI-RADS in the Interpretation of Surveillance Contrast-Enhanced CT after Treatment of Oral Cavity and Oropharyngeal Squamous Cell Carcinoma <i>F.H.J. Elsholtz, et al.</i>	HEAD & NECK
	866	Tumor Response Assessment in Diffuse Intrinsic Pontine Glioma: Comparison of Semiautomated Volumetric, Semiautomated Linear, and Manual Linear Tumor Measurement Strategies <i>L.A. Gilligan, et al.</i>	PEDIATRICS FUNCTIONAL
	874	MR Imaging Correlates for Molecular and Mutational Analyses in Children with Diffuse Intrinsic Pontine Glioma <i>C. Jaimes, et al.</i>	PEDIATRICS FUNCTIONAL
	882	Synthetic MRI of Preterm Infants at Term-Equivalent Age: Evaluation of Diagnostic Image Quality and Automated Brain Volume Segmentation <i>T. Vanderhasselt, et al.</i>	PEDIATRICS FUNCTIONAL
	889	Disrupted Functional and Structural Connectivity in Angelman Syndrome <i>H.M. Yoon, et al.</i>	PEDIATRICS FUNCTIONAL
	898	Balanced Steady-State Free Precession Techniques Improve Detection of Residual Germ Cell Tumor for Treatment Planning <i>W.A. Mehan Jr, et al.</i>	PEDIATRICS
	904	Neuroimaging Findings in Children with Constitutional Mismatch Repair Deficiency Syndrome <i>A. Kerpel, et al.</i>	PEDIATRICS
	911	Utility of Pre-Hematopoietic Cell Transplantation Sinus CT Screening in Children and Adolescents <i>J.H. Harreld, et al.</i>	PEDIATRICS
	917	The Periolandic Sign: A Unique Imaging Finding Observed in Association with Polymerase γ -Related Disorders <i>F.G. Gonçalves, et al.</i>	PEDIATRICS
	923	Cerebellar Watershed Injury in Children <i>J.N. Wright, et al.</i>	PEDIATRICS
	929	Sensitivity of the Inhomogeneous Magnetization Transfer Imaging Technique to Spinal Cord Damage in Multiple Sclerosis <i>H. Rasoanandrianina, et al.</i>	SPINE FUNCTIONAL
	938	MR Myelography for the Detection of CSF-Venous Fistulas <i>J.L. Chazen, et al.</i>	SPINE
	941	35 YEARS AGO IN AJNR	

ONLINE FEATURES

LETTERS

- E26 **Identification of Vortex Cores in Cerebral Aneurysms on 4D Flow MRI** *S. Meckel, et al.*
- E27 **Reply** *K. Futami, et al.*
- E28 **ASPECTS Distorts Infarct Volume Measurement** *R.A. Suss, et al.*
- E29 **Reply** *K. Nael*
-  E30 **How Far Can We Take Vessel Wall MRI for Intracranial Atherosclerosis? The Tissue is Still the Issue** *M.D. Alexander, et al.*
- E32 **Reply** *M.H.T. Zwartbol, et al.*
- E33 **Time to Discontinue Use of the Term Stroke in Neuroradiology**
D.A.L. Ortega, et al.
- E34 **Reply** *M.A. Aftab*

BOOK REVIEWS

R.M. Quencer, Section Editor

Please visit www.ajnrblog.org to read and comment on Book Reviews.



Brain stem nuclei and pathways in a healthy control subject, 9 individual datasets co-registered and averaged, 2-hour 15-minute total scan time.



Indicates Editor's Choices selection



Indicates Fellows' Journal Club selection



Indicates open access to non-subscribers at www.ajnr.org



Indicates article with supplemental on-line table



Indicates article with supplemental on-line photo



Indicates article with supplemental on-line video



Evidence-Based Medicine Level 1



Evidence-Based Medicine Level 2

AJNR *go green*

***AJNR* urges American Society of Neuroradiology members to reduce their environmental footprint by voluntarily suspending their print subscription.**

The savings in paper, printing, transportation, and postage directly fund new electronic enhancements and expanded content.

The digital edition of *AJNR* presents the print version in its entirety, along with extra features including:

- Publication Preview
- Case Collection
- Podcasts
- The *AJNR* News Digest
- The *AJNR* Blog

It also reaches subscribers much faster than print. An electronic table of contents will be sent directly to your mailbox to notify you as soon as it publishes.

Readers can search, reference, and bookmark current and archived content 24 hours a day on www.ajnr.org.

ASNR members who wish to opt out of print can do so by using the *AJNR* Go Green link on the *AJNR* Website (<http://www.ajnr.org/content/subscriber-help-and-services>). Just type your name in the email form to stop print and spare our ecosystem.

IMPORTANT SAFETY INFORMATION¹

WARNING: NEPHROGENIC SYSTEMIC FIBROSIS (NSF)

Gadolinium-based contrast agents (GBCAs) increase the risk for NSF among patients with impaired elimination of the drugs. Avoid use of GBCAs in these patients unless the diagnostic information is essential and not available with non-contrast MRI or other modalities. NSF may result in fatal or debilitating fibrosis affecting the skin, muscle and internal organs.

- The risk for NSF appears highest among patients with:
 - Chronic, severe kidney disease (GFR < 30 mL/min/1.73m²), or
 - Acute kidney injury.
- Screen patients for acute kidney injury and other conditions that may reduce renal function. For patients at risk for chronically reduced renal function (e.g. age > 60 years, hypertension, diabetes), estimate the glomerular filtration rate (GFR) through laboratory testing.
- For patients at highest risk for NSF, do not exceed the recommended DOTAREM dose and allow a sufficient period of time for elimination of the drug from the body prior to any re-administration.

INDICATIONS AND USAGE

DOTAREM[®] (gadoterate meglumine) injection is a prescription gadolinium-based contrast agent indicated for intravenous use with magnetic resonance imaging (MRI) in brain (intracranial), spine and associated tissues in adult and pediatric patients (including term neonates) to detect and visualize areas with disruption of the blood brain barrier (BBB) and/or abnormal vascularity.

CONTRAINDICATIONS

History of clinically important hypersensitivity reactions to DOTAREM.

WARNINGS AND PRECAUTIONS

- Hypersensitivity Reactions: Anaphylactic and anaphylactoid reactions have been reported with DOTAREM, involving cardiovascular, respiratory, and/or cutaneous manifestations. Some patients experienced circulatory collapse and died. In most cases, initial symptoms occurred within minutes of DOTAREM administration and resolved with prompt emergency treatment.
- Before DOTAREM administration, assess all patients for any history of a reaction to contrast media, bronchial asthma and/or allergic disorders. These patients may have an increased risk for a hypersensitivity reaction to DOTAREM.
- Administer DOTAREM only in situations where trained personnel and therapies are promptly available for the treatment of hypersensitivity reactions, including personnel trained in resuscitation.
- Gadolinium Retention: Gadolinium is retained for months or years in several organs. The highest concentrations have been identified in the bone, followed by brain, skin, kidney, liver and spleen. The duration of retention also varies by tissue, and is longest in bone. Linear GBCAs cause more retention than macrocyclic GBCAs.
- Consequences of gadolinium retention in the brain have not been established. Adverse events involving multiple organ systems have been reported in patients with normal renal function without an established causal link to gadolinium retention.
- Acute Kidney Injury: In patients with chronically reduced renal function, acute kidney injury requiring dialysis has occurred with the use of GBCAs. The risk of acute kidney injury may increase with increasing dose of the contrast agent; administer the lowest dose necessary for adequate imaging.
- Extravasation and Injection Site Reactions: Ensure catheter and venous patency before the injection of DOTAREM. Extravasation into tissues during DOTAREM administration may result in tissue irritation.

ADVERSE REACTIONS

- The most common adverse reactions associated with DOTAREM in clinical trials were nausea, headache, injection site pain, injection site coldness and rash.
- Serious adverse reactions in the Postmarketing experience have been reported with DOTAREM. These serious adverse reactions include but are not limited to: arrhythmia, cardiac arrest, respiratory arrest, pharyngeal edema, laryngospasm, bronchospasm, coma and convulsion.

USE IN SPECIFIC POPULATIONS

- **Pregnancy:** GBCAs cross the human placenta and result in fetal exposure and gadolinium retention. Use only if imaging is essential during pregnancy and cannot be delayed.
- **Lactation:** There are no data on the presence of gadoterate in human milk, the effects on the breastfed infant, or the effects on milk production. However, published lactation data on other GBCAs indicate that 0.01 to 0.04% of the maternal gadolinium dose is present in breast milk.
- **Pediatric Use:** The safety and efficacy of DOTAREM at a single dose of 0.1 mmol/kg has been established in pediatric patients from birth (term neonates \geq 37 weeks gestational age) to 17 years of age based on clinical data. The safety of DOTAREM has not been established in preterm neonates. No cases of NSF associated with DOTAREM or any other GBCA have been identified in pediatric patients age 6 years and younger.

You are encouraged to report negative side effects of prescription drugs to the FDA. Visit www.fda.gov/medwatch or call 1-800-FDA-1088.

Please see the full Prescribing Information, including the patient Medication Guide, for additional important safety information.

References: 1. Dotarem [package insert]. Princeton, NJ: Guerbet LLC; Oct 2019. 2. Maravilla K et al. Comparison of Gadoterate Meglumine and Gadobutrol in the Diagnosis of Primary Brain Tumors: A Double-Blind Randomized Controlled Intraindividual Crossover Study (the REMIND Study). 2017 June 29. doi: 10:3174/ajnr.A5316. [Epub ahead of print]. 3. de Kerviler E et al. Adverse reactions to gadoterate meglumine: review of over 25 years of clinical use and more than 50 million doses. Invest Radiol 2016;51:544–51 CrossRef Medline. 4. Endrikat J et al. Safety of gadobutrol: results from 42 clinical phase II to IV studies and postmarketing surveillance after 29 million applications. Invest Radiol 2016;51: 537–43 CrossRef Medline. 5. Port M et al. Efficiency, thermodynamic and kinetic stability of marketed gadolinium chelates and their possible clinical consequences: a critical review. Biometals. 2008;21:469-90. 6. Frenzel T et al. Stability of gadolinium-based magnetic resonance imaging contrast agents in human serum at 37°C. Invest Radiol. 2008;43:817-828.

DOTAREM[®] is a registered trademark of Guerbet LLC, and is available by prescription only.

Gadavisit[®] is a registered trademark of the Bayer group of companies, and is available by prescription only.

DOTAREM[®] (gadoterate meglumine) Injection

MR

Comparison of Dotarem[®] to Gadavist[®] for Overall Visualization and Characterization in the MRI Diagnosis of Primary Brain Tumors



Despite the difference in relaxivity between these 2 GBCAs



There Is No Measurable Difference in Clinical Benefit Observed Between Dotarem[®] and Gadavist^{®2}



as demonstrated by the **REMIND Study**, a multicenter, double-blind, randomized, controlled intraindividual crossover study.²

This study “demonstrates the non-inferiority of gadoterate meglumine [Dotarem[®]] versus gadobutrol [Gadavist[®]] for overall visualization and characterization of primary brain tumors”.² Additionally, there was no preference of the readers for either contrast agent, in most cases, regarding border delineation, internal morphology, and the qualitative degree of contrast enhancement, despite quantitative mean lesion percentage enhancement being higher with gadobutrol.²

- For all readers in the REMIND Study, more than 90% of patients presented with good or excellent overall lesion visualization and characterization with either Dotarem[®] or Gadavist[®].²
- The REMIND Study also demonstrated a low incidence of immediate reported AEs with Dotarem[®] and with Gadavist[®], as shown in multiple previous studies.^{2,3,4}
- Dotarem[®] is the first imaging contrast with a macrocyclic and ionic structure for high thermodynamic and kinetic stability.^{5,6}
- Dotarem[®] is not only trusted for high molecular stability^{5,6}; the REMIND Study demonstrates that it is as effective as Gadavist[®] for MRI diagnosis of primary brain tumors.²

Please see Important Safety information on opposite page. For more information on Dotarem[®], please see Full Prescribing Information including Boxed Warning and Medication Guide.

Guerbet | 

COMMITTED

Learn more at
RemindStudy.com



Introducing
Eclipse 2L
DUAL LUMEN BALLOON CATHETER



Balt's Access Portfolio Delivers Unique Solutions



Visit www.balt-usa.com to learn more



Title: Victory of the Healing Hand in the Fight Against Covid 19, oil painting.
Ajeet Gordhan, MD, Neurointerventional Radiologist, Bloomington, Illinois

To keep fighting against a seemingly invincible enemy at a reminiscent time the world faced a common threat, Winston Churchill said,

"You ask, what is our aim? I can answer in one word. It is victory. Victory at all costs — Victory in spite of all terrors — Victory, however long and hard the road may be, for without victory there is no survival.

Against this pandemic, Covid 19, Victory is our aim.

Tyrosine Kinase Inhibitor Therapy for Brain Metastases in Non-Small-Cell Lung Cancer: A Primer for Radiologists

C. Dodson, T.J. Richards, D.A. Smith, and N.H. Ramaiya



ABSTRACT

SUMMARY: Treatment options for patients who develop brain metastases secondary to non-small-cell lung cancer have rapidly expanded in recent years. As a key adjunct to surgical and radiation therapy options, systemic therapies are now a critical component of the oncologic management of metastatic CNS disease in many patients with non-small-cell lung cancer. The aim of this review article was to provide a guide for radiologists, outlining the role of systemic therapies in metastatic non-small-cell lung cancer, with a focus on tyrosine kinase inhibitors. The critical role of the blood-brain barrier in the development of systemic therapies will be described. The final sections of this review will provide an overview of current imaging-based guidelines for therapy response. The utility of the Response Assessment in Neuro-Oncology criteria will be discussed, with a focus on how to use the response criteria in the assessment of patients treated with systemic and traditional therapies.

ABBREVIATIONS: ALK = anaplastic lymphoma kinase; CTLA-4 = cytotoxic T-lymphocyte-associated protein 4; EGFR = epidermal growth factor receptor; EML4 = echinoderm microtubule-associated protein-like 4; ICI = immune checkpoint inhibitor; NSCLC = non-small-cell lung cancer; PD-1 = programmed cell death protein 1; PFS = progression-free survival; PRES = posterior reversible encephalopathy syndrome; QALY = quality-adjusted life years; RANO = Response Assessment in Neuro-Oncology; RECIST = Response Evaluation Criteria in Solid Tumors; ROS1 = C-ras oncogene 1; SRS = stereotactic radiosurgery; TKI = tyrosine kinase inhibitor; WBRT = whole-brain radiation therapy

In recent years, several systemic therapies have been developed that demonstrate efficacy in non-small-cell lung cancer (NSCLC) metastatic to the brain. It is essential for radiologists to be informed about these novel therapeutic agents to evaluate the intracranial response to therapy on imaging in patients undergoing treatment with these drugs. As the systemic chemotherapeutic options for metastatic NSCLC evolve, the assessment of the response of brain metastases on imaging is becoming ever more critical for evaluating and managing patients with metastatic NSCLC.

Brain metastasis is a serious occurrence in patients with cancer and is observed at the highest frequency in NSCLC among all cancer types, with approximately 50% of patients with NSCLC being affected by brain metastases.¹ Historically, the prognosis for patients with NSCLC diagnosed with brain metastases has been dismal. Before the advent of FDA-approved targeted therapies, the 5-year survival rate was 2.3% for patients with NSCLC following a

diagnosis of brain metastases.² Cytotoxic chemotherapeutics are largely ineffective intracranially due to their inability to cross the BBB. Therefore, the standard treatment for CNS metastasis has traditionally been local interventions such as an operation, stereotactic radiosurgery (SRS), and whole-brain radiation therapy (WBRT).³

However, the recent discovery of targetable driver mutations such as those involving the *epidermal growth factor receptor* (EGFR), *anaplastic lymphoma kinase* (ALK), and *C-ras oncogene 1* (ROS1) genes in NSCLC has led to the creation of small-molecule tyrosine kinase inhibitors (TKIs) that target these driver mutations. These TKIs can also traverse the blood-brain barrier to access the brain parenchyma, which has led to increased survival rates for patients with NSCLC with brain metastases. Before the development of TKIs, studies reported the mean overall survival of patients with NSCLC brain metastases as 5 months with motexafin gadolinium chemotherapy plus WBRT and 8 months with cisplatin and etoposide chemotherapy.^{4,5} The concept of using tyrosine kinase inhibitors to target driver mutations has also been investigated in brain metastases from cancer types other than NSCLC. For instance, the EGFR inhibitor lapatinib has shown efficacy in combination with capecitabine in patients with brain metastases originating from HER-2-positive breast cancer.⁶ TKI therapy has also been shown to reduce the incidence of brain metastases in patients with metastatic renal cell cancer.⁷

Received November 10, 2019; accepted after revision January 6, 2020.

From the Department of Radiology (C.D., T.J.R., D.A.S., N.H.R.), University Hospitals Cleveland Medical Center, Case Western Reserve University, Cleveland, Ohio; and Department of Radiology and Imaging Sciences (T.J.R.), University of Utah Hospital, Salt Lake City, Utah.

Please address correspondence to Daniel A. Smith, MD, University Hospitals Cleveland Medical Center, Case Western Reserve University, Department of Radiology, 11100 Euclid Ave, Cleveland, OH 44106; e-mail: Daniel.Smith3@UHhospitals.org

Indicates open access to non-subscribers at www.ajnr.org

<http://dx.doi.org/10.3174/ajnr.A6477>

In the era of targeted therapy, selection of the most effective course of therapy relies on molecular genetic testing of a biopsy or cytology sample of malignant tissue. For preservation, tissue samples are typically processed in a formalin-fixed, paraffin-embedded block, while cytology samples are prepared in an artificial cell block or a smear.⁸ Joint guidelines from the College of American Pathologists, the International Association for the Study of Lung Cancer, and the Association for Molecular Pathology categorize *EGFR*, *ALK*, and *ROS1* as the 3 “must-test” genes for which testing must be offered at all laboratories conducting molecular testing on lung cancer.⁹ The guidelines also assert that *EGFR*, *ALK*, and *ROS1* testing should be performed on all patients with advanced-stage lung adenocarcinoma. Reverse transcription polymerase chain reaction or next-generation sequencing can be used to detect mutations in *EGFR*, *ALK*, and *ROS1* genes. *ALK* or *ROS1* rearrangements can also be detected by fluorescence in situ hybridization.

Despite the high cost of new targeted therapies, the molecular genetic testing and the TKI medications themselves have been shown to be a relatively cost-effective means of treatment. Narita et al¹⁰ found that *EGFR*-mutation testing and gefitinib therapy are more cost-effective than standard chemotherapy and no *EGFR* testing, with the *EGFR* testing/gefitinib strategy resulting in 0.036 quality-adjusted life years (QALY) per patient and an incremental cost-effectiveness ratio of US \$32,500 per QALY gained. Holleman et al¹¹ demonstrated that osimertinib is the most effective *EGFR*-TKI, with a mean of 2.01 QALY gained per patient at a cost of €128,343 (US \$143,485) per QALY gained. Djalalov et al¹² found that genetic testing for the *EML4* (*echinoderm microtubule-associated protein-like 4*)-*ALK* fusion gene followed by the first-generation *ALK*-inhibitor crizotinib therapy resulted in a gain of 0.011 QALY, with an incremental cost-effectiveness ratio of CaD \$255,970 (US \$220,641) per QALY gained compared with standard chemotherapy. Compared with the first-generation *ALK*-inhibitor crizotinib, second-generation alectinib has resulted in a gain of 0.87 QALY, with an incremental cost-effectiveness ratio of US \$39,312 per QALY.¹³ Of note, most studies on the cost-effectiveness of TKIs have been conducted in Canada, Europe, and Asia, indicating the need for additional studies that examine the cost-effectiveness of these drugs within the American health care system.

While a body of research on the development of targeted therapies for NSCLC brain metastases is rapidly accruing in the field of clinical oncology, much less has been written in the radiology literature. This article, therefore, aims to provide radiologists with a foundational overview of the TKIs that cross the BBB in NSCLC brain metastases and to provide a useful guide for radiologically assessing the effects of these novel drugs in the treatment of NSCLC brain metastases.

Pathophysiology of the Blood-Brain Barrier in Brain Metastasis

To appreciate the imaging features relevant to systemic treatment of brain metastases, an understanding of the pathophysiology of the BBB is critical. The BBB is a selectively permeable,

nonfenestrated layer of endothelial cells that enclose the cerebral capillaries. This endothelial cell layer is surrounded by a supportive layer of extracellular matrix, pericytes, and astrocytes.¹⁴ Tight junctions connect the endothelial cells and allow the BBB to regulate the passage of molecules between cerebral capillaries and the brain parenchyma on the basis of the size and charge of these molecules.¹⁵ The intercellular tight junctions connecting the epithelial cells of the barrier are impermeable to many hydrophilic systemic chemotherapeutic agents, which explains the low intracranial efficacy of these agents.^{16,17} Efflux pumps unique to the BBB inhibit the entry of certain compounds into the BBB endothelial cells and also transport compounds out of the endothelial cells to return them to blood vessels, thereby preventing these compounds from reaching the brain parenchyma. Larger molecules are more likely than small molecules to be substrates of these efflux transporters. The small size of TKIs relative to cytotoxic chemotherapeutics may therefore provide a possible mechanism behind the greater BBB penetration with TKIs compared with cytotoxic chemotherapeutic agents.¹⁸ Additionally, the good cellular permeability of TKIs may also explain this efficacy of TKIs in treating intracranial metastases relative to traditional chemotherapeutics.

Metastasis begins when the metastatic tissue detaches from a primary tumor, enters the extracellular matrix, and migrates into a blood vessel.¹⁵ The circulating tumor cells migrate hematogenously to the site of metastasis, where they extravasate from the blood vessel into the parenchyma of the target organ. In the case of brain metastasis, this extravasation from cerebral capillaries into the brain parenchyma requires BBB penetration. Circulating tumor cells traverse the BBB by interacting with the barrier via mechanisms not yet fully elucidated, after which they establish a secondary tumor in the brain parenchyma.¹⁴ The expression of vascular endothelial growth factors by the metastatic cancer cells allows the metastatic tissue to establish a blood supply.¹⁹ This vascular endothelial growth factor secretion also initiates signaling cascades that cause the endothelium of the BBB to become hyperpermeable, thereby transforming the BBB into a blood-tumor barrier that has increased permeability to some chemotherapeutic agents.¹⁹

Metastatic proliferation is further enhanced by the immune-privileged nature of the brain due to the BBB, as well as the lack of access of many chemotherapeutic drugs to the brain parenchyma, both of which allow NSCLC metastases to establish secondary tumors and thrive in the brain parenchyma. The recent development of targeted therapies that penetrate the BBB affords patients with brain metastases an increased survival that has not previously been achievable with systemic chemotherapeutics (Fig 1).

EGFR-Tyrosine Kinase Inhibitors

EGFR is a transmembrane glycoprotein and a member of the ErbB receptor tyrosine kinase family. When EGFR is bound to the extracellular ligand, its intracellular domain activates several intracellular pathways implicated in cell proliferation, growth, and survival. Activating mutations in *EGFR* result in the constitutive activation of downstream signaling cascades that lead to uncontrolled cell proliferation in NSCLC.

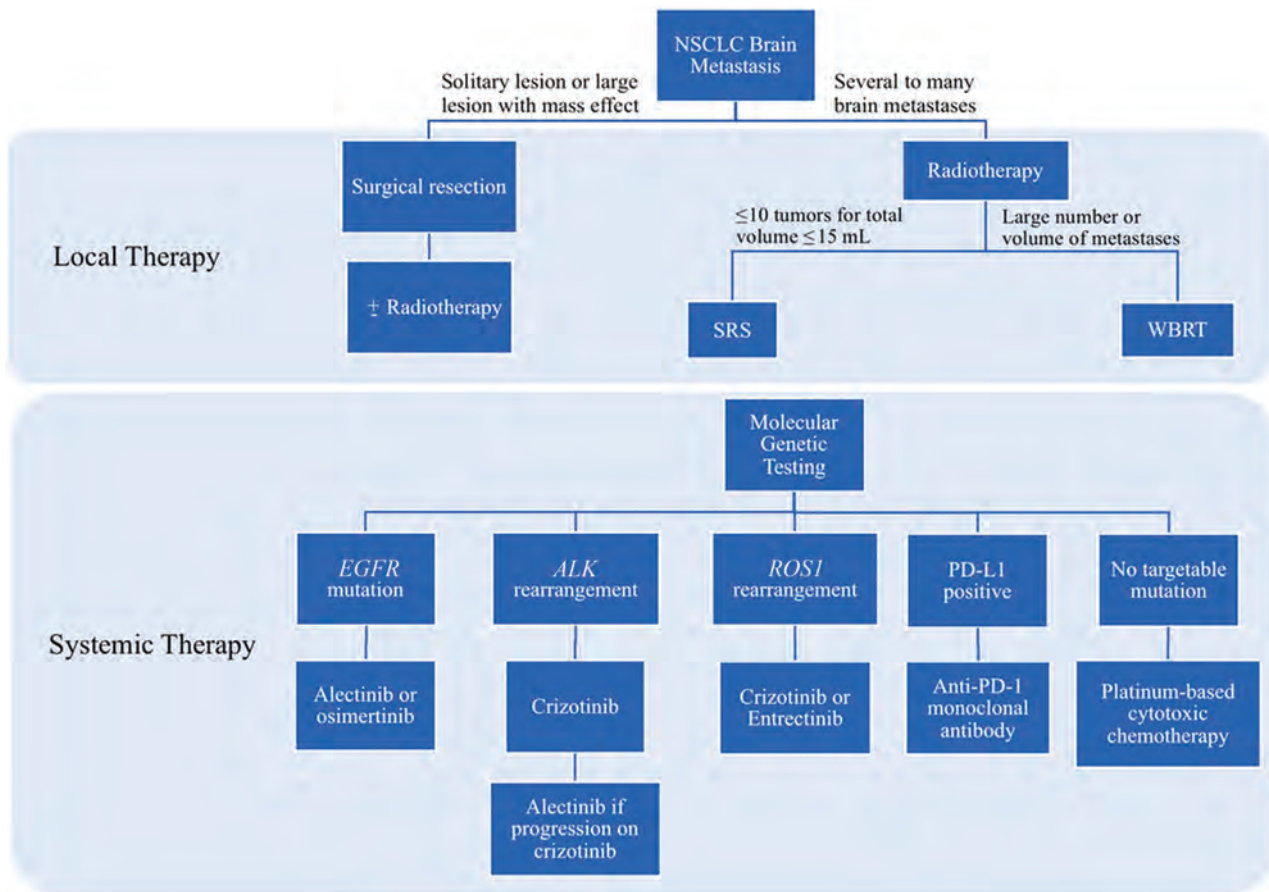


FIG 1. Decision tree for the selection of local and systemic therapies for the treatment of NSCLC brain metastases. PD-L1 indicates programmed death-ligand 1.

Tyrosine kinase inhibitors inhibit *EGFR* by competitively binding to the adenosine triphosphate binding site on the intracellular tyrosine kinase domain of the receptor. This prevents the tyrosine kinase domain from activating intracellular signaling cascades that would otherwise amplify cell proliferation and survival. A positive *EGFR*-mutation status has been associated with a higher incidence of brain metastases in patients with advanced nonsquamous NSCLC, so *EGFR* mutations are especially relevant to the treatment of patients with NSCLC brain metastasis.²⁰ The most common *EGFR* mutations observed in patients with NSCLC are in-frame LREA exon 19 deletions and exon 21 L858R point mutations.²¹

Three generations of TKIs have been developed to treat *EGFR*-mutant NSCLC. The first-generation *EGFR*-TKIs are erlotinib and gefitinib, both of which inhibit *EGFR* by binding reversibly to the kinase domain of the receptor.²² In a Phase II study investigating gefitinib and erlotinib as first-line treatments for patients diagnosed with *EGFR*-mutant NSCLC, a high response rate of 83% was observed in patients with brain metastases treated with either drug, with a median progression-free survival (PFS) of 6.6 months and an overall survival of 15.9 months.²³ Erlotinib has been observed to have a BBB permeation rate of 4.4% in patients following 4 weeks of treatment, with the level of response being proportional to the concentration of the drug in the CSF. In a Phase III study of gefitinib versus carboplatin-paclitaxel in patients with

advanced, *EGFR*-mutated NSCLC and no history of chemotherapy, the gefitinib group had a PFS of 10.8 months, compared with 5.4 months in the traditional chemotherapy group.²⁴ The gefitinib group also had a higher response rate of 73.7% compared with 30.7% in the carboplatin-paclitaxel group.

Despite the frequently promising initial response observed in first-generation TKIs, CNS tumor recurrence is common, and patients with *EGFR*-mutated NSCLC typically develop resistance to erlotinib and gefitinib after a median time of 8–10 months on therapy.²⁵ These issues led to the creation of second-generation *EGFR*-TKIs such as afatinib which, unlike its predecessors, binds irreversibly to the *EGFR*. In a compassionate use program involving patients with NSCLC brain metastases who had failed on platinum-based chemotherapy and had progressed on a first-generation TKI, afatinib produced an overall cerebral response rate of 35%, making afatinib a potentially viable option for patients with NSCLC with brain metastases who have progressed on other chemotherapeutic regimens.²⁶

The secondary T790M mutation in the adenosine triphosphate binding site of *EGFR* is the most common mutation conferring acquired resistance to both first- and second-generation TKIs.²⁷ This mutation is, therefore, partially responsible for the resistance to first- or second-generation *EGFR*-TKIs typically developing after 9–12 months of therapy.²⁸ Osimertinib is an approved third-generation *EGFR*-TKI that can overcome the

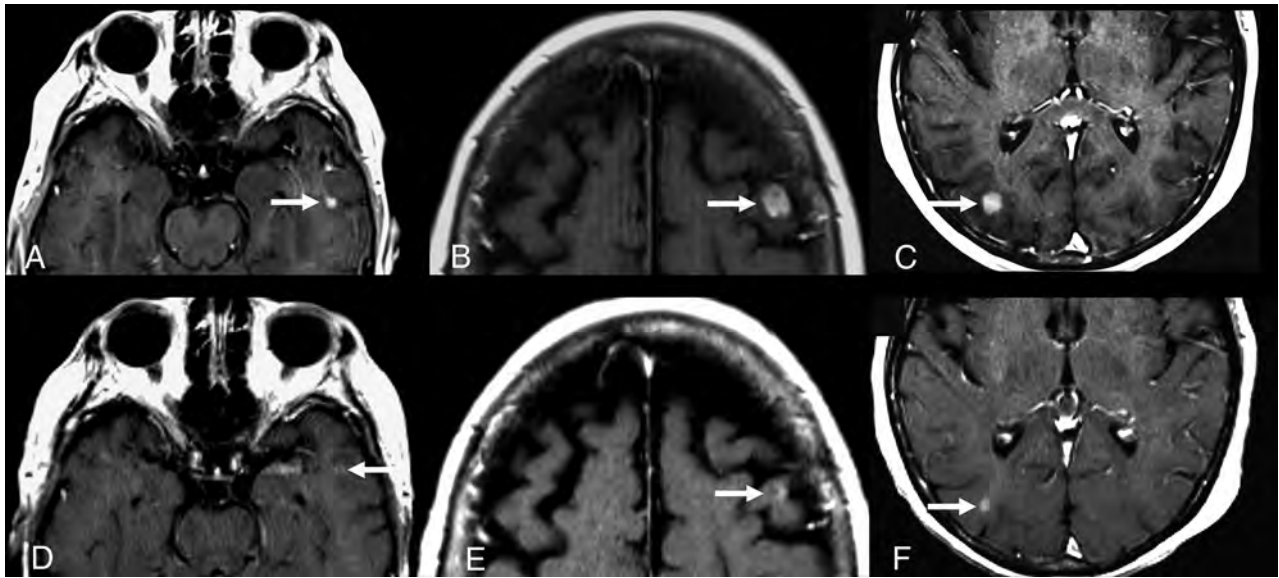


FIG 2. A 73-year-old woman with *EGFR*-mutated NSCLC, which was initially treated with erlotinib for 9 months with an initial partial response of the primary lung tumor. The patient's primary lung tumor then progressed, and the patient developed brain metastases. Repeat genetic analysis showed that the patient's tumor now had a T790M mutation, so she was started on osimertinib. Images captured before (A–C) and 6 weeks after starting treatment with osimertinib (D–F) demonstrate a partial response to therapy of the left temporal (A and D), left frontal (B and E), and right occipital (C and F) enhancing brain metastases (arrows).

T790M mutation in patients who have acquired resistance to first- or second-generation *EGFR* inhibitors (Fig 2). Osimertinib irreversibly binds to *EGFR* and targets both the initial activating *EGFR* mutation as well as the T790M mutation, while sparing wild-type *EGFR*.²⁹ Osimertinib and other experimental third-generation TKIs, unlike their first- and second-generation predecessors, are also mutant-selective in that they exert more potent *EGFR* inhibition on *EGFR*-mutant cells as opposed to *EGFR* wild type cells.³⁰ In the Phase III AZD9291 Versus Gefitinib or Erlotinib in Patients with Locally Advanced or Metastatic Non-small Cell Lung Cancer (FLAURA) study, patients with *EGFR*-mutant, advanced NSCLC were assigned to receive either osimertinib or standard *EGFR*-TKI treatment, which consisted of either erlotinib or gefitinib. A subanalysis of the patients in the FLAURA study with asymptomatic or stable CNS metastases found a 91% CNS objective response rate in the osimertinib arm compared with 68% for the standard *EGFR*-TKI arm.³¹ The median PFS was longer with osimertinib versus standard *EGFR*-TKI therapy (18.9 versus 10.2 months, respectively).³² Due to its superior BBB permeability and intracranial efficacy compared with older TKIs, osimertinib is projected to become the new first-line standard of care in the treatment of NSCLC brain metastases.³⁰

ALK-Tyrosine Kinase Inhibitors

Oncogenic rearrangements involving the *ALK* gene are the second most common mutation in NSCLC and account for approximately 3% of lung adenocarcinoma cases.²¹ The *ALK* gene codes for a transmembrane receptor tyrosine kinase that activates intracellular signaling cascades to promote cell proliferation. The oncogenic mutation of *ALK* consists of the fusion of 2 genes, most frequently *ALK* and *EML4*, to create a fusion of the *ALK* receptor with mutations in the extracellular domain

that allow it to be activated in the absence of ligand binding. Like *EGFR* inhibitors, *ALK*-TKIs inhibit the *ALK* receptor by binding to the intracellular tyrosine kinase domain to prevent downstream signal transduction. Up to 70% of patients with *ALK* rearrangement with NSCLC develop brain metastases, making *ALK* gene rearrangements a prime target for TKIs that can penetrate the blood-brain barrier.²¹

The first TKI developed to target *ALK*-rearranged NSCLC was crizotinib. In a retrospective analysis of the patients with *ALK*-rearranged asymptomatic brain metastases included in the PROFILE 1005 and 1007 clinical trials of crizotinib, crizotinib treatment yielded an intracranial disease control rate of 56% in previously untreated patients with asymptomatic brain metastasis and 62% in previously treated patients.³³ The median intracranial time-to-progression was 7 months for the previously untreated group and 13.2 months for the previously treated group. However, eventual progression of pre-existing intracranial lesions or the development of new intracranial lesions during crizotinib therapy was common; this finding aligns with the observation that resistance is typically acquired within 12–14 months of the initiation of crizotinib therapy.³⁴

Alectinib is a second-generation *ALK*-rearranged TKI that is highly selective for *ALK* and also blocks the L1196M mutation that confers resistance to crizotinib, therefore providing a treatment option to patients whose intracranial disease has progressed on crizotinib (Fig 3).²¹ In an analysis of the 122 patients with NSCLC brain metastasis included in the Phase III ALEX study, alectinib had a higher overall CNS response rate than crizotinib (85.7% versus 71.4%, respectively) and significantly delayed CNS progression compared with crizotinib in patients with advanced *ALK*-rearranged NSCLC.³⁵ Another Phase III trial, while showing the superiority of alectinib over crizotinib in terms of increased PFS and a lower incidence of CNS progression, also found that

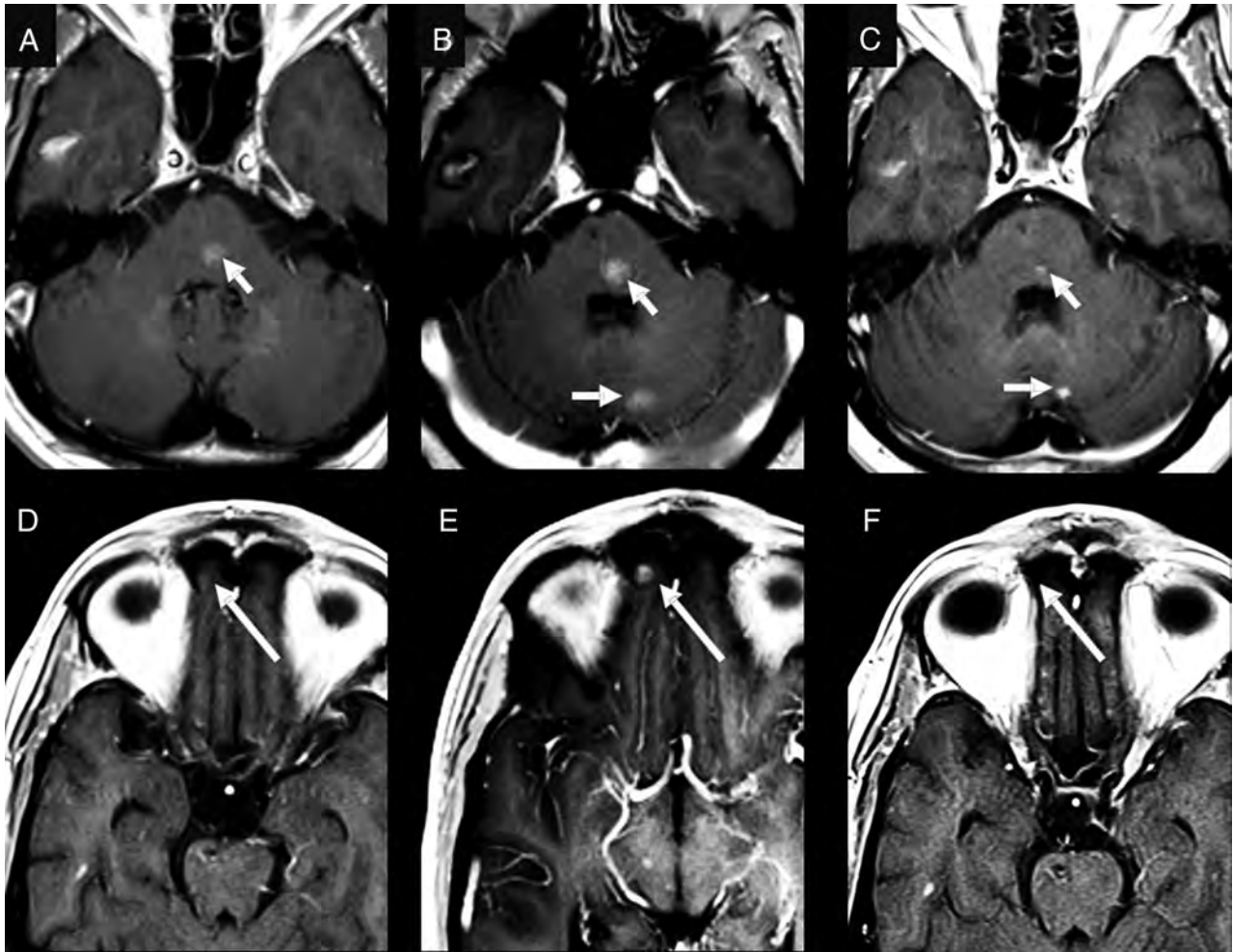


FIG 3. A 58-year-old man who was originally diagnosed with *EGFR* wild-type and was negative for *EML4/ALK* adenocarcinoma of the lung. After 3 years of traditional chemotherapy, the patient developed brain metastases. At that time, a biopsy of the patient's pericardial metastasis came back positive for *EML4/ALK* fusion. Note small metastatic lesions (arrows) at the time of diagnosis of the brain metastases in the pons (A) and medial right orbital gyrus (D). After starting crizotinib, several of the patient's brain metastases, including the lesions in the pons (B) and right medial orbital gyrus (E), increased in size (arrows), and there was development of new lesions such as the lesion in the left cerebellar hemisphere on B (arrow). The patient was then switched to alectinib, which resulted in a partial response in the brain with decreased size of previously identified lesions (arrows) (C and F).

alectinib has a superior toxicity profile compared with crizotinib.³⁶ The *ALK*-TKIs ceritinib, brigatinib, and lorlatinib have also shown efficacy in NSCLC brain metastases.^{10,22-24,37-39}

***ROS1* Tyrosine Kinase Inhibitors**

ROS1 is present in 1%–2% of cases of NSCLC and represents another targetable driver mutation in NSCLC brain metastases. *ROS1* is a tyrosine kinase that can fuse with several different genes to create multiple *ROS1*-fusion receptors that lead to overactivation of downstream pathways within the cell that lead to uncontrolled proliferation. Like *EGFR* and *ALK*, *ROS1* can be inhibited by TKIs that bind to the tyrosine kinase portion within the intracellular domain of the *ROS1* receptor. Owing to the sequence homology shared by the *ALK* and *ROS1* proteins, several *ALK* inhibitors have demonstrated efficacy in *ROS1*-rearranged NSCLC as well.⁴⁰ For instance, crizotinib has demonstrated intracranial efficacy in *ROS1*-rearranged NSCLC (Fig 4). A Phase II trial of crizotinib in advanced *ROS1*+ NSCLC reported an overall response rate of 73.9% and

a PFS of 10.2 months in the 23 patients with measurable CNS lesions at baseline.⁴¹ The *ALK/ROS1*/pan-TRK (pan-tropomyosin receptor kinase) inhibitor entrectinib was also studied in patients with *ROS1*-inhibitor-naïve NSCLC, and the authors reported an objective response in 7 of 11 patients with CNS metastases, as well as a CNS response rate of 71% based on 7 patients with evaluable lesions.⁴²

A Phase II study of the *ALK* inhibitor lorlatinib has also reported an intracranial overall response rate of 56.0% in 25 patients with brain metastases, including a mixture of patients whose lesions were crizotinib-naïve and crizotinib-refractory.⁴³ The *ALK* inhibitor ceritinib was also examined in *ROS1*-rearranged NSCLC in a small Phase II study, which reported intracranial disease control in 5 of the 8 patients with CNS metastases enrolled in the study.⁴⁴

***TKI* Toxicities and Risks**

Overall, *EGFR*-TKIs are well-tolerated, with fewer than 10% of patients discontinuing therapy due to adverse events.⁴⁵ Toxic

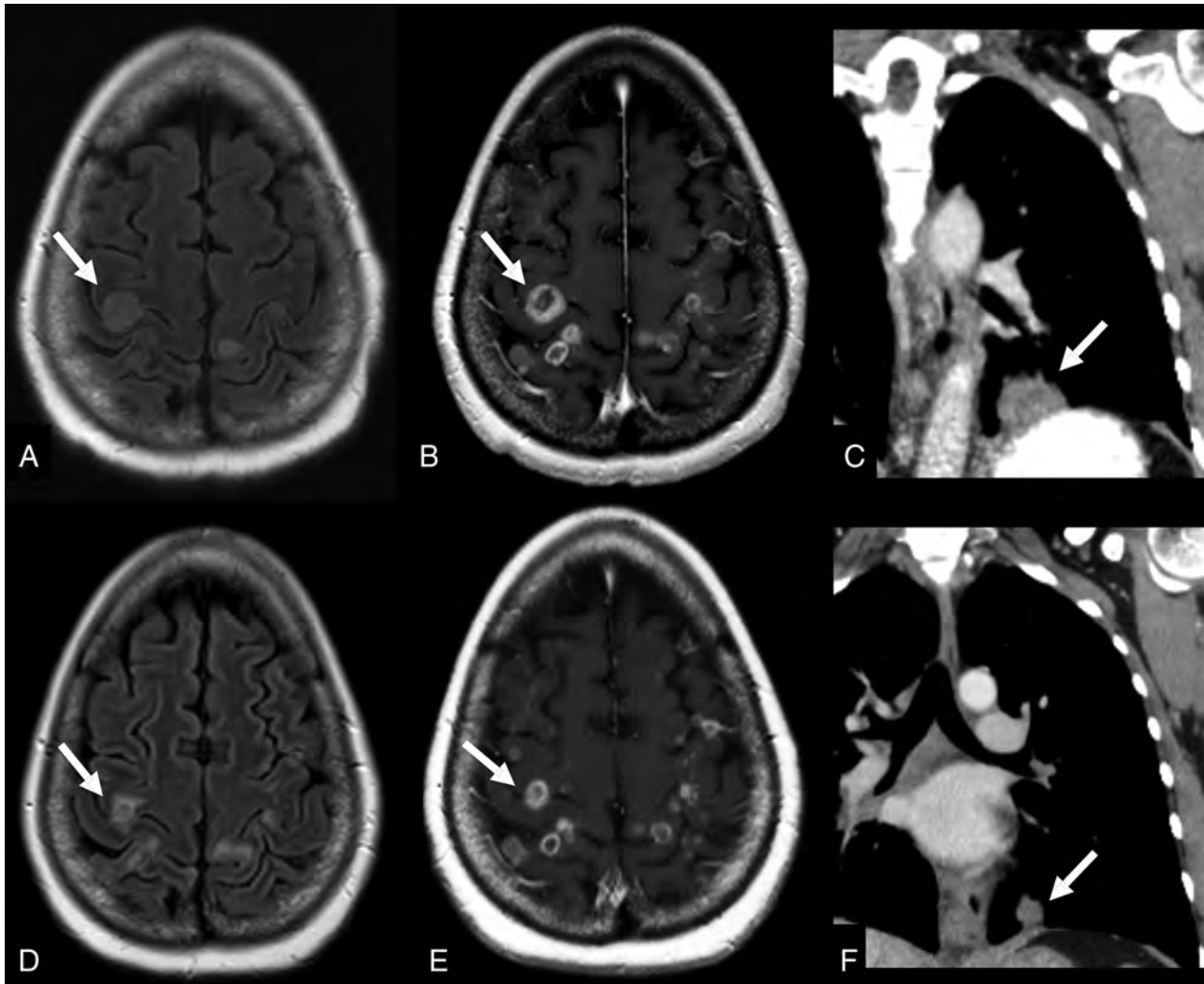


FIG 4. A 50-year-old woman with NSCLC with *ROS1-CD74* (Cluster of Differentiation 74) fusion. The patient was initially started on crizotinib. The primary lung tumor was responsive to therapy, but there was progressive disease in the brain. Given the numerous brain metastases, the patient elected to undergo local therapy with whole-brain radiation. The pretherapy images (A and B) demonstrate multiple peripherally enhancing lesions with surrounding hyperintense FLAIR signal consistent with surrounding vasogenic edema (arrows in A and B). The posttherapy images (D and E) demonstrate a decrease in the size and surrounding edema of the brain metastases (arrows in D and E). The patient was also able to remain on crizotinib for systemic therapy, given the favorable response in the chest (arrows in C and F).

deaths with these 3 *EGFR*-TKIs are rare, with pneumonitis being the most frequent cause in these agents. *ALK* inhibitors have been associated with lung toxicity, with the most frequent serious adverse event on *ALK*-inhibitor therapy being pneumonia.⁴⁶ Crizotinib has also been associated with cardiotoxicities such as bradycardia, complete heart block, QT prolongation, and pericarditis.⁴⁷

No major CNS toxicities have been described for *EGFR*-, *ALK*-, or *ROS1*-TKIs to date. However, radiation necrosis and pseudoprogression have been described in some TKIs following SRS. Pseudoprogression refers to a short-lived increase in lesion size following therapy commonly due to the inflammatory reaction associated with radiation necrosis. Radiation necrosis presenting as pseudoprogression has been reported with alectinib following SRS, as well as with ceritinib following WBRT.^{48,49} A risk with pseudoprogression is mistakenly identifying it as true progression, which could result in unnecessary radiation or surgical CNS

interventions. A high index of suspicion is therefore necessary in identifying radiation necrosis and pseudoprogression in patients with NSCLC brain metastases who have undergone radiation therapy followed by a TKI.

Posterior reversible encephalopathy syndrome (PRES) is a reversible neurologic syndrome that manifests as T2-hyperintense vasogenic edema on MR imaging and presents clinically with acute hypertension, seizures, vision abnormalities, and altered mental status.⁵⁰ PRES is most frequently associated with antiangiogenic TKIs that inhibit the vascular endothelial growth factor because PRES is thought to be related to altered cerebral blood flow regulation. However, cases of PRES have been reported with the *EGFR* inhibitors erlotinib, gefitinib, and osimertinib, as well as the *ALK* inhibitor crizotinib.⁵⁰ Classically, PRES involves the posterior parietal and occipital lobes but can vary in its distribution, with the most common presentation patterns being a dominant parietal-occipital pattern, superior frontal sulcus pattern, or

a linear holohemispheric watershed pattern.⁵¹ As the name suggests, PRES is most often reversible on discontinuation of the offending agent but may progress to hemorrhage or infarction if not promptly treated.

Despite the rare occurrence of radiation necrosis/pseudoprogression or PRES with TKI therapy, the overall risk associated with TKIs remains low. Not only are targeted therapies extending the lives of patients, but they are also doing so with less drug-associated morbidity. Therefore, the minimal toxicities associated with TKIs explain why these medications constitute a powerful breakthrough in the field of thoracic oncology.

Definitive Treatments for Brain Metastases

SRS was originally approved for treatment of up to 3 brain metastases but is demonstrating success in up to 10 lesions at some institutions.⁵²⁻⁵⁴ WBRT is typically used in patients with more numerous brain metastases. However, the neurodegenerative effects of WBRT can cause substantial morbidity and impair quality of life while having only a moderately beneficial effect on overall survival.⁵⁵ To minimize neurocognitive damage from WBRT, novel radiation techniques are currently being explored. Hippocampal-sparing WBRT reduces the radiation exposure of the hippocampus while preserving the therapeutic benefit on the grounds that the hippocampus has a low frequency of brain metastasis occurrences, while WBRT-induced hippocampal damage is frequently associated with neurotoxicity.⁵⁶ The neurodegenerative effects of WBRT have also incited effort to reduce the exposure of the brain to radiation via the expansion of SRS to patients with greater numbers of brain metastases in place of WBRT.⁵⁶

Responses of NSCLC brain metastases to radiation therapy have been shown to improve when radiation therapy is combined with immune checkpoint inhibitors (ICIs). The primary ICIs investigated in NSCLC are the anti-programmed cell death protein 1 (anti-PD-1) monoclonal antibodies nivolumab and pembrolizumab, and the anti-cytotoxic T-lymphocyte-associated protein 4 (CTLA-4) monoclonal antibody ipilimumab. These ICIs block tumor cell binding to PD-1, programmed death-ligand 1, or CTLA-4 on immune cells, respectively, to prevent tumor cells from interacting with immune cells and evading the host immune response. The anti-programmed death ligand 1 monoclonal antibody atezolizumab has also been studied in NSCLC. Atezolizumab functions by binding to the programmed death-ligand 1 on tumor cells rather than immune cells, which, nevertheless, prevents tumor cells from interacting with immune cells and relieves immune cell suppression as is also seen with the anti-PD-1 and anti-CTLA-4 checkpoint inhibitors.

In a cohort study comparing 34 patients with ICI-naïve NSCLC brain metastasis receiving SRS alone with 17 patients receiving SRS concurrently with either nivolumab, pembrolizumab, or atezolizumab, the concurrent SRS/ICI cohort achieved a higher rate of CNS complete response (50% versus 15.6%) and a shorter median time to regression of brain metastases (2.5 versus 3.1 months).⁵⁷ A larger retrospective study analyzed the responses to SRS combined with ipilimumab, nivolumab, or pembrolizumab in 260 patients with NSCLC ($n = 157$), melanoma ($n = 70$), or renal cell carcinoma ($n = 33$) with brain metastases. This study

found that concurrent SRS/ICI use was associated with a longer overall survival (24.7 months) compared with both SRS alone and SRS with nonconcurrent ICI (12.9 and 14.5 months, respectively).⁵⁸ One explanation for this synergy between ICI and SRS is that SRS facilitates increased release of proinflammatory signals, which augment the efficacy of ICI therapy. Notably, there was no increased risk of neurotoxicity with concurrent SRS/ICI therapy compared with SRS alone in either study.

Imaging Features of *EGFR*-, *ALK*-, and *ROS1*-Mutated NSCLC Brain Metastases. Brain metastases from NSCLC with *EGFR*, *ALK*, or *ROS1* mutations most often appear similar to brain metastases from other common primary malignancies. They typically appear round with well-demarcated borders, exhibit a homogeneous or mostly solid pattern of enhancement, and have surrounding vasogenic edema with mass effect. Several recent case reports and case series have noted development of unique, nearly entirely cystic brain metastases in NSCLC treated with TKIs.⁵⁹⁻⁶¹ In one case series including patients with *ALK*-mutated NSCLC, patients undergoing treatment with crizotinib developed brain metastases characterized by a thin rim of malignant cells with a large mucinous center.⁵⁹ These lesions exhibited no-to-minimal peripheral enhancement, no surrounding vasogenic edema, and variable central FLAIR signal, likely related to the amount of proteinaceous content within the central mucinous portion of the lesion.⁵⁹ In all 3 cases, the patient was asymptomatic despite the relatively large size of the lesions.⁵⁹ Another case report described a patient with NSCLC with an unknown genetic mutation status who was treated with erlotinib and developed entirely cystic brain metastases in the subarachnoid space without any associated enhancement.⁶⁰ This patient's lesions responded very well to WBRT, whereas the other cases of cystic metastases after treatment with TKIs did not change significantly after radiation therapy. Another patient with *EGFR*-mutated NSCLC with a cystic brain metastasis after gefitinib progressed to death from mass effect and subsequent brain herniation.⁶¹

Guidelines for Response to Therapy

Due to the poor response of brain metastases to traditional systemic chemotherapy drugs and short life expectancies of these patients in the past, patients with brain metastases were usually excluded from clinical trials. On the rare occasion that these patients were included, they were almost always required to demonstrate stable or treated CNS disease to be eligible for a trial. At least in part due to this limitation, there were no consensus guidelines for monitoring the response of brain metastases to systemic therapy. Trials often extended the Response Evaluation Criteria in Solid Tumors (RECIST)⁶² to evaluate the CNS metastases. Brain metastases were combined with all non-CNS diseases in all other organs as a single compartment for assessment of response. Furthermore, CNS metastases were rarely chosen as target lesions for the assessment of response to therapy. Grouping both CNS and non-CNS metastases as a single compartment is problematic. Traditional systemic chemotherapeutic agents have minimal penetration across the BBB; therefore, CNS lesions may progress while the non-CNS lesions are responding well to therapy. This outcome could force a patient

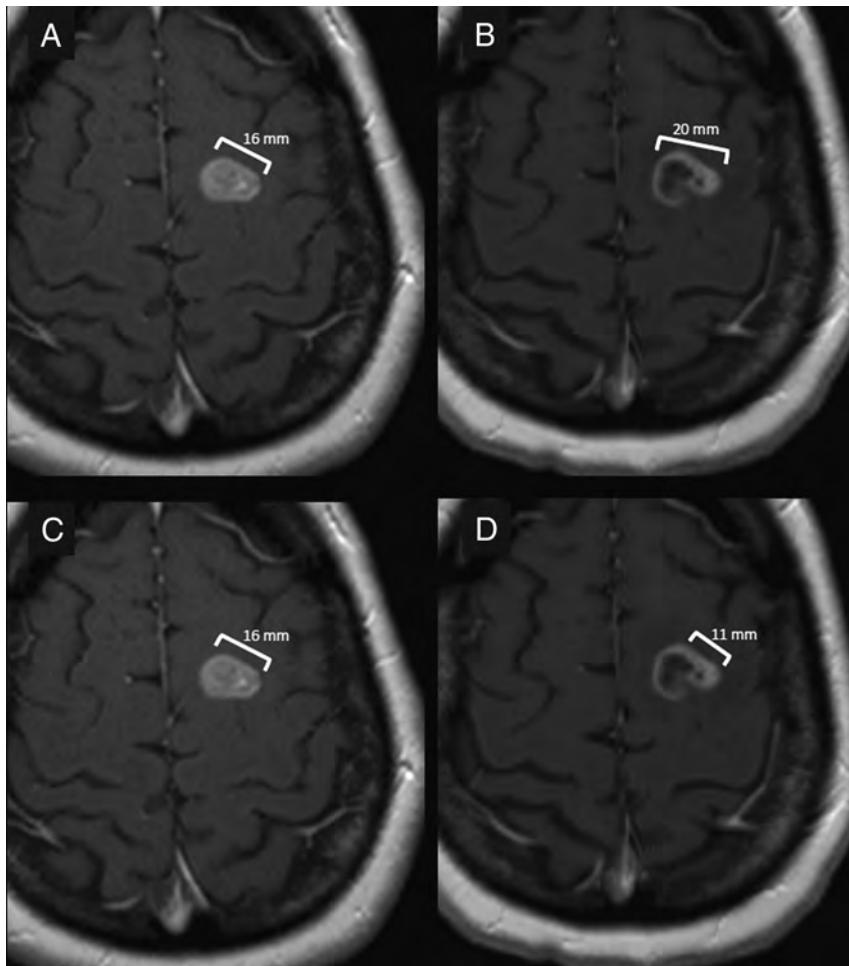


FIG 5. A 58-year-old man with *EGFR*-mutant NSCLC treated with erlotinib. Pretreatment images (A and C) show a solidly enhancing left frontal brain metastasis measuring 17 mm in diameter. Posttreatment images (B and D) demonstrate the implications of different measurement methods on the response to therapy. The measurement on B includes both the cystic and solid components of the lesion and demonstrates an increase of 25% of the lesion size, consistent with progressive disease. The measurement on D was performed according to the RANO criteria specifications, which only include the enhancing nodular component of the lesion, which has a perpendicular diameter of at least 5 mm. This method of measurement calculated a decrease of 31%, which is consistent with partial response to therapy. This patient continued to have a response to therapy and further decrease in the size of this lesion.

to be removed from the clinical trial even in the setting of a strong response to therapy outside the CNS. If the CNS disease and non-CNS disease are treated as separate compartments, locally progressive CNS disease can be treated with local therapy (eg, SRS, WBRT, and so forth), and the patient can remain on systemic therapy if effective in the non-CNS compartment.

Now that TKIs have shown much greater success in treating NSCLC brain metastases, there is a need for consensus guidelines to assess this response. The Response Assessment in Neuro-Oncology (RANO) group set out to address this problem and to create guidelines for monitoring the CNS response, including guidelines for both brain metastases and leptomeningeal disease.^{63,64} While other criteria such as RECIST and RECIST 1.1 are sometimes used in clinical trials that include

patients with brain metastases, the RANO group is the only group to establish criteria pertaining specifically to brain metastases. The remainder of this article will serve as a guide for radiologists to appropriately assess the response to TKIs and other concurrent therapies of brain metastases according to the guidelines established by the RANO group.⁶³

Obtaining Adequate Imaging

The first role of the radiologist in the assessment of brain metastases is to ensure that imaging is obtained with adequate parameters to enable accurate assessment of the response to therapy. MR imaging without and with gadolinium contrast is the ideal imaging technique for assessment of the response to therapy in brain metastases. According to the RANO group, CT with contrast may be used as a substitute in patients with contraindications to MR imaging and/or gadolinium or in areas with limited access to MR imaging; however, MR imaging should be performed whenever possible.⁶³ Initial baseline imaging for comparison with further studies should be performed within 4 weeks of the start of treatment.⁶³ For contrast-enhanced sequences, the MR imaging study should include a postgadolinium T1-weighted sequence with a maximum section thickness of 5 mm and no gap between slices. Ideally, especially in patients with smaller brain metastases or in trials that allow target lesions <1 cm in maximal diameter, a section thickness of ≤ 1.5 mm should be obtained when feasible. The additional MR imaging sequences in the recommended protocol suggested by the RANO group can be found in their article.⁶³

Identifying and Measuring Target Lesions

For a lesion to be eligible as a target lesion, it must fit the RANO definition of a measurable lesion. A measurable lesion, as defined by the RANO criteria, is one with an enhancing component that is at least 10 mm in the longest diameter and 5 mm in the perpendicular, short-axis diameter that is visible on at least 2 consecutive slices and can be reproducibly measured.⁶³ Of note, if the lesion is cystic or mixed cystic and solid, the cystic component should not be included in the measurement (Fig 5). Other features, including cystic-only lesions, leptomeningeal disease, dural-based disease, or lesions with ill-defined borders, are considered nonmeasurable disease (Fig 6).

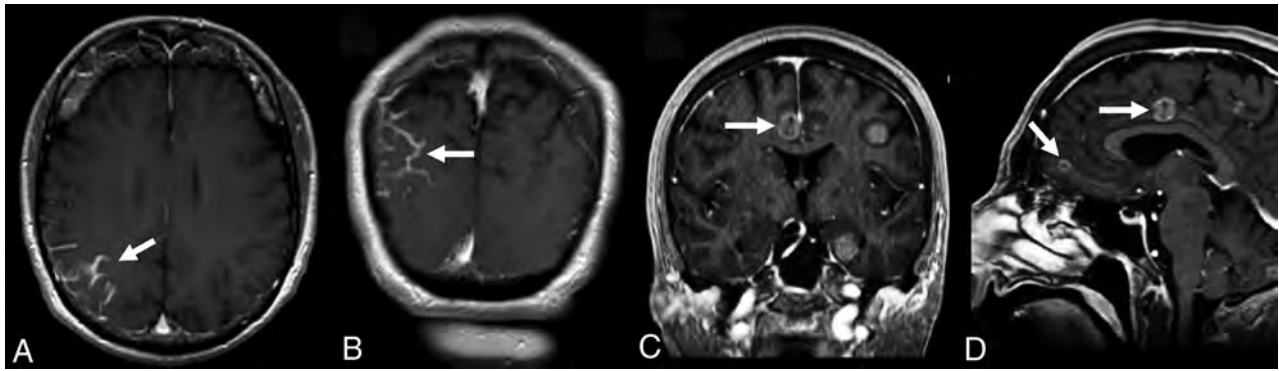


FIG 6. Examples of nonmeasurable disease in a patient with NSCLC brain metastases. *A* and *B*, Leptomeningeal metastatic disease in the right parietal lobe (*white arrows*). *C* and *D*, A different patient with small-cell lung cancer demonstrates completely cystic metastases (*white arrows*) that do not have a measurable solidly enhancing component. Both leptomeningeal disease and completely cystic metastases are considered nonmeasurable disease by the RANO criteria.

Up to 5 measurable lesions should be identified as target lesions. If the patient has >5 measurable lesions, then the target lesions should be selected while giving preference to the following factors:

- Largest size.
- Increasing size on consecutive imaging studies.
- No prior local treatment, including an operation, SRS, and so forth.

After the target lesions are selected, the longest diameter (including only the enhancing nodular component of the lesion) should be recorded for each of the target lesions (Fig 5). The sum of the longest diameter of all target lesions should also be included in the report. If there are no lesions that meet the criteria for a measurable target lesion, then the patient is said to have nonmeasurable disease. The RANO group suggests that studies that include the assessment of the CNS response to therapy as their primary end point should not include patients with nonmeasurable disease.⁶³

Additional factors including a description of morphologic features at initial imaging and the location of brain metastases may prove important in the era of precision medicine and targeted therapies, including TKIs. One study of 144 patients with *EGFR*-mutated NSCLC brain metastases treated with a first- or second-generation *EGFR*-TKI found that erlotinib achieved a longer PFS than gefitinib or afatinib only in patients who demonstrated poor prognostic factors on MR imaging such as tumor necrosis, rim enhancement, or tumor location in the frontal lobe, putamen, or cerebellum.⁶⁵ In patients without these poor prognostic imaging characteristics, the PFS was comparable among erlotinib, gefitinib, and afatinib. This finding suggests that the initial imaging features of brain metastases may be useful in predicting outcomes in patients treated with novel targeted therapies.

Nontarget Lesions

Although the nontarget brain metastases do not need to be measured, they should be identified and included in the baseline report. This is important so that on subsequent follow-up imaging these lesions can also be assessed for progression and new lesions can be easily identified.

Evaluation of Lesions on Follow-Up Imaging

On follow-up imaging, the previously identified target lesions should be found and the largest diameter of each lesion as well as the sum of these unidirectional measurements should be recorded. Next, the nontarget lesions should be compared with measurements on prior studies and results of the evaluation of whether these lesions are increased, decreased, or unchanged in size should be recorded. Even if the target lesions are unchanged or decreased in size, if there is unequivocal and substantial progression of the nontarget lesions, the patient is still considered to have progressive disease. Finally, evaluation for any new brain metastasis should be performed. A clear statement of whether any new lesion is larger than 5 mm in diameter; visible in axial, sagittal, and coronal planes; and definitively not due to artifacts should be given in the report. In the case of questionable new lesions, the patient and oncologist may choose to continue therapy and obtain short-term follow-up imaging to re-evaluate the lesion in question.

Response to Therapy

The RANO criteria for response to therapy in brain metastases take several clinical factors into account, including changes in the corticosteroid dose and Karnofsky Performance Scale. Any significant increase in the corticosteroid dose or worsening in performance status that cannot be returned to baseline is consistent with progressive disease.⁶³ Thus, unless the radiologist has access to both of these factors in the clinical history, it would be sensible to not include the definitive RANO criteria response in a report before discussing the patient with the referring oncology team. However, follow-up imaging is one of the major criteria for determining response to therapy according to the RANO criteria. From an imaging standpoint, the following are the criteria for each possible response to therapy:⁶³

- Complete response: complete resolution of all target and nontarget metastases with no new enhancing lesions.
- Partial response: decrease of at least 30% in the sum of the longest diameter of the target lesions compared with baseline, no change or decrease in the nontarget lesions, and no new lesions.

- Progressive disease: either an increase of at least 20% in the sum of the longest diameter of the target lesions from the nadir, unequivocal progression of nontarget lesions, or any new lesion.
- Stable disease: change in the sum of the longest diameter of the target lesions between 30% decrease and 20% increase, stable or improved nontarget lesions, and no new lesions.

Finally, the RANO group suggests that when reporting the response to therapy in patients with brain metastases, the CNS disease should be separated from the non-CNS disease. For non-CNS disease, the criteria established in RECIST 1.1 are recommended.⁶² This approach gives the flexibility for a trial to calculate both local CNS progression-free survival, non-CNS progression-free survival, and bicompartamental progression-free survival. Any of these outcomes could then be used as a primary end point for the trial. This flexibility is potentially beneficial in situations in which patients have local CNS progression and a favorable response in the non-CNS compartment for undergoing concurrent local CNS therapy and being able to stay in the trial.

When patients with NSCLC with brain metastases are on immunotherapy or have received local therapy with WBRT or SRS, new lesions alone may not constitute progression of disease and instead may be due to pseudoprogression.⁶³ Pseudoprogression refers to a transient increase in tumor size on imaging shortly after treatment due to edema, necrosis, or immune cell infiltration. This initial radiographic growth can mimic true progression, but unlike true progression, it is subsequently followed by a reduction in tumor burden. Pseudoprogression after radiation therapy, especially SRS, is a well-recognized phenomenon in patients with brain metastases and has been shown to occur in up to 25%–30% of patients radiographically after SRS.^{66,67} Studies have also shown that it may occur in at a higher rate in NSCLC-associated brain metastases and that *ALK* mutation may be an added risk factor.⁶⁸ Whether TKI therapy after SRS and/or WBRT is an added risk remains to be determined, and there is conflicting evidence on the topic. Before the use of second-generation *ALK* inhibitors, there were no reports of radiation necrosis during crizotinib use, including when it was used after patients had undergone SRS.^{48,69} There have been reports of radiation necrosis in patients on alectinib for *ALK*-mutated NSCLC months to years after radiation therapy.^{48,70} The RANO criteria do give some guidance in these situations; and often short-term follow-up, advanced MR imaging or PET, or biopsy must be performed to find a more definitive answer.⁶³ Because TKIs are the focus of this article and they have not been established as a risk factor for pseudoprogression, an in-depth discussion of the guidelines pertaining to pseudoprogression will not be included. It is, however, important to keep in mind the possibility of pseudoprogression in these patients in the correct clinical and imaging scenario.

Studies evaluating the best imaging parameters to evaluate the response to TKI therapy have not yet been performed; however, many believe that the unidirectional method proposed by the RANO group may not be the best approach. Some have suggested that volumetric measurements are a more accurate measurement of changes in the number of cancer cells and better account for irregular shapes and cystic changes that frequently occur in brain

metastases after treatment. A study on the treatment of melanoma brain metastases with SRS demonstrated that volumetric measurements were a better predictor of overall survival and the need for salvage WBRT compared with linear measurements.⁷¹ The RANO group does admit that volumetric measurements may prove to be a better method; however, they believe that there are too little data, availability, and standardization of volumetric measurements to recommend this over unidirectional measurements at this time. Furthermore, until volumetric measurements become more automated, they require higher cost and more effort to provide these measurements.

Unlike metastases treated with systemic cytotoxic chemotherapy, which typically demonstrate response to therapy as a shrinkage in size and decreased surrounding edema, metastases treated with SRS and WBRT often undergo more complex morphologic changes after treatment.⁷² Kang et al⁷² described early-stage changes, including central and perilesional edema with an occasional transient increase in the size of the enhancing brain metastasis days after SRS. These changes are followed by central cavitation and necrosis, often with indistinct enhancing borders.⁷² Finally, in the chronic stage, the lesion remains as a peripherally enhancing glial scar without surrounding edema.⁷² Because of these dynamic changes in size with difficult-to-measure centrally necrotic lesions, SRS has been the subject of study for many other imaging biomarkers to predict a response to therapy, including MR diffusion, MR perfusion (especially dynamic contrast enhancement), and PET studies using 3-deoxy-3-[¹⁸F]fluorothymidine or 2-[¹⁸F]fluoro-2-deoxy-d-glucose.⁷³⁻⁷⁷ One study concluded that the response to SRS treatment of brain metastases could be predicted as soon as 7–10 days after treatment using MR diffusion-weighted imaging.⁷⁶ However, after many studies in search of the best biomarkers, factors as simple as whether an increase or decrease in diffusivity predicts a good response to SRS still remain controversial and are likely related to the timing of the follow-up studies.^{73,76,77} Because of the complexity of the physiologic changes happening at the cellular level in brain metastases after different types of treatment, accepting new, advanced MR imaging or PET biomarkers as a means to assess treatment response should not be haphazard. Furthermore, the use of different imaging biomarkers for different types of therapy may be the best means of evaluation. Well-designed prospective studies on imaging biomarkers are needed to fully understand the best biomarkers for assessment of the response to TKIs and other methods of treatment.

In our experience, morphologic changes after TKIs more closely follow the systemic cytotoxic chemotherapy pattern of response including decreased size and surrounding edema of mostly solidly enhancing lesions. However, further studies need to systematically evaluate the pattern of morphologic changes in brain metastases after treatment with TKIs, especially because bizarre imaging appearances, including nearly entirely cystic brain metastases, have been described in patients undergoing treatment with TKIs. Also, if size criteria prove to be the best means of measuring response to therapy, unidirectional, bidirectional, and volumetric measurements should be compared to see which method best predicts early response or progression and long-term patient outcomes.

CONCLUSIONS

In recent years, several systemic therapies have been developed that demonstrate efficacy in NSCLC metastatic to the brain. It is essential for radiologists to be informed about these novel therapeutic agents to evaluate the intracranial response to therapy on imaging in patients undergoing treatment with these drugs. As the systemic chemotherapeutic options for metastatic NSCLC evolve, the assessment of the responses of brain metastases on imaging is becoming ever more critical for evaluating and managing patients with metastatic NSCLC.

REFERENCES

1. Baik CS, Chamberlain MC, Chow LQ. Targeted therapy for brain metastases in EGFR-mutated and ALK-rearranged non-small-cell lung cancer. *J Thorac Oncol* 2015;10:1268–78 CrossRef Medline
2. Hall WA, Djalilian HR, Nussbaum ES, et al. Long-term survival with metastatic cancer to the brain. *Med Oncol* 2000;17:279–86 CrossRef Medline
3. Proto C, Imbimbo M, Gallucci R, et al. Epidermal growth factor receptor tyrosine kinase inhibitors for the treatment of central nervous system metastases from non-small cell lung cancer: the present and the future. *Transl Lung Cancer Res* 2016;5:563–78 CrossRef Medline
4. Mehta MP, Rodrigus P, Terhaard CHJ, et al. Survival and neurologic outcomes in a randomized trial of motexafin gadolinium and whole-brain radiation therapy in brain metastases. *J Clin Oncol* 2003;21:2529–36 CrossRef Medline
5. Franciosi V, Cocconi G, Michiara M, et al. Front-line chemotherapy with cisplatin and etoposide for patients with brain metastases from breast carcinoma, nonsmall cell lung carcinoma, or malignant melanoma: a prospective study. *Cancer* 1999;85:1599–1605 Medline
6. Petrelli F, Ghidini M, Lonati V, et al. The efficacy of lapatinib and capecitabine in HER-2 positive breast cancer with brain metastases: a systematic review and pooled analysis. *Eur J Cancer* 2017;84:141–48 CrossRef Medline
7. Verma J, Jonasch E, Allen P, et al. Impact of tyrosine kinase inhibitors on the incidence of brain metastasis in metastatic renal cell carcinoma. *Cancer* 2011;117:4958–65 CrossRef Medline
8. Kerr KM, López-Ríos F. Precision medicine in NSCLC and pathology: how does ALK fit in the pathway? *Ann. Oncol* 2016;27:ii16–24 CrossRef Medline
9. Lindeman NI, Cagle PT, Aisner DL, et al. Updated molecular testing guideline for the selection of lung cancer patients for treatment with targeted tyrosine kinase inhibitors. *Arch Pathol Lab Med* 2018;142:321–46 CrossRef Medline
10. Narita Y, Matsushima Y, Shirowa T, et al. Cost-effectiveness analysis of EGFR mutation testing and gefitinib as first-line therapy for non-small cell lung cancer. *Lung Cancer* 2015;90:71–77 CrossRef Medline
11. Holleman MS, Al MJ, Zaim R, et al. Cost-effectiveness analysis of the first-line EGFR-TKIs in patients with non-small cell lung cancer harbouring EGFR mutations. *Eur J Health Econ* 2019 Sep 20. [Epub ahead of print] CrossRef Medline
12. Djalalov S, Beça J, Hoch JS, et al. Cost effectiveness of EML4-ALK fusion testing and first-line crizotinib treatment for patients with advanced ALK-positive non-small-cell lung cancer. *J Clin Oncol* 2014;32:1012–19 CrossRef Medline
13. Carlson JJ, Kangho S, Orfanos P, et al. Cost effectiveness of alectinib vs. crizotinib in first-line anaplastic lymphoma kinase-positive advanced non-small-cell lung cancer. *Pharmacoeconomics* 2018;36:495–504 CrossRef Medline
14. Glitza Oliva IC, Schwartsman G, Tawbi H. Advances in the systemic treatment of melanoma brain metastases. *Ann Oncol* 2018;29:1509–20 CrossRef Medline
15. Svokos KA, Sahlia B, Toms SA. Molecular biology of brain metastasis. *Int J Mol Sci* 2014;15:9519–30 CrossRef Medline
16. Löscher W, Potschka H. Blood-brain barrier active efflux transporters: ATP-binding cassette gene family. *NeuroRx* 2005;2:86–98 CrossRef Medline
17. Connell JJ, Chatain G, Cornelissen B, et al. Selective permeabilization of the blood-brain barrier at sites of metastasis. *J Natl Cancer Inst* 2013;105:1634–43 CrossRef Medline
18. Tan J, Li M, Zhong W, et al. Tyrosine kinase inhibitors show different anti-brain metastases efficacy in NSCLC: a direct comparative analysis of icotinib, gefitinib, and erlotinib in a nude mouse model. *Oncotarget* 2017;8:98771–81 CrossRef Medline
19. García-Román J, Zentella-Dehesa A. Vascular permeability changes involved in tumor metastasis. *Cancer Lett* 2013;335:259–69 CrossRef Medline
20. Wang BX, Ou W, Mao XY, et al. Impacts of EGFR mutation and EGFR-TKIs on incidence of brain metastases in advanced non-squamous NSCLC. *Clin Neurol Neurosurg* 2017;160:96–100 CrossRef Medline
21. O’Kane GM, Leighl NB. Systemic therapy of lung cancer CNS metastases using molecularly targeted agents and immune checkpoint inhibitors. *CNS Drugs* 2018;32:527–42 CrossRef Medline
22. Abdallah SM, Wong A. Brain metastases in non-small-cell lung cancer: are tyrosine kinase inhibitors and checkpoint inhibitors now viable options? *Curr Oncol* 2018;25:S103–14 CrossRef Medline
23. Park SJ, Kim HT, Lee DH, et al. Efficacy of epidermal growth factor receptor tyrosine kinase inhibitors for brain metastasis in non-small cell lung cancer patients harboring either exon 19 or 21 mutation. *Lung Cancer* 2012;77:556–60 CrossRef Medline
24. Maemondo M, Inoue A, Kobayashi K, et al; North-East Japan Study Group. Gefitinib or chemotherapy for non-small-cell lung cancer with mutated EGFR. *N Engl J Med* 2010;362:2380–88 CrossRef Medline
25. Pao W, Balak MN, Riely GJ, et al. Molecular analysis of NSCLC patients with acquired resistance to gefitinib or erlotinib. *J Clin Oncol* 2006;24:7078 CrossRef
26. Hoffknecht P, Tufman A, Wehler T, et al; Afatinib Compassionate Use Consortium (ACUC). Efficacy of the irreversible ErbB family blocker afatinib in epidermal growth factor receptor (EGFR) tyrosine kinase inhibitor (TKI)-pretreated non-small-cell lung cancer patients with brain metastases or leptomeningeal disease. *J Thorac Oncol* 2015;10:156–63 CrossRef Medline
27. Yu HA, Arcila ME, Rekhtman N, et al. Analysis of tumor specimens at the time of acquired resistance to EGFR TKI therapy in 155 patients with EGFR mutant lung cancers. *Clin Cancer Res* 2013;19:2240–47 CrossRef Medline
28. Griffin R, Ramirez RA. Molecular targets in non-small cell lung cancer. *Ochsner J* 2017;17:388–92 Medline
29. Malapelle U, Ricciuti B, Baglivo S, et al. Osimertinib. *Recent Results Cancer Res* 2018;211:257–76 CrossRef Medline
30. Tan CS, Kumarakulasinghe NB, Huang YQ, et al. Third generation EGFR TKIs: current data and future directions. *Mol Cancer* 2018;17:1–14 CrossRef Medline
31. Reungwetwattana T, Nakagawa K, Cho BC, et al. CNS response to osimertinib versus standard epidermal growth factor receptor tyrosine kinase inhibitors in patients with untreated EGFR-mutated advanced non-small-cell lung cancer. *J Clin Oncol* 2018 Aug 28. [Epub ahead of print] CrossRef Medline
32. Soria JC, Ohe Y, Vansteenkiste J, et al; FLAURA Investigators. Osimertinib in untreated EGFR-mutated advanced non-small-cell lung cancer. *N Engl J Med* 2018;378:113–25 CrossRef Medline
33. Costa DB, Shaw AT, Ou SH, et al. Clinical experience with crizotinib in patients with advanced ALK-rearranged non-small-cell lung cancer and brain metastases. *J Clin Oncol* 2015;33:1881–88 CrossRef Medline

34. Ricciuti B, De Giglio A, Mecca C, et al. **Precision medicine against ALK-positive non-small cell lung cancer: beyond crizotinib.** *Med Oncol* 2018;35:1–18 CrossRef Medline
35. Gadgeel S, Peters S, Mok T, et al. **Alectinib versus crizotinib in treatment-naïve anaplastic lymphoma kinase-positive (ALK+) non-small-cell lung cancer: CNS efficacy results from the ALEX study.** *Ann Oncol* 2018;29:2214–22 CrossRef Medline
36. Peters S, Camidge DR, Shaw AT, et al; ALEX Trial Investigators. **Alectinib versus crizotinib in untreated ALK-positive non-small-cell lung cancer.** *N Engl J Med* 2017;377:829–38 CrossRef Medline
37. Crinò L, Ahn MJ, De Marinis F, et al. **Multicenter phase II study of whole-body and intracranial activity with ceritinib in patients with ALK-rearranged non-small-cell lung cancer previously treated with chemotherapy and crizotinib: results from ASCEND-2.** *J Clin Oncol* 2016;34:2866–73 CrossRef Medline
38. Camidge DR, Kim HR, Ahn MJ, et al. **Brigatinib versus crizotinib in ALK-positive non-small-cell lung cancer.** *N Engl J Med* 2018;379:2027–39 CrossRef Medline
39. Shaw AT, Felip E, Bauer TM, et al. **Lorlatinib in ALK- or ROS1-rearranged non-small cell lung cancer: an international, multicenter, open-label phase I trial.** *Lancet Oncol* 2017;18:1590–99 CrossRef Medline
40. Ou SHI, Zhu VW. **CNS metastasis in ROS1+ NSCLC: an urgent call to action, to understand, and to overcome.** *Lung Cancer* 2019;130:201–07 CrossRef Medline
41. Wu YL, Yang JC, Kim DW, et al. **Phase II study of crizotinib in East Asian patients with ROS1-positive advanced non-small-cell lung cancer.** *J Clin Oncol* 2018;36:1405–12 CrossRef Medline
42. Ahn M, Cho BC, Siena S, et al. **OA 14.06 entrectinib in patients with locally advanced or metastatic ROS1 fusion-positive non-small cell lung cancer (NSCLC).** *J Thorac Oncol* 2017;12:S178 CrossRef
43. Ou S, Shaw A, Riely G, et al. **OA02.03 clinical activity of lorlatinib in patients with ROS1+ advanced non-small cell lung cancer: phase 2 study cohort EXP-6.** *J Thorac Oncol* 2018;13:S322–23 CrossRef
44. Lim SM, Kim HR, Lee JS, et al. **Open-label, multicenter, phase II study of ceritinib in patients with non-small-cell lung cancer harboring ROS1 rearrangement.** *J Clin Oncol* 2017;35:2613–18 CrossRef Medline
45. Ding PN, Lord SJ, GebSKI V, et al. **Risk of treatment-related toxicities from EGFR tyrosine kinase inhibitors: a meta-analysis of clinical trials of gefitinib, erlotinib, and afatinib in advanced EGFR-mutated non-small cell lung cancer.** *J Thorac Oncol* 2017;12:633–43 CrossRef Medline
46. Hou H, Sun D, Liu K, et al. **The safety and serious adverse events of approved ALK inhibitors in malignancies: a meta-analysis.** *Cancer Manag Res* 2019;11:4109–18 CrossRef Medline
47. Del Valle MF, Chang AY. **Real world experience on treatment, outcome and toxicity of crizotinib in patients with anaplastic lymphoma kinase positive advanced non-small cell lung cancer.** *J Thorac Dis* 2019;11:3864–73 CrossRef Medline
48. Ou SH, Klempler SJ, Azada MC, et al. **Radiation necrosis presenting as pseudoprogression (PsP) during alectinib treatment of previously radiated brain metastases in ALK-positive NSCLC: implications for disease assessment and management.** *Lung Cancer* 2015;88:355–59 CrossRef Medline
49. Song YP, Colaco RJ. **Radiation necrosis: a growing problem in a case of brain metastases following whole brain radiotherapy and stereotactic radiosurgery.** *Cureus* 2018;10:e2037 CrossRef Medline
50. Shah RR. **Anti-angiogenic tyrosine kinase inhibitors and reversible posterior leukoencephalopathy syndrome: could hypomagnesemia be the trigger?** *Drug Saf* 2017;40:373–86 CrossRef Medline
51. Shankar J, Banfield J. **Posterior reversible encephalopathy syndrome: a review.** *Can Assoc Radiol J* 2017;68:147–53 CrossRef Medline
52. Yamamoto M, Serizawa T, Shuto T, et al. **Stereotactic radiosurgery for patients with multiple brain metastases (JLKG0901): a multi-institutional prospective observational study.** *Lancet Oncol* 2014;15:387–95 CrossRef Medline
53. Yamamoto M, Serizawa T, Higuchi Y, et al. **A multi-institutional prospective observational study of stereotactic radiosurgery for patients with multiple brain metastases (JLKG0901 study update): irradiation-related complications and long-term maintenance of Mini-Mental State Examination scores.** *Int J Radiat Oncol Biol Phys* 2017;99:31–40 CrossRef Medline
54. Berghoff A, Preusser M. **New developments in brain metastases.** *Ther Adv Neurol Disord* 2018;11:1756286418785502 CrossRef Medline
55. Jindal V, Gupta S. **Expected paradigm shift in brain metastases therapy: immune checkpoint inhibitors.** *Mol Neurobiol* 2018;55:7072–78 CrossRef Medline
56. Kelly WJ, Shah NJ, Subramaniam DS. **Management of brain metastases in epidermal growth factor receptor mutant non-small-cell lung cancer.** *Front Oncol* 2018;8:208–09 CrossRef Medline
57. Shepard MJ, Xu Z, Donahue J, et al. **Stereotactic radiosurgery with and without checkpoint inhibition for patients with metastatic non-small cell lung cancer to the brain: a matched cohort study.** *J Neurosurg* 2019 Jul 26. [Epub ahead of print] CrossRef Medline
58. Chen L, Douglass J, Kleinberg L, et al. **Concurrent immune checkpoint inhibitors and stereotactic radiosurgery for brain metastases in non-small cell lung cancer, melanoma, and renal cell carcinoma.** *Int J Radiat Oncol Biol Phys* 2018;100:916–25 CrossRef Medline
59. Narayanan V, Honce MJ, Mehrotra S, et al. **Cystic brain metastases occurring in anaplastic lymphoma kinase gene rearranged non-small-cell lung cancer patients receiving crizotinib.** *Clin Lung Cancer* 2016;17:85–90 CrossRef Medline
60. Essenmacher AC, Watal P, Bathla G, et al. **Brain metastases from adenocarcinoma of the lung with truly cystic magnetic resonance imaging appearance.** *Clin Imaging* 2018;52:203–07 CrossRef Medline
61. Zee YK, Chin TM, Wong ASC. **Fatal cystic change of brain metastasis after response to gefitinib in non-small-cell lung cancer.** *J Clin Oncol* 2009;27:145–46 CrossRef Medline
62. Schwartz LH, Litière S, de Vries E, et al. **RECIST 1.1: update and clarification—from the RECIST Committee.** *Eur J Cancer* 2016;62:132–37 CrossRef Medline
63. Lin NU, Lee EQ, Aoyama H, et al; Response Assessment in Neuro-Oncology (RANO) group. **Response assessment criteria for brain metastases: proposal from the RANO group.** *Lancet Oncol* 2015;16:e270–78 CrossRef Medline
64. Chamberlain M, Junck L, Brandsma D, et al. **Leptomeningeal metastases: a RANO proposal for response criteria.** *Neuro Oncol* 2017;19:484–92 CrossRef Medline
65. Lin CY, Chang CC, Su PL, et al. **Brain MRI imaging characteristics predict treatment response and outcome in patients with de novo brain metastasis of EGFR-mutated NSCLC.** *Medicine (Baltimore)* 2019;98:e16766 CrossRef Medline
66. Minniti G, Clarke E, Lanzetta G, et al. **Stereotactic radiosurgery for brain metastases: analysis of outcome and risk of brain radionecrosis.** *Radiat Oncol* 2011;6:48 CrossRef Medline
67. Kohutek ZA, Yamada Y, Chan TA, et al. **Long-term risk of radionecrosis and imaging changes after stereotactic radiosurgery for brain metastases.** *J Neurooncol* 2015;125:149–56 CrossRef Medline
68. Miller JA, Bennett EE, Xiao R, et al. **Association between radiation necrosis and tumor biology after stereotactic radiosurgery for brain metastasis.** *Int J Radiat Oncol Biol Phys* 2016;96:1060–69 CrossRef Medline
69. Gan GN, Weickhardt AJ, Scheier B, et al. **Stereotactic radiation therapy can safely and durably control sites of extra-central nervous system oligoprogressive disease in anaplastic lymphoma kinase-positive lung cancer patients receiving crizotinib.** *Int J Radiat Oncol Biol Phys* 2014;88:892–98 CrossRef Medline
70. Ou SH, Weitz M, Jalas JR, et al. **Alectinib induced CNS radiation necrosis in an ALK + NSCLC patient with a remote (7 years) history of brain radiation.** *Lung Cancer* 2016;96:15–18 CrossRef Medline

71. LeCompte MC, McTyre E, Henson A, et al. **Survival and failure outcomes predicted by brain metastasis volumetric kinetics in melanoma patients following upfront treatment with stereotactic radiosurgery alone.** *Cureus* 2017;9:e1934 CrossRef Medline
72. Kang TW, Kim ST, Byun HS, et al. **Morphological and functional MRI, MRS, perfusion and diffusion changes after radiosurgery of brain metastasis.** *Eur J Radiol* 2009;72:370–80 CrossRef Medline
73. Jakubovic R, Zhou S, Heyn C, et al. **The predictive capacity of apparent diffusion coefficient (ADC) in response assessment of brain metastases following radiation.** *Clin Exp Metastasis* 2016;33:277–84 CrossRef Medline
74. Abdulla DS, Scheffler M, Brandes V, et al. **Monitoring treatment response to erlotinib in EGFR-mutated non-small-cell lung cancer brain metastases using serial O-(2- [18 F]fluoroethyl)-L-tyrosine PET.** *Clin Lung Cancer* 2019;20:e148–51 CrossRef Medline
75. Essig M, Waschkes M, Wenz F, et al. **Assessment of brain metastases with dynamic susceptibility-weighted contrast-enhanced MR imaging: initial results.** *Radiology* 2003;228:193–99 CrossRef Medline
76. Mahmood F, Johannesen HH, Geertsen P, et al. **Repeated diffusion MRI reveals earliest time point for stratification of radiotherapy response in brain metastases.** *Phys Med Biol* 2017;62:2990–3002 CrossRef Medline
77. Huang CF, Chou HH, Tu HT, et al. **Diffusion magnetic resonance imaging as an evaluation of the response of brain metastases treated by stereotactic radiosurgery.** *Surg Neurol* 2008;69:62–68 CrossRef Medline

Advanced Multicompartment Diffusion MRI Models and Their Application in Multiple Sclerosis

 D.A. Lakhani,  K.G. Schilling,  J. Xu, and  F. Bagnato



ABSTRACT

SUMMARY: Conventional MR imaging techniques are sensitive to pathologic changes of the brain and spinal cord seen in MS, but they lack specificity for underlying axonal and myelin integrity. By isolating the signal contribution from different tissue compartments, newly developed advanced multicompartment diffusion MR imaging models have the potential to detect specific tissue subtypes and associated injuries with increased pathologic specificity. These models include neurite orientation dispersion and density imaging, diffusion basis spectrum imaging, multicompartment microscopic diffusion MR imaging with the spherical mean technique, and models enabled through high-gradient diffusion MR imaging. In this review, we provide an appraisal of the current literature on the physics principles, histopathologic validation, and clinical applications of each of these techniques in both brains and spinal cords of patients with MS. We discuss limitations of each of the methods and directions that future research could take to provide additional validation of their roles as biomarkers of axonal and myelin injury in MS.

ABBREVIATIONS: AD = axial diffusivity; D_{ax} = intra-axonal diffusivity; DBSI = diffusion basis spectrum imaging; FF = fiber fraction; IVF = isotropic volume fraction; NDI = neurite density index (also V_{ic} , V_{in} , or f_{icvt}); NODDI = neurite orientation dispersion and density imaging; ODI = orientation dispersion index; RD = radial diffusivity; SMT = spherical mean technique; V_{ax} = intra-axonal volume fraction

MS is an inflammatory-degenerative disease of the CNS affecting approximately 2.3 million people, nearly 900,000 of whom are in the United States.¹

Transient and focal inflammation with variable degrees of demyelination and axonal injury is the pathologic hallmark of MS lesions. The acute inflammatory phase resolves within a few weeks.^{2,3} Thereafter, some lesions undergo repair of injured myelin and axons,⁴ while others may fail to repair and evolve into chronic plaques featured by variable degrees of chronic demyelination and axonal injury.⁴ Axons do not survive chronic

demyelination, leading to axonal atrophy, transection, and subsequent neuronal death. These neurodegenerative processes may also extend outside focal plaques to areas of normal-appearing WM and normal-appearing GM.⁵

Conventional MR imaging (T1WI and T2WI) is highly sensitive to focal tissue injury in MS but lacks specificity to axonal content. Furthermore, T1WI and T2WI do not capture disease processes outside focal lesions; hence, there remains a pressing need to identify an MR imaging biometric that is both sensitive and specific to lesional and nonlesional axonal injury and loss.⁶

Toward this effort, several advanced multicompartment diffusion-based models have been recently developed and applied in MS (On-line Figure). The advantage of these methods over the more commonly used DTI (On-line Figure A) is the ability to isolate the signal contribution from different tissue compartments, thereby increasing the specificity for tissue subtypes and associated injuries. These models include neurite orientation dispersion and density imaging (NODDI), diffusion basis spectrum imaging (DBSI), multicompartment microscopic diffusion MR imaging with the spherical mean technique (SMT), and several models enabled with high-gradient diffusion MR imaging.

While some of these methods are very close to clinical translation and even available on clinical scanners, others lag behind. The need for high-gradient diffusion MR imaging and relatively

Received November 16, 2019; accepted after revision February 3, 2020.

From the Neuroimaging Unit (D.A.L., F.B.), Neuroimmunology Division, Department of Neurology; Division of Internal Medicine (D.A.L.); and Department of Radiology and Radiological Sciences (K.G.S., J.X.), Vanderbilt University Institute of Imaging Sciences, Vanderbilt University Medical Center, Nashville, Tennessee; Department of Radiology (D.A.L.), West Virginia University, Morgantown, West Virginia; and Department of Neurology (F.B.), VA Tennessee Valley Healthcare System, Nashville, Tennessee.

This work was supported by the National Institutes of Health grants R01EB017230 and T32EB001628 (K.G.S.), the National Institutes of Health grant K25 CA168936 (J.X.), and the National MS Society grant PP-1801-29686 (F.B.).

Please address correspondence to Francesca Bagnato, MD, PhD, Neuroimaging Unit, Neuroimmunology Division, Department of Neurology, Vanderbilt University Medical Center, 2201 Children's Way, Suite 1222, Nashville, TN 37212; e-mail: francesca.r.bagnato@vanderbilt.edu

 Indicates article with supplemental on-line tables.

 Indicates article with supplemental on-line photo.

<http://dx.doi.org/10.3174/ajnr.A6484>

long scanning times is still an important limiting factor to a widespread application of some of these models.

In this review, we appraise the current literature on the physics principles, histopathologic validation, and clinical applications of each of these techniques in both brain and spinal cord imaging of patients with MS. We also discuss limitations of each of the methods and future directions for translational research to provide additional validation for their role as a proxy for axonal injury in MS.

Neurite Orientation Dispersion and Density Imaging

The NODDI model was developed to provide a clinically feasible technique for in vivo mapping of neurite orientation, dispersion, and density.⁷ The advantage of NODDI is the requirement of a moderate number of diffusion-weighted images acquired with only 2 b-shells (b-values), in contrast to other multicompartment models that need large gradient strengths or extensive scan times.⁷

Principles of Physics. NODDI is a multicompartmental model that distinguishes 3 microstructural environments: intracellular (or intra-axonal), extracellular (or extra-axonal), and CSF compartments (On-line Figure B). By affecting diffusion in a unique way, each compartment results in a separate MR imaging signal.

The intracellular component is represented by the intradendrites and intra-axonal spaces. Due to the highly restricted nature of diffusion in this space, the intracellular component is modeled as a set of geometric “sticks,” or infinitely thin cylinders, with diffusion completely restricted perpendicular to these sticks but unhindered along them. The diffusivity along a stick is assumed to be fixed at $1.7 \times 10^{-3} \text{ mm}^2/\text{s}$. This set of sticks can be arranged in many distributions of orientations, eg, all coherently aligned in a single direction or more dispersed and spread over a range of orientations. The distribution of neurites (ie, sticks) is described by an average direction and a concentration parameter, which describes the orientation dispersion around the main direction.

The extracellular component represents the space around the neurites or axons, which is occupied by glial cells and neuronal cell bodies. In contrast to the restricted intracellular space, the diffusion in this space is “hindered” by neurites and is modeled as a simple anisotropic Gaussian distribution (as in DTI). The parallel and perpendicular diffusivities of the tensor in extracellular space are physically determined by the neurite morphology itself (ie, the intrinsic diffusivity and the neurite dispersion).

The CSF compartment is modeled as isotropic Gaussian diffusion with a fixed isotropic diffusivity ($3.0 \times 10^{-3} \text{ mm}^2/\text{s}$).

Thus, the NODDI model results in metrics describing orientation, shape, diffusivities, and fractions of the different compartments. As reported in On-line Table 1, NODDI produces a number of clinically relevant indices: 1) the intracellular volume fraction, represented by the neurite density index (referred to in the literature as NDI, V_{ic} , V_{in} , or f_{icvt}), that ranges from 0 to 1, denoting complete loss or full preservation of axons, respectively; 2) the neurite orientation dispersion index (ODI), which ranges from 0, representing perfectly coherently oriented WM structures, to 1, representing isotropically dispersed neurites; and 3)

the isotropic volume fraction (often abbreviated as IVF, V_{iso} , or f_{iso}), which can be interpreted as the voxel volume fraction of free water (ie, CSF).

Fixing the intrinsic and isotropic diffusivities and deriving the extracellular diffusivities from the dispersion index reduces the number of free parameters and simplifies the fitting of the model.⁸⁻¹⁰

Histopathologic Validation. Grussu et al¹¹ used the thoracic spine tissue of a patient with primary-progressive MS and a lumbar spine specimen of a patient with secondary-progressive MS, as well as of 2 healthy controls. The authors used circular variance as a histologic marker of neurite orientation variability, and the myelin staining fraction, astrocyte staining fraction, microglia staining fraction, and neurofilament staining fraction as markers of myelin, astrocytes, microglia, and axon contents, respectively. Correlations were seen between ODI and circular variance in the normal-appearing WM of both healthy controls ($r = 0.84$, $P < .001$) and patients with MS ($r = 0.60$, $P = .001$), as well as between ODI and the myelin staining fraction in MS samples ($r = 0.40$, $P < .05$). Negative correlations were seen between NDI and circular variance ($r = -0.78$, $P < .001$) in healthy controls and between NDI and the myelin staining fraction ($r = 0.74$, $P < .001$), neurofilament staining fraction ($r = 0.56$, $P < .01$), and the microglia staining fraction ($r = 0.49$, $P < .01$) in patients with MS. No significant correlations were observed between IVF and histology markers. The authors found similar but less specific results with DTI-derived indices, in that several DTI-derived metrics correlated with histopathologic counterparts of myelin injury (like NODDI) as well as astrocyte/microglia infiltrates. In addition, none of the DTI indices showed a correlation with circular variance. These key findings highlight the ability of NODDI to show a different layer of pathology not captured by conventional DTI, eg, changes in the complexity of neurite arborizations.

Clinical Applications. Several cross-sectional studies have been performed to test the clinical feasibility and the ability of NODDI to differentiate tissue injury in MS and its associations with patients' disabilities. NODDI acquisition has been reported as ~22 minutes for whole-brain imaging ($0.4 \times 0.4 \times 2 \text{ mm}^3$ resolution, 2 b-shells, and 90 directions)¹² and ~18 minutes for a single section of the cervical spinal cord ($1.25 \times 1.25 \text{ mm} \times 10 \text{ mm}^3$, 2 b-shells, and 96 directions).¹³

We detail significant clinical findings reported in all published clinical studies in On-line Table 2. In summary, it was noted that when reaching a statistically significant difference, NDI/ V_{ic} values were always lower in lesions compared with normal-appearing WM,^{12,14-16} in normal-appearing WM compared with the normal WM of healthy controls (both in brains^{14,16,17} and spinal cord^{13,17}), and in the spinal cord normal-appearing GM compared with the GM of healthy controls.¹³ These results were consistent across patients with relapsing-remitting¹²⁻¹⁷ or secondary-progressive MS.^{12,16,17} However, thus far, only values of NDI measured in both the cortex¹⁸ and the spinal cord¹⁷ were found to be associated with clinical disability measured with the Expanded Disability Status

Scale¹⁹ in patients with both relapsing-remitting^{17,18} and secondary-progressive^{17,18} MS.

On the contrary, ODI measurements yielded more contradictory results because ODI measurements were higher in lesions compared with normal-appearing WM in some studies focused on patients with relapsing-remitting MS^{13,14,18} and lower in others focused on either relapsing-remitting or mixed MS populations.^{12,15} Similarly, while Schneider et al¹⁵ found lower levels of ODI in the brain normal-appearing WM of patients with relapsing-remitting MS; By et al¹⁵ reported opposite trends in the spinal cord of a similar population of patients. Only cortical ODI measures were associated with clinical decline in patients with both relapsing-remitting^{14,18} and secondary-progressive¹⁸ MS.

Summary of Advantages and Limitations. NODDI appears to offer a clinically feasible technique that adds a layer of pathologic sensitivity and specificity to the detection of MS disease. A high interstudy variability is observed with ODI, thus making its interpretation complex. This finding is not surprising because by depicting the degree of tissue organization, ODI is a more granular, and therefore variable, measure of disease variability. It is proposed that ODI is more informative if used to assess longitudinal changes of individual patients rather than to assess comparisons between patients. On the contrary, although not always sensitive to disease, NDI/ V_{ic} appears to capture some degree of change in axonal content, which is also measurable in perilesional tissue.¹⁶

A few technical limitations need to be acknowledged regarding this model: 1) NODDI simplifications limit the model to simple fiber geometries, 2) the fixed diffusivities may not be true in altered physiology of the disease, and may bias measurements, and 3) debate remains on the relationship (and absolute values) of the intrinsic intra- and extracellular diffusivities.⁸⁻¹⁰

Thus, further work is needed to untangle these technical challenges, and to investigate the efficacy of NODDI-derived metrics as biomarkers of neurodegeneration, by assessing the sensitivity to tissue injury and clinical measures in larger cohorts of patients followed longitudinally over time.

Multicompartment Microscopic Diffusion MR Imaging with the Spherical Mean Technique

The SMT estimates microscopic features specific to the intra- and extraneurite compartments in the CNS. The use of the spherical mean technique is the most relevant advantage of this method, in that the SMT minimizes the confounding effects derived from axonal fiber crossings, curving, and orientation dispersion. SMT is suitable for clinical applications that require information on axonal volume fraction as well as axonal directions if one obtains spherical deconvolution.

Principles of Physics. SMT requires ≥ 2 b-shells (each with multiple diffusion directions) and assumes diffusion-weighted signals arising from intra- and extra-axonal spaces (On-line Figure C), resulting in the apparent intra-axonal volume fraction (V_{ax}) and the apparent extra-axonal volume fraction. Instead of approximating the whole intra- and extra-axonal spaces using single diffusion tensors, SMT assumes that signals arise from many “per-axon” diffusion tensors in arbitrary directions.²⁰ By averaging the same b-value diffusion MR imaging signals over all directions,

one can remove the orientation dependence of signals. Moreover, SMT assumes the following: 1) the intra-axonal radial diffusivity (RD) is zero due to the very small axon sizes in the CNS, and 2) the axial diffusivity (AD) is the same in both intra- and extra-axonal spaces due to the lack of restriction per axon. By such means, SMT can separate intra- and extra-axonal signals and 2 independent microstructural parameters, ie, the V_{ax} and the apparent intra-axonal diffusivity (D_{ax}) can be fit from the data. Other microstructure parameters, such as extra-axonal RD, can be calculated from V_{ax} and D_{ax} (On-line Table 1).

Histopathologic Validation. There are no studies in either humans with MS or animal models of MS that validated SMT-derived metrics against histopathologic counterparts; however, there is histopathologic validation of SMT in other models of diseases. Kaden et al²¹ studied the mouse model of the tuberous sclerosis complex and evaluated microscopic features specific to intra- and extraneurite compartments. The tuberous sclerosis animal model is more suitable for detecting CNS axonal injury than the MS model of experimental autoimmune encephalomyelitis because it is free from the inflammatory component that contaminates data from experimental autoimmune encephalomyelitis. V_{ax} and D_{ax} were measured in several WM tracts of the brain, including the genu, midbody, splenium of the corpus callosum, and anterior commissure in both tuberous sclerosis and control mice. V_{ax} values were lower ($P < .05$) and D_{ax} values were higher ($P < .05$) in the WM of animals with tuberous sclerosis compared with controls. Furthermore, a decrease in the myelinated axon fraction (with the myelin fraction excluded, $P < .001$) was mirrored by a reduction of the MR imaging-based V_{ax} . Although obtained with a different disease model, the provided validation against axonal histology is fundamental. It is applicable to any condition affecting myelin and axonal integrity and supports the ability of SMT to quantify axonal content without artifactual effects from fiber-crossing and orientation dispersion.

Clinical Application. Only 2 studies investigating the feasibility and applicability of SMT in the brains²² and spinal cords²³ of patients with MS have been performed thus far. The authors reported acquisition times between ~ 18 minutes²³ (single-section C-spine, $1.25 \times 1.25 \times 10$ mm resolution, 2 b-shells, with 32 and 64 directions) and ~ 22 minutes (full brain coverage, $0.4 \times 0.4 \times 2$ mm resolution, 90 directions).²² The implementation of a recently developed multiband technique can remarkably reduce the scan time while keeping similar image quality. For example, a multiband factor of 3 can reduce the total scan time of SMT from ~ 22 minutes to ~ 10 minutes.

In brains²² and spinal cords²³ of patients with MS, V_{ax} and D_{ax} (brain only²²) differed between lesions and normal-appearing WM. Decreased values of V_{ax} were also observed in normal-appearing WM compared with normal WM of healthy controls (spinal cord only²³). Reduction in acquisition schemes by 50% did not affect the sensitivity of SMT in distinguishing all 3 tissue subtypes.²³

Grussu et al²⁴ studied the diffusion time-dependence of IVF, ODI, V_{ax} , and D_{ax} in 3 healthy controls and quoted percentage

changes of these parameters in the diffusion time range of 29–76 ms. Increases in IVF (4.1%) and V_{ax} (2%) and decreases in the ODI (–16%) and D_{ax} (–5.4%) as a function of the diffusion time were noted in the motor columns of the spinal cord. Furthermore, increases in the IVF (3.7%) and decreases in the ODI (–15%), V_{ax} (–5.1%), and D_{ax} (–11.5%) were measured in the WM of the sensory columns of the spinal cord. The results suggest a diffusion time-dependence of NODDI- and SMT-derived metrics, which will provide new opportunities to optimize these methodologies for spinal cord imaging.

Summary of Advantages and Limitations. By taking the averages of diffusion signals over all directions and making no assumptions about the orientation of fibers, SMT removes the orientation dependence of diffusion MR imaging signals. These elements simplify data analysis and improve the SNR because they remarkably reduce the interscan variability. Histopathologic evidence supports the ability of SMT to isolate signal contributions from axons. In clinical studies, both V_{ax} and D_{ax} have shown the potential to differentiate tissue subtypes in the brains and spinal cords of patients with MS. Even by reducing the acquisition time by 50%, the SMT metrics were found to be equally sensitive in differentiating these tissue subtypes.²³ Both metrics, however, have failed to show correlation with the clinical measure of disease. This issue may be related simply to the relatively small sample size of cross-sectional studies performed thus far. Larger studies with longitudinal designs are warranted to elucidate the role of SMT-derived metrics as biomarkers of neurodegeneration in MS.

Diffusion Basis Spectrum Imaging

DBSI was proposed to resolve multiple tensor-like populations of water that may arise not only in healthy tissue but also from axon injury, inflammation, and demyelination.²⁵ Despite solid histopathologic validation studies, clinical applications of this technique are limited.

Principles of Physics. DBSI models diffusion as a combination of multiple discrete anisotropic tensors and a spectrum of isotropic diffusion tensors (On-line Figure D). The discrete anisotropic tensors are intended to represent myelinated and unmyelinated axons oriented in varying directions. The isotropic tensors, then, represent the integration of multiple pools of water, typically separated into the restricted spectrum from $0 \leq$ apparent diffusion coefficient $\leq 0.3 \times 10^{-3} \text{ mm}^2/\text{s}$, which may reflect cellularity. The nonrestricted isotropic diffusion spectrum from $0.3 \times 10^{-3} \text{ mm}^2/\text{s} <$ apparent diffusion coefficient $< 3.0 \times 10^{-3} \text{ mm}^2/\text{s}$ reflects extracellular edema and CSF. Thus, in DBSI, the diffusion signal is modeled as a summation of many diffusion tensors and an integration of free water with varying diffusivities, involves fitting many free variables, and uses a complex signal-fitting approach.

DBSI results in estimates of several anisotropic diffusion components (representing intra-axonal water molecules), each weighted by signal intensity fractions (referred to as their fiber ratios), oriented in the direction of the fiber population, and associated with their own parallel and perpendicular diffusivity.²⁵ Thus, just like DTI, DBSI results in metrics of RD, AD,

fractional anisotropy, and the fraction of anisotropic components (called the fiber fraction [FF]) (On-line Table 1). In addition, the fraction of water molecules of highly restricted isotropic structures can be measured (referred to as the restricted isotropic diffusion fraction or as the cell ratio in the original implementation), as well as that of the less restricted isotropic water (referred to as the water ratio).

Histopathologic Validation. Shirani et al²⁶ studied histopathologic correlates of DBSI in comparison with DTI in a single tumefactive lesion of a patient with newly diagnosed MS. DTI-derived AD and RD and DBSI-derived RD were increased, while DTI- and DBSI-derived fractional anisotropy were decreased in the lesion compared with the normal WM. DBSI-derived FF was also minimally decreased in the lesional area. Histopathologic analyses showed features of demyelination with increased inflammation and cellularity, but little axonal damage. Overall, the authors concluded that DBSI more selectively depicted demyelination and cellular increase and was not affected by the presence of edema, which, instead, biased the DTI-derived AD values.

Wang et al²⁷ studied postmortem examinations of the cervical spinal cords of 2 patients with relapsing-remitting MS and 1 with primary-progressive MS. The authors found correlations between FF and silver stain ($r = 0.7\text{--}0.8$, $P < .001$, in 3/3 samples); DBS-derived RD and Luxol fast blue stain ($r = -0.4\text{--}-0.84$, $P < .05$, in 3/3 samples); and restricted fraction and hematoxylin stain, reflecting the number of nucleated cells ($r = 0.3\text{--}0.8$, $P < .05$, in 2/3 samples). No significant correlations were seen between DBSI-derived AD and silver stain.

To assess the performance of DBSI and DTI metrics in the presence of CSF contamination, Wang et al²⁷ compared values derived from regions in the center of the corpus callosum (representing pure axonal fibers) and from areas of the WM bordering the lateral ventricles (representing CSF contamination) in 5 healthy controls. DBSI-derived AD and RD for each of these voxels were indistinguishable, while CSF contamination substantially altered DTI-derived AD and RD.

Furthermore, DBSI and DTI values were derived from regions at the crossing between the corona radiata and the corpus callosum; and within the corona radiata and the corpus callosum in 5 healthy controls, to assess the effect of fiber-crossing. DBSI AD and RD values were similar, while DTI AD and RD values differed between the corpus callosum and regions at the crossing between the corpus callosum and the corona radiata. DBSI AD values did not differ between the pure corona radiata and corona radiata fibers extracted from the region of crossing with the corpus callosum.

In conclusion, contrary to DTI, DBSI-derived AD and RD values were not influenced by CSF contamination and fiber-crossing.

Clinical Application. Shirani et al²⁸ applied DBSI in patients with relapsing-remitting MS ($n = 22$, disease duration = 2.0–18.8 years), secondary-progressive MS ($n = 16$, disease duration = 15.4–39.0 years), and primary-progressive MS ($n = 17$, disease duration = 6.5–18.3 years). They used recursive partitioning, a nonparametric decision tree-based regression and classification, to assess the ability of DBSI-derived metrics to classify patients with different disease subtypes. FF and restricted isotropic fraction classified 35/55 patients (63%) into the

correct MS subtype. Similarly, FF, nonrestricted isotropic fraction and RD measured in the normal-appearing WM of the corpus callosum correctly classified 37/55 patients (67%). No differences were seen in the FF, isotropic restricted fraction, isotropic nonrestricted fraction, RD and AD between WM lesions and normal-appearing WM among patients with relapsing-remitting, secondary-progressive, and primary-progressive MS.

Summary of Advantages and Limitations. The performance of DBSI has been extensively validated against histopathology in humans, and DBSI was shown to perform better than conventional DTI in the presence of edema. Accordingly, DBSI has shown promising results for assessing axonal quantity (DBSI-AD and -FF) while correcting for signal impurity derived from fluid contamination and fiber-crossing. Clinical applications of this methodology are in their infancy. Initial studies support the notion that DBSI correctly classifies the phenotype of about two-thirds of patients with MS. Additional studies are necessary to further elucidate its role *in vivo*. Similarly, sensitivity and specificity validations are lacking in simulated and physical phantom environments, and further investigation of precision and bias is necessary.

High-Gradient Diffusion MR Imaging

Principles of Physics. This method is similar to the previously developed AxCaliber method,²⁹ which maps the mean axon diameter and water fractions of axons and CSF.³⁰ It assumes diffusion signals arising from 3 nonexchanging compartments: restricted diffusion in the intra-axonal space, hindered diffusion in the extra-axonal space, and free diffusion in CSF (On-line Figure E). Unlike NODDI and SMT, this method assumes that axons have nonzero diameters and typically require diffusion data with multiple diffusion times and multiple b-values. By assuming that axons are cylinders, analytic models can be fit to diffusion data to extract quantitative microstructural information, such as mean axon diameter and apparent intra-axonal volume fraction (On-line Table 1). Note that the obtained mean axon diameter is volume-weighted rather than an arithmetical mean value, the latter predominantly used previously in the pathology literature.³⁰ It is challenging to fit comprehensive analytic equations to diffusion-weighted signal data from a voxel consisting of axonal fibers in >1 direction (such as fiber-crossing, curving, and dispersion). Therefore, this method was initially used only in regions with 1 dominant axonal fiber direction, such as the corpus callosum or the spinal cord.^{31,32} A recent report, however, has extended the application of this method to different WM tracts in the brain.³³ This extended method assumes that axonal fibers are oriented in a principal direction, which makes it possible to average DWI signals perpendicular to this principal fiber orientation. By such a means, a volume-weighted axon diameter index can be obtained in all white matter tracts in the brain, as shown in On-line Figure E.

There are existing debates on the ability of this method to fit the axon diameter. Early studies of AxCaliber *in vivo* were found to overestimate axon diameters in the corpus callosum.³⁰ Gradient strengths can definitely alleviate this issue, yet it is recognized that the reported mean axon diameters in the corpus

callosum in healthy subjects are still overestimated compared with the histologic findings.^{31,34,35} Moreover, a recent study showed that the extra-axonal diffusion dominates the overall diffusion signals in the typical diffusion time range; thus, it should be used with caution to interpret the fitted axon diameter *in vivo*.³⁶ The high-gradient diffusion method requires special gradient coils with gradient strengths up to 300 mT/m, which is much stronger than the 30–80 mT/m gradient strength on typical commercial MR imaging systems. This requirement is an important obstacle to clinical translation.

Clinical Application. Huang et al^{31,37} studied the clinical feasibility and applicability of high-gradient diffusion MR imaging in MS. The authors reported a scanning time of ~51 minutes for a whole-brain acquisition at a 2-mm isotropic resolution.³⁷ Six patients with relapsing-remitting MS (disease duration, 1–11 years) and 6 healthy controls were initially imaged with the aim of characterizing axonal disease in MS lesions and normal-appearing WM. Increased axonal diameter, decreased restricted fraction, increased free water fraction, and reduced mean axon density were described in lesions compared with normal-appearing WM, but not between normal-appearing WM and normal WM.³¹

Recently, the same group³⁷ reported data from a larger patient population, illustrated in On-line Table 2. Similarly, Santis et al³⁸ found increased axonal diameters and decreased restricted volume fraction/axonal density in lesions compared with the normal-appearing WM of the corpus callosum, in normal-appearing WM compared with normal WM, as well as in the normal-appearing WM of patients with secondary-progressive MS compared with that of patients with relapsing-remitting MS.

Summary of Advantages and Limitations. Clinical studies show the potential for high-gradient diffusion MR imaging to differentiate tissues with different degrees of axonal pathology. The physics underlying the use of high-gradient diffusion MR imaging limit its ability to quantify axon diameter in the presence of fiber-crossing. Furthermore, no histopathologic validation has been performed, a factor that currently hampers extrapolating the full significance from the *in vivo* data. It is interesting to note that the axonal diameter measured using this technique were larger in patients as compared to that of healthy controls. The finding may reflect the well-known pathologic course of axon death.³⁹ Axons undergo remodeling with initial swelling before atrophy and cell death. Thus, the time when patients are imaged may determine the direction of group differences one can find.

CONCLUSIONS

There is an urgent need to discover a biometric of neurodegeneration and repair, which can be used to untangle MS disease progression before it manifests as an irreversible disability. Advanced, multi-shell-based diffusion methods have the potential to add pathologic specificity to imaging findings, and hence serve as biomarker of neurodegeneration and neuroregeneration. Additional work is required, however, to translate these methods to clinical application.

Most of these techniques have 2 main technical advantages. First, they use conventional, off-the-shelf diffusion MR imaging pulse sequences, which are widely available on clinical MR imaging

scanners. This use removes any obstacle toward their translation to routine clinical imaging. Second, most of these diffusion methods have their data analysis codes open to the public, making it easy to implement independent studies. However, technical improvements based on the implementation of multibands are warranted to enhance clinical reliability.^{40,41} These changes will aim for faster acquisitions with higher signal-to-noise ratio. Effort will also be devoted to the implementation of postprocessing techniques for the spinal cord and the development of atlases that can more accurately couple these advanced imaging metrics with anatomic landmarks.

From a histopathologic validation standpoint, the provided evidence is solid but remains limited because it is based on a small number of samples or animal studies using a different model of neurodegeneration. Ideally, postmortem studies on human brains are the closest ones for studying human disease. These studies, however, have the limitations of formalin fixation, which substantially alters diffusivity properties and shortens the T1 and T2 relaxation times of tissues compared with their in vivo state.⁴² Furthermore, there is a time-dependent effect of formalin fixation on diffusivity. Data show that scanning different brains at a consistent postfixation interval leads to different absolute measurements between samples, which could, in turn, lead to erroneous conclusions.⁴³

Histopathologic validation of lesions requiring biopsy is also an efficient method but has the caveat that lesions undergoing biopsy are usually atypically aggressive. While not resembling, in full, MS pathology, these evaluations still offer a solid validation method for the imaging-pathologic correlates. Similarly, animal studies, while again offering a disease model that may not resemble, in full, that of MS, do offer opportunities to validate histologic counterparts of imaging data. It is unlikely, however, that individual centers will be able to offer a full spectrum of validation; and to this end, collaborative efforts are certainly crucial to delineate the solidity and reproducibility of individual findings.

From a clinical standpoint, it appears that metrics derived from each of the discussed techniques are sensitive to different degrees of pathology in MS for both the brain and spinal cord. A common criticism of those methods is that changes measured in different tissue types using metrics derived from advanced diffusion models may, at times, be like those measured using conventional DTI or other quantitative techniques. Even if the criticism is valid, given the physics principles underpinning each of those techniques, advanced multicompartiment diffusion MR imaging models offer a novel and superior way to visualize and quantify pathology. Thus, even if the effect size is similar, all these models add a substantial layer of pathologic specificity to disease detection.

Whether this increased pathologic specificity corresponds to an improved ability to explain disability remains to be assessed. While data thus far do not seem to necessarily suggest so, none of the presented studies have been powered to address this question. It is also likely that across-time changes of these proposed measures, rather than single-time-point assessments, are reflective of across-time disease progression. Additional larger clinical studies to address this question are the next step. It is indeed likely, and most relevant clinically, that individual patient changes across time, rather than between-subject cross-sectional comparisons, are going to be both more informative and explicative of the pathologic and clinical evolution of MS. This consideration is

particularly relevant in lieu of the fact that axonal size and volume change with time as a function of the pathologic processes. Swelling and enlargement often at times precede shrinkage and transection,^{5,39} and this feature must be taken into consideration when comparing data from different patient cohorts or even when comparing patients with healthy controls in cross-sectional evaluations.

Last, but not less important, intercenter reliability measures must be estimated. Lack of intercenter and interscanner consistency is an important drawback and will consequently hinder clinical translation of any biomarker.

Future research based on cooperative effort aiming to fill the gap in the histopathologic, clinical, and technical knowledge as detailed above is most warranted.

ACKNOWLEDGMENTS

The authors would like to thank Dr Seth Smith for the design and conceptualization of the On-line Figure and Dr Karina Ciccone for thoroughly reviewing the manuscript for grammar and appropriateness of the delivered message.

Disclosures: Francesca Bagnato—*UNRELATED*: Speaker honoraria from EMD-Serono and Novartis. She serves/ed as site PI of multicenter studies sponsored by EMD-Serono and Novartis. Paid to the individual.

REFERENCES

1. Wallin MT, Culpepper WJ, Campbell JD, et al; US Multiple Sclerosis Prevalence Workgroup. **The prevalence of MS in the United States: a population-based estimate using health claims data.** *Neurology* 2019;92:e1029–40 CrossRef Medline
2. Bagnato F, Jeffries N, Richert ND, et al. **Evolution of T1 black holes in patients with multiple sclerosis imaged monthly for 4 years.** *Brain* 2003;126:1782–89 CrossRef Medline
3. Cotton F, Weiner HL, Jolesz FA, et al. **MRI contrast uptake in new lesions in relapsing-remitting MS followed at weekly intervals.** *Neurology* 2003;60:640–46 CrossRef Medline
4. Patrikios P, Stadelmann C, Kutzelnigg A, et al. **Remyelination is extensive in a subset of multiple sclerosis patients.** *Brain* 2006;129:3165–72 CrossRef Medline
5. Frischer JM, Bramow S, Dal-Bianco A, et al. **The relation between inflammation and neurodegeneration in multiple sclerosis brains.** *Brain* 2009;132:1175–89 CrossRef Medline
6. Fox RJ, Thompson A, Baker D, et al. **Setting a research agenda for progressive multiple sclerosis: the International Collaborative on Progressive MS.** *Mult Scler* 2012;18:1534–40 CrossRef Medline
7. Zhang H, Schneider T, Wheeler-Kingshott CA, et al. **NODDI: practical in vivo neurite orientation dispersion and density imaging of the human brain.** *Neuroimage* 2012;61:1000–16 CrossRef Medline
8. Hutchinson EB, Avram AV, Irfanoglu MO, et al. **Analysis of the effects of noise, DWI sampling, and value of assumed parameters in diffusion MRI models.** *Magn Reson Med* 2017;78:1767–80 CrossRef Medline
9. Kunz N, da Silva AR, Jelescu IO. **Intra- and extra-axonal axial diffusivities in the white matter: which one is faster?** *Neuroimage* 2018;181:314–22 CrossRef Medline
10. Lee HH, Fieremans E, Novikov DS. **What dominates the time dependence of diffusion transverse to axons: intra- or extra-axonal water?** *Neuroimage* 2018;182:500–10 CrossRef Medline
11. Grussu F, Schneider T, Tur C, et al. **Neurite dispersion: a new marker of multiple sclerosis spinal cord pathology?** *Ann Clin Transl Neurol* 2017;4:663–79 CrossRef Medline

12. Chen A, Franco G, Smith S, et al. **Measuring white matter axonal injury in patients with multiple sclerosis.** In: *Proceedings of the American Academy of Neurology Annual Meeting*, Philadelphia, Pennsylvania. May 4–10, 2019
13. By S, Xu J, Box BA, et al. **Application and evaluation of NODDI in the cervical spinal cord of multiple sclerosis patients.** *Neuroimage Clin* 2017;15:333–42 CrossRef Medline
14. Granberg T, Fan Q, Treaba CA, et al. **In vivo characterization of cortical and white matter neuroaxonal pathology in early multiple sclerosis.** *Brain* 2017;140:2912–26 CrossRef Medline
15. Schneider T, Brownlee W, Zhang H, et al. **Sensitivity of multi-shell NODDI to multiple sclerosis white matter changes: a pilot study.** *Funct Neurol* 2017;32:97–101 CrossRef Medline
16. Mustafi SM, Harezlak J, Kodiweera C, et al. **Detecting white matter alterations in multiple sclerosis using advanced diffusion magnetic resonance imaging.** *Neural Regen Res* 2019;14:114–23 CrossRef Medline
17. Collorone S, Cawley N, Grussu F, et al. **Reduced neurite density in the brain and cervical spinal cord in relapsing-remitting multiple sclerosis: a NODDI study.** *Mult Scler* 2019 Nov 4. [Epub ahead of print] CrossRef Medline
18. Spanò B, Giulietti G, Pisani V, et al. **Disruption of neurite morphology parallels MS progression.** *Neurol Neuroimmunol Neuroinflamm* 2018;5:e502 CrossRef Medline
19. Kurtzke JF. **Rating neurologic impairment in multiple sclerosis: an Expanded Disability Status Scale (EDSS).** *Neurology* 1983;33:1444–52 CrossRef Medline
20. Kaden E, Kruggel F, Alexander DC. **Quantitative mapping of the per-axon diffusion coefficients in brain white matter.** *Magn Reson Med* 2016;75:1752–53 CrossRef Medline
21. Kaden E, Kelm ND, Carson RP, et al. **Multi-compartment microscopic diffusion imaging.** *Neuroimage* 2016;139:346–59 CrossRef Medline
22. Bagnato F, Franco G, Li H, et al. **Probing axons using multi-compartmental diffusion in multiple sclerosis.** *Ann Clin Transl Neurol* 2019;6:1595–1605 CrossRef
23. By S, Xu J, Box BA, et al. **Multi-compartmental diffusion characterization of the human cervical spinal cord in vivo using the spherical mean technique.** *NMR Biomed* 2018;31:e3894 CrossRef Medline
24. Grussu F, Ianuş A, Tur C, et al. **Relevance of time-dependence for clinically viable diffusion imaging of the spinal cord.** *Magn Reson Med* 2019;81:1247–64 CrossRef Medline
25. Wang Y, Wang Q, Haldar JP, et al. **Quantification of increased cellularity during inflammatory demyelination.** *Brain* 2011;134:3590–3601 CrossRef Medline
26. Shirani A, Sun P, Schmidt RE, et al. **Histopathological correlation of diffusion basis spectrum imaging metrics of a biopsy-proven inflammatory demyelinating brain lesion: a brief report.** *Mult Scler* 2019;25:1937–41 CrossRef
27. Wang Y, Sun P, Wang Q, et al. **Differentiation and quantification of inflammation, demyelination and axon injury or loss in multiple sclerosis.** *Brain* 2015;138:1223–38 CrossRef Medline
28. Shirani A, Sun P, Trinkaus K, et al. **Diffusion basis spectrum imaging for identifying pathologies in MS subtypes.** *Ann Clin Transl Neurol* 2019;6:2323–27 CrossRef Medline
29. Assaf Y, Blumenfeld-Katzir T, Yovel Y, et al. **AxCaliber: a method for measuring axon diameter distribution from diffusion MRI.** *Magn Reson Med* 2008;59:1347–54 CrossRef
30. Alexander DC, Hubbard PL, Hall MG, et al. **Orientationally invariant indices of axon diameter and density from diffusion MRI.** *Neuroimage* 2010;52:1374–89 CrossRef Medline
31. Huang SY, Tobyne SM, Nummenmaa A, et al. **Characterization of axonal disease in patients with multiple sclerosis using high-gradient-diffusion MR imaging.** *Radiology* 2016;280:244–51 CrossRef Medline
32. Duval T, McNab JA, Setsompop K, et al. **In vivo mapping of human spinal cord microstructure at 300mT/m.** *Neuroimage* 2015;118:494–507 CrossRef Medline
33. Huang SY, Tian Q, Fan Q, et al. **High-gradient diffusion MRI reveals distinct estimates of axon diameter index within different white matter tracts in the in vivo human brain.** *Brain Struct Funct* 2019 Sep 28. [Epub ahead of print] CrossRef Medline
34. Huang SY, Nummenmaa A, Witzel T, et al. **The impact of gradient strength on in vivo diffusion MRI estimates of axon diameter.** *Neuroimage* 2015;106:464–72 CrossRef Medline
35. Aboitiz F, Scheibel AB, Fisher RS, et al. **Fiber composition of the human corpus callosum.** *Brain Res* 1992;598:143–53 CrossRef Medline
36. Burcaw LM, Fieremans E, Novikov DS. **Mesoscopic structure of neuronal tracts from time-dependent diffusion.** *Neuroimage* 2015;114:18–37 CrossRef Medline
37. Huang SY, Fan Q, Machado N, et al. **Corpus callosum axon diameter relates to cognitive impairment in multiple sclerosis.** *Ann Clin Transl Neurol* 2019;6:882–92 CrossRef Medline
38. Santis SD, Herranz E, Treaba CA, et al. **Whole brain in vivo axonal diameter mapping in multiple sclerosis.** In: *Proceedings of the International Engineering in Medicine and Biology Conference*, Berlin, Germany. July 23–27, 2019; 204–07
39. Kutzelnigg A, Lucchinetti CF, Stadelmann C, et al. **Cortical demyelination and diffuse white matter injury in multiple sclerosis.** *Brain* 2005;128:2705–12 CrossRef Medline
40. Feinberg DA, Setsompop K. **Ultra-fast MRI of the human brain with simultaneous multi-slice imaging.** *J Magn Reson* 2013;229:90–100 CrossRef Medline
41. Veraart J, Novikov DS, Christiaens D, et al. **Denoising of diffusion MRI using random matrix theory.** *Neuroimage* 2016;142:394–406 CrossRef Medline
42. Shepherd TM, Thelwall PE, Stanisz GJ, et al. **Aldehyde fixative solutions alter the water relaxation and diffusion properties of nervous tissue.** *Magn Reson Med* 2009;62:26–34 CrossRef Medline
43. Shatil AS, Uddin MN, Matsuda KM, et al. **Quantitative ex vivo MRI changes due to progressive formalin fixation in whole human brain specimens: longitudinal characterization of diffusion, relaxometry, and myelin water fraction measurements at 3T.** *Front Med (Lausanne)* 2018;5:31 CrossRef Medline
44. Cutter GR, Baier ML, Rudick RA, et al. **Development of a multiple sclerosis functional composite as a clinical trial outcome measure.** *Brain* 1999;122:871–82 CrossRef Medline

Methylphenidate Effects on Cortical Thickness in Children and Adults with Attention-Deficit/Hyperactivity Disorder: A Randomized Clinical Trial

K.B. Walhovd, I. Amlien, A. Schranter, D.A. Rohani, I. Groote, A. Bjørnerud, A.M. Fjell, and L. Reneman



ABSTRACT

BACKGROUND AND PURPOSE: Although methylphenidate is frequently used to treat children with attention-deficit/hyperactivity disorder, it is currently unknown how methylphenidate affects brain development. In a randomized controlled trial, we investigated whether the cortical effects of methylphenidate are modulated by age.

MATERIALS AND METHODS: Between June 1, 2011, and June 15, 2015, we conducted a randomized, double-blind, placebo-controlled trial (Effects of Psychotropic Drugs on Developing Brain-Methylphenidate) in 99 males with attention-deficit/hyperactivity disorder (according to *Diagnostic and Statistical Manual of Mental Disorders, 4th Edition*, criteria) from referral centers in the greater Amsterdam area in the Netherlands. The trial was registered on March 24, 2011 (identifier NL34509.000.10) and subsequently at the Netherlands National Trial Register (identifier NTR3103). Participants (first enrolled October 13, 2011) were 10–12 years or 23–40 years of age and randomized to treatment with either methylphenidate or a placebo for 16 weeks. Our main outcome was a change in cortical thickness in predefined ROIs as measured by MR imaging pre- and posttreatment.

RESULTS: We observed a time \times medication \times age interaction ($F[1,88.825] = 4.316, P < .05$) for the right medial cortex ROI, where methylphenidate treatment yielded less cortical thinning in children, but not in adults or the placebo groups.

CONCLUSIONS: Our finding that the effects of methylphenidate on right medial cortical thickness differ between children and adults infers that the drug affects gray matter development in this brain region. This warrants replication in larger groups with longer follow-up to determine whether this effect can also be observed in other cortical brain regions and whether it may have long-term consequences.

ABBREVIATIONS: ADHD = attention-deficit/hyperactivity disorder; MNI = Montreal Neurological Institute; RCT = randomized controlled trial

The psychostimulant methylphenidate is among the drugs most frequently prescribed to children for treatment of attention-deficit/hyperactivity disorder (ADHD).^{1,2} Randomized controlled trials (RCTs) have shown that methylphenidate suppresses children's physical growth during treatment,^{3,4} but they have not included measures of brain development. However, longitudinal brain maturation studies using MR imaging indicate that children with ADHD, on average, deviate from controls in

their brain developmental trajectories, including regionally thinner cortices and lower basal ganglia volumes.^{5,6} Recent highly powered cross-sectional studies on subcortical volumes and cortical thickness and surface area have shown ADHD case-control differences, with higher effect sizes in children than adults.^{7,8} In these observational cross-sectional studies, the authors found no influence of psychostimulant medication on subcortical volumes or cortical thickness of the areas showing group differences, but in smaller surface areas of regions of the frontal cortex in children taking the medication.^{7,8} Prospective studies on children with ADHD using-versus-not using psychostimulants have yielded

Received February 1, 2020; accepted after revision April 8.

From the Department of Psychology (K.B.W., I.A., D.A.R., A.B., A.M.F.), Center for Lifespan Changes in Brain and Cognition, and Institute of Physics (A.B.), Faculty of Mathematics and Natural Sciences, University of Oslo, Oslo, Norway; Departments of Radiology and Nuclear Medicine (K.B.W., A.M.F.) and Diagnostic Physics (I.G., A.B.), Oslo University Hospital, Oslo, Norway; and Department of Radiology and Nuclear Medicine (A.S., A.B., L.R.), Amsterdam UMC, Academic Medical Center, Amsterdam, the Netherlands.

This study was funded by faculty resources of the Academic Medical Center, University of Amsterdam, and grant 11.32050.26 from the European Research Area Network Priority Medicines for Children (Sixth Framework Programme).

Clinical Trial registry name and registration number: Central Committee on Research Involving Human Subjects (an independent registry, identifier NL34509.000.10) and the Netherlands National Trial Register (identifier NTR3103).

Please address correspondence to Liesbeth Reneman, MD, PhD, Amsterdam UMC, Academic Medical Center, Department of Radiology and Nuclear Medicine, G1-222 Meibergdreef 9 1105 AZ Amsterdam, the Netherlands; e-mail: l.reneman@amsterdamumc.nl

Indicates open access to non-subscribers at www.ajnr.org

Indicates article with supplemental on-line appendix, photo, and trial protocol.

Indicates article with supplemental on-line photo.
<http://dx.doi.org/10.3174/ajnr.A6560>

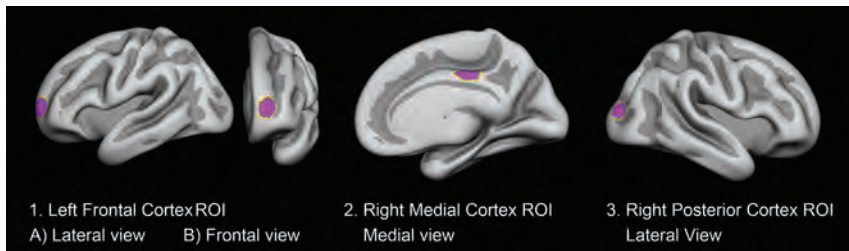


FIG 1. ROIs investigated. Cortical ROIs were determined on the basis of the MNI coordinates of the vertices corresponding to peak group differences in the observational prospective study of psychostimulant treatment and the developing cortex by Shaw et al.⁹ Labels were created at the corresponding vertices on the FreeSurfer average surface. The labels were dilated 15 times, resulting in hexagon-shaped ROIs, covering approximately 550 mm² when transformed to the individual participants' brain surfaces. Shown here are the following: 1) the left frontal cortex ROI in lateral (A) and frontal (B) view; 2) the right medial cortex ROI in the medial view; and 3) the right posterior cortex ROI in the lateral view.

some evidence for medication-associated differences for cortical thickness changes,⁹ but an absence of such evidence for basal ganglia trajectories.⁵ However, such observational studies are limited by possible selection effects. Moreover, the cortical differences observed have been in terms of greater thinning of the cortex in the right medial frontal motor region, the left middle/inferior frontal gyrus, and the right posterior parieto-occipital region in children with ADHD not taking psychostimulants,⁹ and different effects of psychostimulant medication can be expected during development, when the brain changes at a higher rate than in adulthood.¹⁰

We recently reported age-dependent effects of methylphenidate on changes in cerebral blood flow of the dopaminergic system (our predefined primary aim), as measured by pharmacologic MR imaging, in young-versus-adult patients with ADHD.¹¹ Because our RCT is the first study that examines the effects of methylphenidate on brain development, this means that there are only limited and indirect data available to perform a sample-size calculation. Our goal for this research was to be able to detect differences in the age-dependent effect of methylphenidate on the brain if these differences are in the magnitude of a standardized effect size of 1.25 (see also On-line Research Protocol, page 18). A secondary aim of the Effects of Psychotropic Drugs on Developing Brain (ePOD) study is to assess the effects of methylphenidate treatment on cortical changes in children and adults with ADHD in a double-blind RCT. Due to ongoing development of the dopaminergic system during childhood and adolescence, we hypothesized that methylphenidate treatment would be associated with reduced cortical thinning (rate of change) in the left frontal, right posterior, and right medial cortices⁹ and that this would be observed in children only, not in adults. In addition to testing this hypothesis, we also explored possible cortical effects in a vertex-wise whole-brain analysis and possible relations between cortical change and change in ADHD symptom severity.

MATERIALS AND METHODS

Trial Design

The ePOD-Methylphenidate RCT was a 16-week double-blind, randomized, placebo-controlled, multicenter trial of the use

of methylphenidate and a blinded end point evaluation in psychostimulant treatment-naïve patients with ADHD.^{11,12} The length of the trial was dictated by the waiting list for treatment. In the Netherlands at the time of the execution of this trial, a waiting list of 17 weeks was very common before (child and adolescent) psychiatric evaluation could take place and treatment could commence. It is in this timeframe that the current study was executed, to ensure only a very small or no delay in the placebo group before active treatment could take place. The timeframe was thus chosen so that patients treated with a placebo would not be harmed by study participation (for further details, see the On-line Research Protocol). The primary outcome measure of the ePOD-Methylphenidate trial was to report on the effect modification by age of the methylphenidate treatment on the outgrowth of the dopaminergic system.¹¹

Here, we report our secondary outcome. A prior article dealt with the effect of methylphenidate on white matter development,¹³ whereas this article assesses the effects on the rate of change in cortical thickness of selected ROIs assessed using structural MR imaging in exactly the same sample of children and adults with ADHD, randomly assigned to either placebo or active treatment with methylphenidate, pre- and posttreatment. The selection of ROIs was based on prior results from an observational prospective study of psychostimulant treatment and the developing cortex by Shaw et al.⁹ The ROIs chosen for investigation are shown in Fig 1. The study protocol applied the code of medical ethics and was registered by the Central Committee on Research Involving Human Subjects (an independent registry) on March 24, 2011 (identifier NL34509.000.10) and subsequently at the Netherlands National Trial Register (identifier NTR3103), with enrollment of the first patient on October 13, 2011. In addition, the institutional review board of the Academic Medical Center approved the study. The full protocol is described elsewhere.¹² The trial ended on June 15, 2015, and was monitored by the Clinical Research Unit of the Academic Medical Center, University of Amsterdam, the Netherlands. All patients and parents or legal representatives of the children provided written informed consent.

Participants

Participants were psychostimulant treatment-naïve, 50 boys (10–12 years of age) and 49 men (23–40 years of age), diagnosed as having ADHD and recruited through clinical programs at the Department of Child and Adolescent Psychiatry at Triversum (Alkmaar, the Netherlands), De Bascule Academic Center for Child and Adolescent Psychiatry (Amsterdam), and PsyQ mental health facility (The Hague). As laid out in the protocol, the cutoff point of 10–12 years of age for the pediatric population was chosen because the peak prevalence of ADHD has been found to be

10 years of age,¹⁴ and also because several MR imaging parameters show greater age differences in early than later childhood.¹⁵ One hundred thirty-one individuals were screened for eligibility. All included met strict criteria for ADHD (all subtypes) according to the *Diagnostic and Statistical Manual of Mental Disorders, 4th Edition (DSM-IV)*¹⁶ and were diagnosed by an experienced psychiatrist. Diagnoses were confirmed with diagnostic interviews.^{17,18} More detailed inclusion and exclusion criteria are available in the On-line Appendix and On-line Research Protocol (see also Schrantee et al).¹¹

Intervention, Randomization, and Blinding

Patients were randomly assigned to either methylphenidate or placebo treatment.¹¹ The treating physicians prescribed the study medication under double-blind conditions on clinical guidance in accord with Dutch treatment guidelines. Medication dosages were titrated per individual, under supervision of a child and adolescent psychiatrist. Adult participants received coaching sessions, and parents of children received psychoeducation. Adherence to the study medication was monitored, and the compliance rate (0.0–1.0) was calculated (On-line Appendix).

Outcomes

Primary Outcome Measure of ROI Cortical Thickness Change. Imaging was performed using 1 of two 3T MR imaging systems (scanner 1, Intera; scanner 2, Achieva; Philips Healthcare). All participants were scanned on the same scanner pre- and postintervention. Anatomic 3D T1-weighted fast-field echo sequences were acquired and used for cortical surface analyses. Cortical thickness measures were derived using FreeSurfer (<http://surfer.nmr.mgh.harvard.edu>), Version 5.3. Cortical thickness was estimated vertex-wise across the brain surface using an automated approach.^{19–23} Scans were rated for the presence of motion and were excluded unless rated (1 = no sign of motion, or 2 = minor signs of motion, but no major distortion and acceptable reconstruction). An ROI approach was considered the viable option, given the necessarily restricted participant numbers of this RCT. Montreal Neurological Institute (MNI) coordinates of the vertices corresponding to peak group differences in the observational study⁹ were converted to Talairach coordinates, and labels were created at the corresponding vertices on the FreeSurfer average surface. The MNI coordinates for peak group differences forming the basis for the cortical ROIs were as follows: left frontal: –26, 61, 6; right medial frontal: 6, –23, 40; right posterior: 30, –93, 12. The labels were dilated 15 times, resulting in hexagon-shaped ROIs covering approximately 550 mm² when transformed to the individual participant's brain surface (Fig 1). Surface measures were extracted from the individual participants (Fig 1 and On-line Appendix).

Statistical Analyses

Analyses of ROI values were performed using SPSS, Version 24 (IBM), per reviewer request; analyses on handedness were later added, performed using SPSS, Version 26 (<https://www.ibm.com/analytics/data-science/predictive-analytics/spss-statistical-software>). One-way ANOVA was used to test differences in baseline brain characteristics, scan interval, scan movement ratings, compliance

rates, and age for children and adults separately. Linear mixed models with age group (children, adults) × treatment group (placebo, methylphenidate) × time (pre-, posttreatment), as well as the main effects and interactions of each, were set up to test interaction effects on rates of change, using maximum likelihood estimation, with the covariance structure set to compound symmetry. For further analysis of medication effects per age group, we split the sample by age and set up similar linear mixed models with treatment group (placebo, methylphenidate) × time (pre-, posttreatment), as well as the main effects and interactions of each, to test interaction effects on rates of change within each age group for all ROIs separately. The significance level was set at $P < .05$.

While the ROI analysis was the primary outcome measure given the small number, an exploratory vertex-wise analysis on the whole cortical mantle²⁴ was also performed (see On-line Appendix for details). In addition, cortical ROI change scores were correlated with the change in symptom severity pre- and posttreatment to explore possible relations.

RESULTS

Randomization and Baseline Characteristics

A total of 99 patients with ADHD were randomized to methylphenidate or placebo treatment. After randomization, 1 adult disclosed previous methylphenidate treatment and was therefore excluded from the analyses. On inspection of the scans, it was found in the child placebo group that one subject had a relatively large posterior cyst causing possible displacement of brain ROIs and another had an abnormality in the right frontal lobe that seemed to affect reconstructions of surfaces in the lateral cortex (by neuroradiologic follow-up thought to possibly be a benign tumor). Both of these individuals were therefore excluded from the current analyses. Forty-eight children and 47 adults were included in the primary analysis (CONSORT flow diagram, based on a template from <http://www.consort-statement.org/consort-statement/flow-diagram>, Fig 2). Of these, 1 child and 2 adults had invalid baseline data, and 1 child had invalid follow-up data due to scan motion or poor scan quality, leading to flawed image reconstruction. Note that 1 of the adults whose baseline data did not pass quality control was also among the ones who discontinued intervention. Treatment medication adherence data were missing for 1 child in the placebo group and for 3 children in the methylphenidate treatment group. No serious adverse events were noted in any of the individuals studied.

Sample characteristics are given in the Table (for in-depth clinical descriptives and behavioral measures used, see the On-line Appendix and Schrantee et al,¹¹ Schmand et al,²⁵ Rosler et al,²⁶ Oosterlaan et al,²⁷ and Wechsler²⁸). There were no significant differences in baseline age, ADHD symptom severity, reported handedness (proportion right-handed), estimated intelligence quotient, or ROI brain characteristics or scan interval or movement ratings between the placebo and medication groups. For the children, no tendency ($P < .10$) toward differences between treatment groups was observed. However, for the adults, there was a tendency toward a thicker cortex in the right posterior ROI ($P = .072$) at baseline in the placebo group and a greater compliance rate in the treatment group ($P = .096$). Because outcome ROI analyses were

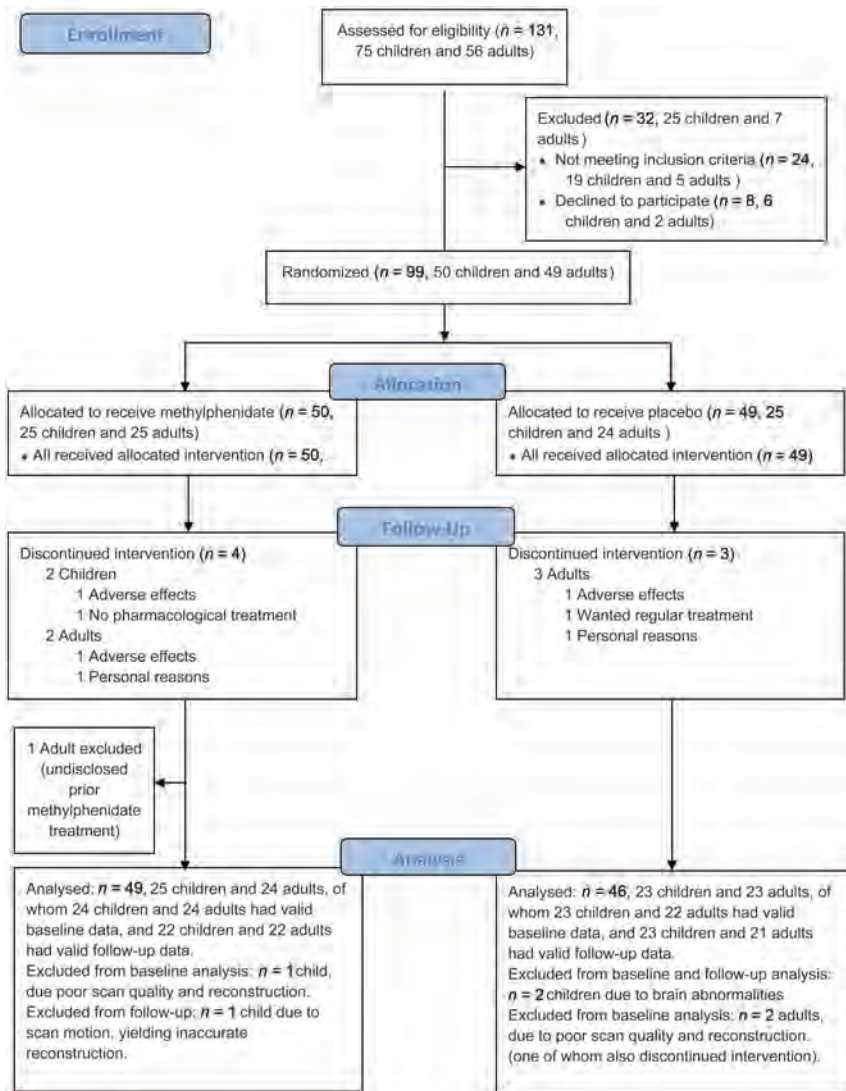


FIG 2. Consolidated standards of reporting trials flow diagram. Patients were randomized to either methylphenidate or placebo.

for longitudinal cortical thickness change only, we chose not to correct for intracranial volume in the analyses.

Main Outcome of the ROI Cortical Thickness Change

Cortical thickness values for the groups pre- and posttreatment are shown in Fig 3, and individual data are shown in On-line Fig 1. Analyses using linear mixed models with scan time as a repeat measure \times age \times medication group showed, for the right medial cortex ROI a main effect of age ($F[1,95.606] = 199.713, P < .001$), likely reflecting expected age-related thinning, and an interaction of medication group \times age group \times time ($F[1,88.825] = 4.316, P = .041$). As shown in Fig 3, in the children, the methylphenidate group showed increasing thickness, while the placebo group showed cortical thinning, whereas in adults, both groups showed cortical thinning. Although there were no significant baseline differences, slight differences were seen at baseline throughout the ROIs across age and medication groups, which also contributed to

the identified interaction. The individual data plots did, however, not reveal striking outliers at any time point. Relatively lesser thinning in children in the methylphenidate treatment group was also seen in the right posterior cortex ROI, but not in the left frontal cortex ROI. However, no significant 3-way interaction effects of medication group \times age group \times time were found, except for the right medial cortex ROI. Other significant fixed effects in these analyses were limited to a main effect of age on the left frontal cortex ($F[1,96.308] = 46.788, P < .001$) and the right posterior cortex ($F[1,96.289] = 51.361, P < .001$), for which an interaction of age group \times medication group was also found ($F[1,96.289] = 3.973, P = .049$). This effect appeared to be due to the child medication group having, on average, thicker cortices with the adult medication group having, on average, thinner cortices than the same-age placebo groups.

The analyses per age group confirmed an interaction of medication group \times time ($F[1,44.893] = 4.793, P = .034$) in the young group only for the right medial cortex ROI. In the per-age group analyses, no other significant interaction effects were found, only a main effect of the medication group in the adults for the right posterior cortex ROI ($F[1,47.274] = 4.483, P = .040$), reflecting a thicker cortex in the adult placebo group at both time points. However, there were no trends toward the interaction of medication group \times time for this ROI ($P = .986$). For comparison with previous results from the longer observational study from which the ROIs were derived,⁹ the present change rate for the right medial cortex ROI was converted to a rate of change per year, shown in Fig 4. The mean rates of change in cortical thickness for this region were quite similar across studies, but confidence intervals were larger in the present study.

The exploratory vertex-wise whole-brain analyses did not reveal any significant interaction between group and treatment on the thickness rate of change in any region when corrected for multiple comparisons (false discovery rate, $P < .05$). One-way ANOVA confirmed an effect of group on symptom change in the present sample, with post-, minus pre-treatment scores being lower for the methylphenidate than for the placebo groups ($F[1,42] = 5.551, P = .023$, and $F[1,41] = 5.857, P = .020$ for children and adults, respectively). Mean posttreatment ADHD symptom-severity scores in children were 30.2 ± 10.1 ($n = 22$) versus 21.7 ± 10.5 ($n = 22$) for the placebo and methylphenidate groups,

Sample characteristics for those included at baseline with valid MRIs, age, intelligence quotient, reported handedness, ADHD symptom severity, and brain ROIs, as well as scan movement ratings at baseline and follow-up and scan interval and compliance rates for those included in the analyses, divided by age and medication group^a

	Children				Adults			
	Methylphenidate Hydrochloride (n = 25)		Placebo (n = 23)		Methylphenidate Hydrochloride (n = 24)		Placebo (n = 23)	
	Mean	SD	Mean	SD	Mean	SD	Mean	SD
Age at baseline (yr)	11.4	0.8	11.4	0.9	28.2	4.4	29.0	5.0
Estimated intelligence quotient ^b	104.8	21.0	102.8	15.7	107.9	8.8	107.9	6.4
ADHD symptom severity	36.6	6.2	38.4	8.2	31.8	9.9	31.0	9.9
Proportion right-handed	0.840	0.374	0.913	0.288	0.958	0.204	0.826	0.388
Left frontal cortex thickness, Tp1 (mm) ^c	2.805	0.229	2.763	0.236	2.471	0.170	2.553	0.164
Right medial cortex thickness, Tp1 (mm) ^c	2.724	0.115	2.770	0.097	2.434	0.128	2.438	0.120
Right posterior cortex thickness, Tp1 (mm) ^c	2.409	0.142	2.384	0.172	2.151	0.157	2.223	0.096
Scan movement Tp1 ^c	1.2	0.4	1.2	0.4	1.0	0.0	1.1	0.2
Scan movement Tp2 ^d	1.3	0.5	1.2	0.4	1.1	0.2	1.0	0.0
Compliance rate percentage ^e	83.5	15.5	79.0	18.1	90.0	8.0	85.7	8.4
Scan interval (day) ^f	122.3	4.2	121.4	3.9	110.8	27.5	111.7	24.6

Note:—Tp indicates time point; Tp1, baseline time point; and Tp2, follow-up time point.

^a There were no significant ($P < .05$) differences in these characteristics across participants randomized to methylphenidate or placebo treatment.

^b Available for 21 children and 22 adults in the placebo group and all 25 children and 22 adults in the methylphenidate group.

^c Available for those with scans included at baseline: 23 children and 22 adults in the placebo group and 24 children and 24 adults in methylphenidate group.

^d Available for those with scans included at follow-up: 23 children and 21 adults in placebo group and 22 children and 22 adults in methylphenidate group.

^e Available for 22 children and 21 adults in the placebo group and 20 children and 22 adults in the methylphenidate group.

^f Available for those included who did not drop out: 23 children and 21 adults in placebo group and 23 children and 22 adults in methylphenidate group.

respectively. Mean posttreatment ADHD symptom-severity scores in adults were 26.5 ± 7.9 ($n = 21$) versus 20.1 ± 6.7 ($n = 22$) for the placebo and methylphenidate groups, respectively. However, there were no significant relationships between symptom-severity change and the estimated rate of ROI cortical change per year in either children or adults.

DISCUSSION

The present results yield partial support for the hypothesis that methylphenidate treatment in development is associated with reduced cortical thinning,⁹ as identified here in the right medial cortex. The 3-way interaction of treatment group \times age group \times time for this region also indicates that similar effects were not seen in adulthood, in line with the hypothesis. However, for the 2 other cortical ROIs previously indicated,⁹ in the left frontal and right posterior cortices, no significant medication group \times time interactions were observed in the current RCT.

The only partial overlap and noted discrepancies of findings across the current study and the previous observational study of children and adolescents⁹ may be due to several factors: First, in the observational study, decisions regarding psychostimulant treatment were the joint responsibility of the patients, their families, and their physicians,⁹ whereas in this study, participants were randomized. While there were no significant differences in baseline characteristics in terms of age, ADHD symptom severity, and clinical impairment across treatment groups in either study,^{9,11} it may still be more likely that groups self-selecting medication/no medication differed on some dimensions. Second, the current follow-up interval is considerably shorter than that of the observational study, ie, 4 months versus 4 years. There are

substantial cortical changes in the relevant age ranges,^{10,29-32} and it may be that additional or other effects would be seen in a longer RCT. However, for ethical and practical reasons, a much longer RCT with patients with ADHD, children in particular, is deemed impossible to perform. Of note, when converted to the mean rate of change per year, the present results for the right medial cortex resemble those found across longer time intervals in the observational study.⁹ Third, the MR imaging measures used in the previous observational study⁹ and the present one vary in terms of scanner platforms and field strengths (1.5T versus 3T), sequence parameters, and cortical reconstructions and segmentations. The observational study⁹ used CIVET (<https://sourceforge.net/projects/civet/>) software for cortical reconstruction and thickness estimation, whereas FreeSurfer¹⁹⁻²³ was used in the present study. The measurement of cortical thickness requires that the analysis be performed at the nodes of a 3D polygonal mesh,³³ capturing the distance between the WM surface and the intersection between the outer cortical boundary and the CSF. This is in accordance with a geometric definition, which can vary across methods, so the way cortical thickness is quantified is of importance for the end results. Of note, the normal maturational cortical trajectories measured by CIVET and FreeSurfer can be discrepant.³⁴ Moreover, the exact re-creation of the cortical effect sites identified in the observational study⁹ was not possible; therefore, smaller ROIs were drawn around the peak effects.

Methodologic issues aside, the present results yield an indication toward thicker regional cortices with methylphenidate treatment in childhood specifically, as shown in the 3-way interaction of treatment group \times age group \times time for the right medial cortex, with absence of any treatment group \times time interactions in

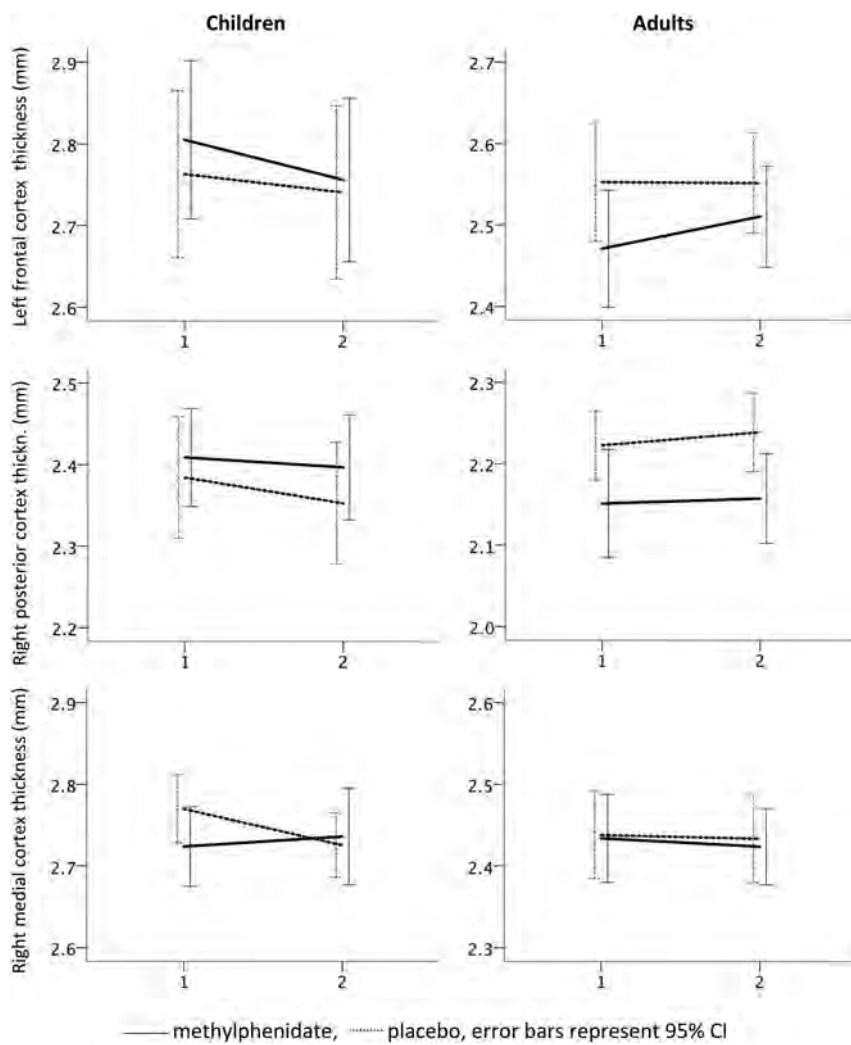


FIG 3. Differences in rates of cortical thickness change of the ROIs in children and adults taking methylphenidate or placebo medication. For each ROI, at the y-axis, cortical thickness in millimeters (in left frontal, right posterior, and right medial cortices) is shown at baseline (x-axis time point 1) and at the end point (x-axis time point 2) of the trial. Note that as cortical thickness differs across regions and age groups, different origin values for cortical thickness are given across panels to enable visualization, but the scale is otherwise the same, and increments on the y-axes invariably represent 0.1mm. Mean rates of change are shown with *dotted lines* for the placebo group and *solid lines* for the methylphenidate group. *Error bars* represent the 95% confidence intervals.

adults. This finding corresponds to evidence from animal models, indicating that psychotropic drugs affect the brain in a differential manner depending on the age of exposure.^{35,36} The results also align with findings of age-dependent effects of methylphenidate on cerebral perfusion and the blood flow response of the dopaminergic system in the same sample studied here.³⁷ Hence, the present data on cortical thickness changes are in line with the neurochemical imprinting hypothesis,³⁶ to some extent also being at play at a macrostructural level.

To the extent that brain differences among ADHD case-controls are predominantly found in children rather than adults, as was recently reported,^{7,8} it is also given that such differences can only be influenced when they are present in childhood. In large recent cross-sectional studies on observational cohorts, no effect of psychostimulant medication on subcortical volumes⁸ or the cortical thickness of regions showing patient-control group differences (fusiform gyrus, temporal pole)⁷ were found. There are, as mentioned above, multiple methodologic challenges to studying the effects of medication in a pure observational setting. The absence of such observational cross-sectional medication effects on cortical thickness could mean that such effects are not present in the studied regions or that any such effects are transient. It could, however, also be that medication may cause persistent changes, even if they can only be detected at the level of brain structure for a limited time.

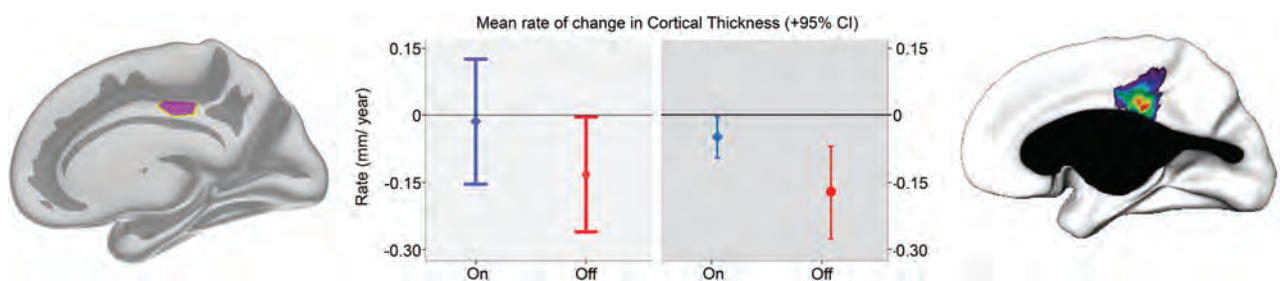


FIG 4. Mean rate of change in cortical thickness estimated per year for the present RCT and the previous observational study for the right medial cortex region. For children receiving methylphenidate (blue) and placebo (red), cortical change values for the right medial ROI across the duration of the present RCT were converted to an estimated mean rate of change in cortical thickness per year (left panel). This was done for comparison with previous results (right panel) from the observational study from which the ROI was derived (Shaw et al⁹), reporting on the mean rate of cortical change per year across a period of about 4 years.

Limitations

There are several limitations to the present study. First, the sample was too small for detection of effects in a whole-brain analysis. Thus, although there were no significant baseline differences, slight differences were seen throughout the ROIs across age and medication groups, and baseline differences also contributed to the identified interaction. The vast normal variation in brain anatomy, including cortical measures,^{38–40} unfortunately makes it unlikely that relatively small groups will have completely identical values. Second, because we did not detect significant relationships between changes in cortical ROIs and changes in symptom severity, the functional significance remains uncertain. ADHD symptom severity was not related to subcortical differences in a recent cross-sectional mega-analysis either,⁸ so direct morphometric-functional relationships may not necessarily be expected. However, it would be of interest in future larger studies to investigate whether both baseline and longitudinal differences in cortical thickness are associated with a differential response to medication. Third, the follow-up interval was relatively short, and while changes in cortical thickness can be reliably detected across time at intervals even shorter than the present ones,⁴¹ medication effects may develop differently across a longer time. It is unknown why the right medial frontal cortical region, rather than the left frontal and left posterior cortical ROIs, showed the hypothesized effect in the present study. There was no reason to expect a differential strength of effects based on the previous observational study.⁹ We do not believe it is necessary to speculate about possible causes for this in this relatively small sample in which we also do not find correlations with symptom severity in any of the ROIs. Furthermore, it is beyond the scope of the present article to address functional imaging changes, but changes in cortical thickness with medication may likely also relate to and possibly interact with functional imaging changes, such as blood oxygen level-dependent functional signal variability.⁴²

Finally, macrostructural MR imaging measures cannot pinpoint the neural changes underlying the observed differences in thickness. Neurogenesis does not take place in the cortex in these age ranges,⁴³ but a number of other processes may be at play, inclusive of differences in growth and regressive changes, astrocytes, dendritic branching, synaptic pruning, intracortical myelination, dendritic spine formation, and vascular changes.^{44–50} Preferably, animal models should combine high-resolution MR imaging and histologic methods to elucidate the neural fundament. The present results warrant replication in larger groups and possibly with longer follow-up, to determine whether the effects are permanent and whether they have long-term functional correlates.

CONCLUSIONS

The results of this RCT yield partial support for the hypothesis that methylphenidate treatment in development is associated with reduced cortical thinning in childhood, but not adulthood. This was identified here in the right medial cortex, but not in 2 other cortical ROIs previously indicated.⁹ Because significant relationships between changes in cortical ROIs and changes in symptom severity were not observed, the functional significance

remains uncertain. Replication of the effects in prolonged studies in larger groups would be required to determine both possible temporal dynamics and functional significance of cortical effects.

Disclosures: Inge Amlien—RELATED: Grant: UNINETT Sigma2 NS9084S, Comments: computer resources (storage/processing). Atle Bjørnerud—UNRELATED: Employment: Oslo University Hospital and University of Oslo.

REFERENCES

1. Burcu M, Zito JM, Metcalfe L, et al. **Trends in stimulant medication use in commercially insured youths and adults, 2010–2014.** *JAMA Psychiatry* 2016;73:992–93 CrossRef Medline
2. Trip AM, Visser ST, Kalverdijk LJ, et al. **Large increase of the use of psycho-stimulants among youth in the Netherlands between 1996 and 2006.** *Br J Clin Pharmacol* 2009;67:466–68 CrossRef Medline
3. Group M. **National Institute of Mental Health Multimodal Treatment Study of ADHD follow-up: 24-month outcomes of treatment strategies for attention-deficit/hyperactivity disorder.** *Pediatrics* 2004;113:754–61 CrossRef Medline
4. Swanson J, Greenhill L, Wigal T, et al. **Stimulant-related reductions of growth rates in the PATS.** *J Am Acad Child Adolesc Psychiatry* 2006;45:1304–13 CrossRef
5. Shaw P, De Rossi P, Watson B, et al. **Mapping the development of the basal ganglia in children with attention-deficit/hyperactivity disorder.** *J Am Acad Child Adolesc Psychiatry*.2014;53:780–89.e711 CrossRef Medline
6. Shaw P, Malek M, Watson B, et al. **Development of cortical surface area and gyrification in attention-deficit/hyperactivity disorder.** *Biol Psychiatry* 2012;72:191–97 CrossRef Medline
7. Hoogman M, Muetzel R, Guimaraes JP, et al. **Brain imaging of the cortex in ADHD: a coordinated analysis of large-scale clinical and population-based samples.** *Am J Psychiatry* 2019;176:531–42 CrossRef Medline
8. Hoogman M, Bralten J, Hibar DP, et al. **Subcortical brain volume differences in participants with attention-deficit hyperactivity disorder in children and adults: a cross-sectional mega-analysis.** *Lancet Psychiatry* 2017;4:310–19 CrossRef Medline
9. Shaw P, Sharp WS, Morrison M, et al. **Psychostimulant treatment and the developing cortex in attention-deficit hyperactivity disorder.** *Am J Psychiatry* 2009;166:58–63 CrossRef Medline
10. Tamnes CK, Walhovd KB, Dale AM, et al; Alzheimer's Disease Neuroimaging Initiative. **Brain development and aging: overlapping and unique patterns of change.** *Neuroimage* 2013;68:63–74 CrossRef Medline
11. Schrantee A, Tamminga HG, Bouziane C, et al. **Age-dependent effects of methylphenidate on the human dopaminergic system in young vs adult patients with attention-deficit/hyperactivity disorder: a randomized clinical trial.** *JAMA Psychiatry* 2016;73:955–62 CrossRef Medline
12. Bottelier MA, Schouw ML, Klomp A, et al. **The effects of Psychotropic drugs On Developing brain (ePOD) study: methods and design.** *BMC Psychiatry* 2014;14:48 CrossRef Medline
13. Bouziane C, Filatova OG, Schrantee A, et al. **White matter by diffusion MRI following methylphenidate treatment: a randomized control trial in males with attention-deficit/hyperactivity disorder.** *Radiology* 2019;293:186–92 CrossRef Medline
14. Burd L, Klug MG, Coumbe MJ, et al. **Children and adolescents with attention-deficit-hyperactivity disorder. 1: prevalence and cost of care.** *J Child Neurol* 2003;18:555–61 CrossRef Medline
15. Ben Bashat D, Ben Sira L, Graif M, et al. **Normal white matter development from infancy to adulthood: comparing diffusion tensor and high b value diffusion weighted MR images.** *J Magn Reson Imaging* 2005;21:503–11 CrossRef Medline
16. Association AP. *Diagnostic and Statistical Manual of Mental Health Disorders.* 4th ed. American Psychiatric Association; 1994
17. Ferdinand R, van der Ende J, Nimh DI. *Diagnostic Interview Schedule for Children* (in Dutch). Erasmus MC-Sophia; 2000

18. Kooij J, Francken M. **Diagnostic Interview for ADHD in Adults (DIVA)**. 2010. https://www.divacenter.eu/Content/Downloads/DIVA_2_NL_FORMULIER.pdf. Accessed April 28, 2020
19. Fischl B, Sereno MI, Dale AM. **Cortical surface-based analysis. II: inflation, flattening, and a surface-based coordinate system**. *Neuroimage* 1999;9:195–207 CrossRef Medline
20. Fischl B, Dale AM. **Measuring the thickness of the human cerebral cortex from magnetic resonance images**. *Proc Natl Acad Sci U S A* 2000;97:11050–55 CrossRef Medline
21. Dale AM, Sereno MI. **Improved localization of cortical activity by combining EEG and MEG with MRI cortical surface reconstruction: a linear approach**. *J Cogn Neurosci* 1993;5:162–76 CrossRef Medline
22. Dale AM, Fischl B, Sereno MI. **Cortical surface-based analysis. I: segmentation and surface reconstruction**. *Neuroimage* 1999;9:179–94 CrossRef Medline
23. Segonne F, Grimson E, Fischl B. **A genetic algorithm for the topology correction of cortical surfaces**. *Inf Process Med Imaging* 2005;19:393–405 Medline
24. Reuter M, Schmansky NJ, Rosas HD, et al. **Within-subject template estimation for unbiased longitudinal image analysis**. *Neuroimage* 2012;61:1402–18 CrossRef Medline
25. Schmand B, Bakker D, Saan R, et al. **The Dutch Reading Test for Adults: a measure of premorbid intelligence level (in Dutch)**. *Tijdschr Gerontol Geriatr* 1991;22:15–19 Medline
26. Rosler M, Retz W, Thome J, et al. **Psychopathological rating scales for diagnostic use in adults with attention-deficit/hyperactivity disorder (ADHD)**. *Eur Arch Psychiatry Clin Neurosci* 2006;256 (Suppl 1):i3–11 CrossRef Medline
27. Oosterlaan J, Scheres A, Antrop I, et al. **Vragenlijst voor Gedragsproblemen bij Kinderen (VvGK)**. [Dutch Translation of the Disruptive Behavior Disorders Rating Scale]. Harcourt Test Publishers; 1998
28. Wechsler D. **Manual for the Wechsler Intelligence Scale for Children-Revised**. Psychological Corporation; 1974
29. Walhovd KB, Tamnes CK, Bjornerud A, et al. **Maturation of cortico-subcortical structural networks: segregation and overlap of medial temporal and fronto-striatal systems in development**. *Cereb Cortex* 2015;25:1835–41 CrossRef Medline
30. Tamnes CK, Walhovd KB, Grydeland H, et al. **Longitudinal working memory development is related to structural maturation of frontal and parietal cortices**. *J Cogn Neurosci* 2013;25:1611–23 CrossRef Medline
31. Fjell AM, Grydeland H, Krogsrud SK, et al. **Development and aging of cortical thickness correspond to genetic organization patterns**. *Proc Natl Acad Sci U S A* 2015;112:15462–67 CrossRef Medline
32. Walhovd KB, Krogsrud SK, Amlien IK, et al. **Neurodevelopmental origins of lifespan changes in brain and cognition**. *Proc Natl Acad Sci U S A* 2016;113:9357–62 CrossRef Medline
33. Lerch JP, Evans AC. **Cortical thickness analysis examined through power analysis and a population simulation**. *Neuroimage* 2005;24:163–73 CrossRef Medline
34. Walhovd KB, Fjell AM, Giedd J, et al. **Through thick and thin: a need to reconcile contradictory results on trajectories in human cortical development**. *Cereb Cortex* 2017;27:1472–81 CrossRef Medline
35. Urban KR, Waterhouse BD, Gao WJ. **Distinct age-dependent effects of methylphenidate on developing and adult prefrontal neurons**. *Biol Psychiatry* 2012;72:880–88 CrossRef Medline
36. Andersen SL, Navalta CP. **Altering the course of neurodevelopment: a framework for understanding the enduring effects of psychotropic drugs**. *Int J Dev Neurosci* 2004;22:423–40 CrossRef Medline
37. Schrantee A, Mutsaerts H, Bouziane C, et al. **The age-dependent effects of a single-dose methylphenidate challenge on cerebral perfusion in patients with attention-deficit/hyperactivity disorder**. *Neuroimage Clin* 2017;13:123–29 CrossRef Medline
38. Tamnes CK, Ostby Y, Walhovd KB, et al. **Neuroanatomical correlates of executive functions in children and adolescents: a magnetic resonance imaging (MRI) study of cortical thickness**. *Neuropsychologia* 2010;48:2496–2508 CrossRef Medline
39. Tamnes CK, Ostby Y, Fjell AM, et al. **Brain maturation in adolescence and young adulthood: regional age-related changes in cortical thickness and white matter volume and microstructure**. *Cereb Cortex* 2010;20:534–48 CrossRef Medline
40. Storsve AB, Fjell AM, Tamnes CK, et al. **Differential longitudinal changes in cortical thickness, surface area and volume across the adult life span: regions of accelerating and decelerating change**. *J Neurosci* 2014;34:8488–98 CrossRef Medline
41. Engvig A, Fjell AM, Westlye LT, et al. **Effects of memory training on cortical thickness in the elderly**. *Neuroimage* 2010;52:1667–76 CrossRef Medline
42. Pur DR, Eagleson RA, de Ribapierre A, et al. **Moderating effect of cortical thickness on BOLD signal variability age-related changes**. *Front Aging Neurosci* 2019;11:46 CrossRef Medline
43. Bhardwaj RD, Curtis MA, Spalding KL, et al. **Neocortical neurogenesis in humans is restricted to development**. *Proc Natl Acad Sci U S A* 2006;103:12564–68 CrossRef Medline
44. Zatorre RJ, Fields RD, Johansen-Berg H. **Plasticity in gray and white: neuroimaging changes in brain structure during learning**. *Nat Neurosci* 2012;15:528–36 CrossRef Medline
45. Shafee R, Buckner RL, Fischl B. **Gray matter myelination of 1555 human brains using partial volume corrected MRI images**. *Neuroimage* 2015;105:473–85 CrossRef Medline
46. Huttenlocher PR, De Courten C, Garey LJ, et al. **Synaptic development in human cerebral cortex**. *Int J Neurol* 1982;16-17:144–54 Medline
47. Huttenlocher PR, Dabholkar AS. **Regional differences in synaptogenesis in human cerebral cortex**. *The Journal of Comparative Neurology* 1997;387:167–78 CrossRef Medline
48. Huttenlocher PR. **Morphometric study of human cerebral cortex development**. *Neuropsychologia* 1990;28:517–27 CrossRef Medline
49. Huttenlocher PR. **Synapse elimination and plasticity in developing human cerebral cortex**. *Am J Ment Defic* 1984;88:488–96 Medline
50. Huttenlocher PR. **Synaptic density in human frontal cortex: developmental changes and effects of aging**. *Brain Res* 1979;163:195–205 CrossRef Medline

Scientific Collaboration across Time and Space: Bibliometric Analysis of the *American Journal of Neuroradiology*, 1980–2018

V.M. Zohrabian, L.H. Staib, M. Castillo, and L. Wang



ABSTRACT

BACKGROUND AND PURPOSE: Scientific collaboration is traditionally acknowledged through coauthorship. Studies on this topic are few in the neuroimaging literature. This study is a bibliometric analysis of the *American Journal of Neuroradiology (AJNR)* between 1980 and 2018, with the primary aim of evaluating changes in article collaboration.

MATERIALS AND METHODS: Full bibliographic records from 1980 to 2018 were retrieved. Yearly metrics calculated included the number of articles published, the average number of authors, and the average number of affiliations per article. The levels of evidence of 160 random articles were determined. Geographic characteristics of author affiliations were analyzed. Changes across time were evaluated using linear regression, while Spearman rank-order correlation was used to determine relationships between level of evidence and time, number of authors, and number of affiliations.

RESULTS: There was a steady linear growth in the number of articles ($R^2 = 0.70$, $P < 1e-10$) from 1980 to 2018. There were clear linear increases in the average number of authors ($R^2 = 0.91$, $P < 1e-15$) and affiliations ($R^2 = 0.90$, $P < 1e-15$) per article. There was a significant correlation between level of evidence and time period (Spearman $\rho = -0.42$, $P < 1e-7$), indicating that articles trended toward better methodologic quality or strength of results over time. A significant correlation existed between the level of evidence and the number of authors (Spearman $\rho = -0.39$, $P < 1e-6$). There were linear increases in the average number of different geographic locales of authors per article by country/region ($R^2 = 0.80$, $P < 1e-13$), state/province ($R^2 = 0.88$, $P < 1e-15$), and locality/city/town ($R^2 = 0.86$, $P < 1e-15$).

CONCLUSIONS: From 1980 to 2018, as the quantity of articles published in the *AJNR* increased, their level of evidence improved, while an increasing number of authors with different affiliations and from different geographic locales collaborated on these articles.

ABBREVIATION: WOS = Web of Science

Bibliometric analyses continue to gain traction in the scientific literature as they use quantitative approaches to evaluate and compare research across countries, institutions, investigators, and journals. In more than a decade, only a very small number of studies in the *American Journal of Neuroradiology (AJNR)*, the official journal of the American Society of Neuroradiology, have centered on bibliometrics. Whereas most of these have highlighted citation numbers or Impact Factors,¹⁻⁵ few have underscored authorships or affiliations.⁶⁻⁹ Furthermore, even though a number of these inquiries have demonstrated continually increasing international contributions to the *AJNR*,⁷⁻⁹ none have

focused on collaborations among researchers from different geographic areas. One prior study found high interdisciplinary cooperation in neurointerventional research published in the *AJNR* between 2003 and 2012, yet it did not examine other types of collaboration.¹⁰ Scientific collaboration, so valuable to the dissemination of knowledge and production of high-quality research,¹¹ is traditionally acknowledged through coauthorship and, therefore, can be measured by the number of authors and affiliations. In this study, we hypothesized that collaborative efforts among researchers with different affiliations and from different geographic locales, both domestic and international, have grown with time. We conducted a systematic, in-depth analysis of the characteristics and trends of articles published in the *AJNR* between 1980 and 2018, with the primary aim of evaluating changes in collaboration during 4 decades.

MATERIALS AND METHODS

Institutional review board approval was not required because human subjects were not involved. The Web of Science (WOS) (Clarivate Analytics) was determined to be the optimal

Received January 14, 2020; accepted after revision March 2.

From the Department of Radiology and Biomedical Imaging (V.M.Z., L.H.S.), Yale School of Medicine, New Haven, Connecticut; Department of Radiology (M.C.), University of North Carolina at Chapel Hill, Chapel Hill, North Carolina; and Cushing/Whitney Medical Library (L.W.), Yale University, New Haven, Connecticut.

Please address correspondence to Vahe M. Zohrabian, MD, Yale School of Medicine, PO Box 208042, New Haven, CT 06520-8042; e-mail: vahe.zohrabian@yale.edu



Indicates article with supplemental on-line photos.

<http://dx.doi.org/10.3174/ajnr.A6523>

Table 1: Evidence-based medicine ratings, adapted from the AJNR Web site

Level	Study Type
1	Randomized controlled trial
2	Prospective cohort study
3	Retrospective cohort study, case-control study
4	Case series
5	Mechanism-based reasoning

bibliographic data source for this study. Full bibliographic records of all items ($n = 14,758$) published in the *AJNR* from January 1, 1980, to December 31, 2018, were retrieved from the WOS and saved as tab delimited data files. A custom script was written in Ruby, an open-source programming language, to extract a subset of the bibliographic records to include only those with a document type of “Article” ($n = 10,789$), defined in WOS as “reports of research on original works,” which include “research papers, features, brief communications, case reports, technical notes, chronology, and full papers that were published in a journal and/or presented at a symposium or conference.”¹² This process excluded any comments, editorials, replies, letters, and reviews from our dataset. This subset of 10,789 bibliographic records served as the basis of all statistical analyses in this study.

The script also extracted all unique author affiliation addresses ($n = 29,577$) from the 10,789 bibliographic records and sent them individually to Google’s Geocoding API, which returned standardized geographic locations of those addresses at the locality/city/town, state/province, and country/region levels. The geocoding results were checked for accuracy at the country/region level, and inaccuracies ($n = 1293$) were manually corrected.

The script grouped records by publication year and calculated the following metrics for each year: number of articles published, average number of authors per article, average number of affiliations per article, average number of affiliation countries/regions per article, average number of affiliation states/provinces per article, and average number of affiliation localities/cities/towns per article.

The script also generated a random sample of 20 records for each 5-year period between 1980 and 2014 and an additional 20 random records for the 4-year period between 2015 and 2018, totaling 160 records. Two trained individuals retrieved the full text of each of the articles and independently assigned a level of evidence (levels 1–5) to each according to the evidence-based medicine ratings guidelines published on the *AJNR* Web site, as in Table 1.¹³ After independent review, any disagreements were resolved by consensus.

The articles were also substratified by country/region of origin or the geographic affiliation of the primary author for the study. The countries/regions of origin were determined for most of the articles ($n = 10,230$, 95%). The affiliation country/region of the last/senior author, when available, was established as the article origin. For the purposes of this study, we presumed that the last/senior author’s institution was the focal point of the work and where the work originated. For articles without such information, an origin was recognized if only a single affiliation country/region was listed for the article.

Visual representations of international collaboration across time were achieved by plotting network diagrams using Cytoscape (Cytoscape Consortium, Version 3.7.2, 2019; <https://cytoscape.org/download.html>). The “nodes” in the diagrams represented countries/regions with articles that had at least 1 coauthor from a different country/region, and the size of the nodes represented the number of such articles. The nodes were linked by “edges,” the thickness of which represented the number of articles with coauthors from the pair of connected countries/regions. The network diagrams were scaled using Cytoscape for better readability.

All data were tabulated and statistical analyses performed using R statistical and computing software (Version 3.3.2, 2016; <http://www.r-project.org/>). Changes with time were evaluated using linear regression. The Spearman rank-order correlation was used to assess relationships between level of evidence and time, number of authors, and number of affiliations.

RESULTS

Number of Articles

A total of 10,789 articles published in *AJNR* between 1980 and 2018 met the inclusion criteria for this bibliometric study. As shown in On-line Fig 1, there was a steady linear growth in the number of articles published yearly in the *AJNR* since 1980 ($R^2 = 0.70$, $P < 1e-10$), from 85 articles in 1980 to 321 articles in 2018. Article counts increased, on average, by 6.4 each year.

Number of Authors and Affiliations

On-line Fig 2 shows linear increases in the average number of authors ($R^2 = 0.91$, $P < 1e-15$) and affiliations ($R^2 = 0.90$, $P < 1e-15$) per article. The average number of authors per article increased by 0.10 per year. The average number of affiliations per article increased by 0.08 per year. The average number of authors per article was 3.4 in 1980, 5.3 in 2000, and 8.0 in 2016. The average number of affiliations represented in each article was 1.6 in 1980, 2.5 in 2000, and 4.4 in 2016.

Level of Evidence

There was a significant correlation between the level of evidence and time period (Spearman $\rho = -0.42$, $P < 1e-7$), indicating that articles trended toward better methodologic quality or strength of results across time, as shown in On-line Fig 3. For example, the proportion of level 5 articles decreased, while level 3 and 4 articles increased during the 4 decades.

Level of Evidence and Number of Authors and Affiliations

A significant correlation was found between the level of evidence and the number of authors (Spearman $\rho = -0.39$, $P < 1e-6$), as shown in On-line Fig 4. The proportion of level 5 articles decreased as the number of authors increased. However, no significant relationship was found between the level of evidence and the number of affiliations (Spearman $\rho = -0.15$, $P = .054$, not significant).

Geographic Locales of Author Affiliations

Authors from the United States were, by far, the largest contributors to *AJNR*, appearing in 6270 (58%) articles. The United States

Table 2: Number of articles with at least N affiliation countries/regions

Time Span	n = 2	n = 3	n = 4	n = 5	n = 6	n = 7	n = 8	n = 9	n = 10
All	1456	250	74	36	21	8	4	2	2
1980–1989	72	5	1	0	0	0	0	0	0
1990–1999	183	12	1	0	0	0	0	0	0
2000–2009	453	65	12	6	4	0	0	0	0
2010–2018	748	168	60	30	17	8	4	2	2

Table 3: Percentages of AJNR articles with all authors from the same geographic locales^a

Time Span	Same Country/Region	Same State/Province	Same Locality/City/Town
1980–1989	96%	82%	74%
1990–1999	93%	72%	65%
2000–2009	87%	58%	50%
2010–2018	75%	43%	37%

^aHere, “All” refers to all authors in the author line of a single article being from the same geographic locale, either the same country/region, state/province, or locality/city/town.

Table 4: Percentage of international collaboration articles involving the United States

	No. of Collaborating Countries/Regions	No. of International Collaborating Articles	No. of International Collaborating Articles Involving the United States	% of International Collaborating Articles Involving the United States
1980–1989	24	72	53	74%
1990–1999	32	183	125	68%
2000–2009	47	453	317	70%
2010–2018	57	748	465	62%

Table 5: Top 5 countries/regions collaborating internationally in AJNR, 1980–2018

Country	Article Count
United States	960
Germany	291
Canada	255
France	187
United Kingdom	171

was followed by Japan (9%), Germany (7%), and Canada (5%) as the next largest contributing countries.

As in On-line Fig 5, more than half ($n = 5658$, 55%) of AJNR articles published between 1980 and 2018 (whose origins could be determined) originated from the United States. The United States was followed by Japan (8%), Germany (5%), and Canada (4%) as the next largest origin countries.

A detailed assessment of geographic locales of author affiliations in each article was performed. On-line Fig 6 demonstrates linear increases in the average number of different geographic locales of author affiliations per article from 1980 to 2018 by country/region ($R^2 = 0.80$, $P < 1e-13$), state/province ($R^2 = 0.88$, $P < 1e-15$), and locality/city/town ($R^2 = 0.86$, $P < 1e-15$). The average number of countries/regions represented in each article increased by 0.01 per year. The average number of states/provinces per article increased by 0.03 per year. The average number of localities/cities/towns per article increased by 0.04 per year. Of the 10,789 articles analyzed, 1456 (14%) were the result of collaborations between at least 2 countries/regions, and 250 (2%), among at least 3. These numbers trended upward across the decades, as shown in Table 2. Furthermore, as shown in Table 3, the

percentages of AJNR articles by authors from the same country/region, state/province, and locality/city/town decreased during the 4 time periods, with the largest decrease occurring at the locality/city/town level. For example, 74% of AJNR articles were by authors from the same locality/city/town during 1980–1989. That percentage dropped to 37% during 2010–2018. At the state/province level, the percentage dropped from 82% to 43%, while at the country/region level, it dropped from 96% to 75%.

Nearly all countries/regions were increasingly involved in international collaborations across time. On-line Fig 7 reveals that on the basis of the change between the last 2 decades, China had the largest gain in international collaborations (606%), followed by Norway (340%), Spain (338%), and France (319%). The United States (147%), Germany (145%), and Japan (108%), on the other hand, demonstrated more modest gains during the past 2 decades. Table 4 demonstrates

that the United States held a decreasing share of the “international collaboration pie” across time because the percentage of such articles involving the United States decreased from 1980–1989 (74%) to 2010–2018 (62%).

The complexity of the network diagrams increased during the 4 time periods, 1980–1989 (On-line Fig 8A), 1990–1999 (On-line Fig 8B), 2000–2009 (On-line Fig 8C), and 2010–2018 (On-line Fig 8D). Between 1980 and 1989, only 24 countries/regions (in 39 pairs) published articles in the AJNR with international coauthors. These numbers increased to 57 and 368, respectively, between 2010 and 2018. The top 5 countries/regions that collaborated internationally in the AJNR, and the top 3 collaboration pairs overall (1980–2018) are presented in Tables 5 and 6.

DISCUSSION

Collaboration enhances the quality of scientific research. Collaboration allows sharing of knowledge, facilitates acquisition of specialized and new expertise, fosters creativity, and promotes innovation. While macro-level collaborations are typically large initiatives by collaborating nations or international organizations, meso-level collaborations are usually among academic institutions, sometimes across national boundaries.¹⁴ Micro-level collaborations, on the other hand, involve individual researchers or small groups of individual researchers working together.¹⁴ The formal acknowledgment of scientific collaboration is traditionally through coauthorship and can be measured by the number of authors and affiliations. In this study, we performed in-depth bibliometric analyses of the characteristics and trends of AJNR articles published during the past 4 decades, from 1980 to 2018. We

Table 6: Top 3 pairs overall collaborating internationally in AJNR, 1980–2018

Country 1	Country 2	Pair Count
Germany	United States	149
Canada	United States	147
Japan	United States	109

examined article counts, level of evidence, number of authors, and the number and geography of author affiliations and, in doing so, proved that collaboration has increased across the years.

In examining collaborations, we established that the average number of authors per article increased by 0.10 per year, from 3.4 per article in 1980 to 8.0 per article in 2018. Multiple prior studies have likewise demonstrated a trend toward a greater number of authors per article, which may, in part, be due to increasing scientific complexity and specialization.^{15–17} Our manual analysis of a small random sample of 160 articles revealed that the level of evidence has improved since 1980, trending toward better methodologic quality or strength of results. Whereas studies published in 1980 were all level 4 or 5, studies in 2015 were mostly level 2 or 3. Furthermore, we demonstrated a significant association between the level of evidence and the number of authors so that more methodologically robust studies tended to have a larger number of authors and vice-versa. However, this finding is a correlation, and we have not proved that the number of authors and the level of evidence are causally related. A prior study showed that the number of authors per article was larger for original research than for case reports and review articles.¹⁸ On the other hand, increasing authorship may be merely because publications are an increasingly central part of recruitment, promotion, and retention of faculty in academic medicine.^{16,19–21} In fact, increasing coauthorship in the biomedical literature has been subject to debate, especially in the radiology literature, because several authors have noted increasing trends of inappropriate authorship during several decades.^{15,22–25}

A recently published analysis of the impact of the recommendations of the International Committee of Medical Journal Editors on 49 clinical radiology journals between 1946 and 2013 found that overall authorship increased with time, independent of the journal of publication, country of publication, publication type, and language of publication. Moreover, of the top 10 radiology journals by volume, *AJNR* ranked above the average for change in authorship with time.¹⁸ Therefore, authors are reminded to strictly adhere to the guidelines of the International Committee of Medical Journal Editors, which are specified on the *AJNR* Web site, to ensure proper attribution of authorship.

In our examination, we also established that the average number of affiliations per article increased by 0.08 per year. However, no significant association was found between the level of evidence and the number of affiliations. We speculate that access to intra-institutional diversity of expertise has improved with time and has helped in conducting studies that required more methodologic rigor.

Authors from the United States were, by far, the largest contributors to the *AJNR*, appearing in 6270 (58%) articles. The United States was followed by Japan (9%), Germany (7%), and

Canada (5%). During the 4 decades, however, the percentage of articles with authors from the United States declined (–30%), from 80% in 1980–1989 to 50% in 2010–2018, while the percentages of articles with authors from other countries/regions increased, with China and Germany demonstrating the largest increases (+7%). The United States was the origin country for more than half ($n = 5658$, 55%) of all *AJNR* articles published between 1980 and 2018 whose origins could be determined, which is not surprising because *AJNR* is the official journal of the American Society of Neuroradiology. The United States was followed by Japan (8%), Germany (5%), and Canada (4%) as the next largest origin countries. However, the percentage of articles originating from the United States declined (–36%) with time, from 80% in 1980–1989 to 44% in 2010–2018, while South Korea (+6%) and China (+5%) demonstrated the largest gains.

Our data are consistent with a previously published work that has shown that although the United States is the largest contributor of articles to selected journals in clinical radiology between 1991 and 2000 (43.2%), the relative shares of the United States, United Kingdom, and Canada have decreased, whereas those of Japan, France, Germany, Italy, South Korea, Spain, Switzerland, Turkey, Austria, and China have increased.²⁶ Additionally, a study in the *American Journal of Roentgenology* found that from 1980 to 1982, ten percent of the articles originated from institutions outside the United States, but between 1990 and 1992, international articles accounted for 25% of published articles.²⁷ A follow-up of the study found that while the total number of published articles from most nations increased from 1980 to 2002, Korea, Japan, and Germany made the largest advances.²⁸ Moreover, our study confirmed a prior work in the *AJNR*, which noted a relative decline in contributions from the United States since 1992 and proposed that articles from China, India, and Eastern Europe would continue to increase as the economies of these countries expanded and became more integrated with the rest of the world through globalization.⁹

Most interesting, beyond merely observing increasing international contributions in the *AJNR*, when the geography of coauthors' affiliations was examined, we confirmed a trend toward increasing national and international collaborations on articles during 4 decades. This is demonstrated by an increase in the average number of geographic locales per article by year in On-line Fig 6 and is visually portrayed by the increasing complexity and interconnectivity of the network diagrams in On-line Fig 8A–D. Internationally, the United States and Germany ($n = 149$), the United States and Canada ($n = 147$), and the United States and Japan ($n = 109$) collaborated on the greatest number of articles between 1980 and 2018, though nearly all countries/regions demonstrated increasing international collaboration. China demonstrated the largest gain, with a 606% increase between 2000 and 2009 and 2010 and 2018, followed by Norway (340%), Spain (338%), and France (319%). On the other hand, the United States demonstrated a more modest gain of 147% during these last 2 decades, followed by Germany (145%) and Japan (108%).

As the volume of international collaboration increased across time, the relative percentage of each country/region declined. For example, although the United States, both as an origin and collaborating country, contributed the largest number of *AJNR* articles during the 4 decades, its relative share in international collaboration

decreased with time, as shown by the declining percentages of international collaboration articles involving the United States in Table 4. A trend of increasing collaboration across academic borders in science and engineering and the social sciences has been noted on a much larger scale by Jones et al.²⁹ In examining 4.2 million research articles published between 1975 and 2005, the researchers demonstrated that multi-university collaborations grew from 10% of articles in 1975 to 30%–35% of articles in 2005, while single-author articles became increasingly rare during the same time period.²⁹ However, the researchers also found that the average distance between collaborators grew only slightly, from 725–750 miles in 1975 to 800 miles in 2005.²⁹ This latter finding is also substantiated in our study because we found that the percentage of articles by authors from the same country/region decreased to a much lesser extent during the 4 decades than the percentages of those by authors from the same state/province, and especially the same locality/city/town, as shown in Table 3.

The digital age has lowered the transaction costs for international collaboration by breaking down barriers related to physical distance and variations in technology.³⁰ Technologic advancements have made it much easier to communicate, and a multitude of Web sites and apps have enabled users to create and share content in the virtual space. Social media and social collaborative networks, which saw a revolution in the 21st century, have permeated nearly every aspect of personal and professional lives. The number of social media users worldwide has more than doubled in less than a decade, from 0.97 billion in 2010 to 2.62 billion in 2018.³¹ As artificial intelligence and machine learning continue to transform social media platforms, they will likely become even more pervasive. While earlier studies have shown a low frequency of social media use among scientists,^{32–34} the landscape is quickly changing, with a recent survey in *Nature* revealing that more than 95% of respondents have used some form of social media or social collaborative network for professional purposes, that 50% of professional users access Facebook on a daily basis, and that most respondents use social media for discovering and/or reading scientific content.³⁵ Most interesting, in our study, we noted that the most rapid change in the average number of geographic locales per article took place since 2006, in the midst of the social media revolution, as shown in On-line Fig 6. However, this trend, albeit more modest, is also observed in the 1980s to 1990s, long before the Internet and social media boom, implying that additional factors are responsible for growth in collaboration.

There are several limitations to our study, most of which pertain to data extraction. At the time of this study, we were not able to dissect author affiliations down to institutional or departmental levels because such information in a structured, consistent format was not immediately available for retrieval. Instead, we had to rely on geographic location data parsed from author affiliation addresses by Google's Geocoding API. Although fairly accurate, we found that results returned from the API had some inaccuracies at the country/region level at a rate of 4.37% (1293 of 29,577), affecting 9.39% (1013 of 10,789) of all records. These inaccuracies were manually corrected, but only at the country/region level. Due to resource constraints, it was not practical to check and correct for inaccuracies at the state/province and

locality/city/town levels; therefore, geocoding inaccuracy rates at these levels are not known. However, on the basis of our cursory review of records and the low inaccuracy rate for country/region, these inaccuracies are likely minor.

Additionally, we realize that in some instances, authors may have recorded multiple affiliations. Unfortunately, data from WOS do not specify primary or secondary affiliations. In our study, authors and affiliations were analyzed separately most of the time. In those cases, all authors and affiliations were considered. The linkage between authors and affiliations was only relevant when determining country/region of origin for each article. In that case, we had to choose 1 (and only 1) affiliation for the last author and use the country/region for that affiliation as the country/region of origin for the article. For this specific analysis, affiliations were considered only at the country/region level, and very few articles ($n = 26$) had last/senior author affiliations spanning multiple countries/regions, representing only 0.25% of articles whose countries/regions of origin were determined ($n = 10,230$) and 0.24% of all articles in our dataset ($n = 10,789$). Given the very small number of such articles, any potential inaccuracies caused by multiple affiliations were likely minimal.

Furthermore, in assigning country of origin, we presumed that the last author's institution was the focal point of the work that was done and geographically where the work originated. In the radiology literature, the convention is that the first author is the greatest contributor to the work and is its principal writer, whereas the last author is the more senior and experienced one responsible for its content. Because scholarly output is an increasingly important part of promotion, younger researchers need to publish as first authors early in their academic careers when they may be still be in training, change specialties, or switch institutions or even countries altogether. Because senior authors tend to be higher on the academic ladder, their affiliations are less likely to change. However, this latter point is an inference based on anecdotal evidence and may not be entirely consistent. Moreover, the records we analyzed were of those published between 1980 and 2018. When we compared metrics by decades, the last decade (2010–2018) was 1 year shorter than the other decades. Consequently, when we generated a smaller sample for level-of-evidence grading by 5-year periods, the last period (2015–2018) was shorter by 1 year. However, because we were interested in examining larger trends across decades, inclusion of data from 1 additional year was not likely to considerably alter our findings.

Finally, our study uses the number of authors and the geography of affiliations as proxies for collaboration. As discussed earlier, inappropriate authorship is a problem facing not only radiology, but all of medicine. To what extent inappropriate authorship was represented in our bibliographic sample and how this may have influenced our findings are not known. Future studies might use sophisticated metrics for collaboration, such as a collaborative index, degree of collaboration, collaborative coefficient, modified collaborative coefficient, and degree of centrality, as well as examine relationships of these metrics with research productivity, journal Impact Factor, and number of citations. Larger analyses might also be stratified by article topic or category, for example, brain, spine, head and

neck, and interventional procedures, to ascertain differences in levels of evidence as well as to quantify levels of evidence for countries of origin and correlate these findings with changes in the number of articles from these countries across time.

CONCLUSIONS

Scientific collaboration is essential for the dissemination of knowledge and production of high-quality research. From 1980 to 2018, as the quantity of articles published in the *AJNR* increased, their level of evidence improved, while an increasing number of authors with different affiliations and from different geographic locales collaborated on these articles.

REFERENCES

1. Castillo M. Citations and open access: questionable benefits. *AJNR Am J Neuroradiol* 2009;30:215–16 CrossRef Medline
2. Castillo M. Measuring academic output: the H-index. *AJNR Am J Neuroradiol* 2010;31:783–84 CrossRef Medline
3. Choudhri AF, Castillo M. Subspecialty virtual Impact Factors within a dedicated neuroimaging journal. *AJNR Am J Neuroradiol* 2015;36:1810–13 CrossRef Medline
4. McDonald RJ, Cloft HJ, Kallmes DF. Fate of submitted manuscripts rejected from the American Journal of Neuroradiology: outcomes and commentary. *AJNR Am J Neuroradiol* 2007;28:1430–34 CrossRef Medline
5. McDonald RJ, Cloft HJ, Kallmes DF. Fate of manuscripts previously rejected by the American Journal of Neuroradiology: a follow-up analysis. *AJNR Am J Neuroradiol* 2009;30:253–56 CrossRef Medline
6. Huntley JH, Pakpoor J, Yousem DM. The top 20 most prolific authors in the American Journal of Neuroradiology: what is their impact? *AJNR Am J Neuroradiol* 2018;39:2182–86 CrossRef Medline
7. Emamzadehfar S, Eslami V, Yousem DM, et al. Disproportionate international contributions to subspecialties of neuroradiology in the American Journal of Neuroradiology. *AJNR Am J Neuroradiol* 2019;40:E3–E4 CrossRef Medline
8. Charkhchi P, Mirbolouk M, Jalilian R, et al. Who's contributing most to American neuroscience journals: American or foreign authors? *AJNR Am J Neuroradiol* 2018;39:1001–07 CrossRef Medline
9. Cloft HJ, Cloft KJ. How American is the American Journal of Neuroradiology? *AJNR Am J Neuroradiol* 2007;28:601 Medline
10. Lee JY, Yoon DY, Yoon SD, et al. Neurointerventional research between 2003 and 2012: slow growth, high interdisciplinary collaboration, and a low level of funding. *AJNR Am J Neuroradiol* 2014;35:1877–82 CrossRef Medline
11. Freeman RB, Huang W. Collaboration: strength in diversity. *Nature* 2014;513:305 CrossRef Medline
12. *Searching the Document Type Field: Web of Science Core Collection Help*. Clarivate Analytics; 2018. https://images.webofknowledge.com/images/help/WOS/hs_document_type.html. Accessed October 10, 2019
13. *Evidence-Based Medicine Ratings*. American J of Neuroradiology; 2019. <http://www.ajnr.org/page/content/EBM>
14. Abbasi A, Hossain L, Uddin S, et al. Evolutionary dynamics of scientific collaboration networks: multi-levels and cross-time analysis. *Scientometrics* 2011;89:687–710 CrossRef
15. Chew FS. Coauthorship in radiology journals. *AJR Am J Roentgenol* 1988;150:23–26 CrossRef Medline
16. Weeks WB, Wallace AE, Kimberly BC. Changes in authorship patterns in prestigious US medical journals. *Soc Sci Med* 2004;59:1949–54 CrossRef Medline
17. Gaeta TJ. Authorship: “law” and order. *Acad Emerg Med* 1999;6:297–301 CrossRef Medline
18. Dang W, McInnes MD, Kielar AZ, et al. A comprehensive analysis of authorship in radiology journals. *PLoS One* 2015;10:e0139005 CrossRef Medline
19. Drenth JP. Multiple authorship: the contribution of senior authors. *JAMA* 1998;280:219–21 CrossRef Medline
20. Levsy ME, Rosin A, Coon TP, et al. A descriptive analysis of authorship within medical journals, 1995–2005. *South Med J* 2007;100:371–75 CrossRef Medline
21. Baerlocher MO, Gautam T, Newton M, et al. Changing author counts in five major general medicine journals: effect of author contribution forms. *J Clin Epidemiol* 2009;62:875–77 CrossRef Medline
22. Chew FS. The scientific literature in diagnostic radiology for American readers: a survey and analysis of journals, papers, and authors. *AJR Am J Roentgenol* 1986;147:1055–61 CrossRef Medline
23. Mussurakis S. Coauthorship trends in the leading radiological journals. *Acta Radiology* 1993;34:316–20 Medline
24. Baek S, Yoon DY, Cho YK, et al. Trend toward an increase in authorship for leading radiology journals. *AJR Am J Roentgenol* 2015;205:924–28 CrossRef Medline
25. Chow DS, Ha R, Filippi CG. Increased rates of authorship in radiology publications: a bibliometric analysis of 142,576 articles published worldwide by radiologists between 1991 and 2012. *AJR Am J Roentgenol* 2015;204:W52–57 CrossRef Medline
26. Rahman M, Haque TL, Fukui T. Research articles published in clinical radiology journals: trend of contribution from different countries. *Acad Radiology* 2005;12:825–29 CrossRef Medline
27. Elster AD, Chen MY. The internationalization of the American Journal of Roentgenology: 1980–1992. *AJR Am J Roentgenol* 1994;162:519–22 CrossRef Medline
28. Chen MY, Jenkins CB, Elster AD. Internationalization of the American Journal of Roentgenology: 1980–2002. *AJR Am J Roentgenol* 2003;181:907–12 CrossRef Medline
29. Jones BF, Wuchty S, Uzzi B. Multi-university research teams: shifting impact, geography, and stratification in science. *Science* 2008;322:1259–62 CrossRef Medline
30. Sun H, Puterbaugh MD. Using social media to promote international collaboration. *Pennsylvania Libraries: Research & Practice* 2013;1:60–74 CrossRef
31. J. Clement. Number of social network users worldwide from 2010 to 2021. August 14, 2019. <https://www.statista.com/statistics/278414/number-of-worldwide-social-network-users/>. Accessed January 10, 2020
32. Priem J, Costello K, Dzuba T. Prevalence and use of Twitter among scholars. January 15, 2015. <https://s3-eu-west-1.amazonaws.com/pfigshare-u-files/232738/5uniposter.png>. Accessed January 10, 2020
33. Wilkinson C, Weitkamp E. A case study in serendipity: environmental researchers use of traditional and social media for dissemination. *PLoS One* 2013;8:e84339 CrossRef Medline
34. Collins K, Shiffman D, Rock J. How are scientists using social media in the workplace? *PLoS One* 2016;11:e0162680 CrossRef Medline
35. Nature Research. *Springer Nature 2017_Social Media Survey*. 2017

Medicare for All: Considerations for Neuroradiologists

T.H. Nguyen, J.M. Milburn, R. Duszak, J. Savoie, M. Horný, and J.A. Hirsch

ABSTRACT

SUMMARY: The year 2019 featured extensive debates on transforming the United States multipayer health care system into a single-payer system. At a time when reimbursement structures are in flux and potential changes in government may affect health care, it is important for neuroradiologists to remain informed on how emerging policies may impact their practices. The purpose of this article is to examine potential ramifications for neuroradiologist reimbursement with the Medicare for All legislative proposals. An institution-specific analysis is presented to illustrate general Medicare for All principles in discussing issues applicable to practices nationwide.

ABBREVIATIONS: MFA = Medicare for All; PC = professional component

Senator Bernie Sanders originally introduced the Medicare for All (MFA) Act in 2017, which aimed to establish a single national health insurance program. At that time, the bill was supported by only 16 other senators and eventually died in the 115th Congress. Fast forward 2 years: Several 2020 presidential candidates now emphatically endorse MFA, aligned with the fact that during the past decade, the support by the public for a national health plan has grown.¹ In April 2019, Senator Sanders reintroduced his MFA bill with expanded covered services.² This came on the heels of an additional MFA bill proposed in the House of Representatives in February 2019 by Representative Pramila Jayapal.³ Other politicians have proposed offering public health insurance while preserving private options.⁴ With health care reform at the center of national debate during this election year, it is important for physicians to be abreast of potential landmark health care legislation. While varying plans have been proposed on how to reform US health care, only the 2 aforementioned MFA Acts have been formally introduced in Congress at the time of this writing. The fundamental objectives common to both bills are summarized in Table 1. In this article, we use the term “MFA” specifically in reference to both Medicare for All Acts of 2019.

The financial impact of MFA implementation on individual radiology practices would depend on the case mix of services of each practice, the payer mix for each patient service, and reimbursement rates currently negotiated with private payers. The current payment models of the practice (eg, fee-for-service, bundled payments, or global budget) are also determinants of the potential impact of MFA on that particular practice. The MFA bills do not specifically address payment models; therefore, it is unclear how these would be affected. Thus, it is uncertain what would happen with reimbursement penalties and bonuses under the Merit-Based Incentive Payment System and Medicare Access and CHIP Reauthorization Act of 2015.

The ambiguity in MFA makes it difficult to predict the effect of MFA on a practice. However, the salient feature in the MFA legislative proposals is essentially transitioning the US multipayer health care system to a single-payer system. The goal of this Practice Perspectives is to discuss issues neuroradiologists may encounter in such a transition. We also provide an institution-specific analysis to illustrate the degree of impact this shift can have on a practice. The analysis is based on the case mix of the primary author’s institution and reimbursement figures for its locale. Medicare global, professional component (PC), and technical component fees were determined using the Medicare Physician Fee Schedule for 2019.⁵ Private reimbursement rates for noncapitated services provided by in-network providers to patients with primary residence in Louisiana or Mississippi (the Data Use Agreement prohibited us from reporting state-level metrics for Louisiana only) were extracted from the IBM MarketScan Commercial Claims and Encounters Database for the year 2017. All payments were adjusted for inflation using the seasonally-adjusted Consumer Price Index for Medical Care obtained from the Federal Reserve

Received January 16, 2020; accepted after revision March 7.

From the Department of Radiology (T.H.N., J.M.), Ochsner Health System, New Orleans, Louisiana; Department of Radiology and Imaging Sciences (R.D., M.H.), Emory University School of Medicine, Atlanta, Georgia; Imaging Services Administration (J.S.), University of Southern California Keck School of Medicine, Los Angeles, California; Department of Health Policy and Management (M.H.), Emory University Rollins School of Public Health, Atlanta, Georgia; and Department of Radiology (J.A.H.), Massachusetts General Hospital, Boston, Massachusetts.

Please address correspondence to Theresa H. Nguyen, MD, Department of Radiology, Ochsner Health System, 1514 Jefferson Hwy, New Orleans, LA, 70121; e-mail: Theresa.Nguyen@ochsner.org; @TheNguyenMD
<http://dx.doi.org/10.3174/ajnr.A6524>

Bank of St. Louis and expressed in 2019 US dollars.⁶ Medicaid fees in this study represent hospital-based Medicaid PC fee averages in Louisiana for the respective examinations and were provided by the radiology finance department of our lead study site. Although the analysis is institution-specific, it serves as a real-world example to illustrate general issues that apply to practices nationwide.

Financial Implications for Providers

In the United States, approximately 49% of the general population receives health insurance through their employers; 20%, through Medicaid; and 14%, through Medicare. About 9% of the population is uninsured. Other coverage comprises individual/nongroup insurance (6%) and military (1%).⁷ Under MFA, private health insurers would be prohibited from offering benefits included in the public program. The transition from a multipayer to single-payer system could have negative financial consequences for many radiologists because private insurer fees typically exceed those of Medicare.^{8,9} With regard to neuroradiology, brain MR imaging payments from private insurers were shown to

be more than twice as high as Medicare fee-for-service payments in a 2018 study published by the Congressional Budget Office.⁸

The difference between Medicare and private insurance fees is affected by factors including the negotiating power of a practice with private insurers, case mix, and the Geographic Practice Cost Index. As an example of variation between Medicare and private insurance reimbursement for a neuroradiology practice, Table 2 shows a brain examination case mix from the primary author's radiology department with fees from Medicare and estimated average reimbursements from private insurers.

The shift to MFA could be especially disruptive for practices that currently treat a large portion of privately insured patients because private insurer fees are typically higher than those of Medicare throughout the country.⁸⁻¹⁰ Conversely, MFA could increase revenue for some practices by reducing their uncompensated care for uninsured patients as well as by increasing their reimbursement for care of patients currently covered by lower-paying Medicaid.¹¹ Previous research found the average national Medicaid-to-Medicare fee index is 0.72,¹² though inpatient Medicaid fees vary on the basis of specific hospital cost-to-charge ratios. Some also

argue that MFA would reduce costs for providers by decreasing their administrative burdens.¹³ Furthermore, practices might benefit from reduced time between when services are rendered and reimbursed. A current advantage of Medicare over private insurers is that Medicare often reimburses sooner.

Table 1: Fundamental objectives of the Medicare for All Acts of 2019^{2,3}

Objectives
Establishment of a national health insurance program administered by the government that would cover all US residents
Creation of a nation health budget
Elimination of cost-sharing (deductibles, coinsurance, copayments) and balance billing for covered services
Interdiction against duplicate benefits from private health insurers or employers

Table 2: Example of neuroradiology case mix and 2019 Medicare fees compared with private insurance^{5,6a}

Examination (CPT)	No. of Examinations (2019)	Case Mix (%)	NR	Medicare		PI		Medicare	
				Global	Global	PC	PI PC	TC	PI TC
CT head (70450)	44,300	69.5	\$0	\$115.20	\$369.82	\$43.72	\$74.54	\$71.48	\$295.28
CT head with contrast (70460)	50	0.1	\$0	\$162.76	\$420.63	\$58.56	\$95.97	\$104.20	\$324.66
CT head without and with contrast (70470)	564	0.9	\$0	\$190.09	\$437.57	\$65.34	\$106.08	\$124.74	\$331.49
MR imaging brain (70551)	9400	14.7	\$0	\$224.92	\$550.98	\$76.16	\$131.26	\$148.77	\$419.72
MR imaging brain with contrast (70552)	244	0.4	\$0	\$311.96	\$486.19	\$91.71	\$158.49	\$220.24	\$327.70
MR imaging brain without and with contrast (70553)	9225	14.5	\$0	\$368.27	\$911.65	\$117.39	\$217.90	\$250.88	\$693.75
Total	63,783	100.0							

Note:—NR indicates nonreimbursed; PI, private insurance; TC, technical component; CPT, Current Procedural Terminology.

^a Medicare fees are based on the Medicare Physician Fee Schedule database with the following criteria: year 2019 and MAC locality 0720201.⁵ There was no difference between Medicare facility and nonfacility fees. Private insurance fees were obtained from IBM MarketScan Commercial Claims and Encounters Database for the year 2017. Payments were adjusted for inflation using the Consumer Price Index for Medical Care obtained from the Federal Reserve Bank of St. Louis and expressed in 2019 US Dollars.⁶

Table 3: Case mix and professional component fees by payer type

CPT	Examination	Case Mix	Uninsured	Medicare ⁵	Medicaid ^a	Private Insurance ⁶
70551	MR imaging brain WO contrast	15%	\$0	\$74.64	\$72.08	\$131.26
74178	CT Abd/pelvis WO/W contrast	15%	\$0	\$102.53	\$88.15	\$173.22
76770	US Abd complete	10%	\$0	\$37.14	\$32.59	\$63.33
77067	Screening mammogram	20%	\$0	\$38.79	\$37.86	\$63.67
71046	XR chest single	40%	\$0	\$10.25	\$8.52	\$18.70
	Total	100%				

Note:—W indicates with; WO, without; Abd, abdomen; US, ultrasound; XR, x-ray.

^a Medicaid fees represent hospital-based Medicaid PC fee averages in Louisiana for the respective examinations and were provided by the Radiology Finance Department of our lead study site.

To illustrate the impact on reimbursement in transitioning to a single-payer system, we present in Table 3, a simplified hypothetical general radiology case mix of 5 examinations, including MR imaging of the brain. These data are based on the case mix from the primary author's radiology department and reimbursement figures for this locale to provide as realistic an example as possible of radiology reimbursement in the US multipayer system. Current Procedural Terminology codes were used to obtain volumes of the corresponding examinations performed in the first half of 2019. The finance department of the institution providing these data advised against publishing department-specific reimbursement data. With this condition, the analysis includes commonly performed examinations outside neuroradiology because high-volume studies typically make up a large proportion of overall reimbursements. Furthermore, a variety of imaging modalities more accurately reflects the impact on neuroradiologists who tend to practice in broader radiology environments.

In the general Louisiana population, approximately 13.1% of individuals are enrolled in Medicare, while about half have private health insurance.⁷ Typically, Medicare enrollees use more health services than privately insured individuals, which is reflected in the inpatient population payer mix (Medicare accounts for 25.8%) derived from national data.^{14,15} Table 4 presents these examples of payer mixes. The payer mix of a typical radiology practice in Louisiana likely lies between these 2 examples if the practice performs both inpatient and outpatient imaging.

If we assume no change in the use of health services, if all patients in Louisiana were transitioned to Medicare at current Medicare PC fees, overall PC reimbursements for all 5 examinations in this analysis would decrease—with MR imaging of the

brain leading that decline. The estimated revenue reduction for our simplified radiology case mix is 14%–20% (Table 5). Given the larger decrease for MR imaging payments, practices with higher percentages of MR imaging brain examinations could be more affected. The change in reimbursement is smaller in the inpatient scenario because Medicare and Medicaid currently make up larger proportions of payers in this setting.

Considerations for Neuroradiology Practices

The 14%–20% figure in Table 5 pertains to the primary author's institution and is meant to serve as an example in discussing generalizable topics under MFA. A separate study by Galvani et al¹⁶ projected a 7.4% reduction if all physician and clinical services were reimbursed at Medicare rates. For practices that own equipment, technical fees contribute largely to the total cost of an imaging study. Louisiana Medicaid does not reimburse the technical component separately but rather reimburses for an imaging examination either by full service if the provider owns the equipment or by the PC alone.¹⁷ Other states may have nuanced differences in the way Medicaid reimburses the technical component.

The size of a practice is an important determinant of reimbursement. Because larger practices tend to negotiate higher prices with private health plans than smaller practices, smaller groups may experience less drastic reimbursement decreases under MFA. There is also a smaller reduction in the inpatient payer scenario because Medicare and Medicaid make up larger proportions of payers in this setting. This is concordant with the hypothesis that practices with more privately insured patients will experience more drastic reimbursement reductions compared with those that treat a high percentage of Medicare, Medicaid, and uninsured patients. Louisiana has a high proportion of Medicaid patients and around an average proportion of uninsured patients compared with the national US averages.⁷ In accounting for uncompensated care and lower PC fees from Medicaid, this analysis still showed an overall decrease in PC reimbursement in a Medicare single-payer scenario. Neuroradiologists in states with higher proportions of privately insured patients may experience a more drastic impact on reimbursements under MFA.

The analysis does not factor in fluctuations in imaging volume that may occur in a single-payer system. The volume of imaging examinations would likely increase due to decreased

Table 4: Examples of payer mix

Payer Type	Louisiana General Population Payer Mix ^a	Inpatient Population Payer Mix ^b
Private insurance	50.5%	35.6%
Medicare	13.1%	25.8%
Medicaid	28.3%	31.9%
Uninsured	8.1%	6.7%
Total	100%	100%

^a Based on data from the Kaiser Family Foundation 2017.⁷ The source data included an additional payer type "Other Public," which comprised military and the Veterans Health Administration. Our payer mix percentages were weighted to exclude this additional group, which made up 1% of the original mix.

^b Derived from data from the Health Care Cost and Utilization Project and U.S. Census Bureau 2017.^{14,15}

Table 5: Change in professional component reimbursement under Medicare for All at a radiology practice in Louisiana

Examination	Payer Type Scenario					
	100% Medicare	Current General Population Payer Mix	% Difference	Current Inpatient Payer Mix	% Difference	
MR imaging brain WO contrast	\$74.64	\$96.46	–23%	\$89.14	–16%	
CT Abd/pelvis WO/W contrast	\$102.53	\$125.85	–19%	\$117.11	–12%	
US Abd complete	\$37.14	\$46.07	–19%	\$42.80	–13%	
Screening mammogram	\$38.79	\$47.95	–19%	\$44.81	–13%	
XR chest single	\$10.25	\$13.20	–22%	\$12.13	–15%	
% Change if all uninsured, Medicaid, and privately insured patients are transitioned to Medicare			–20%		–14%	

Note:—W indicates with; WO, without; Abd, abdomen; US, ultrasound; XR, x-ray.

cost-sharing for patients.¹⁸ Further research is also needed to examine realistic cost-savings opportunities (eg, administrative costs) in evaluating the overall financial impact of MFA on radiology.

The estimated decrease in PC reimbursement in this analysis is based on 2019 Medicare PC fees. The Medicare Physician Fee Schedule for 2020 entailed cuts in reimbursement for radiology to boost reimbursement for care-related evaluation and management services. It is estimated this change will cost radiologists \$450 million in 1 year alone, and \$5.6 billion during the next decade.¹⁹ We also note that with reimbursement changes following passages of the Patient Protection and Affordable Care Act and Medicare Access and CHIP Reauthorization Act of 2015, it is also possible that fee-for-service may be substantially or completely replaced by alternative payment models (eg, bundled or episode-based payments, capitated payments, global budgets, and government salaried providers).¹³

Is Medicare for All Better for Our Patients?

Compared with patients in other high-income countries, Americans are more likely to report financial barriers to health care,^{20,21} with a third of US adults reporting difficulty paying medical bills in 2018.²² This situation is often sensationalized in the media, creating a perception that the US health care industry takes advantage of sick people. Such a belief can undermine public trust in our health care system. Below, we discuss concerns commonly brought up by American patients and concerns regarding MFA.

In 2018, approximately 30.4 million persons in the United States were uninsured.²³ MFA would certainly extend coverage to more patients, and proponents of this system argue that increasing access to preventative care will reduce overall health care costs (eg, by decreasing emergency department use or hospital admissions for acute exacerbations of chronic illnesses). Prior research found that extending Medicaid coverage resulted in more health care use, including emergency department visits, without immediate improvement in health measures such as blood pressure or cardiovascular risk. It did, however, reduce the prevalence of depression and medical debt.²⁴

In addition to expanding coverage, proponents argue that MFA would provide more stable coverage. Currently, many Americans receive health insurance through their employers, and changing jobs can result in coverage fluctuations. MFA does not address how the government would feasibly absorb this cost from employers and risks encountering similar issues as other countries if unprepared. Several countries with highly regarded universal health care systems now struggle to finance their health care systems. Since 2010, the National Health Service budget of the United Kingdom has fallen short of its health care costs, resulting in longer wait times for patients, reduced payments to providers, and calls for tax increases.²⁵⁻²⁷ Canada and Australia have faced similar issues of unsustainable rising health care costs, with consequent restrictions on services and increased reliance on private insurance.^{28,29}

The above is not a critique of the principle of universal health insurance but rather of how health care costs have become unsustainable despite a variety of coverage designs. In reforming health

care, current politics seems to focus more on who will pay for care rather than on strategies and resources to promote healthier lifestyles. Modern challenges, such as increases in the prevalence of chronic diseases, risk overwhelming the health care system. Although MFA aims to increase access to care, any such legislation will likely have a minimal effect on the root causes of contemporary issues such as sedentary lifestyles and poor diet. While we have focused mainly on financial implications, we acknowledge that there are innumerable other factors to consider in evaluating health care systems.

In summary, implementation of a single-payer system might solve some problems but would likely introduce several others. As key stakeholders in health care, neuroradiologists should scrutinize how emerging legislation will affect their practices and patients.

Disclosures: Richard Duszak—RELATED: Grant: Harvey L. Neiman Health Policy Institute.* Michal Horný—RELATED: Grant: Harvey L. Neiman Health Policy Institute.* Joshua A. Hirsch—UNRELATED: Consultancy: Medtronic, Relievent, Comments: Medtronic consultant, Relevant Data-Monitoring Committee; Grants/Grants Pending: Harvey L. Neiman Health Policy Institute. *Money paid to the institution.

REFERENCES

1. **Public Opinion on Single-Payer, National Health Plans, and Expanding Access to Medicare Coverage.** KFF. February 21, 2019. <https://www.kff.org/slideshow/public-opinion-on-single-payer-national-health-plans-and-expanding-access-to-medicare-coverage/>. Accessed June 11, 2019
2. **Medicare for All Act of 2019. S.S. 1129 from 116th Congress. B. Sanders, Author.** <https://www.congress.gov/116/bills/s/1129/BILLS-116s1129is.pdf>. Accessed May 10, 2019
3. **Medicare for All Act of 2019, H.R. 1384 from 116th Congress. J. Pramila, Author.** <https://www.congress.gov/bill/116th-congress/house-bill/1384>. Accessed May 10, 2019
4. Uhrmacher K, Schaul K, Firozi P, et al. **Where 2020 Democrats stand on Medicare-for-all.** *The Washington Post*. March 5, 2019. <https://www.washingtonpost.com/graphics/politics/policy-2020/medicare-for-all/>. Accessed August 17, 2019
5. U.S. Centers for Medicare & Medicaid Services. 2019. Physician Fee Schedule Search. <https://www.cms.gov/apps/physician-fee-schedule/search/search-criteria.aspx>. Accessed November 1, 2019
6. Federal Reserve Bank of St. Louis, U.S. Bureau of Labor Statistics. **Consumer Price Index for All Urban Consumers: Medical Care in U.S. City Average.** February 2020. <https://fred.stlouisfed.org/series/CPIMEDSL>. Accessed February 10, 2020
7. Kaiser Family Foundation. **Health Insurance Coverage of the Total Population. 2008–2018** <https://www.kff.org/other/state-indicator/total-population/?currentTimeframe=0&sortModel=%7B%22colId%22:%22Location%22,%22sort%22:%22asc%22%7D>. Accessed July 9, 2019
8. Congressional Budget Office. **An Analysis of Private-Sector Prices for Physicians' Services: Working Paper 2018-01. United States. January 12, 2018.** <https://www.cbo.gov/publication/53441>. Accessed June 11, 2019
9. Maeda JM, Marder WD, Karaca Z, et al. **Variation in hospital inpatient prices across small geographic areas.** *Am J Manag Care* 2014;20:907–16 Medline
10. Hargraves J, Biniek J; Health Care Cost Institute. **Comparing Commercial and Medicare Rates for Select Anesthesia ER, and Radiology Services by State.** July 23, 2019. <https://healthcostinstitute.org/out-of-network-billing/median-allowed-amounts-esi-2017>. Accessed September 17, 2019
11. Zuckerman Skopec L, Epstein M, et al. Urban Institute. **Medicaid Physician Fees after the ACA Primary Care Fee Bump.** March 2017. <https://www.urban.org/sites/default/files/publication/88836/>

- 2001180-medicaid-physician-fees-after-the-aca-primary-care-fee-bump_0.pdf. Accessed September 17, 2019
12. **Medicaid-to-Medicare Fee Index; State Health Facts.** 2016. <https://www.kff.org/medicaid/state-indicator/medicaid-to-medicare-fee-index/?currentTimeframe=0&selectedRows=%7B%22wrapups%22:%7B%22united-states%22:%7B%7D%7D%7D&sortModel=%7B%22colId%22:%22Location%22,%22sort%22:%22asc%22%7D>. Accessed August 15, 2019
 13. Congressional Budget Office. **Key Design Components and Considerations for Establishing a Single-Payer Health Care System.** May 2019. <https://www.cbo.gov/system/files/2019-05/55150-singlepayer.pdf>. Accessed June 11, 2019
 14. Sun RA, Karaca Z, Wong HS. **Trends in Hospital Inpatient Stays by Age and Payer, 2000–2015. H-CUP Statistical Brief.** January 2018. www.hcup-us.ahrq.gov/reports/statbriefs/sb235-Inpatient-Stays-Age-PayerTrends.pdf. Accessed October 20, 2019
 15. **Health Insurance Coverage Status and Type of Coverage by Selected Characteristics.** 2017. United States Census Bureau. <https://www.census.gov/data/tables/>. Accessed November 5, 2019
 16. Galvani AP, Parpia AS, Foster EM, et al. **Improving the prognosis of health care in the USA.** *Lancet* 2020;395:524–33 CrossRef Medline
 17. Louisiana Department of Health. **Professional services provider manual. Chapter Five of the Medicaid Services Manual.** <https://www.lamedicaid.com/provweb1/Providermanuals/manuals/PS/PS.pdf>. Accessed January 3, 2020
 18. Manning WG, Newhouse JP, Duan N, et al. Health Insurance and the Demand for Medical Care: Evidence from a Randomized Experiment. In: Manning WG, Newhouse JP, Duan N, et al. *RAND Report.* RAND Corporation: 1988
 19. Stempniak M. **ACR disappointed as feds finalize policy that could cost field billions.** *RADIOLOGY BUSINESS.* November 4, 2019. <https://www.radiologybusiness.com/topics/policy/american-college-radiology-cms-physician-fee-schedule>. Accessed November 10, 2019
 20. Osborn R, Squires D, Doty MM, et al. **New survey of eleven countries, US adults still struggle with access to and affordability of health care.** *Health Aff (Millwood)* 2016;35:2327–36 CrossRef Medline
 21. **2016 Commonwealth Fund International Health Policy Survey of Adults.** March–June 2016. <https://www.commonwealthfund.org/publications/surveys/2016/nov/2016-commonwealth-fund-international-health-policy-survey-adults>. Accessed June 17, 2019
 22. Collins SR, Bhupal HK, Doty M. **Health Insurance Coverage Eight Years After the ACA: Fewer Uninsured Americans and Shorter Coverage Gaps, But More Underinsured.** *Commonwealth Fund, February 2019.* Accessed June 4, 2019
 23. Cohen RA, Terlizzi EP, Martinez ME. **Health insurance coverage: early release of estimates from the National Health Interview Survey, 2018.** National Center for Health Statistics. May 2019. <https://www.cdc.gov/nchs/data/nhis/earlyrelease/insur201905.pdf>. Accessed June 17, 2019
 24. Baicker K, Allen HL, Wright BJ, et al. **The effect of Medicaid on medication use among poor adults: evidence from Oregon.** *Health Aff (Millwood)* 2017;36:2110–14 CrossRef Medline
 25. Martinson ML, Teitler JO, Reichman NE. **Health across the life span in the United States and England.** *Am J Epidemiol* 2011;173:858–65 CrossRef Medline
 26. Torjesen I. **Taxes must rise to fund 5% budget increase the NHS needs.** *BMJ* 2018;361:k2337 CrossRef Medline
 27. **Financial sustainability of the NHS. Report by the Comptroller and Auditor General of The National Audit Office. Presented to the House of Commons 785 Session. 2016–17.** November 22, 2016. <https://www.nao.org.uk/wp-content/uploads/2016/11/Financial-Sustainability-of-the-NHS.pdf>. Accessed August 18, 2019
 28. Barua B, Palacios M, Emes J. **The Sustainability of Health Care Spending in Canada 2017.** Fraser Institute. <https://www.fraserinstitute.org/sites/default/files/sustainability-of-health-care-spending-in-canada-2017-execsum.pdf>. Accessed June 3, 2019
 29. Stoelwinder J. **Sustaining universal health care in Australia: Introducing dynamic efficiency.** *CEDA, Healthcare: Reform or Ration.* <https://www.ceda.com.au/CEDA/media/ResearchCatalogue/Documents/PDFs/15366-healthcarefinal1.pdf>. Accessed June 3, 2019

Direct In Vivo MRI Discrimination of Brain Stem Nuclei and Pathways

T.M. Shepherd, B. Ades-Aron, M. Bruno, H.M. Schambra, and M.J. Hoch



ABSTRACT

BACKGROUND AND PURPOSE: The brain stem is a complex configuration of small nuclei and pathways for motor, sensory, and autonomic control that are essential for life, yet internal brain stem anatomy is difficult to characterize in living subjects. We hypothesized that the 3D fast gray matter acquisition T1 inversion recovery sequence, which uses a short inversion time to suppress signal from white matter, could improve contrast resolution of brain stem pathways and nuclei with 3T MR imaging.

MATERIALS AND METHODS: After preliminary optimization for contrast resolution, the fast gray matter acquisition T1 inversion recovery sequence was performed in 10 healthy subjects (5 women; mean age, 28.8 ± 4.8 years) with the following parameters: TR/TE/TI = 3000/2.55/410 ms, flip angle = 4° , isotropic resolution = 0.8 mm, with 4 averages (acquired separately and averaged outside *k*-space to reduce motion; total scan time = 58 minutes). One subject returned for an additional 5-average study that was combined with a previous session to create a highest quality atlas for anatomic assignments. A 1-mm isotropic resolution, 12-minute version, proved successful in a patient with a prior infarct.

RESULTS: The fast gray matter acquisition T1 inversion recovery sequence generated excellent contrast resolution of small brain stem pathways in all 3 planes for all 10 subjects. Several nuclei could be resolved directly by image contrast alone or indirectly located due to bordering visualized structures (eg, locus coeruleus and pedunculopontine nucleus).

CONCLUSIONS: The fast gray matter acquisition T1 inversion recovery sequence has the potential to provide imaging correlates to clinical conditions that affect the brain stem, improve neurosurgical navigation, validate diffusion tractography of the brain stem, and generate a 3D atlas for automatic parcellation of specific brain stem structures.

ABBREVIATION: FGATIR = fast gray matter acquisition T1 inversion recovery

The human brain stem represents the complex interdigitation of compact anatomic pathways and nuclei that control or modulate motor, sensory, autonomic, and cognitive functions. Many brain stem structures are essential for survival.¹ Patients can experience profound symptoms and disability even from small focal brain stem lesions due to ischemic stroke, multiple sclerosis, infections, vascular malformations, or tumors.²⁻⁶ Histopathologic changes in specific brain stem structures can lead to neurodegeneration associated with movement disorders, such as Parkinson disease, progressive

supranuclear palsy, and multiple system atrophy.⁷⁻¹¹ Even with state-of-the-art clinical MR imaging, it remains challenging to confidently localize the spatial locations of specific brain stem structures or to detect early pathologic changes to these structures in individual patients before postmortem examination.

To estimate the location of a particular brain stem structure in current practice, clinicians triangulate on the basis of surface landmarks, limited MR imaging-visible internal features, and mental representations of histology-stained sections from the same superior-inferior level. Systematic dissections of normal cadaver brains may improve the accuracy of this qualitative approach, particularly

Received January 28, 2020; accepted after revision March 19.

From the Departments of Radiology (T.M.S., B.A.-A., M.B.), Electrical and Computer Engineering (B.A.-A.), and Neurology (H.M.S.), New York University, New York, New York; and Department of Radiology (M.J.H.), University of Pennsylvania, Philadelphia, Pennsylvania.

T.M.S. received research support from the National Institute of Aging (1K23 AG048622-01). HMS received research support from National Library of Medicine (R01LM013316) and National Institute of Neurological Disorders and Stroke (K02 NS104207). H.M.S., T.M.S., and B.A.-A. received research support from the National Institute of Neurological Disorders and Stroke (R01 NS10696). This work was supported, in part, by the Center for Advanced Imaging Innovation and Research, a National Institutes of Health National Institute of Biomedical Technology resource center (grant P41EB017183).

Please address correspondence to Timothy Shepherd, MD, PhD, Department of Radiology, 660 First Ave, Room 226, New York, NY, 10016; e-mail: timothy.shepherd@nyumc.org; @tim0shepherd

Indicates open access to non-subscribers at www.ajnr.org

Indicates article with supplemental on-line photos.

Indicates article with supplemental on-line videos.

<http://dx.doi.org/10.3174/ajnr.A6542>

to better identify safe entry zones for surgical procedures of the brain stem.^{12,13} However, this overall approach does not account for anatomic distortion that frequently occurs with pathology (ie, no one performs surgery on the normal brain stem). Unfortunately, most stereotactic imaging-based brain atlases have emphasized resolution of cortex, white matter, or specific functional neurosurgery targets within the diencephalon.¹⁴⁻¹⁸ Detailed image-based parcellation for internal brain stem anatomy remains scant.^{19,20} The widely used FreeSurfer (<http://surfer.nmr.mgh.harvard.edu>) parcellation provides a single atlas label for the *entire* brain stem, and the more recent brain stem substructures algorithm only divides the brain stem into “midbrain,” “pons,” and “medulla.”²¹⁻²³

High-field MR imaging of postmortem, isolated brain stem specimens reveals the potential for MR imaging contrast resolution of internal brain stem anatomy comparable with histology,²⁴⁻²⁷ though external validity is limited because this requires 8+ hours of scanning-dissected, coil-optimized individual specimens that may have altered MR imaging properties due to fixation and the postmortem interval.^{28,29} Improved internal brain stem contrast also can be obtained with *in vivo* MR imaging using 7T systems,³⁰⁻³³ susceptibility mapping,^{34,35} relaxometry,^{30,35,36} or various representations/models of diffusion contrast.³⁷⁻³⁹ Diffusion tractography approaches can putatively identify many internal pathways and features of the brain stem.^{36,39} However, diffusion tractography is prone to spurious tract generation and true-positive segmentations are challenging to validate.⁴⁰ Furthermore, diffusion contrast is often altered by underlying pathology (unfortunately when identifying brain stem structures is most needed clinically).

Several groups have previously reported novel MR imaging sequences that manipulate T1 relaxation to suppress signal from white matter and maximize internal contrast within the thalamus and basal ganglia for direct targeting during functional neurosurgery.⁴¹⁻⁴⁶ These sequences have various acronyms, but perhaps the most relevant was fast gray matter acquisition T1 inversion recovery (FGATIR).⁴² Optimization of image contrast by manipulation of MR imaging sequence parameters was described in detail previously—the key concept is suppression of signal from voxels that contain myelin, even if the tissue does not contain classic white matter bundles by histology (eg, individual thalamic nuclei). Here, we demonstrate the tremendous advantages of also applying this MR imaging contrast mechanism for the direct identification of many internal brain stem structures in individual living subjects.

MATERIALS AND METHODS

This study was compliant with the New York University institutional review board and requirements of the Health Insurance Portability and Accountability Act. The data that support the findings of this study are available from the corresponding author on reasonable request. Healthy adult volunteers were imaged using a 3T Magnetom Prisma scanner with a 64-channel head and neck coil (Siemens). The sequence used here differs minimally from the originally reported FGATIR MR imaging sequence,⁴² or the more recent fluid and white matter suppression (FLAWS) component⁴³ of the updated MP2RAGE sequence.⁴⁴ For simplicity, we refer to the sequence used as FGATIR throughout the remainder of this report. For all experiments described below, parallel imaging was not used, the radiofrequency mode was “fast,” and “prescan normalize” was used (per

manufacturer). Complete protocol details will be provided to interested readers. We empirically developed a protocol to obtain excellent contrast and spatial resolution to discriminate brain stem structures as determined by consensus between 2 board-certified diagnostic neuroradiologists with expertise in brain stem neuroanatomy.

We first explored how to use signal averaging during image reconstruction to improve contrast resolution of brain stem structures using a 1-mm isotropic resolution sequence with the following parameters: TR/TE/TI = 3000/2.4/410 ms, nonselective 180° inversion pulse, flip angle = 6°, 256 × 256 matrix, 256-mm-square FOV, 160 × 1 mm sagittal slices, bandwidth = 320 Hz/pixel, time = 12 minutes 9 seconds per 1 average. Due to the relatively long scan time per signal average and potential for subtle-but-compounding motion artifacts, we compared obtaining 4 averages in *k*-space before Fourier image transformation (the standard approach to signal averaging) versus when 4 averages were obtained independently, reconstructed to image space, spatially coregistered using a 6-*df* rigid-body transform with FMRIB Linear Image Registration Tool (FLIRT; <http://www.fmrib.ox.ac.uk/fsl/fslwiki/FLIRT>), and finally averaged together. While there is a signal-to-noise penalty for not obtaining multiple averages in *k*-space before Fourier image transformation,⁴⁷ this approach (4 separate 12-minute 9-second scans versus a continuous scan time of 48 minutes 36 seconds) resulted in less image degradation from subtle head motion, even in cooperative, tolerant, and experienced volunteers.

Next, we compared contrast resolution between 1- and 0.8-mm isotropic resolution in which the latter sequence parameters were the following: TR/TE/TI = 3000/2.11/410 ms, nonselective 180° inversion pulse, flip angle = 6°, matrix = 288 × 288, FOV = 230 mm square, 192 × 0.8 mm sagittal slices, bandwidth = 460 Hz/pixel, time = 14 minutes 26 seconds per 1 average. The image quality and fine anatomic detail of the 0.8-mm isotropic resolution were preferred by both neuroradiologists. Then, a single subject underwent the 0.8-mm isotropic protocol in 2 separate sessions with 4 and 5 individual averages (57 minutes 44 seconds and 72 minutes 10 seconds, respectively). Within-session averages were coregistered using 6-*df* rigid-body transforms, and data between the 2 scan sessions were aligned using a 12-*df* affine transform. Individual averages were then combined sequentially to assess image-quality improvement with additional averages. The 9-average dataset was used for annotating the relevant brain stem anatomy in this report; however, 4 averages were more practical for multiple subjects and appeared to provide sufficient contrast resolution for most individual brain stem structures (per both neuroradiologists). Ten right-handed subjects (5 women, 28.8 ± 4.8 years of age, mean Edinburgh Handedness Inventory score = 86 ± 19) then were each imaged using 4 individual averages of the 0.8-mm FGATIR protocol to assess inter-subject variability in brain stem anatomy. Anatomic assignment of structures was determined by consensus between the 2 neuroradiologists using commonly available references and standard nomenclature.⁴⁸⁻⁵⁰ Note that axial images were created parallel to the commissural plane, while coronal images were parallel to the rhomboid fossa (which is not orthogonal to the commissural plane) (On-line Fig 1). For all figures, please see the Table for the specific labeled structures.

Key summary of labels for multiplanar anatomic images of the brain stem (Figs 1–6 and On-line Fig 2)

Label	Structure	Label	Structure
1	Mammillary body	32	Principal inferior olivary nucleus
2	Cerebral peduncle	33	Glossopharyngeal nerve
3	Pallido- and corticonigral tracts	34	Medullary pyramid
4	Substantia nigra, pars reticularis	35	Olivocerebellar fibers
5	Substantia nigra, pars compacta	36	Area postrema
6	Oculomotor nerve	37	Spinal trigeminal nucleus
7	Red nucleus	38	Cuneate nucleus
8	Medial lemniscus	39	Central gray matter
9	Spinothalamic tract	40	Internal arcuate fibers and sensory decussation
10	Central tegmental tract	41	Spinocerebellar tracts
11	Periaqueductal gray	42	Cuneate fasciculus
12	Medial longitudinal fasciculus	43	Gracile fasciculus
13	Inferior colliculus	44	Pyramidal decussation
14	Lateral lemniscus	45	Subthalamic nucleus
15	Decussation of superior cerebellar peduncles	46	Dentatorubrothalamic tract
16	Superior cerebellar peduncles	47	Posterior perforated substance
17	Rubrospinal tract	48	Habenulopeduncular tract
18	Corticospinal tract	49	Gracile nucleus
19	Pontocerebellar fibers	50	Lateral geniculate nucleus
20	Pontine nuclei	51	Medial geniculate nucleus
21	Trigeminal nerve	52	Superior colliculus
22	Sensory and motor trigeminal nuclei	53	Posterior commissure
23	Internal genu of facial nerve	54	Commissure of superior colliculus
24	Superior olivary nucleus	55	Brachium of the inferior colliculus
25	Middle cerebellar peduncle	56	Obex
26	Vestibular nuclear complex	57	Interpeduncular nucleus
27	Abducens nucleus	58	Tectospinal tract
28	Facial nerve	59	Trochlear nucleus
29	Vestibulocochlear nerve	60	Mesencephalic reticular formation
30	Trapezoid body	61	Ventral trigeminothalamic tract
31	Inferior cerebellar peduncle		

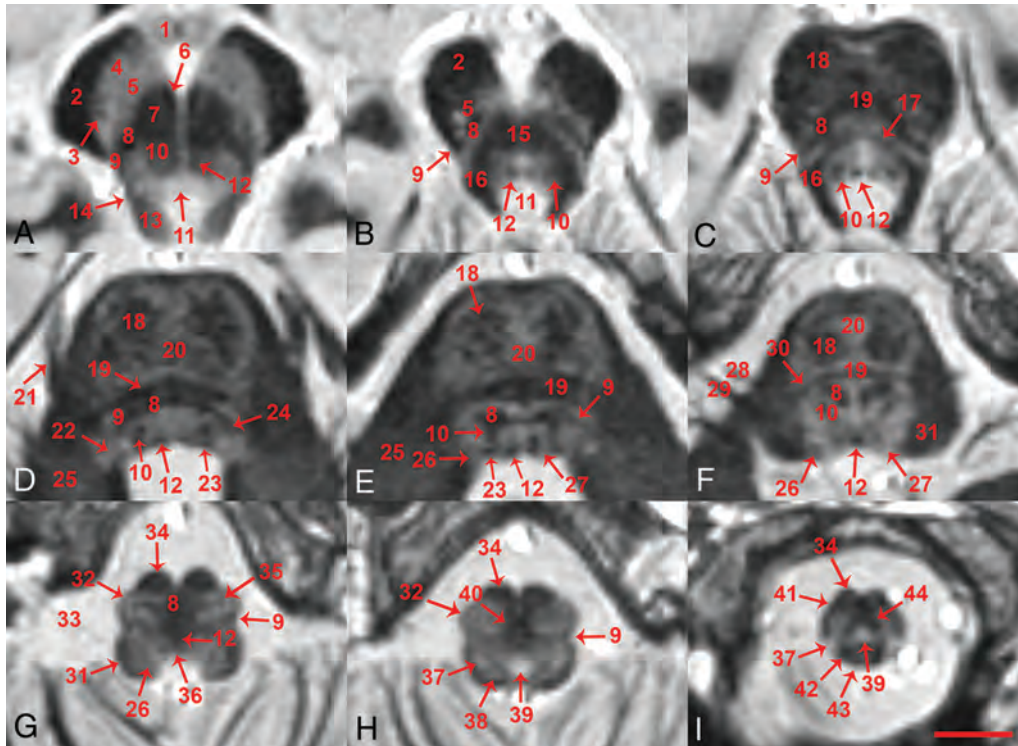


FIG 1. Superior-to-inferior axial in vivo MR images parallel to the intercommissural plane for the brain stem (number denotes the position below the plane), including the superior midbrain (A, 8.8 mm), inferior midbrain (B, 15.2 mm), midbrain-pons junction (C, 18.4 mm), superior midpons (D, 25.5 mm), inferior midpons (E, 29.5 mm), inferior pons (F, 35.9 mm), superior or “open” medulla (G, 43.1 mm), closed medulla at the sensory decussation (H, 47.1 mm) and motor decussation (I, 55.1 mm). A 26-year-old healthy control female subject, 0.8-mm isotropic resolution, 9 individual datasets coregistered and averaged, 2 imaging sessions with ~2-hour 15-minute total scan time (scale bar = 5 mm). Please see the Table and Results section for explanation of labeled structures.

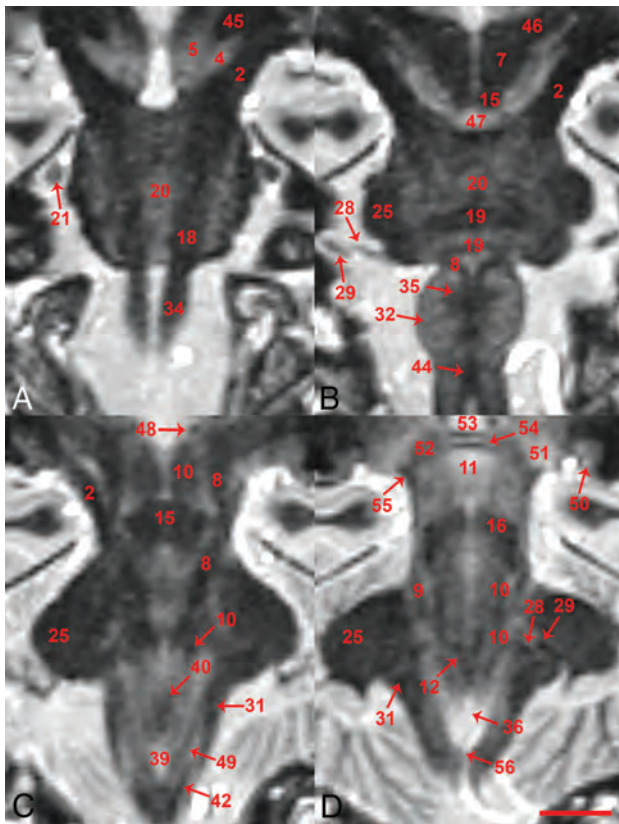


FIG 2. Anterior-to-posterior coronal in vivo MR images for the brain stem including 13.5-, 9-, 4.5-, and 1.5-mm anterior and parallel to the rhomboid fossa (A–D, respectively). A 26-year-old healthy control female subject, 0.8-mm isotropic resolution, 9 individual datasets coregistered and averaged, 2× imaging sessions, ~2-hour 15-minute total scan time (scale bar = 5 mm). Note this orientation is parallel to the long axis of the brain stem, but not orthogonal to the intercommissural plane. Please see the Table and the Results section for explanation of labeled structures.

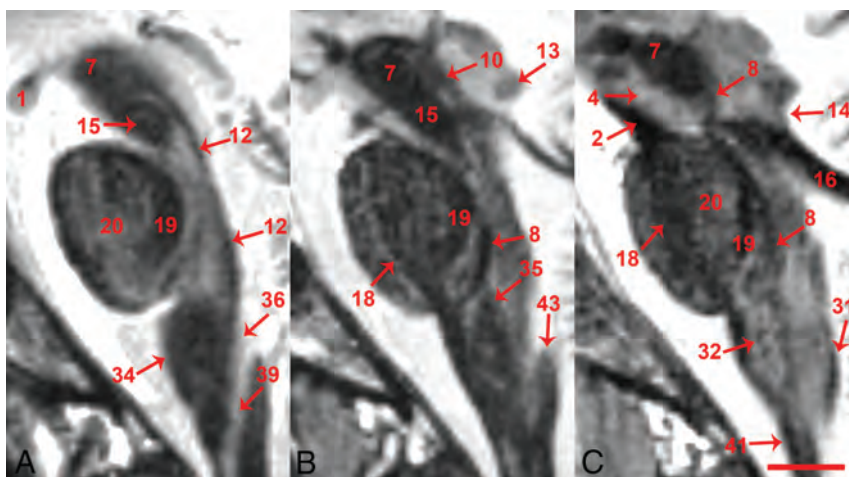


FIG 3. Medial-to-lateral sagittal in vivo MR images parallel to the interhemispheric plane and ventral medullary fissure for the brain stem including 1.2-, 2-, and 6-mm lateral to the midline (A, B, and C, respectively). A 26-year-old healthy control female subject, 0.8-mm isotropic resolution, 9 individual datasets coregistered and averaged, 2× imaging sessions, ~2-hour 15-minute total scan time (scale bar = 5 mm). Please see the Table and results section for explanation of labeled structures.

Finally, to demonstrate clinical feasibility, we performed a single average, 1-mm isotropic resolution FGATIR sequence (~12 minutes) in a patient with hemiplegia after ischemic stroke involving the corticospinal tract.

RESULTS

The FGATIR sequence provided novel MR imaging–derived contrast throughout the in vivo brain stem and allowed the direct identification of many small functionally important structures. Structure identification by 2 neuroradiologists was facilitated by 3-plane cross-referencing. Selected serial axial images illustrate contrast resolution of internal brain stem anatomy at canonical levels (Fig 1). Selected coronal and sagittal images also reveal excellent contrast resolution of internal brain stem anatomy (Figs 2 and 3, respectively). Such longitudinal images demonstrate the superior-inferior course of several brain stem pathways and the potential for the 0.8-mm isotropic FGATIR to enhance our understanding of the 3D organization of the brain stem. Videos of axial, coronal, and sagittal images through the brain stem are provided to interested readers on-line (On-line Videos 1–3).

Within the brain stem, the signal intensity or brightness of a specific structure appeared inversely correlated with the intensity of myelin staining in postmortem histology atlases.^{48–50} Blood in the vertebral arteries and dural venous sinuses appeared the brightest. The next most hyperintense structures were CSF and adjacent gray matter such as the periaqueductal gray and area postrema, the latter a circumventricular organ with an altered extracellular matrix and vascular structure.^{51,52} The third most hyperintense structures were more central gray matter within the brain stem such as the substantia nigra and pontine nuclei. Structures with intermediate hyperintensity were less compact or less densely myelinated structures like the inferior colliculi, central tegmental tract, and corticonigral pathways. Dark structures were classic myelinated brain stem pathways such as the medial longitudinal fasciculus, medial lemniscus, and pontocerebellar fibers. The darkest structures were densely myelinated pathways, including the medullary pyramids, superior/middle cerebellar peduncles, and larger cranial nerves. Cortical bone in the central skull base and the tectorial membrane also appeared very dark. Of note, the signal intensity (and shape) of the corticospinal tract varied along its course, appearing dark within the cerebral peduncles and medullary pyramids, but more diffuse and relatively brighter within the basis pontis. This appearance may represent interdigitation of pontine nuclei and pontocerebellar projections between white matter fascicles of the corticospinal tract.^{48–50,53}

Labeling in the figures emphasizes unambiguous structures that can be identified well on the images. Most of these labeled structures are well-known to clinicians familiar with brain stem anatomy (eg, the medial

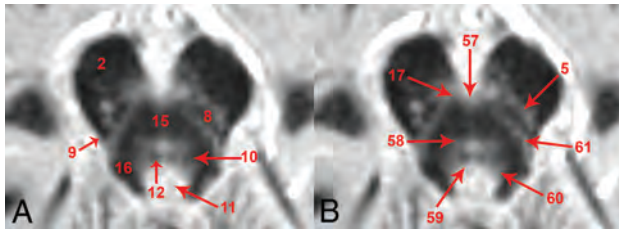


FIG 4. Direct, unambiguous identification of many myelinated structures in the inferior midbrain (A) also helps improve the spatial accuracy for indirect localization of bordering brain stem nuclei and pathways that are less densely myelinated at this level (B). The ventral trigeminothalamic tract⁶¹ is located between the decussation of the superior cerebellar peduncles and medial lemniscus. Subtle dark bumps on the anterior and posterior aspects of the decussation¹⁵ are consistent with the rubrospinal¹⁷ and tectospinal tracts,⁵⁸ respectively. The bright midline structure anterolateral to the medial longitudinal fasciculus⁸ should be the substantia nigra pars compacta.⁵ The reticular formation⁶⁰ is the bright region posterolateral to the medial longitudinal fasciculus and central tegmental tract,¹⁰ and anterolateral to the periaqueductal gray.¹¹ This region will also contain the locus coeruleus. The trochlear nucleus⁵⁹ should be along the posterior border of the medial longitudinal fasciculus. The interpeduncular nucleus⁵⁷ is off-midline anterior to the decussation of the superior cerebellar peduncles. Similar indirect localization can be derived at other brain stem levels, but is beyond the scope of this initial report.

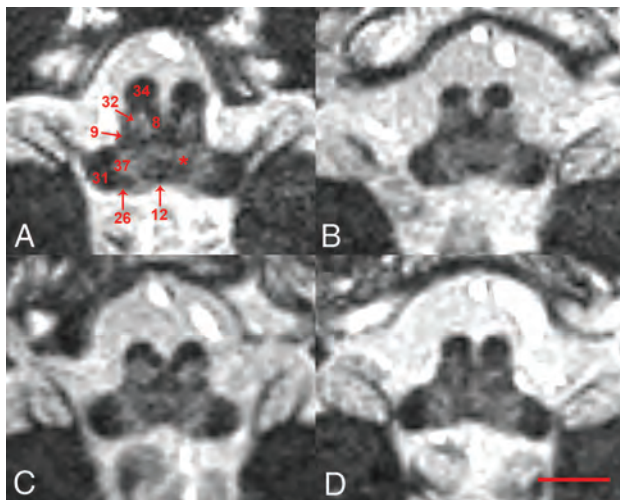


FIG 5. Axial in vivo MR images of the pontomedullary junction (superior to Fig 1F) selected from 4 different healthy adult controls (2 men) suggest reproducibility of overall image contrast across individuals and sexes (0.8-mm isotropic resolution, 4 averages, 58-minute total scan time, scale bar = 5 mm). The putative location of the pontomedullary reticular formation, a structure of interest for predicting limb function recovery after stroke, is denoted with an *asterisk*.

longitudinal fasciculus). Directly labeled visible structures also can be used to generate more exact indirect localization for other bordering internal brain stem structures. Figure 4 provides a highly detailed example of this approach for the inferior midbrain where the likely positions of multiple additional structures can be estimated relative to the borders and anatomic spaces formed between the medial longitudinal fasciculus, medial lemniscus, and decussation of the superior cerebellar peduncles. Annotation at this level of detail with descriptions of functional relevance is possible

throughout the brain stem, but is beyond the scope of this initial report. Other selected examples of indirect localization that may be of general interest include the oculomotor complex (bright region posteromedial to the central tegmental tract in Fig 1A), pedunculo-pontine nucleus (bright region medial to the medial lemniscus and lateral to the decussation of the superior cerebellar peduncles, in Fig 1B), locus coeruleus (bright region posterior to the central tegmental tract and medial to the superior cerebellar peduncle in Fig 1C), and facial nucleus (bright region posterolateral to the central tegmental tract and medial to the cerebellar peduncles in Fig 1F). An inferior notch along the medial aspect of the left middle cerebellar peduncle with gray matter signal intensity in Fig 2D is the cochlear nucleus.

There also are subtle features in the images that are difficult to assign with certainty (and sometimes only visualized on 1 side) that likely correspond to specific structures better resolved with postmortem MR microscopy⁵³ and histology atlases.^{48–50} Limited visualization may be from partial volume effects due to the small size of the structures relative to 0.8-mm isotropic voxels and/or less contrast relative to surrounding nervous tissue. On the right side of Fig 1B, there is an arc-like medially concave dark structure oriented anterior-posterior, consistent with the expected location of the left oculomotor nerve. In Fig 1C, -D, the tectospinal tract appears as a faint dark dotlike structure anterior to the medial lemniscus, particularly on the left side. In Fig 1E, the left tectospinal tract is more obvious, but there is marked asymmetry compared with the subject's right side. Also, in Fig 1E, the indistinct anterior margin of the medial lemniscus may represent the anteromedial continuation of the trapezoid body. In Fig 2D, an intermediate signal intensity line oriented inferomedial to superolateral, dividing the area postrema (on the right side of the image), may be the sulcus limitans. Some structures also are better recognized when the imaging plane is transverse to the structure. For example, the facial nerve in the lateral midpons is difficult to appreciate in the axial plane (Fig 1F), but better resolved in the coronal plane (Fig 2D).

The FGATIR images did not discriminate all brain stem structures well. It was not possible to distinguish the corticospinal tract from other white matter in the cerebral peduncle (Fig 1A). Boundaries of the medial lemniscus, tectospinal tract, and medial longitudinal fasciculus, which are adjacent to one another in an anterior-posterior orientation within the medulla, remain indistinct (Fig 1G). The inverse relationship of MR imaging signal intensity to white matter content described above also was not entirely consistent. For example, the red nucleus appeared isointense to enveloping cerebellorubral and cerebellothalamic fibers on MR imaging, but these structures are more distinct with classic white matter staining on histology.^{48,49}

Contrast discrimination of structures improved with more signal averages for the FGATIR sequence with 0.8-mm isotropic resolution, but subjectively yielded less improvement beyond 4 averages (On-line Fig 2). Thus, a 4-average protocol was used to image 10 healthy volunteers (~1-hour scan time) to assess individual variability in contrast (Fig 5). We observed subtle differences in morphology (eg, compare the medullary pyramids in A and C) or contrast resolution (eg, compare sensory decussation in A and D), but the overall contrast and the structures observed appeared consistent across individuals. In some subjects, the

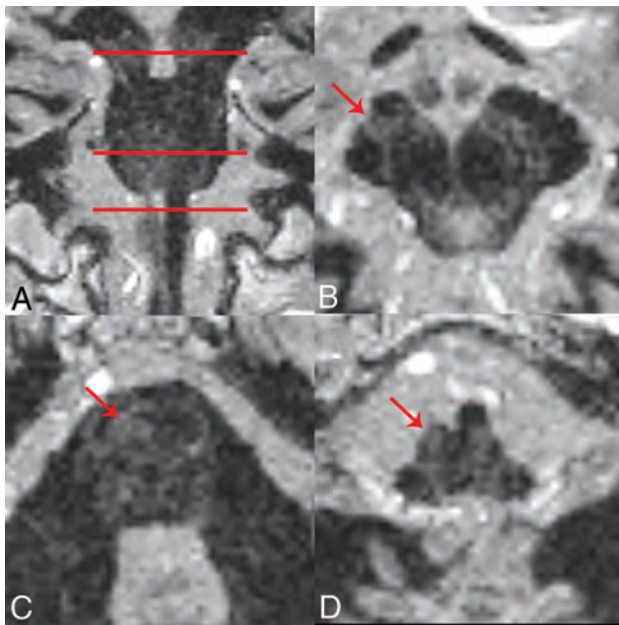


FIG 6. Example of the 1-mm isotropic resolution FGATIR sequence obtained in a 53-year-old woman with a remote prior right middle cerebral artery infarct involving the posterior fronto-insular cortex and subjacent basal ganglia (not shown). *A*, The axial planes for *B–D*. There is asymmetric absence of the compact dark corticospinal tract (red arrows) in the middle third of the right cerebral peduncle of the midbrain (*B*), right central basis pontis (*C*), and right medullary pyramid (*D*). These images appear very similar to myelin-stained histology changes of the brain stem after chronic right-sided infarct published in a popular neuroanatomy atlas.⁴⁸ This clinical example illustrates the feasibility of detecting brain stem pathology in patients using the faster, but lower 1-mm isotropic spatial resolution.

corticospinal tract signal intensity appeared asymmetrically darker on the left within the basis pontis (eg, Fig 1E). A similar observation has been reported in postmortem T2-weighted MR imaging microscopy of brain stems.⁵⁴

To demonstrate clinical feasibility, we used the 1-average, 1-mm isotropic FGATIR (theoretically increasing available intravoxel signal by ~95%) to obtain images in a consented patient with prior right-sided infarct (Fig 6). Here we observed loss of the normal right corticospinal tract signal intensity in the cerebral peduncle and basis pontis, with complete absence of the right medullary pyramid. These findings were spatially remote from the site of ischemic stroke (right basal ganglia and internal capsule) and consistent with trans-synaptic degeneration of the tract.

DISCUSSION

Better discrimination of internal brain stem anatomy is critical for building knowledge about brain stem structure-function relationships in health, normal aging, and disease.^{3,7,8} In current clinical practice, however, brain stem structure location can only be inferred indirectly on axial MR images on the basis of a priori knowledge of anatomy derived from histology (or postmortem MR microscopy), the superior-inferior position and surface landmarks, and limited internal contrast on clinical MR imaging. Current research atlases for imaging data like FreeSurfer^{22,23} provide limited detail for the internal brain stem anatomy. Here, we

identified brain stem anatomy using the FGATIR sequence, which uses a short inversion time to suppress signal from myelin. Previous groups using FGATIR (or similar contrast) emphasized applications for whole-brain segmentation or identification of diencephalic and spinal cord structures.^{41–46} FGATIR not only enables the direct visualization of brain stem structures, but also the brain stem structures identified can be used for more precise indirect localization of additional bordering brain stem structures (eg, Fig 4). Internal brain stem contrast can be generated directly using FGATIR without the need for postprocessing, modeling assumptions, or ultra-high-field MR imaging systems. Contrast was consistent across multiple subjects and was feasible to obtain in patients with stroke.

Other MR imaging methods have provided some contrast resolution of internal brain stem anatomy, but are clinically or technically limited. Submillimeter isotropic resolution MR microscopy images can be obtained from isolated postmortem brain stem samples;^{24–27} however, these protocols required 8–200 hours of scanning using ultra-high-field magnets and radiofrequency coils smaller than the human head, making this approach impractical for living subjects. Maps of diffusion parameters and tractography provide improved contrast resolution of internal brain stem anatomy.^{36,39} However, diffusion MR imaging resolution of submillimeter brain stem pathways is challenging *in vivo* due to signal-to-noise limitations. Reliance on high-resolution diffusion MR imaging for anatomic localization can also be problematic due to inherent geometric distortion, particularly in structures near the skull base, and results in spatial misregistration with volumetric sequences. Unlike FGATIR, diffusion MR imaging contrast depends on complex mathematic representations or models that have proved challenging to validate *in vivo*.⁴⁰ FGATIR may provide complementary contrast for validating brain stem diffusion tractography or for independently extracting diffusion values from brain stem structures/regions. Joint reconstruction of multiple MR imaging contrasts, including FGATIR, may provide the best contrast resolution of brain stem anatomy.⁵⁵

The 1-mm isotropic FGATIR acquisition with 1 average (~12-minute acquisition) is a relatively long acquisition for clinical MR imaging protocols, but appears feasible in patients (Fig 6), particularly in specific clinical circumstances that justify such a long scan. For example, the FGATIR sequence was originally developed for functional neurosurgery to improve deep brain stimulator electrode placement within the subthalamic nucleus.⁴² We plan to implement FGATIR in clinical patients to better localize specific brain stem structures affected by focal lesions (eg, infarcts, demyelinating, or inflammatory lesions). This sequence also may prove helpful for planning surgical biopsies or anatomic corridors for tumor resection.^{12,13} The 800- μ m isotropic data require 3–4 averages for useful contrast resolution, which may be susceptible to motion-related image degradation in noncompliant individuals. This concern may be addressed by applying several recently developed methods to accelerate FGATIR acquisitions, including sliding window reconstructions of *k*-space,⁵⁶ compressed sensing image reconstruction of undersampled data,⁵⁷ and deep learning approaches to improve suboptimal image contrast produced by shortened scan times.^{58,59} Clinical feasibility also can be supported through the use of a diffeomorphic template for coregistration of limited contrast

FGATIR images from individual patients⁶⁰ or by training a neural network to recognize small brain stem structures with limited FGATIR contrast.⁵⁸

Using FGATIR to depict brain stem anatomy has other potential limitations. Not all brain stem structures were directly resolved by FGATIR. We identified brain stem structures on the basis of correspondences to labeled myelin-stained histology images in published atlases,⁴⁸⁻⁵⁰ but direct structure-function correlations in the same brain would be helpful. Like diffusion MR imaging, FGATIR image contrast in the brain stem also could change with aging or disease. Such changes occur in other non-diffusion-weighted scans of the brain stem such as neuromelanin MR imaging in subjects with Parkinson disease.⁶¹ In our ongoing work, FGATIR-based contrast in older patients with stroke and essential tremor appears similar to that in age-matched healthy controls and younger subjects (unpublished data). However, the effects of aging and disease on FGATIR contrast require systematic investigation.

To date, the teaching, clinical targeting, and research of brain stem structures have largely relied on neuroanatomic atlases that have limitations. Most brain stem plates in the Haines atlas are from a single individual with trans-synaptic degeneration of the corticospinal tract due to internal capsule infarction.⁴⁸ The Schaltenbrand brain atlas, widely used for functional neurosurgery in the United States, relies predominately on 3 thalami of different sizes and limited spatial overlap.⁶² This atlas also provided annotated images of only 1 brain stem in the axial plane.¹⁷ MR imaging data with FGATIR contrast have some advantages over traditional neuroanatomy atlases that use postmortem histology. First, the 3D imaging datasets enable simultaneous localization and visualization of specific structures in multiple planes. Depiction of brain stem anatomy is not limited to the plane of section like histologic sampling, and specific oblique image reconstructions can be obtained to emphasize certain key spatial relationships. Second, collections of MR imaging data are less expensive and less time-intensive, providing greater opportunity to characterize brain stem structure variations across multiple individual brains. We intend to collect FGATIR data from a large cohort of subjects to create a diffeomorphic template with atlas labels^{60,63,64} for the human brain stem. These data could be used to investigate size and shape differences in the brain stem and as an independent method for extracting quantitative data from MR imaging and PET data in future investigations of small brain stem structure changes associated with aging and different diseases.^{65,66}

CONCLUSIONS

The FGATIR sequence provided excellent novel contrast resolution of internal brain stem pathways and nuclei at 3T in healthy living subjects. The 1-mm isotropic resolution protocol was clinically feasible (~12-minute acquisition) and may immediately help with structure-function correlations or surgical corridor planning in the brain stem for individual patients. The FGATIR sequence also provided image contrast that may be helpful to complement and/or validate other advanced MR imaging methods for brain stem anatomy such as diffusion tractography.

Disclosures: Timothy M. Shepherd—UNRELATED: Stock/Stock Options: MICroStructure Imaging, Heidi M. Schambra—RELATED: Grant: National Institutes of Health,

Comments: grant R01 NS10696*; UNRELATED: Grants/Grants Pending: National Institutes of Health.* *Money paid to the institution.

REFERENCES

1. Carpenter MB, Strong OS, Truex RC. *Human Neuroanatomy (Formerly Strong and Elwyn's Human Neuroanatomy)*. 7th ed. Lippincott Williams & Wilkins; 1976
2. Ortiz de Mendivil A, Alcalá-Galiano A, Ochoa M, et al. **Brainstem stroke: anatomy, clinical and radiological findings.** *Semin Ultrasound CT MR* 2013;34:131–41 CrossRef Medline
3. Tintore M, Rovira A, Arrambide G, et al. **Brainstem lesions in clinically isolated syndromes.** *Neurology* 2010;75:1933–38 CrossRef Medline
4. Tan IL, Mowry EM, Steele S, et al. **Brain stem encephalitis: etiologies, treatment, and predictors of outcome.** *J Neurol* 2013;260:2312–19 CrossRef Medline
5. Han SJ, Englot DJ, Kim H, et al. **Brainstem arteriovenous malformations: anatomical subtypes, assessment of “occlusion in situ” technique, and microsurgical results.** *J Neurosurg* 2015;122:107–17 CrossRef Medline
6. Donaldson SS, Laningham F, Fisher PG. **Advances toward an understanding of brainstem gliomas.** *J Clin Oncol* 2006;24:1266–72 CrossRef Medline
7. Dickson DW. **Parkinson's disease and parkinsonism: neuropathology.** *Cold Spring Harb Perspect Med* 2012;2 CrossRef Medline
8. Seidel K, Mahlke J, Siswanto S, et al. **The brainstem pathologies of Parkinson's disease and dementia with Lewy bodies.** *Brain Pathol* 2015;25:121–35 CrossRef Medline
9. Dugger BN, Tu M, Murray ME, et al. **Disease specificity and pathologic progression of tau pathology in brain stem nuclei of Alzheimer's disease and progressive supranuclear palsy.** *Neurosci Lett* 2011;491:122–26 CrossRef Medline
10. Santpere G, Ferrer I. **Delineation of early changes in cases with progressive supranuclear palsy-like pathology: astrocytes in striatum are primary targets of tau phosphorylation and GFAP oxidation.** *Brain Pathol* 2009;19:177–87 CrossRef Medline
11. Bretschneider J, Irwin DJ, Boluda S, et al. **Progression of alpha-synuclein pathology in multiple system atrophy of the cerebellar type.** *Neuropathol Appl Neurobiol* 2017;43:315–29 CrossRef Medline
12. Yagmurlu K, Rhoton AL Jr, Tanriover N, et al. **Three-dimensional microsurgical anatomy and the safe entry zones of the brainstem.** *Neurosurgery* 2014;(Suppl 4):602–19; discussion 619–20 CrossRef Medline
13. Martinez JA, de Oliveira E, Tedeschi H, et al. **Microsurgical anatomy of the brain stem.** *Operative Techniques in Neurosurgery* 2000;3:80–86 CrossRef
14. Talairach J, Tournoux P. *Co-Planar Stereotaxic Atlas of the Human Brain: 3-Dimensional Proportional System—An Approach to Cerebral Imaging*. Thieme Medical Publishers; 1988
15. Talairach J, Tournoux P, Missir O. *Referentially Oriented Cerebral MRI Anatomy: An Atlas of Stereotaxic Anatomical Correlations for Gray and White Matter*. Thieme Verlag; 1993
16. Ono M, Abernathy CD, Kubik S. *Atlas of the Cerebral Sulci*. Thieme; 1990
17. Schaltenbrand G, Hassler R, Wahren W. *Atlas of Stereotaxy of the Human Brain*. 2nd ed. Thieme; 1997
18. Cohn MC, Hudgins PA, Sheppard SK, et al. **Pre- and postoperative MR evaluation of stereotactic pallidotomy.** *AJNR Am J Neuroradiol* 1998;19:1075–80 Medline
19. Niemann K, van den Boom R, Haeselbarth K, et al. **A brainstem stereotactic atlas in a three-dimensional magnetic resonance imaging navigation system: first experiences with atlas-to-patient registration.** *J Neurosurg* 1999;90:891–901 CrossRef Medline
20. Afshar F, Watkins S, Yap JC. *Stereotaxic Atlas of the Human Brainstem and Cerebellar Nuclei: A Variability Study*. Raven Press; 1978
21. Fischl B. **FreeSurfer.** *Neuroimage* 2012;62:774–81 CrossRef Medline
22. Iglesias JE, Van Leemput K, Bhatt P, et al; Alzheimer's Disease Neuroimaging Initiative. **Bayesian segmentation of brainstem structures in MRI.** *Neuroimage* 2015;113:184–95 CrossRef Medline

23. FreeSurfer. <http://surfer.nmr.mgh.harvard.edu/>. Accessed September 24, 2019
24. Aggarwal M, Zhang J, Pletnikova O, et al. **Feasibility of creating a high-resolution 3D diffusion tensor imaging based atlas of the human brainstem: a case study at 11.7 T.** *Neuroimage* 2013;74:117–27 CrossRef Medline
25. Soria G, De Notaris M, Tudela R, et al. **Improved assessment of ex vivo brainstem neuroanatomy with high-resolution MRI and DTI at 7 Tesla.** *Anat Rec (Hoboken)* 2011;294:1035–44 CrossRef Medline
26. Calabrese E, Hickey P, Hulette C, et al. **Postmortem diffusion MRI of the human brainstem and thalamus for deep brain stimulator electrode localization.** *Hum Brain Mapp* 2015;36:3167–78 CrossRef Medline
27. Naidich T, Castillo M, Cha S, et al. *Imaging of the Brain*. Saunders; 2012
28. Shepherd TM, Thelwall PE, Stanisz GJ, et al. **Aldehyde fixative solutions alter the water relaxation and diffusion properties of nervous tissue.** *Magn Reson Med* 2009;62:26–34 CrossRef Medline
29. Shepherd TM, Flint JJ, Thelwall PE, et al. **Postmortem interval alters the water relaxation and diffusion properties of rat nervous tissue: implications for MRI studies of human autopsy samples.** *Neuroimage* 2009;44:820–26 CrossRef Medline
30. Deistung A, Schäfer A, Schweser F, et al. **High-resolution MR imaging of the human brain stem in vivo at 7 Tesla.** *Front Hum Neurosci* 2013;7:710 CrossRef Medline
31. Gizewski ER, Maderwald S, Linn J, et al. **High-resolution anatomy of the human brain stem using 7-T MRI: improved detection of inner structures and nerves?** *Neuroradiology* 2014;56:177–86 CrossRef Medline
32. Cho ZH, Calamante F, Chi JG. *7.0 Tesla MRI Brain White Matter Atlas*. 2nd ed. Springer-Verlag; 2015
33. Eapen M, Zald DH, Gatenby JC, et al. **Using high-resolution MR imaging at 7T to evaluate the anatomy of the midbrain dopaminergic system.** *AJNR Am J Neuroradiol* 2011;32:688–94 CrossRef Medline
34. Manova ES, Habib CA, Boikov AS, et al. **Characterizing the mesencephalon using susceptibility-weighted imaging.** *AJNR Am J Neuroradiol* 2009;30:569–74 CrossRef Medline
35. Hashido T, Saito S. **Quantitative T1, T2, and T2* mapping and semi-quantitative neuromelanin-sensitive magnetic resonance imaging of the human midbrain.** *PLoS One* 2016;11:e0165160 CrossRef Medline
36. Hoch MJ, Chung S, Ben-Eliezer N, et al. **New clinically feasible 3T MRI protocol to discriminate internal brain stem anatomy.** *AJNR Am J Neuroradiol* 2016;37:1058–65 CrossRef Medline
37. Naganawa S, Yamazaki M, Kawai H, et al. **Anatomical details of the brainstem and cranial nerves visualized by high resolution read-out-segmented multi-shot echo-planar diffusion-weighted images using unidirectional MPG at 3 T.** *Magn Reson Med Sci* 2011;10:269–75 CrossRef Medline
38. Nagae-Poetscher LM, Jiang H, Wakana S, et al. **High-resolution diffusion tensor imaging of the brain stem at 3 T.** *AJNR Am J Neuroradiol* 2004;25:1325–30 Medline
39. Habas C, Cabanis EA. **Anatomical parcellation of the brainstem and cerebellar white matter: a preliminary probabilistic tractography study at 3 T.** *Neuroradiology* 2007;49:849–63 CrossRef Medline
40. Maier-Hein KH, Neher PF, Houde JC, et al. **The challenge of mapping the human connectome based on diffusion tractography.** *Nat Commun* 2017;8:1349 CrossRef Medline
41. Reich CA, Hudgins PA, Sheppard SK, et al. **A high-resolution fast spin-echo inversion-recovery sequence for preoperative localization of the internal globus pallidus.** *AJNR Am J Neuroradiol* 2000;21:928–31 Medline
42. Sudhyadhom A, Haq IU, Foote KD, et al. **A high resolution and high contrast MRI for differentiation of subcortical structures for DBS targeting: the fast gray matter acquisition t1 inversion recovery (FGATIR).** *Neuroimage* 2009;47(Suppl 2):T44–52 CrossRef Medline
43. Tanner M, Gambarota G, Kober T, et al. **Fluid and white matter suppression with the MP2RAGE sequence.** *J Magn Reson Imaging* 2012;35:1063–70 CrossRef Medline
44. Marques JP, Gruetter R. **New developments and applications of the MP2RAGE sequence: focusing the contrast and high spatial resolution R1 mapping.** *PLoS One* 2013;8:e69294 CrossRef Medline
45. Tourdias T, Saranathan M, Levesque IR, et al. **Visualization of intrathalamic nuclei with optimized white-matter-nulled MPRAGE at 7T.** *Neuroimage* 2014;84:534–45 CrossRef Medline
46. Zerroug A, Gabrillargues J, Coll G, et al. **Personalized mapping of the deep brain with a white matter attenuated inversion recovery (WAIR) sequence at 1.5-Tesla: experience based on a series of 156 patients.** *Neurochirurgie* 2016;62:183–89 CrossRef Medline
47. Mitchell DG, Cohen MS. *MRI Principles*. 2nd ed. Saunders; 2004
48. Haines DE. *Neuroanatomy: An Atlas of Structures, Sections and Systems*. 6th ed. Lippincott Williams & Wilkins; 2004
49. DeArmond SJ, Fusco MM, Dewey MM. *Structure of the Human Brain: A Photographic Atlas*. 3rd ed. Oxford University Press; 1989
50. Warner JJ, Samuels MS. *Atlas of Neuroanatomy: With Systems Organization and Case Correlations*. Butterworth-Heinemann; 2001
51. Pécsai K, Kálmán M. **Extracellular matrix components mark the territories of circumventricular organs.** *Neurosci Lett* 2014;566:36–41 CrossRef Medline
52. Duvernoy HM, Risold PY. **The circumventricular organs: an atlas of comparative anatomy and vascularization.** *Brain Res Rev* 2007;56:119–47 CrossRef Medline
53. Naidich TP, Duvernoy HM, Delman BN, et al. *Duvernoy's Atlas of the Human Brain Stem and Cerebellum*. Springer-Verlag, Vienna; 2009
54. Hoch MJ, Bruno MT, Faustina A, et al. **3T MRI whole-brain microscopy discrimination of subcortical anatomy, Part 1: brain stem.** *AJNR Am J Neuroradiol* 2019;40:401–07 CrossRef Medline
55. Manjón JV, Coupé P, Buades A, et al. **MRI superresolution using self-similarity and image priors.** *Int J Biomed Imaging* 2010;2010:425891 CrossRef Medline
56. d'Arcy JA, Collins DJ, Rowland IJ, et al. **Applications of sliding window reconstruction with Cartesian sampling for dynamic contrast enhanced MRI.** *NMR Biomed* 2002;15:174–83 CrossRef Medline
57. Lustig M, Donoho D, Pauly JM. **Sparse MRI: the application of compressed sensing for rapid MR imaging.** *Magn Reson Med* 2007;58:1182–95 CrossRef Medline
58. Akkus Z, Galimzianova A, Hoogi A, et al. **Deep learning for brain MRI segmentation: state of the art and future directions.** *J Digit Imaging* 2017;30:449–59 CrossRef Medline
59. Zhang K, Zuo W, Chen Y, et al. **Beyond a Gaussian denoiser: residual learning of deep CNN for image denoising.** *IEEE Trans Image Process* 2017;26:3142–55 CrossRef Medline
60. Avants BB, Yushkevich P, Pluta J, et al. **The optimal template effect in hippocampus studies of diseased populations.** *Neuroimage* 2010;49:2457–66 CrossRef Medline
61. Xing Y, Sapuan A, Dineen RA, et al. **Life span pigmentation changes of the substantia nigra detected by neuromelanin-sensitive MRI.** *Mov Disord* 2018;33:1792–99 CrossRef Medline
62. Niemann K, van Nieuwenhofen I. **One atlas: three anatomies—relationships of the Schaltenbrand and Wharen microscopic data.** *Acta Neurochir (Wien)* 1999;141:1025–38 CrossRef Medline
63. Avants BB, Tustison NJ, Song G, et al. **A reproducible evaluation of ANTs similarity metric performance in brain image registration.** *Neuroimage* 2011;54:2033–44 CrossRef Medline
64. Wang H, Yushkevich P. **Multi-atlas segmentation with joint label fusion and corrective learning: an open source implementation.** *Front Neuroinform* 2013;7:27 CrossRef Medline
65. Lambert C, Chowdhury R, Fitzgerald TH, et al. **Characterizing aging in the human brainstem using quantitative multimodal MRI analysis.** *Front Hum Neurosci* 2013;7:462 CrossRef Medline
66. Nye JA, Purselle D, Plisson C, et al. **Decreased brainstem and putamen SERT binding potential in depressed suicide attempters using [¹¹C]-zient PET imaging.** *Depress Anxiety* 2013;30:902–07 CrossRef Medline

Acetazolamide-Loaded Dynamic 7T MR Quantitative Susceptibility Mapping in Major Cerebral Artery Steno-Occlusive Disease: Comparison with PET

K. Fujimoto, I. Uwano, M. Sasaki, S. Oshida, S. Tsutsui, W. Yanagihara, S. Fujiwara, M. Kobayashi, Y. Kubo, K. Yoshida, K. Terasaki, and K. Ogasawara



ABSTRACT

BACKGROUND AND PURPOSE: Dynamic changes in cerebrovascular reactivity after acetazolamide administration vary markedly among patients with major cerebral arterial steno-occlusive disease. MR quantitative susceptibility mapping can dynamically quantify the cerebral magnetic susceptibility. The purpose of this study was to determine whether dynamic changes in susceptibility after administration of acetazolamide on 7T quantitative susceptibility mapping are associated with pre-existing states of CBV and the cerebral metabolic rate of oxygen in the cerebral hemispheres with major cerebral arterial steno-occlusive disease.

MATERIALS AND METHODS: Sixty-five patients underwent 7T MR imaging at baseline and at 5, 10, 15, and 20 minutes after acetazolamide administration. Differences between the susceptibility of venous structures and surrounding brain tissue were calculated in the quantitative susceptibility mapping images. Susceptibility differences at 5, 10, 15, and 20 minutes after acetazolamide administration relative to baseline were calculated in 97 cerebral hemispheres with major cerebral arterial steno-occlusive disease. CBV and the cerebral metabolic rate of oxygen were also calculated using ^{15}O -gas PET in the resting state.

RESULTS: Dynamic changes of susceptibility after acetazolamide administration were classified into 3 patterns: abnormally increasing 5 or 10 minutes after acetazolamide administration; abnormally decreasing within 20 minutes after acetazolamide administration; and remaining unchanged after acetazolamide administration. CBV was significantly greater in the first pattern than in the latter 2. The cerebral metabolic rate of oxygen differed significantly in descending order from the first to middle to last pattern.

CONCLUSIONS: Dynamic changes of susceptibility after acetazolamide administration on 7T MR quantitative susceptibility mapping are associated with pre-existing states of CBV and the cerebral metabolic rate of oxygen in major cerebral arterial steno-occlusive disease.

ABBREVIATIONS: ACZ = acetazolamide; BOLD = blood oxygen level-dependent; CMRO₂ = cerebral metabolic rate of oxygen; CVR = cerebrovascular reactivity; OEF = oxygen extraction fraction; QSM = quantitative susceptibility mapping; RS = relative susceptibility

When the chronic progression of major cerebral arterial steno-occlusive disease reduces cerebral perfusion pressure, cerebrovascular autoregulatory mechanisms attempt to preserve CBF through the dilation of precapillary resistance vessels;

this is referred to as stage 1 ischemia.¹⁻³ In stage 1 ischemia, cerebrovascular reactivity (CVR) to acetazolamide (ACZ), which reflects the degree of cerebrovascular autoregulatory vasodilation, starts to decrease.¹⁻³ However, autoregulatory capacity cannot compensate for further reductions in cerebral perfusion pressure, which result in a decline in CBF; this is referred to as stage 2 ischemia, or misery perfusion.¹⁻³ CVR to ACZ is exhausted in this stage.¹⁻³ In the clinical setting, CVR to ACZ is measured using perfusion SPECT,⁴ dynamic susceptibility contrast perfusion MR imaging,⁵ and transcranial Doppler ultrasonography.⁶

MR imaging is capable of quantifying the blood oxygen level-dependent (BOLD) changes in venous structures and/or brain parenchyma induced by differences in magnetic susceptibility between oxy- and deoxyhemoglobin.⁷⁻⁹ Wu et al¹⁰ continuously measured CVR to ACZ using BOLD imaging with 3T MR imaging in patients with steno-occlusive disease of major cerebral arteries and demonstrated that overall, BOLD signal began

Received March 4, 2019; accepted after revision March 1, 2020.

From the Department of Neurosurgery (K.F., S.O., S.T., W.Y., S.F., M.K., Y.K., K.Y., K.O.), Division of Ultrahigh Field MRI, Institute for Biomedical Sciences (I.U., M.S.), and Cyclotron Research Center (K.T.), Iwate Medical University School of Medicine, Morioka, Japan.

This study was funded by a grant-in-aid for the Private University Research Branding Project from the Ministry of Education, Culture, Sports, Science and Technology-supported program; and scientific research from the Japan Society for the Promotion of Science (JP18K09002).

Please address correspondence to Kuniaki Ogasawara, M.D., Department of Neurosurgery, Iwate Medical University, Uchimaru 19-1, Morioka 020-8505, Japan; e-mail: kuogasa@iwate-med.ac.jp

Indicates open access to non-subscribers at www.ajnr.org

Indicates article with supplemental on-line table.

<http://dx.doi.org/10.3174/ajnr.A6508>

increasing immediately after ACZ administration, approaching a plateau at ~8.5 minutes after administration. However, in some patients, BOLD signal showed a more severely reduced relative reactivity at 6–7 minutes after the initiation of ACZ infusion and progressive partial recovery toward a pre-ACZ administration value at 10–11 minutes.¹⁰ These findings suggested that dynamic changes to susceptibility after ACZ administration vary markedly among such patients. CVR to ACZ itself may depend on the pre-existing state of vasodilation, which can be assessed using CBV, and pre-existing dilated vessels show little or no response to ACZ.^{1–3} We hypothesized that a pre-existing state of cerebral metabolism is another condition impacting CVR to ACZ; ACZ acts via enzyme reaction, and a reduction in this enzyme reaction causes a slow, decreased CVR to ACZ. Cerebral metabolism, which can be assessed using the cerebral metabolic rate of oxygen (CMRO₂), may be reduced in such a state.

A postprocessing technique known as quantitative susceptibility mapping (QSM) on MR imaging can quantify the magnetic susceptibility of venous structures and/or brain parenchyma from T2*-weighted magnitude/phase images, which are easily obtained using a commercial scanner.¹¹ Several investigators have measured CVR to ACZ using QSM on 3T MR imaging and suggested that QSM is sensitive to dynamic modulation of the oxygen extraction fraction (OEF) during hemodynamic augmentation.¹² A recent study using QSM with a 7T scanner reported that it offered profound susceptibility effects and optimized postprocessing techniques.¹³ The scan time for this mapping is relatively short (3 minutes 25 seconds), and it may also enable imaging of dynamic changes in blood oxygenation levels in venous structures and/or brain parenchyma.

Therefore, the purpose of the present study was to determine whether dynamic changes in susceptibility after ACZ administration on 7T QSM are associated with pre-existing CBV and CMRO₂ on PET in patients with ICA or MCA steno-occlusive disease.

MATERIALS AND METHODS

All procedures performed in studies involving human participants were in accordance with the institutional ethics committee, and written, informed consent was obtained from all subjects or their next of kin before patient participation.

Healthy Subjects

To obtain healthy control values from brain ¹⁵O-gas PET studies, we enrolled 10 healthy adult men (mean age, 47 ± 8 years; age range, 35–60 years) who had no history of diabetes mellitus, dyslipidemia, or hypertension and had an absence of asymptomatic lacunar infarction and leukoaraiosis on conventional brain MR imaging.

Patient Inclusion Criteria

We prospectively selected patients who provided written informed consent to participate and who met the following basic inclusion criteria: presence of clinical symptoms suggesting ischemic episodes in the MCA or ICA territory at 1–6 months before visiting our institution; useful residual function (0, 1, or 2 on the mRS); presence of uni- or bilateral MCA (M1 portion) or extra- or intracranial ICA stenosis (>70% or 50% for the ICA and MCA, respectively) or occlusion on angiography; and absence of infarcts in the

entire cortical area supplied by the M4 branch of the MCA on T1WI and T2WI, and DWI.

MR Imaging Protocol and Generation of QSM

A 7T MR scanner (Discovery MR950; GE Healthcare) with quadrature transmission and 32-channel receive head coils was used. QSM source data were obtained using a 3D spoiled gradient recalled acquisition technique with flow compensation (TR, 30 ms; TE, 15 ms; flip angle, 20°; FOV, 256 mm; acquisition matrix size, 512 × 256; section thickness, 2 mm; number of slices, 160; reconstruction voxel size after zero-fill interpolation, 0.5 mm³; and scan time, 3 minutes 25 seconds).¹³ Magnitude and real/imaginary phase images were regenerated from this acquisition.

First, each patient underwent the above-mentioned MR imaging at baseline. Next, ACZ (1000 mg; range, 13–19 mg/kg body weight) was dissolved in physiologic saline (20 mL); this solution was then administered intravenously for 1 minute. The MR imaging was performed in the same fashion 4 times so that each midscan time was 5, 10, 15, and 20 minutes after the end of intravenous administration of ACZ.

Before the start of this ACZ challenge study, 30 other cerebral hemispheres with ICA or MCA steno-occlusive disease underwent 5 MR imaging scans with the same timing without ACZ administration to assess the minute-to-minute test-retest variability of susceptibility as measured using QSM.

QSM images were generated from the source images using an in-house program with a multiple dipole-inversion combination with *k*-space segmentation¹⁴ and regularization-enabled sophisticated harmonic artifact reduction for phase data methods,¹⁵ as described previously.¹³ A 2D Gaussian low-pass filter with a kernel size of 60% of the total image power in each section was applied to extract iron deposition in deep nuclei, hemosiderin deposition, dural sinuses, and large venous structures, and a 2D Gaussian high-pass filter of 2% was applied to extract small venous structures.¹³ Subsequently, small venous structures were determined by multiplying the Gaussian high-pass filter-processed binary images and the logical negations of Gaussian low-pass filter-processed binary images under the threshold for binarization of ≥2 SDs.¹³

The difference between the average susceptibility of venous structures and surrounding brain tissue was calculated in each voxel of interest of 25 mm³ in the processed QSM images.¹³ The susceptibility difference was finally displayed with a smoothing procedure. To validate a correlation between baseline OEF obtained from QSM images and pre-existing OEF obtained on PET, we generated OEF maps from baseline QSM images before ACZ challenge in accordance with a previous study.¹³

Brain ¹⁵O-Gas PET Study

Patients who were scheduled to undergo MR imaging studies with the ACZ challenge underwent PET studies in a resting state without ACZ challenge. PET studies were performed using a SET-3000GCT/M scanner (PET/CT; Shimadzu) (full width at half maximum for in-plane and axial spatial resolutions of 3.5 and 4.2 mm, respectively) within 5 days before MR imaging. Before the PET scans, a 3-minute transmission scan with a

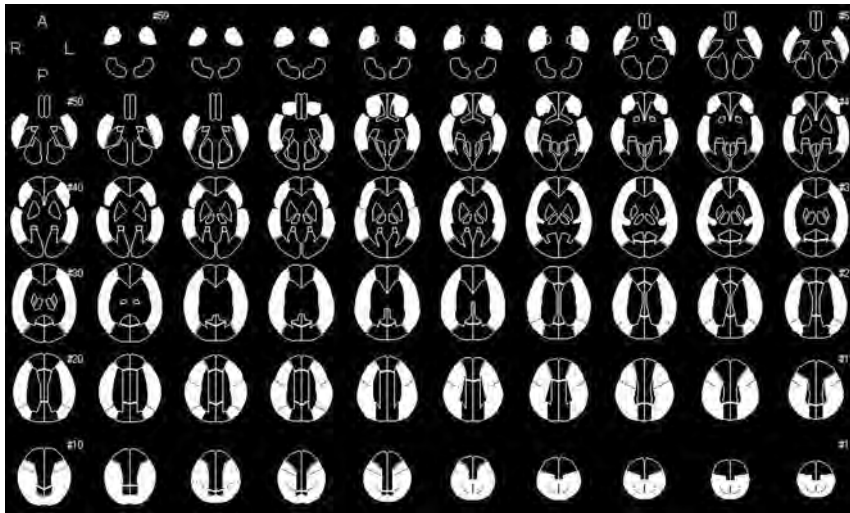


FIG 1. Diagrams showing the 318 ROIs for the 3D stereotaxic ROI template. *White ROIs indicate territories perfused by bilateral MCAs.*

cesium 137 (^{137}Cs) point source was conducted using a bismuth germanate transmission detector ring that was coaxially attached to the gadolinium silica oxide emission detector ring. Next, CBF was measured while the patient inhaled C^{15}O_2 continuously through a mask. The CMRO_2 and OEF were measured during continuous inhalation of $^{15}\text{O}_2$; these data were collected for 5 minutes. CBV was measured during a single breath of C^{15}O . Finally, CBF, OEF, and CMRO_2 were calculated using the steady-state method¹⁶ and then corrected on the basis of CBV.¹⁷

Image Data Analyses

Image data analyses were performed according to previously reported methods.¹³ By means of SPM, Version 12 (<http://www.fil.ion.ucl.ac.uk/spm/software/spm12>),¹⁸ PET images that were coregistered to QSM source images, as well as QSM images after Gaussian smoothing ($\sigma = 10$ pixel), were warped to Montreal Neurological Institute coordinates. Next, 318 constant ROIs were placed in both the cerebral and cerebellar hemispheres automatically using a 3D stereotaxic ROI template with SPM.¹⁹ The ROIs were then grouped into a total of 10 segments—callosomarginal, pericallosal, precentral, central, parietal, angular, temporal, posterior, hippocampal, and cerebellar—in each hemisphere according to the arterial supply. Five of these 10 segments (precentral, central, parietal, angular, and temporal) perfused by the MCA were then combined and defined as an MCA ROI (Fig 1).

Mean susceptibility differences on QSM images and CBF, CBV, OEF, and CMRO_2 on PET images were measured using image-analysis software (ITK-SNAP; www.itksnap.org)²⁰ in the MCA ROI in the cerebral hemisphere with ICA or MCA stenocclusive disease. In each MCA ROI of each cerebral hemisphere with ACZ challenge, relative susceptibility (RS, %) was calculated as follows: $100 \times$ susceptibility difference at each time (5, 10, 15, or 20 minutes) after ACZ administration on QSM images/susceptibility difference in the baseline on QSM images. In each MCA ROI of each cerebral hemisphere without ACZ challenge, RS was also calculated as follows: $100 \times$ susceptibility difference on QSM images

in the second, third, fourth, or fifth MR imaging/susceptibility difference on QSM images in the first MR imaging. When RS at 5 (RS_5), 10 (RS_{10}), 15 (RS_{15}), or 20 (RS_{20}) minutes after ACZ administration was higher than the upper limit of the 95% CI of RS in the second, third, fourth, or fifth MR imaging, respectively, in the 30 cerebral hemispheres without ACZ challenge, the former RS was defined as abnormally increased. When RS_5 , RS_{10} , RS_{15} , or RS_{20} was lower than the lower limit of the 95% CI of RS in the second, third, fourth, or fifth MR imaging, respectively, in the 30 cerebral hemispheres without ACZ challenge, the former RS was defined as abnormally decreased. In each MCA ROI of each patient, a chronological change in RS after ACZ administration was classified

on the basis of the presence or absence of an abnormal increase or decrease in RS at any time point.

In each MCA ROI of each patient, when CBV was greater than the upper limit of the 95% CI of control values obtained from 20 cerebral hemispheres of 10 healthy subjects, this ROI was defined as having abnormally elevated CBV; when the CMRO_2 was lower than the lower limit of the 95% CI of control values, this ROI was defined as showing abnormally reduced CMRO_2 .

Statistical Analysis

Data are expressed as the mean \pm SD. Pearson correlation coefficients were used to assess correlations between baseline QSM-OEF and pre-existing PET-OEF. A difference in RS at each time point after ACZ administration was evaluated using the Friedman test. When this difference was significant, differences among RS values at each time after ACZ administration were compared using the Wilcoxon signed rank test followed by the Holm method. A difference in CBF, CBV, OEF, or CMRO_2 among ≥ 3 groups was evaluated using the Kruskal-Wallis test. When this difference was significant, differences among CBF, CBV, OEF, or CMRO_2 in each group were compared using the Mann-Whitney *U* test followed by the Holm method. A difference in CBV or CMRO_2 among 2 groups was evaluated using the Mann-Whitney *U* test. *P* values $< .05$ were considered statistically significant for all assessments.

RESULTS

During the 30-month study period, a total of 89 patients successfully underwent 7T MR imaging without severe adverse effects. In 4 of these patients, data sufficient to generate QSM were not obtained because of motion artifacts; these 4 patients were excluded from the analysis. Therefore, 85 patients (65 and 20 with and without ACZ challenge, respectively) were finally enrolled in the study.

Among these 85 patients (46 men, 39 women; mean age, 55 ± 12 years; age range, 30–76 years), 60 had hypertension, 32 had diabetes mellitus, and 55 had dyslipidemia. Thirty-seven, 27, 3, and 17 patients had bilateral ICA (bilateral extracranial diseases in 27; bilateral intracranial diseases in 5; unilateral extracranial disease and contralateral intracranial disease in 5), unilateral ICA (extracranial disease in 22; intracranial disease in 5), the M1 portion diseases of bilateral MCA, and unilateral M1 portion steno-occlusive disease, respectively. The remaining patient had unilateral extracranial ICA and contralateral M1 portion steno-occlusive diseases. Therefore, 127 MCA ROIs of the 127 cerebral hemispheres with MCA or ICA steno-occlusive disease (97 and 30 with and without ACZ challenge, respectively) were eventually analyzed.

The 95% CI of RS values in the second, third, fourth, and fifth MR imaging in 30 MCA ROIs without ACZ challenge were 91.85%–108.55%, 90.81%–109.33%, 90.59%–109.49%, and 90.70%–109.22%, respectively. No difference was observed among each RS. The 95% CIs of CBV and CMRO₂ obtained from 20 MCA ROIs of 10 healthy subjects were 2.45–5.01 mL/100 g and 2.31–4.70 mL/100 g/min, respectively.

A significant correlation was observed between baseline QSM-OEF and pre-existing PET-OEF ($r = 0.865$; $P \leq .0001$) (Fig 2).

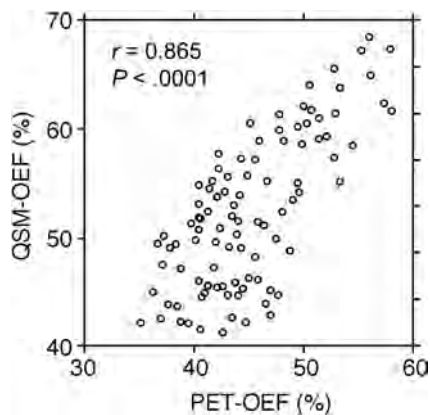


FIG 2. Correlations between baseline QSM-OEF before ACZ administration and pre-existing PET-OEF in 97 MCA ROIs.

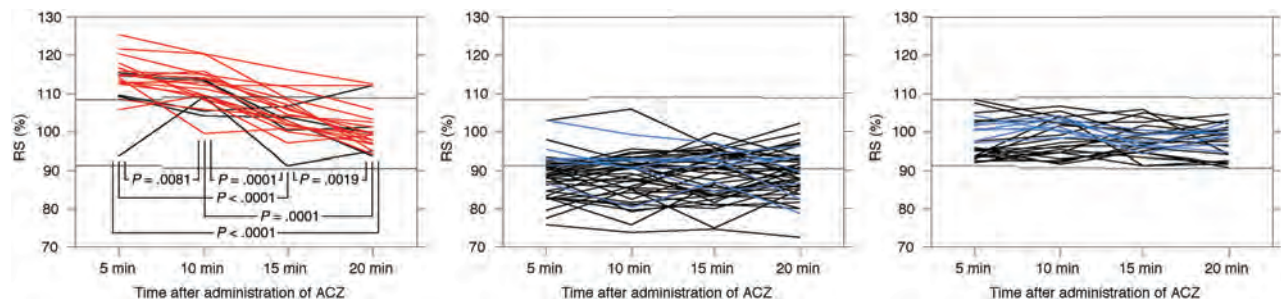


FIG 3. Chronological changes in RS after ACZ administration in 97 MCA ROIs. Left, middle, and right graphs show the 22 MCA ROIs with abnormally increased RS at ≥ 1 time point, the 47 MCA ROIs with abnormally decreased RS at ≥ 1 time point, and the 28 MCA ROIs without abnormally increased or decreased RS at any time point, respectively. Red, blue, and black lines denote ROIs with abnormally elevated CBV, an abnormally decreased cerebral metabolic rate of oxygen, and neither, respectively. Upper and lower dotted horizontal lines denote the upper and lower limits of the 95% CI of controls without ACZ challenge, respectively.

Figure 3 shows chronological changes in RS after ACZ administration for the 97 MCA ROIs. Patterns of these changes were classified into the following 3 groups: RS was abnormally increased at ≥ 1 time point in 22 MCA ROIs; RS was abnormally decreased at ≥ 1 time point in 47 MCA ROIs; and RS remained within the 95% CI of controls at all time points (defined as unchanged RS) in 28 MCA ROIs. None of the MCA ROIs exhibited an abnormally increased RS and an abnormally decreased RS at different time points.

Of the 22 MCA ROIs with abnormally increased RS, 2 exhibited abnormally increased RS at all time points; 1 exhibited abnormally increased RS₅, RS₁₀, and RS₁₅; eleven exhibited abnormally increased RS₅ and RS₁₀; one exhibited abnormally increased RS₅ and RS₂₀; five exhibited abnormally increased RS₅ alone; and 2 exhibited abnormally increased RS₁₀ alone.

Of the 47 MCA ROIs with abnormally decreased RS, 18 exhibited abnormally decreased RS at all time points; 3 exhibited abnormally decreased RS₅, RS₁₀, and RS₁₅; three exhibited abnormally decreased RS₅, RS₁₀, and RS₂₀; two exhibited abnormally decreased RS₅, RS₁₅, and RS₂₀; one exhibited abnormally decreased RS₁₀, RS₁₅, and RS₂₀; one exhibited abnormally decreased RS₅ and RS₁₀; one exhibited abnormally decreased RS₁₅ and RS₂₀; nine exhibited abnormally decreased RS₅ alone; 3 exhibited abnormally decreased RS₁₀ alone; 2 exhibited abnormally decreased RS₁₅ alone; and 4 exhibited abnormally decreased RS₂₀ alone.

In the 22 MCA ROIs with abnormally increased RS, RS differed significantly among 4 time points: RS₅ ($113.84 \pm 6.28\%$; $P = .0081$ for RS₁₀; $P < .0001$ for RS₁₅; $P < .0001$ for RS₂₀), RS₁₀ ($111.58 \pm 5.06\%$; $P = .0001$ for RS₁₅; $P = .0001$ for RS₂₀), RS₁₅ ($104.72 \pm 5.43\%$; $P = .0019$ for RS₂₀), and RS₂₀ ($100.93 \pm 5.55\%$) in descending order (Fig 3). In the 47 MCA ROIs with abnormally decreased RS, no significant differences were observed among RS₅ ($88.69 \pm 5.56\%$), RS₁₀ ($88.55 \pm 5.98\%$), RS₁₅ ($88.71 \pm 5.87\%$), and RS₂₀ ($89.00 \pm 5.83\%$). In the 28 MCA ROIs with unchanged RS, no significant differences were observed among RS₅ ($97.89 \pm 4.89\%$), RS₁₀ ($99.06 \pm 4.47\%$), RS₁₅ ($97.85 \pm 3.74\%$), and RS₂₀ ($97.80 \pm 3.78\%$).

The On-line Table shows comparisons of pre-existing CBV and CMRO₂ among MCA ROIs with abnormally increased RS, abnormally decreased RS, unchanged RS, and MCA ROIs in healthy subjects as controls. CBV was significantly greater in

MCA ROIs with abnormally increased RS than in those with abnormally decreased RS, unchanged RS, or controls. No significant differences in CBV were identified in other any comparisons. Of the 22 MCA ROIs with abnormally increased RS, 17 (77%) had abnormally elevated CBV. In contrast, none of the patients with abnormally decreased RS or unchanged RS had abnormally elevated CBV. No significant differences in CMRO₂ were apparent between controls and MCA ROIs with abnormally increased RS. Regarding other comparisons, the CMRO₂ differed significantly in descending order, as follows: controls or abnormally increased RS, abnormally decreased RS, and unchanged RS. Of the 28 MCA ROIs with unchanged RS, 8 (29%) showed abnormally reduced CMRO₂. In contrast, of the 47 MCA ROIs with abnormally decreased RS, only 7 (14%) had abnormally reduced CMRO₂, and no MCA ROIs with abnormally increased RS had abnormally reduced CMRO₂. Furthermore, in the 47 MCA ROIs with abnormally decreased RS, whereas CBV did not differ significantly in the 11 MCA ROIs with unchanged RS₅ (3.35 ± 0.84 mL/100 g) and the 36 MCA ROIs with abnormally decreased RS₅ (3.40 ± 0.3862 mL/100 g), CMRO₂ was significantly lower in the former MCA ROIs (2.65 ± 0.52 mL/100 g/min) than in the latter (3.06 ± 0.38 mL/100 g/min; $P = .0182$).

Representative chronological images of susceptibility difference obtained from QSM after ACZ administration and PET images performed before MR imaging in a patient with abnormally increased CBV in the symptomatic cerebral hemisphere are shown in Fig 4.

DISCUSSION

The present study demonstrated that dynamic changes in susceptibility after ACZ administration on 7T QSM are associated with pre-existing CBV and CMRO₂ on PET in patients with ICA or MCA steno-occlusive disease.

In this study, ACZ was administered intravenously for 1 minute. This method has been applied for measuring CVR on brain perfusion SPECT in adult patients with ICA or MCA steno-occlusive disease.^{4,21} Considering the adverse effects of ACZ administration performed in the same fashion, 63% of patients reportedly developed only minor symptoms such as headache, nausea, dizziness, tinnitus, numbness of the extremities, and general malaise, and these symptoms resolved within 72 hours after ACZ administration.²² These patients experienced neither severe general symptoms nor neurologic deficits.²² Similarly, no patients in the present study experienced such severe adverse effects due to ACZ administration.

A study using ¹⁵O PET demonstrated that while CBF increased at 10 and 20 minutes after ACZ administration in healthy humans, CMRO₂ was unchanged compared with preadministration.²³ Changes in susceptibility after ACZ administration on QSM theoretically reflect both changes in CBF and oxygen metabolism by ACZ. Although whether CMRO₂ after ACZ administration is constant in patients with cerebrovascular diseases remains unknown, dynamic changes in susceptibility after ACZ administration on QSM may more strongly reflect changes in CBF than changes in oxygen metabolism: Increases and decreases in the susceptibility may predominantly indicate decreases and increases in CBF, respectively. One study of CVR to ACZ using QSM on 3T MR imaging showed that OEF decreased from baseline to 16 minutes

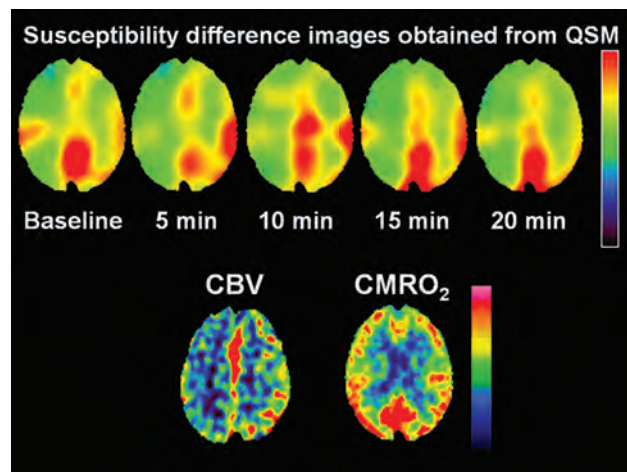


FIG 4. A 55-year-old man with transient ischemic attacks of right hemiparesis and bilateral MCA stenosis. Susceptibility on susceptibility difference images (upper) obtained from QSM is increased at 5 and 10 minutes after ACZ administration in the left cerebral hemisphere compared with baseline, suggesting early steal phenomenon. The susceptibility in that hemisphere begins to decline at 15 minutes after ACZ administration and reaches below baseline at 20 minutes after ACZ administration. By contrast, susceptibility in the right cerebral hemisphere is decreased at 5 minutes after ACZ administration compared with baseline and is gradually increased at 10 and 15 minutes after ACZ administration. However, the susceptibility in that hemisphere at 20 minutes after ACZ administration remains below baseline. ¹⁵O-gas PET images at resting state (lower images) show an increase in CBV and CMRO₂ within normal limits in the left cerebral hemisphere.

after ACZ administration in the cerebral hemisphere with anterior circulation steno-occlusive disease, as well as in the cerebral hemisphere without such disease, and the decrease was more substantial in the latter.¹² These changes in susceptibility might be caused by changes of CBF.¹²

In the present study, dynamic changes of susceptibility after ACZ administration were classified into 3 patterns: abnormally increasing, peaking at 5 or 10 minutes after ACZ administration and later returning toward baseline; abnormally decreasing within 20 minutes after ACZ administration and maintaining this decrease; and remaining unchanged after ACZ administration. A dynamic change comprising an abnormal increase in susceptibility early after ACZ administration and subsequent return was comparable with a finding obtained using continuous measurements of BOLD signal after ACZ administration.¹⁰ In MCA ROIs with such dynamic changes, pre-existing CBV was abnormally elevated and pre-existing CMRO₂ was normally maintained. Mean transit time (MMT) is a function of CBV/CBF, and an increase in CBV usually implies a long MMT in MCA or ICA steno-occlusive disease. A long MMT can result in low drug delivery, leading to little or no CVR immediately after ACZ administration in the region affected by such a condition, whereas CVR in surrounding or other brain tissues with a normal MMT reacts rapidly because of normal drug delivery. In addition, the small arterioles or intraparenchymal vessels are dilated in regions with an increase in CBV. These pre-existing dilated

vessels cannot respond immediately after ACZ administration, whereas normal vessels in surrounding or other brain tissue rapidly dilate. These differences in CVR to ACZ administration lead to a sudden reduction in cerebral perfusion pressure of normal vessels relative to pre-existing dilated vessels. This dynamically developed pressure gradient may result in the early steal of blood flow from pre-existing dilated vessels to normal vessels. Subsequently, pre-existing dilated vessels may gradually respond to ACZ, and a vasodilation effect of ACZ in normal vessels may gradually reduce with time. Such mechanisms could explain the abnormal increase in susceptibility early after ACZ administration (early steal phenomenon) and subsequent return.

A dynamic change of the abnormal decrease in susceptibility within 20 minutes after ACZ administration and maintenance of this decrease might imply an increase in CBF—that is, normal CVR to ACZ. Actually, in MCA ROIs showing such a dynamic change, pre-existing CBV was normal. Pre-existing CMRO₂ was reduced compared with that in controls but remained within normal limits in 86% of MCA ROIs showing that susceptibility change. On the other hand, pre-existing CMRO₂ was reduced more in MCA ROIs with an abnormal decrease in susceptibility ≥ 10 minutes after ACZ administration than in those with an abnormal decrease in susceptibility 5 minutes after ACZ administration. Because CBV did not differ significantly between these 2 groups, the difference in dynamic change after ACZ administration might be attributable to pre-existing CMRO₂. ACZ acts via carbonic anhydrase, and a reduction in its activity slows CVR to ACZ. The activity of carbonic anhydrase may depend on cerebral metabolism. This hypothesis may also explain the maintenance of unchanged susceptibility after ACZ administration. In MCA ROIs with such a dynamic change in susceptibility, pre-existing CBV was normal, but pre-existing CMRO₂ was quite markedly reduced; this finding suggests that the activity of carbonic anhydrase was severely reduced and cerebral vessels were unresponsive to ACZ.

Using continuous measurement of CVR to ACZ with BOLD imaging, Wu et al¹⁰ demonstrated that BOLD signal began increasing gradually following ACZ administration, approaching a plateau at ~ 8.5 minutes after administration in the cerebral hemisphere without ICA or MCA steno-occlusive disease. This dynamic change in susceptibility differed compared with that of MCA ROIs with normal CBV and normal CMRO₂ in the present study: an abnormal decrease in susceptibility 5 minutes after ACZ administration and maintenance of this decrease. The difference in peak susceptibility may be due to the method of ACZ administration. ACZ (1000 mg) was administered intravenously for 3–5 minutes in the study by Wu et al and for 1 minute in the present study.

A preoperative decrease in CVR to ACZ or a preoperative increase in CBV in the cerebral hemisphere ipsilateral to carotid endarterectomy or carotid artery stent placement for cervical ICA stenosis or arterial bypass surgery for Moyamoya disease has been identified as a powerful and independent predictor of postoperative cerebral hyperperfusion.^{21,24,25} Postoperative cerebral hyperperfusion induces unilateral headache, face and eye pain, seizure, and focal symptoms that occur secondary to cerebral edema or intracerebral hemorrhage.^{21,25} This phenomenon, even when

asymptomatic, induces slight-but-diffuse brain damage, resulting in postoperative cognitive decline.²⁶ Identification of reduced CVR to ACZ or elevated CBV therefore enables improved risk stratification for such patients. However, the predictive accuracy of CVR to ACZ on brain perfusion SPECT is not always high, with a positive-predictive value of $< 50\%$.^{21,24} Our findings that dynamic changes in susceptibility, particularly susceptibility 5 minutes after ACZ administration, detected increased CBV with high positive (77%) and negative (100%) predictive values suggests that these dynamic changes may predict the risk of cerebrovascular adverse events more accurately than conventional measurements of CVR to ACZ. In addition, the examination time of the present method using 7T QSM was < 12 minutes if the susceptibility change was measured until a midscan time of 5 minutes after ACZ administration.

QSM source data were obtained with a section thickness of 2 mm. Such a thick section may reduce the accuracy of susceptibility on QSM due to the partial volume effect for small veins.^{11,13} As another limitation, the scan time for 7T QSM is 3 minutes 25 seconds longer than that for BOLD or QSM imaging with 3T MR imaging.¹⁰ Shortening the scan time may help clarify dynamic changes in susceptibility after ACZ administration. Furthermore, considerable variation in cerebral hemodynamics might be anticipated within an MCA ROI, especially in the borderzone,¹² and use of the MCA ROI might reduce such hemodynamic variation. Ranges of CBV in the cerebral gray matter are quite large. This high heterogeneity might also be reduced using MCA ROI analysis.

CONCLUSIONS

The present study demonstrated that the dynamic changes in susceptibility after ACZ administration on 7T QSM are associated with pre-existing CBV and CMRO₂ on PET in patients with ICA or MCA steno-occlusive disease.

Disclosures: Makoto Sasaki—UNRELATED: Consultancy: Actelion Pharmaceuticals, Micron Technology; Grants/Grants Pending: Hitachi; Ministry of Education, Culture, Sports, Science and Technology; Agency for Medical Research and Development; Ministry of Health, Labour and Welfare*; Payment for Lectures Including Service on Speakers Bureaus: Actelion Pharmaceuticals, Mitsubishi Tanabe Pharma, Bayer AG, Nihon Medi-Physics Co., Ltd, Eisai Co., Ltd, Fujifilm, Daiichi Sankyo, Boehringer-Ingelheim.jp, Otsuka America Pharmaceutical, CHUGAI PHARMACEUTICAL, Astellas Pharma, Ono Pharmaceutical. *Money paid to the institution.

REFERENCES

1. Baron JC, Boussier MG, Rey A, et al. **Reversal of focal “misery-perfusion syndrome” by extra-intracranial arterial bypass in hemodynamic cerebral ischemia: a case study with ¹⁵O positron emission tomography.** *Stroke* 1981;12:454–59 CrossRef Medline
2. Gibbs JM, Leenders KL, Wise RJ, et al. **Evaluation of cerebral perfusion reserve in patients with carotid-artery occlusion.** *Lancet* 1984;1:310–14 CrossRef
3. Powers WJ, Raichle ME. **Positron emission tomography and its application to the study of cerebrovascular disease in man.** *Stroke* 1985;16:361–76 CrossRef Medline
4. Ogasawara K, Ito H, Sasoh M, et al. **Quantitative measurement of regional cerebrovascular reactivity to acetazolamide using ¹²³I-N-isopropyl-p-iodoamphetamine autoradiography with SPECT: validation study using H₂¹⁵O with PET.** *J Nucl Med* 2003;44:520–25 Medline
5. Wiart M, Berthezène Y, Adeleine P, et al. **Vasodilatory response of border zones to acetazolamide before and after endarterectomy: an echo planar imaging-dynamic susceptibility contrast-enhanced**

- MRI study in patients with high-grade unilateral internal carotid artery stenosis. *Stroke* 2000;31:1561–65 CrossRef Medline
6. Aries M, Elting JW, De Keyser J, et al. **Cerebral autoregulation in stroke: a review of transcranial Doppler studies.** *Stroke* 2010;41:2697–2704 CrossRef Medline
 7. Zhang J, Liu T, Gupta A, et al. **Quantitative mapping of cerebral metabolic rate of oxygen (CMRO2) using quantitative susceptibility mapping (QSM).** *Magn Reson Med* 2015;74:945–52 CrossRef Medline
 8. De Vis JB, Petersen ET, Bhogal A, et al. **Calibrated MRI to evaluate cerebral hemodynamics in patients with an internal carotid artery occlusion.** *J Cereb Blood Flow Metab* 2015;35:1015–23 CrossRef Medline
 9. Liu Z, Li Y. **Cortical cerebral blood flow, oxygen extraction fraction, and metabolic rate in patients with middle cerebral artery stenosis or acute stroke.** *AJNR Am J Neuroradiol* 2016;37:607–14 CrossRef Medline
 10. Wu J, Dehkharghani S, Nahab F, et al. **Acetazolamide-augmented dynamic BOLD (aczBOLD) imaging for assessing cerebrovascular reactivity in chronic steno-occlusive disease of the anterior circulation: an initial experience.** *Neuroimage Clin* 2017;13:116–22 CrossRef Medline
 11. Kudo K, Liu T, Murakami T, et al. **Oxygen extraction fraction measurement using quantitative susceptibility mapping: comparison with positron emission tomography.** *J Cereb Blood Flow Metab* 2016;36:1424–33 CrossRef Medline
 12. Leatherday C, Dehkharghani S, Nahab F, et al. **Cerebral MR oximetry during acetazolamide augmentation: beyond cerebrovascular reactivity in hemodynamic failure.** *J Magn Reson Imaging* 2019;50:175–82 CrossRef Medline
 13. Uwano I, Kudo K, Sato R, et al. **Noninvasive assessment of oxygen extraction fraction in chronic ischemia using quantitative susceptibility mapping at 7 Tesla.** *Stroke* 2017;48:2136–41 CrossRef Medline
 14. Sato R, Shirai T, Taniguchi Y, et al. **Quantitative susceptibility mapping using the multiple dipole-inversion combination with k-space segmentation method.** *Magn Reson Med Sci* 2017;16:340–50 CrossRef Medline
 15. Sun H, Wilman AH. **Background field removal using spherical mean value filtering and Tikhonov regularization.** *Magn Reson Med* 2014;71:1151–57 CrossRef Medline
 16. Frackowiak RS, Lenzi GL, Jones T, et al. **Quantitative measurement of regional cerebral blood flow and oxygen metabolism in man using 15O and positron emission tomography: theory, procedure, and normal values.** *J Comput Assist Tomogr* 1980;4:727–36 CrossRef Medline
 17. Lammertsma AA, Jones T. **Correction for the presence of intravascular oxygen-15 in the steady-state technique for measuring regional oxygen extraction ratio in the brain, I; description of the method.** *J Cereb Blood Flow Metab* 1983;3:416–24 CrossRef Medline
 18. Ashburner J. **SPM: a history.** *Neuroimage* 2012;62:791–800 CrossRef Medline
 19. Takeuchi R, Matsuda H, Yoshioka K, et al. **Cerebral blood flow SPET in transient global amnesia with automated ROI analysis by 3DSRT.** *Eur J Nucl Med Mol Imaging* 2004;31:578–89 CrossRef Medline
 20. Yushkevich PA, Piven J, Hazlett HC, et al. **User-guided 3D active contour segmentation of anatomical structures: significantly improved efficiency and reliability.** *Neuroimage* 2006;31:1116–28 CrossRef Medline
 21. Oshida S, Ogasawara K, Saura H, et al. **Does preoperative measurement of cerebral blood flow with acetazolamide challenge in addition to preoperative measurement of cerebral blood flow at the resting state increase the predictive accuracy of development of cerebral hyperperfusion after carotid endarterectomy? Results from 500 cases with brain perfusion single-photon emission computed tomography study.** *Neurol Med Chir (Tokyo)* 2015;55:141–48 CrossRef Medline
 22. Saito H, Ogasawara K, Suzuki T, et al. **Adverse effects of intravenous acetazolamide administration for evaluation of cerebrovascular reactivity using brain perfusion single-photon emission computed tomography in patients with major cerebral artery steno-occlusive diseases.** *Neurol Med Chir (Tokyo)* 2011;51:479–83 CrossRef Medline
 23. Okazawa H, Yamauchi H, Sugimoto K, et al. **Effects of acetazolamide on cerebral blood flow, blood volume, and oxygen metabolism: a positron emission tomography study with healthy volunteers.** *J Cereb Blood Flow Metab* 2001;21:1472–79 CrossRef Medline
 24. Yoshimura S, Kitajima H, Enomoto Y, et al. **Staged angioplasty for carotid artery stenosis to prevent postoperative hyperperfusion.** *Neurosurgery* 2009;64(3 Suppl):ons122–28; discussion ons128–29 CrossRef Medline
 25. Uchino H, Kuroda S, Hirata K, et al. **Predictors and clinical features of postoperative hyperperfusion after surgical revascularization for Moyamoya disease: a serial single photon emission CT/positron emission tomography study.** *Stroke* 2012;43:2610–16 CrossRef Medline
 26. Chida K, Ogasawara K, Suga Y, et al. **Postoperative cortical neural loss associated with cerebral hyperperfusion and cognitive impairment following carotid endarterectomy: ¹²³I-iomazenil SPECT study.** *Stroke* 2009;40:448–53 CrossRef Medline

Spatial Resolution and the Magnitude of Infarct Volume Measurement Error in DWI in Acute Ischemic Stroke

J.M. Ospel, A. Jaffray, V. Schulze-Zachau, S. Kozerke, and C. Federau



ABSTRACT

BACKGROUND AND PURPOSE: Infarct volume in acute ischemic stroke is an important prognostic marker and determines endovascular treatment decisions. This study evaluates the magnitude and potential clinical impact of the error related to partial volume effects in infarct volume measurement on diffusion-weighted MR imaging in acute stroke and explores how increasing spatial resolution could reduce this error.

MATERIALS AND METHODS: Diffusion-weighted imaging of 393 patients with acute stroke, of whom 56 had anterior circulation large-vessel occlusion, was coregistered to standard space. Lesion boundaries were manually segmented. A 3D lesion-volume model was resampled for voxel sizes from $4 \times 4 \times 8$ to $1 \times 1 \times 2$ mm, and the surface-volume, corresponding to the partial volume error, was calculated. The number of cases with anterior circulation large-vessel occlusion, in which the endovascular therapy core threshold of 70 mL was contained within the margin of error, was calculated as a function of imaging resolution.

RESULTS: The mean infarct core volume was 27.2 ± 49.9 mL. The mean surface volume was 14.7 ± 20.8 mL for $2 \times 2 \times 4$ mm resolution and 7.4 ± 10.7 mL for $1 \times 1 \times 2$ mm resolution. With a resolution of $2 \times 2 \times 4$ mm, 70 mL was contained within the margin of error in 7/56 cases (12.5%) with large-vessel occlusion, while with a $1 \times 1 \times 2$ mm voxel size, the margin of error was 3/56 (5%). The lesion-volume range of potentially misclassified lesions dropped from 46.5–94.1 mL for a $2 \times 2 \times 4$ mm resolution to 64.4–80.1 mL for a $1 \times 1 \times 2$ mm resolution.

CONCLUSIONS: Partial volume effect is an important source of error in infarct volume measurement in acute stroke. Increasing spatial resolution substantially decreases the mean error. Standard use of high-resolution DWI should be considered to increase the reliability of infarct volume measurements.

ABBREVIATION: LVO = large-vessel occlusion

Infarct core volume is a known predictor of outcome in patients with acute stroke; smaller infarct cores are associated with better outcomes and higher rates of functional independence. In patients with a small infarct core, thrombectomy leads to a more favorable result.^{1–4} Diffusion-weighted imaging is considered the

criterion standard for infarct core measurement. A large infarct core, usually above 70 mL, was considered a contraindication for endovascular therapy in many clinical trials and is commonly used as a threshold in clinical practice.^{5–7}

The accuracy of DWI-based infarct core measurement is limited by several factors. For example, although DWI hyperintense lesions are generally considered to represent irreversibly damaged tissue, reversible DWI lesions have been reported.^{8,9} Another important potential source of error is partial volume effects at the border of the lesion due to the finite spatial resolution reconstruction.

The surface volume (ie, the volume of the surface voxels) represents the volume in which misclassification can occur due to the partial volume effect and is an established measure of spatial resolution-induced measurement error.¹⁰ This error is equal to the number of voxels composing the surface, multiplied by the individual voxel volume used in image reconstruction (Fig 1). Because of the complex shapes of most large stroke lesions (eg, those with a gyriform pattern), volume measurement error due

Received December 11, 2019; accepted after revision March 6, 2020.

From the Department of Radiology (J.M.O., V.S.-Z., C.F.), University Hospital Basel, University of Basel, Basel, Switzerland; Department of Clinical Neurosciences (J.M.O.), University of Calgary, Calgary, Canada; and Institute for Biomedical Engineering (A.J., S.K., C.F.), University of Zurich, Zurich, Switzerland.

This work was supported, in part, by the Swiss Heart Association.

Preliminary results of this study previously presented at: Annual Meeting of the American Society of Neuroradiology, May 18–23, 2019; Boston, Massachusetts.

Please address correspondence to Christian Federau, MD, Institute for Biomedical Engineering, University of Zurich, Gloriastr 35, 8092 Zürich, Switzerland; e-mail: christian.federau@gmail.com; @johanna_ospel

Indicates article with supplemental on-line appendix.

Indicates article with supplemental on-line photos.

<http://dx.doi.org/10.3174/ajnr.A6520>

to partial volume effects could potentially lead to an erroneous choice of therapy.

The purpose of our study was to assess the magnitude and potential therapeutic impact of errors related to partial volume effects in infarct core volume measurement on DWI in acute stroke. Furthermore, we aimed to evaluate to what extent increasing the spatial resolution could reduce this error.

MATERIALS AND METHODS

Patients

Approval from the local ethics committee was obtained for this anonymized, retrospective evaluation. MR imaging examinations of patients who presented in the emergency department of the University Hospital of Basel with symptoms of acute ischemic stroke between August 2010 and November 2017 were reviewed and considered for this study. A subgroup analysis was performed in the group with anterior circulation large-vessel occlusion (LVO) who be considered endovascular treatment-eligible according to

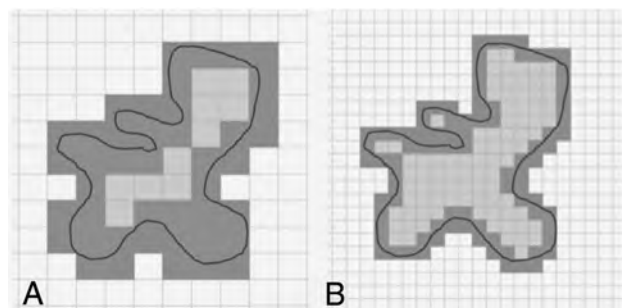


FIG 1. Inaccuracy of volumetric measurements at the lesion surface. The grid represents voxel boundaries; the *solid line* represents an acute ischemic lesion. *Voxels outlined in gray* are the surface voxels, ie, those voxels with lesion margins. The sum of the surface voxel volume is a measure of the potential measurement error due to partial volume effects, which results from discretization at the lesion surface (the net volume uncertainty per surface voxel has been defined as half of the volume of the voxel in both the positive and negative directions). Standard resolution leads to large surface volume and thus has the potential for large measurement errors (A). Increasing the spatial resolution substantially reduces the surface volume and thereby decreases the potential measurement error (B).

their occlusion site based on current American Heart Association/American Stroke Association guidelines.¹¹

Technical Parameters

MR imaging examinations were performed on a Magnetom Skyra 3T, a Magnetom Skyra fit 3T, or a Magnetom Avanto fit 1.5T scanner (Siemens) and included diffusion-weighted (acquired at $b = 1000 \text{ s/mm}^2$), fluid-attenuated inversion recovery, and susceptibility-weighted images. The Table provides a summary of the acquisition parameters.

Image Postprocessing

All diffusion-weighted images were coregistered to the standard Montreal Neurological Institute template (<http://www.bic.mni.mcgill.ca/ServicesAtlases/ICBM152NLin2009>) space rotated in the anterior/posterior commissure direction, using an affine transformation and a mutual information loss, and resampled to a standard resolution of $128 \times 128 \times 40$ voxels with the Advanced Normalization Tools library (<http://stnava.github.io/ANTs/>). Images were then saved back in the DICOM format using a homemade C++ code.

Infarct Core Segmentation

Infarct cores, if present, were manually segmented by 2 radiologists (J.M.O., V.S.-Z.) on the coregistered $b=1000 \text{ s/mm}^2$ DWI using an open-source DICOM viewing software (horosproject.org). Tissue was identified as infarct on the basis of hyperintensity compared with the surrounding tissue and the contralateral hemisphere. Imaging artifacts resembling infarct cores were distinguished from real infarct cores on the basis of contextual information from the whole image including symmetry/bilaterality, presence of metals, other causative materials, and typical anatomic location near the skull base or on brain-bone/air interfaces. Parenchymal hematomas in continuation with or within infarcts were included in the segmentation. In case of doubt, to distinguish hyperintensity due to acute infarction from leukoaraiosis and chronic white matter changes, we reviewed the other available MR images, including the $b = 0 \text{ s/mm}^2$ images and fluid-attenuated inversion recovery images.

Diffusion-weighted imaging acquisition parameters

Parameter	Mean	SD	Range
Section thickness (mm)	3.03	0.22	3–5
TR (ms)	6989.76	1518.53	3550–9600
TE (ms)	99.59	3.32	59–104
Interslice gap (mm)	0.6	—	0.6–0.6
Sequence duration (sec)	583	168	312–984
Field strength	1.5T: $n = 251$ (63.9%) 3T: $n = 142$ (36.1%)		
Matrix size	128: $n = 282$ (71.8%) 162: $n = 106$ (27.0%) 192: $n = 5$ (1.3%)		
In-plane resolution	$2.00 \times 2.00 \text{ mm}$: $n = 318$ (81.0%) $1.36 \times 1.36 \text{ mm}$: $n = 46$ (11.7%) $1.20 \times 1.20 \text{ mm}$: $n = 4$ (1.0%) $1.13 \times 1.13 \text{ mm}$: $n = 1$ (0.3%) $0.68 \times 0.68 \text{ mm}$: $n = 24$ (6.1%)		

Note:— indicates that there was no SD as the interslice gap was 0.6 mm in all cases.

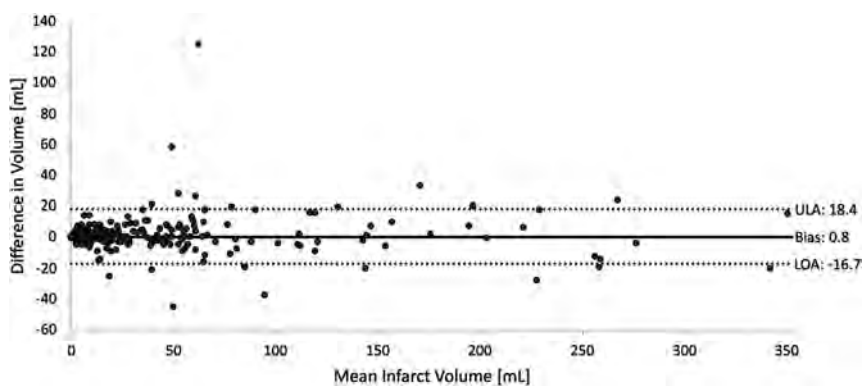


FIG 2. Interreader agreement of manual infarct core segmentation. Bias (0.82 mL) is shown with a solid line. Lower limits of agreement (LOA, -16.74 mL) and upper limits of agreements (ULA, 18.38 mL) are marked with dashed lines.

Lesion Tessellation

Section-by-section parameterization of segmented ischemic cores using spline interpolants was performed to reconstruct lesion boundaries with arbitrarily high in-plane resolution, and tessellated surfaces were reconstructed from the interpolated lesion boundary points, thereby providing lesion boundaries of varying in-plane resolutions. Reconstruction of the high-resolution 3D lesions with voxels of fixed size within the tessellated surface boundaries was then performed for a continuous range of voxel sizes from $4 \times 4 \times 8$ to $1 \times 1 \times 2$ mm using a Matlab routine (MathWorks). Section-by-section parameterization and lesion tessellation are illustrated in detail in the On-line Appendix.

Data Analysis and Statistics

Differences in the segmented stroke volumes between the 2 radiologists were visualized with a Bland-Altman plot. Infarct core volumes and infarct core surface volumes were calculated for both readers and were averaged for further analysis. Means and SDs were calculated for averaged stroke volume and surface volume, and the number of patients in whom the margin of error (ie, mean infarct volume \pm 50% of the mean surface volume) contained 70 mL, which is the commonly used decision threshold for endovascular treatment,^{5,6} was calculated for each voxel size. A Spearman correlation was performed to assess the relationship of spatial resolution and surface volume. Correlation coefficients and corresponding *P* values were calculated for each patient and averaged.

RESULTS

Data Base Characteristics

MR imaging examinations of 393 patients with DWI-hyperintense lesions consistent with acute infarction were included in this study (220 male patients, 56.0%). The mean age was 71.6 ± 14.2 years. Fifty-six patients had an anterior circulation large-vessel occlusion (26 male patients, 46.4%; mean age, 71.7 ± 14.9 years; median NIHSS score, 8; interquartile range, 12–17.5), with a median time from symptom onset to MR imaging of 26 hours (interquartile range, 21.8–30.8 hours). These included 34 M1 segment middle cerebral artery occlusions, 21 terminal internal carotid

artery occlusions, and 1 A1 segment anterior cerebral artery occlusion.

Human Segmentation

Comparison of segmentation volumes performed by both radiologists showed good agreement: In 380/393 (96.03%), the difference was within the limits of agreement (Fig 2). Mean infarct volume was 27.2 ± 49.9 mL, and 69.4 ± 81.1 mL in the subgroup of patients with anterior circulation LVO. Thirty-two of 393 (8.1%) infarct volumes were above 70 mL. In 8/393 (2.0%) infarct volumes, the readers disagreed on whether the infarct volume was greater or less than 70 mL. On-line Fig 3 shows how human segmentations were performed on an exemplary case.

Volume Error Related to Partial Volume Effects

The mean surface volume (ie, volume error related to partial volume effects) was 14.7 ± 20.8 mL for a reconstruction voxel size of $2 \times 2 \times 4$ mm and 7.4 ± 10.7 mL for a size of $1 \times 1 \times 2$ mm. In the patients with anterior circulation LVO, the mean surface volume was 64.8 ± 31.1 mL for a reconstruction voxel size of $2 \times 2 \times 4$ mm and 17.7 ± 16.3 mL for a size of $1 \times 1 \times 2$ mm. Figure 3 shows the simulation results for additional spatial resolution steps. There was a strong and highly significant correlation between spatial resolution and surface volume ($P = 0.903$, $P < .001$).

Volume Range Containing the Clinical-Decision Volume Threshold of 70 mL as Function of Reconstruction Resolution

With a reconstruction voxel size of $2 \times 2 \times 4$ mm, the clinical-decision volume threshold of 70 mL was contained in a lesion volume ranging from 46.5 to 94.1 mL—that is, lesions as small as 46.5 mL could have been erroneously classified as >70 mL due to partial volume effects, and lesions of 94.1 mL volume could have been erroneously classified as <70 mL (Fig 4B). Reducing the reconstruction voxel size to $1 \times 1 \times 2$ mm resulted to the clinical-decision volume threshold being contained in the range of 64.4–80.1 mL (Fig 4C).

Number of Patients with Anterior Circulation LVO within the Range of Measurement Error

In the patients with anterior circulation LVO, the clinical-decision volume threshold of 70 mL was contained within the range of measurement error in 7/56 cases (12.5%) with a resolution of $4 \times 2 \times 2$ mm and in 3/56 cases (5.3%) with a resolution of $1 \times 1 \times 2$ mm (Fig 5).

DISCUSSION

Accurate determination of infarct volume in acute ischemic stroke is crucial because infarct core volume was used as an exclusion criterion in several randomized controlled trials^{6,11} and has become a key decision driver in endovascular therapy decision-

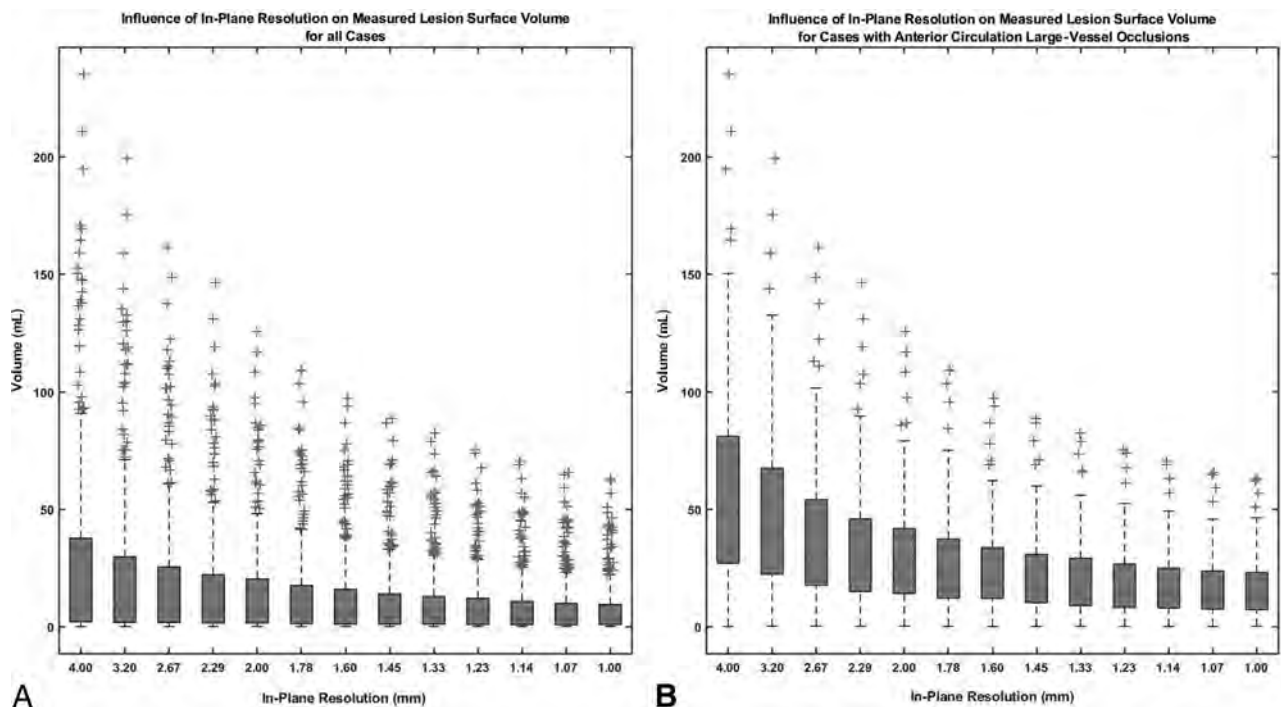


FIG 3. Surface volume as a function of spatial resolution for all cases (A) and for the cases with anterior circulation large-vessel occlusion (B). Surface volume (median and interquartile range) are shown on the y-axis, and spatial resolution, on the x-axis. With increasing spatial resolution, a marked decrease in surface volume can be observed.

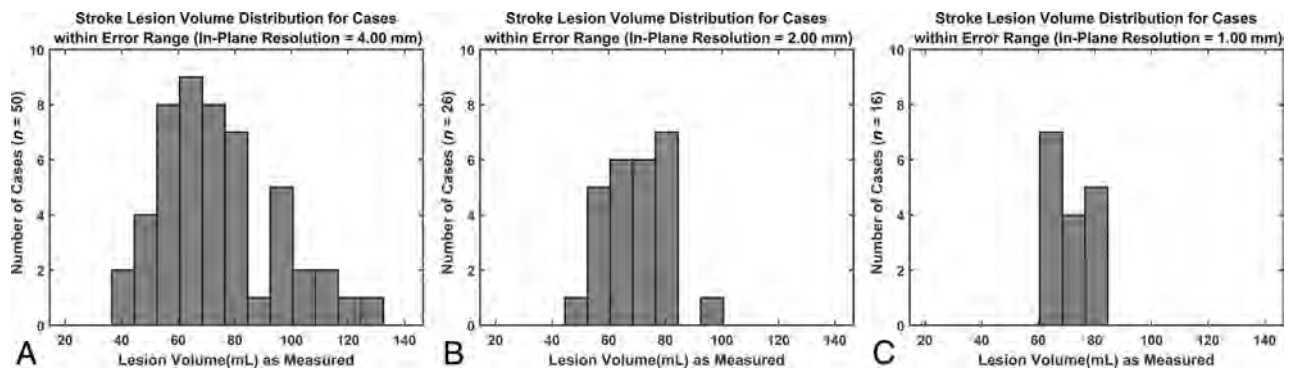


FIG 4. Distribution of stroke lesion volumes for the cases in which 70 mL is contained within the margin of measurement error for voxel sizes of $4 \times 4 \times 8$ mm (A), $2 \times 2 \times 4$ mm (B), and $1 \times 1 \times 2$ mm (C). With increasing spatial resolution, the range of lesion volumes for which the margin of error contains 70 mL is reduced. Lesion ranges were as follows: $4 \times 4 \times 8$ mm (A): 40.96–126.46 mL; $2 \times 2 \times 4$ mm (B): 46.5–94.1 mL; and $1 \times 1 \times 2$ mm (C): 64.35–80.13 mL.

making. Our study demonstrates the importance of spatial resolution when performing DWI-based infarct measurements in the context of acute stroke imaging: With a reconstruction resolution of $2 \times 2 \times 4$ mm, the mean error in our patient cohort was 14.7 mL, and a resolution of $1 \times 1 \times 2$ mm led to a noteworthy decrease of the error to 7.4 mL. The same held true for the number of cases in which 70 mL was contained within the margin of error in volume measurements (from 12.5% of cases with LVO using a $2 \times 2 \times 4$ mm resolution to 5% of cases using a $1 \times 1 \times 2$ mm resolution), while the range of lesion volumes measured in these cases decreased from 46.5–94.1 to 64.4–80.1 mL.

Our findings suggest that DWI in the context of acute stroke should be acquired with the maximal resolution possible. Of note,

the maximal achievable resolution is variable across scanners and depends mostly on the imaging gradient strength. While the increase in resolution implies a decrease in the signal-to-noise ratio, this should be acceptable because of the high contrast of the DWI findings positive for lesions compared with the normal brain parenchyma. In case the signal-to-noise ratio needs to be improved, scan time could be increased.¹² However, stroke outcomes are highly time-dependent, and treatment delays should, therefore, be avoided. If a high-resolution DWI sequence were to be used in the acute setting, its acquisition time has to be relatively short. High-resolution DWI sequences with acquisition times of <5 minutes are available and have been shown to increase lesion conspicuity and the overall number of visible lesions in acute ischemic stroke.^{13,14}

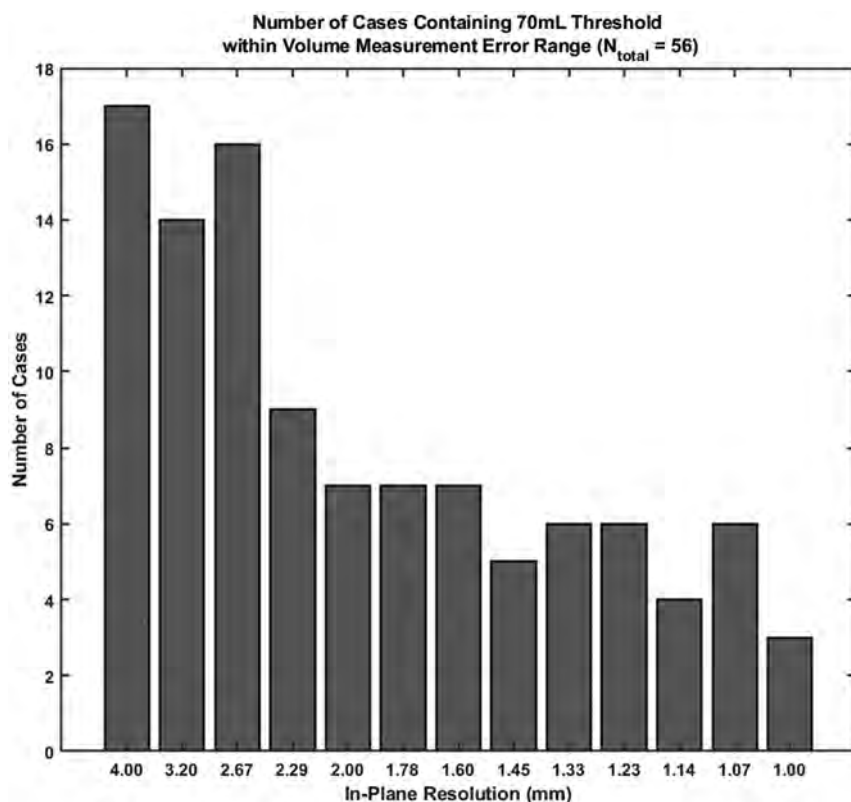


FIG 5. The number of cases in which 70 mL is contained within the margin of error (y-axis) for the cases with anterior circulation large-vessel occlusion, ie, cases in which a treatment error could have resulted on the basis of a 70-mL threshold, as a function of spatial resolution (x-axis). With increasing spatial resolution, the number of cases in which the margin of error contains 70 mL is reduced.

Several further sources of errors that can occur in DWI-based infarct core measurement were not considered in this work, such as inhomogeneities in the B_0 and diffusion-weighted gradient and imaging gradient fields,^{2,3} errors in section selection, and motion artifacts.^{15,16} Because the effect of these errors is multiplicative, our results most probably substantially underestimated the real volume measurement error. Reducing measurement error due to partial volume averaging is even more important in patients with larger, complex-shaped infarcts (ie, gyriform, white matter-sparing infarct patterns) because the lesion surface and hence the potential error due to partial volume averaging are particularly large in such patients.

Limitations

Our study has several limitations: First, this was a single-center study. The images used were mostly acquired after thrombolytic or endovascular therapy, but it is reasonable to assume that the sizes and shapes of the lesions were similar to lesions in the therapeutic window. Infarct segmentation was performed manually, possibly introducing some inaccuracy, though interreader agreement of the infarct segmentations was good. We performed a “virtual increase” using lesion tessellation to simulate high-resolution DWI, and not “real” high-resolution DWI, which has been shown to be feasible at and beyond the smallest voxel size simulated in this study but yields its own set of challenges that have not been addressed in this study. These include a decrease in signal-to-noise ratio with voxel size and

increased motion artifacts due to longer required scan times. Furthermore, endovascular therapy trials that used DWI for infarct core measurement and established the 70-mL threshold might have had the very same measurement inaccuracy described in this article but were nevertheless able to show the clinical significance of this threshold. DWI volume is used in most multicentric studies as a surrogate marker for stroke severity, for example in the Diffusion Weighted Imaging Evaluation for Understanding Stroke Evolution Study 2 (DEFUSE 2) studies,¹⁷ but in clinical practice, pretreatment MR imaging is performed only in a limited number of centers. Despite these limitations, our study provides preliminary exploratory evidence for the magnitude of infarct core measurement error on DWI that can arise due to partial volume averaging and offers a starting point for future investigations on how to reduce these inaccuracies.

CONCLUSIONS

When one performs DWI-based volumetric stroke infarct measurements with routinely used spatial resolutions, measurement errors due to partial volume averaging are substantial and can potentially affect clinical decision-making. Thus, infarct volumes derived from DWI should be interpreted with caution. The magnitude of error can be minimized when spatial resolution is increased. Because fast and robust high-resolution DWI sequences are available, they should be used in acute stroke imaging whenever possible to accurately measure infarct cores and come to a solid, well-informed endovascular therapy decision.

Disclosures: Johanna M. Ospel—RELATED: Grant: University of Basel Research Foundation, Julia Bangerter-Rhyner Foundation, Freiwillige Akademische Gesellschaft Basel, Comments: research scholarships. Christian Federau—RELATED: Grant: Swiss National Science Foundation.* Victor Schulze-Zachau—UNRELATED: Employment: employment as resident physician at the University Hospital Basel.* Money paid to institution.

REFERENCES

- Ozdemir O, Giray S, Arlier Z, et al. Predictors of a good outcome after endovascular stroke treatment with stent retrievers. *ScientificWorldJournal* 2015;2015:403726 CrossRef Medline
- Xie Y, Oppenheim C, Guillemin F, et al; THRACE Investigators. Pretreatment lesional volume impacts clinical outcome and thrombectomy efficacy. *Ann Neurol* 2018;83:178–85 CrossRef Medline
- Yoo AJ, Chaudhry ZA, Nogueira RG, et al. Infarct volume is a pivotal biomarker after intra-arterial stroke therapy. *Stroke* 2012;43:1323–30 CrossRef Medline
- Campbell BC, Donnan GA, Mitchell PJ, et al. Endovascular thrombectomy for stroke: current best practice and future goals. *Stroke Vasc Neurol* 2016;1:16–22 CrossRef Medline

5. Albers GW, Marks MP, Kemp S, et al; DEFUSE 3 Investigators. **Thrombectomy for stroke at 6 to 16 hours with selection by perfusion imaging.** *N Engl J Med* 2018;378:708–18 CrossRef Medline
6. Campbell BC, Mitchell PJ, Kleinig TJ, et al; EXTEND-IA Investigators. **Endovascular therapy for ischemic stroke with perfusion-imaging selection.** *N Engl J Med* 2015;372:1009–18 CrossRef Medline
7. Yoo AJ, Verduzco LA, Schaefer PW, et al. **MRI-based selection for intra-arterial stroke therapy: value of pretreatment diffusion-weighted imaging lesion volume in selecting patients with acute stroke who will benefit from early recanalization.** *Stroke* 2009;40:2046–54 CrossRef Medline
8. Yoo J, Choi JW, Lee SJ, et al. **Ischemic diffusion lesion reversal after endovascular treatment.** *Stroke* 2019;50:1504–09 CrossRef Medline
9. Edlow BL, Hurwitz S, Edlow JA. **Diagnosis of DWI-negative acute ischemic stroke: a meta-analysis.** *Neurology* 2017;89:256–62 CrossRef Medline
10. Schuleri KH, Centola M, George RT, et al. **Characterization of perinfarct zone heterogeneity by contrast-enhanced multidetector computed tomography: a comparison with magnetic resonance imaging.** *J Am Coll Cardiol* 2009;53:1699–1707 CrossRef Medline
11. Nogueira RG, Jadhav AP, Haussen DC, et al; DAWN Trial Investigators. **Thrombectomy 6 to 24 hours after stroke with a mismatch between deficit and infarct.** *N Engl J Med* 2018;378:11–21 CrossRef Medline
12. Federau C, Gallichan D. **Motion-correction enabled ultra-high resolution in-vivo 7T-MRI of the brain.** *PLoS One* 2016;11:e0154974 CrossRef Medline
13. Benameur K, Bykowski JL, Luby M, et al. **Higher prevalence of cortical lesions observed in patients with acute stroke using high-resolution diffusion-weighted imaging.** *AJNR Am J Neuroradiol* 2006;27:1987–89 Medline
14. Hotter B, Galinovic I, Kunze C, et al. **High-resolution diffusion-weighted imaging identifies ischemic lesions in a majority of transient ischemic attack patients.** *Ann Neurol* 2019;86:452–57 CrossRef Medline
15. Goyal M, Menon BK, Derdeyn CP. **Perfusion imaging in acute ischemic stroke: let us improve the science before changing clinical practice.** *Radiology* 2013;266:16–21 CrossRef Medline
16. Sheth KN, Terry JB, Nogueira RG, et al. **Advanced modality imaging evaluation in acute ischemic stroke may lead to delayed endovascular reperfusion therapy without improvement in clinical outcomes.** *J Neurointerv Surg* 2013;(Suppl 1):i62–65 CrossRef Medline
17. Federau C, Christensen S, Mlynash M, et al. **Comparison of stroke volume evolution on diffusion-weighted imaging and fluid-attenuated inversion recovery following endovascular thrombectomy.** *Int J Stroke* 2017;12:510–18 CrossRef Medline

Structural Connectivity and Cortical Thickness Alterations in Transient Global Amnesia

J. Hodel, X. Leclerc, M. Zuber, S. Gerber, P. Besson, V. Marcaud, V. Roubeau, H. Brasme, I. Ganzoui, D. Ducreux, J.-P. Pruvo, M. Bertoux, M. Zins, and R. Lopes



ABSTRACT

BACKGROUND AND PURPOSE: Transient global amnesia (TGA) is a sudden onset of anterograde and retrograde amnesia. We aimed to assess differences in terms of cortical thickness and structural brain connectome between patients with TGA (at acute and delayed postrecovery stages) and matched controls.

MATERIALS AND METHODS: We report on 18 consecutive patients with TGA who underwent 3T MR imaging, including DTI and MPRAGE sequences, at the acute (mean delay postonset: 44 hours) and delayed post-recovery (mean delay: 35 days) stages. Structural connectome was assessed in patients with TGA and in 18 age- and sex-matched controls by using probabilistic fiber-tracking and segmentation of 164 cortical/subcortical structures (“nodes”). Connectivity graphs were computed and global network metrics were calculated. Network-based statistical analysis (NBS) was applied to compare patients with TGA at each stage with controls. We also compared cortical thickness between patients with TGA and healthy controls.

RESULTS: Global network metrics were not altered in patients with TGA. NBS-analysis showed structural connectome alterations in patients with TGA compared with controls, in core regions involving the limbic network, with 113 nodes and 114 connections (33 left intrahemispheric, 31 right intrahemispheric, and 50 interhemispheric connections) showing significantly decreased structural connectivity ($P < .05$ NBS corrected, t -values ranging from 3.03 to 8.73). Lower cortical thickness compared with controls was associated with these structural alterations in patients with TGA, involving the orbitofrontal, cingulate, and inferior temporal cortices. All the abnormalities were visible at both acute and delayed postrecovery stages.

CONCLUSIONS: Our preliminary study suggests there are structural abnormalities of the limbic network in patients with TGA compared with controls, including decreased structural connectivity and cortical thickness.

ABBREVIATIONS: TGA = transient global amnesia; TOF-MRA = time-of-flight MRA; VBM = voxel-based morphometry; AUC = area under the curve; FDR = false discovery rate; NBS = network-based statistical analysis

Transient global amnesia (TGA) is characterized by a sudden onset of an anterograde and retrograde amnesia that lasts up to 24 hours.¹ The pathogenesis of TGA remains unclear, however long-term cognitive performance is similar between patients with TGA and healthy controls.² Hippocampal punctate hyperintensities can be observed in up to 70% of patients with TGA by using diffusion-weighted imaging.³ Such lesions are better detected on an optimized DWI sequence^{4,5} and may be related to a delayed neuronal loss within the hippocampus cornu ammonis 1-subfield (CA1-subfield).⁶

Several neuroimaging studies revealed more widespread abnormalities in patients with TGA. Using cortical morphometry, pre-existing structural abnormalities were reported in patients with TGA mainly involving the default mode network.^{7,8} The thalamus and the prefrontal cortex have been reported to be functionally altered during TGA by using positron emission tomography assessment.⁹⁻¹¹ Using single-photon emission CT, Jang et al¹² found that anterior lesions on DWI were associated with hypoperfusion of the frontal and anterior temporal areas whereas posterior lesions were associated with

Received October 17, 2019; accepted after revision March 12, 2020.

From the Departments of Radiology (J.H., S.G., I.G., M.Z.), and Neurology (M.Z., V.M., V.R., H.B.), Saint Joseph Hospital, Paris, France; Department of Neuroradiology (X.L., J.-P.P., R.L.), Roger Salengro Hospital, Lille, France; INSERM UMR S919 (M.Z.), Université Paris Descartes, Sorbonne Paris Cité, Paris, France; Department of Radiology (P.B.), Northwestern University, Feinberg School of Medicine, Chicago, Illinois; Department of Neuroradiology (D.D.), Bicêtre Hospital, Kremlin-Bicêtre, France; and University of Lille (M.B., R.L.), Inserm U1171, CHU Lille, F-59000, Lille, France.

Please address correspondence to Jérôme Hodel, MD, PhD, Department of Radiology, Saint Joseph Hospital, Paris, France; e-mail: jerome.hodel@gmail.com; @ci2clab

Indicates article with supplemental on-line appendix and table.

Indicates article with supplemental on-line photos.

<http://dx.doi.org/10.3174/ajnr.A6530>

hypoperfusion of the parietal, posterior temporal, occipital, and cerebellar areas. More recently, 2 resting-state functional MR imaging studies revealed a decreased functional connectivity in TGA. Peer et al¹³ showed functional alterations involving the episodic memory network including the frontal regions, cingulate cortex, and basal ganglia. Zidda et al¹⁴ demonstrated alterations of the executive and salience networks including frontal and prefrontal regions, cingulate gyrus, parietal, insular and hippocampus.

However, the connectivity alterations at the acute stage of TGA, and their evolution at delayed postrecovery stage, have not been investigated yet by brain morphometry or whole-brain structural connectome. Considering the clinical phenomenology of TGA and previous neuroimaging studies, we hypothesized that the structural connectome could also be altered in patients with TGA, particularly within the limbic network that includes the hippocampus, temporal pole, parahippocampal gyrus, amygdala, anterior and posterior cingulate gyrus, and medial and lateral orbitofrontal cortex. To test this hypothesis, we aimed to assess differences in terms of cortical thickness and structural brain connectome between patients with TGA (at acute and delayed postrecovery stages) and matched controls.

MATERIALS AND METHODS

Participants

The Institutional Review Board approved this prospective study. Informed written consent was obtained according to ethical standard procedures. During a study inclusion of 2 years, the inclusion criteria were the following:

- 1) Right-handed patient.
- 2) Diagnosis of TGA according to Hodges and Warlow criteria¹ including: a) presence of an anterograde amnesia that is witnessed by an observer, b) no clouding of consciousness or loss of personal identity, c) cognitive impairment limited to amnesia, d) no focal neurologic or epileptic signs, e) no recent history of head trauma or seizures, and f) resolution of symptoms within 24 hours.
- 3) No personal history of prior episodes of TGA, drug abuse, or neurologic or psychiatric disorders.
- 4) Neurologic examination considered as normal at acute and delayed postrecovery stages.
- 5) 3T MRI available at both acute (less than 48 hours after onset) and delayed (between 30 to 40 days after onset) stages.

Exclusion criteria included: age under 18 years, contraindication for 3T MR imaging, brain lesion or motion artifacts detected on MR images. We excluded patients and controls in case of 1) white matter hyperintensities with a score of 2 or 3 according to the Fazekas scale, 2) acute or old brain infarct(s), 3) more than 3 microbleeds, or 4) brain tumor, because these brain lesions may have potentially altered the tractography of the fibers. Hippocampal hyperintensity was not exclusionary for patients with TGA.

The recruitment of healthy controls was based on clinical examination (including the Mini-Mental State Examination), socio-demographic factors, and MR imaging data. The healthy

volunteers were selected from a cohort of healthy subjects once the cohort of patients with TGA was fully established. Indeed, each control was selected to correspond to a patient with TGA in terms of sex and age. The exclusion criteria applied to patients with TGA and controls. Both patients with TGA and healthy volunteers had no personal history of prior episodes of TGA, drug abuse, neurologic or psychiatric disorders, and had normal structural MR imaging.

MR Imaging Acquisition

Patients with TGA and healthy controls were scanned at the same site by using 3T MR imaging (Discovery MR750; GE Healthcare) with the same MR sequences: 1) 3D T1-weighted MPRAGE: TR/TE, 2530/1.74 ms; flip angle, 70°; matrix, 256 x 256; isotropic 1-mm voxels; acquisition time, 7 minutes; 2) single-shot echo-planar diffusion tensor imaging: TR/TE, 8080/83 ms; flip angle, 90°; matrix, 128 x 128; isotropic 2-mm voxels; $10 b = 0$ s/mm² images (“b0 images”) and 64 directional gradients at $b = 1000$ seconds/mm²; acquisition time, 10 minutes. DTI trace images and apparent diffusion coefficient maps were systematically generated. In all patients and healthy controls, the MR imaging protocol also included axial T2-weighted, 3D FLAIR, time-of-flight MRA (TOF-MRA), and susceptibility-weighted MR images.

Analysis of Conventional MR Images

In each subject, 2 senior neuroradiologists (J.H. and X.L.) analyzed in consensus all the MR images available to ensure the lack of brain lesions, and in search of potential hippocampal lesions on DTI trace images and ADC maps.

Image Pre-processing and Whole-Brain Tractography

For each participant, MPRAGE images were segmented in 74 cortical regions and 8 subcortical regions per hemisphere by using FreeSurfer software (v5.3.0, <http://surfer.nmr.mgh.harvard.edu/>). Moreover, the cortical thickness map in native space was generated by FreeSurfer software. DTI data were preprocessed for eddy current distortions and motion artifacts by using FSL software (FMRIB Software Library; <http://www.fmrib.ox.ac.uk/fsl/>), and the MPRAGE image was nonlinearly registered to the mean b0 image by using ANTS software (<http://stnava.github.io/ANTs/>). Whole-brain fiber-tracking was performed by using the MRtrix3 software package (<http://www.mrtrix.org/>). The algorithm generated 1,000,000 fibers of minimum length 20 mm. All steps are detailed in On-line Appendix and were manually checked for errors by visual inspection. In this study, image preprocessing and analysis were performed without knowledge of the presence of hippocampal hyperintensities on DTI trace images.

Network Construction

The nodes of graph G represented the 164 brain ROIs and edges, the brain subcortical and cortical structure connections. For any pair of nodes I and J, an edge was added to G if at least 1 fiber tract connected these 2 ROIs. Moreover, the edge was weighted by the sum of fiber tracts connecting these 2 ROIs divided by the volume of the 2 ROIs. Thus, for each subject, a 164 x 164 symmetric weighted graph was constructed.

Statistical Analyses

Demographic Data. Between-group difference in age and sex between controls and patients was assessed by student and χ^2 tests, respectively.

Network Topology Analysis. The weighted graph G was thresholded at different levels of sparsities that ranged from $T = 10\%$ to 35% by using increments of 1% , in keeping the highest weighted edges. Then, further analysis was based on the binarized graph G_T for each subject.

At each threshold, global network metrics were calculated by using GRETNA toolbox (<https://www.nitrc.org/projects/gretna/>): clustering coefficient (C_p), shortest path length (L_p), global efficiency (E_g), and local efficiency (E_{loc}). The metrics were described by Rubinov et al¹⁵. The area under the curve (AUC) for each network metric was calculated to provide a summarized scalar for topologic organization of brain networks independent of a single threshold selection.¹⁶ Non-parametric permutation tests (20,000 permutations) were used to test between-group differences in AUC values of network metrics (ie, clustering coefficient, mean path length, local efficiency, and global efficiency). Patients with TGA between acute and delayed stages ($n = 18$) and with age-matched controls ($n = 18$) were compared by using paired and 2-sample t -tests, respectively. The results are presented at a statistical threshold of $P < .05$ (false discovery rate (FDR)-corrected).

Structural Connectivity Analysis. To further identify altered structural connections in patients with TGA between acute and delayed stages compared with controls, network-based statistical analysis (NBS) was used on the unthresholded corrected graph, which is a validated nonparametric statistical approach for controlling family-wise error in connectome analyses.¹⁷ NBS was applied to compare patients and controls by paired and 2-sample t -tests as follows:¹ mean connectivity strength changes were calculated with permutation tests,² network components of interconnected edges that survived a p -value of $.005$ uncorrected were retained,³ and the size of the largest cluster was calculated. To generate an empirical null distribution for evaluating the statistical significance of the cluster sizes, groups were randomly shuffled (20,000 permutations), then the largest cluster size null distribution was obtained by repeating steps 1, 2, and 3. The significance level of altered components in the NBS analysis was set to $.05$ (NBS-corrected).

Cortical Thickness and Subcortical Volumetric Analyses

Because our purpose was to assess the between-group differences in cortical thickness and subcortical volumetry within brain regions associated with structural connectivity alterations, an ROI analysis was also performed. The mean cortical thickness of cortical ROI and volumetry of subcortical ROI were measured by FreeSurfer software and compared between patients with TGA at acute and delayed stages and controls to assess if connectivity alterations were associated with cortical thickness or subcortical volumetry differences between groups. Nonparametric permutation tests (20,000 permutations) were used to test between-group

differences. The results are presented at a statistical threshold of $P < .05$ (FDR-corrected).

RESULTS

Participants

During the 2-year inclusion period, 24 consecutive patients were diagnosed with TGA in our institution. Of these 24 patients, 4 presented motion artifacts on MR imaging and MR imaging was not available at the delayed postrecovery stage in 2. Finally, 18 patients with TGA (14 women, mean age 64.5 years, range: 40–80 years, all right-handed) were included in the study. All patients ($n = 18$) underwent 3T MR imaging (Discovery MR750) at both acute (mean scan time from onset: 44 hours, range: 24–51 hours) and delayed postrecovery (mean scan time from onset: 35 days, range: 31–39 days) TGA stages. Characteristics of patients with TGA are shown in the Table.

In addition, 18 age and sex-matched, right-handed, healthy volunteers served as controls. The controls perfectly matched with patients in terms of sex (18 subjects including 14 [78%] females) and were close in terms of age (the mean age of patients was 64 ± 11 years; it was 61 ± 13 years in controls). The comparison between patients with TGA and controls did not show any significant statistical difference for age ($P = .46$) or sex ($P = .1$).

Hippocampal Hyperintensities on DTI Trace Images

Punctate hyperintensities were visible on DTI trace images in 12 of the 18 patients with TGA. Results are detailed in the Table. There were no abnormalities detected in controls. Postprocessing data showed no correlation between hippocampal hyperintensities and structural connectivity ($P = .38$, Mann-Whitney test) or volume of hippocampus ($P = .61$, Mann-Whitney test).

Network Topology

No differences of the global network metrics were observed between patients with TGA at acute and delayed stages and healthy controls (Fig 1).

Structural Connectivity

NBS Comparing patients with TGA at Acute Phase and Healthy Controls. In comparison with controls, a cluster of 113 nodes and 114 connections (33 left intrahemispheric, 31 right intrahemispheric, and 50 interhemispheric connections) had significantly decreased structural connectivity (ie, decreased number of fiber tracts) ($P < .05$ NBS corrected, t values ranging from 3.03 to 8.73) in patients with TGA at acute phase (Fig 2A and On-line Table).

In this widespread network, structural changes in patients with TGA were more prominent in core regions (ie, showing the highest number of altered connections) including: left hippocampus, left frontomarginal gyrus and sulcus, left middle anterior part of the cingulate gyrus and sulcus, left subcallosal gyrus, left planum polare of the superior temporal gyrus, left superior segment of the circular sulcus of the insula, left superior and transverse occipital sulci, left and right opercular part of the inferior frontal gyri, right inferior temporal gyrus, right anterior segment of the circular sulcus of the insula, right superior frontal sulcus, right parieto-occipital sulcus, and right pericallosal sulcus (Fig 2B).

Characteristics of patients

No.	Sex	Age	Precipitating Event	Hippocampal Lesions on DTI Trace Images at the Acute Stage of TGA				
				Laterality	Number	Head	Location Body	Tail
1	F	73	No	0	0	0	0	0
2	F	70	Stressful event	Bilateral	2	0	2	0
3	M	69	No	Bilateral	2	1	0	1
4	F	76	Stressful event	0	1	1	0	0
5	F	56	No	Right	1	1	0	0
6	F	61	Stressful event	Bilateral	4	1	0	2
7	F	65	Physical activity	0	0	0	0	0
8	F	62	No	0	0	0	0	0
9	F	67	Stressful event	0	0	0	0	0
10	F	80	Stressful event	Right	1	1	0	0
11	F	62	Stressful event	0	0	0	0	0
12	M	57	Physical activity	Bilateral	3	0	2	1
13	F	40	Physical activity	0	0	0	0	0
14	M	69	No	Bilateral	2	0	2	0
15	F	70	Stressful event	Bilateral	3	2	0	1
16	M	43	Physical activity	Bilateral	2	2	0	0
17	F	78	Physical activity	Left	1	0	0	1
18	F	63	No	Bilateral	2	0	0	2

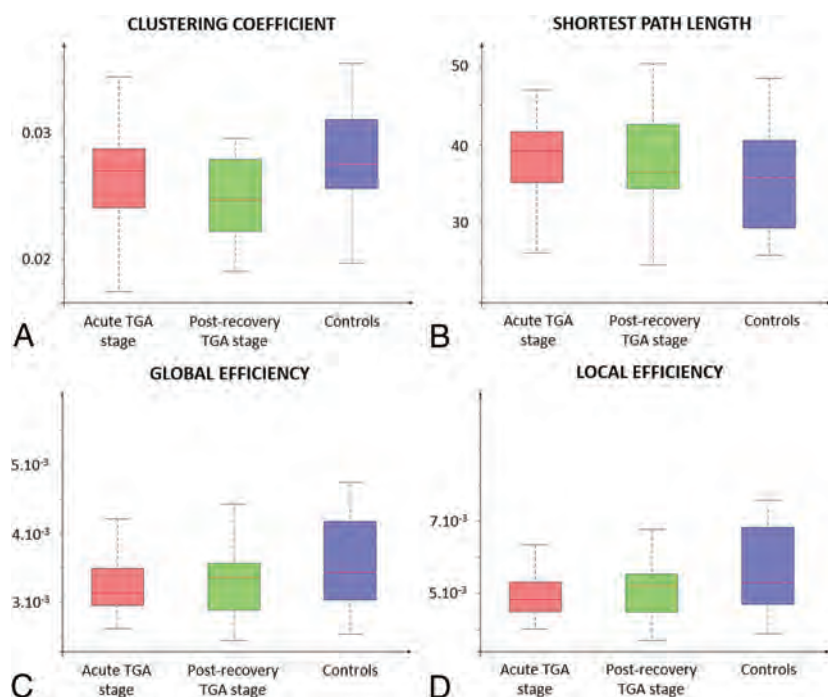


FIG 1. Global properties of the structural connectome based on normalized values of number of fibers comparing patients with TGA at acute and post-recovery stages with healthy controls. The normalization was done by dividing the number of fibers by the sum of ROI surface or volume. Clustering coefficient, shortest path length, global efficiency and local efficiency metrics were compared between groups. For each TGA stage, the global network metrics did not significantly differ between patients with TGA and controls.

NBS Comparing Patients with TGA at Acute and Delayed Stages. No statistical difference in structural connectivity was observed between acute and delayed stages in patients with TGA.

Cortical Thickness and Subcortical Volumetry

In comparison with controls, lower cortical thickness was observed in patients with TGA at the acute stage in the following cortical regions: left and right frontomarginal gyrus and

sulcus, left orbital gyri, left transverse frontopolar gyri and sulci, left middle-anterior part of the cingulate gyrus and sulcus, left lateral orbital sulcus, left posterior-ventral cingulate gyrus, left subcallosal gyrus, left lateral occipito-temporal gyrus, right long insular gyrus and central sulcus of the insula, right triangular part of the inferior frontal gyrus, and right opercular part of the inferior frontal gyrus (Online Figs 1 and 2). No between-group difference was observed in subcortical regions.

Longitudinal Follow-Up at the Delayed Post-recovery TGA Stage

All the structural abnormalities observed in patients with TGA (ie, decreased structural connectivity and decreased cortical thickness and subcortical volumetry) remained completely stable at the delayed stage, in each patient with TGA.

DISCUSSION

This is the first study evaluating NBS-corrected structural connectome and cortical thickness in TGA at both acute and postrecovery stages. We found lower structural connectivity and cortical thickness in some core regions of the limbic network in patients with TGA. This preliminary study highlights the potential value of advanced MR imaging to improve our understanding of TGA. Our findings and those of the other available studies may be of use to determine the most relevant neuropsychological tests in patients with TGA, potentially reducing the time and cost of future research protocols.

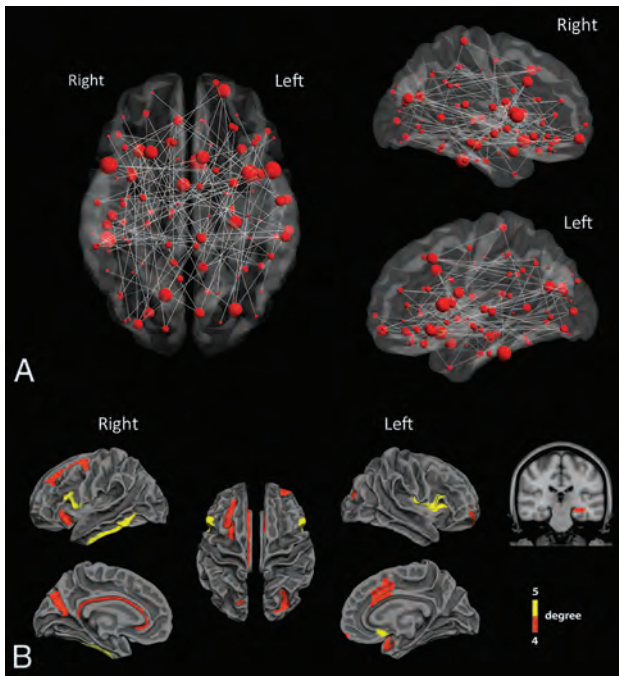


FIG 2. Altered structural connections in patients with TGA. *A*, Structural connectivity differences between controls and patients with TGA at acute phase. The gray lines mean significant decrease of connectivity in patients compared with controls. The red dots represent the location of ROIs and their size is proportional to the number of significant connections. A network of 113 ROIs and 114 connections had significantly decreased structural connectivity in patients with TGA ($P < .05$ NBS corrected, t -values ranging from 3.03–8.73). *B*, In this widespread network, the cortical and subcortical regions (nodes) with a number of significantly altered connections between patients and controls greater than 4 were mainly located in inferior and mesial temporal, cingulate, and frontal cortices.

Of note the topologic organization of the structural connectome was not altered in patients with TGA. Rather than a global disorganization, our study suggests altered connectivity of a specific network in patients with TGA. Such findings are in agreement with neuropsychological studies demonstrating a selective disorder of episodic memory in TGA without impairment of other components of memory.^{18,19} Indeed, as suggested by previous SPECT, PET, tract-based spatial statistics, and fMRI studies,^{10,12–14,20–22} the present study leads to the concept of TGA as a network disease.

We found structural alterations in several brain regions that are all known to be involved in different stages or components of memory processing, including: hippocampus, temporal lobe, orbitofrontal cortex, and parieto-occipital sulcus or cingulum. Indeed, most of these regions are directly involved in memory processing, in strategic or executive-based processing of mnemonic information meant to ensure its successful encoding or retrieval. The orbitofrontal and dorsal anterior cingulate cortices are involved in value-based modulations and temporal context-processing during memory (the ability to replace events or their aspects in the right time).^{23,24} The frontomarginal and dorsal anterior cingulate regions are involved in prospective memory and future-thinking,^{25,26} as well as in inhibitory control during encoding and retrieval. The ventral lateral frontal regions tap into

incidental and intentional memory encoding.²⁷ The retrosplenial cortex is also assumed to perform the translation between egocentric and allocentric representations formed into the hippocampus, mostly during navigation.²⁸

Interestingly, some brain regions with decreased connectivity are also involved in meta-cognitive processing. The dorsal anterior cingulate regions, together with the subcallosal cortex and the insula are all involved in mnemonic monitoring processes such as self-assessment of encoding or retrieval and confidence in self-performance.^{29,30} This network appears critical to ensure successful memory given its connections to frontal and medial temporal regions, parahippocampal cingulate bundle and fornix.³¹ Overall, this network allows for strong interactions between memory processing and meta-cognitive processes so that associative regions could interact with interoceptive cortex and salience regions to promote accurate judgment of self-memory performance³² as well as self-projection in different spatial and temporal dimensions.²⁶

To compare the cortical thickness between patients and controls we performed an ROI analysis, which is potentially more sensitive than the voxel-based approach previously used in patients with TGA.⁸ Decreased cortical thickness involved the orbitofrontal, cingulate, and inferior temporal cortices of patients with TGA. Interestingly, several regions of the limbic network showed alterations of both structural connectivity and cortical thickness (left subcallosal gyrus, left lateral orbital sulcus, left middle anterior cingulate cortex, and right opercular inferior frontal gyrus), further strengthening our results.

Our study has some limitations. There was no patient scanned during the hyperacute phase. Because TGA is both rare and short-lived, neuroimaging studies performed during an attack of amnesia are also rare. In this pilot study, the reference standard for the diagnosis of TGA was based on the Hodges and Warlow criteria that are widely used in the clinical practice¹ and completely recovered after the event. Further studies are required to correlate the structural abnormalities with neuropsychological assessments of cognitive and emotional functions.

CONCLUSIONS

Compared with controls, both structural connectivity and cortical thickness were significantly decreased in the limbic network in patients with TGA. This preliminary study highlights the potential value of advanced MR imaging to improve our understanding of TGA and may be of use to plan further prospective studies.

REFERENCES

- Hodges JR, Warlow CP. **Syndromes of transient amnesia: towards a classification. A study of 153 cases.** *J Neurol Neurosurg Psychiatry* 1990;53:834–43 CrossRef
- Jager T, Bazner H, Kliegel M, et al. **The transience and nature of cognitive impairments in transient global amnesia: a meta-analysis.** *J Clin Exp Neuropsychol* 2008;31:8–19 CrossRef
- Bartsch T, Alfke K, Deuschl G, et al. **Evolution of hippocampal CA-1 diffusion lesions in transient global amnesia.** *Ann Neurol* 2007; 62:475–80 CrossRef

4. Weon YC, Kim JH, Lee JS, et al. **Optimal diffusion-weighted imaging protocol for lesion detection in transient global amnesia.** *AJNR Am J Neuroradiol* 2008;29:1324–28 CrossRef
5. Sartoretti T, Sartoretti E, Binkert C, et al. **Diffusion-weighted zonal oblique multislice-epi enhances the detection of small lesions with diffusion restriction in the brain stem and hippocampus: a clinical report of selected cases.** *AJNR Am J Neuroradiol* 2018; 39:1255–59 CrossRef
6. Nakada T, Kwee IL, Fujii Y, et al. **High-field, T2 reversed MRI of the hippocampus in transient global amnesia.** *Neurology* 2005;64: 1170–74 CrossRef
7. Park KM, Han YH, Kim TH, et al. **Pre-existing structural abnormalities of the limbic system in transient global amnesia.** *J Clin Neurosci* 2015;22:843–47 CrossRef
8. Kim HC, Lee BI, Kim SE, et al. **Cortical morphology in patients with transient global amnesia.** *Brain Behav* 2017;7:e00872 CrossRef
9. Baron JC, Petit-Taboué MC, Le Doze F, et al. **Right frontal cortex hypometabolism in transient global amnesia. A PET study.** *Brain* 1994;117:545–52 CrossRef
10. Eustache F, Desgranges B, Petit-Taboué MC, et al. **Transient global amnesia: implicit/explicit memory dissociation and PET assessment of brain perfusion and oxygen metabolism in the acute stage.** *J Neurol Neurosurg Psychiatry* 1997;63:357–67 CrossRef
11. Guillery B, Desgranges B, de la Sayette V, et al. **Transient global amnesia: concomitant episodic memory and positron emission tomography assessment in two additional patients.** *Neuroscience Letters* 2002;325:62–66 CrossRef
12. Jang JW, Park YH, Park SY, et al. **Longitudinal cerebral perfusion change in transient global amnesia related to left posterior medial network disruption.** *PLoS One* 2015;10:e0145658 CrossRef
13. Peer M, Nitzan M, Goldberg I, et al. **Reversible functional connectivity disturbances during transient global amnesia.** *Ann Neurol* 2014;75:634–43 CrossRef
14. Zidda F, Griebel M, Ebert A, et al. **Resting-state connectivity alterations during transient global amnesia.** *NeuroImage Clin* 2019;23: 101869 CrossRef
15. Rubinov M, Sporns O. **Complex network measures of brain connectivity: uses and interpretations.** *NeuroImage* 2010;52:1059–69 CrossRef
16. Achard S, Salvador R, Whitcher B, et al. **A resilient, low-frequency, small-world human brain functional network with highly connected association cortical hubs.** *J Neurosci* 2006;26:63–72 CrossRef
17. Zalesky A, Fornito A, Bullmore ET. **Network-based statistic: identifying differences in brain networks.** *NeuroImage* 2010;53:1197–207 CrossRef
18. Bartsch T, Deuschl G. **Transient global amnesia: functional anatomy and clinical implications.** *Lancet Neurol* 2010;9:205–14 CrossRef
19. Guillery-Girard B, Quinette P, Desgranges B, et al. **Long-term memory following transient global amnesia: an investigation of episodic and semantic memory.** *Acta Neurol Scand* 2006;114:329–33 CrossRef
20. LaBar KS, Gitelman DR, Parrish TB, et al. **Functional changes in temporal lobe activity during transient global amnesia.** *Neurology* 2002;58:638–41 CrossRef
21. Chung YA, Jeong J, Yang DW, et al. **A Tc-99m SPECT study of regional cerebral blood flow in patients with transient global amnesia.** *NeuroImage* 2009;47:50–55 CrossRef
22. Park KM, Lee BI, Kim SE. **Is transient global amnesia a network disease?** *Eur Neurol* 2018;80:345–54 CrossRef
23. Frank LE, Preston AR, Zeithamova D. **Functional connectivity between memory and reward centers across task and rest track memory sensitivity to reward.** *Cogn, Affect Behav Neurosci* 2019; 19:503–22 CrossRef
24. Duarte A, Henson RN, Knight RT, et al. **Orbito-frontal cortex is necessary for temporal context memory.** *J Cogn Neurosci* 2010;22: 1819–31 CrossRef
25. Volle E, Gonen-Yaacovi G, Costello Ade L, et al. **The role of rostral prefrontal cortex in prospective memory: a voxel-based lesion study.** *Neuropsychologia* 2011;49:2185–98 CrossRef
26. Burgess PW, Gonen-Yaacovi G, Volle E. **Functional neuroimaging studies of prospective memory: what have we learnt so far?** *Neuropsychologia* 2011;49:2246–57 CrossRef
27. Fletcher PC, Henson RN. **Frontal lobes and human memory: insights from functional neuroimaging.** *Brain* 2001;124:849–81 CrossRef
28. Lambrey S, Doeller C, Berthoz A, et al. **Imagining being somewhere else: neural basis of changing perspective in space.** *Cereb Cortex* 2012;22:166–74 CrossRef
29. Hebscher M, Barkan-Abramski M, Goldsmith M, et al. **Memory, decision-making, and the ventromedial prefrontal cortex (vmPFC): the roles of subcallosal and posterior orbitofrontal cortices in monitoring and control processes.** *Cereb Cortex* 2016;26:4590–601 CrossRef
30. Vaccaro AG, Fleming SM. **Thinking about thinking: a coordinate-based meta-analysis of neuroimaging studies of metacognitive judgements.** *Brain Neurosci Adv* 2018;2:239821281881059 CrossRef
31. Bubb EJ, Kinnavane L, Aggleton JP. **Hippocampal - diencephalic - cingulate networks for memory and emotion: An anatomical guide.** *Brain Neurosci Adv* 2017;1:239821281772344 CrossRef
32. Fleming SM, Dolan RJ. **The neural basis of metacognitive ability.** *Phil Trans R Soc B* 2012;367:1338–49 CrossRef

The Impact of Intracortical Lesions on Volumes of Subcortical Structures in Multiple Sclerosis

I. Kalinin, G. Makshakov, and E. Evdoshenko



ABSTRACT

BACKGROUND AND PURPOSE: Recent studies showed thalamic atrophy in the early stages of MS. We investigated the impact of intracortical lesions on the volumes of subcortical structures (especially the thalamus) compared with other lesions in MS.

MATERIALS AND METHODS: Seventy-one patients with MS were included. The volumes of intracortical lesions and white matter lesions were identified on double inversion recovery and FLAIR, respectively, by using 3D Slicer. Volumes of white matter T1 hypointensities and subcortical gray matter, thalamus, caudate, putamen, and pallidum volumes were calculated using FreeSurfer. Age, MS duration, and the Expanded Disability Status Scale score were assessed.

RESULTS: Patients with intracortical lesions were older ($P = .003$), had longer disease duration ($P < .001$), and higher Expanded Disability Status Scale scores ($P = .02$). The presence of intracortical lesions was associated with a significant decrease of subcortical gray matter volume ($P = .02$). In our multiple regression model, intracortical lesion volume was the only predictor of thalamic volume ($R^2 = 0.4$, $b^* = -0.28$, $P = .03$) independent of white matter lesion volume and T1 hypointensity volume. White matter lesion volume showed an impact on subcortical gray matter volume in patients with relapsing-remitting MS ($P = .04$) and those with disease duration of <5 years ($P = .04$) and on thalamic volume in patients with Expanded Disability Status Scale scores of <4.0 ($P = .01$). By contrast, intracortical lesion volume showed an impact on subcortical gray matter and thalamic volumes in the secondary-progressive MS subgroup ($P = .02$ and $P < .001$) in patients with a long-standing disease course ($P < .001$ and $P = .001$) and more profound disability ($P < .001$ and $P < .001$).

CONCLUSIONS: Thalamic atrophy was explained better by intracortical lesions than by white matter lesion and T1 hypointensity volumes, especially in patients with more profound disability.

ABBREVIATIONS: DIR = double inversion recovery; EDSS = Expanded Disability Status Scale; iCL = intracortical lesion; ICV = intracranial volume; PPMS = primary-progressive MS; RRMS = relapsing-remitting MS; SPMS = secondary-progressive MS; TIH = T1 hypointensities; WMH = white matter hypointensities; WML = white matter lesions; SGMS = subcortical grey matter structures; b^* = standardized regression coefficients

Multiple sclerosis (MS) is a chronic debilitating disease of the CNS. Atrophy of subcortical gray matter structures (SGMS) is associated with cognitive dysfunction, fatigue, and overall disability in MS.¹ Among all SGMS, most attention is riveted on the thalamus, a gateway for cortical areas and a relay between the cortex and basal ganglia.²

Volumetric MR imaging studies showed thalamic atrophy at early stages of the disease, including clinically and radiologically isolated syndromes.^{3,4} Thalamic atrophy was associated with fatigue,^{5,6} cognitive impairments,^{7,8} decrease of walking speed,⁹ and higher disability.^{10,11} Measuring thalamic volume may be a good surrogate biomarker for clinical trials and, probably, routine practice.^{4,11,12}

Thalamic atrophy in MS can be related to either primary damage in the thalamus or distant damage of afferent or efferent thalamic fibers.¹ Primary damage includes inflammation and neurodegeneration followed by demyelination, neuronal loss, neuronal shrinkage, and axonal damage.^{7,13} Distant damage occurs due to mechanisms of Wallerian or transneuronal degeneration as a result of gray matter (GM)¹⁴ and white matter (WM)¹⁵ pathology.

In early MS, most lesions are located in the WM with less prominent involvement of the GM.¹⁶ Cortical demyelination spreads as the disease progresses, and it is most prominent in the secondary-progressive phase.¹⁷ However, thalamic atrophy is prominent in early stages and continues throughout the disease course.¹¹ The

Received December 12, 2019; accepted after revision February 27, 2020.

From the SPb Center of Multiple Sclerosis and AID (SBIH City Clinical Hospital No. 3), St. Petersburg, Russia.

The study was supported by a research grant from the Russian Science Foundation (project No. 16-15-10203).

Please address correspondence to Evgeniy Evdoshenko, MD, SPb Center of Multiple Sclerosis and AID (SBIH City Clinical Hospital No. 3), 197110, 11 Dinamo Ave, St. Petersburg, Russia; e-mail: e.evdoshenko@centremms.com

Indicates open access to non-subscribers at www.ajnr.org

Indicates article with supplemental on-line table.

<http://dx.doi.org/10.3174/ajnr.A6513>

differential impact of localization of demyelinating lesions on the thalamus and SGMS atrophy is unclear. In a neuropathological study of Vercellino et al,¹⁸ demyelination of subcortical GM correlates well with cortical, but not WM, demyelination. By contrast, in the MR imaging study by Henry et al,¹⁹ in patients with clinically isolated syndrome, the evidence of a direct connection between thalamic atrophy and white matter lesions (WML) was shown. In the MR imaging study of Ruggieri et al,¹⁴ atrophy of SGMS, eg, the thalamus, correlated with the number and volume of cortical lesions. The negative correlation of T1 black hole load and SGMS atrophy in patients with relapsing-remitting MS (RRMS) was shown.²⁰

To date, not enough data demonstrate the differentiated impact of cortical and WM pathology on subcortical gray matter atrophy. In this study, we aimed to investigate the impact of cortical lesions on volumes of the thalamus and other subcortical structures compared with other lesion locations (eg, WML and T1 white matter hypointensities (WMH) in MS.

MATERIALS AND METHODS

Study Population

This study had a cross-sectional design with retrospective analysis of data. Seventy-one patients with MS were included. The study was approved by the Local Ethics Committee of the SBIH City Clinical Hospital No. 31, and all subjects provided their written informed consent.

The inclusion criteria were as follows: patients of both sexes with multiple sclerosis, defined with the McDonald 2017 criteria; 18–65 years of age at MR imaging; and providing informed consent. The exclusion criteria were as follows: patients with relapses or steroid use within 30 days before MR imaging; a medical history associated with brain pathology (excluding MS); and pregnancy.

All data were collected for the time of MR imaging study and included sex, age, disease duration (time from the first relapse till the date of MR imaging), and Expanded Disability Status Scale (EDSS) score.

MR Imaging Acquisition Protocol

MR imaging was performed on General Electric (GE) Signa (GE Healthcare) 3T machine with isometric voxels (1 × 1 × 1 mm); model discovery, 750w; receive channels, 24. MR imaging sequence protocol was as follows—T1 CUBE (GE Healthcare): imaging plane, sagittal; imaging resolution, 1 × 1 × 1 mm; TR, 7.68 ms; TE, 3.12 ms; TI, 400 ms; flip angle, 11°; echo-train length, 1; bandwidth, 244 Hz/pixel; FLAIR CUBE: imaging plane, sagittal; imaging resolution, 1 × 1 × 1 mm; TR, 6500 ms; TE, 90 ms; TI, 1956 ms; flip angle, 90°; echo-train length, 140; bandwidth, 122 Hz/pixel; and double inversion recovery (DIR) CUBE: imaging plane, sagittal; imaging resolution, 1 × 1 × 1 mm; TR, 7000 ms; TE, 90 ms; TI, 2897 ms; flip angle, 90°; echo-train length, 160; bandwidth, 140 Hz/pixel.

For this project, we defined only intracortical lesions (iCLs) that were confined within the cortex, with sparing of the white matter and detected using the DIR sequence.¹⁹ WML were detected on FLAIR. Lesion volumes were manually counted using 3D Slicer (<http://www.slicer.org>) by 2 independent neuroscientists with experience in lesion segmentation (G.M., I.K.)

based on predefined criteria. All inconsistencies were solved by agreement.

Volumes of white matter hypointensities, detected on T1 (T1H); subcortical gray matter volume; and thalamus, caudate, putamen, and pallidum volumes were measured automatically using FreeSurfer (<https://surfer.nmr.mgh.harvard.edu/>). To normalize lesion volumes for brain size, we used ROBEX (<https://www.nitrc.org/projects/robex>) to count the intracranial volume (ICV) and then transformed all volumes in milliliters to percentage of ICV using the following formula:

$$\frac{\text{Volume}}{\text{ICV}} \times 100\%.$$

Statistical Analysis

All datasets were checked for normality with the Kolmogorov-Smirnov test.

On the first step, we divided all patients in 2 groups according to their intracortical lesion status, positive and negative for iCLs to compare demographic, clinical, and radiologic features of both groups depending on the iCL status. A comparison between iCL-negative and iCL-positive groups was performed with nonparametric (Mann-Whitney *U* test) tests. To compare the categorical data (the sex and MS phenotype), we used the Pearson χ^2 test. We considered $P < .05$ as significant. Data are presented as mean (SD) or as median (25th, 75th quartile).

On the second step, we attempted to assess the impact of iCL on volumes of subcortical structures using multivariate analysis of covariance, corrected for age and sex. Then we assessed the impact of iCL on volumes of subcortical structures compared with white matter lesions and T1 WMH using multiple regression analysis. Furthermore, using regression analysis, we estimated the impact of iCL in different disease categories, such as the following: 1) patients with relapsing-remitting MS (RRMS), secondary-progressive MS (SPMS), and primary-progressive MS (PPMS); 2) disease duration before and after 5 years; and 3) EDSS score <4.0 and ≥4.0. Volumes of iCL, WML, WMH, age, and disease duration were included as covariates.

RESULTS

Forty-three (61%) women and 28 (39%) men were included in the study. The median age was 37 years (interquartile range (difference between 75th and 25th percentiles), 29–49 years). According to the disease phenotype, there were 54/71 (76%) patients with RRMS, 12/71 (17%) with SPMS, and 5/71 (7%) with PPMS. The median EDSS score and disease duration were 3 months (interquartile range, 2–4.5 months) and 53 months (interquartile range, 15–122) months, respectively.

iCLs were detected in 55/71 (77%) patients. An example of a purely iCL is shown in Fig 1. On the basis of iCL status, patients were divided into groups positive and negative for iCL. Clinical and imaging data were compared between these 2 groups. No difference in the disease phenotype (RRMS, SPMS, PPMS) was detected between groups ($P = .11$). Patients with iCLs were older ($P = .003$) and had longer disease duration ($P < .001$) and the highest EDSS scores ($P = .02$). Results are shown in the Table 1.

The presence of iCLs was associated with a significant decrease of subcortical gray matter volume ($P = .02$) and atrophy of the caudate, putamen, and pallidum ($P = .03$, $P = .02$, $P = .005$, respectively). Results are presented in Table 2 and Fig 2; examples of the volume measurements of the thalamus in patients positive and negative for iCL are shown in the Fig 3.

Generalized linear model analysis of covariance revealed a significant impact of the volume of iCLs (% ICV) on the volumes of subcortical gray matter ($F = 20.8$, $P < .001$), thalamus ($F = 16.15$, $P < .001$), caudate ($F = 7.4$, $P = .008$), putamen ($F = 7.15$, $P = .009$), and pallidum ($F = 8.88$, $P = .004$). Age significantly predicted the total volumes of subcortical gray matter ($F = 7.76$, $P = .007$) and the putamen ($F = 24.7$, $P < .001$). Sex was not a significant predictor in this model.

Our multiple regression model explained 43% of variance ($R^2 = 0.43$), and iCL volume was the only predictor of the thalamic volume ($b^* = -0.28$, $P = .03$) independent of the volume of WML and T1H. iCL volume did not demonstrate an impact on volumes of other structures. T1H volume predicted

subcortical gray matter volume ($R^2 = 0.52$, $b^* = -0.41$, $P = .02$) independent of the volumes of iCLs and WML.

Subgroup Analysis

Disease Phenotype. In patients with RRMS, only the WML volume had a significant impact on subcortical gray matter volume ($R^2 = 0.49$, $b^* = -0.49$, $P = .04$) and putamen volume ($R^2 = 0.27$, $b^* = -0.57$, $P = .04$).

By contrast, in the SPMS subgroup, iCL lesion volume showed a significant impact on subcortical gray matter volume ($R^2 = 0.81$, $b^* = -0.44$, $P = .02$) and thalamic volume ($R^2 = 0.89$, $b^* = -0.78$, $P < .001$). Volumes of T1H explained only subcortical gray matter volume ($R^2 = 0.81$, $b^* = -1.11$, $P = .04$). Volumes of WML showed no significant associations.

We did not perform multiple regression for the PPMS subgroup due to the low number of patients (4 subjects).

Disease Duration. In the iCL-positive group, 20 patients had disease duration of <5 years and 35 patients had disease duration of >5 years.

In patients with MS with disease duration of <5 years, only the volume of WML had a significant impact on subcortical gray matter volume ($R^2 = 0.34$, $b^* = -0.70$, $P = .04$), putamen volume ($R^2 = 0.36$, $b^* = -0.79$, $P = .02$), and pallidum volume ($R^2 = 0.32$, $b^* = -0.77$, $P = .03$).

In patients with long-standing disease course (>5 years), we showed significant impact of iCL volume on subcortical gray matter volume ($R^2 = 0.71$, $b^* = -0.41$, $P < .001$), thalamus ($R^2 = 0.55$, $b^* = -0.50$, $P = .001$), and caudate volumes ($R^2 = 0.49$, $b^* = -0.59$, $P = .01$). The volume of T1H was associated with subcortical gray matter volume ($R^2 = 0.71$, $b^* = -0.62$, $P = .001$). Volumes of WML showed no significant associations.

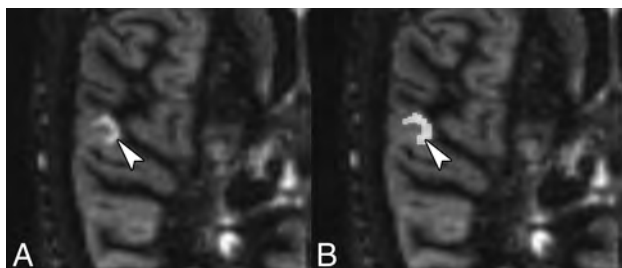


FIG 1. An example of a purely intracortical lesion (arrowhead) (A) on the DIR MR image and its manual segmentation using 3D Slicer (B).

Table 1: Demographic characteristics according to iCL status

	iCL-Negative Subgroup (n = 16)	iCL-Positive Subgroup (n = 55)	P Value
No. (%) women	10/16 (63)	33/55 (43)	.86 ^a
Median age at MR imaging (yr) (25th, 75th percentile)	27 (25–36.5)	40 (32–53)	.003 ^b
Median disease duration (mo) (25th, 75th percentile)	15 (9–34.5)	77 (26–171)	<.001 ^b
Median EDSS score (25th, 75th percentile)	2 (1.25–3)	3.5 (2–4.5)	.02 ^b
MS phenotype (No.) (%)			
Relapsing-remitting	15 (94)	39 (71)	
Secondary-progressive	0	12 (22)	
Primary-progressive	1 (6)	4 (7)	.11 ^a

^aTo compare, the Pearson χ^2 test was used.

^bSignificant difference.

Table 2: Brain morphometry analysis according to the iCL status

Structures, Median, and (25th, 75th Percentile)	iCL-Negative Subgroup (n = 16)	iCL-Positive Subgroup (n = 55)	P Value
Median of ICV (mL) (25th, 75th percentile)	1374.49 (1282.47–1482.68)	1343.47 (1260.50–1432.01)	.53
Subcortical gray matter volume (median) % ICV (25th, 75th percentile)	4.36 (3.93–4.42)	4.01 (3.75–4.23)	.02 ^a
Thalamus volume (median) % ICV (25th, 75th percentile)	1.03 (0.99–1.097)	0.99 (0.93–1.09)	.22
Caudate volume (median) % ICV (25th, 75th percentile)	0.56 (0.48–0.598)	0.49 (0.46–0.55)	.03 ^a
Putamen volume (median) % ICV (25th, 75th percentile)	0.81 (0.75–0.88)	0.74 (0.68–0.82)	.02 ^a
Pallidum volume (median) % ICV (25th, 75th percentile)	0.23 (0.20–0.25)	0.20 (0.17–0.22)	.005 ^a
Volume of WML (median) % ICV (25th, 75th percentile)	0.39 (0.16–0.57)	0.65 (0.31–1.34)	.01 ^a
iCL lesions volume (median) % ICV (25th, 75th percentile)	–	0.008 (0.004–0.02)	–

^aSignificant difference.

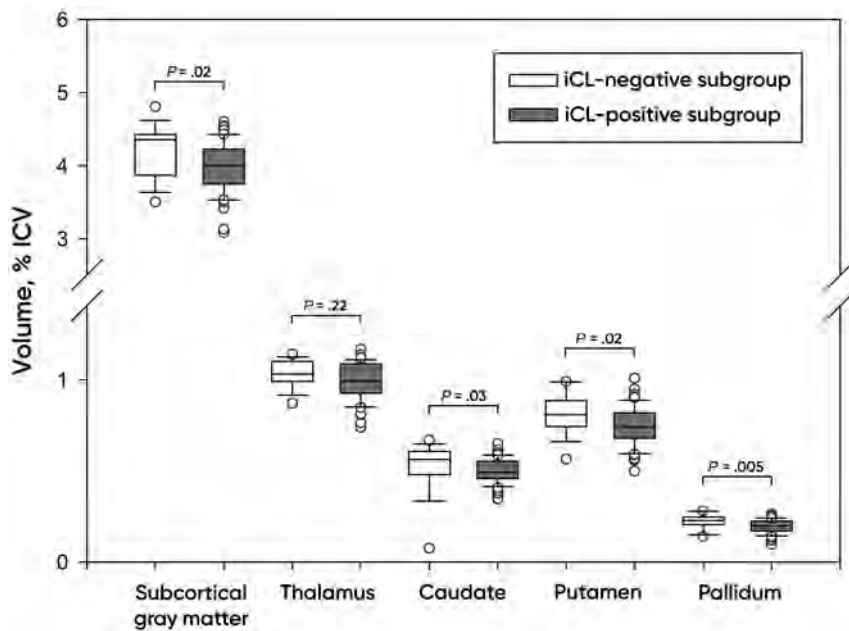


FIG 2. Brain volumes according to the iCL status. Plots of the median, 10th, 25th, 75th, and 90th percentiles as vertical boxes with error bars.

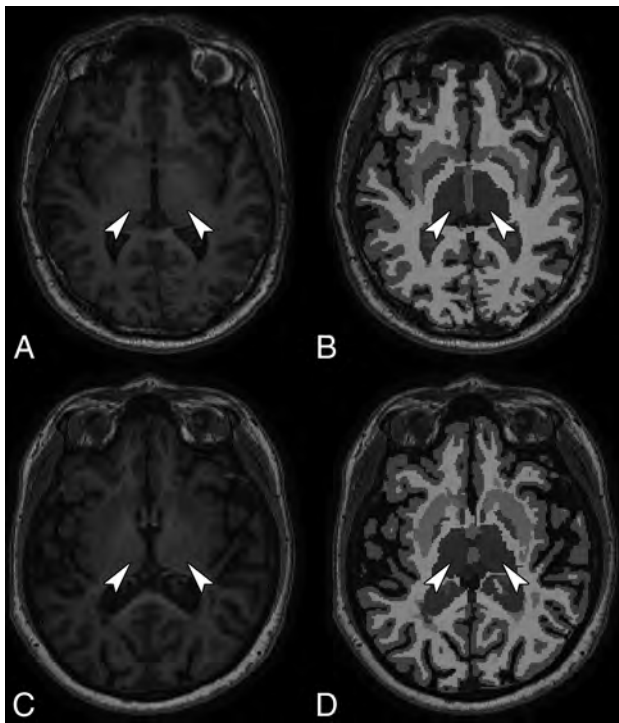


FIG 3. Examples of the volume measurement of the thalamus (arrowheads) in iCL-negative (A and B) and iCL-positive patients (C and D) using FreeSurfer (T1-weighted MR image).

EDSS Score. In the iCL-positive group, 28 patients had EDSS scores of <4 , and 27 patients had EDSS scores ≥ 4.0 .

In the subgroup of patients with MS with EDSS scores of <4.0 , the only significant impact was shown for the volume of WML on thalamic volume ($R^2 = 0.34$, $b^* = -0.60$, $P = .01$).

In patients with EDSS score ≥ 4.0 , iCL lesion volume showed a significant impact on subcortical gray matter volume ($R^2 = 0.77$, $b^* = -0.56$, $P < .001$), thalamic volume ($R^2 = 0.55$, $b^* = -0.60$, $P < .001$), and caudate volume ($R^2 = 0.57$, $b^* = -0.44$, $P = .007$).

The volume of T1H was associated with subcortical gray matter ($R^2 = 0.77$, $b^* = -0.79$, $P = .002$) and thalamic volumes ($R^2 = 0.55$, $b^* = -0.74$, $P = .03$). Volumes of WML showed no significant associations.

All data can be found in the Online Table.

DISCUSSION

In this study, we assessed the impact of iCL on volumes of subcortical structures compared with WML and T1H in MS.

Our findings demonstrate that the volumes of iCLs may impact the volumes of subcortical gray matter structures,

especially on the thalamus in MS. iCL volume was the only predictor of thalamic volume independent of volumes of WML and T1H.

The more interesting results were found in subgroup analysis. Volumes of WML impacted subcortical gray matter volume in patients with RRMS, patients with disease duration of <5 years, and the volume of the thalamus in patients with EDSS scores of <4.0 . These findings are in line with those of the study of Tao et al,²⁰ which has shown a correlation between the volume of WML and thalamic atrophy in patients with RRMS. Acute inflammation, related to the formation of WML, is the major driving force during the RRMS phase, with some diminishing inflammatory activity in the progressive phase.²¹ Hence, our findings are highly relevant to this concept. iCLs have a different pathogenesis and may prevail in progressive forms of MS, becoming more important to atrophy of subcortical structures.²²

iCL volume impacted subcortical gray matter and thalamic volume in patients with long-standing disease course and more profound disability. Although we found that iCL volume impacts subcortical gray matter and thalamic volumes in the SPMS subgroup, we had no iCL-negative patients with SPMS for comparison. In fact, the presence of cortical demyelination has been shown in pathology studies;²³ however, MR imaging methods like the DIR sequence may not be sensitive enough to detect iCLs.²⁴ Cortical pathology in our iCL-negative subgroup may not have been prominent enough to be detected with the DIR sequence, so in fact, this study may represent only a part of disease mechanisms due to technical limitations.

Because in the early stages of disease, white matter pathology predominates over cortical pathology,²⁵ we suppose, that in this case, thalamic atrophy can be caused by distant damage of afferent or efferent thalamic fibers. This supposition is in line with previous MR imaging studies that supposed that atrophy of the

subcortical gray matter structures preceded cortical atrophy in early MS.^{19,26} Rocca et al⁴ observed that white matter lesions contribute to thalamic tissue loss. In another study, Henry et al¹⁹ demonstrated that only WML in the region of thalamocortical fibers significantly correlated with thalamic atrophy in patients with clinically isolated syndrome.

Cortical demyelination becomes much more prominent in the chronic disease stages.¹⁷ iCLs can result in thalamic atrophy due to retrograde degeneration of thalamocortical radiations.¹⁴ This finding is in accordance with previously published neuropathologic and MR imaging that showed a correlation between cortical demyelination and cortical lesions with thalamic atrophy.^{14,18}

Our study had some limitations. We had a rather small sample size (71 patients in total and 55 with iCLs). The design of the study was not prospective, so the dynamics of changes were not evaluated. A low number of patients with PPMS (4 subjects) made it impossible to perform multiple regression for this subgroup. In addition, we had no healthy controls or a control group of patients with other neurodegenerative disorders with pathology of the basal ganglia.

CONCLUSIONS

Thalamic atrophy was explained better by intracortical lesions, than by white matter lesions and T1 white matter hypointensities, especially in patients with disease duration of >5 years and EDSS scores of ≥ 4.0 .

Disclosures: Ivan Kalinin—UNRELATED: Travel/Accommodations/Meeting Expenses Unrelated to Activities Listed: travel grants, Comments: ECTRIMS 2018, EAN 2019, 27th Annual Meeting of the Charcot Foundation 2019. Gleb Makshakov—RELATED: Grant: Russian Scientific Fund, Comments: Russian Scientific Fund grant application No. 16-15-203, received in 2016–2018*; UNRELATED: Payment for Lectures Including Service on Speakers Bureaus: Genzyme, Janssen, Roche, Comments: honoraria for lectures and speaking in the past 2 years; Travel/Accommodations/Meeting Expenses Unrelated to Activities Listed: travel grants, Comments: ECTRIMS 2015, 2016, 2017, 2018, and 2019 meetings. Evgeniy Evdoshenko—RELATED: Grant: Russian Science Foundation (Application No. 16-15-203), received in 2016–2018*; UNRELATED: Payment for Lectures Including Service on Speakers Bureaus: Merck, Biogen, Roche, Johnson & Johnson, Novartis, GlaxoSmithKline, Sanofi, Genzyme, Genierum, Comments: honoraria for lectures and speaking in the past 2 years. *Money paid to the institution.

REFERENCES

1. Capone F, Collorone S, Cortese R, et al. **Fatigue in multiple sclerosis: the role of thalamus.** *Mult Scler* 2020;26:6–16 CrossRef Medline
2. Minagar A, Barnett MH, Benedict RH, et al. **The thalamus and multiple sclerosis: modern views on pathologic, imaging, and clinical aspects.** *Neurology* 2013;80:210–19 CrossRef Medline
3. Azevedo CJ, Overton E, Khadka S, et al. **Early CNS neurodegeneration in radiologically isolated syndrome.** *Neurol Neuroimmunol Neuroinflamm* 2015;2:e102 CrossRef Medline
4. Rocca MA, Mesaros S, Pagani E, et al. **Thalamic damage and long-term progression of disability in multiple sclerosis.** *Radiology* 2010;257:463–69 CrossRef Medline
5. Calabrese M, Rinaldi F, Grossi P, et al. **Basal ganglia and frontal/parietal cortical atrophy is associated with fatigue in relapsing-remitting multiple sclerosis.** *Mult Scler* 2010;16:1220–28 CrossRef Medline

6. Bernitsas E, Yarraguntla K, Bao F, et al. **Structural and neuronal integrity measures of fatigue severity in multiple sclerosis.** *Brain Sci* 2017;7 CrossRef Medline
7. Houtchens MK, Benedict RH, Killiany R, et al. **Thalamic atrophy and cognition in multiple sclerosis.** *Neurology* 2007;69:1213–23 CrossRef Medline
8. Batista S, Zivadinov R, Hoogs M, et al. **Basal ganglia, thalamus and neocortical atrophy predicting slowed cognitive processing in multiple sclerosis.** *J Neurol* 2012;259:139–46 CrossRef Medline
9. Motl RW, Zivadinov R, Bergsland N, et al. **Thalamus volume and ambulation in multiple sclerosis: a cross-sectional study.** *Neurodegener Dis Manag* 2016;6:23–29 CrossRef Medline
10. Rasche L, Scheel M, Otte K, et al. **MRI markers and functional performance in patients with CIS and MS: a cross-sectional study.** *Front Neurol* 2018;9 CrossRef Medline
11. Azevedo C, Cen S, Khadka S, et al. **Thalamic atrophy in multiple sclerosis: A magnetic resonance imaging marker of neurodegeneration throughout disease.** *Ann Neurol* 2018;83:223–34 CrossRef Medline
12. Solomon A, Watts R, Dewey B, et al. **MRI evaluation of thalamic volume differentiates MS from common mimics.** *Neurol Neuroimmunol Neuroinflamm* 2017;4:e387 CrossRef Medline
13. Cifelli A, Arridge M, Jezzard P, et al. **Thalamic neurodegeneration in multiple sclerosis.** *Ann Neurol* 2002;52:650–53 CrossRef Medline
14. Ruggieri S, Petracca M, Miller A, et al. **Association of deep gray matter damage with cortical and spinal cord degeneration in primary progressive multiple sclerosis.** *JAMA Neurol* 2015;72:1466–74 CrossRef Medline
15. Kipp M, Wagenknecht N, Beyer C, et al. **Thalamus pathology in multiple sclerosis: from biology to clinical application.** *Cell Mol Life Sci* 2015;72:1127–47 CrossRef Medline
16. Kutzelnigg A, Lucchinetti C, Stadelmann C, et al. **Cortical demyelination and diffuse white matter injury in multiple sclerosis.** *Brain* 2005;128:2705–12 CrossRef Medline
17. Geurts J, Barkhof F. **Grey matter pathology in multiple sclerosis.** *Lancet Neurol* 2008;7:841–51 CrossRef Medline
18. Vercellino M, Masera S, Lorenzatti M, et al. **Demyelination, inflammation, and neurodegeneration in multiple sclerosis deep gray matter.** *J Neuropathol Exp Neurol* 2009;68:489–502 CrossRef Medline
19. Henry RG, Shieh M, Okuda DT, et al. **Regional grey matter atrophy in clinically isolated syndromes at presentation.** *J Neurol Neurosurg Psychiatry* 2008;79:1236–44 CrossRef Medline
20. Tao G, Datta S, He R, et al. **Deep gray matter atrophy in multiple sclerosis: a tensor based morphometry.** *J Neurol Sci* 2009;282:39–46 CrossRef Medline
21. Frischer J, Bramow S, Dal-Bianco A, et al. **The relation between inflammation and neurodegeneration in multiple sclerosis brains.** *Brain* 2009;132:1175–89 CrossRef Medline
22. Popescu B, Pirko I, Lucchinetti C. **Pathology of multiple sclerosis.** *Continuum (Minneapolis)* 2013;19:901–21 CrossRef Medline
23. Lucchinetti C, Popescu B, Bunyan R, et al. **Inflammatory cortical demyelination in early multiple sclerosis.** *N Engl J Med* 2011;365:2188–97 CrossRef Medline
24. Favaretto A, Poggiali D, Lazzarotto A, et al. **The parallel analysis of phase sensitive inversion recovery (PSIR) and double inversion recovery (DIR) images significantly improves the detection of cortical lesions in multiple sclerosis (MS) since clinical onset.** *PLoS One* 2015;10:e0127805 CrossRef Medline
25. Popescu BF, Lucchinetti CF. **Meningeal and cortical grey matter pathology in multiple sclerosis.** *BMC Neurol* 2012;12:11 CrossRef Medline
26. Sepulcre J, Sastre-Garriga J, Cercignani M, et al. **Regional gray matter atrophy in early primary progressive multiple sclerosis: a voxel-based morphometry study.** *Arch Neurol* 2006;63:1175–80 CrossRef Medline

Aging and the Brain: A Quantitative Study of Clinical CT Images

K.A. Cauley, Y. Hu, and S.W. Fielden



ABSTRACT

BACKGROUND AND PURPOSE: Though CT is a highly calibrated imaging modality, head CT is typically interpreted qualitatively. Our aim was to initiate the establishment of a reference quantitative database for clinical head CT.

MATERIALS AND METHODS: An automated segmentation algorithm was developed and applied to 354 clinical head CT scans with radiographically normal findings (ages, 18–101 years; 203 women) to measure brain volume, brain parenchymal fraction, brain radiodensity, and brain parenchymal radiomass. Brain parenchymal fraction was modeled using quantile regression analysis.

RESULTS: Brain parenchymal fraction is highly correlated with age ($R^2 = 0.908$ for men and 0.950 for women), with 11% overall brain volume loss in the adult life span (1%/year from 20 to 50 years and 2%/year after 50 years of age). Third-order polynomial quantile regression curves for brain parenchymal fraction were rationalized and statistically validated. Total brain parenchymal radiodensity shows a decline as a function of age (14.9% for men, 14.7% for women; slopes not significantly different, $P = .760$). Age-related loss of brain radiomass (the product of volume and radiodensity) is approximately 20% for both sexes, significantly greater than the loss of brain volume ($P < .001$).

CONCLUSIONS: An automated segmentation algorithm has been developed and applied to clinical head CT images to initiate the development of a reference database for quantitative brain CT imaging. Such a database can be subject to quantile regression analysis to stratify patient brain CT scans by metrics such as brain parenchymal fraction, radiodensity, and radiomass, to aid in the identification of statistical outliers and lend quantitative assessment to image interpretation.

ABBREVIATIONS: BPF = brain parenchymal fraction; TIV = total intracranial volume; SD = standard deviation

Abnormalities in brain volumetrics have been associated with congenital and acquired diseases. Most *in vivo* studies have been performed with MR imaging of healthy volunteers and measure global and regional volume loss.^{1–8} Lack of an accepted normative database, together with evidence that measurements are influenced by differences in postprocessing methods, has limited quantitative reporting.⁹

Among adults, MR imaging has been used to identify abnormalities of global brain volume in multiple sclerosis,^{10,11} amyotrophic lateral sclerosis,¹² and age-related dementia,¹³ with brain parenchymal fraction (BPF) permitting normalization for subject variability.^{14,15} MR imaging also suggests that brain volume is reduced by antipsychotic medications,¹⁶ steroids,¹⁷ alcohol use,¹⁸ and radiation and chemotherapy¹⁹ among other things. Changes in brain radiodensity or radiomass (the product of volume and radiodensity), as a function of disease states are relatively unexplored topics. Identifying and quantifying tissue loss through volumetric measures, measures of radiodensity or radiomass, may aid in the diagnosis or monitoring of brain pathology. To account for intrasubject variability as well as variability as a function of age and sex, correlating metrics with pathology requires a reference database. The initiation of such a reference database is the goal of the current study.

CT imaging appears highly suitable for *in vivo* study of the brain because it is routinely acquired in the clinical setting and is less subject to motion artifacts than MR imaging. Radiodensity characteristics of the brain and skull enable automated volumetric and radiodensity assessment. Furthermore, the relatively low

Received November 17, 2019; accepted after revision January 30, 2020.

From the Department of Radiology (K.A.C., S.W.F.), Geisinger Medical Center, Danville Pennsylvania; Department of Imaging Science and Innovation (S.W.F.), Geisinger Health System, Lewisburg, Pennsylvania; and Department of Imaging Science and Innovation (Y.H.), Geisinger Medical Center, Danville Pennsylvania. Dr Cauley is currently affiliated with Virtual Radiologic, Eden Prairie, Minnesota.

This work was supported by a grant from Geisinger Clinical Research Fund to K.A.C. and S.W.F., SRC-L-58.

Please address correspondence to Keith A. Cauley, MD, Virtual Radiologic, 11995 Singletree Lane, No. 500, Eden Prairie, MN 55344; e-mail: keithcauley@hotmail.com

Indicates article with supplemental on-line tables.

<http://dx.doi.org/10.3174/ajnr.A6510>

clinical threshold for performing CT provides large numbers of studies with radiographically normal findings, enabling the generation of a large reference database for statistical analysis.

In the current study, we report brain volumes from 354 subjects, both before and after normalization to the intracranial volume, expressed as a function of age and sex. Total radiodensity and radiomass estimations are also calculated. Statistical methods are used with quantile regression applied to brain parenchymal fraction measures. We propose that a clinical database can be used to quantitatively assess new cases in the context of a clinical peer group.

MATERIALS AND METHODS

Study Design

This study was limited to a retrospective analysis of head CTs performed on patients who were identified from the clinical PACS. The study was approved by this institutional review board (Geisinger Medical Center), and a waiver of consent was granted.

Study Cohort

All studies were from a single CT scanner during a 2-year time interval (January 1, 2015, to December 31, 2016). Selected cases were scanned for nonspecific symptoms (headache, syncope, vertigo), were without known systemic disease, and were discharged without incident. All control cases were interpreted as having normal findings (without acute or chronic abnormal findings) by 2 board-certified neuroradiologists.

Imaging Data

The CT scanner (LightSpeed VCT; GE Healthcare) primarily serves the emergency department of a level 1 trauma center. The axial acquisition noncontrast head CT protocol consists of 135 kV(peak) and modulated milliampere, minimum 50 and maximum 290 mA; rotation time, 0.75 seconds, acquired from the foramen magnum through the vertex with a standard 512×512 matrix; and 24-cm FOV at 5.0-mm section thickness. The scanner undergoes a daily quality assurance procedure, which assesses the radiodensity of water. This value must be within allowable limits, generally 0–5 HU. Drift or trending is rarely observed. In addition, scanners undergo an annual inspection by a medical physicist using the American College of Radiology phantom. Acceptable ranges of Hounsfield units for clinical scanners are broad (–7 to +7 HU for water, 110–135 HU for acrylic). This testing is extended to all kV

(peak) values used by the scanner. Additionally, service engineers routinely test the calibration at preventive maintenance.

Image Processing and Analysis

DICOM images were converted to the Neuroimaging Informatics Technology Initiative data format using MRIConvert-2.0.7 (<https://www.softpedia.com/get/Science-CAD/MRIConvert.shtml>). Images were first thresholded from –15 to 50 HU to grossly remove background and skull. Brain extraction was then applied using the FSL Brain Extraction Tool (<http://fsl.fmrib.ox.ac.uk/fsl/fslwiki/BET>) with a fractional intensity threshold of 0.01. All cases were carefully reviewed for the integrity of brain extraction. For segmentation, a 3-tissue-compartment segmentation using the FMRIB Automated Segmentation Tool (<http://fsl.fmrib.ox.ac.uk/fsl/fslwiki/fast>) was used, with the resulting white matter and gray matter compartments combined into a single brain compartment (Fig 1). The brain parenchymal fraction (BPF) was calculated as the ratio of brain volume to total intracranial volume, consisting of brain plus CSF space. Brain radiomass was calculated as the product of mean brain radiodensity and brain volume.

Statistical Methods

Statistical analysis was performed using GraphPad Prism software, Version 7.0c for Mac OS X (GraphPad Software). Polynomial regression models were performed in R Studio (Version 1.2.1335; <http://rstudio.org/download/desktop>). The overall polynomial regression of third degree of age was fitted on the BPF, after adjusting for sex. For male and female subgroups, quantile regression was adopted to characterize BPF, with the polynomial term of age. Models were evaluated using leave-one-out cross-validation, and root-mean-square errors were computed for predictive accuracy. At a .1 significance level, significant differences were observed in BPF between men and women.

RESULTS

Brain Parenchymal Volume

A scatterplot of brain parenchymal volume from adult male and female subjects as a function of age is shown in Fig 2A. The mean brain volume for men is $1209 \pm 133.6 \text{ cm}^3$, and for women, $1056 \pm 107.4 \text{ cm}^3$. Across all ages, whole-brain volumes were approximately 10% smaller for female subjects. The slopes of the linear regression trendlines for brain volume (men, $R = 0.413$, $R^2 = 0.17$; women, $R = 0.425$, $R^2 = 0.18$) are not significantly different between the sexes ($P = .5451$) (On-line Table 1). The loss of brain volume calculated from the linear trendline from 20 to 100 years is 14.0% for men and 13.9% for women, without a significant difference.

Brain Parenchymal Fraction

BPF from adult male and female subjects as a function of age is shown in Fig 2B. The brain parenchymal fraction ranges from approximately 0.9 to 0.75, showing a curvilinear decline with age. The mean BPF is 0.843 for women and 0.847 for men and the difference was

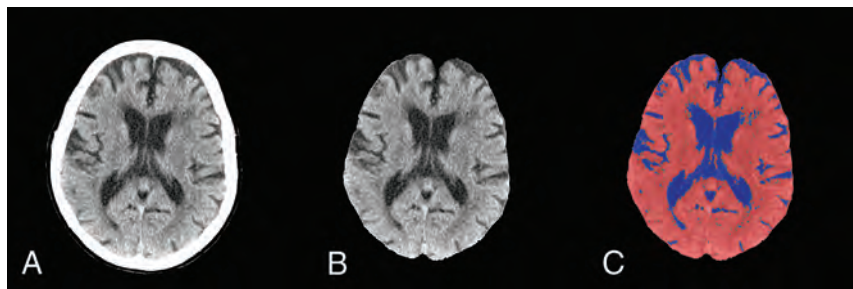


FIG 1. Brain extraction and CSF segmentation. A, Raw head CT image. B, Brain extracted image; volume = TIV (total intracranial volume). C, Thresholded to identify CSF. BPF = TIV–CSF volume/TIV.

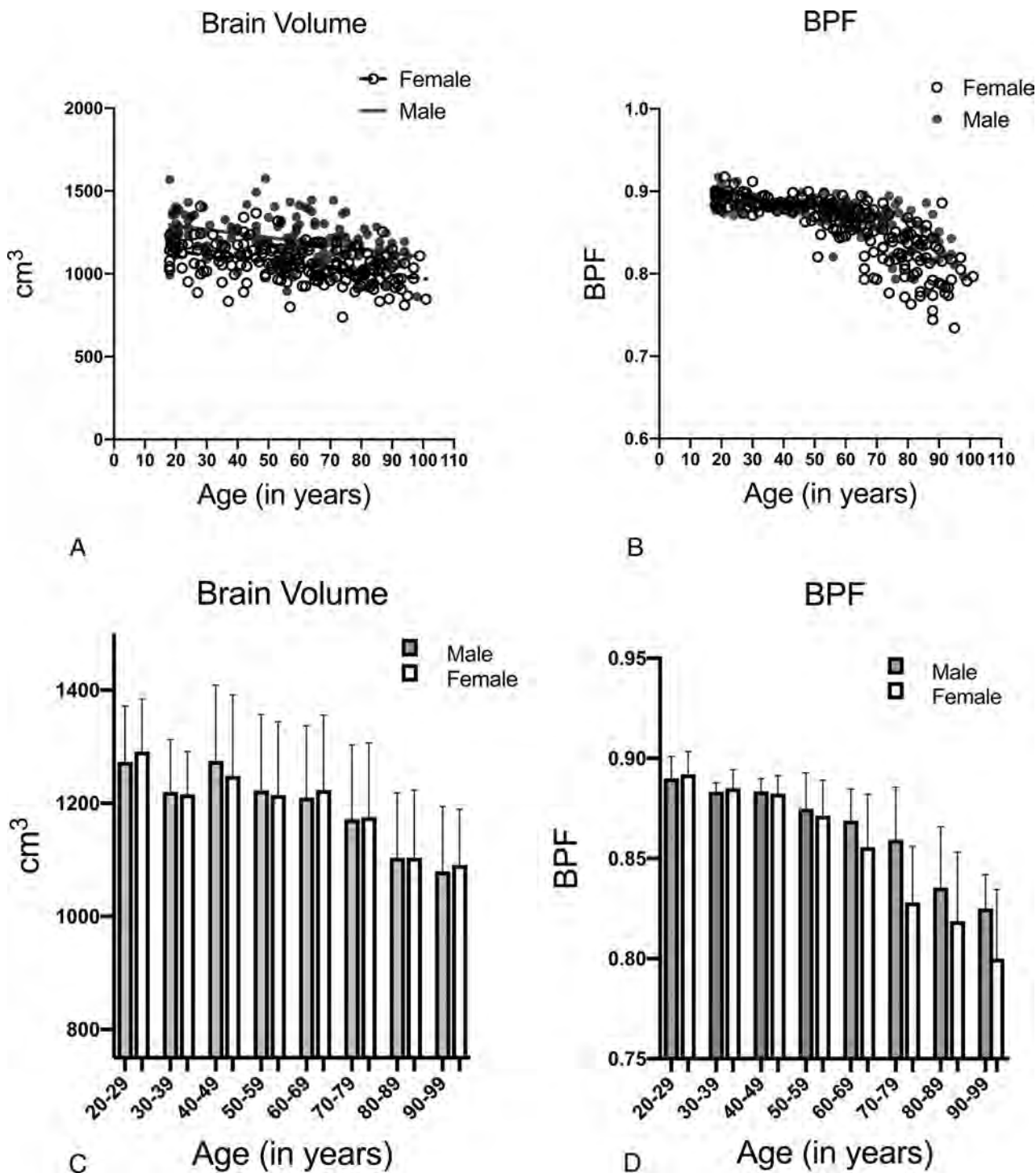


FIG 2. A, Brain volume as a function of age and sex. B, Brain parenchymal fraction as a function of age and sex. C, Bar chart of brain volume with decade age grouping, with SDs. Gray bars indicate men; white bars, women. D, Bar chart of BPF with decade age grouping, with SDs. Gray bars indicate men; white bars, women.

not significant between the sexes (Student *t* test, $P = .48$). Linear regression with age shows $R^2 = 0.51$ for men and 0.62 for women. BPF shows a decreased coefficient of variation relative to brain volume (3.085% vs 11.06% for men, 4.632% vs 10.2% for women; male data is shown in On-line Table 1).

The bar charts (Fig 2C and 2D) show decade groupings of the age cohorts. The BPF shows increased correlation with age, with

decreased SD relative to brain volume measure. Statistical correlations of brain parenchymal volume and BPF are shown in On-line Table 2.

Brain Parenchymal Density

The brain parenchymal density (Fig 3A) is taken as the mean Hounsfield unit number for total brain parenchyma. Considerable

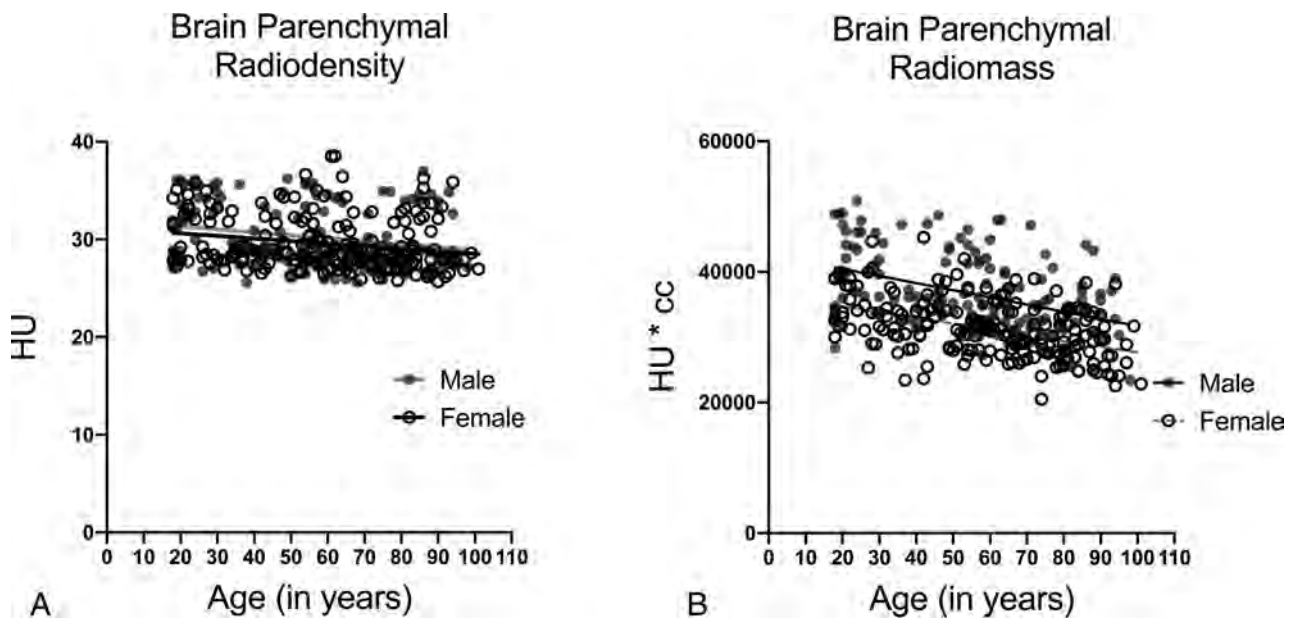


FIG 3. A, Brain parenchymal radiodensity as a function of age and sex. B, Estimated brain radiomass (volume \times radiodensity) as a function of age and sex.

variation is seen in the mean parenchymal density for both sexes. The mean Hounsfield unit density for men is 30.29 ± 3.20 , and for women, 29.58 ± 2.70 . Male mean brain parenchymal density is slightly-but-significantly greater than for women ($P = .0263$). The mean brain parenchymal density declines significantly with age from 31.34 to 28.91 for men ($P < .0061$, -7.74%) and from 30.64 to 28.54 for women ($P = .0026$, -6.8%). The slopes of the linear regression lines are not significantly different ($P = .76$). Analysis by decade grouping by age shows that the third decade (20–29 years) is significantly different from the older groups (male data shown in On-line Table 3).

Brain Parenchymal Radiomass

Brain volume multiplied by brain radiodensity yields total brain radiomass, measured as cubic centimeter \times Hounsfield unit (Fig 3B). The mean brain radiomass was $36,671.6 \pm 5954$ for men and $29,291 \pm 8816$ for women, with female brain radiomass being consistently approximately 20% less than for men. For women, the brain mass was 34,876 at 18 years and 27,673 at 100 years, a 20.7% decline. For men, the brain mass was 40,679 at 18 years and 31,709 at 100 years, a 22% decline, with differences in regression slopes not significant ($P = .325$). Significance between decade cohorts is achieved between the third decade and the older decade cohorts (male data shown in On-line Table 3).

Quantile Regression

BPF was chosen to illustrate quantile regression. The overall polynomial regression of third degree of age was fitted on the brain parenchymal fraction, after adjusting for sex. Overall polynomial regression indicated differences between men and women (mean difference = -0.005 ; 95% confidence interval, 0.01 to $-1e-04$; $P = .046$). Therefore, we fitted a quantile regression model of third degree of age on brain parenchymal fraction for men (Fig 4A) and

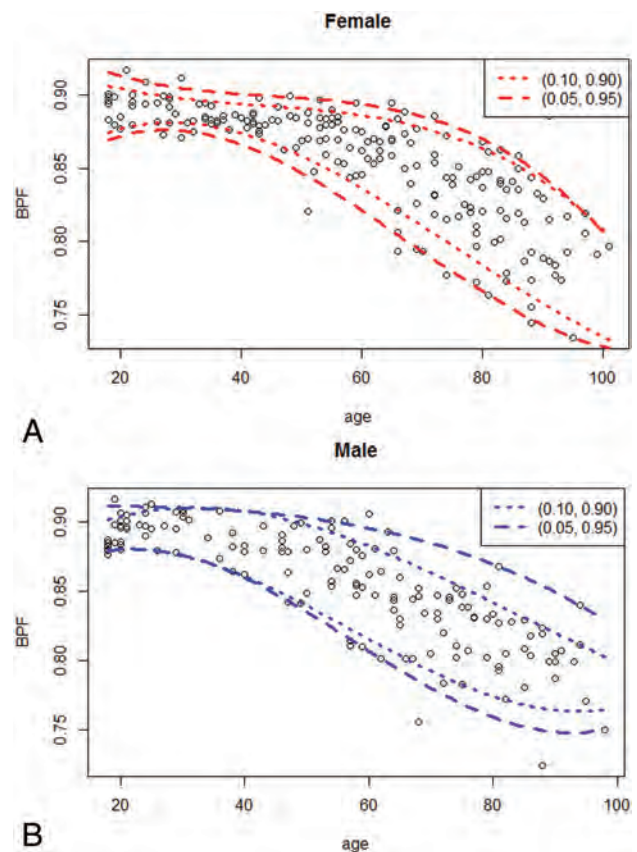


FIG 4. Quantile regression of brain parenchymal fraction. Scatterplot of BPF as a function of age for female patients (A) and male patients (B). Quantile regression lines are drawn by polynomial curve fitting with 5th and 95th percentile as *dashed lines*, and 10th and 90th percentile as *dotted lines*. Polynomial coefficients are shown in Table 1.

Coefficients of polynomial regression models

	Overall	Men (0.05-Tile)	Men (0.95-Tile)	Women (0.05-Tile)	Women (0.95-Tile)
Intercept	0.86	8.32E-01	9.12E-01	8.11E-01	9.54E-01
Age	-0.58	4.74E-03	-4.91E-05	5.21E-03	-3.13E-03
Age ²	-0.13	-1.32E-04	3.21E-06	-1.19E-04	6.37E-05
Age ³	0.04	7.63E-07	-1.15E-07	5.88E-07	-4.72E-07

women (Fig 4B), respectively, with a polynomial curve of third degree of age plotted at 0.05-tile and 0.95-tile, and 0.10-tile and 0.90-tile. The coefficients of the polynomial regression models are shown in the Table.

DISCUSSION

Our study is a quantitative analysis of clinical images. Most brain studies of this type are performed with MR imaging, on healthy volunteers under ideal conditions. The goal of the current study was the development of a clinical tool; our study is derived from clinical images so that patients can be compared with their clinical peer group using the same imaging technique under identical conditions. While current image interpretation is largely qualitative, an automated quantitative analysis together with statistical methods such as quantile regression enables a quantitative assessment of brain parameters.

The data show large variance in brain volumes, consistent with previous reports that total brain size can vary almost 2-fold among individuals of the same age.²⁰ Adult brain volumes are consistent with published literature, with our study focusing on the parenchymal volume.^{4,21,22} The female brain parenchymal volume is 1056 cm³, approximately 12.6% smaller than for men (mean parenchymal volume, 1209 cm³) not adjusted for body size, with a near-linear 14.9% decrease in male brain volume and 14.7% decrease in female brain volume during the adult life span (18–100 years), also consistent with previous reports.^{3,4}

The BPF is taken as a ratio of brain parenchymal volume to the intracranial volume^{9,23} and serves to normalize the brain volume to account for variations in head size, with increased sensitivity for age-related atrophy or pathology.^{12,13,15,23,24} To our knowledge, the BPF has not been previously derived from head CT imaging. Because brain volume can vary as much as 2-fold even in the younger population, the CT BPF shows considerably less variation, decreasing from approximately 0.9 in early adulthood to 0.75 in late life, as has been noted in an MR imaging study of volunteers.³ BPF shows significantly greater correlation with age than brain volume (On-line Tables 1–3).

CT has the advantage over MR imaging in that the image signal intensity is a direct measure of the radiodensity and is a calibrated and scaled metric. Previous studies have found declines in Hounsfield units with aging,^{25,26} whereas other studies report no change.^{27,28} Global variant brain tissue density has been shown to correlate with acute and chronic pathology.^{29,30} Imprecisions of machine calibration may contribute to the variance in radiodensity; however, several patterns are evident. First, there is a significant negative trendline slope of radiodensity as a function of age for both men and women ($P < .001$). Second, the radiodensity of the 20- to 29-year group in both sexes is statistically significantly higher than in older groups (On-line Tables 1–3). These data

argue for an age-dependent decline in brain tissue radiodensity. A decline in brain tissue density may correlate with neuronal loss and/or an increase in lipid or water content. Myelin is less dense than water, and relative loss of myelin would not be expected to result in decreased density.

Most imaging studies of brain atrophy measure the loss of tissue volume only. CT enables assessment of tissue radiodensity, with the product of radiodensity and volume, yielding an estimate of total brain radiomass. Radiomass can be correlated with mass measures from postmortem data. An authoritative postmortem study by Svennerholm et al³¹ showed a 20% decrease in brain parenchymal mass from 20 to 100 years of age for women and 22% for men. Our study of decade age cohorts shows a 22% decrease from the third to the 10th decade for both sexes. The data of Svennerholm et al also showed that the average female brain mass is 16% smaller than the male brain mass, whereas the brain volume is only 10% smaller. Both sets of data illustrate that brain mass declines significantly more than is reflected by a measure of brain volume alone.

Quantile regression is used as a quantitative method for comparing a given case with the total pool of reference cases. BPF was chosen for illustration. Third-order polynomial was best fit for the data. Small-but-measurable differences were seen between men and women, with slightly greater volume loss in men at older ages (Table). Similar regressions could be performed for each type of quantitative metric. New cases could be described in terms of the quantile position relative to the reference database.

Study Limitations

A potential criticism of this database is that included studies may not be “normal” because each study is obtained for a clinical reason. The goal of this study was not to identify true normal but to characterize the clinical population and develop a clinically useful database with which future studies might be compared. A large database together with statistical methods will approximate normalcy (i.e., the law of large numbers applies) or at least provide a clinically useful reference. CT entails radiation exposure and recruiting large numbers of healthy volunteers from the clinical archive facilitates the development of a large database of both sexes across the life span.

All data for this study originated from a single CT scanner. Although contemporary scanners are highly calibrated, differences between scanners or scan protocols could introduce an additional variable. Measured volumes and BPFs would be expected to show little variance across scanners, though measured Hounsfield units may vary.³² Data from different scanners may be merged using statistical methods such as *z* scoring; more rigorous calibration standards may be necessary for broad implementation of a standard database.

CONCLUSIONS

This study demonstrates that a large pool of clinical CT data can be subject to automated analysis to yield brain metrics supported by the existing literature. The total brain metrics of BPF, brain parenchymal density, and brain parenchymal mass derived from CT images are novel reports and show high correlation with loss of brain matter as a function of the aging process. Clinical head CT data can be subject to analytic methods to quantitatively assess new studies in the context of a clinical peer group.

Disclosures: Keith Cauley—RELATED: Grant: Geisinger Clinical Research Grant, Comments: internal research grant, no money paid to me; UNRELATED: Employment: Geisinger Medical Center.

REFERENCES

1. Autti T, Raininko R, Vanhanen SL, et al. **MRI of the normal brain from early childhood to middle age, I: appearances on T2- and proton density-weighted images and occurrence of incidental high-signal foci.** *Neuroradiology* 1994;36:644–68 CrossRef Medline
2. Coffey CE, Lucke JF, Saxton JA, et al. **Sex differences in brain aging: a quantitative magnetic resonance imaging study.** *Arch Neurol* 1998;55:169–79 CrossRef Medline
3. Condon B, Grant R, Hadley D, et al. **Brain and intracranial cavity volumes: in vivo determination by MRI.** *Acta Neurol Scand* 1988;78:387–93 CrossRef Medline
4. Courchesne E, Chisum HJ, Townsend J, et al. **Normal brain development and aging: quantitative analysis at in vivo MR imaging in healthy volunteers.** *Radiology* 2000;216:672–82 CrossRef Medline
5. Ge Y, Grossman RI, Babb JS, et al. **Age-related total gray matter and white matter changes in normal adult brain, Part I: volumetric MR imaging analysis.** *AJNR Am J Neuroradiol* 2002;23:1327–33 Medline
6. Jernigan TL, Archibald SL, Berhow MT, et al. **Cerebral structure on MRI, Part I: Localization of age-related changes.** *Biol Psychiatry* 1991;29:55–67 CrossRef Medline
7. Pfefferbaum A, Mathalon DH, Sullivan EV, et al. **A quantitative magnetic resonance imaging study of changes in brain morphology from infancy to late adulthood.** *Arch Neurol* 1994;51:874–87 CrossRef Medline
8. Xu J, Kobayashi S, Yamaguchi S, et al. **Gender effects on age-related changes in brain structure.** *AJNR Am J Neuroradiol* 2000;21:112–18 Medline
9. Vagberg M, Granasen G, Svenningsson A. **Brain parenchymal fraction in healthy adults—a systematic review of the literature.** *PLoS One* 2017;12:e0170018 CrossRef Medline
10. Losseff NA, Wang L, Lai HM, et al. **Progressive cerebral atrophy in multiple sclerosis. A serial MRI study.** *Brain* 1996;119:2009–19 CrossRef
11. Simon JH, Jacobs LD, Champion MK, et al. **A longitudinal study of brain atrophy in relapsing multiple sclerosis: the Multiple Sclerosis Collaborative Research Group (MSCRG).** *Neurology* 1999;53:139–48 CrossRef Medline
12. Rajagopalan V, Pioro EP. **Brain parenchymal fraction: a relatively simple MRI measure to clinically distinguish ALS phenotypes.** *Biomed Res Int* 2015;2015:693206 CrossRef Medline
13. Fjell AM, McEvoy L, Holland D, et al; Alzheimer's Disease Neuroimaging Initiative. **Brain changes in older adults at very low risk for Alzheimer's disease.** *J Neurosci* 2013;33:8237–42 CrossRef Medline
14. Reardon PK, Seidlitz J, Vandekar S, et al. **Normative brain size variation and brain shape diversity in humans.** *Science* 2018;360:1222–27 CrossRef Medline
15. Vagberg M, Lindqvist T, Ambarki K, et al. **Automated determination of brain parenchymal fraction in multiple sclerosis.** *AJNR Am J Neuroradiol* 2013;34:498–504 CrossRef Medline
16. Moncrieff J, Leo J. **A systematic review of the effects of antipsychotic drugs on brain volume.** *Psychol Med* 2010;40:1409–02 CrossRef Medline
17. Zivadinov R. **Steroids and brain atrophy in multiple sclerosis.** *J Neurol Sci* 2005;233:73–81 CrossRef Medline
18. Paul CA, Au R, Fredman L, et al. **Association of alcohol consumption with brain volume in the Framingham study.** *Arch Neurol* 2008;65:1363–67 CrossRef Medline
19. Prust MJ, Jafari-Khouzani K, Kalpathy-Cramer J, et al. **Standard chemoradiation for glioblastoma results in progressive brain volume loss.** *Neurology* 2015;85:683–91 CrossRef Medline
20. Giedd JN, Raznahan A, Alexander-Bloch A, et al. **Child psychiatry branch of the National Institute of Mental Health longitudinal structural magnetic resonance imaging study of human brain development.** *Neuropsychopharmacology* 2015;40:43–49 CrossRef Medline
21. Matsumae M, Kikinis R, Morocz IA, et al. **Age-related changes in intracranial compartment volumes in normal adults assessed by magnetic resonance imaging.** *J Neurosurg* 1996;84:982–91 CrossRef Medline
22. Blatter DD, Bigler ED, Gale SD, et al. **Quantitative volumetric analysis of brain MR: normative database spanning 5 decades of life.** *AJNR Am J Neuroradiol* 1995;16:241–51 Medline
23. Rudick RA, Fisher E, Lee JC, et al. **Use of the brain parenchymal fraction to measure whole brain atrophy in relapsing-remitting MS: Multiple Sclerosis Collaborative Research Group.** *Neurology* 1999;53:1698–1704 CrossRef Medline
24. Fjell AM, Walhovd KB, Fennema-Notestine C, et al. **One-year brain atrophy evident in healthy aging.** *J Neurosci* 2009;29:15223–31 CrossRef Medline
25. Meyer JS, Takashima S, Terayama Y, et al. **CT changes associated with normal aging of the human brain.** *J Neurol Sci* 1994;123:200–08 CrossRef Medline
26. Stafford JL, Albert MS, Naeser MA, et al. **Age-related differences in computed tomographic scan measurements.** *Arch Neurol* 1988;45:409–15 CrossRef Medline
27. Cala LA, Thickbroom GW, Black JL, et al. **Brain density and cerebrospinal fluid space size: CT of normal volunteers.** *AJNR Am J Neuroradiol* 1981;2:41–47 Medline
28. Schwartz M, Creasey H, Grady CL, et al. **Computed tomographic analysis of brain morphometrics in 30 healthy men, aged 21 to 81 years.** *Ann Neurol* 1985;17:146–57 CrossRef Medline
29. Cauley KA, Fielden SW. **A radiodensity histogram study of the brain in multiple sclerosis.** *Tomography* 2018;4:194–203 CrossRef Medline
30. Inaba K, Teixeira PG, David JS, et al. **Computed tomographic brain density measurement as a predictor of elevated intracranial pressure in blunt head trauma.** *Am Surg* 2007;73:1023–26 Medline
31. Svennerholm L, Bostrom K, Jungbjer B. **Changes in weight and compositions of major membrane components of human brain during the span of adult human life of Swedes.** *Acta Neuropathol* 1997;94:345–52 CrossRef Medline
32. Cauley KA, Hu Y, Och J, et al. **Modeling early postnatal brain growth and development with CT: changes in the brain radiodensity histogram from birth to 2 years.** *AJNR Am J Neuroradiol* 2018;39:775–78 CrossRef Medline

Prognostic Value of Preoperative MRI Metrics for Diffuse Lower-Grade Glioma Molecular Subtypes

P. Darvishi, P.P. Batchala, J.T. Patrie, L.M. Poisson, M.-B. Lopes, R. Jain, C.E. Fadul, D. Schiff, and S.H. Patel

ABSTRACT

BACKGROUND AND PURPOSE: Despite the improved prognostic relevance of the 2016 WHO molecular-based classification of lower-grade gliomas, variability in clinical outcome persists within existing molecular subtypes. Our aim was to determine prognostically significant metrics on preoperative MR imaging for lower-grade gliomas within currently defined molecular categories.

MATERIALS AND METHODS: We undertook a retrospective analysis of 306 patients with lower-grade gliomas accrued from an institutional data base and The Cancer Genome Atlas. Two neuroradiologists in consensus analyzed preoperative MRIs of each lower-grade glioma to determine the following: tumor size, tumor location, number of involved lobes, corpus callosum involvement, hydrocephalus, midline shift, eloquent cortex involvement, ependymal extension, margins, contrast enhancement, and necrosis. Adjusted hazard ratios determined the association between MR imaging metrics and overall survival per molecular subtype, after adjustment for patient age, patient sex, World Health Organization grade, and surgical resection status.

RESULTS: For *isocitrate dehydrogenase* (*IDH*) wild-type lower-grade gliomas, tumor size (hazard ratio, 3.82; 95% CI, 1.94–7.75; $P < .001$), number of involved lobes (hazard ratio, 1.70; 95% CI, 1.28–2.27; $P < .001$), hydrocephalus (hazard ratio, 4.43; 95% CI, 1.12–17.54; $P = .034$), midline shift (hazard ratio, 1.16; 95% CI, 1.03–1.30; $P = .013$), margins ($P = .031$), and contrast enhancement (hazard ratio, 0.34; 95% CI, 0.13–0.90; $P = .030$) were associated with overall survival. For *IDH*-mutant 1p/19q-codeleted lower-grade gliomas, tumor size (hazard ratio, 2.85; 95% CI, 1.06–7.70; $P = .039$) and ependymal extension (hazard ratio, 6.34; 95% CI, 1.07–37.59; $P = .042$) were associated with overall survival.

CONCLUSIONS: MR imaging metrics offers prognostic information for patients with lower-grade gliomas within molecularly defined classes, with the greatest prognostic value for *IDH* wild-type lower-grade gliomas.

ABBREVIATIONS: LGG = lower-grade glioma; HR = hazard ratio; *IDH* = *isocitrate dehydrogenase*; *IDH*mut-Codel = *IDH* mutation and a whole-arm deletion of chromosome arms 1p and 19q; *IDH*mut-Noncodel = *IDH*-mutant lacking 1p/19q codeletion; *IDH*wild-type = *IDH* wild-type; IQR = interquartile range; OS overall survival; TCIA = The Cancer Imaging Archive; *TERT* = telomerase reverse transcriptase; WHO = World Health Organization

Recognition of the biologic and prognostic significance of molecular-based characterization of diffuse lower-grade gliomas (LGGs) heralded major revisions to their classification by the World Health Organization (WHO) in 2016.^{1–3} LGGs encompass WHO grade II and III astrocytic and oligodendroglial tumors, most of which have a prognostically favorable mutation in the *isocitrate dehydrogenase* (*IDH*) gene.^{2,4} Oligodendrogliomas are defined by the presence of both an *IDH* mutation and a whole-

arm deletion of chromosome arms 1p and 19q (*IDH*mut-Codel), which confer added prognostic and therapeutic favorability.^{5,6} *IDH*-mutant astrocytomas (*IDH*mut-Noncodel) lack 1p/19q codeletion and typically have tumor protein p53 and alpha-thalassemia/mental retardation syndrome X-linked (*ATRX* chromatin remodeler, [*ATRX*]) gene mutations.^{7,8} *IDH* wild-type LGGs (*IDH*wild-type) are generally associated with far worse clinical outcomes and largely comprise neoplasms that are genotypically similar to primary glioblastoma.^{1,9}

Despite improved clinical applicability of the revised classification system, there remains substantial heterogeneity in clinical outcomes within existing subtypes of LGGs.^{10–12} While numerous

Received November 27, 2019; accepted after revision February 29, 2020.

From the Departments of Radiology and Medical Imaging (P.D., P.P.B., S.H.P.); Public Health Sciences (J.T.P.); Pathology, Divisions of Neuropathology and Molecular Diagnostics (M.-B.L.); and Division of Neuro-Oncology (C.E.F., D.S.), University of Virginia Health System, Charlottesville, Virginia; Department of Public Health (L.M.P.), Henry Ford Health System, Detroit, Michigan; and Departments of Radiology (R.J.) and Neurosurgery (R.J.), New York University School of Medicine, New York, New York.

S.H. Patel was supported by the Radiological Society of North America Research Scholar Grant (RSCH1819).

Please address correspondence to Sohil H. Patel, MD, Department of Radiology and Medical Imaging, University of Virginia Health System, PO Box 800170, Charlottesville, VA 22908; e-mail: shp4k@virginia.edu
<http://dx.doi.org/10.3174/ajnr.A6511>

studies have reported neuroimaging features that predict currently defined glioma molecular subtypes,¹³⁻²⁰ neuroimaging features might additionally contain information that allows prognostic stratification of gliomas within currently defined molecular categories. The purpose of our investigation was to determine whether neuroimaging features on preoperative anatomic MR imaging have prognostic significance for LGGs within currently defined molecular categories.

MATERIALS AND METHODS

This was a retrospective study with institutional review board approval (University of Virginia Health System, Charlottesville, Virginia) as well as Health Insurance Portability and Accountability Act compliance.

Patient Selection

Cases were accrued from a diffuse LGG data base maintained at our institution ($n = 255$) as well as from The Cancer Imaging

Archive (TCIA) ($n = 198$).²¹ Inclusion criteria were the following: 1) known *IDH* mutation status and 1p/19q-codeletion status; 2) known surgical resection status (gross total resection, subtotal resection, or biopsy); and 3) available preoperative MR imaging including (at a minimum) precontrast T1WI, contrast-enhanced T1WI, and either T2WI or FLAIR.

From the institutional dataset, 178 cases met the inclusion criteria; 43 cases were excluded for lack of *IDH* and/or 1p/19q-codeletion status, and 34 cases were excluded for lack of requisite preoperative MR imaging. From the TCIA cohort, 128 cases met the inclusion criteria; 1 case was excluded for lack of *IDH* and 1p/19q-codeletion status and 69 cases lacked requisite preoperative MR imaging. In total, our study cohort included 306 cases. Overall survival times were available for all included patients, defined as the time between the date of pathologic diagnosis to the date of death or last contact.

Neuroimaging and Analysis

Two neuroradiologists with 6 and 14 years of experience, blinded to molecular status, WHO grade, patient demographics, and clinical outcome, analyzed the preoperative MR imaging to determine the following metrics:—1) tumor size: maximum long-axis diameter (centimeters); 2) location: any glioma signal abnormality/enhancement involving the basal ganglia, thalamus, or brain stem (yes = central; no = peripheral); 3) number (n) of involved lobes: each of the following counted as 1 lobe (per hemisphere)—frontal lobe, parietal lobe, temporal lobe, insula, occipital lobe, brain stem/cerebellum; 4) corpus callosum involvement: any glioma signal abnormality/enhancement involving the corpus callosum (yes or no); 5) hydrocephalus: (yes or no); 6) midline shift: greatest degree of contralateral brain displacement (centimeters); 7) eloquent cortex involvement: any glioma signal abnormality/enhancement involving the eloquent cortex, defined per Chang et al²² (yes or no); 8) ependymal extension: any glioma signal abnormality/enhancement involving the ventricular ependyma (yes or no); 9) margins: <33%, 33%–66%, or >66% sharp/circumscribed glioma margins; 10) contrast enhancement: any glioma contrast enhancement (yes or no); and 11) necrosis: any region of glioma necrosis characterized by peripheral contrast enhancement and central nonenhancement (yes or no).

Neuropathology

Pathologic data for patients in the institutional dataset were retrieved from the electronic medical record. Molecular markers were tested in the Clinical Laboratory Improvement Amendments–certified molecular pathology laboratory at our institution. A clinically validated *IDH1* antibody was used to determine *IDH* mutation status.^{23,24} Clinically validated pyrosequencing assays (PyroMark Q24 system; <https://www.qiagen.com/us/shop/automated-solutions/pyro-mark-q24/>) were used in immunohistochemistry-negative cases in accordance with the manufacturers to determine *IDH1/IDH2* mutation status.

Table 1: Patient characteristics for each molecular subtype

	<i>IDH</i> mut-Codel	<i>IDH</i> mut-Noncodel	<i>IDH</i> wt
Total patients ^a	104 (34.0%)	129 (42.2%)	73 (23.9%)
Female sex	58 (55.8%)	61 (47.3%)	35 (47.9%)
Age ^b	48 (17–74)	35 (17–70)	57 (19–76)
WHO grade			
II	72 (69.2%)	83 (64.3%)	34 (46.6%)
III	32 (30.8%)	46 (35.7%)	39 (53.3%)

^aData are listed as count (percentage of total cohort).

^bData are listed as median (range). Other data are listed as count (percentage of cases within given molecular subtype).

Table 2: Empiric distribution summaries for the preoperative MR imaging metrics according to LGG molecular subtype

MR Imaging Metric	<i>IDH</i> mut-Codel	<i>IDH</i> mut-Noncodel	<i>IDH</i> wt
Tumor size (cm)			
Median	6.6	6.9	6.2
IQR (1st to 3rd quartile)	(5.2–8.6)	(5.3–9.3)	(4.6–8.4)
Range (minimum–maximum)	(1.9–14.2)	(1.7–15.3)	(1.1–15.0)
Location			
Central	26 (25.0%)	43 (33.3%)	29 (39.7%)
Peripheral	78 (75.0%)	86 (66.7%)	44 (60.3%)
No. of involved lobes			
Median	2.0	2.0	2.0
IQR (1st to 3rd quartile)	(1.0–3.0)	(1.0–3.0)	(1.0–3.0)
Range (minimum–maximum)	(1.0–6.0)	(1.0–9.0)	(1.0–8.0)
Corpus callosum extension	44 (42.3%)	46 (35.7%)	18 (24.2%)
Hydrocephalus	12 (11.5%)	27 (20.9%)	7 (9.6%)
Midline shift (cm)			
Median	0.00	0.30	0.00
IQR (1st to 3rd quartile)	(0.00–0.43)	(0.00–0.80)	(0.00–0.10)
Range (minimum–maximum)	(0.00–2.70)	(0.00–1.90)	(0.00–1.40)
Eloquent cortex	33 (31.7%)	45 (34.9%)	24 (32.9%)
Ependymal extension	65 (62.5%)	80 (62.0%)	58 (79.5%)
Margin			
<33% sharp/circumscribed	32 (30.8%)	31 (24.0%)	28 (38.4%)
33%–66% sharp/circumscribed	55 (52.9%)	38 (29.5%)	31 (42.5%)
>66% sharp/circumscribed	17 (16.3%)	60 (46.5%)	14 (19.2%)
Contrast enhancement	21 (31.8%)	51 (39.5%)	30 (41.1%)
Necrosis	17 (16.3%)	14 (10.9%)	18 (24.7%)

The 1p/19q-codeletion status was determined by fluorescence in situ hybridization; dual-color human probes localizing the 1p, 1q, 19p, and 19q loci were used (Vysis LSI 1p36/1q25 and LSI 19q13/

19p13 FISH Probe Kit; Abbott Laboratories, Abbott Park, IL). Histopathologic and molecular data for the TCIA cohort were retrieved from supplemental material in Ceccarelli et al.²⁵

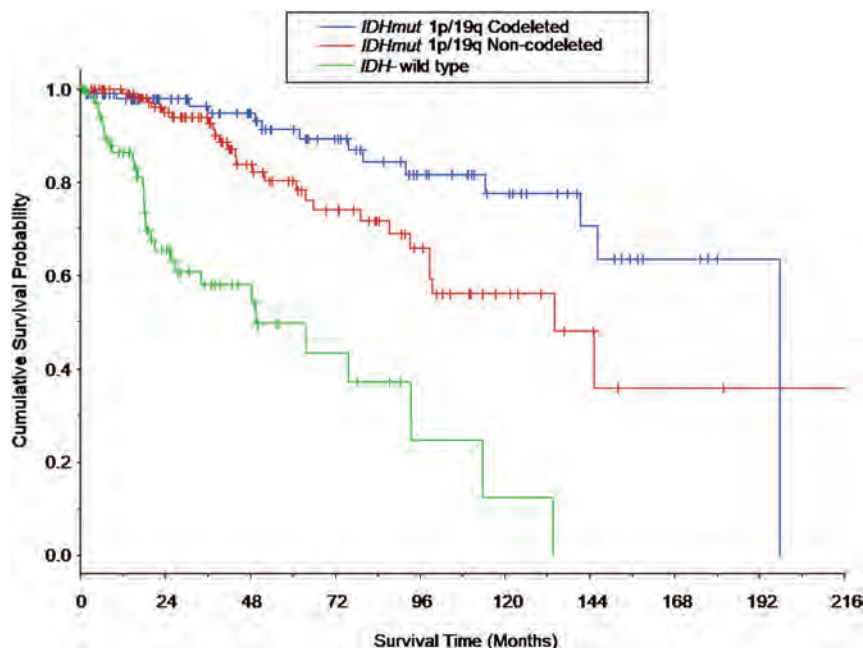


FIG 1. Kaplan-Meier survival curves based on the LGG molecular subtype. Vertical tick marks identify right-censored survival times. The survival curves differed among all 3 LGG molecular subtypes (*IDH*-mutant 1p/19q-codeleted molecular subtype versus *IDH*-mutant 1p/19q-noncodeleted molecular subtype: $P = .021$; *IDH*-mutant 1p/19q-codeleted molecular subtype versus *IDH* wild-type molecular subtype: $P < .001$; and *IDH*-mutant 1p/19q-noncodeleted molecular subtype versus *IDH*-wild type molecular subtype: $P < .001$). Survival curves for patients who composed a subset of the current patient cohort are shown in Patel et al,⁴⁶ in 2019.

Statistical Analysis

Data Summarization. Categorical variables are summarized by frequencies and percentages, and continuous scaled data are summarized by the median, the interquartile range (IQR), and the range of the empiric distribution.

Survival Analyses. Cox proportional hazards regression was used to examine the prognostic utility of the preoperative MR imaging metrics to predict survival within the currently defined molecular categories of LGGs. The survival analyses were conducted per molecular category (ie, *IDH*mut-Codel, *IDH*mut-NonCodel, and *IDH*wt) and per MR imaging metrics. For each MR imaging metric, a multivariate Cox proportional hazards regression analysis was conducted in which the MR imaging metric of interest served as the primary predictor variable and patient age, patient sex, WHO grade, and surgical resection status served as concomitant adjustment variables. The follow-up times of survivors were treated as right-censored survival times in the Cox model. With

Table 3: Associations between preoperative MR imaging metrics and overall survival per LGG molecular subtype, after adjustment for patient age, sex, tumor grade, and surgical resection status^a

Relative Comparison (Non-Reference:Reference) ^b	<i>IDH</i> mut-Codel	<i>IDH</i> mut-Noncodel	<i>IDH</i> wt
Tumor size (3rd to 1st quartile)	2.85 (1.06–7.70) ($P = .039$)	2.90 (1.54–5.48) ($P < .001$)	3.82 (1.94–7.75) ($P < .001$)
Location (central:peripheral)	0.59 (0.16–2.18) ($P = .430$)	0.50 (0.22–1.17) ($P = .101$)	0.78 (0.36–1.70) ($P = .534$)
No. of involved lobes ($X + 1:X$)	1.37 (0.84–2.23) ($P = .211$)	1.25 (0.99–1.58) ($P = .065$)	1.70 (1.28–2.27) ($P = .001$)
Corpus callosum extension (yes:no)	2.60 (0.69–9.84) ($P = .160$)	1.42 (0.59–3.41) ($P = .433$)	1.89 (0.78–4.58) ($P = .160$)
Hydrocephalus (yes:no)	2.57 (0.42–15.81) ($P = .308$)	0.63 (0.19–2.11) ($P = .457$)	4.43 (1.12–17.54) ($P = .034$)
Midline shift (3rd to 1st quartile)	1.32 (0.77–2.26) ($P = .320$)	1.14 (0.54–2.41) ($P = .730$)	1.16 (1.03–1.30) ($P = .013$)
Eloquent cortex (yes:no)	1.00 (0.29–3.43) ($P = .740$)	1.91 (0.77–4.78) ($P = .165$)	2.01 (0.90–4.49) ($P = .087$)
Ependymal extension (yes:no)	6.34 (1.07–37.59) ($P = .042$)	1.72 (0.64–4.64) ($P = .289$)	1.51 (0.52–4.35) ($P = .447$)
Margins (global test P value) ^c	($P = .775$)	($P = .190$)	($P = .031$)
33%–66%:<33% ^d	1.57 (0.42–5.97) ($P = .505$)	0.51 (0.19–1.33) ($P = .166$)	0.39 (0.17–0.90) ($P = .027$)
>66%:<33% ^d	0.98 (0.09–10.85) ($P = .985$)	0.39 (0.13–1.19) ($P = .098$)	0.24 (0.06–1.05) ($P = .057$)
>66%:33%–66% ^d	0.62 (0.06–6.40) ($P = .688$)	0.77 (0.24–2.38) ($P = .646$)	0.63 (0.14–2.87) ($P = .554$)
Contrast enhancement (yes:no)	3.11 (0.71–13.68) ($P = .132$)	1.67 (0.62–4.51) ($P = .313$)	0.34 (0.13–0.90) ($P = .030$)
Necrosis (yes:no)	1.84 (0.32–10.78) ($P = .498$)	0.28 (0.03–2.42) ($P = .247$)	1.93 (0.82–4.58) ($P = .134$)

^a Data are listed as adjusted hazard ratios (95% confidence interval) and corresponding P values.

^b Relative comparison (nonreference:reference) identifies the nonreference predictor variable value/level and the reference predictor variable value/level at which the adjusted instantaneous risk of death ratio (ie, hazard ratio) was evaluated. For example (3rd:1st quartile) represents a comparison of the adjusted instantaneous risk of death (ie, hazard) between 2 patients, 1 patient whose predictor variable value is at the 3rd quartile of the predictor variable empiric distribution (nonreference) and 1 patient whose predictor variable value is at the 1st quartile of the predictor variable empiric distribution (reference). A relative comparison denoted as ($X + 1:1$) represents a comparison of the adjusted instantaneous risk of death (ie, hazard) between 2 patients, 1 patient whose predictor variable value is $X + 1$ units (nonreference) and 1 patient whose predictor variable value is X units (reference). A relative comparison, denoted as (yes:no), represents a comparison of the adjusted instantaneous risk of death (ie, hazard) between 2 patients, 1 patient who has the factor of interest (nonreference = yes) and 1 patient who does not have the factor of interest (reference = no). Note, if the adjusted hazard ratio is >1 (<1), it indicates that the estimate for the instantaneous risk of death is greater (less) for the patient who has the nonreference predictor value/level.

^c Global test P value is the P value for testing the null hypothesis that the instantaneous risk of death is same for all “margin” categories.

^d Percentage of LGGs displaying sharp/circumscribed margin.

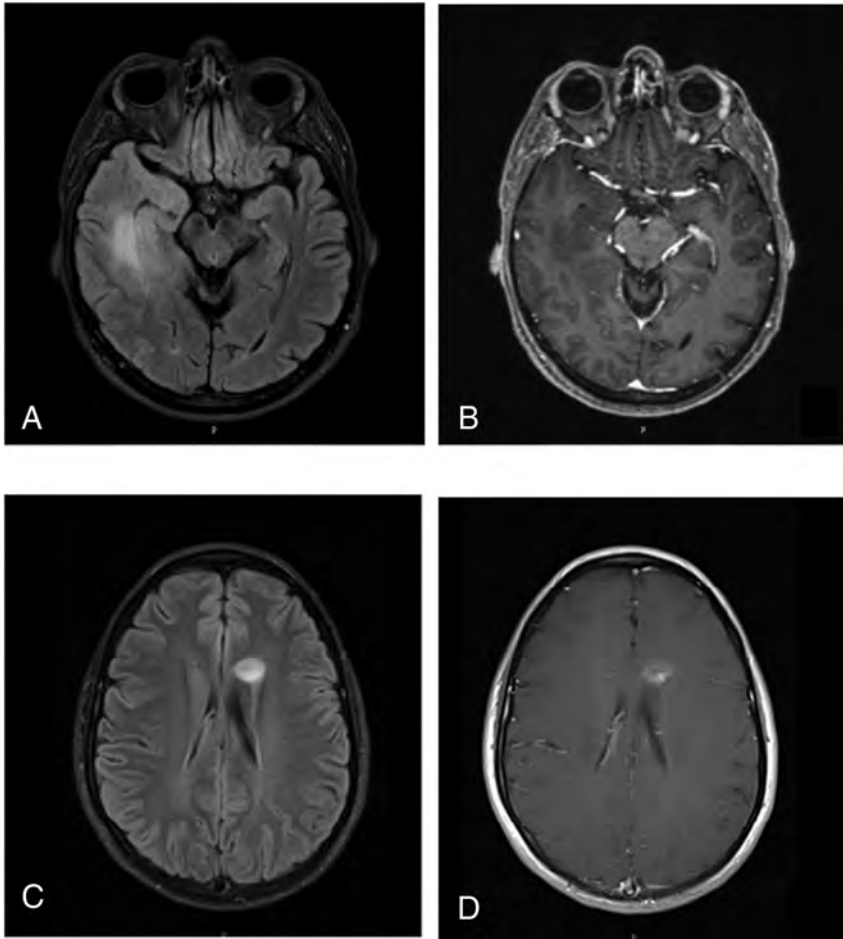


FIG 2. Representative cases of *IDHwt* LGGs. A 51-year-old man with an *IDH* wild-type diffuse astrocytoma. FLAIR (A) shows a 6-cm mass in the right temporal lobe with ill-defined margins. Contrast-enhanced T1WI (B) shows no contrast enhancement of the mass. This patient is deceased, with a survival time of 262 days. Further molecular testing in this case was positive for *TERT* promoter (−124 C > T) mutation. A 26-year-old woman with an *IDH* wild-type diffuse astrocytoma. FLAIR (C) and contrast-enhanced T1WI (D) show a 1.6-cm left frontal lobe mass with fairly well-circumscribed margins and contrast enhancement. This patient was alive at last follow-up, with a survival time of 2757 days. Further molecular testing in this case was positive for the *BRAF* V600E mutation.

regard to hypothesis testing, the Wald χ^2 test was used to test the null hypothesis that the instantaneous risk of death (ie, hazard) is not associated with the values/categories of the MR imaging metric of interest after adjustment for patient age, patient sex, WHO grade, and surgical resection status. A $P \leq .05$ decision rule was used as the null hypothesis rejection criterion for the tests of association.

Tumor Grade Analyses. MR imaging metrics versus WHO grade association were examined via multivariate logistic regression, per LGG molecular subtype. The dependent variable of the multivariate logistic regression model was an indicator variable (Y) that distinguished WHO grade III tumors ($Y = 1$) from WHO grade II tumors ($Y = 0$), and the MR imaging metrics served as the predictor variables. Regarding hypothesis testing, the type III Wald χ^2 test was used to test the null hypothesis that the adjusted odds for a tumor being WHO grade III are not associated with

the MR imaging metric. A $P \leq .05$ decision rule was used as the null hypothesis rejection criterion.

RESULTS

The study population included 306 patients, with 154 women (50.3%) and 152 men (49.7%). Patient characteristics per LGG molecular subtype are shown in Table 1, and preoperative MR imaging metric empiric distribution summaries per LGG molecular subtype are shown in Table 2.

Survival curves for overall survival (OS) are shown in Fig 1 for the LGG molecular subtypes. OS differed among all the LGG molecular subtypes ($P < .022$ for all comparisons), with patients with *IDHwt* LGGs having the shortest median OS (49.5 months; 95% CI lower bound, 25.5 months), followed by the patients with *IDHmut*-Noncodel (134.6 months; 95% CI lower bound, 98.7 months), and patients with *IDHmut*-Codel (196.6 months, 95% CI lower bound, 141.4 months).

The associations between preoperative MR imaging metrics and OS per LGG molecular subtype are expressed as hazard ratios (HRs) in Table 3, after adjustment for patient age, patient sex, tumor grade, and surgical resection status. For *IDHwt* LGGs, greater tumor size (HR, 3.82; 95% CI, 1.94–7.75; $P < .001$), greater number of involved lobes (HR, 1.70; 95% CI, 1.28–2.27; $P < .001$), hydrocephalus (HR, 4.43; 95% CI, 1.12–17.54; $P = .034$), greater degree of midline shift (HR, 1.16; 95% CI, 1.03–1.30; $P = .013$), and less circumscribed margins ($P = .031$) were associated with shorter OS, whereas the presence of contrast enhancement (HR, 0.34; 95% CI, 0.13–0.90; $P = .030$) was associated with longer OS (Fig 2). For *IDHmut*-Noncodel LGGs, greater tumor size (HR, 2.90; 95% CI, 1.54–5.48; $P = .001$) was associated with shorter OS. For *IDHmut*-Codel LGGs, greater tumor size (HR, 2.85; 95% CI, 1.06–7.70; $P = .039$) and ependymal extension (HR, 6.34; 95% CI, 1.07–37.59; $P = .042$) were associated with shorter OS.

A secondary analysis determined unique associations between MR imaging metrics and tumor grade (II or III) per LGG molecular subtype (Table 4). Contrast enhancement was associated with grade III for both *IDHwt* LGGs (OR, 16.75; 95% CI, 3.47–80.86; $P < .001$) and *IDHmut*-Noncodel LGGs (OR, 6.08; 95% CI, 2.12–17.41; $P = .001$), but not for *IDHmut*-Codel LGGs. For *IDHwt* LGGs, ependymal extension was associated with grade II (OR, 0.09; 95% CI, 0.01–0.59; $P = .012$), and for *IDHmut*-Noncodel LGGs, central

Table 4: Associations between preoperative MR imaging metrics and WHO grade III per molecular subtype^a

Relative Comparison (Non-Reference:Reference) ^b	IDHmut-Codel	IDHmut-Noncodel	IDHwt
Tumor size (3rd to 1st quartile)	0.97 (0.18–5.26) (<i>P</i> = .975)	1.24 (0.34–4.57) (<i>P</i> = .742)	1.60 (0.31–8.17) (<i>P</i> = .573)
Location (central:peripheral)	1.55 (0.22–10.49) (<i>P</i> = .654)	0.21 (0.05–0.80) (<i>P</i> = .035)	0.42 (0.10–1.84) (<i>P</i> = .252)
No. of involved lobes (X + 1:X)	1.45 (0.64–3.30) (<i>P</i> = .370)	1.12 (0.65–1.94) (<i>P</i> = .673)	0.96 (0.48–1.92) (<i>P</i> = .906)
Corpus callosum extension (yes:no)	1.88 (0.39–9.05) (<i>P</i> = .430)	2.51 (0.72–8.76) (<i>P</i> = .149)	1.46 (0.25–8.35) (<i>P</i> = .672)
Hydrocephalus (yes:no)	8.55 (0.33–223.32) (<i>P</i> = .197)	2.07 (0.50–8.54) (<i>P</i> = .313)	0.26 (0.01–5.09) (<i>P</i> = .372)
Midline shift (3rd to 1st quartile)	0.88 (0.37–2.10) (<i>P</i> = .774)	0.55 (0.16–1.85) (<i>P</i> = .331)	1.31 (0.91–1.89) (<i>P</i> = .148)
Eloquent cortex (yes:no)	1.71 (0.49–5.99) (<i>P</i> = .402)	1.87 (0.69–5.09) (<i>P</i> = .220)	0.35 (0.08–1.54) (<i>P</i> = .165)
Ependymal extension (yes:no)	1.68 (0.28–10.07) (<i>P</i> = .570)	0.65 (0.15–2.86) (<i>P</i> = .571)	0.09 (0.01–0.59) (<i>P</i> = .012)
Margins (global test) ^c	<i>P</i> = .970	<i>P</i> = .360	<i>P</i> = .221
33%–66%:<33% ^d	1.20 (0.28–5.23) (<i>P</i> = .804)	1.47 (0.37–5.79) (<i>P</i> = .583)	1.62 (0.24–10.84) (<i>P</i> = .619)
>66%:<33% ^d	1.16 (0.15–9.17) (<i>P</i> = .888)	0.64 (0.12–3.56) (<i>P</i> = .614)	0.27 (0.02–3.35) (<i>P</i> = .305)
>66%:33%–66% ^d	0.96 (0.17–5.56) (<i>P</i> = .967)	0.44 (0.13–1.42) (<i>P</i> = .170)	0.16 (0.02–1.28) (<i>P</i> = .084)
Contrast enhancement (yes:no)	1.73 (0.47–6.43) (<i>P</i> = .411)	6.08 (2.12–17.41) (<i>P</i> = .001)	16.75 (3.47–80.86) (<i>P</i> < .001)
Necrosis (yes:no)	9.68 (0.83–112.49) (<i>P</i> = .070)	0.61 (0.08–4.67) (<i>P</i> = .632)	0.67 (0.13–3.36) (<i>P</i> = .630)

^a Note that for the multivariate logistic regression analysis, WHO grade III tumors were assigned the value 1 and WHO grade II tumors were assigned the value 0. Data are listed as adjusted odds ratios, (95% confidence interval) and corresponding *P* value determined by a Wald type III χ^2 test.

^b Relative comparison (nonreference:reference) identifies the nonreference predictor variable value/level and the reference predictor variable value/level at which the adjusted odds ratio was evaluated. For example (3rd:1st Quartile) represents a comparison of the adjusted odds for tumor grade III between 2 patients, 1 patient whose predictor variable value is at the 3rd quartile of the predictor variable empiric distribution (nonreference) and 1 patient whose predictor variable value is at the 1st quartile of the predictor variable empiric distribution (reference). A relative comparison denoted as (X + 1:X) represents a comparison of the adjusted odds for tumor grade III between 2 patients, 1 patient whose predictor variable value equals X + 1 (nonreference) and 1 patient whose predictor variable value equals X (reference). A relative comparison denoted as (yes:no) represents a comparison of the adjusted odds for a tumor grade III between 2 patients, 1 patient who has the factor of interest (nonreference = yes) and 1 patient who does not have the factor of interest (reference = no). Note, if the adjusted odds ratio is >1 (<1), it indicates that the estimate for the adjusted odds for a tumor grade III is greater (less) for the patient who has the nonreference predictor value/level.

^c Global test *P* value is the *P* value for testing the null hypothesis that the adjusted odds ratio is same for all “margin” categories.

^d Percentage of LGG displaying sharp/circumscribed margin.

location was associated with grade II (OR, 0.21; 95% CI, 0.05–0.80; *P* = .035).

DISCUSSION

Despite the markedly improved prognostic relevance of the 2016 WHO classification of LGGs, clinical outcome variability persists for LGGs within existing molecular subtypes.^{26–29} For each LGG molecular subtype, we separately explored the association between preoperative MR imaging metrics and patient OS after adjustment for WHO grade, surgical resection status, patient age, and patient sex. We further explored the relationship between MR imaging metrics and tumor grade separately for each LGG subtype. Among our results, we found that preoperative MR imaging features have more prognostic value for IDHwt LGGs than for IDH-mutant LGGs. Tumor size is significantly associated with OS in all LGG molecular subtypes, and MR imaging associations with tumor grade vary among LGG molecular subtypes.

Our finding that preoperative MR imaging has the greatest prognostic value for the IDHwt subtype is potentially explained by the increasingly well-recognized biologic and clinical heterogeneity of IDHwt LGGs, in particular based on molecular alterations such as telomerase reverse transcriptase (*TERT*) promoter mutation (Fig 2A, -B), *epidermal growth factor receptor (EGFR)* gene amplification, and chromosome 7/10 alterations.^{12,26,27,30} These molecular alterations have not yet been formally incorporated into the WHO classification scheme, and it is conceivable that some of our neuroimaging metrics correlated with these prognostically significant molecular alterations among our IDHwt cohort. We further speculate that our apparently counter-intuitive finding of a positive correlation between contrast enhancement and survival time for the IDHwt cohort could be explained by the potential inclusion of *B-raf proto-oncogene*

(*BRAF*)-mutant IDHwt gliomas in our cohort (Fig 2C, -D). *BRAF*-mutant diffuse gliomas commonly demonstrate contrast enhancement and are associated with favorable clinical outcomes.^{31–33}

On the other hand, we found relatively few significant associations with overall survival for the IDH-mutant LGG subtypes. These results might reflect that the IDH-mutant LGG subtypes represent more uniform genomic entities compared with the IDHwt subtype. Nonetheless, for both IDHmut-Noncodel and IDHmut-Codel subtypes, larger tumor size was associated with worse OS. Moreover, we found that ependymal extension is associated with worse OS for the IDHmut-Codel subtype. It is known that subventricular zone extension by glioblastoma portends a worse prognosis, possibly due to recruitment of migratory progenitor cells in this location.³⁴ It is unclear whether a similar process contributes to a more aggressive clinical course among the IDHmut-Codel LGGs, and further investigation into the impact of ependymal extension in the IDHmut-Codel subtype could build on our results.

To our knowledge, the literature investigating prognostically relevant imaging metrics in molecularly defined LGG subtypes is sparse. Perhaps the most applicable study is by Wu et al,³⁵ in 2019, who found that tumor size and elevated relative cerebral blood volume on preoperative imaging correlate with a more aggressive subtype of IDHmut-Noncodel gliomas. While our results support these findings in regard to tumor size, we observed a similar relationship for IDHmut-Codel and IDHwt subgroups as well. Small sample size and lack of adjustment for WHO grade by Wu et al are limitations that may have contributed to differences observed between our studies. Suchorska et al,³⁶ in 2019, found that contrast enhancement is a viable prognostic metric for IDH-mutant subgroups, a finding that was not reproduced in our study. Finally, the apparent diffusion

coefficient has been reported as a potential prognostic marker for *IDHwt* LGGs.³⁷

Multiple prior studies have investigated imaging findings that correlate with WHO grade.^{38–42} However, to the best of our knowledge, we are the first to report the relationship between neuroimaging metrics and WHO grade separately for each LGG molecular subtype. Our results indicate that contrast enhancement predicts WHO grade III for the *IDHmut-Noncodel* and *IDHwt* LGGs, but not for *IDHmut-Codel* LGGs. A previous study of oligodendrogliomas by White et al,⁴³ in 2005, also reported no association between contrast enhancement and WHO grade; however, 1p/19q testing was not undertaken in their study, and their cohort was small ($n = 24$). Our results strengthen this conclusion and may serve to modify the well-established dictum that contrast enhancement correlates with tumor grade in adult diffuse gliomas.^{44,45}

While efforts to identify preoperative neuroimaging predictors of LGG molecular status are valuable, the clinical utility is frequently limited because nearly all such cases undergo biopsy or resection for a definitive pathologic diagnosis. Our investigation aimed to uncover simple neuroimaging metrics that could relay prognostic information for LGGs beyond what can be inferred from their molecular and histologic characterization. An added strength of our study design was the adjustment of our analysis for both tumor grade and surgical resection status. The extent of surgical resection in particular is well-recognized for its impact on the overall survival of a patient with LGG.^{46,47}

Nonetheless, our study has limitations. This is a retrospective study and thus inherently limited by design in its ability to infer relationships beyond association. Further prospective multi-institutional investigations would be necessary to confirm our results. Another potential limitation is the binary method of analysis for several metrics (eg, yes or no contrast enhancement). While this method was chosen to reduce ambiguity in the data acquisition and maintain a simple set of imaging metrics, a more graded approach to measurement may allow a more nuanced and potentially revealing analysis. Similarly, we measured “tumor size” as a single long-axis diameter, and volumetric measurements based on 3D MR imaging acquisitions would be preferable. Furthermore, we investigated a limited set of MR imaging pulse sequences (pre-contrast T1WI, contrast-enhanced T1WI, and either T2WI or FLAIR), and additional study into the prognostic value of more advanced techniques (eg, perfusion-weighted imaging, diffusion tensor imaging, susceptibility-weighted imaging) might be fruitful. We did not adjust our analysis for nonsurgical treatment (eg, chemotherapy and radiation therapy), which presumably varied across our cohort. Finally, future investigations evaluating links between MR imaging metrics and molecular alterations pertinent to *IDHwt* LGGs, such as *BRAF* or *TERT* mutations, would be highly valuable.

CONCLUSIONS

Preoperative MR imaging metrics offer prognostic information for patients with LGG within molecularly defined classes. Multiple neuroimaging features had unique prognostic significance for the *IDHwt* subtype, including hydrocephalus, midline

shift, margin features, and contrast enhancement, likely reflecting the known biologic and clinical heterogeneity of *IDHwt* LGGs. Contrast enhancement was associated with WHO grade III among *IDHwt* and *IDHmut-Noncodel* LGGs, but not *IDHmut-Codel* LGGs.

Disclosures: Laila M. Poisson—UNRELATED: Grants/Grants Pending: National Cancer Institute, Comments: R01CA222146.* Maria-Beatriz Lopes—UNRELATED: Grants/Grants Pending: Focus Ultrasound Foundation*; Royalties: Elsevier, Comments: textbook chapter. Rajan Jain—UNRELATED: Consultancy: Cancer Panels; Royalties: Thieme. Camilo E. Fadul—UNRELATED: Grants/Grants Pending: Novartis.* David Schiff—UNRELATED: Board Membership: Orbus Therapeutics, Comments: Data and Safety Monitoring Committee Chair for clinical trial; Royalties: UpToDate. Sohil H. Patel—RELATED: Grant: Radiological Society of North America Scholar Grant, Comments: RSCH1819.* *Money paid to the institution.

REFERENCES

1. Brat DJ, Verhaak RG, Aldape KD, et al; Cancer Genome Atlas Research Network. **Comprehensive, integrative genomic analysis of diffuse lower-grade gliomas.** *N Engl J Med* 2015;372:2481–98 CrossRef Medline
2. Eckel-Passow JE, Lachance DH, Molinaro AM, et al. **Glioma groups based on 1p/19q, IDH, and TERT promoter mutations in tumors.** *N Engl J Med* 2015;372:2499–2508 CrossRef Medline
3. Louis DN, Perry A, Reifenberger G, et al. **The 2016 World Health Organization classification of tumors of the central nervous system: a summary.** *Acta Neuropathol* 2016;131:803–20 CrossRef Medline
4. Yan H, Parsons DW, Jin G, et al. **IDH1 and IDH2 mutations in gliomas.** *N Engl J Med* 2009;360:765–73 CrossRef Medline
5. Chamberlain MC, Born D. **Prognostic significance of relative 1p/19q codeletion in oligodendroglial tumors.** *J Neurooncol* 2015;125:249–51 CrossRef Medline
6. Aldape K, Burger PC, Perry A. **Clinicopathologic aspects of 1p/19q loss and the diagnosis of oligodendroglioma.** *Arch Pathol Lab Med* 2007;131:242–51 Medline
7. Liu X, Gerges N, Korshunov A, et al. **Frequent ATRX mutations and loss of expression in adult diffuse astrocytic tumors carrying IDH1/IDH2 and TP53 mutations.** *Acta Neuropathol* 2012;124:615–25 CrossRef Medline
8. Kannan K, Inagaki A, Silber J, et al. **Whole-exome sequencing identifies ATRX mutation as a key molecular determinant in lower-grade glioma.** *Oncotarget* 2012;3:1194–1203 CrossRef Medline
9. Reuss DE, Kratz A, Sahm F, et al. **Adult IDH wild type astrocytomas biologically and clinically resolve into other tumor entities.** *Acta Neuropathol* 2015;130:407–17 CrossRef Medline
10. Gleize V, Alentorn A, Connen de Kérillis L, et al; POLA network. **CIC inactivating mutations identify aggressive subset of 1p19q codeleted gliomas.** *Ann Neurol* 2015;78:355–74 CrossRef Medline
11. Reis GF, Pekmezci M, Hansen HM, et al. **CDKN2A loss is associated with shortened overall survival in lower-grade (World Health Organization grades II-III) astrocytomas.** *J Neuropathol Exp Neurol* 2015;74:442–42 CrossRef Medline
12. Aibaidula A, Chan AK, Shi Z, et al. **Adult IDH wild-type lower-grade gliomas should be further stratified.** *Neuro Oncol* 2017;19:1327–37 CrossRef Medline
13. Park YW, Han K, Ahn SS, et al. **Prediction of IDH1-mutation and 1p/19q-codeletion status using preoperative MR imaging phenotypes in lower grade gliomas.** *AJNR Am J Neuroradiol* 2018;39:37–42 CrossRef Medline
14. Lasocki A, Gaillard F, Gorelik A, et al. **MRI features can predict 1p/19q status in intracranial gliomas.** *AJNR Am J Neuroradiol* 2018;39:687–92 CrossRef Medline
15. Smits M, van den Bent MJ. **Imaging correlates of adult glioma genotypes.** *Radiology* 2017;284:316–31 CrossRef Medline

16. Jenkinson MD, Du Plessis DG, Smith TS, et al. **Histological growth patterns and genotype in oligodendroglial tumours: correlation with MRI features.** *Brain* 2006;129:1884–91 CrossRef Medline
17. Megyesi JF, Kachur E, Lee DH, et al. **Imaging correlates of molecular signatures in oligodendrogliomas.** *Clin Cancer Res* 2004;10:4303–06 CrossRef Medline
18. Patel SH, Poisson LM, Brat DJ, et al. **T2–FLAIR mismatch, an imaging biomarker for IDH and 1p/19q status in lower-grade gliomas: a TCGA/TCIA project.** *Clin Cancer Res* 2017;23:6078–85 CrossRef Medline
19. Batchala PP, Muttikkal TJ, Donahue JH, et al. **Neuroimaging-based classification algorithm for predicting 1p/19q-codeletion status in IDH-mutant lower grade gliomas.** *AJNR Am J Neuroradiol* 2019;40:426–32 CrossRef Medline
20. Aliotta E, Nourzadeh H, Batchala P, et al. **Molecular subtype classification in lower-grade glioma with accelerated DTI.** *AJNR Am J Neuroradiol* 2019;40:1458–63 CrossRef Medline
21. Radiology Data from The Cancer Genome Atlas Low Grade Glioma [TCGA-LGG] collection. *The Cancer Imaging Archive*. <https://www.cancerimagingarchive.net>. Accessed April 11, 2019
22. Chang EF, Smith JS, Chang SM, et al. **Preoperative prognostic classification system for hemispheric low-grade gliomas in adults.** *J Neurosurg* 2008;109:817–24 CrossRef Medline
23. Capper D, Weissert S, Balsl J, et al. **Characterization of R132H mutation-specific IDH1 antibody binding in brain tumors.** *Brain Pathol* 2010;20:245–54 CrossRef Medline
24. Capper D, Zentgraf H, Balsl J, et al. **Monoclonal antibody specific for IDH1 R132H mutation.** *Acta Neuropathol* 2009;118:599–601 CrossRef Medline
25. Ceccarelli M, Barthel FP, Malta TM, et al; TCGA Research Network. **Molecular profiling reveals biologically discrete subsets and pathways of progression in diffuse glioma.** *Cell* 2016;164:550–63 CrossRef Medline
26. Di Carlo DT, Duffau H, Cagnazzo F, et al. **IDH wild-type WHO grade II diffuse low-grade gliomas: a heterogeneous family with different outcomes—systematic review and meta-analysis.** *Neurosurg Rev* 2018 Jun 26. [Epub ahead of print] CrossRef Medline
27. Poulen G, Goze C, Rigau V, et al. **Huge heterogeneity in survival in a subset of adult patients with resected, wild-type isocitrate dehydrogenase status, WHO grade II astrocytomas.** *J Neurosurg* 2018 Apr 20. [Epub ahead of print] CrossRef Medline
28. Wijnenga M, French PJ, Dubbink HJ, et al. **Prognostic relevance of mutations and copy number alterations assessed with targeted next generation sequencing in IDH mutant grade II glioma.** *J Neurooncol* 2018;139:349–57 CrossRef Medline
29. Wijnenga MM, Dubbink HJ, French PJ, et al. **Molecular and clinical heterogeneity of adult diffuse low-grade IDH wild-type gliomas: assessment of TERT promoter mutation and chromosome 7 and 10 copy number status allows superior prognostic stratification.** *Acta Neuropathol* 2017;134:957–59 CrossRef Medline
30. Brat DJ, Aldape K, Colman H, et al. **cIMPACT-NOW update 3: recommended diagnostic criteria for “Diffuse astrocytic glioma, IDH-wildtype, with molecular features of glioblastoma, WHO grade IV.”** *Acta Neuropathol* 2018;136:805–10 CrossRef Medline
31. Chi AS, Batchelor T, Yang D, et al. **BRAF V600E mutation identifies a subset of low-grade diffusely infiltrating gliomas in adults.** *J Clin Oncol* 2013;31:e233–36 CrossRef Medline
32. Chan AY, Zhang RQ, Aibaidula A, et al. **BRAF mutation marks out specific subgroups of glioma.** *Glioma* 2018;1:168 CrossRef
33. Aibaidula A, Chan AK, Shi Z, et al. **Adult IDH wild-type lower-grade gliomas should be further stratified.** *Neuro-Oncology* 2017;19:1327–37 CrossRef Medline
34. Jafri NF, Clarke JL, Weinberg V, et al. **Relationship of glioblastoma multiforme to the subventricular zone is associated with survival.** *Neuro-Oncology* 2013;15:91–96 CrossRef Medline
35. Wu CC, Jain R, Neto L, et al. **MR imaging phenotype correlates with extent of genome-wide copy number abundance in IDH mutant gliomas.** *Neuroradiology* 2019;61:1023–31 CrossRef Medline
36. Suchorska B, Schüller U, Biczok A, et al. **Contrast enhancement is a prognostic factor in IDH1/2 mutant, but not in wild-type WHO grade II/III glioma as confirmed by machine learning.** *Eur J Cancer* 2019;107:15–27 CrossRef Medline
37. Wu C, Jain R, Radmanesh A, et al. **Predicting genotype and survival in glioma using standard clinical MR imaging apparent diffusion coefficient images: a pilot study from the Cancer Genome Atlas.** *AJNR Am J Neuroradiol* 2018;39:1814–20 CrossRef Medline
38. Hakyemez B, Erdogan C, Ercan I, et al. **High-grade and low-grade gliomas: differentiation by using perfusion MR imaging.** *Clin Radiol* 2005;60:493–502 CrossRef Medline
39. Komatsu K, Wanibuchi M, Mikami T, et al. **Arterial spin labeling method as a supplemental predictor to distinguish between high- and low-grade gliomas.** *World Neurosurg* 2018;114:e495–500 CrossRef Medline
40. Togao O, Hiwatashi A, Yamashita K, et al. **Differentiation of high-grade and low-grade diffuse gliomas by intravoxel incoherent motion MR imaging.** *Neuro-Oncology* 2016;18:132–41 CrossRef Medline
41. Leu K, Ott GA, Lai A, et al. **Perfusion and diffusion MRI signatures in histologic and genetic subtypes of WHO grade II–III diffuse gliomas.** *J Neurooncol* 2017;134:177–88 CrossRef Medline
42. Delgado AF, Delgado AF. **Discrimination between glioma grades II and III using dynamic susceptibility perfusion MRI: a meta-analysis.** *AJNR Am J Neuroradiol* 2017;38:1348–55 CrossRef Medline
43. White M, Zhang Y, Kirby P, et al. **Can tumor contrast enhancement be used as a criterion for differentiating tumor grades of oligodendrogliomas?** *AJNR Am J Neuroradiol* 2005;26:784–90
44. Smirniotopoulos JG, Murphy FM, Rushing EJ, et al. **Patterns of contrast enhancement in the brain and meninges.** *Radiographics* 2007;27:525–51 CrossRef Medline
45. Young GS. **Advanced MRI of adult brain tumors.** *Neurol Clin* 2007;25:947–73 CrossRef Medline
46. Patel SH, Bansal AG, Young EB, et al. **Extent of surgical resection in lower-grade glioma: differential impact based on molecular subtype.** *AJNR Am J Neuroradiol* 2019;40:1149–55 CrossRef Medline
47. Wijnenga MM, French PJ, Dubbink HJ, et al. **The impact of surgery in molecularly defined low-grade glioma: an integrated clinical, radiological, and molecular analysis.** *Neuro Oncol* 2018;20:103–12 CrossRef Medline

A Critical Assessment of the Golden Hour and the Impact of Procedural Timing in Stroke Thrombectomy

 A.P. Wessell,  H.D.P. Carvalho,  E. Le,  G. Cannarsa,  M.J. Kole,  J.A. Stokum,  T. Chryssikos,  T.R. Miller,  S. Chaturvedi,  D. Gandhi,  K. Yarbrough,  S.R. Satti, and  G. Jindal



ABSTRACT

BACKGROUND AND PURPOSE: Previous studies in acute ischemic stroke have demonstrated the importance of minimizing delays to endovascular treatment and keeping thrombectomy procedural times at <30–60 minutes. The purpose of this study was to investigate the impact of thrombectomy procedural times on clinical outcomes.

MATERIALS AND METHODS: We retrospectively compared 319 patients having undergone thrombectomy according to procedural time (<30 minutes, 30–60 minutes, and >60 minutes) and time from stroke onset to endovascular therapy (≤ 6 or >6 hours). Clinical characteristics of patients with postprocedural intracranial hemorrhage were also assessed. Logistic regression was used to determine independent predictors of poor outcome at 90 days (mRS ≥ 3).

RESULTS: Greater age (OR, 1.03; 95% CI, 1.01–1.06; $P = .016$), higher admission NIHSS score (OR, 1.10; 95% CI, 1.04–1.16; $P = .001$), history of diabetes mellitus (OR, 1.96; 95% CI, 1.05–3.65; $P = .034$), and postprocedural intracranial hemorrhage were independently associated with greater odds of poor outcome. Modified TICI scale scores of 2c (OR, 0.11; 95% CI, 0.04–0.28; $P < .001$) and 3 (OR, 0.15; 95% CI, 0.06–0.38; $P < .001$) were associated with reduced odds of poor outcome. Although not statistically significant on univariate analysis, onset to endovascular therapy of >6 hours was independently associated with increased odds of poor outcome (OR, 2.20; 95% CI, 1.11–4.36; $P = .024$) in the final multivariate model (area under the curve = 0.820). Procedural time was not independently associated with clinical outcome in the final multivariate model ($P > .05$).

CONCLUSIONS: Thrombectomy procedural times beyond 60 minutes are associated with lower revascularization rates and worse 90-day outcomes. Procedural time itself was not an independent predictor of outcome. While stroke thrombectomy procedures should be performed rapidly, our study emphasizes the significance of achieving revascularization despite the requisite procedural time. However, the potential for revascularization must be weighed against the risks associated with multiple thrombectomy attempts.

ABBREVIATIONS: ICH = intracranial hemorrhage; mTICI = modified TICI; OTE = onset to endovascular therapy; sICH = symptomatic intracranial hemorrhage

Ischemic stroke is a major source of morbidity and the fifth leading cause of death in the United States.¹ Mechanical thrombectomy has been well-established as the standard of care for acute ischemic stroke treatment in selected patients presenting with a large-vessel occlusion.^{2,3} Advances in prehospital stroke care and triage, along with technical advances in mechanical thrombectomy,

have resulted in significant improvement in timing, revascularization rates, and clinical outcomes following stroke thrombectomy.^{2,4}

In recent years, there has been investigation into the impact of procedural timing on clinical outcomes. The time from groin puncture to revascularization of <60 minutes, termed the “golden hour,” has been associated with improved outcomes following stroke thrombectomy.⁵ Additionally, a shorter time from stroke onset to endovascular therapy (OTE) has been linked to more favorable outcomes, including significant early recovery and increased odds of discharge to home. Notably, the association between OTE and improved outcome has been shown to be most significant within the first 2 hours following stroke onset, termed the “2 golden hours.”⁶

In the current study, we investigated the significance of thrombectomy procedure duration and the time from stroke onset to endovascular treatment on clinical outcomes after

Received September 20, 2019; accepted after revision March 4, 2020.

From the Division of Interventional Neuroradiology (H.D.P.C., E.L., T.R.M., D.G., G.J.); Departments of Neurosurgery (A.P.W., G.C., M.J.K., J.A.S., T.C.) and Neurology (S.C., K.Y.), University of Maryland Medical Center, Baltimore, Maryland; and Department of Neurointerventional Surgery (S.R.S.), Christiana Care Health System, Newark, Delaware.

Please address correspondence to Aaron P. Wessell, MD, Department of Neurosurgery, University of Maryland Medical Center, 22 S Greene St, S12D, Baltimore, MD; e-mail: apwessell@gmail.com

 Indicates article with supplemental on-line table.

<http://dx.doi.org/10.3174/ajnr.A6556>

mechanical thrombectomy. Additionally, we investigated the impact of revascularization and postprocedural intracranial hemorrhage (ICH), among other variables, on clinical outcomes in patients treated with mechanical thrombectomy.

MATERIALS AND METHODS

This study was conducted with local institutional review board approval (University of Maryland, Baltimore). We performed a retrospective review of a prospectively maintained data base of all patients undergoing mechanical thrombectomy for the treatment of acute ischemic stroke at a single comprehensive stroke center from April 2012 through February 2019. Patients eligible for inclusion in the study included patients 18 years of age or older who underwent mechanical thrombectomy within 24 hours of stroke onset for treatment of an acute ischemic stroke involving the anterior cerebral circulation.

Data collected included patient demographics, clinical presentation, procedural details, angiographic/radiographic findings, and clinical outcome at 90-day follow-up. Anterior circulation occlusions were defined as occlusions of the ICA, M1 segment of the MCA, or M2 segment of the MCA. Angiographic revascularization grade classified according to the modified TICI score (mTICI) was determined by the neurointerventional surgeon performing the procedure with subsequent verification via independent review of the posttreatment angiogram by an attending neurointerventional surgeon (D.G., T.R.M., G.J., E.L.) and 1 neurointerventional fellow. Differences were adjudicated in a consensus reading when necessary. Successful revascularization was defined as mTICI 2b, 2c, or 3.⁷

A thrombectomy pass was defined as any stent retrieval thrombectomy attempt or an attempt using aspiration without a stent retriever. Procedural time was grouped according to groin puncture to procedure end time of <30 minutes, 30–60 minutes, or >60 minutes. Procedural time was also dichotomized to less than or greater than 30 minutes for additional analyses. OTE was defined as the time from stroke onset or last known well to groin puncture. Patients were dichotomized according to OTE ≤6 hours or >6 hours. Postprocedural ICH was identified on postthrombectomy CT or MR imaging of the brain. Symptomatic intracranial hemorrhage (sICH) was defined as a deterioration in neurologic examination findings attributed to the hemorrhage, as defined by the European Cooperative Acute Stroke Study III definition.^{8,9} The primary outcome of interest was the mRS score at 90 days based on assessment by a neurologist or specialty-trained neurology nurse who did not perform the thrombectomy procedure. An mRS score of 0–2 was considered a good clinical outcome, and 3–6, a poor clinical outcome.

Procedures were performed using institutional protocols and standard of care. Patient selection for thrombectomy was based on findings from noncontrast CT, CT angiography, and/or MR imaging/MR angiography. Exclusion criteria for the study were the following: 1) mild stroke symptoms, defined as admission NIHSS score of less than four; 2) the presence of a completed large territorial infarction observed on noncontrast CT (ASPECTS <4) or MR imaging (>90-mL infarct volume); 3) functional dependence at baseline, defined as a prestroke mRS less than three; 4) intracranial hemorrhage noted within the

targeted stroke territory; or 5) >24 hours from time of known stroke onset. Any discrepancy in the ASPECTS or eligibility for thrombectomy was adjudicated by multidisciplinary consensus between the attending neurointerventional surgeon and attending stroke neurologist. Procedures were performed in a biplane neuroangiography suite (Artis zee; Siemens) by 1 of 4 attending neurointerventional surgeons. Procedures were completed with the patient under moderate/conscious sedation or general anesthesia at the discretion of the attending neurointerventional surgeon.

Statistical Analysis

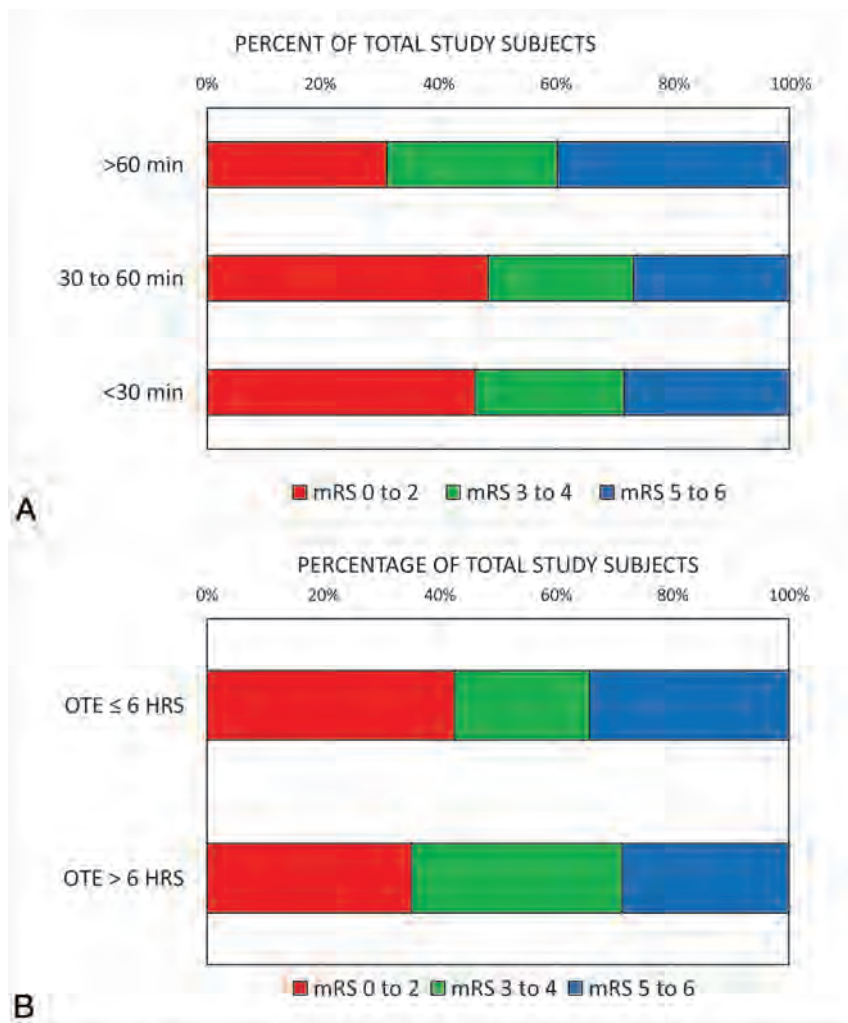
The distribution, frequency, and mean values of all clinical and demographic variables were assessed. We compared patients grouped according to procedural time of <30 minutes, 30–60 minutes, or >60 minutes and OTE of ≤6 hours or >6 hours using the χ^2 test for categorical variables and the Student *t* test/ANOVA for continuous variables. Bivariate analysis was used to compare clinical characteristics among patients who had postprocedural symptomatic hemorrhage and all other patients. Univariate and multivariate logistic regression was used to determine independent predictors of poor outcome at 90 days defined by mRS scores of 3–6.

Logistic regression was performed on all 319 patients. Variables on univariate analysis with a *P* value ≤ .10 were included in the final multivariable logistic regression. Select variables with *P* values >.10 on univariate analysis were included in the final logistic regression model due to their clinical relevance. The following variables were included in the final multivariate model: age, NIHSS score, tPA, medical history (hypertension, diabetes mellitus, hyperlipidemia, atrial fibrillation, smoking), OTE of ≤6 hours, procedural time (<30 minutes, 30–60 minutes, >60 minutes), mTICI score, moderate sedation versus general anesthesia, number of thrombectomy passes, and postprocedural ICH. The number of thrombectomy passes was grouped according to 1 pass, 2 passes, or ≥3 passes for all analyses. mTICI scores were categorized as ≤2a, 2b, 2c, or 3 for logistic regression analysis. We assessed potential interactions among all independent variables before inclusion in the final model. A receiver operating characteristic analysis was performed to measure the predictive power of the final regression model. All analyses were conducted using STATA/SE (Version 16 for Windows; StataCorp). A *P* value < .05 was considered statistically significant for all tests.

RESULTS

Total Cohort Demographics, Clinical/Procedural Characteristics, and Outcomes

Three hundred thirty-four eligible patients underwent mechanical thrombectomy for ischemic stroke during the study period. Patients were excluded due to ischemic stroke involving the posterior circulation (*n* = 12), missing clinical information (*n* = 1), and loss to follow-up (*n* = 2), leaving a total of 319 study subjects. The average patient age was 65.10 ± 0.78 years. The mean admission NIHSS score was 17.71 ± 0.31. Sixty-four percent of patients had an occlusion of the M1 segment, while 22% and 14% had occlusions of the ICA and M2 segment, respectively.



Abbreviations: mRS, modified Rankin Scale; OTE, onset-to-endovascular therapy.

FIGURE. Distribution of 90-day mRS outcome according to procedural time <30 minutes, 30–60 minutes, >60 minutes (A); and onset to endovascular therapy ≤6 hours or OTE >6 hours (B).

Revascularization (mTICI 2b, 2c, 3) was achieved in 79% of cases, and full revascularization (mTICI 2c or 3), in 56% of cases. Mean groin puncture to procedure end time was 58.7 (2.0) minutes. Forty percent of patients ($n=129$) from the 319 study subjects achieved a good outcome at 90 days. Patient demographics, clinical characteristics, procedural data, and outcomes are outlined in the On-line Table.

Procedural Time

A comparison of patients grouped according to procedural time of <30 minutes ($n=74$), 30–60 minutes ($n=112$), and >60 minutes ($n=133$) is outlined in the On-line Table. There was no statistically significant difference in patient age, admission NIHSS score, IV-tPA usage, occlusion site/side, medical history, and time from stroke onset-to-endovascular therapy ($P>.05$). Shorter procedural times were associated with greater revascularization rates and fewer thrombectomy passes ($P<.001$) (On-line Table). Patients with procedural times of <30 minutes and 30–60 minutes had greater rates of good outcome at 90 days (46% and 48%,

respectively) relative to those with a procedural time of >60 minutes (31%) ($P=.012$) (Fig 1A).

Stroke Onset to Endovascular Therapy

The mean time from stroke onset or last known well time to endovascular therapy was 244.29 ± 67.24 minutes in the OTE ≤6 hours group and 646.93 ± 312.86 minutes in the OTE >6 hours group ($P<.001$). The admission NIHSS score was greater for patients in the OTE ≤6 hours group (18.46 ± 5.35 versus 15.85 ± 5.75 ; $P<.001$), and there was a trend toward a greater percentage of M1 occlusions relative to ICA or M2 occlusions among patients in the OTE ≤6 hours group ($P=.060$). Patients with OTE of ≤6 hours were more likely to receive tPA before thrombectomy relative to patients with OTE >6 hours (57% versus 25%; $P<.001$). The mean time from groin puncture to procedure end was greater among patients in the OTE ≤6 hours group (61.47 ± 37.5 minutes versus 51.74 ± 30.37 minutes; $P=.029$). There was no significant difference in revascularization rates or the number of thrombectomy passes between the ≤6 hours versus >6 hours OTE groups. A comparison of patient demographics and clinical characteristics according to OTE ≤6 hours or >6 hours is shown in the On-line Table. Forty-three percent of patients in the OTE ≤6 hours group achieved a good outcome at 90 days relative to 35% in the OTE >6 hours group ($P=.225$) (Fig 1B).

Postprocedural Hemorrhage

Fifty-seven patients (18%) had a postprocedural ICH following thrombectomy, 16 of whom (5%) developed an sICH. There was no difference in admission NIHSS, tPA usage, occlusion site, mTICI score, or OTE among patients with symptomatic hemorrhage compared with all other patients. While not statistically significant, there was a trend toward the presence of sICH in patients with procedural times of >30 minutes versus <30 minutes ($P=.099$). The development of sICH was associated with a greater number of thrombectomy passes ($P=.019$). All patients who developed sICH ($n=16$) experienced poor outcomes at 90 days (Table 1).

Independent Predictors of Poor Outcome

On univariate analysis, several patient demographic and clinical characteristics were associated with poor clinical outcome at

Table 1: Clinical and procedural characteristics associated with postthrombectomy symptomatic hemorrhage^a

Variable	Postprocedural Symptomatic Hemorrhage (n = 16)	Asymptomatic/No Hemorrhage (n = 303)	P Value
NIHSS	17.88 (6.48)	17.70 (5.55)	.905
tPA	9 (56%)	145 (48%)	.521
Occlusion site			
ICA	3 (19%)	67 (22%)	.927
M1	11 (69%)	194 (64%)	
M2	2 (13%)	42 (14%)	
mTICI scale			
mTICI 0	0 (0%)	25 (8%)	.425
mTICI 1	1 (6%)	11 (4%)	
mTICI 2a	3 (19%)	25 (8%)	
mTICI 2b	4 (25%)	71 (23%)	
mTICI 2c	1 (6%)	56 (18%)	
mTICI 3	7 (44%)	115 (38%)	
OTE (min)	308.06 (87.68)	361.85 (258.76)	.408
Groin puncture to procedure end (min)	64.45 (35.01)	58.39 (35.97)	.512
Procedural sedation			
Moderate sedation	9 (56%)	166 (55%)	.909
General anesthesia	7 (44%)	137 (45%)	
No. thrombectomy passes			
1 Pass	4 (25%)	109 (36%)	.019
2 Passes	2 (12%)	104 (34%)	
≥3 Passes	10 (63%)	90 (30%)	
Procedure time			
<30 min	1 (6%)	73 (24%)	.099
≥30 min	15 (94%)	230 (76%)	
mRS at 90 days			
mRS 0–2 (good)	0 (0%)	129 (43%)	.001
mRS 3–6 (poor)	16 (100%)	174 (57%)	
Death	10 (63%)	59 (19%)	<.001

^aContinuous variables are expressed as mean (±standard error or SD). Categorical binary variables are expressed as No. (%). $P < .05$ is considered statistically significant.

90 days (Table 2). On multivariable logistic regression, greater age (OR, 1.03; 95% CI, 1.01–1.06; $P = .016$), higher admission NIHSS score (OR, 1.10; 95% CI, 1.04–1.16; $P = .001$), ICH (OR, 3.48; 95% CI, 1.55–7.82; $P = .003$), and a history of diabetes mellitus (OR, 1.96; 95% CI, 1.05–3.65; $P = .034$) were independently associated with greater odds of poor outcome. Modified TICI scale scores of 2c (OR, 0.11; 95% CI, 0.04–0.28; $P < .001$) and 3 (OR, 0.15; 95% CI, 0.06–0.38; $P < .001$) were associated with reduced odds of poor outcome. Although not significant on univariate analysis, OTE >6 hours was independently associated with increased odds of poor outcome (OR, 2.20; 95% CI, 1.11–4.36; $P = .024$) after adjusting for confounding variables included in the final multivariate model (area under the curve = 0.820). Although procedural times of <30 minutes and 30–60 minutes had significantly better rates of good outcome at 90 days relative to those with procedural times of >60 minutes, procedural time itself and the number of thrombectomy passes did not have an independent association with clinical outcome on the final multivariable logistic regression (Table 2). An additional bivariate analysis comparing patients grouped according to procedural times less than or ≥30 minutes showed no significant difference in outcome (mRS 0–2: 46% versus 39%, respectively; $P = .271$).

DISCUSSION

The golden hour in stroke thrombectomy, defined by Spiotta et al⁵ as a procedural time of ≤60 minutes, has been associated with improved outcomes in comparison with longer procedural times. Subsequent recent reports by Alawieh et al¹⁰ and Huang et al¹¹ have reinforced the importance of shorter procedural times, noting worse outcomes and greater rates of sICH among patients with extended procedural times, specifically those extending beyond 30 minutes. Similar to these recent reports,^{10,11} greater rates of good functional outcomes among patients who underwent procedures lasting <30 minutes or 30–60 minutes relative to procedures of >60 minutes ($P = .012$) were found. Our data also demonstrate a trend toward an increased risk of sICH in those with procedural times of >30 minutes. Final TICI scores were significantly different across the procedural time groups. When we accounted for this notable discrepancy in the final multivariate regression analysis, procedural time and the number of thrombectomy passes were no longer independent predictors of outcome. Procedural time, when dichotomized to less than or greater than 30 minutes

was, again, not independently associated with outcomes on multivariate analysis.^{10,11} Our results differ in this regard when compared with the reports by Alawieh et al¹⁰ and Huang et al.¹¹

Our results are similar, however, to recent findings of Tonetti et al¹² and Jindal et al.¹³ The data from these studies suggest that the treatment effect still favors recanalization for patients, despite requiring a higher number of thrombectomy passes. Both of these groups concluded that successful recanalization should be pursued despite the number of attempts necessary. Our findings deviate from those reported in the original description of the first pass effect by Zaidat et al.¹⁴ However, the data from this report did not account for lower rates of revascularization in higher pass cohorts. We continue to believe that it is critical to expedite thrombectomy procedures as much as possible because lengthy procedures delay revascularization and confer some additional risk to the patient with each subsequent thrombectomy pass.

More recently, the 2 golden hours, coined by Peretz et al,⁶ defined the crucial 2-hour period between the time of stroke onset to endovascular therapy in which patients experience the greatest benefit from mechanical thrombectomy. These results are consistent with those of prior reports that described the importance of early stroke intervention.^{6,15,16} Our data similarly demonstrate that OTE >6 hours is associated with increased odds of poor outcome (OR, 2.20; 95% CI, 1.11–4.36; $P = .024$) on

Table 2: Results of univariate and multivariate logistic regression analysis of clinical parameters and poor outcome (mRS 3–6) at 90 days^a

Variable	Univariate			Multivariate		
	OR	95% CI	P Value	OR	95% CI	P Value
Age	1.03	1.01–1.05	<.001	1.03	1.01–1.06	.016
NIHSS score	1.10	1.05–1.15	<.001	1.10	1.04–1.16	.001
tPA	0.66	0.42–1.03	.067	0.75	0.42–1.37	.354
Medical history						
Hypertension	1.60	0.96–2.68	.071	1.44	0.74–2.80	.283
Diabetes mellitus	1.82	1.09–3.04	.021	1.96	1.05–3.65	.034
Hyperlipidemia	1.47	0.93–2.31	.099	1.23	0.67–2.26	.502
Atrial fibrillation	1.91	1.18–3.10	.008	1.46	0.78–2.76	.239
Smoking	0.64	0.41–1.01	.051	0.75	0.42–1.32	.319
Procedural timing						
OTE >6 hr ^b	1.37	0.82–2.26	.226	2.20	1.11–4.36	.024
Procedure <30 min	0.75	0.44–1.26	.272	Ref		
Procedure 30–60 min	0.61	0.37–0.97	.038	0.58	0.27–1.25	.163
Procedure >60 min	2.01	1.26–3.21	.003	1.32	0.57–2.08	.515
mTICI scale						
mTICI ≤2a	4.85	2.37–9.93	<.001	Ref		
mTICI 2b	1.74	0.99–3.02	.050	0.52	0.20–1.33	.169
mTICI 2c	0.39	0.21–0.69	.001	0.11	0.04–0.28	<.001
mTICI 3	0.50	0.31–0.79	.003	0.15	0.06–0.38	<.001
Procedural sedation						
Moderate sedation	0.58	0.37–0.92	.019	Ref		
General anesthesia	1.72	1.09–2.72	.019	1.46	0.80–2.65	.213
Thrombectomy passes						
1 Pass	0.53	0.33–0.84	.007	Ref		
2 Passes ^b	1.05	0.65–1.69	.834	1.40	0.70–2.79	.343
≥3 Passes	1.93	1.16–3.19	.011	1.62	0.72–3.67	.244
ICH	2.26	1.18–4.35	.014	3.48	1.55–7.82	.003

Note:—Ref indicates reference.

^a $P < .05$ considered statistically significant; area under the curve = 0.820 for final logistic regression model.

^b Not statistically significant on univariate analysis but included in final model due to clinical relevance.

multivariable logistic regression analysis. An OTE of >6 hours was associated with lower rates of tPA usage, lower NIHSS scores, and a trend toward more M2-level occlusions. These factors are known to impact outcomes, and these were accounted for in our multivariate analysis. Patients in the OTE >6 hours group also had shorter procedural times than those in the OTE ≤6 hours group (51.74 [30.37] minutes versus 61.47 [37.58] minutes; $P = .029$); this finding may reflect an operator tendency to spend less time on patients in the “late window” and/or might be related to the higher incidence of M2 occlusions seen in the OTE >6 hours group. We did not evaluate the impact of the 2 golden hours of OTE on patient outcomes, because only 15 of our patients were treated within 2 hours of onset. Most of our patients with stroke treated with thrombectomy were transferred to our facility from outside hospitals during the study period.⁶

Greater age and NIHSS scores, which are well-established predictors of outcome following stroke, were independent predictors of poor outcome in our final multivariate analysis ($P < .05$).^{2,17} Postprocedural ICH was associated with poor outcomes on multivariate analysis, and all patients with sICH experienced a poor outcome at 90 days. This outcome is similar to that in prior reports.¹⁰ Also similar to prior reports, a history of diabetes mellitus was found to be predictive of poor outcome (OR, 1.96; 95% CI, 1.05–3.65; $P = .034$).^{13,18}

The present study has limitations. This is a single-center retrospective study, and the triage and thrombectomy techniques

we used evolved during the course of the study. A single-center series, however, does ensure some homogeneity with regard to periprocedural and procedural care. Angiographic TICI scoring was initially performed by the operating physician, but subsequent verification of TICI scoring was performed by only 1 attending physician and 1 neurointerventional fellow. Although we created a thorough multivariate model to predict poor outcome with a high degree of predictive accuracy (area under the curve = 0.820), it is possible that we failed to include unmeasured markers of disease severity or other relevant confounding variables. While we attempted to account for differences between the 2 OTE groups in the multivariate analysis, these differences represent a limitation in comparing these groups. Moreover, although we included 319 patients, a larger, higher-powered study is likely needed to help us more precisely understand the role of procedural time itself on outcomes after stroke thrombectomy, because longer procedures and a greater number of thrombectomy attempts confer added risk to the patient.

CONCLUSIONS

When accounting for lower rates of revascularization in longer procedures, procedural time was not in itself highly predictive of patient outcomes. Thus, our study emphasizes the significance of achieving revascularization despite the requisite procedural time. However, pursuing longer procedures must be weighed against

the added risk of intracranial hemorrhage associated with multiple thrombectomy attempts.

Disclosures: Gregory Cannarsa—UNRELATED: Employment: University of Maryland Medical Center. Timothy R. Miller—UNRELATED: Grants/Grants Pending: active grants: August, 01, 2013, to present; Co-Inv, Principal Investigator: Gaurav Jindal, (1%) "ULTRA: Ultra Coils from Start to Finish for the Endovascular Repair of Small Intracranial Aneurysms"; multicenter trial sponsor: Stryker; award amount: \$744,774; assist in patient recruitment, data collection, September 1, 2014, to present; Co-Inv, Site Principal Investigator: Dheeraj Gandhi, (1%) "BARREL: Prospective, Multi-Center, "Single-Arm Study of the Reverse Medical Barrel™ Vascular Reconstruction Device (VRD) for Adjunctive Treatment to Embolic Coils for Wide-Neck, Intracranial, Bifurcating/Branching Aneurysms of Middle Cerebral and Basilar Arteries"; multicenter trial, sponsor: Medtronic; award amount: \$26,232; assist in patient recruitment, data collection, September 15, 2015, to present; Co-Inv, Site Principal Investigator: Gaurav Jindal (1%) "A Prospective, Multi-center, Single Arm Study to Evaluate the Safety and Effectiveness of the CODMAN ENTERPRISE® Vascular Reconstruction Device and Delivery System when Used in Conjunction with Endovascular Coil Embolization in the Treatment of Wide-necked Saccular Intracranial Aneurysms"; multicenter trial, Sponsor: Cerenovus, DePuy Synthes; award amount: \$99,995; assist in patient recruitment, data collection, January 30, 2018, to present; Co-Inv, Site Principal Investigator: Howard Eisenberg, (1%) "A Pivotal Clinical Trial of the Management of the Medically-Refractory Dyskinesia Symptoms or Motor Fluctuation of Advanced Idiopathic Parkinson's Disease With Unilateral Lesioning of the Globus Pallidum Using the ExAblate Neuro System"; multicenter trial, sponsor: InSightec; award amount: \$830,971; assist in treatment planning and execution, February 21, 2018, to present; Co-Inv, Site Principal Investigator: Gaurav Jindal, (1%) "Ruptured Aneurysms Treated with Hydrogel Coils—RAGE"; multicenter trial, sponsor: MicroVention; award amount: \$126,350; assist in patient recruitment, data collection, July 11, 2018, to present; Co-Inv, Site Principal Investigator: Graeme Woodworth, (1%) "A Study to Evaluate the Safety and Feasibility of Exablate Model 4000 Type-2 to Temporally Mediate Blood-Brain Barrier Disruption (BBBD) in Patients with Suspected Glioblastoma in the Setting of Planned Surgical Interventions"; single-center trial, sponsor: InSightec; award amount: \$239,027; assist in treatment planning and execution, August 16, 2018, to present; Co-Inv, Site Principal Investigator: Dheeraj Gandhi, (1%) "PHIL DAVF: Study of PHIL Embolic System in the Treatment of Intracranial Dural Arteriovenous Fistulas"; multicenter trial; sponsor: MicroVention; award amount: \$130,000; assist in patient recruitment, data collection, completed grants, January 13, 2016, to June 1, 2019; Site Principal Investigator, (3%) "Apollo Onyx Delivery Micro Catheter Post Market Safety Study"; multicenter trial, sponsor: Medtronic; award amount: \$32,500; assist in patient recruitment, data gathering, data analysis, November 2, 2011, to June 2, 2017; Co-Inv, Site Principal Investigator: Gaurav Jindal, (1%) "Hydrogel Endovascular Aneurysm Treatment Trial (HEAT)"; multicenter trial, sponsor: Stryker; award amount: \$34,889; assist in patient recruitment, data collection, November 16, 2013, to November 25, 2014; Co-Inv, Site Principal Investigator: Elias Melhem, (1%) "Gadobutrol Enhanced MRA of the Supra-aortic Vessels"; multicenter trial, sponsor: Bayer; award amount: \$79,295; assist in patient recruitment, data collection; November 25, 2013, to December 11, 2017; Site Principal Investigator, (5%) "Trevor Retriever Registry: Post Market Surveillance Study"; multicenter trial, sponsor: Stryker; award amount: \$337,430; assist in patient recruitment, data gathering, data analysis, November 10, 2014, to August 20, 2015; Co-Inv, Site Principal Investigator: Dheeraj Gandhi, (1%) "A Pivotal Study of MicroVention, Inc: Neurovascular Self-expanding Retrievable Stent System LVIS"; multicenter trial; sponsor: MicroVention, award amount: \$45,350; assist in patient recruitment, data collection, December 8, 2015, to April 3, 2017; Co-Inv, Site Principal Investigator: Gaurav Jindal, (1%) "Systemic Evaluation of Patients Treated with Neurothrombectomy Devices for Acute Ischemic Stroke (STRATIS) Registry"; multicenter acute stroke registry, sponsor: Medtronic; award amount: \$96,000; assist in patient recruitment, data collection, December 20, 2015, to July 21, 2016; Principal Investigator, (3%) "Pipeline Flex versus Classic Retrospective Study"; single-center retrospective trial; sponsor: Medtronic; award amount: \$20,000; assist in study design, data gathering, data analysis.* Seemant Chaturvedi—RELATED: Grant: National Institute of Neurological Disorders and Stroke, Comments: Carotid Revascularization and Medical Management for Asymptomatic Carotid Stenosis Trial (CREST-2) Executive Committee*; UNRELATED: Board Membership: *New England Journal of Medicine Journal Watch Neurology, Comments:* Associate Editor. Dheeraj Gandhi—RELATED: Grant: MicroVention, Comments: National Principal Investigator on a grant (SOFAST)*; UNRELATED: Grants/Grants Pending: Ultrasound Foundation, National Institutes of Health*; Royalties: Cambridge Press. Sudhakar R. Satti—UNRELATED: Consultancy: Stryker, Cerenovus, Medtronic, Terumo, Penumbra. Gaurav Jindal—RELATED: Grant: Stryker Neurovascular and MicroVention, Comments: research-related grant funding*; UNRELATED: Grants/Grants Pending: Stryker Neurovascular and MicroVention, Comments: research-related grant funding*; Payment for Lectures Including Service on Speakers Bureaus: Penumbra, Comments: payment for 1 lecture. *Money paid to the institution.

REFERENCES

1. Lloyd-Jones D, Adams R, Carnethon M, et al; American Heart Association Statistics Committee and Stroke Statistics Subcommittee. **Heart disease and stroke statistics—2009 update: a report from the American Heart Association Statistics Committee and Stroke Statistics Subcommittee.** *Circulation* 2009;119:480–86 CrossRef Medline
2. Goyal M, Menon BK, van Zwam WH, et al. **Endovascular thrombectomy after large-vessel ischaemic stroke: a meta-analysis of individual patient data from five randomised trials.** *Lancet* 2016;387:1723–31 CrossRef Medline
3. Hill MD, Goyal M. **Treat fast but abandon time from ischemic stroke onset as a criterion for treatment: the DAWN and DEFUSE-3 trials.** *Int J Stroke* 2018;13:344–47 CrossRef Medline
4. Audebert HJ, Saver JL, Starkman S, et al. **Prehospital stroke care: new prospects for treatment and clinical research.** *Neurology* 2013;81:501–08 CrossRef Medline
5. Spiotta AM, Vargas J, Turner R, et al. **The golden hour of stroke intervention: effect of thrombectomy procedural time in acute ischemic stroke on outcome.** *J NeuroInterv Surg* 2014;6:511–16 CrossRef Medline
6. Peretz S, Raphaeli G, Borenstein N, et al. **Effect of time from onset to endovascular therapy on outcomes: the National Acute Stroke Israeli (NASIS)-REVASC registry.** *J Neurointerv Surg* 2020;12:13–18 CrossRef Medline
7. Zaidat OO, Yoo AJ, Khatri P, et al; STIR Thrombolysis in Cerebral Infarction (TICI) Task Force. **Recommendations on angiographic revascularization grading standards for acute ischemic stroke: a consensus statement.** *Stroke* 2013;44:2650–63 CrossRef Medline
8. Yaghi S, Eisenberger A, Willey JZ. **Symptomatic intracerebral hemorrhage in acute ischemic stroke after thrombolysis with intravenous recombinant tissue plasminogen activator: a review of natural history and treatment.** *JAMA Neurol* 2014;71:1181–85 CrossRef Medline
9. Hacke W, Kaste M, Bluhmki E, et al. **Thrombolysis with alteplase 3 to 4.5 hours after acute ischemic stroke.** *N Engl J Med* 2008;359:1317–29 CrossRef Medline
10. Alawieh A, Vargas J, Fargen KM, et al. **Impact of procedure time on outcomes of thrombectomy for stroke.** *J Am Coll Cardiol* 2019;73:879–90 CrossRef Medline
11. Huang X, Cai Q, Xiao L, et al. **Influence of procedure time on outcome and hemorrhagic transformation in stroke patients undergoing thrombectomy.** *J Neurol* 2019;266:2560–70 CrossRef Medline
12. Tonetti DA, Desai SM, Casillo S, et al. **Successful reperfusion, rather than number of passes, predicts clinical outcome after mechanical thrombectomy.** *J Neurointerv Surg* 2019 Nov 1. [Epub ahead of print] CrossRef Medline
13. Jindal G, Carvalho HP, Wessel A, et al. **Beyond the first pass: revascularization remains critical in stroke thrombectomy.** *J Neurointerv Surg* 2019;11:1095–99 CrossRef Medline
14. Zaidat OO, Castonguay AC, Linfante I, et al. **First pass effect: a new measure for stroke thrombectomy devices.** *Stroke* 2018;49:660–66 CrossRef Medline
15. Mulder M, Jansen IG, Goldhoorn RB, et al; MR CLEAN Registry Investigators. **Time to endovascular treatment and outcome in acute ischemic stroke: MR CLEAN Registry results.** *Circulation* 2018;138:232–40 CrossRef Medline
16. Alawieh A, Pierce AK, Vargas J, et al. **The golden 35 min of stroke intervention with ADAPT: effect of thrombectomy procedural time in acute ischemic stroke on outcome.** *J Neurointerv Surg* 2018;10:213–20 CrossRef Medline
17. Kleine JF, Beller E, Zimmer C, et al. **Lenticulostriate infarctions after successful mechanical thrombectomy in middle cerebral artery occlusion.** *J Neurointerv Surg* 2017;9:234–39 CrossRef Medline
18. Jia Q, Zhao X, Wang C, et al. **Diabetes and poor outcomes within 6 months after acute ischemic stroke: the China National Stroke Registry.** *Stroke* 2011;42:2758–62 CrossRef Medline

Predictors of Cerebral Aneurysm Rupture after Coil Embolization: Single-Center Experience with Recanalized Aneurysms

Y. Funakoshi, H. Imamura, S. Tani, H. Adachi, R. Fukumitsu, T. Sunohara, Y. Omura, Y. Matsui, N. Sasaki, T. Fukuda, R. Akiyama, K. Horiuchi, S. Kajiuira, M. Shigeyasu, K. Iihara, and N. Sakai



ABSTRACT

BACKGROUND AND PURPOSE: Recanalization after coil embolization is widely studied. However, there are limited data on how recanalized aneurysms rupture. Herein, we describe our experience with the rupture of recanalized aneurysms and discuss the type of recanalized aneurysms at greatest rupture risk.

MATERIALS AND METHODS: A total of 426 unruptured aneurysms and 169 ruptured aneurysms underwent coil embolization in our institution between January 2009 and December 2017. Recanalization occurred in 38 (8.9%) of 426 unruptured aneurysms (unruptured group) and 37 (21.9%) of 169 ruptured aneurysms (ruptured group). The Modified Raymond-Roy classification on DSA was used to categorize the recanalization type. Follow-up DSA was scheduled until 6 months after treatment, and follow-up MRA was scheduled yearly. If recanalization was suspected on MRA, DSA was performed.

RESULTS: In the unruptured group, the median follow-up term was 74.0 months. Retreatment for recanalization was performed in 18 aneurysms. Four of 20 untreated recanalized aneurysms (0.94% of total coiled aneurysms) ruptured. In untreated recanalized aneurysms, class IIIb aneurysms ruptured significantly more frequently than class II and IIIa ($P = .025$). In the ruptured group, the median follow-up term was 28.0 months. Retreatment for recanalization was performed in 16 aneurysms. Four of 21 untreated recanalized aneurysms (2.37% of total coiled aneurysms) ruptured. Class IIIb aneurysms ruptured significantly more frequently than class II and IIIa ($P = .02$).

CONCLUSIONS: The types of recanalization after coil embolization may be predictors of rupture. Coiled aneurysms with class IIIb recanalization should undergo early retreatment because of an increased rupture risk.

ABBREVIATIONS: AcomA = anterior communicating artery; PcomA = posterior communicating artery

Endovascular coiling of cerebral aneurysms is widely performed, with continued improvement in related techniques and devices.^{1,2} However, an important problem with endovascular coiling is recanalization after coil embolization. Coiled aneurysms that show major recanalization require additional coiling to prevent rupture. The incidence of recanalization after coiling ranges from 6.1% to 33.6%,^{3,4} and the reported risk factors for recanalization include aneurysm morphologic features, coil compaction and/or migration, and various endovascular embolization techniques.³⁻⁵

Although recanalization after coil embolization has been previously evaluated, there are insufficient data on the way in which recanalized aneurysms rupture. Thus, in the present study, we describe our experience with the rupture of aneurysms that have recanalized after coil embolization in Kobe City Medical Center General Hospital and discuss the type of recanalized aneurysms at greatest risk of rupture and the appropriate timing of follow-up angiography and retreatment.

MATERIALS AND METHODS

Patient and Aneurysm Characteristics

Between January 2009 and December 2017, coil embolization was performed in a total of 426 unruptured aneurysms and 169 ruptured aneurysms in our institution, excluding fusiform aneurysms, dissecting aneurysms, infectious aneurysms, and aneurysms combined with arteriovenous malformations or Moyamoya disease. Aneurysms that underwent parent artery occlusion and that were treated with an off-label stent used in a clinical trial and a stent in the acute phase of rupture, recanalized aneurysms previously

Received December 15, 2019; accepted after revision February 22, 2020.

From the Department of Neurosurgery (Y.F., H.I., S.T., H.A., R.F., T.S., Y.O., Y.M., N.Sasaki, T.F., R.A., K.H., S.K., M.S., N.Sakai), Kobe City Medical Center General Hospital, Kobe, Japan; and Department of Neurosurgery (K.I.), Graduate School of Medical Sciences, Kyushu University, Fukuoka, Japan.

Please address correspondence to Yusuke Funakoshi, MD, Department of Neurosurgery, Graduate School of Medical Sciences, Kyushu University, 3-1-1 Maidashi, Higashi-ku, Fukuoka 812-8582, Japan; e-mail: sflwan0610@gmail.com

 Indicates article with supplemental on-line table.

<http://dx.doi.org/10.3174/ajnr.A6558>

Table 1: Patient and aneurysm characteristics, volume embolization ratio, use of stents, and follow-up term^a

Patient characteristic	Unruptured Group		Ruptured Group	
	All Aneurysms (n = 426)	Recanalized Aneurysms (n = 38)	All Aneurysms (n = 169)	Recanalized Aneurysms (n = 37)
Age (yr)	63.0 (52.0–70.0)	65.0 (49.8–71.3)	66.0 (52.0–77.5)	59.0 (44.5–76.5)
Male sex	105 (24.6%)	6 (15.8%)	56 (33.1%)	10 (27.0%)
Aneurysm location				
ICA-cavernous	12 (2.8%)	2 (5.3%)	0 (0.0%)	0 (0.0%)
ICA-paraclinoid	188 (44.1%)	9 (23.7%)	5 (3.0%)	2 (5.4%)
ICA-PcomA	49 (11.5%)	9 (23.7%)	55 (32.5%)	16 (43.2%)
ICA-AchoA	10 (2.3%)	0 (0.0%)	13 (7.7%)	4 (10.8%)
ICA-bifurcation	11 (2.6%)	2 (5.3%)	3 (1.8%)	0 (0.0%)
MCA	6 (1.4%)	0 (0.0%)	4 (2.4%)	0 (0.0%)
AcomA	66 (15.5%)	1 (2.6%)	57 (33.7%)	11 (29.7%)
VA	15 (3.5%)	4 (10.5%)	8 (4.7%)	1 (2.7%)
BA-SCA	16 (3.8%)	2 (5.3%)	2 (1.2%)	1 (2.7%)
BA-bifurcation	41 (9.6%)	9 (23.7%)	12 (7.1%)	2 (5.4%)
Others	12 (2.8%)	0 (0.0%)	10 (5.9%)	0 (0.0%)
Aneurysm size				
Dome	6.2 (4.9–8.4)	10.1 (7.0–14.1)	6.5 (5.0–9.3)	7.7 (5.4–13.0)
Neck	3.8 (2.9–5.1)	5.9 (4.7–7.7)	3.2 (2.4–4.2)	4.0 (2.7–5.9)
Endovascular procedures				
VER	26.9 (21.9–32.8)	23.0 (18.0–29.2)	25.8 (19.8–33.2)	23.7 (18.9–29.5)
Without stent	240 (56.3%)	19 (50.0%)	169 (100.0%)	37 (100.0%)
With stent	186 (43.7%)	19 (50.0%)	0 (0.0%)	0 (0.0%)
Follow-up				
Duration (mo)	58.5 (24.0–86.0)	74.0 (30.5–96.3)	18.0 (3.0–48.0)	28.0 (10.0–56.0)

Note:—AchoA indicates anterior choroidal artery; VA, vertebral artery; BA, basilar artery; SCA, superior cerebellar artery; VER, volume embolization ratio.

^a Unruptured group indicates unruptured aneurysms that underwent coil embolization; ruptured group, ruptured aneurysms that underwent coil embolization. Data are Unruptured Group (n = 426); Recanalization after coil embolization occurred in 38 of 426 unruptured aneurysms. Ruptured Group (n = 169); Recanalization after coil embolization occurred in 37 of 169 ruptured aneurysms.

treated with coiling, and aneurysms that reruptured in the acute phase (<1 month after the initial rupture) were excluded from the present study. Recanalization after coil embolization occurred in 38 of 426 (8.9%) unruptured aneurysms (unruptured group) and 37 of 169 (21.9%) ruptured aneurysms (ruptured group). Table 1 summarizes the characteristics of the patients and recanalized aneurysms, endovascular procedures, and follow-up term in these 2 groups compared with all patients and aneurysms.

The present investigation was approved by our local ethics committee (institutional review board of Kobe City Medical Center General Hospital). The study was conducted in accordance with the 1964 Declaration of Helsinki (as revised in Fortaleza, Brazil, October 2013).

Perioperative Antiplatelet Management

Patients undergoing coil embolization for unruptured aneurysms were generally administered dual-antiplatelet therapy with 100 mg of aspirin and 75 mg of clopidogrel daily for at least 7 days before the procedure. Either aspirin or clopidogrel was decreased gradually from 6 months after the procedure and discontinued after at least 1 year. Single-antiplatelet therapy was generally discontinued after 1 or 2 years. When stent-assisted coil embolization was performed, antiplatelet activity was assessed using aspirin and P2Y₁₂ assays (VerifyNow; Accumetrics) on the day before the procedure. When the aspirin reaction unit measurements were >550, the aspirin dose was increased to 200 mg daily. When the P2Y₁₂ reaction unit measurements were >220, a

loading dose of 20 mg of prasugrel was given, and the dose was then decreased to 3.75 mg from the following day. Prasugrel was decreased gradually from 6 months after the procedure. Although prasugrel and either aspirin or clopidogrel were discontinued after 1 year, single-antiplatelet therapy was continued as a life-long treatment. Patients undergoing coil embolization for ruptured aneurysms were generally administered single-antiplatelet therapy with aspirin or cilostazol. Single-antiplatelet therapy was discontinued depending on the DSA findings.

Endovascular Procedures

Preoperative DSA findings were used to determine the best approach and technique for the endovascular procedure (ie, simple technique, double-catheter technique, balloon-assisted coil embolization, or stent-assisted coil embolization). The procedure was performed by a neurovascular team, including a board-certified neuroendovascular surgeon. The procedure for unruptured aneurysms was generally performed with the patient under local anesthesia, because neurologic evaluation can be performed during the procedure. The procedure for ruptured aneurysms was performed with the patient under general anesthesia. All patients received heparin after an arterial puncture to maintain an elevated activated clotting time of approximately 300 seconds during the procedure for unruptured aneurysms and approximately 250 seconds for ruptured aneurysms. The volume embolization ratio was measured on DSA after the procedure, and the angiographic findings were evaluated.

Evaluation of Coiled Aneurysms

The Raymond-Roy occlusion classification is the standard for evaluating aneurysm occlusion, while the Modified Raymond-Roy classification was recently reported to be a predictor of progressive occlusion or recurrence (Fig 1).⁶ In the Modified Raymond-Roy classification, complete obliteration is defined as class I, a residual neck is defined as class II, and a residual aneurysm is defined as class III.⁶ Class III is further separated into class IIIa (contrast within the coil interstices) and IIIb (contrast along the aneurysm wall).⁶ The present study used the Modified Raymond-Roy classification to evaluate aneurysm occlusion and recanalization. Any further filling of the aneurysm sac across

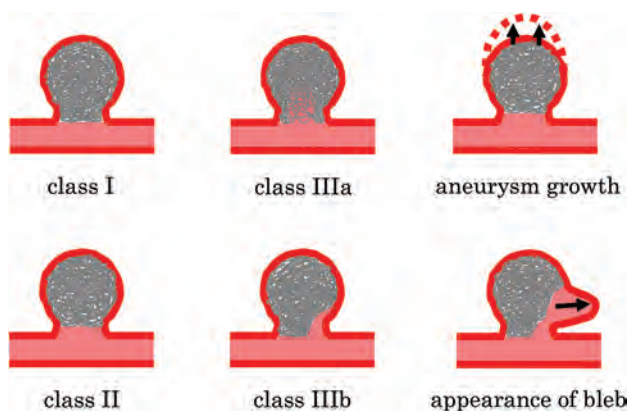


FIG 1. Illustration of the Modified Raymond-Roy classification and additional definitions of the type of recanalization used in the present study. Class I: complete obliteration; class II: residual neck; class IIIa: residual aneurysm with contrast within the coil interstices; class IIIb: residual aneurysm with contrast along the aneurysm wall. The appearance of new blebs was distinguished from an increase in the diameter of the coiled aneurysm. Except for the appearance of new blebs, an increase in the diameter of the coiled aneurysm was termed “aneurysm growth.”

time on follow-up DSA was termed “recanalization.” The appearance of new blebs was distinguished from an increase in the diameter of the coiled aneurysm. Except for the appearance of new blebs, an increase in the diameter of the coiled aneurysm was termed “aneurysm growth” (Fig 1).

Two observers, who were board-certified neuroendovascular surgeons, evaluated aneurysm occlusion and recanalization using the Modified Raymond-Roy classification, and 1 investigator evaluated these parameters twice to verify inter- and intrarater reliability.

Follow-Up

In the unruptured group, follow-up DSA was scheduled at 6 months after treatment, and follow-up MRA (using $\geq 1.5T$ magnet strength) was scheduled yearly. In the ruptured group, follow-up DSA was generally scheduled for 1 week after treatment to evaluate vasospasm and for 1 month after treatment to detect early recanalization. From 6 months after treatment, follow-up evaluations were performed as described for the unruptured group. In principle, the diagnosis of recanalization was based only on DSA findings. If recanalization was suspected on follow-up MRA, DSA was performed. When recanalization was identified on follow-up DSA, the patient was scheduled to undergo retreatment or an earlier follow-up DSA.

Statistical Analysis

Statistical analyses were performed using statistical software (JMP software, Version 14; SAS Institute). Sex, aneurysm location, use of a stent, type of recanalization, aneurysm growth, and the appearance of new blebs were evaluated using the χ^2 test or the Fisher exact test. Age, aneurysm dome diameter, aneurysm neck size, and volume embolization ratio were analyzed using the Mann-Whitney *U* test. $P < .05$ was considered statistically significant.

RESULTS

Outcomes of Aneurysms and Patients

Outcomes of aneurysms and patients are summarized in Table 2. In the unruptured group, the median follow-up term of recanalized aneurysms was 74.0 months. The type of recanalization on follow-up DSA, the timing of retreatment and rupture, and the type of recanalization immediately before retreatment and rupture are shown in Table 3. From a total of 38 recanalized aneurysms, the type of recanalization on final DSA was classified as class II in 3 (7.9%) aneurysms, class IIIa in 12 (31.6%), and class IIIb in 23 (60.5%). On follow-up DSA, aneurysm growth was identified in 12 (31.6%) aneurysms, and the appearance of new blebs, in 2 (5.3%) aneurysms. Retreatment was performed in 18 (47.4%) aneurysms,

Table 2: Outcomes of aneurysms and patients

	Unruptured Group ^a	Ruptured Group ^a
Type of recanalization on final DSA		
Class II	3 (7.9%)	7 (18.9%)
Class IIIa	12 (31.6%)	7 (18.9%)
Class IIIb	23 (60.5%)	23 (62.2%)
Aneurysm growth	12 (31.6%)	3 (8.1%)
Appearance of bleb	2 (5.3%)	1 (2.7%)
Retreatment	18 (47.4%)	16 (43.2%)
Rupture	4 (10.5%)	4 (10.8%)
Rupture risk (/aneurysm)	0.94%	2.37%
Rupture risk (/yr)	0.20%	0.97%
Final mRS score without ruptured recanalized aneurysm ^b		
0–2	31 (91.2%)	21/33 (63.6%)
3–4	1 (2.9%)	6/33 (18.2%)
5–6	2 (5.9%)	6/33 (18.2%)
Final mRS score with ruptured recanalized aneurysm ^c		
0–2	2 (50.0%)	1 (25.0%)
3–4	0 (0.0%)	2 (50.0%)
5–6	2 (50.0%)	1 (25.0%)

^a Unruptured Group ($n = 38$); Ruptured Group ($n = 37$).

^b Unruptured Group ($n = 34$); Ruptured Group ($n = 33$).

^c Unruptured Group ($n = 4$); Ruptured Group ($n = 4$).

Table 3: Type of aneurysm occlusion and recanalization on follow-up DSA, the timing of retreatment and rupture, and the type of recanalization immediately before retreatment and rupture in the unruptured group^a

	Initial (n = 38) (n = 38)	6 Months (n = 36) (n = 38)	1 Year (n = 16) (n = 37)	2 Years (n = 3) (n = 35)	3 Years (n = 0) (n = 26)	4 Years (n = 0) (n = 26)	5 Years (n = 1) (n = 23)	6 Years (n = 1) (n = 22)	7 Years (n = 0) (n = 16)	8 Years (n = 1) (n = 13)
Type of aneurysm occlusion and recanalization										
I	5	2	0	0	0	0	0	0	0	0
II	10	4	1	0	0	0	0	0	0	0
IIIa	12	13	9	1	0	0	0	1	0	0
IIIb	11	17	6	2	0	0	1	0	0	1
Type of recanalization of retreated recanalized aneurysms										
IIIa	0	1	3	0	0	0	0	1	0	0
IIIb	0	8	2	1	0	0	1	0	0	1
Type of recanalization of ruptured recanalized aneurysms										
IIIa	0	0	0	0	0	0	0	0	0	0
IIIb	1	1	1	0	0	0	0	1	0	0

^a The first row of numbers in parentheses indicates the number of cases that underwent follow-up DSA at that time; the second row of numbers in parentheses, the number of cases that underwent follow-up MRA at that time.

Table 4: Type of aneurysm occlusion and recanalization on follow-up DSA, the timing of retreatment and rupture, and the type of recanalization immediately before retreatment and rupture in the ruptured group^a

	Initial (n = 37) (n = 37)	1 Week (n = 37) (n = 37)	1 Month (n = 34) (n = 37)	6 Months (n = 19) (n = 29)	1 Year (n = 12) (n = 28)	2 Years (n = 0) (n = 22)	3 Years (n = 0) (n = 18)	4 Years (n = 0) (n = 13)	5 Years (n = 0) (n = 9)	6 Years (n = 0) (n = 6)
Type of aneurysm occlusion and recanalization										
I	14	9	3	0	0	0	0	0	0	0
II	17	19	13	5	2	0	0	0	0	0
IIIa	2	2	3	5	3	0	0	0	0	0
IIIb	4	7	15	9	7	0	0	0	0	0
Type of recanalization of retreated recanalized aneurysms										
IIIa	0	0	0	2	1	0	0	0	0	0
IIIb	0	0	11	1	1	0	0	0	0	0
Type of recanalization of ruptured recanalized aneurysms										
IIIa	—	—	0	0	0	0	0	0	0	0
IIIb	—	—	2	1	0	1	0	0	0	0

Note:— indicates not available.

^a Aneurysms that reruptured in the acute phase (<1 month after the initial rupture) were excluded. The first-row of number in parentheses indicates the number of cases that underwent follow-up DSA at that time. The second-row of number in parentheses indicates the number of cases that underwent follow-up MRA at that time.

while 20 (52.6%) were untreated. The 2 aneurysms with the appearance of new blebs were retreated. Four of the 20 untreated aneurysms ruptured, 0.94% of the total coiled aneurysms ruptured, and the rupture risk was 0.20% per year. Thirty-one (91.2%) of 34 patients without a ruptured recanalized aneurysm had a final mRS of 0–2, while 2 (50.0%) of 4 patients with a ruptured recanalized aneurysm had a final mRS of 0–2.

In the ruptured group, the median follow-up term of recanalized aneurysms was 28.0 months. The type of recanalization on follow-up DSA, the timing of retreatment and rupture, and the type of recanalization immediately before retreatment and rupture are shown in Table 4. From a total of 37 recanalized aneurysms, the type of recanalization on final DSA was classified as class II in 7 (18.9%) aneurysms, class IIIa in 7 (18.9%), and class IIIb in 23 (62.2%). On

follow-up DSA, aneurysm growth was identified in 3 (8.1%) aneurysms, and new blebs appeared in 1 (2.7%) aneurysm. Retreatment was performed in 16 (43.2%) aneurysms, and 21 (56.8%) were untreated. The aneurysm with the appearance of new blebs was retreated. Four of the 21 untreated aneurysms ruptured, 2.37% of the total coiled aneurysms ruptured, and the rupture risk was 0.97% per year. Twenty-one (63.6%) of 33 patients without a ruptured recanalized aneurysm had a final mRS of 0–2, while 1 (25.0%) of 4 patients with a ruptured recanalized aneurysm had a final mRS of 0–2.

Factors Associated with Rupture after Coil Embolization

Factors associated with rupture after coil embolization are summarized in Tables 5 and 6 for the unruptured and ruptured groups,

Table 5: Factors associated with rupture after coil embolization in untreated recanalized aneurysms in the unruptured group^a

	Untreated Recanalized Aneurysms (n = 20)		
	Unruptured (n = 16)	Ruptured (n = 4)	P Value
Age (yr)	67.0 (60.3–72.8)	63.0 (55.8–70.3)	.570
Sex			
Male	1 (6.3%)	1 (25.0%)	.264
Female	15 (93.7%)	3 (75.0%)	
Location			
ICA	5 (31.2%)	1 (25.0%)	.937
ICA-PcomA	4 (25.0%)	1 (25.0%)	
AcomA	1 (6.3%)	0 (0.0%)	
Posterior	6 (37.5%)	2 (50.0%)	
Dome	9.2 (7.6–13.4)	9.9 (6.6–11.1)	.813
Neck	5.5 (4.4–7.0)	4.5 (3.2–8.8)	.741
VER	22.1 (13.9–26.1)	25.1 (18.5–37.3)	.321
Use of stent			
No	9 (56.3%)	2 (50.0%)	.822
Yes	7 (43.7%)	2 (50.0%)	
Type of recanalization on final DSA			
II + IIIa	10 (62.5%)	0 (0.0%)	.025 ^b
IIIb	6 (37.5%)	4 (100.0%)	
Aneurysm growth			
No	13 (81.3%)	3 (75.0%)	.780
Yes	3 (18.7%)	1 (25.0%)	

Note:—ICA indicates ICA other than ICA-PcomA; VA, vertebral artery; BA, basilar artery; SCA, superior cerebellar artery; VER, volume embolization ratio; Posterior, posterior circulation including the VA, BA-SCA, and BA-bifurcation.

^a Data are recanalized aneurysms in the unruptured group (n = 38): Twenty of 38 recanalized aneurysms were untreated. Among 20 untreated recanalized aneurysms, 16 aneurysms unruptured and 4 aneurysms ruptured.

^b Statistical significance.

Table 6: Factors associated with rupture after coil embolization in untreated recanalized aneurysms in the ruptured group^a

	Untreated Recanalized Aneurysms (n = 21)		
	Unruptured (n = 17)	Ruptured (n = 4)	P Value
Age (yr)	62.0 (44.5–78.0)	55.5 (47.5–75.5)	.929
Sex			
Male	6 (35.3%)	1 (25.0%)	.694
Female	11 (64.7%)	3 (75.0%)	
Location			
ICA	3 (17.7%)	0 (0.0%)	.628
ICA-PcomA	9 (52.9%)	2 (50.0%)	
AcomA	4 (23.5%)	2 (50.0%)	
Posterior	1 (5.9%)	0 (0.0%)	
Dome	6.2 (5.2–8.7)	9.4 (5.3–14.4)	.347
Neck	3.2 (2.5–4.6)	5.2 (3.6–9.1)	.066
VER	24.9 (21.3–29.5)	25.5 (16.7–28.5)	.741
Use of stent			
No	17 (100.0%)	4 (100.0%)	—
Yes	0 (0.0%)	0 (0.0%)	
Type of recanalization on final DSA			
II + IIIa	11 (64.7%)	0 (0.0%)	.020 ^b
IIIb	6 (35.3%)	4 (100.0%)	
Aneurysm growth			
No	16 (94.1%)	4 (100.0%)	.619
Yes	1 (5.9%)	0 (0.0%)	

Note:— indicates not available.

^a Data are recanalized aneurysms in the ruptured group (n = 37): Twenty-one of 37 recanalized aneurysms were untreated. Among 21 untreated recanalized aneurysms, 17 aneurysms unruptured and 4 aneurysms ruptured.

^b Statistical significance.

respectively. In the unruptured group, 4 class IIIb recanalized aneurysms ruptured of the 20 untreated recanalized aneurysms, and there was a significant difference in the frequency of rupture between classes II and IIIa ($P = .025$).

In the ruptured group, 4 class IIIb recanalized aneurysms ruptured of the 21 untreated recanalized aneurysms, and there was a trend toward a larger median aneurysm neck diameter in the ruptured recanalized aneurysms (5.2 mm) compared with the unruptured recanalized aneurysms (3.2 mm; $P = .066$). Class IIIb recanalized aneurysms ruptured significantly more frequently than classes II and IIIa ($P = .020$).

Rupture of Recanalized Aneurysms

The cases of ruptured recanalized aneurysm are summarized in the On-line Table. The DSA findings of ruptured recanalized aneurysms in the unruptured and ruptured groups are shown in Figs 2 and 3, respectively. In patient 4 in the unruptured group, DSA could not be performed when the recanalized aneurysm ruptured. Thus, the MRA findings are shown instead. In the unruptured group, 4 recanalized aneurysms ruptured. In patient 1 with a large basilar artery–bifurcation aneurysm, the type of recanalization changed from class II to IIIb, and the aneurysm ruptured at 8 months after coil embolization. In patient 2 with an ICA–posterior communicating artery (PcomA) aneurysm, patient 3 with an ICA–paraclinoid aneurysm, and patient 4 with a large basilar artery–bifurcation aneurysm, the type of recanalization was class IIIb, and the aneurysms ruptured with a new bleb formation at 76, 2, and 24 months after coil embolization, respectively. All 4 patients with ruptured recanalized aneurysms were receiving continued antiplatelet therapy at the time of rupture.

In the ruptured group, 4 recanalized aneurysms ruptured. In patients 1 and 2, both with an anterior communicating artery (AcomA) aneurysm, the type of recanalization changed from class II to IIIb, and both aneurysms ruptured with formation of a new bleb at 1 month after coil embolization. In patients 3 and 4, both with an ICA-PcomA aneurysm, the type of recanalization was class IIIb, and the aneurysms ruptured at 29 and 7 months after coil embolization, respectively. All 4 patients with ruptured recanalized aneurysms were receiving continued antiplatelet therapy at the time of rupture. Recanalized aneurysms in the ruptured group tended to rupture earlier than those in the unruptured group.

DISCUSSION

The epidemiology, natural history, management options, and familial screening of unruptured aneurysm are well-established.^{7–11} Several studies have also reported treatment outcomes for ruptured

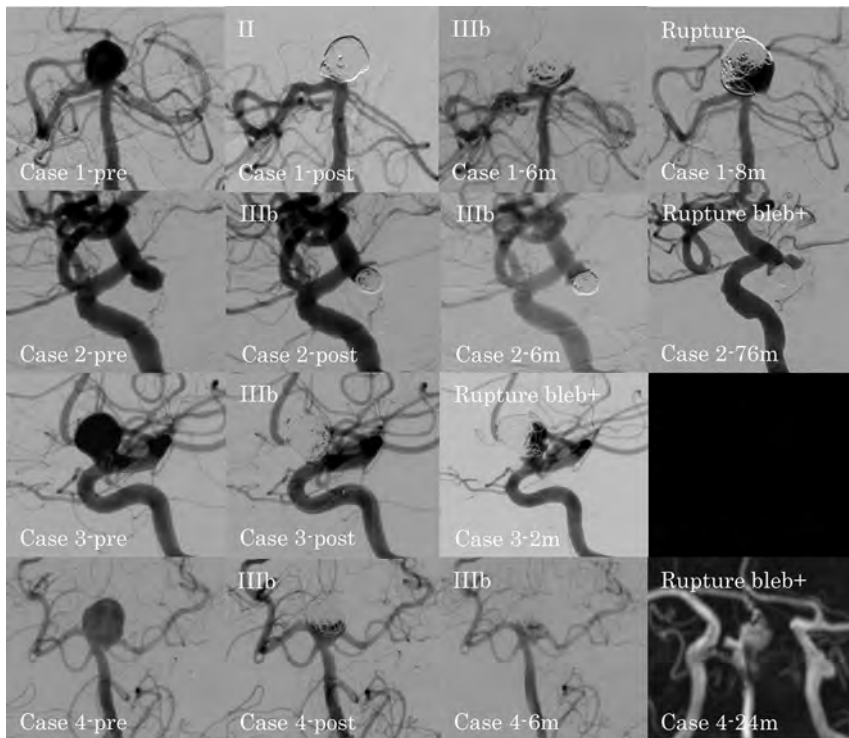


FIG 2. DSA findings for ruptured recanalized aneurysms in the unruptured group. Case 1-pre: preprocedural basilar artery–bifurcation aneurysm; case 1-post: class II aneurysm occlusion immediately after the procedure; case 1-6m: class IIIb recanalization at 6 months after the procedure; case 1-8m: ruptured recanalized aneurysm with a new bleb at 8 months after the procedure; case 2-pre: preprocedural ICA–posterior communicating artery aneurysm; case 2-post: class IIIb aneurysm occlusion immediately after the procedure; case 2-6m: progression of the class IIIb recanalization at 6 months after the procedure; case 2-76m: ruptured recanalized aneurysm with a new bleb at 76 months after the procedure; case 3-pre: preprocedural paraclinoid-ICA aneurysm; case 3-post: class IIIb aneurysm occlusion immediately after the procedure; case 3-2m: ruptured recanalized aneurysm with a new bleb at 2 months after the procedure; case 4-pre: preprocedural basilar artery–bifurcation aneurysm; case 4-post: class IIIb aneurysm occlusion immediately after the procedure; case 4-6m: no change at 6 months after the procedure; case 4-24m: MRA shows the ruptured recanalized aneurysm with a new bleb at 24 months after the procedure.

aneurysms.^{1,12-14} Aneurysms are widely treated by endovascular coiling, which has become the standard treatment because of its clinical efficacy.^{1,2} However, recanalization is an important problem that can occur after coil embolization and can result in aneurysm rupture. Although numerous studies have evaluated recanalization in unruptured aneurysms after coil embolization, there are insufficient data on how recanalized aneurysms rupture. In addition, in ruptured aneurysms, although long-term follow-up data from the International Subarachnoid Aneurysm Trial (ISAT) showed that the risk of rerupture of coiled aneurysms was 0.156%,¹⁵ there are no detailed data on how the coiled aneurysms recanalized and ruptured. Thus, the present study evaluated whether the type of recanalization affected the risk of aneurysm rupture.

In general, large aneurysms are more likely to recanalize than small aneurysms,^{5,16-18} and recanalization rates after stent-assisted coil embolization are lower than those after simple coil embolization.¹⁹⁻²¹ In addition, recanalization is affected by hemodynamic force.²² Computational fluid dynamics studies have shown that maximum wall shear stress increases at sites of blood flow impingement near remnant necks.²³ This repetitive flow

impingement and subsequent wall shear stress increments may lead to recanalization.¹⁹

Recanalization is a risk factor for rupture of coiled aneurysms because major recanalization can result in aneurysm rupture. However, not all recanalized aneurysms rupture, and the risk of rupture seems to depend on the type of recanalization. The Modified Raymond-Roy classification is an indicator of how aneurysms are occluded, and it can be used to predict progressive occlusion or recurrence.⁶ Because the type of occlusion is a predictor of recanalization, the types of occlusion and recanalization may be predictors of rupture of coiled aneurysms. In the present study, although the aneurysm neck diameter of the ruptured recanalized aneurysms tended to be larger than that of the unruptured recanalized aneurysms in the ruptured group ($P = .066$), the type of recanalization was the only significant factor in both the unruptured ($P = .025$) and ruptured ($P = .020$) groups. There was no rupture of coiled aneurysms with class II and IIIa recanalization (ie, no contrast along the aneurysm wall). However, 4 recanalized aneurysms with class IIIb recanalization (ie, contrast along the aneurysm wall) ruptured in each group. Although there were few ruptured aneurysms and statistical evaluation was insufficient, the present study has important information regarding

how the occlusion and recanalization of coiled aneurysms affected the risk of rupture.

A previous study reported that the risk factors for early recanalization of coiled aneurysms within 6 months included posterior circulation aneurysms, SAH presentation, a second coiling procedure for recanalization, and an aneurysm of >7 mm.¹⁸ In addition, long-term follow-up is recommended even for aneurysms of 4–7 mm because of the risk of late recanalization.¹⁸ In the present study, recanalized aneurysms in the ruptured group tended to rupture earlier than those in the unruptured group. In our institution, on the basis of our experience, follow-up DSA was scheduled at 6 months after treatment for unruptured aneurysms; for ruptured aneurysms, follow-up DSA was scheduled at 1 week after treatment to evaluate vasospasm and at 1 month after treatment to detect early recanalization. The recanalized aneurysms in patients 1 and 2 in the ruptured group ruptured at 1 month after treatment (just before the scheduled follow-up DSA).

In the present study, most retreatments for recanalization in the ruptured group were performed at 1–6 months after the initial treatment. Follow-up DSA within 1 month can prevent the rupture

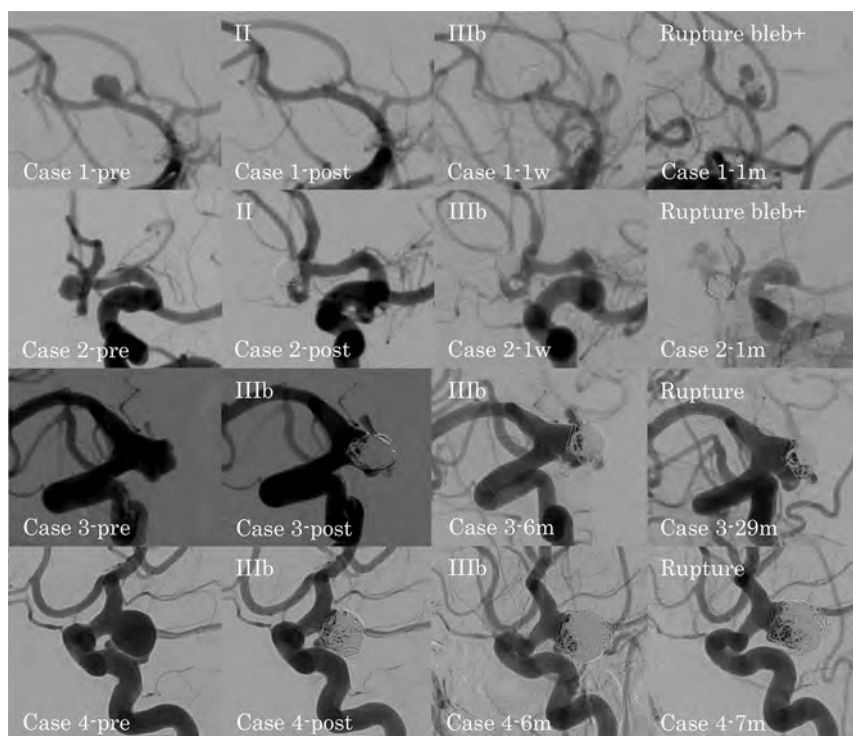


FIG 3. DSA findings for ruptured recanalized aneurysms in the ruptured group. Case 1-pre: pre-procedural anterior communicating artery aneurysm; case 1-post: class II aneurysm occlusion immediately after the procedure; case 1-1w: class IIIb recanalization at 1 week after the procedure; case 1-1m: ruptured recanalized aneurysm with a new bleb at 1 month after the procedure; case 2-pre: pre-procedural anterior communicating artery aneurysm; case 2-post: class II aneurysm occlusion immediately after the procedure; case 2-1w: class IIIb recanalization at 1 week after the procedure; case 2-1m: ruptured recanalized aneurysm with a new bleb at 1 month after the procedure; case 3-pre: pre-procedural ICA-posterior communicating artery aneurysm; case 3-post: class IIIb aneurysm occlusion immediately after the procedure; case 3-6m: progression of the class IIIb recanalization at 6 months after the procedure; case 3-29m: ruptured recanalized aneurysm at 29 months after the procedure; case 4-pre: pre-procedural ICA-posterior communicating artery aneurysm; case 4-post: class IIIb aneurysm occlusion immediately after the procedure; case 4-6m: progression of the class IIIb recanalization at 6 months after the procedure; case 4-7m: ruptured recanalized aneurysm at 7 months after the procedure.

of some recanalized aneurysms. For unruptured aneurysms, follow-up DSA at 6 months after coil embolization is considered reasonable. Compared with the ruptured group, the timing of coiled aneurysm rupture in the unruptured group tended to be later in the present study. Most retreatments for recanalization in the unruptured group were performed at 6 months to 1 year after the initial treatment. Although retreatment at this time can prevent the rupture of recanalized aneurysms, there are rare exceptions that rupture shortly after coil embolization: For example, the unruptured aneurysm after coil embolization in patient 3 ruptured at 2 months after treatment. In addition, there were cases in both the unruptured and ruptured groups in which the coiled aneurysms ruptured during long-term follow-up. Coiled aneurysms with class IIIb recanalization should undergo early retreatment because of the high risk of rupture. Although coiled aneurysms with class II or IIIa recanalization should also be retreated if possible, these aneurysms can be treated with conservative therapy because of the low risk of rupture. However, class II or IIIa recanalization can progress into class IIIb recanalization. Thus, follow-up examinations are essential.

Periprocedural antiplatelet therapy was associated with a low risk of symptomatic thromboembolic events after coil embolization for aneurysms.²⁴ In the present study, all patients with ruptured recanalized aneurysms were receiving continued antiplatelet therapy at the time of rupture. In particular, long-term dual-antiplatelet therapy was continued, considering the thromboembolic event in patient 4 in the ruptured group. Long-term single-antiplatelet therapy was also continued in patient 2 in the unruptured group and in patient 3 in the ruptured group. Although it is unclear whether antiplatelet therapy in the present cases could influence the rupture of recanalized aneurysms, indiscriminate continuation of antiplatelet therapy should be avoided.

The risk of rupture for aneurysms with growth is 12 times higher than that for aneurysms without growth.²⁵ In the present study, although some coiled aneurysms showed aneurysm growth and the appearance of new blebs, there were no significant differences in aneurysm growth in the unruptured ($P = .780$) and ruptured ($P = .619$) groups. The appearance of new blebs was also not a significant risk factor for rupture of recanalized aneurysms. However, all aneurysms with the appearance of new blebs on follow-up DSA were retreated, and

the appearance of new blebs was detected in 3 of 4 ruptured recanalized aneurysms in the unruptured group and in 2 of 4 ruptured recanalized aneurysms in the ruptured group at the time of rupture. Although it is difficult to detect the appearance of new blebs on follow-up DSA because aneurysms with formation of new blebs can rupture early, the appearance of new blebs can be a risk factor for rupture of recanalized aneurysms and thus must not be overlooked. Additionally, the appearance of new blebs both on follow-up DSA and at the time of rupture was identified only in coiled aneurysms with class IIIb recanalization; this finding may be because blood flow along the aneurysm wall can form new blebs. In recanalized aneurysms, the type of recanalization can be important because class IIIb recanalization can result in the appearance of new blebs, which may be a risk factor for early rupture of recanalized aneurysms.

Study Limitations

The present study was a nonrandomized retrospective observation study, though the series comprised consecutive cases. In addition,

interpretation of the radiographic data was performed in a non-blinded manner. Although there were 4 cases of ruptured recanalized aneurysms in both the unruptured and ruptured groups, the number of ruptured recanalized aneurysms was small. Thus, statistical multivariate analysis could not be performed, though multiple factors can be related to rupture of recanalized aneurysms. Because the ruptured group included many severe cases that could not be followed up at our institution, there was also a lack of cases with sufficient data. Furthermore, because retreatment was generally performed in cases in which retreatment for recanalized aneurysms was possible and the patient provided consent, the true course of recanalized aneurysms leading to rupture without retreatment remains unclear.

CONCLUSIONS

The present study determined the type of recanalized aneurysm at risk of rupture on the basis of our experience. The types of aneurysm occlusion and recanalization are predictors of the rupture of coiled aneurysms. Coiled aneurysms with class IIIB recanalization should undergo early retreatment because of the high risk of rupture.

ACKNOWLEDGMENTS

We thank Kelly Zammit, BVSc, from Edanz Editing (www.edanzediting.com/ac), for editing a draft of the manuscript.

Disclosures: Hirotooshi Imamura—UNRELATED: Payment for Lectures Including Service on Speakers Bureaus: Medtronic, Nobuyuki Sakai—UNRELATED: Grants/Grants Pending: Terumo, Medtronic, Comments: modest*; Payment for Lectures Including Service on Speakers Bureaus: Biomedical Solutions, Stryker, Terumo, Comments: modest. *Money paid to the institution.

REFERENCES

- Molyneux A, Kerr R, Stratton I, et al; International Subarachnoid Aneurysm Trial (ISAT) Collaborative Group. **International Subarachnoid Aneurysm Trial (ISAT) of neurosurgical clipping versus endovascular coiling in 2143 patients with ruptured intracranial aneurysms: a randomised trial.** *Lancet* 2002;360:1267–74 CrossRef Medline
- Lin N, Cahill KS, Frerichs KU, et al. **Treatment of ruptured and unruptured cerebral aneurysms in the USA: a paradigm shift.** *J NeuroIntervent Surg* 2018;10:i69–76 CrossRef Medline
- Ries T, Siemonsen S, Thomalla G, et al. **Long-term follow-up of cerebral aneurysms after endovascular therapy-prediction and outcome of retreatment.** *AJNR Am J Neuroradiol* 2007;28:1755–61 CrossRef Medline
- Zhang Q, Jing L, Liu J, et al. **Predisposing factors for recanalization of cerebral aneurysms after endovascular embolization: a multivariate study.** *J Neurointerv Surg* 2018;10:252–57 CrossRef Medline
- Jeon JP, Cho YD, Rhim JK, et al. **Extended monitoring of coiled aneurysms completely occluded at 6-month follow-up: late recanalization rate and related risk factors.** *Eur Radiol* 2016;26:3319–26 CrossRef Medline
- Mascitelli JR, Moyle H, Oermann EK, et al. **An update to the Raymond-Roy occlusion classification of intracranial aneurysms treated with coil embolization.** *J Neurointervent Surg* 2015;7:496–502 CrossRef Medline
- Wiebers DO, Whisnant JP, Huston J 3rd, et al. **Unruptured intracranial aneurysms: natural history, clinical outcome, and risks of surgical and endovascular treatment.** *Lancet* 2003;362:103–10 CrossRef
- Sonobe M, Yamazaki T, Yonekura M, et al. **Small unruptured intracranial aneurysm verification study: SUAVE study, Japan.** *Stroke* 2010;41:1969–77 CrossRef
- Morita A, Kirino T, Hashi K, et al. **The natural course of unruptured cerebral aneurysms in a Japanese cohort.** *N Engl J Med* 2012;366:2474–82 CrossRef Medline
- Brown RD, Broderick JP. **Unruptured intracranial aneurysms: epidemiology, natural history, management options, and familial screening.** *Lancet Neurol* 2014;13:393–404 CrossRef Medline
- Darsaut TE, Findlay JM, Magro E, et al. **Surgical clipping or endovascular coiling for unruptured intracranial aneurysms: a pragmatic randomised trial.** *J Neurol Neurosurg Psychiatry* 2017;88:663–68 CrossRef Medline
- CARAT Investigators. **Rates of delayed rebleeding from intracranial aneurysms are low after surgical and endovascular treatment.** *Stroke* 2006;37:1437–42 Medline
- McDougall CG, Spetzler RF, Zabramski JM, et al. **The Barrow Ruptured Aneurysm Trial.** *J Neurosurg* 2012;116:135–44 CrossRef Medline
- Lindgren A, Vergouwen MD, van der Schaaf IC, et al. **Endovascular coiling versus neurosurgical clipping for people with aneurysmal subarachnoid hemorrhage.** *Stroke* 2019;50:e102 CrossRef
- Molyneux AJ, Kerr RS, Birks J, et al. **Risk of recurrent subarachnoid haemorrhage, death, or dependence and standardised mortality ratios after clipping or coiling of an intracranial aneurysm in the International Subarachnoid Aneurysm Trial (ISAT): long-term follow-up.** *Lancet Neurol* 2009;8:427–33 CrossRef Medline
- Cognard C, Weill A, Spelle L, et al. **Long-term angiographic follow-up of 169 intracranial berry aneurysms occluded with detachable coils.** *Radiology* 1999;212:348–56 CrossRef Medline
- Ogilvy CS, Chua MH, Fusco MR, et al. **Validation of a system to predict recanalization after endovascular treatment of intracranial aneurysms.** *Neurosurgery* 2015;77:168–73 CrossRef Medline
- Jeon JP, Cho YD, Yoo DH, et al. **Risk factor analysis of recanalization timing in coiled aneurysms: early versus late recanalization.** *AJNR Am J Neuroradiol* 2017;38:1765–70 CrossRef Medline
- Luo CB, Teng MMH, Chang FC, et al. **Stent-assisted coil embolization of intracranial aneurysms: a single center experience.** *J Chin Med Assoc* 2012;75:322–28 CrossRef Medline
- Hwang SK, Hwang G, Bang JS, et al. **Endovascular Enterprise stent-assisted coil embolization for wide-necked unruptured intracranial aneurysms.** *J Clin Neurosci* 2013;20:1276–79 CrossRef Medline
- Jeon JP, Cho YD, Rhim JK, et al. **Fate of coiled aneurysms with minor recanalization at 6 months: rate of progression to further recanalization and related risk factors.** *AJNR Am J Neuroradiol* 2016;37:1490–95 CrossRef Medline
- Park W, Song Y, Park KJ, et al. **Hemodynamic characteristics regarding recanalization of completely coiled aneurysms: computational fluid dynamic analysis using virtual models comparison.** *Neurointervention* 2016;11:30–36 CrossRef Medline
- Ortega J, Hartman J, Rodriguez J, et al. **Post-treatment hemodynamics of a basilar aneurysm and bifurcation.** *Ann Biomed Eng* 2008;36:1531–46 CrossRef Medline
- Almekhlafi MA, Al Sultan AS, Kuczynski AM, et al. **Antiplatelet therapy for prevention of thromboembolic complications in coiling-only procedures for unruptured brain aneurysms.** *J Neurointerv Surg* 2020;12:298–302 CrossRef Medline
- Villablanca JP, Duckwiler GR, Jahan R, et al. **Natural history of asymptomatic unruptured cerebral aneurysms evaluated at CT angiography: growth and rupture incidence and correlation with epidemiologic risk factors.** *Radiology* 2013;269:258–65 CrossRef Medline

Signal of Carotid Intraplaque Hemorrhage on MR T1-Weighted Imaging: Association with Acute Cerebral Infarct

D. Yang, Y. Liu, Y. Han, D. Li, W. Wang, R. Li, C. Yuan, and X. Zhao



ABSTRACT

BACKGROUND AND PURPOSE: Identifying the mere presence of carotid intraplaque hemorrhage would be insufficient to accurately discriminate the presence of acute cerebral infarct. We aimed to investigate the association between signal intensity ratios of carotid intraplaque hemorrhage on T1-weighted MR imaging and acute cerebral infarct in patients with hemorrhagic carotid plaques using MR vessel wall imaging.

MATERIALS AND METHODS: Symptomatic patients with carotid intraplaque hemorrhage were included. The signal intensity ratios of carotid intraplaque hemorrhage against muscle on T1-weighted, TOF, and MPRAGE images were measured. The acute cerebral infarct was determined on the hemisphere ipsilateral to the carotid intraplaque hemorrhage. The association between signal intensity ratios of carotid intraplaque hemorrhage and acute cerebral infarct was analyzed.

RESULTS: Of 109 included patients (mean, 66.8 ± 9.9 years of age; 96 men), 40 (36.7%) had acute cerebral infarct. Patients with acute cerebral infarct had significantly higher signal intensity ratios of carotid intraplaque hemorrhage on T1-weighted images than those without (Median, 1.44; 25–75 Percentiles, 1.14–1.82 versus Median, 1.27; 25–75 Percentiles, 1.06–1.55, $P = .022$). Logistic regression analysis revealed that the signal intensity ratio of carotid intraplaque hemorrhage on T1-weighted images was significantly associated with acute cerebral infarct before (OR, 4.08; 95% CI, 1.34–12.40; $P = .013$) and after (OR, 3.34; 95% CI, 1.08–10.31; $P = .036$) adjustment for clinical confounding factors. However, this association was not significant when further adjusted for occlusion of the carotid artery ($P = .058$) and volumes of intraplaque hemorrhage and lipid-rich necrotic core ($P = .458$).

CONCLUSIONS: The signal intensity ratio of carotid intraplaque hemorrhage on T1-weighted images is associated with acute cerebral infarct in symptomatic patients with carotid hemorrhagic plaques. This association is independent of traditional risk factors but not of the size of plaque composition. The possibility of applying T1 signals of carotid intraplaque hemorrhage to predict subsequent cerebrovascular ischemic events needs to be prospectively verified.

ABBREVIATIONS: ACI = acute cerebral infarct; IPH = intraplaque hemorrhage; LRNC = lipid-rich necrotic core; SIR = signal intensity ratio

In China, stroke has become the leading cause of death and disability in recent years.¹ It is well established that carotid atherosclerotic disease is one of the important causes of ischemic stroke.² Previous studies have demonstrated that the presence of

carotid intraplaque hemorrhage (IPH) is one of the features of vulnerable plaques³ and is a strong predictor of cerebrovascular ischemic events.^{4–7} Fryer et al⁸ reported that, in symptomatic plaques, the incidence of a larger amount of hemorrhage (involving $\geq 50\%$ of the plaque thickness) was much more common and IPH may occur at many stages in the evolution of the plaque. Investigators found that the presence of IPH was also observed in asymptomatic carotid atherosclerotic plaques and plaques with 0% stenosis.^{9,10} A prospective study by

Received October 30, 2019; accepted after revision February 29, 2020.

From the Beijing Institute of Brain Disorders (D.Y., Y.H., D.L.), Laboratory of Brain Disorders, Ministry of Science and Technology, Collaborative Innovation Center for Brain Disorders, Capital Medical University, Beijing, China; Department of Biomedical Engineering (D.Y., Y.H., D.L., R.L., X.Z.), Center for Biomedical Imaging Research, Tsinghua University School of Medicine, Beijing, China; Department of Radiology (Y.L., W.W.), The Affiliated Hospital of Yangzhou University, Yangzhou University, Yangzhou, China; and Department of Radiology (C.Y.), University of Washington, Seattle, Washington.

Drs Dandan Yang and Yang Liu are co-first authors who contributed equally to this study.

This study was supported by grants from the National Natural Science Foundation of China (81771825), Beijing Municipal Science and Technology Commission (D17110003017003), and Ministry of Science and Technology of China (2017YFC1307904).

Please address correspondence to Xihai Zhao, MD, PhD, Center for Biomedical Imaging Research, Department of Biomedical Engineering, Tsinghua University School of Medicine, Haidian District, Beijing, 100084, China; e-mail: xihai.zhao@tsinghua.edu.cn

Indicates open access to non-subscribers at www.ajnr.org

Indicates article with supplemental on-line photo.

<http://dx.doi.org/10.3174/ajnr.A6498>

Table 1: Parameters of carotid MR vessel wall and brain imaging

	Carotid Artery Imaging				Brain Imaging	
	TIWI	T2WI	TOF	MPRAGE	DWI ^a	TIWI
Sequence	TSE	TSE	FFE	FFE	EPI	FFE
TR (ms)	800	4800	20	8.8	2724	308
TE (ms)	10	50	4.9	5.3	86	4.6
Flip angle	90°	90°	20°	15°	90°	90°
FOV (cm ²)	14 × 14	14 × 14	14 × 14	14 × 14	23 × 23	23 × 23
Matrix size	256 × 256	256 × 256	256 × 256	256 × 256	128 × 126	400 × 256
Slice thickness (mm ^b)	2	2	1	1	5.5	5.5

Note.—FFE indicates fast-field echo; TSE, turbo spin echo; EPI, echo planar imaging; TR, repetition time; TE, echo time; FOV, field of view.

^a DWI: $b = 0, 1000 \text{ s/mm}^2$.

^b Values represent the acquired slice thickness.

Sun et al¹¹ suggested that carotid IPH could persist for years with no clinical symptoms. However, the presence of IPH could accelerate the progression of atherosclerotic plaque and increase the risk of plaque rupture.¹² Therefore, identifying the mere presence of IPH would be insufficient to precisely predict the presence of cerebrovascular ischemic events.

T1-weighted MR images have commonly been used to detect IPH due to the degradation of hemorrhage into methemoglobin, which leads to T1-shortening¹³ and correspondingly causes high signal intensity on T1-weighted MR images. Previous studies have indicated the importance of the signal intensity ratios (SIRs) of carotid plaques on different MR images, which could be taken into account for factors beyond the presence of IPH.^{14,15} A recent study by Wang et al¹⁶ indicated that the SIRs of carotid IPH on heavily T1-weighted images on the symptomatic side were higher than those on the asymptomatic side in symptomatic patients with bilateral carotid IPHs. However, this study targeted only the patients with bilateral carotid IPHs with small sample sizes and measured SIRs of carotid IPH on one T1 sequence of MPRAGE. In addition, the acute cerebral infarct (ACI) lesions in that study on the symptomatic side were not distinct.

The purpose of this study was to investigate the association between the SIRs of carotid IPH on different T1-weighted MR images and the presence of ipsilateral ACI lesions in patients with hemorrhagic carotid plaques using multicontrast MR vessel wall imaging.

MATERIALS AND METHODS

Patients

All patients were enrolled from a cross-sectional, multicenter study of Chinese Atherosclerosis Risk Evaluation (CARE-II), which aimed to assess the prevalence and characteristics of carotid high-risk atherosclerotic plaques in Chinese patients with recent ischemic stroke or transient ischemic attack using multicontrast MR vessel wall imaging. The study protocol of the CARE-II study has been reported previously.¹⁷ The inclusion criteria are as follows: 1) 18–80 years of age, 2) a recent stroke or transient ischemic attack (<2 weeks after the onset of symptoms), 3) atherosclerotic plaques in at least one carotid artery determined by B-mode sonography, and 4) carotid plaques with IPH confirmed by MR vessel wall imaging. Patients with the following conditions were excluded from this study: 1) cardioembolic or hemorrhagic stroke, 2) a history of radiation therapy to the neck, or 3) contraindications to MR imaging. All patients underwent

carotid multicontrast MR vessel wall imaging and clinically routine brain MR imaging. The demographics and clinical characteristics of all patients including age, sex, body mass index, history of smoking, hypertension, diabetes, hyperlipidemia, statin use, antihypertension medication use, coronary heart disease, and lipid levels were acquired from the medical records. The study protocol was approved by the institutional review board of Tsinghua University and local institutions, and a written consent form was obtained from each subject.

Carotid and Brain MR Imaging

All patients underwent carotid and brain MR imaging on 3T MR scanners (Achieva TX; Philips Healthcare, Best, the Netherlands) with 8-channel phased array carotid coils and head coils. A standardized multisequence protocol was performed for the carotid artery by acquiring TOF, T1-weighted, and MPRAGE sequences. Carotid artery imaging was centered on the carotid artery bifurcation on the symptomatic side. Standard brain MR images were acquired using T1-weighted and DWI sequences. The imaging parameters are detailed in Table 1.

MR Image Analysis

All the carotid images were reviewed in consensus by 2 experienced radiologists who had >3 years of experience in neurovascular imaging, blinded to clinical information using custom-designed software (CASCADE; University of Washington, Seattle, Washington).¹⁸ All carotid images were registered with the landmark of carotid bifurcation. The lumen and outer wall boundaries were manually traced. The lumen, wall, total vessel areas, and the mean wall thickness on each axial image were measured. Normalized wall index, defined as wall area divided by the total vessel area, was calculated. The presence or absence of calcification, lipid-rich necrotic core (LRNC), IPH, and fibrous cap rupture at each axial location was identified according to the published criteria, which were validated by histology.¹⁹ In particular, the identification of carotid IPH was mainly based on a pattern of hyperintense signal intensity on MPRAGE images (1.5 times the signal intensity compared with adjacent muscle).²⁰ The volume of each plaque component, including calcification, LRNC, and IPH, and the corresponding percentage volume (volume of each carotid plaque component divided by plaque volume) were calculated. The volume of carotid plaque was calculated as the sum of the plaque area within slices multiplied by slice thickness. The length of carotid IPH was defined as the

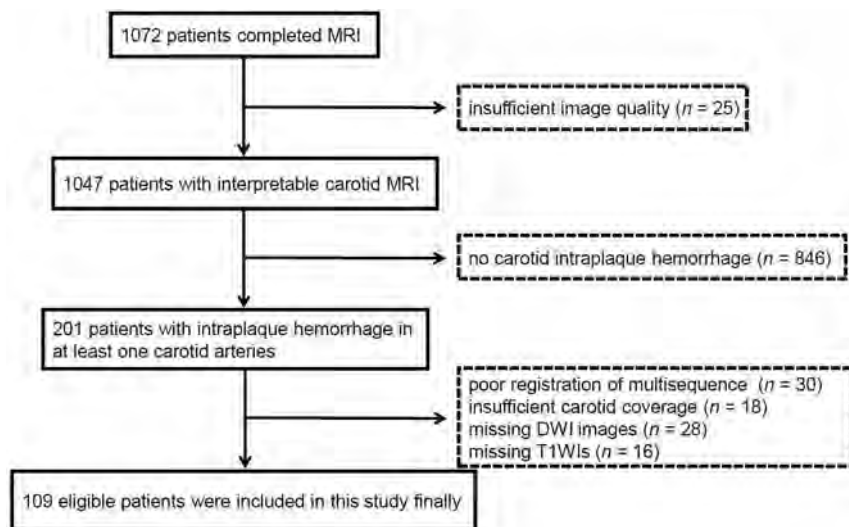


FIG 1. Flow chart of the study sample.

Table 2: Clinical characteristics of study population

	Mean \pm SD or (No.) (%)		P Value ^a
	Patients with ACI (n = 40)	Patients without ACI (n = 69)	
Age (yr)	64.2 \pm 10.2	68.3 \pm 9.5	.035
Sex, male	37 (92.5)	59 (85.5)	.366
Body mass index (kg/m ²)	25.1 \pm 3.6	24.0 \pm 2.7	.117
History of smoking	30 (75.0)	38 (55.1)	.038
History of hypertension	33 (82.5)	58 (84.1)	.833
Systolic blood pressure (mm Hg)	144.2 \pm 20.9	143.9 \pm 21.3	.840
Diastolic blood pressure (mm Hg)	85.2 \pm 9.2	85.8 \pm 14.1	.720
History of hyperlipidemia	21 (52.5)	39 (56.5)	.684
LDL (mmol/L)	2.7 \pm 1.0	3.0 \pm 1.0	.182
HDL (mmol/L)	1.1 \pm 0.2	1.1 \pm 0.2	.780
TC (mmol/L)	4.3 \pm 1.2	4.7 \pm 1.1	.161
TG (mmol/L)	1.9 \pm 1.2	2.0 \pm 1.1	.519
History of diabetes mellitus	15 (37.5)	25 (36.2)	.895
History of coronary heart disease	11 (27.5)	14 (20.3)	.388
Statin use	15 (37.5)	25 (36.2)	.895
Antihypertension medication use	28 (70.0)	49 (71.0)	.911
TIA	12 (30.0)	32 (46.4)	.108
Recent stroke	28 (70.0)	37 (53.6)	.108

Note:—LDL indicates low-density lipoprotein cholesterol; HDL, high-density lipoprotein cholesterol; TC, total cholesterol; TG, triglycerides; TIA, transient ischemia attack.

^a P values were calculated by the Mann-Whitney U test or Fisher exact test.

number of slices with carotid IPH on MPRAGE images multiplied by slice thickness. The ROIs were drawn to enclose the IPH region and the adjacent muscle, respectively, on each axial MPRAGE image with IPH and were automatically mapped to other MR imaging sequences (On-line Figure). The maximum signal intensity of carotid IPH and the mean signal intensity of the adjacent sternocleidomastoid muscle on T1-weighted, TOF, and MPRAGE images were recorded.

The SIR of carotid IPH against muscle on different imaging sequences was calculated by dividing the maximum signal intensity of the IPH by the mean signal intensity of the sternocleidomastoid muscle on each axial image.²¹ Luminal stenosis was measured by radiologists on TOF MR angiography using the NASCET criteria.²² In the present study, we included some

subjects with total luminal occlusion. In analyzing these subjects, we usually reviewed only the slices without luminal occlusion. Brain MR images were evaluated by 2 experienced radiologists who had >3 years of experience in neurovascular imaging with consensus, blinded to clinical information and carotid MR images. The presence or absence of ACI lesions in the internal carotid artery territory was determined on the hemisphere ipsilateral to carotid IPH. ACI was defined as lesions that showed hyperintensity on DWI ($b = 1000$ s/mm²), but iso- or hypointensity on T1-weighted images.

Statistical Analysis

For patients with bilateral carotid IPHs, the MR imaging features of the carotid artery associated with symptoms were selected for final statistical analysis. The continuous variables were presented as mean \pm SD or median and interquartile range, and the binary variables were expressed as count and percentage. The plaque features on carotid MR imaging were compared between patients with and without ACI using the independent *t* test, Mann-Whitney *U* test, χ^2 test, or Fisher exact test. Univariate and multivariate logistic regressions were performed to calculate the OR and corresponding 95% CI of the carotid SIR of carotid IPH against muscle features on different sequences in discriminating the presence of ipsilateral ACI lesions before and after adjustment for confounding factors. $P < .05$ was considered statistically significant. All statistical analyses were performed using SPSS 16.0 (IBM, Armonk, New York).

RESULTS

The flow chart of patient recruitment in this study is shown in Fig 1. In total, 201 patients with carotid IPH in at least one carotid artery were recruited in this study. Of the 201 patients, 92 patients were excluded due to the following reasons: 1) poor registration of multisequences ($n = 30$); 2) insufficient coverage for carotid images ($n = 18$); 3) missing DWI images ($n = 28$); and 4) missing carotid T1-weighted images ($n = 16$). Finally, 109 patients with carotid IPH were qualified for the final analysis.

Clinical Characteristics

Of the 109 patients, 40 (36.7%) had ACI lesions in the ipsilateral hemispheres of carotid IPH, of which 28 (70%) had a recent stroke and 12 (30%) had a transient ischemic attack. The clinical

characteristics between patients with and without ipsilateral ACI lesions are presented in Table 2. Patients with ipsilateral ACI lesions were younger (mean, 64.2 ± 10.2 versus 68.3 ± 9.5 years of age, $P = .035$) and had a higher prevalence of smoking (75.0% versus 55.1%, $P = .038$) compared with those without. No significant differences were found in other clinical characteristics between patients with and without ipsilateral ACI.

Plaque Morphology and Component Characteristics

The comparison results on the carotid plaque morphologic and compositional characteristics between patients with and without ipsilateral ACI lesions are shown in Table 3. Patients with ipsilateral ACI lesions had significantly greater mean wall area ($48.3 \pm$

14.9 versus 41.5 ± 11.1 mm², $P = .028$), mean wall thickness (1.9 ± 0.6 versus 1.6 ± 0.4 mm, $P = .010$), and a higher prevalence of total luminal occlusion of the carotid artery (52.5% versus 15.9%, $P < .001$) than those without. There were no statistically significant differences in other carotid plaque burden measurements, including lumen area, total vessel area, mean normalized wall index and carotid plaque volume between the two groups (all $P > .05$). Of all 109 patients, 93 (85.3%) had carotid calcification and 37 (33.9%) had carotid fibrous cap rupture. There were no significant differences in the prevalence of calcification ($P = .526$) and fibrous cap rupture ($P = .859$) between patients with and without ipsilateral ACI lesions. Patients with ipsilateral ACI lesions had a significantly larger volume of LRNC (312.7 [174.1–625.3] versus 227.7 [122.1–351.4] mm³, $P = .038$), a larger percentage LRNC volume (29.4% versus 23.6%, $P = .039$), and a larger IPH volume (93.2 [31.4–201.2] versus 56.4 [21.9–104.9] mm³, $P = .016$) than those without. No significant differences were found in the percentage of IPH volume, volume of calcification, percentage of calcification volume, and carotid plaque length between the two groups (all, $P > .05$).

IPH Signal Characteristics

Patients with ipsilateral ACI lesions were found to have significantly higher SIRs of carotid IPH (1.44 [1.14–1.82] versus 1.27 [1.06–1.55], $P = .022$) on T1-weighted images than those without (Fig 2). No significant differences were found in the SIRs of carotid IPH on TOF (1.36 [1.11–1.72] versus 1.19 [0.92–1.58], $P = .096$) and

Table 3: Comparison of carotid plaque morphologic and compositional characteristics between patients with and without ipsilateral ACI lesions

	Mean \pm SD. (No.) (%) or Median (25–75 Percentiles)		P Value ^a
	Patients with ACI (n = 40)	Patients without ACI (n = 69)	
Mean lumen area (mm ²)	35.5 \pm 13.5	36.5 \pm 12.4	.555
Mean wall area (mm ²)	48.3 \pm 14.9	41.5 \pm 11.1	.028
Mean total vessel area (mm ²)	83.8 \pm 20.6	78.0 \pm 18.6	.172
Mean wall thickness (mm)	1.9 \pm 0.6	1.6 \pm 0.4	.010
Mean normalized wall index (%)	57.9 \pm 11.3	53.6 \pm 9.1	.087
Total luminal occlusion	21 (52.5%)	11 (15.9%)	<.001
Plaque volume (mm ³)	1240.7 \pm 535.2	1064.4 \pm 414.1	.159
Presence of calcification	33 (82.5)	60 (87.0)	.526
Presence of FCR	14 (35.0)	23 (33.3)	.859
Volume of calcification (mm ³) ^b	35.8 (12.4–87.3)	36.2 (15.8–79.6)	.794
Percentage calcification volume (%) ^b	3.1 (1.3–6.4)	3.5 (1.9–7.7)	.312
Volume of LRNC (mm ³) ^b	312.7 (174.1–625.3)	227.7 (122.1–351.4)	.038
Percentage LRNC volume (%) ^b	29.4 (17.9–42.1)	23.6 (14.0–34.0)	.039
Volume of IPH (mm ³) ^b	93.2 (31.4–201.2)	56.4 (21.9–104.9)	.016
Percentage IPH volume (%) ^b	7.9 (3.0–17.0)	5.4 (2.5–10.1)	.074
IPH length (mm)	12.0 (4.5–17.5)	10.0 (4.0–14.0)	.101

Note:—FCR indicates fibrous cap rupture.

^a P values are based on the Mann-Whitney U test or Fisher exact test between patients with and without ipsilateral ACI lesions.

^b Only patients with the corresponding component present were included in the comparison.

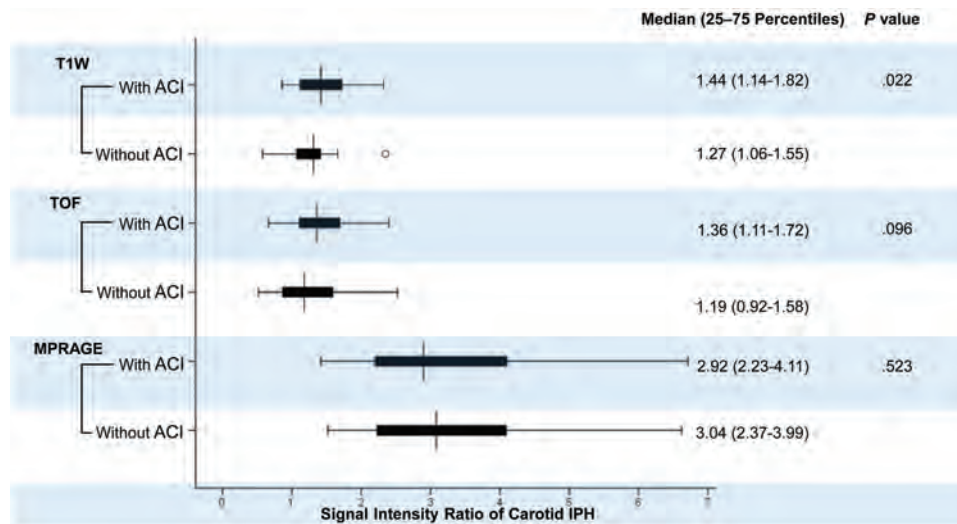


FIG 2. Boxplots of the SIR of carotid IPH on different T1-weighted MR imaging sequences in patients with and without ACI. Patients with ipsilateral ACI lesions had significantly higher SIRs of carotid IPH on T1-weighted images than those without.

Table 4: Association between signal intensity ratio of carotid IPH and the presence of ipsilateral ACI lesions

SIR _{IPH-to-muscle} on MR Image	Presence of ACI											
	Univariate Regression			Multivariate Model 1 ^a			Multivariate Model 2 ^a			Multivariate Model 3 ^a		
	OR	95% CI	P ^b	OR	95% CI	P ^b	OR	95% CI	P ^b	OR	95% CI	P ^b
T1-weighted	4.08	1.34–12.40	.013	3.34	1.08–10.31	.036	3.12	0.96–10.11	.058	1.57	0.48–5.20	.458
TOF	1.98	0.80–4.93	.141	2.54	0.94–6.82	.065	2.70	0.90–8.13	.077	1.21	0.37–3.93	.756
MPRAGE	0.86	0.51–1.45	.561	0.85	0.48–1.48	.557	0.98	0.53–1.79	.941	0.56	0.28–1.12	.101

Note:—SIR_{IPH-to-muscle} indicates the maximum signal intensity of carotid IPH/the mean signal intensity of the sternocleidomastoid muscle.

^a Multivariate model 1 was adjusted for age, sex, and history of smoking; model 2 was further adjusted using model 1 and total luminal occlusion of the carotid artery. Model 3 was further adjusted using model 1 and the volume of carotid IPH and LRNC.

^b Associations between patients with and without ipsilateral ACI lesions were assessed using the OR values.

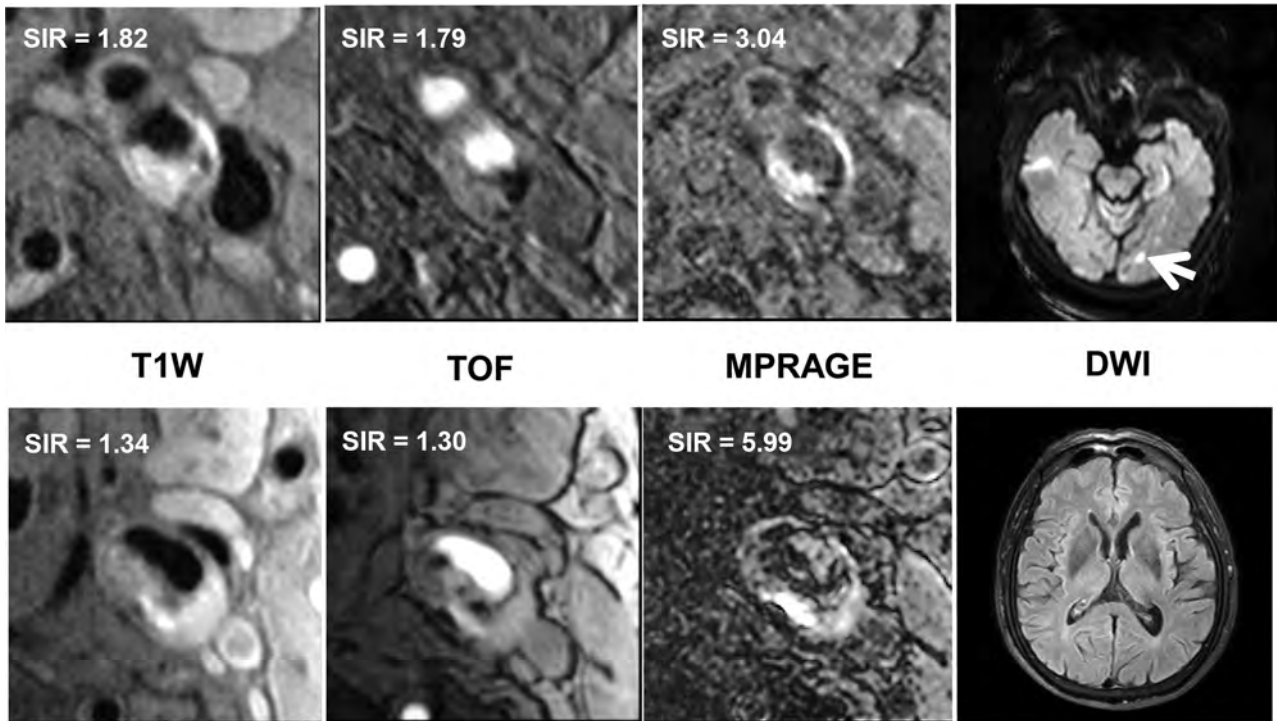


FIG 3. Comparison of the SIR of carotid IPH on T1-weighted MR imaging sequences, including T1-weighted, TOF, and MPRAGE, between patients with ACI (4 images above, hyperintense on DWI as the arrow indicates) and without ACI (4 images below, no abnormality on DWI). It shows that the patient with the higher SIR on T1-weighted images had ACI lesions in the ipsilateral hemisphere.

MPRAGE (2.92 [2.23–4.11] versus 3.04 [2.37–3.99], $P = .523$) images between patients with and without ipsilateral ACI lesions (Fig 2).

Association between SIRs of Carotid IPH and the Ipsilateral ACI

Univariate regression analysis (Table 4) revealed that the SIRs of carotid IPH on T1-weighted images were significantly associated with the presence of ipsilateral ACI lesions (OR, 4.08; 95% CI, 1.34–12.40; $P = .013$). After adjustment for clinical confounding factors of age, sex, and history of smoking (model 1), this association remained statistically significant (OR, 3.34; 95% CI, 1.08–10.31; $P = .036$). After further adjustment for total luminal occlusion of the carotid artery (model 2), this association appeared marginally significant (OR, 3.12; 95% CI, 0.96–10.11; $P = .058$). However, after further adjustment for the volume of carotid IPH and LRNC (model 3), this association was not significant (OR, 1.57; 95% CI, 0.48–5.20; $P = .458$). Figure 3 shows

that a patient with higher SIRs of carotid IPH against muscle on T1-weighted images had ACI lesions in the ipsilateral hemisphere on DWI. There were no significant associations between SIRs of carotid IPH on TOF and MPRAGE images and the presence of ACI lesions before and after adjustment for clinical confounding factors, total luminal occlusion of the carotid artery, and the size of carotid IPH and LRNC (all, $P > .05$; Table 4).

DISCUSSION

The present study investigated the association between the SIRs of carotid IPH on different T1-weighted MR imaging sequences and ipsilateral ACI lesions in patients with carotid hemorrhagic plaques using multicontrast MR vessel wall imaging. Although we found that patients with ipsilateral ACI lesions had significantly higher SIRs of carotid IPH on T1-weighted images than those without statistically, there was still an overlap in the SIRs of carotid IPH on T1-weighted images between the

two groups. Only extremely low (range, 1.06–1.14) or high (range, 1.55–1.82) SIR values will allow a fairly accurate prediction of whether an ACI is present. Further studies are warranted combining SIRs of IPH with other metrics for predicting ACI, particularly for those IPHs with SIRs within this overlap. Furthermore, there was a significant association between the SIR of carotid IPH on T1-weighted images and the presence of ipsilateral ACI lesions, which was independent of traditional risk factors. After further adjustment for total luminal occlusion of the carotid artery, this association appeared marginally significant. This finding implies that the association between the SIRs of IPH on T1-weighted images and ACI might be influenced by the luminal occlusion. However, this association was not significant after further adjustment for the volume of carotid IPH and LRNC, suggesting that the differences of carotid SIRs on T1-weighted images between the two groups might be, in part, attributed to the different sizes of carotid IPH and LRNC. Our findings might provide additional imaging information in predicting the presence of cerebrovascular ischemic events beyond the mere presence of IPH.

In the present study, patients with ACI lesions were found to be younger than those without, which was consistent with the study by Turin et al,²³ in which a lifetime risk of stroke was higher in younger age than in older age. Another recent study by Feigin et al²⁴ indicated that the global lifetime risk of stroke declined with age in patients older than 70 years, due to age-related competing risks from other diseases.²⁵ In addition, the present study also demonstrated that patients with ipsilateral ACI lesions were more likely to smoke than those without, which was in line with previous studies. Wolf et al²⁶ and Donnan et al²⁷ have reported that cigarette smoking was an independent risk factor for cerebral infarct. Nicotine has been considered a key component that contributes to the influence of cigarette smoking on the cerebral infarct. Li et al²⁸ demonstrated that mitochondrial oxidative stress induced by nicotine may have important implications for the pathogenesis and pathophysiology of ischemic stroke.

In this study, we assessed the association between the SIRs of carotid IPH on different MR images and ipsilateral ACI lesions in symptomatic patients with carotid hemorrhagic plaques. We found that the SIRs of carotid IPH on T1-weighted images were associated with the presence of ipsilateral ACI lesions in symptomatic patients regardless of clinical confounding factors, including age, sex, and a history of smoking. However, this association was not significant after further adjustment for total luminal occlusion of the carotid artery and the volume of carotid IPH and LRNC. In contrast, previous studies that included patients both with and without carotid IPH also demonstrated the association between the T1-weighted signal of carotid plaque and cerebral ischemic lesions. Takemoto et al²⁹ reported that a higher T1-weighted signal intensity of carotid plaque was present more often in symptomatic patients with lesions positive for cerebral ischemia on DWI. In a study of patients with carotid artery stenosis scheduled for carotid endarterectomy or carotid artery stenting, Kurosaki et al³⁰ documented that plaques with higher signal intensity on T1-weighted images were at higher risk of

causing ischemic events. However, the mechanism for the association between the SIRs of carotid IPH on T1-weighted images and the presence of ACI remained unclear.

Previous studies have demonstrated that the signal intensity of IPH was associated with the age of hemorrhage within plaques, and high signal intensity of IPH on T1-weighted images may indicate a recent hemorrhage.³¹ In addition, the increasing size of IPH, which means a higher concentration of methemoglobin locally within the plaque, may also play a role in the occurrence of stronger SIRs of IPH on T1-weighted images. A study by Leung and Moody³² revealed that erythrocyte degradation caused intraplaque deposition of methemoglobin, which had a strong T1-shortening effect. In the present study, no significant association was found between SIRs of carotid IPH on T1-weighted images and the presence of ACI when adjusted for clinical confounding factors and carotid IPH and LRNC volume, suggesting that the difference in carotid SIRs on T1-weighted images between the two patient groups might be, in part, attributed to the different sizes of IPH and LRNC.

In addition, we found that patients with ACI lesions had significantly larger carotid IPH and LRNC, respectively, than those without. Takaya et al⁵ reported that carotid plaques with a larger area of IPH (hazard ratio for a 10-mm² increase, 2.6; 95% CI, 1.4–4.6; $P = .006$) were significantly associated with subsequent ipsilateral carotid cerebrovascular events. However, the mechanism for this phenomenon remained uncertain. Previous studies indicated that the volume of IPH was significantly independently associated with minor fibrous cap disruption in carotid arteries (OR, 2.152; 95% CI, 1.241–3.730; $P = .006$).³³ Another study by Zhao et al³⁴ indicated that patients with larger LRNC plaques might have larger cerebral infarcts. This phenomenon might be because that the large LRNC volume would accompany a larger fibrous cap area and increase the risk of rupture. Therefore, the size of carotid IPH and LRNC may influence, in part, the association between SIRs of carotid IPH and ACI. In this study, it is possible that carotid SIRs on T1-weighted imaging may combine both IPH and LRNC. Histologically, it is hypothesized that IPH occurs within the large lipid-rich necrotic core. Although the IPH was outlined on MPRAGE images, it is possible to include the LRNC in the ROI of IPH when the IPH is inhomogeneous. Our findings suggest that the SIR of IPH might be a surrogate for the size of the IPH or LRNC in predicting ACI.

An interesting issue we observed is that the SIRs of carotid IPH on MPRAGE images in patients with ipsilateral ACI lesions tended to be similar to those without (Median, 2.92; 25–75 Percentiles, 2.23–4.11 versus Median, 3.04; 25–75 Percentiles, 2.37–3.99, $P = .523$), a finding that was inconsistent with those in previous studies. A recent study by Wang et al¹⁶ indicated that carotid IPH signals on MPRAGE images on the symptomatic side were significantly higher (mean, 5.8 ± 2.4 versus 4.7 ± 1.8 , $P = .004$) than those on the asymptomatic side in symptomatic patients with bilateral carotid IPHs. There were a number of methodologic differences, including different sampling techniques and sample sizes, between the study by Wang et al¹⁶ and the present study. For example, in our study, patients included were divided into two groups due to the presence or absence of ACI lesions on DWI, while in the study by Wang et

al, carotid plaques with IPH were divided into symptomatic and asymptomatic sides according to the recent symptoms, and the ACI lesions in that study on the symptomatic side were not distinct. More studies need to be performed to investigate the differences in this issue.

There are some limitations to this study. First, it only investigated the association between the SIRs of carotid IPH and ischemic stroke but did not analyze the difference in the age of IPH between patients with and without ACI lesions. The age of IPH may influence the association between the SIRs of IPH and ipsilateral ACI lesions. Future studies are warranted. Second, the current in-plane spatial resolution used in this study was 0.55 mm, which is limited to accurately quantifying small IPHs. Third, in this study, approximately one-fourth of the 201 patients were excluded due to “poor registration of multisequences,” suggesting that the method, at least in a certain number of subjects, is just not feasible. Future studies with larger samples and more improved technical methods are needed. Finally, although patients were recruited from a multicenter study, carotid IPH signal measurements on different sequences were performed on a single platform using a unified MR imaging protocol. Future studies using similar but not identical techniques are needed.

CONCLUSIONS

The signal intensity ratio of carotid IPH on T1-weighted images is associated with ACI in symptomatic patients with carotid hemorrhagic plaques. This association is independent of traditional risk factors but not of the size of plaque compositions. The possibility of applying T1 signals of carotid IPH to predict subsequent cerebrovascular ischemic events needs to be prospectively verified.

Disclosures: Chun Yuan—RELATED: Grant: Philips Healthcare; UNRELATED: Grants/Grants Pending: National Institutes of Health, Philips Healthcare.* Money paid to the institution.

REFERENCES

1. Liu L, Wang D, Wong KS, et al. **Stroke and stroke care in China: huge burden, significant workload, and a national priority.** *Stroke* 2011;42:3651–54 CrossRef Medline
2. Barnett HJ, Gunton RW, Eliasziw M, et al. **Causes and severity of ischemic stroke in patients with internal carotid artery stenosis.** *JAMA* 2000;283:1429–36 CrossRef Medline
3. Underhill HR, Hatsukami TS, Cai J, et al. **A noninvasive imaging approach to assess plaque severity: the carotid atherosclerosis score.** *AJNR Am J Neuroradiol* 2010;31:1068–75 CrossRef Medline
4. Hosseini AA, Kandiyil N, Macsweeney ST, et al. **Carotid plaque hemorrhage on magnetic resonance imaging strongly predicts recurrent ischemia and stroke.** *Ann Neurol* 2013;73:774–84 CrossRef Medline
5. Takaya N, Yuan C, Chu B, et al. **Association between carotid plaque characteristics and subsequent ischemic cerebrovascular events: a prospective assessment with MRI—initial results.** *Stroke* 2006;37:818–23 CrossRef Medline
6. Singh N, Moody AR, Gladstone DJ, et al. **Moderate carotid artery stenosis: MR imaging—depicted intraplaque hemorrhage predicts risk of cerebrovascular ischemic events in asymptomatic men.** *Radiology* 2009;252:502–08 CrossRef Medline
7. McNally JS, McLaughlin MS, Hinckley PJ, et al. **Intraluminal thrombus, intraplaque hemorrhage, plaque thickness, and current smoking optimally predict carotid stroke.** *Stroke* 2015;46:84–90 CrossRef Medline
8. Fryer JA, Myers PC, Appleberg M. **Carotid intraplaque hemorrhage: significance of neovascularity.** *J Vasc Surg* 1987;6:341–49 CrossRef Medline
9. Dong L, Underhill HR, Yu W, et al. **Geometric and compositional appearance of atheroma in an angiographically normal carotid artery in patients with atherosclerosis.** *AJNR Am J Neuroradiol* 2010;31:311–16 CrossRef Medline
10. Cai Y, He L, Yuan C, et al. **Atherosclerotic plaque features and distribution in bilateral carotid arteries of asymptomatic elderly population: a 3D multicontrast MR vessel wall imaging study.** *Eur J Radiol* 2017;96:6–11 CrossRef Medline
11. Sun J, Underhill HR, Hippe DS, et al. **Sustained acceleration in carotid atherosclerotic plaque progression with intraplaque hemorrhage: a long-term time course study.** *JACC Cardiovasc Imaging* 2012;5:798–804 CrossRef Medline
12. Takaya N, Yuan C, Chu B, et al. **Presence of intraplaque hemorrhage stimulates progression of carotid atherosclerotic plaques: a high-resolution magnetic resonance imaging study.** *Circulation* 2005;111:2768–75 CrossRef Medline
13. Moody AR, Murphy RE, Morgan PS, et al. **Characterization of complicated carotid plaque with magnetic resonance direct thrombus imaging in patients with cerebral ischemia.** *Circulation* 2003;107:3047–52 CrossRef Medline
14. Yamada K, Yoshimura S, Shirakawa M, et al. **Asymptomatic moderate carotid artery stenosis with intraplaque hemorrhage: progression of degree of stenosis and new ischemic stroke.** *J Clin Neurosci* 2019;63:95–99 CrossRef Medline
15. Yamada K, Kawasaki M, Yoshimura S, et al. **High-intensity signal in carotid plaque on routine 3D-TOF-MRA is a risk factor of ischemic stroke.** *Cerebrovasc Dis* 2016;41:13–18 CrossRef Medline
16. Wang X, Sun J, Zhao X, et al; CARE-II study investigators. **Ipsilateral plaques display higher T1 signals than contralateral plaques in recently symptomatic patients with bilateral carotid intraplaque hemorrhage.** *Atherosclerosis* 2017;257:78–85 CrossRef Medline
17. Zhao X, Li R, Hippe DS, et al; CARE-II Investigators. **Chinese Atherosclerosis Risk Evaluation (CARE II) study: a novel cross-sectional, multicentre study of the prevalence of high-risk atherosclerotic carotid plaque in Chinese patients with ischaemic cerebrovascular events—design and rationale.** *Stroke Vasc Neurol* 2017;2:15–20 CrossRef Medline
18. Kerwin W, Xu D, Liu F, et al. **Magnetic resonance imaging of carotid atherosclerosis: plaque analysis.** *Top Magn Reson Imaging* 2007;18:371–78 CrossRef Medline
19. Cai JM, Hatsukami TS, Ferguson MS, et al. **Classification of human carotid atherosclerotic lesions with in vivo multicontrast magnetic resonance imaging.** *Circulation* 2002;106:1368–73 CrossRef Medline
20. Li D, Zhao H, Chen X, et al. **Identification of intraplaque haemorrhage in carotid artery by simultaneous non-contrast angiography and intraPlaque haemorrhage (SNAP) imaging: a magnetic resonance vessel wall imaging study.** *Eur Radiol* 2018;28:1681–86 CrossRef Medline
21. Eto A, Kinoshita Y, Matsumoto Y, et al. **Relationship between the carotid plaque T1 relaxation time and the plaque-to-muscle signal intensity ratio on black-blood magnetic resonance imaging scans.** *J Stroke Cerebrovasc Dis* 2016;25:2580–84 CrossRef Medline
22. **North American Symptomatic Carotid Endarterectomy Trial: methods, patient characteristics, and progress.** *Stroke* 1991;22:711–20 CrossRef Medline
23. Turin TC, Okamura T, Afzal AR, et al. **Hypertension and lifetime risk of stroke.** *J Hypertens* 2016;34:116–22 CrossRef Medline
24. Feigin VL, Nguyen G, Cercy K, et al; GBD 2016 Lifetime Risk of Stroke Collaborators. **Global, regional, and country-specific lifetime risks of stroke.** *N Engl J Med* 2018;379:2429–37 CrossRef Medline
25. Naghavi M, Abajobir AA, Abbafati C, et al. **Global, regional, and national age-sex specific mortality for 264 causes of death, 1980–2016: a systematic analysis for the Global Burden of Disease Study.** *Lancet* 2017;390:1151–16 CrossRef Medline

26. Wolf PA, D'Agostino RB, Kannel WB, et al. **Cigarette smoking as a risk factor for stroke: the Framingham Study.** *JAMA* 1988;259:1025–29 Medline
27. Donnan GA, McNeil JJ, Adena MA, et al. **Smoking as a risk factor for cerebral ischaemia.** *Lancet* 1989;2:643–47 CrossRef Medline
28. Li C, Sun H, Arrick DM, et al. **Chronic nicotine exposure exacerbates transient focal cerebral ischemia-induced brain injury.** *J Appl Physiol* 2016;120:328–33 CrossRef Medline
29. Takemoto K, Ueba T, Takano K, et al. **Quantitative evaluation using the plaque/muscle ratio index panels predicts plaque type and risk of embolism in patients undergoing carotid artery stenting.** *Clin Neurol Neurosurg* 2013;115:1298–1303 CrossRef Medline
30. Kurosaki Y, Yoshida K, Fukumitsu R, et al. **Carotid artery plaque assessment using quantitative expansive remodeling evaluation and MRI plaque signal intensity.** *J Neurosurg* 2016;124:736–42 CrossRef Medline
31. Chu B, Kampschulte A, Ferguson MS, et al. **Hemorrhage in the atherosclerotic carotid plaque: a high-resolution MRI study.** *Stroke* 2004;35:1079–84 CrossRef Medline
32. Leung G, Moody AR. **MR imaging depicts oxidative stress induced by methemoglobin.** *Radiology* 2010;257:470–76 CrossRef Medline
33. Cui Y, Qiao H, Ma L, et al. **Association of age and size of carotid artery intraplaque hemorrhage and minor fibrous cap disruption: a high-resolution magnetic resonance imaging study.** *J Atheroscler Thromb* 2018;25:1222–30 CrossRef Medline
34. Zhao H, Zhao X, Liu X, et al. **Association of carotid atherosclerotic plaque features with acute ischemic stroke: a magnetic resonance imaging study.** *Eur J Radiol* 2013;82:e465–70 CrossRef Medline

Distinguishing Recurrent Thyroid Cancer from Residual Nonmalignant Thyroid Tissue Using Multiphasic Multidetector CT

J.M. Debnam, N. Guha-Thakurta, J. Sun, W. Wei, M.E. Zafereo, M.E. Cabanillas, N.M. Buisson, and D. Schellingerhout



ABSTRACT

BACKGROUND AND PURPOSE: During thyroidectomy incomplete resection of the thyroid gland may occur. This complicates the imaging surveillance of these patients as residual thyroid needs to be distinguished from local recurrence. Therefore, the purpose of this study was to determine if multiphasic multi-detector computed tomography (4D-MDCT) can differentiate residual nonmalignant thyroid tissue and recurrent thyroid carcinoma after thyroidectomy.

MATERIALS AND METHODS: In this retrospective study, Hounsfield unit values on multiphasic multidetector CT in precontrast, arterial (25 seconds), venous (55 seconds), and delayed (85 seconds) phases were compared in 29 lesions of recurrent thyroid cancer, 29 with normal thyroid, and 29 with diseased thyroid (thyroiditis/multinodular thyroid). The comparison of Hounsfield unit values among lesion types by phase was performed using ANOVA. The performance of Hounsfield unit values to predict recurrence was evaluated by logistic regression and receiver operating characteristic analysis.

RESULTS: All 3 tissue types had near-parallel enhancement characteristics, with a wash-in–washout pattern. Statistically different Hounsfield unit density was noted between the recurrence (lowest Hounsfield unit), diseased (intermediate Hounsfield unit), and normal (highest Hounsfield unit) thyroid groups throughout all 4 phases ($P < .001$ for each group and in each phase). Dichotomized recurrence-versus-diseased/normal thyroid tissue with univariate logistic regression analysis demonstrated that the area under the receiver operating characteristic curve for differentiating benign from malignant thyroid for the various phases of enhancement was greatest in the precontrast phase at 0.983 (95% CI, 0.954–1), with a cutoff value of ≤ 62 (sensitivity/specificity, 0.966/0.983) followed by the arterial phase.

CONCLUSIONS: Recurrent thyroid carcinoma can be distinguished from residual nonmalignant thyroid tissue using multiphasic multidetector CT with high accuracy. The maximum information for discrimination is in the precontrast images, then the arterial phase. An optimal clinical protocol could be built from any number of phases but should include a precontrast phase.

ABBREVIATIONS: 4D-MDCT = multiphasic multidetector CT; ROC = receiver operating characteristic

In the United States, between 1975 and 2013, the incidence of thyroid cancer increased by 211% and the average annual increases in incidence and mortality rates were 3.6% and 1.1%, respectively.¹ Papillary thyroid carcinoma, the least aggressive type of thyroid

cancer, accounts for most new cases.² In patients with thyroid cancer, thyroid surgery is the mainstay of treatment.^{3,4}

After the operation, approximately 20%–30% of patients experience local recurrence of soft-tissue or nodal metastases.⁵ Routine follow-up imaging to detect early recurrence includes CT and sonography to assess structural recurrence and thyroid-stimulating hormone and thyroglobulin levels for biochemical assessment.⁶

During thyroidectomy, an area of difficulty for surgeons is the Berry ligament, which tethers the thyroid to the trachea, because the recurrent laryngeal nerve is generally intimately associated with this ligament.⁷ In inexperienced hands, incomplete resection of the thyroid at the Berry ligament may occur as a result of the surgeon's attempt to avoid damaging this nerve.⁸ D'Andrea et al⁹ studied the rate of residual thyroid tissue after total thyroidectomy and found that 34 of 102 patients (33.3%) had "significant thyroid tissue remnants" in the thyroid bed.

Received October 8, 2019; accepted after revision February 24, 2020.

From the Departments of Diagnostic Radiology, Section of Neuroradiology (J.M.D., N.G.-T., N.M.B., D.S.); Biostatistics (J.S., W.W.); Head and Neck Surgery, Division of Surgery (M.E.Z.); Endocrine Neoplasia and Hormonal Disorders (M.E.C.); and Cancer Systems Imaging (D.S.); The University of Texas MD Anderson Cancer Center, Houston, Texas.

The University of Texas MD Anderson Cancer Center is supported, in part, by the National Institutes of Health through Cancer Center Support Grant CA016672.

Please address correspondence to J. Matthew Debnam, MD, The University of Texas MD Anderson Cancer Center, 1400 Pressler Blvd, Unit 1482, Houston, TX 77030; e-mail: Matthew.Debnam@mdanderson.org

Indicates open access to non-subscribers at www.ajnr.org

<http://dx.doi.org/10.3174/ajnr.A6519>

The problem this creates in the imaging follow-up of these patients is that residual tissue needs to be correctly characterized as either benign or malignant. Accurate delineation of thyroid bed tissue as residual thyroid may avoid an unnecessary operation with complications including damage to the recurrent laryngeal nerve as well as the inherent risks of anesthesia. On the other hand, treatment of recurrent disease is necessary to avoid unfavorable outcomes including locoregional complications such as invasion of the trachea and esophagus and to avoid distant metastases.¹⁰

Differentiation between these 2 entities is not always straightforward.⁷ An additional diagnostic challenge is superimposed if there is background benign thyroid disease in the residual thyroid tissue, such as thyroiditis or a multinodular goiter.¹¹ To the best of our knowledge, no prior studies have addressed this issue using CT.

In this study, we address this gap in imaging knowledge and determine whether multiphasic multidetector CT (4D-MDCT) can be used to characterize residual thyroid tissue after an operation as either benign or malignant. 4D-MDCT involves high-resolution helical CT before and during the administration of a bolus of iodinated contrast at specific points in time to allow the changing distribution of contrast to be assessed. 4D-MDCT is in common clinical use for the localization of parathyroid adenomas, which show characteristic contrast handling attributes that allow accurate localization.¹²⁻¹⁷

We hypothesized that 4D-MDCT can be used similarly to differentiate recurrent thyroid carcinoma from residual normal and diseased thyroid tissue. We also hypothesized that recurrent tumor and normal and diseased thyroid would have diagnostic patterns of contrast enhancement that allow them to be clearly discriminated.

MATERIALS AND METHODS

Our institutional review board approved this study and waived the requirement for informed consent. Data were acquired in compliance with all applicable Health Insurance Portability and Accountability Act regulations.

Study Population

We reviewed the medical records of 152 consecutive patients who underwent 4D-MDCT of the thyroid beds for localization of suspected recurrent thyroid carcinoma following total thyroidectomy. In these patients, recurrent lesions were suspected due to an elevated thyroglobulin level, surveillance CT findings, surveillance ultrasound findings, and/or the results of an ultrasound-guided fine-needle aspiration. For inclusion in this group (group 1), patients were required to have pathologically proved disease by either fine-needle aspiration or subsequent surgical resection. The 4D-MDCT studies in group 1 were performed between 48 days and 14 years 9 months (mean, 4 years 3 months) after thyroidectomy.

Seventy-five separate patients underwent 4D-MDCT for localization of a parathyroid adenoma. From these patients, we identified 2 groups of patients: patients with a normal thyroid, defined as a homogeneously enhancing thyroid gland on 4D-MDCT (group 2); and patients with a diseased-but-nonmalignant

thyroid, defined as a thyroiditis with increased vascular flow or benign multinodular goiter on sonography or pathology, and a heterogeneously enhancing thyroid gland on 4D-MDCT (group 3). For inclusion in the study, patients with a normal or diseased thyroid had to have no evidence of a primary cancer either at the time of the 4D-MDCT study or previously.

The medical records were searched until equal numbers of recurrent lesions (group 1) and both normal thyroid (group 2) and diseased thyroid (group 3) cases in each group were identified. The review was completed when there were an equal number of cases in each of the 3 study groups.

Image Acquisition

The 4D-MDCT examinations were performed on a multidetector CT LightSpeed scanner (GE Healthcare) with the following parameters: 140 kV, 220–250 mA, and a 1.25-mm section thickness covering the neck from the bottom of the orbits to the arch of the aorta. We acquired 4 phases: an initial noncontrast helix and then 3 additional helices acquired after intravenous contrast agent injection in the arterial phase (25 seconds after the start of the contrast injection), venous phase (55 seconds after injection), and delayed phase (85 seconds after injection).

ROI Analysis

CT images were transferred to an ADW-2 workstation (GE Healthcare) with Volume Share 2, Version 4.4, software. A head and neck radiologist (J.M.D.) with >15 years of experience in head and neck radiology who was not blinded to the tissue type results drew ROIs around the recurrent lesions and areas of normal and diseased thyroid using freehand contouring. In the freehand contouring technique (Fig 1), the ROI was contoured to the visual outline of the lesion or the thyroid gland through the different phases of enhancement, with no requirement for the ROI size to remain constant. The outline from the largest area of enhancement representing the entire lesion was copied onto a similar site on the pre-contrast phase image. An attempt was made to place the contour 1 mm from the edge of the lesion to minimize the effects of partial volume averaging. Any visible surgical clips or calcifications associated with the lesions were excluded.

Mean, SD, and minimum-maximum of the grouped data were calculated to compare recurrence, normal thyroid, and diseased thyroid Hounsfield unit values through the 4 phases of enhancement. First, ANOVA was used to compare Hounsfield unit values among 3 tissue types. Tukey-Kramer adjustment was used to control the overall type I error rate at 5%. A 2-sample *t* test was used to compare Hounsfield unit values of dichotomized cases of recurrence versus benign thyroid (normal and diseased combined). Second, a univariate logistic regression model was used to associate Hounsfield units with tissue status (recurrence versus benign thyroid). As a high correlation among the different phases was determined, a multivariate model was reduced to a univariate model by the backward deletion. Third, the performance of Hounsfield units to discriminate recurrence from benign thyroid tissue using both the results of the univariate and bivariate analyses was evaluated using receiver operating characteristic (ROC) curve analysis. ROC analysis was used to determine the optimal cutoff point by maximizing the Youden index, sensitivity + specificity–1. Next, ROC

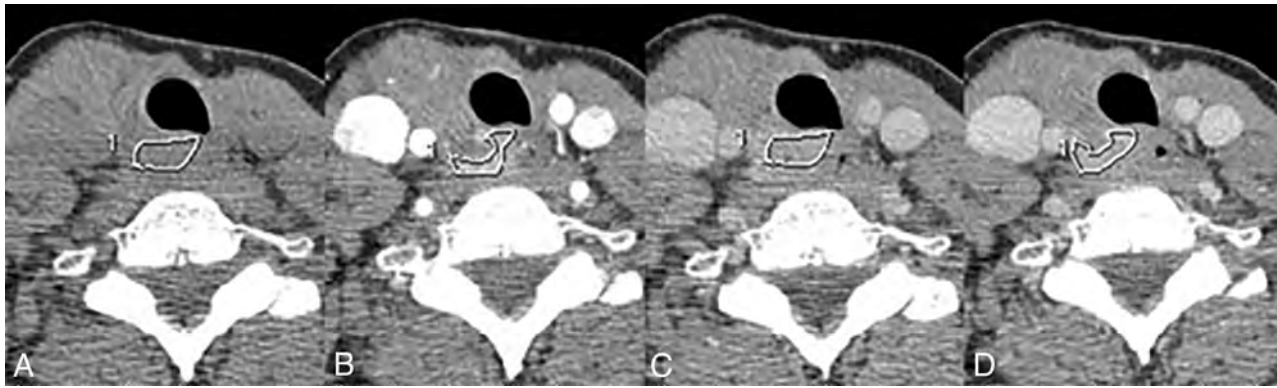


FIG 1. Freehand contouring method of drawing the ROI. In the freehand contouring method, the borders of the lesion were traced on images in the arterial (B), venous (C), and delayed (D) phases of enhancement, with no requirement for the ROI size to remain constant. The largest area, the venous phase in this example, was then copied onto the (A) precontrast phase, where the lesion contrast with background was typically worse.

Table 1: Summary of Hounsfield units by phase and lesion type using 3 categories—normal, diseased, and recurrent

Group	No.	Mean	SD	F	P Value ^a	Tukey HSD Comparisons		
						Disease	Normal	Recurrence
Precontrast								
Normal	29	109.03	16.19	133.73	<.001			
Disease	29	88.07	17.54				<0.001	<0.0001
Recurrence	29	37.09	17.91					<0.0001
Arterial								
Normal	29	233.93	32.56	105.45	<.001			
Disease	29	185.24	36.25				<0.0001	<0.0001
Recurrence	29	99.98	37.67					<0.001
Venous								
Normal	29	191.72	29.5	72.52	<.001			
Disease	29	161.03	36.74				0.0017	<0.0001
Recurrence	29	90.61	31.69					<0.0001
Delayed								
Normal	29	172.31	24.55	67.46	<.001			
Disease	29	144.07	31.06				0.0008	<0.001
Recurrence	29	87.83	28.6					<0.0001

Note:—HSD indicates honestly significant difference.

^aP values were from ANOVA.

curve analysis of Hounsfield units to discriminate recurrence from benign thyroid tissue was performed using univariate and multivariate analyses with 2, 3, or 4 combinations of the various 4 phases (precontrast, arterial, venous, and delayed).

Similar overall root mean square error values were then calculated for each phase. Matrix scatterplots with Pearson correlation were used to compare the Hounsfield unit density through the 4 phases. All tests were 2-sided, and $P \leq .05$ was considered statistically significant. Statistical analysis was performed using SAS, Version 9.4 (SAS Institute) and R statistical and computing software, Version 3.5.3 (<http://www.r-project.org/>).

RESULTS

Study Population

Twenty-nine recurrent thyroid cancer lesions (group 1) were identified in 24 patients (16 women, 8 men; 21–80 years of age; mean, 52.5 ± 15.8 years); 5 patients each had 2 separate lesions. The types of primary thyroid cancer were as follows: papillary thyroid carcinoma ($n=21$), follicular variant papillary thyroid carcinoma, ($n=3$), medullary thyroid carcinoma ($n=3$), and Hurthle cell

Table 2: Summary of Hounsfield units by phase and lesion type using 2 categories—recurrence and benign (includes both normal and diseased thyroid)

Phase/Group	No.	Mean	SD	Min	Max	P Value
Precontrast						
Benign thyroid	58	98.55	19.79	54	138	<.001
Recurrence	29	37.09	17.91	10.8	93	
Arterial						
Benign thyroid	58	209.59	42.06	131	331	<.001
Recurrence	29	99.98	37.67	39.7	174	
Venous						
Benign thyroid	58	176.38	36.47	96	263	<.001
Recurrence	29	90.61	31.69	28.2	156	
Delayed						
Benign thyroid	58	158.19	31.19	94	238	<.001
Recurrence	29	87.83	28.6	24.2	155	

Note:—Min indicates minimum; Max, maximum.

carcinoma ($n=2$). Sixteen of 24 patients (19 lesions) received radioactive iodine following thyroidectomy. The lesions ranged in size from 0.7 to 2.4 cm (mean, 1.2 ± 0.4 cm) and were diagnosed by surgical resection ($n=28$) or fine-needle aspiration ($n=1$). Twenty-nine patients with normal thyroid (group 2) (25 women,

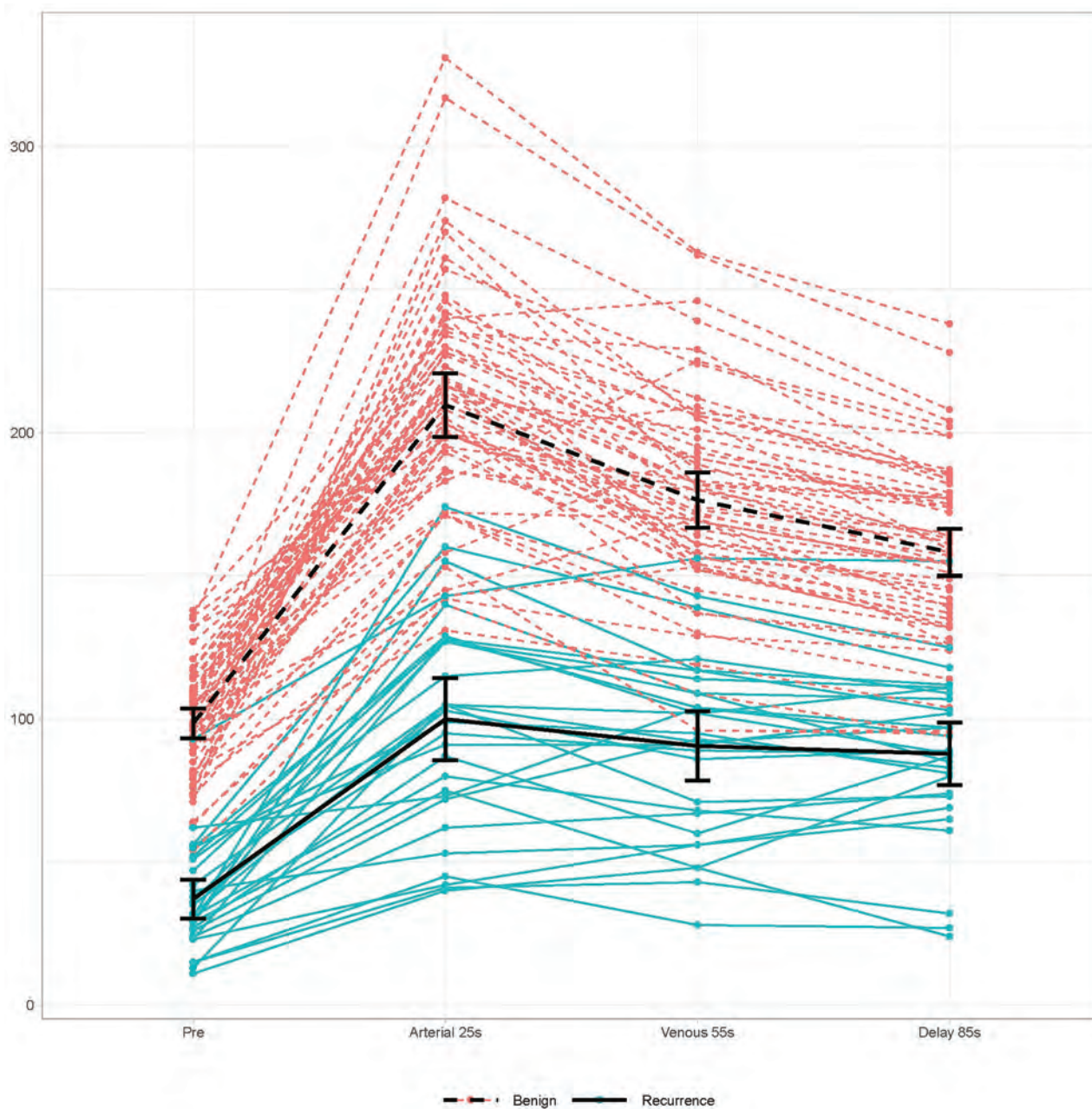


FIG 2. Line graphs with error bars show the evolution of Hounsfield unit density across time for the recurrent disease (blue solid lines) and benign thyroid (red dashed lines) groups through the 4 phases. The peak Hounsfield unit density for both groups occurred in the arterial phase followed by washout of contrast.

4 men; 34–85 years of age; mean, 63 ± 13.2 years) and 29 patients with diseased thyroid (group 3) (18 multinodular goiters, 11 cases of thyroiditis) (23 women, 6 men; 45–86 years of age; mean, 63.5 ± 10.9 years) were also included.

Discrimination among Normal, Diseased, and Recurrent Thyroid

Hounsfield unit densities for recurrent, normal, and diseased thyroids were compared precontrast and at 25 (arterial), 55 (venous), and 85 (delayed) seconds. ANOVA analysis showed that recurrent disease demonstrated significantly lower Hounsfield unit values in all 4 phases compared with diseased thyroid

($P < .001$). Diseased thyroid also had a significantly lower values than normal thyroid (Table 1). Combined benign thyroid (normal and diseased thyroid) was also significantly different from recurrence ($P < .001$) in all 4 phases using a 2-sample t test (Table 2). A line graph with error bars was drawn to show this evolution of Hounsfield unit density with time for the recurrent disease and benign thyroid groups (Fig 2).

Statistical Analysis

On univariate logistic regression analysis of benign thyroid versus recurrence, the odds ratios for differentiating the various phases were as follows: precontrast odds ratio, 0.856 (95% CI, 0.767–

09.11); arterial OR, 0.92 (95% CI, 0.867–0.952); venous OR, 0.928 (95% CI, 0.892–0.954); and delayed OR, 0.916 (95% CI, 0.874–0.946). Statistically significant differences were noted in each phase ($P < .001$) (Table 3). ROC curve analysis of Hounsfield units to discriminate recurrence from benign thyroid showed that the area under the ROC curve was slightly greater in the precontrast phase (0.983) than in the arterial (0.979), venous (0.965), and delayed phases (0.957) (Fig 3). The area under the curve, 95% confidence intervals, optimal Hounsfield unit cutoff, sensitivity, and specificity are provided in Table 4. Similar ROC curve analysis of Hounsfield units using univariate and multivariate analyses with combinations of 2, 3, or 4 of the 4 phases (precontrast, arterial, venous, and delayed) (Table 5) showed that the area under the ROC curve was slightly greater compared with the precontrast phase alone. However, compared

with the precontrast phase, none of these combinations were statistically significant ($P > .05$) (Table 5).

The optimal cutoff point to differentiate benign thyroid from recurrence in each of the 4 phases by ROC analysis was as follows: precontrast, ≤ 62 HU; arterial phase, ≤ 129 HU; venous phase, ≤ 120.6 HU; and delayed phase, ≤ 125 HU (Fig 4). Overall root mean square error values were as follows: precontrast, 34.8; arterial, 29.5; venous, 26.4; and delayed, 26.

To validate these findings, we made an effort to combine the phases into an indicator with better performance, but matrix scatterplots revealed 2 outlier cases that were misclassified regardless of phase, indicating that a combination of phases could not be used to improve performance (though there might be clinical reasons to include >1 phase).

Table 3: Summary of univariate logistic regression model using Hounsfield units to predict lesion status (benign thyroid and recurrence)

Phase	Odds Ratio	95% LCL	95% UCL	P Value
Precontrast	0.856	0.767	0.911	<.001
Arterial	0.92	0.867	0.952	<.001
Venous	0.928	0.892	0.954	<.001
Delayed	0.916	0.874	0.946	<.001

Note:—LCL indicates lower control limit; UCL, upper control limit.

DISCUSSION

Our results demonstrate that 4D-MDCT can be used to distinguish recurrent thyroid carcinoma from benign thyroid tissue, including both normal and diseased nonmalignant thyroids. In all 4 phases, the Hounsfield unit value was significantly lower for recurrent thyroid carcinoma than for benign tissue, with diseased thyroid intermediate between recurrent and normal thyroid. The mean time-enhancement curves ran parallel and did not cross in any phase. Based on the ROC curve analysis, the best single phase to distinguish recurrent disease from benign thyroid

tissue, both normal and diseased, was the precontrast phase with a cutoff value of ≥ 62 HU, yielding a sensitivity of 0.966 and specificity of 0.983. Arterial, venous, and delayed phases each followed with cutoff values of 129, 120.6, and 125, respectively, with sensitivity/specificities of 0.828/1, 0.897/0.931, and 0.966/0.879, respectively. Each individual phase, in other words, yields quite acceptable performance, but the precontrast phase, according to our data, contains the most diagnostic information for this application. The ROC curve analysis of univariate and multivariate data showed that the area under the curve could be slightly improved from 0.983 (precontrast phase alone) in various phase combinations of 2, 3, and 4 phases, but none of these were statistically significant ($P > .05$) in comparison with the precontrast phase alone.

On precontrast MDCT, both normal and diseased thyroid had a higher Hounsfield unit density compared with recurrence. This is attributed, at least in part, to the iodine content of normal thyroid tissue and the inclusion of this thyroid tissue in the ROI measurements of the diseased thyroid.

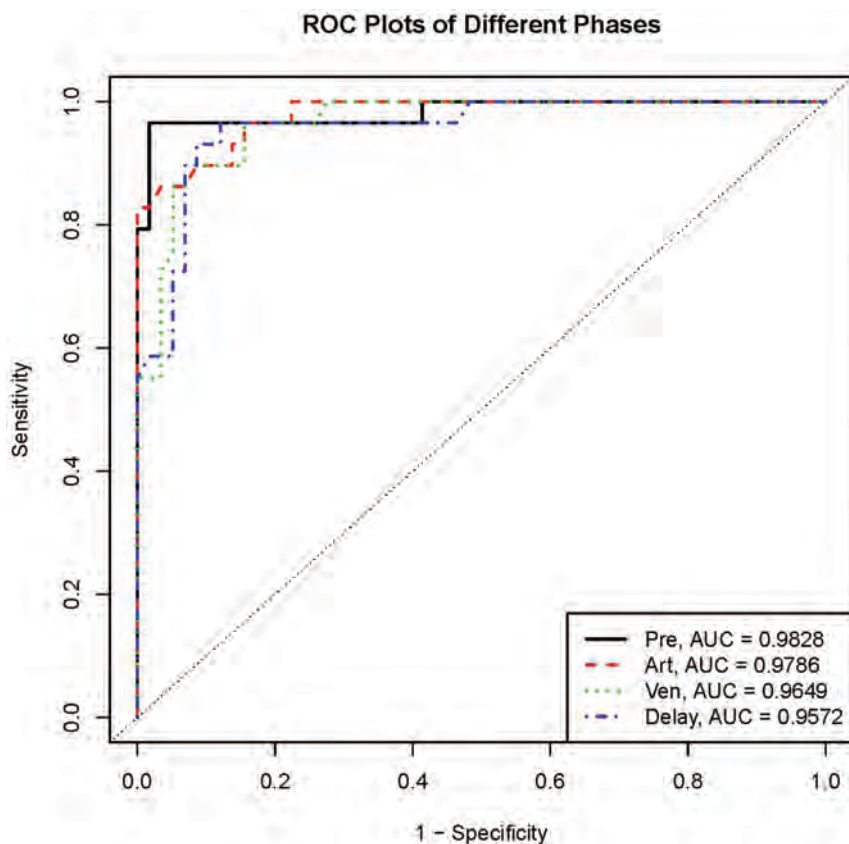


FIG 3. ROC plots comparing recurrent and benign thyroid through 4 phases. The greatest area under the curve was in the precontrast (Pre) phase followed by the arterial (Art), venous (Ven), and delayed (Delay) phases.

Table 4: Area under ROC curve (univariate analysis)

Phase	AUC	95% LCL	95% UCL	Optimal Cutoff (HU)	Sensitivity	Specificity
Precontrast	0.983	0.954	1	62	0.966	0.983
Arterial	0.979	0.955	1	129	0.828	1
Venous	0.965	0.933	0.997	120.6	0.897	0.931
Delayed	0.957	0.916	0.998	125	0.966	0.879

Note:—AUC indicates area under the curve; HU, Hounsfield unit; LCL, lower control limit; UCL, upper control limit.

Table 5: Area under ROC curve for multivariate analysis with P values compared with precontrast phase alone

Phase	AUC	P Value
Precontrast	0.983	
Arterial	0.979	.8
Venous	0.965	.21
Delayed	0.957	.04
Precontrast, arterial	0.994	.26
Precontrast, venous	0.985	.28
Precontrast, delayed	0.983	NA
Arterial, venous	0.979	.8
Arterial, delayed	0.977	.73
Venous, delayed	0.964	.2
Precontrast, arterial, venous	0.995	.26
Precontrast, arterial, delayed	0.995	.29
Precontrast, venous, delayed	0.987	.57
Arterial, venous, delayed	0.979	.81
Precontrast, arterial, venous, delayed	0.996	.37

Note:—NA indicates not applicable; AUC, area under the curve.

Histologically, the thyroid gland is composed of epithelial cells surrounding follicles. Thyroid hormones produced from thyroglobulin and iodide are stored within colloid and account for 25% of the iodide of the body. Because colloid volume is about 3 times greater than the epithelial cell volume,¹⁸ the high electron density of the iodine colloid leads the high attenuation of the thyroid on MDCT.¹⁹⁻²¹ Our results are confirmed in a report by Han et al,²² who studied the appearance of the thyroid gland using PET/CT. They found that thyroid density is proportional to colloid volume and inversely proportional to the cellular component of the thyroid and FDG avidity. A study by Hunter et al¹⁷ compared the 4D-CT enhancement pattern of normal thyroid tissues with parathyroid adenomas on multiphasic multidetector CT. They noted that the higher density of the thyroid gland in the “precontrast phase [as this phase] allows distinction between the iodine-rich thyroid and the surrounding tissue.”

Fitzgerald et al²³ studied the 4D-MDCT patterns of benign and malignant thyroid nodules. Their results in the precontrast phase were similar to ours because the precontrast attenuation of malignant nodules was significantly lower than that of benign lesions (36 versus 61 HU, $P = .05$). In addition to the inclusion of normal hyperdense thyroid tissue in our study, the innate higher density of benign nodules compared with malignant nodules described by Fitzgerald et al may also contribute to our findings of the higher density of benign and diseased thyroid compared with recurrent disease.

Lee et al²⁴ studied the significance of incidental thyroid nodules detected on non-contrast-enhanced low-dose CT for lung cancer screening and found that a “mean attenuation value of 55 HU or more ($P = .036$) and the presence of dense calcifications

($P = .048$)” were associated with malignancy. In our study, recurrent disease had a mean of 37 HU in the precontrast phase. The divergence between their findings and ours is likely related to the inclusion of calcification in the study of Lee et al, which was specifically excluded in our study.

In the arterial phase, we found an increase in Hounsfield unit values within normal thyroid tissue, diseased thyroid, and recurrence. Similarly, the study by Hunter et al¹⁷ found that the peak enhancement of normal thyroid tissue in the arterial phase (25 seconds) was approximately 50 HU over baseline and parathyroid adenomas increased approximately 100 HU from baseline. Ours and the study of Hunter et al also found the greatest separation between thyroid tissue and recurrence, and adenomas and thyroid tissue in the arterial phase, respectively. Fitzgerald et al²³ found no significant difference in HU values between the benign (128 HU) and malignant nodules (144 HU) in the arterial phase ($P = .7$). Differences between their study and ours are likely related to the inclusion of normal thyroid tissue in the diseased thyroid group in our study, which would not be present in the thyroid nodules studied by Fitzgerald et al.²³

In our study, there was washout of contrast in the delayed and late phases in all 3 studied groups. Similarly, Hunter et al¹⁷ found washout of enhancement of thyroid tissue and parathyroid adenomas in the delayed (55 seconds) and late (100 seconds) phases. Fitzgerald et al²³ found no significant difference in Hounsfield unit values between the benign (74 HU) and malignant nodules (98 HU) in the delayed phase ($P = .3$). Again, this difference is likely related to the inclusion of hyperdense thyroid tissue in the normal and diseased thyroid group in our study.

Yoon et al²⁵ examined 734 patients with incidental thyroid nodules, 9% of which were malignant. They found that nodular or rim calcifications and Hounsfield unit values of >130 HU on postcontrast CT with a 45-second delay were suggestive of malignancy. On venous phase imaging (55 seconds), we found mean Hounsfield unit values of 91 HU for recurrent thyroid carcinoma. We speculate that the differences in results between our study and that of Yoon et al²⁵ may also be related to the presence of calcifications in the incidentally detected thyroid carcinomas described in their study.

Limitations include the retrospective nature of the study and the relatively small number of patients (29 in each category). Another limitation is that the lesions in our study may have been detected earlier in their development, given that the patients in our study were being screened for recurrence. During a longer time course, recurrence and residual tissue may have a different appearance. However, the current study design is useful in the early follow-up period when such information is most useful clinically and could be used to decide on questions

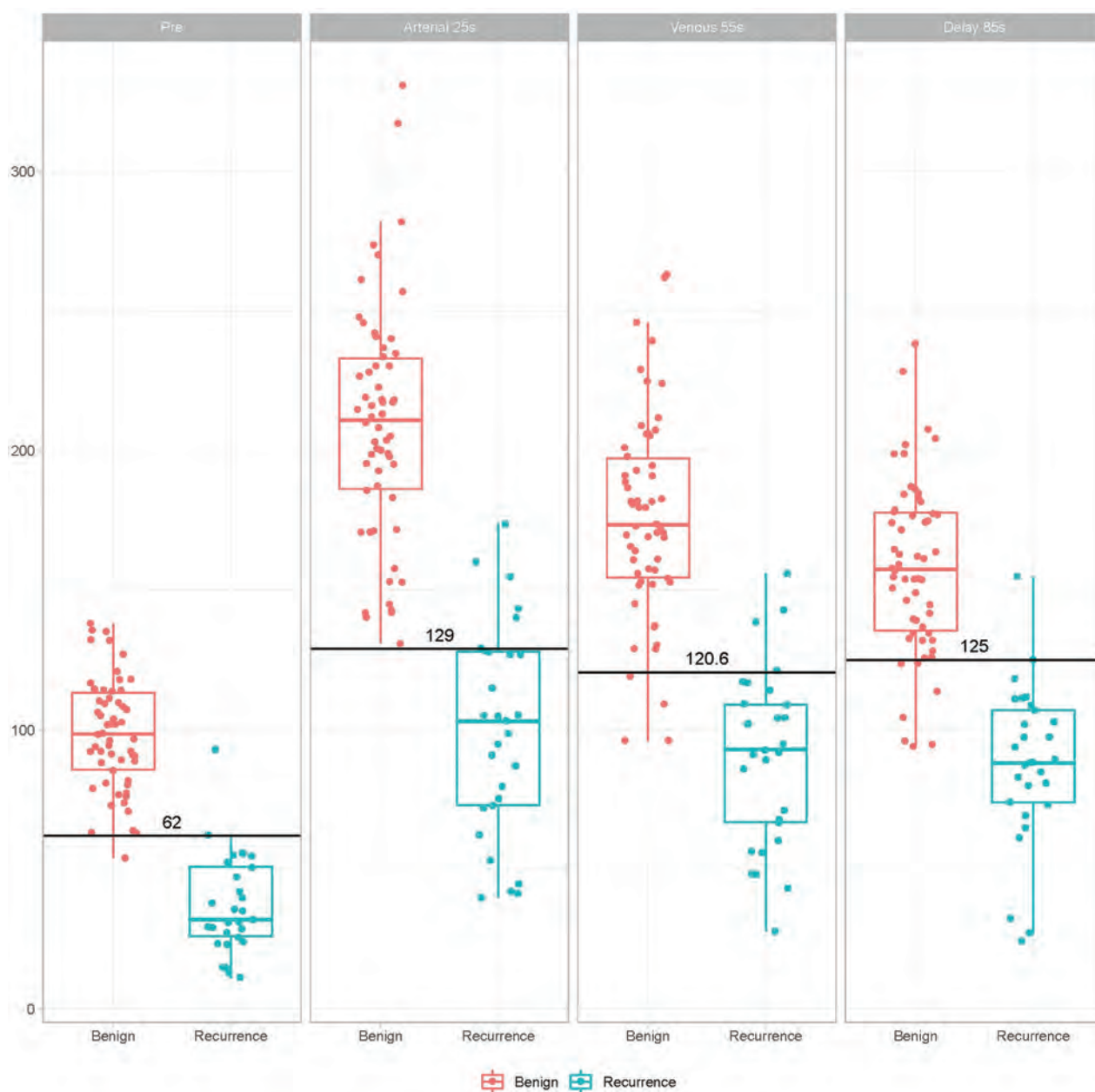


FIG 4. Logistic regression analysis determined the optimal cutoff Hounsfield unit value in each of the 4 phases. The least overlap was present in the precontrast phase with a value of ≤ 62 HU.

such as re-operation. Another limitation is that patients with a multinodular thyroid as part of the diseased thyroid group could conceivably have had an undetected indolent thyroid cancer. In addition, the use of radioactive iodine for the treatment of thyroid cancer might alter the imaging appearance of benign thyroid tissue from what we observed. After radioactive ablation therapy, residual thyroid tissue undergoes fibrosis and appears sonographically as an avascular heterogeneously hypoechoic mass.^{26,27} Caution should be used when extrapolating work done in the thyroid gland that has been treated with radioactive iodine to our current findings in the postthyroidectomy population. Further investigation is needed in this area.

Approximately 27 mSv of radiation is administered during a 4D-MDCT examination, with a roughly equal contribution from

each phase. Because approximately 3 mSv is the estimated yearly natural background radiation exposure, the 4D-MDCT dose in our study is equivalent to the dose received naturally in 9 years.²⁸ The dose for a CT study could potentially be cut to about 6.75 mSv if only 1 phase is acquired (but see next paragraph).

CONCLUSIONS

Our data suggest that the precontrast imaging for characterizing residual tissue after thyroidectomy actually contains the most valuable information and should certainly be a component of any imaging protocol performed for this purpose. The choice of which phase or phases to include is informed but not dictated by our work. Clinical needs might demand that contrast-enhanced sequences be a part of the imaging protocol (for example to

demonstrate lymph nodes and vascular anatomy). Individual radiologists and practices can use the data found in this study to optimally select those imaging phases needed in their practice and balance the need for clinical information against radiation burden, as their patients' needs might require. Prospective clinical imaging trials using these cutoff values are justified.

Disclosures: Mark E. Zafereo—UNRELATED: Grants/Grants Pending: Merck, Eli Lilly, GenePro, Comments: research funding for clinical trials.* Maria E. Cabanillas—UNRELATED: Consultancy: Blueprint Medicines, Ignyta, Bayer Onyx, Loxo Oncology; Grants/Grants Pending: Eisai, Exelixis, Genentech, Kura Oncology; Payment for Lectures Including Service on Speakers Bureaus: various Continuing Medical Education lectures with multiple sponsors; Travel/Accommodations/Meeting Expenses Unrelated to Activities Listed: various Continuing Medical Education lectures.*Money paid to the institution.

REFERENCES

- Lim H, Devesa SS, Sosa JA, et al. **Trends in thyroid cancer incidence and mortality in the United States, 1974-2013.** *JAMA* 2017;317:1338-48 CrossRef Medline
- Howlader N, Noone AM, Krapcho M, et al. **SEER Cancer Statistics Review, 1975-2013, National Cancer Institute. Updated September 12, 2016.** http://seer.cancer.gov/csr/1975_2013/. Accessed October 30, 2018
- Liu FH, Kuo SF, Hsueh C, et al. **Postoperative recurrence of papillary thyroid carcinoma with lymph node metastasis.** *J Surg Oncol* 2015;112:149-54 CrossRef Medline
- Hessel A, Chalian AA, Clayman GL. **Surgical management of recurrent thyroid cancer.** *Neuroimaging Clin N Am* 2008;18:517-25 CrossRef Medline
- Busaidy NL, Cabanillas ME. **Differentiated thyroid cancer: management of patients with radioiodine nonresponsive disease.** *J Thyroid Res* 2012;2012:618985 CrossRef Medline
- Grant CS. **Recurrence of papillary thyroid cancer after optimized surgery.** *Gland Surg* 2015;4:52-62 CrossRef Medline
- Fratkin MJ, Newsome HH Jr, Sharpe AR Jr, et al. **Cervical distribution of iodine 131 following total thyroidectomy for thyroid cancer.** *Arch Surg* 1983;118:864-67 CrossRef Medline
- Salvatori M, Raffaelli M, Castaldi P, et al. **Evaluation of the surgical completeness after total thyroidectomy for differentiated thyroid carcinoma.** *Eur J Surg Oncol* 2007;33:648-54 CrossRef Medline
- D'Andrea V, Cantisani V, Catania A, et al. **Thyroid tissue remnants after "total thyroidectomy."** *Il Giornale di chirurgia* 2009;30:339-44 https://www.researchgate.net/publication/26794592_Thyroid_tissue_remnants_after_total_thyroidectomy. Accessed October 30, 2018
- Sapuppo G, Tavarelli M, Belfiore A, et al. **Time to separate persistent from recurrent differentiated thyroid cancer: different conditions with different outcomes.** *J Clin Endocrinol Metab* 2019;104:258-65 CrossRef Medline
- Shin JH, Han BK, Ko EY, et al. **Sonographic findings in the surgical bed after thyroidectomy: comparison of recurrent tumors and nonrecurrent lesions.** *J Ultrasound Med* 2007;26:1359-66 CrossRef Medline
- Rodgers SE, Hunter GJ, Hamberg LM, et al. **Improved preoperative planning for directed parathyroidectomy with 4-dimensional computed tomography.** *Surgery* 2006;140:932-40 CrossRef Medline
- Lubitz CC, Hunter GJ, Hamberg LM, et al. **Accuracy of 4-dimensional computed tomography in poorly localized patients with primary hyperparathyroidism.** *Surgery* 2010;148:1129-37 CrossRef Medline
- Vu TH, Guha-Thakurta N, Harrell RK, et al. **Imaging characteristics of hyperfunctioning parathyroid adenomas using multiphase multidetector computed tomography: a quantitative and qualitative approach.** *J Comput Assist Tomogr* 2011;35:560-67 CrossRef Medline
- Chazen JL, Gupta A, Dunning A, et al. **Diagnostic accuracy of 4D-CT for parathyroid adenomas and hyperplasia.** *AJNR Am J Neuroradiol* 2012;33:429-33 CrossRef Medline
- Kelly HR, Hamberg LM, Hunter GJ. **4D-CT for preoperative localization of abnormal parathyroid glands in patients with hyperparathyroidism: accuracy and ability to stratify patients by unilateral versus bilateral disease in surgery-naive and re-exploration patients.** *AJNR Am J Neuroradiol* 2014;35:176-81 CrossRef Medline
- Hunter GJ, Schellingerhout D, Vu TH, et al. **Accuracy of 4DCT for the localization of abnormal parathyroid glands in patients with primary hyperparathyroidism.** *Radiology* 2012;25:789-95 CrossRef Medline
- Knobel M, Bisi H, de Araujo Peres C, et al. **Studies on functional and morphological aspects in human multinodular simple goiter tissues.** *Endocr Pathol* 1993;4:205-14 CrossRef Ref
- Silverman PM, Newman GE, Korobkin M, et al. **Computed tomography in the evaluation of thyroid disease.** *AJR Am J Roentgenol* 1984;142:897-902 CrossRef Medline
- Iida Y, Konishi J, Harioka T, et al. **Thyroid CT number and its relationship to iodine concentration.** *Radiology* 1983;147:793-95 CrossRef Medline
- Kaneko T, Matsumoto M, Fukui K, et al. **Clinical evaluation of thyroid CT values in various thyroid conditions.** *J Comput Tomogr* 1979;3:1-4 CrossRef Medline
- Han YM, Kim YC, Park EK, et al. **Diagnostic value of CT density in patients with diffusely increased FDG uptake in the thyroid gland on PET/CT images.** *AJR Am J Roentgenol* 2010;195:223-28 CrossRef Medline
- Fitzgerald RT, Kuruva M, David R, et al. **Characterization of thyroid nodules by 4-dimensional computed tomography: initial experience.** *J Comput Assist Tomogr* 2017;41:195-98 CrossRef Medline
- Lee JH, Jeong SY, Kim YH. **Clinical significance of incidental thyroid nodules identified on low-dose CT for lung cancer screening.** *Multidiscip Respir Med* 2013;8:56 CrossRef Medline
- Yoon DY, Chang SK, Choi CS, et al. **The prevalence and significance of incidental thyroid nodules identified on computed tomography.** *J Comput Assist Tomogr* 2008;32:810-15 CrossRef Medline
- Fajardo LF. **Basic mechanisms and general morphology of radiation injury.** *Semin Roentgenol* 1993;28:297-302 CrossRef Medline
- Pacella CM, Bizzarri G, Spiezia S, et al. **Thyroid tissue: US-guided percutaneous laser thermal ablation.** *Radiology* 2004;232:272-80 CrossRef Medline
- National Council on Radiation Protection and Measurements. **Ionizing radiation exposure of the population of the United States. Report No. 160. 2009.** <https://ncrponline.org/publications/reports/ncrp-report-160/>. Accessed October 30, 2018

MRI Signal Intensity and Electron Ultrastructure Classification Predict the Long-Term Outcome of Skull Base Chordomas

J. Bai, J. Shi, S. Zhang, C. Zhang, Y. Zhai, S. Wang, M. Li, C. Li, P. Zhao, S. Geng, S. Gui, L. Jing, and Y. Zhang



ABSTRACT

BACKGROUND AND PURPOSE: MR imaging is a useful and widely used evaluation for chordomas. Prior studies have classified chordomas into cell-dense type and matrix-rich type according to the ultrastructural features. However, the relationship between the MR imaging signal intensity and ultrastructural classification is unknown. We hypothesized that MR imaging signal intensity may predict both tumor ultrastructural classification and prognosis.

MATERIALS AND METHODS: Seventy-nine patients with skull base chordomas who underwent 95 operations were included in this retrospective single-center series. Preoperative tumor-to-pons MR imaging signal intensity ratios were calculated and designated as ratio on T1 FLAIR sequence (R_{T1}), ratio on T2 sequence (R_{T2}), and ratio on enhanced T1 FLAIR sequence (R_{EN}), respectively. We assessed the relationships among signal intensity ratios, ultrastructural classification, and survival.

RESULTS: Compared with the matrix-rich type group, the cell-dense type chordomas showed lower R_{T2} (cell-dense type: 1.90 ± 0.38 ; matrix-rich type: 2.61 ± 0.60 $P < .001$). The model of predicting cell-dense type based on R_{T2} had an area under the curve of 0.83 (95% CI, 0.75–0.92). In patients without radiation therapy, both progression-free survival ($P = .003$) and overall survival ($P = .002$) were longer in the matrix-rich type group than in the cell-dense type group. R_{EN} was a risk factor for progression-free survival (hazard ratio = 10.24; 95% CI, 1.73–60.79); R_{T2} was a protective factor for overall survival (hazard ratio = 0.33; 95% CI, 0.12–0.87); and R_{EN} was a risk factor for overall survival (hazard ratio = 4.76; 95% CI, 1.51–15.01).

CONCLUSIONS: The difference in MR imaging signal intensity in chordomas can be explained by electron microscopic features. Both signal intensity ratios and electron microscopic features may be prognostic factors.

ABBREVIATIONS: CDT = cell-dense type; MRT = matrix-rich type; OS = overall survival; PFS = progression-free survival; R_{T1} , R_{T2} , and R_{EN} = ratios of tumor-to-pons signal intensity in the T1 FLAIR sequence, T2 sequence, and enhanced T1 FLAIR sequence, respectively.

Chordoma is a rare malignant tumor with an overall incidence of 0.08 per 100,000 in the United States.¹ These tumors occur mainly in the sacrum, followed by the skull base and spine.² Skull base chordomas account for 1% of all brain tumors and 4% of all primary bone tumors.³ Chordomas generally grow slowly; however, recurrence is common because en bloc resection is difficult in the

skull base.^{3–5} The recurrence intervals are distinctively variable among patients due to biologic variability among and within patients. This difference also impacts the treatment plan; for example, some patients should receive radiation therapy as early as possible, and others can wait.⁶ Previous studies by our group and others^{5–12} have demonstrated several risk factors related to long-term survival, such as the expression level of Ki-67, *Platelet-derived growth factor receptor β* (*PDGFR- β*) and *SNF5*, resection extent, age, postsurgery radiation therapy, and histopathologic findings. On the basis of our previous study on the electron microscopic ultrastructural characteristics of chordomas, we have classified chordomas into 2 different groups: cell-dense type (CDT) and matrix-rich

Received October 1, 2019; accepted after revision March 8, 2020.

From the Department of Neurosurgery (J.B., P.Z., S. Geng, S. Gui, Y. Zhang), Beijing Tiantan Hospital, Capital Medical University, Beijing, China; Beijing Neurosurgical Institute (J.B., S.Z., C.Z., Y. Zhai, S.W., M.L., C.L., Y. Zhang), Capital Medical University, Beijing, China; China National Clinical Research Center for Neurological Diseases (J.B., P.Z., S. Geng, S. Gui, Y. Zhang), Beijing, China; Department of Neurosurgery (J.S.), Tsinghua University Yuquan Hospital, Beijing, China; Department of Neurosurgery (S.Z.), Anshan Central Hospital, Anshan, China; Department of Neurosurgery (Y. Zhai), First Affiliated Hospital, Zhengzhou University, Zhengzhou, China; and Department of Health Statistics (L.J.), Shanxi Medical University, Taiyuan, China.

J. Bai and J. Shi contributed equally to this work.

This work was supported by the Beijing Municipal Science and Technology Commission (No. Z171100000117002) and the Research Special Fund for Public Welfare Industry of Health (No. 201402008).

Please address correspondence to Yazhuo Zhang, MD, Beijing Neurosurgery Institute, Nansihuan Xilu No. 119, Fengtai District, Beijing, 100070, China; e-mail: zyz2004520@yeah.net

Indicates open access to non-subscribers at www.ajnr.org

<http://dx.doi.org/10.3174/ajnr.A6557>

Table 1: Key points for the differential diagnosis of cell-dense and matrix-rich types according to the ultrastructures of chordomas^a

	Cell-Dense Type	Matrix-Rich Type
Tumor cell content in a low-power field ($\times 3000$)	Densely arranged	Seldom or none
Extracellular matrix content	Relatively sparse	Abundant
Complex of rough endoplasmic reticulum and the mitochondria	Rich	Relatively seldom
Nuclei and chromatin	Abnormal nuclei with condensed, deeply staining heterochromatin	Regularly shaped nuclei, mainly with loosely arranged euchromatin
Cell junctions	Desmosomes are obvious	Few desmosomes
Collagen fibrils	Type III collagen fibrils can be found	Seldom
Exocytosis	Easily found	Seldom

^a Reprinted with permission from Bai et al¹³ and Elsevier.

type (MRT).¹³ We also demonstrated the association between clinical outcomes and electron microscopic features of tumor specimens.¹³ We have shown that CDT is predictive of poorer outcomes, higher risk of recurrence, and shorter survival, though these findings were derived from a small sample size ($n = 27$).

MR imaging allows a differential diagnosis between chordomas and other tumors using signal intensity.^{14,15} Recent studies have suggested that MR imaging signal intensity ratios on different sequences (ratio of tumor-to-pons signal intensity on T1 FLAIR [R_{T1}]; ratio of tumor-to-pons signal intensity on T2 [R_{T2}]; ratio of tumor-to-pons signal intensity on enhanced T1 FLAIR [R_{EN}]) are useful in predicting outcomes. Tian et al¹⁶ revealed that higher R_{T2} predicted diminished tumor progression and higher R_{EN} predicted more rapid tumor progression; this correlation between R_{EN} and recurrence or progression was also shown by Lin et al¹⁷ However, neither of these studies showed evidence for the possible explanation of signal intensity difference.

We hypothesized that ultrastructural morphologic characters could explain the mechanism of different signal intensities. Hence, this study aimed to explore the relationships among MR imaging signal intensity ratio, the electronic microscopic feature, and survival, which may provide meaningful preoperative prognostic information and help apply better individual-based treatment strategies.

MATERIALS AND METHODS

Patients

Data from 127 patients who underwent an operation by the same surgical team between July 2012 and July 2016 were reviewed retrospectively from the chordoma data base of the neuroendoscopic ward in Beijing Tiantan Hospital. The present series were classified into CDT and MRT according to the electronic features (Table 1).¹³ Overall, in contrast to the features in the MRT tumors, tumor density was high in CDT tumors; thus, the extracellular matrix was sparse.¹³ Only the patients with both electron microscopy images and preoperative MR imaging available were included for further analysis; thus, 79 patients were enrolled in the present study. Among these patients, 27 cases were previously reported.¹³ The relevant clinical information was collected from the inpatient digital archives, including sex, age, tumor status (primary or recurrent tumor), presurgery radiation therapy, tumor blood supply (rich or not rich, with a rich blood supply being defined by having a tumor-resection surface that bled easily and was difficult to suction cleanly, while a blood supply was that was not rich was defined by having a tumor resection surface that bled less easily and was easy to suction

cleanly), resection rate ($\geq 90\%$ or $< 90\%$), and histopathology (Ki-67 level, conventional chordoma, or chondroid chordoma). As a retrospective observational study of de-identified data without any additional therapy or monitoring procedures, this study did not need approval from the Ethics Committee of Beijing Tiantan Hospital.

MR Imaging Scans and Image Evaluation

The patients underwent preoperative MR imaging with a 3T MR imaging scanner (Siemens, Erlangen, Germany). Axial unenhanced T1 FLAIR and T2-weighted images were obtained with the following parameters, respectively: TR/TE range = 1850–2500/9.4–19.8 ms and 4500–6000/84–97 ms. Postcontrast scanning was performed 2 minutes after gadopentetate dimeglumine injection, with a concentration of 0.2 mL/kg (0.5 mol/L). The TR/TE ranges for the enhanced T1 FLAIR sequence were 1850–2500/9.4–19.8 ms. The section thickness was 3.0–50.5 mm.

The images were analyzed on our PACS. Operator-defined ROIs were placed in the tumor and the pons. The mean signal intensity of the tumor was normalized by dividing by the mean signal intensity of the corresponding pons on axial T1 FLAIR (R_{T1}), T2 (R_{T2}), and enhanced T1 FLAIR (R_{EN}), respectively.

Follow-Up

The follow-up period was calculated from the date of the first operation in Beijing Tiantan Hospital to the last follow-up in March 2019 or the date of death, whichever occurred first. The median follow-up time in this series was 52 months (range, 1–118 months), and 7 patients were lost to follow-up. Progression-free survival (PFS) was calculated from the date of the operation to the date of tumor recurrence or progression of residual tumor, which was confirmed by the imaging findings; and overall survival (OS) was defined as the time from diagnosis to disease-specific death or to the last follow-up time. Patients were censored at the last follow-up date if no death occurred or on the date of death if death was not disease-specific.^{5,12}

Statistical Analysis

Statistical analyses were performed with SPSS software, Version 24 (IBM). *T* tests or Mann-Whitney *U* tests were used to analyze the continuous variables between groups. A χ^2 test was used in analyzing the distributions of categorical variables between groups. To evaluate the relationship between signal intensity ratio and electron microscopic classification, we included the signal intensity ratios (R_{T1} , R_{T2} , R_{EN}) in univariate analyses separately; multivariate analysis was performed using logistic regression. The area under the receiver operating characteristic curve was calculated to estimate the accuracy.

Table 2: Demographics of the 79 patients undergoing chordoma surgery in Beijing Tiantan Hospital between July 2012 and July 2016

	Total	MRT	CDT	P
No. of cases	79	39	40	
Tumor status				
Primary	37	24	13	.01
Recurrent	42	15	27	
Sex				
Male	43	21	22	.918
Female	36	18	18	
Age (mean) (yr)				
Primary	47.8 ± 17.4	42.3 ± 18.2	58.2 ± 9.97	.006
Recurrent	47.1 ± 15.3	46.5 ± 16.5	47.6 ± 14.9	.828
Total	47.5 ± 16.2	43.9 ± 17.5	51.0 ± 14.3	.050
Histopathology				
Conventional	71	35	36	1.000
Chondroid	8	4	4	
Blood supply ^a				
Rich	21	7	14	.073
Not rich	55	31	24	
Resection grade				
≥90%	43	23	20	.423
<90%	36	16	20	
Survival status				
Alive	42	27	15	.018
Died	26	8	18	
NA ^b	11	4	7	
Presurgery radiation therapy				
Yes	17	5	12	.063
No	62	34	28	
Postsurgery radiation therapy				
Yes	30	14	16	.667
No	43	21	22	
NA ^c	6	4	2	
PFS (mo) ^d	40.3 ± 5.4	52.2 ± 5.7	18.7 ± 6.9	.003
OS (mo)	100.5 ± 7.1	113.9 ± 6.3	88.9 ± 9.3	.018

Note:—NA indicates not applicable.

^a Operative notes on 3 cases showed no specified blood supply.

^b Including both patients lost to follow-up and patients who did not die of chordomas.

^c Including the patients whose radiation therapy information was not available.

^d Patients without radiation therapy (*n* = 32).

OS and PFS were estimated using the Kaplan-Meier method, and survival curves for the 2 electron microscopic classifications were compared using the log-rank test. Statistically significant variables in the univariate analyses were included in the multivariate Cox proportional hazards regression model, using forward stepwise variable selection, to find significant predictors of recurrence and survival. A *P* value < .05 was considered statistically significant.

RESULTS

Clinical Characteristics and Electron Microscopic Classifications

Seventy-nine cases fit the inclusion criteria and were enrolled in the study (Table 2), which included 37 cases with newly diagnosed primary tumors and 42 cases with recurrent tumors or progression of residual tumors after prior operations. CDT chordomas were more common in recurrent tumors than in primary tumors (*P* = .01). There were 43 men and 36 women, and the mean age was 47.5 ± 16.2 years. Seventy-one cases were confirmed as conventional chordomas, and 8 were chondroid chordomas. Among them, 47 patients

received adjuvant radiation therapy, while the other 32 patients received no radiation therapy. Because no medical treatment was approved for chordoma, no patients received any drug treatment.

According to the electron microscopic classification,¹³ 39 cases were classified as MRT and 40 cases were classified as CDT in the first operation. The MRT tumor cells were loosely arranged, the extracellular matrix was abundant, and the tumor cells showed bubble-like vacuoles. CDT tumors displayed relatively tightly arranged tumor cells, a less abundant matrix, and vacuoles not as rich as those in MRT cells (Fig 1). In the patients with primary tumors, patients with MRT tumors were younger than patients with CDT tumors (42.3 ± 18.2 years versus 58.2 ± 9.97 years, *P* = .006).

Sixty-five patients underwent 1 operation during follow-up, and 14 patients underwent repeat operations due to tumor recurrence or progression of residual tumor. No patients underwent a repeat operation because of an incomplete initial resection. Among those 14 patients, 12 patients underwent 2 operations and 2 patients underwent 3 operations. Therefore, a total of 79 patients with 95 operations were included in the following analysis (Table 3). The median PFS for the patients who underwent a repeat operation was 10.0 months (range, 2–42

months). Among the patients who underwent 2 operations, 6 patients were diagnosed with CDT tumors in both operations, 3 patients were diagnosed with MRT tumors in both operations, 2 patients were diagnosed with a MRT tumor in the first operation and a CDT tumor in the second operation, and 1 patient was diagnosed with a CDT tumor in the first operation and an MRT tumor in the second operation. Among the 2 patients who had 3 operations, one was diagnosed each time with CDT tumors, while the other was diagnosed twice with CDT tumors and once with an MRT tumor.

Relationship between Signal Intensity Ratio and Electron Microscopic Classifications

Presurgery MR images of 95 operations were pooled and analyzed. The CDT chordomas showed lower signal intensity than MRT chordomas on T2-weighted images (Table 4 and Fig 2). The *R*_{T1} values of CDT chordomas were higher than those of MRT chordomas. The *R*_{EN} value was also higher in patients with CDT than in those with MRT. When only 37 primary tumors were considered, the difference was still significant (Table 4).

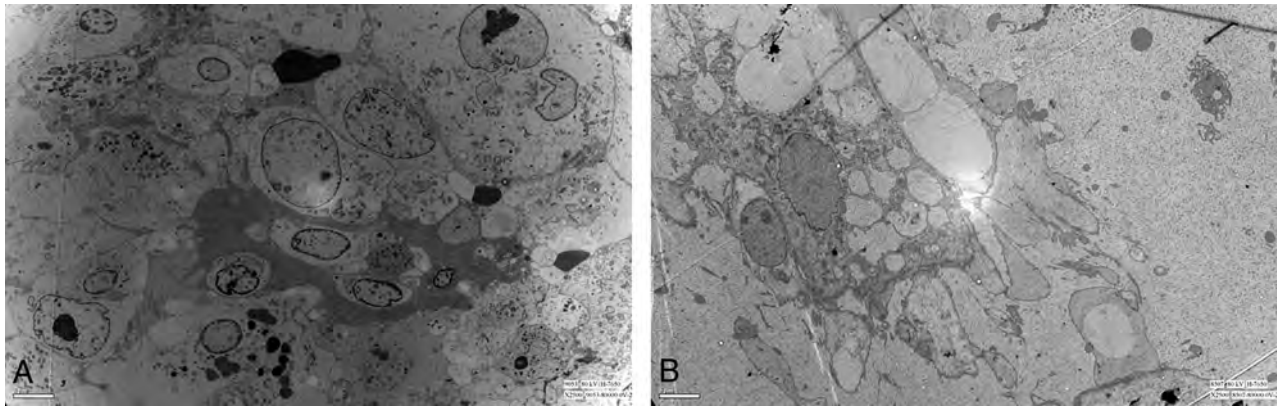


FIG 1. The electron microscopic features of the 2 classifications for skull base chordomas in low-power fields ($\times 2500$). *A*, In a cell-dense type chordoma, the physaliphorous cells are relatively tightly arranged and there is little extracellular matrix present. The vacuoles are not as rich as those observed in matrix-rich type tumor cells. The nuclei vary in size and condensed nuclei are found. *B*, In a matrix-rich type chordoma, the physaliphorous cells are sparse, and abundant extracellular matrix contents exist. The vacuoles are rich and apparent. The nuclei are slightly atypical.

Table 3: Details for the electron microscopic classification

Surgery No./Electron Microscopic Classification	Tumor Status ^a	No. of Cases
1 Operation ($n = 65$)		
CDT	Primary	6
	Recurrent	23
MRT	Primary	22
	Recurrent	14
2 Operations ($n = 12$)		
Both CDTs	Primary	3
	Recurrent	3
Both MRTs	Primary	3
	Recurrent	0
First MRT, second CDT	Primary	1
	Recurrent	1
First CDT, second MRT	Primary	1
	Recurrent	0
3 Operations ($n = 2$)		
3 CDTs	Primary	1
	Recurrent	0
2 CDTs, 1 MRT ^b	Primary	0
	Recurrent	1

^a The tumor status when the first operation was performed in our hospital.

^b The second operation was diagnosed as MRT.

Table 4: Comparison of signal intensity ratios between CDT and MRT

Signal Intensity Ratio	Electron Microscopic Classification		P
	CDT	MRT	
Entire cohort ($n = 95$)			
R _{T2}	1.90 \pm 0.38	2.61 \pm 0.60	<.001
R _{T1}	0.63 \pm 0.14	0.56 \pm 0.13	.016
R _{EN}	1.19 \pm 0.42	0.99 \pm 0.41	.022
Primary tumors ($n = 37$)			
R _{T2}	1.99 \pm 0.39	2.69 \pm 0.53	<.001
R _{T1}	0.67 \pm 0.18	0.55 \pm 0.13	.019
R _{EN}	1.17 \pm 0.42	0.89 \pm 0.32	.024
Recurrent tumors ($n = 58$)			
R _{T2}	1.87 \pm 0.38	2.50 \pm 0.67	.001
R _{T1}	0.62 \pm 0.13	0.58 \pm 0.13	.307
R _{EN}	1.19 \pm 0.43	1.11 \pm 0.49	.526

However, when only recurrent tumors were analyzed, both R_{T1} and R_{EN} were no longer statistically different, while R_{T2} was still significantly different (Table 4).

Logistic regression analysis was then conducted to predict electron microscopic classification. A univariate analysis indicated that recurrent tumor ($P = .004$) and decreased R_{T2} ($P < .001$) and increased R_{T1} and R_{EN} ($P = .019$ and 0.027 , respectively) were significant variables for predicting CDT, while presurgery radiation therapy and histopathology subtype were not significant variables ($P > .05$). From the multivariate analysis, R_{T2} was the only significant independent predictor of CDTs ($P < .001$). The area under the receiver operating characteristic curve was 0.83 (95% CI, 0.75–0.92) with only R_{T2} in the model.

Relationship between Electron Microscopic Classifications and PFS and OS

At follow-up, 26 patients (32.9%) had died of disease progression. Concerning the 32 patients without radiation therapy, 9 patients had died, including 2 patients in the MRT group and 7 patients in the CDT group. Among the 95 operations, 59 tumors (62.1%) had recurred.

When all 95 operations were analyzed together, the PFS was significantly longer in the MRT group than in the CDT group, with median PFS values of 36.0 months (interquartile range, 14–73 months) and 10 months (interquartile range, 6–42 months), respectively ($P = .003$). When the tumors without radiation therapy were considered, the PFS was 56 months (interquartile range, 34–undefined months) in the MRT group and 10 months (interquartile range, 5–24 months) in the CDT group ($P = .003$) (Fig 3A).

The OS was significantly longer in the MRT group than in the CDT group, with a median OS of 132.0 months (interquartile range, 82–undefined months) and 96.0 months (interquartile range, 48–114 months), respectively ($n = 79$; $P = .018$). When just the tumors without radiation therapy ($n = 32$) were considered, the MRT group showed a

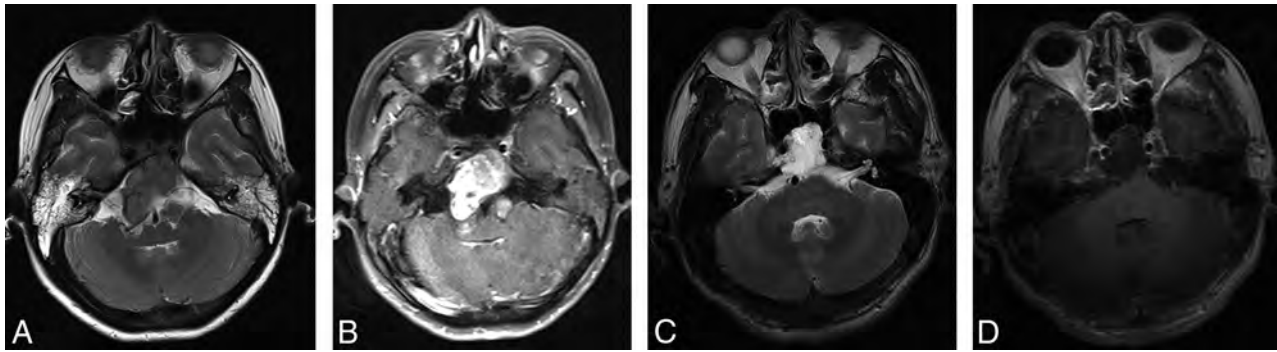


FIG 2. Representative MR images of the 2 classified chordomas. A and B, The cell-dense type chordomas. A, T2-weighted MR imaging shows a low signal intensity, recurrent chordoma in the clival region. B, Contrast-enhanced MR imaging shows the lesion with marked enhancement. C and D, Matrix-rich type chordomas with high signal intensity on T2-weighted images and low signal intensity on contrast-enhanced MR imaging, respectively.

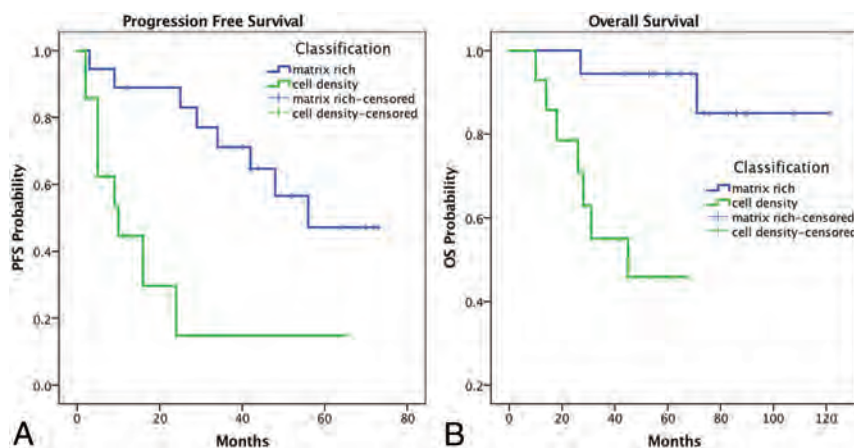


FIG 3. Kaplan-Meier analysis illustrating PFS and OS of 32 patients with chordomas without adjuvant radiation therapy. A, The patients with matrix-rich type chordomas have a significantly longer PFS than the patients with cell-dense type chordomas ($P = .003$). B, The OS of patients with matrix-rich type chordomas is significantly longer than that of those with cell-dense type chordomas ($P = .002$).

significantly longer OS than the CDT group, with 2 deaths in the MRT group compared with 7 deaths in the CDT group ($P = .002$) (Fig 3B).

Relationship between MR Imaging Signal Intensity Ratio and PFS and OS

To test for possible risk factors for recurrence, sex, tumor blood supply, and resection rate were included in the univariate analyses among patients not receiving radiation therapy ($n = 32$). Blood supply and resection rate were associated with recurrence ($P = .015$ and $.019$, respectively). When these 2 parameters were combined with MR imaging signal intensity ratios and age in the multivariate analysis, R_{EN} and blood supply were significant risk factors for PFS (R_{EN} : hazard ratio = 10.24; 95% CI, 1.73–60.79; $P = .010$; blood supply: hazard ratio = 0.87; 95% CI, 1.15–13.01; $P = .029$).

Univariate Cox regression analyses indicated that postsurgery radiation therapy and resection rate ($P = .023$ and $.036$, respectively) were potentially significant prognostic factors

for OS in all 79 cases. In the multivariable analysis, R_{T2} and postsurgery radiation therapy were significant protective factors for OS (hazard ratio = 0.33; 95% CI, 0.12–0.87; $P = .026$; and hazard ratio = 0.12; 95% CI, 0.03–0.41; $P = .001$, respectively). R_{EN} was associated with significantly lower OS (hazard ratio = 0.76; 95% CI, 1.51–15.01; $P = .008$).

Relationship between MR Imaging Signal Intensity Ratio and Expression of Ki-67

The Ki-67 levels were available in 53 samples, which were collected from pathologic reports. The median Ki-67 level was 2% (range, 0%–20%) in 23 MRT chordomas, and the median Ki-67 level was 5% (range, 1%–20%) in 30 CDT chordomas. The expression of Ki-

67 was significantly higher in the CDT group than in the MRT group ($P = .033$).

DISCUSSION

Skull base chordoma can be an aggressive malignancy with poor prognosis. We previously demonstrated that electron microscopic features of chordomas were variable and could be classified into 2 morphologic types, CDT and MRT.¹³ In the present study, we show that electron microscopic classification is a valid predictor of survival. Patients with CDT had a significantly shorter PFS and OS than those with MRT, even after adjusting for the adjuvant radiation therapy. We further demonstrated that the different electron microscopic features of chordomas exhibited different MR imaging signal intensity ratios, especially R_{T2} , and CDT chordomas had lower R_{T2} than MRT chordomas. In a recent radiomics study of the differentiation among primary chordoma, giant-cell tumor, and metastatic tumor of the sacrum, the radiomics model constructed on the basis of T2-weighted and contrast-enhanced T1-weighted MR imaging provided good predictive values.¹⁸ Another radiomics

study also found that T2-weighted and contrast-enhanced T1-weighted MR imaging provided more useful information in differentiating chordoma from chondrosarcoma, compared with T1-weighted MR imaging.¹⁹ An additional study reported that both T2-weighted and contrast-enhanced T1-weighted MR imaging are helpful in differentiating recurrent tumors from postoperative changes.³ In the present study, we additionally found that lower R_{T2} was a relatively accurate indicator for CDT (area under the receiver operating characteristic curve = 0.83; 95% CI, 0.75–0.92), which is applicable in both primary chordomas and recurrent chordomas.

In CDT chordomas, the tumor cells are rich and contact tightly with each other focally, and the extracellular matrix contents are relatively thin. Conversely, in MRT chordomas, the tumor cells are sparsely arranged and the extracellular matrix contents are abundant.¹³ These morphologic characteristics were also confirmed by hematoxylin-eosin staining under low-power microscopy.²⁰ There were numerous vacuoles of various sizes in the cytoplasm of MRT chordomas, while the vacuoles were absent or less obvious in CDT chordomas. Furthermore, the karyoplasm ratio increased occasionally in CDT tumor cells,¹³ which led to reduced fluid content in tumor cells. Both high fluid content in the physaliphorous cells and extracellular matrix likely contribute to the high signal intensity in T2-weighted MR imaging in MRT chordomas.^{3,14,15} Similar findings have been reported in liposarcoma and breast tumors, in which histopathologic components of loose myxoid stroma generate high T2 signal.^{21,22} To our knowledge, this is the first study focusing on the MR imaging signal intensity and electron microscopic features. The results partially-but-directly explain the pathologic basis of the different MR imaging signal intensities among chordomas.

Previous studies^{15,23} demonstrated that poorly differentiated chordomas exhibited no extracellular myxoid stroma or very minimal matrix in pathologic slides and low signal intensity in T2-weighted MR imaging, and this subset of patients has decreased survival compared with those with conventional or chondroid chordomas. Although there were no poorly differentiated chordomas in our series, CDT chordomas do have a sparser extracellular matrix and higher tumor cell density, characteristics that make it reasonable to suggest that our results are comparable with those of these studies^{15,23} and that R_{T2} is also qualified in poorly differentiated chordomas.

In the patients who underwent 1 operation by our team, we found a higher ratio of CDT in recurrent tumors (27/42, 64.3%) than in primary tumors (13/37, 35.1%) (Table 2). This finding indicates that recurrent chordomas are more prone to be CDT tumors than primary chordomas. In the patients who underwent >1 resection by our team, some tumors recurred as a different electron microscopic type from their previous surgical result. These findings may indicate that the tumor cells were heterogeneously arranged,²⁴ and the tiny amount of tissue in the electron microscopic sample may not exactly represent the whole tumor. With MR imaging analysis, the sampling error is greatly reduced because ROIs are selected by drawing the largest possible elliptical area within the tumor but avoiding areas of hemorrhage, necrosis, cyst, or calcification.^{15,17,25} This feature may also indicate the emergence of new malignant cell populations within the recurrent tumor when the MRT tumors recurred as CDT tumors in some cases. Additionally,

we found that most of the tumors that underwent multiple resections eventually evolved into CDTs (10/14) (Table 3). A previous study reported that 2 primary sacral chordomas with high signal intensity in T2-weighted images recurred with poorly differentiated chordomas with intermediate signal intensity on T2-weighted images.¹⁴ This occurrence suggests that decreasing T2 signal intensity may represent increasing malignancy. Recently, we confirmed that Ki-67 was associated with poor prognosis.⁷ In the present study, we found higher Ki-67 levels in CDT tumors than in MRT tumors. The finding suggests that there is a more aggressive proliferation ability in CDT chordomas.¹³ Furthermore, we found that CDT tumors were more likely to recur.¹³ Taken together, we believe that the extent of malignancy increases in most chordomas when they recur, and this progression can be observed by both electron microscopic diagnosis and MR signal intensity.

MR imaging is important not only for diagnosing and differentiating disease but also in predicting prognosis.^{3,16,24} Among the 32 patients who did not undergo adjuvant radiation therapy in the present series, R_{EN} and tumor blood supply were demonstrated as independent factors for PFS. Tian et al¹⁶ and Lin et al¹⁷ have also had similar results, which suggested that R_{EN} was a risk factor for PFS. Tian et al¹⁶ also found that tumors with higher R_{EN} had more tumor blood supply. A recent radiomic analysis of 148 skull base chordomas showed that both radiomic signature (which was based on preoperative axial T1 FLAIR, T2-weighted, and enhanced T1 FLAIR) and blood supply were independent markers of tumor progression.²⁵ These 4 independent studies provide convincing evidence to conclude that the high R_{EN} and rich blood supply of chordomas can be used as prognostic indicators for rapid recurrence or progression.

We also demonstrated that R_{T2} and postsurgery radiation therapy are protective factors for survival and that R_{EN} is a risk factor for OS. Radiation therapy has been recommended as a standard procedure in chordoma treatment,² and many studies also showed that adjuvant radiation therapy improves outcomes.^{4,5,26} To our knowledge, the correlation between signal intensity ratio and OS in chordomas has not been studied previously, and the precise mechanism of our findings needs further research. However, considering that 79 cases are a relatively large sample size for the low incidence and prevalence of chordoma and the statistical significance of our findings, our results are meaningful. Therefore, MR imaging signal intensity ratios are useful clinical indicators for risk stratification of patients with chordomas or treatment-plan ranking.

Limitations

The main limitation of this study is that the time interval between the operation and adjuvant radiation therapy was not available in the present data base, and radiation therapy most likely positively influences recurrence intervals.^{4,5} Furthermore, radiation therapy has been shown to impact the MR imaging enhancement parameters.²⁴ Therefore, we were unable to control for the effect of radiation therapy in the progression-free survival models. Another limitation is that this is a retrospective study for which some clinical information was missing; for example, the tumor blood supply of 3 tumors was not recorded in the archives. A study showed that lower ADC values may predict tumor

progression in postsurgery chordomas²⁷ and may also predict tumor-control probability in skull base chordomas treated with carbon ion therapy.²⁸ This probability suggests that the relationship between ADC values and electronic microscopic characteristics will also be worth investigating. However, diffusion-weighted MR imaging was previously not routinely performed in our hospital; therefore, ADC values were also not available in the present data base. These deficiencies will be remedied in our future study.¹⁵

CONCLUSIONS

MR imaging signal intensity ratio could distinguish CDT from MRT preoperatively, particularly R_{T2} values. The electron microscopic features may be the basis of the MR imaging signal intensity difference. Patients with CDT chordomas have significantly shorter PFS and OS than those with MRT chordomas. A higher R_{T2} correlates with an increased likelihood of MRT chordoma and longer survival, while R_{EN} is an independent adverse prognostic factor for both PFS and OS.

REFERENCES

- McMaster ML, Goldstein AM, Bromley CM, et al. **Chordoma: incidence and survival patterns in the United States, 1973.** *Cancer Causes Control* 2001;12:1–11 CrossRef Medline
- Stacchiotti S, Sommer J; Chordoma Global Consensus Group. **Building a global consensus approach to chordoma: a position paper from the medical and patient community.** *Lancet Oncol* 2015;16:e71–83 CrossRef Medline
- Erdem E, Angtuaco EC, Van Hemert R, et al. **Comprehensive review of intracranial chordoma.** *Radiographics* 2003;23:995–1009 CrossRef Medline
- Walcott BP, Nahed BV, Mohyeldin A, et al. **Chordoma: current concepts, management, and future directions.** *Lancet Oncol* 2012;13:e69–76 CrossRef Medline
- Tauziède-Espariat A, Bresson D, Polivka M, et al. **Prognostic and therapeutic markers in chordomas: a study of 287 tumors.** *J Neuropathol Exp Neurol* 2016;75:111–20 CrossRef Medline
- Beccaria K, Tauziède-Espariat A, Monnien F, et al. **Pediatric chordomas: results of a multicentric study of 40 children and proposal for a histopathological prognostic grading system and new therapeutic strategies.** *J Neuropathol Exp Neurol* 2018;77:207–15 CrossRef Medline
- Zhang S, Bai J, Li M, et al. **Predictive value of transforming growth factor- α and Ki-67 for the prognosis of skull base chordoma.** *World Neurosurg* 2019;129:e199–206 CrossRef Medline
- Zhai Y, Bai J, Wang S, et al. **Analysis of clinical factors and PDGFR- β in predicting prognosis of patients with clival chordoma.** *J Neurosurg* 2018;129:1429–37 CrossRef Medline
- Li M, Zhai Y, Bai J, et al. **SNF5 as a prognostic factor in skull base chordoma.** *J Neurooncol* 2018;137:139–46 CrossRef Medline
- Zhai Y, Bai J, Wang S, et al. **Differences in dural penetration of clival chordomas are associated with different prognosis and expression of platelet-derived growth factor receptor- β .** *World Neurosurg* 2017;98:288–95 CrossRef Medline
- Tian K, Wang L, Wang K, et al. **Analysis of clinical features and outcomes of skull base chordoma in different age-groups.** *World Neurosurg* 2016;92:407–17 CrossRef Medline
- Wang L, Wu Z, Tian K, et al. **Clinical features and surgical outcomes of patients with skull base chordoma: a retrospective analysis of 238 patients.** *J Neurosurg* 2017;127:1257–67 CrossRef Medline
- Bai J, Zhai Y, Wang S, et al. **Prognostic value of a category based on electron microscopic features of clival chordomas.** *World Neurosurg* 2017;99:282–87 CrossRef Medline
- Sung MS, Lee GK, Kang HS, et al. **Sacroccygeal chordoma: MR imaging in 30 patients.** *Skeletal Radiol* 2005;34:87–94 CrossRef Medline
- Yeom KW, Lober RM, Mobley BC, et al. **Diffusion-weighted MRI: distinction of skull base chordoma from chondrosarcoma.** *AJNR Am J Neuroradiol* 2013;34:1056–61 CrossRef Medline
- Tian K, Wang L, Ma J, et al. **MR imaging grading system for skull base chordoma.** *AJNR Am J Neuroradiol* 2017;38:1206–11 CrossRef Medline
- Lin E, Scognamiglio T, Zhao Y, et al. **Prognostic implications of gadolinium enhancement of skull base chordomas.** *AJNR Am J Neuroradiol* 2018;39:1509–15 CrossRef Medline
- Yin P, Mao N, Zhao C, et al. **A triple-classification radiomics model for the differentiation of primary chordoma, giant cell tumor, and metastatic tumor of sacrum based on T2-weighted and contrast-enhanced T1-weighted MRI.** *J Magn Reson Imaging* 2019;49:752–59 CrossRef Medline
- Li L, Wang K, Ma X, et al. **Radiomic analysis of multiparametric magnetic resonance imaging for differentiating skull base chordoma and chondrosarcoma.** *Eur J Radiol* 2019;118:81–87 CrossRef Medline
- von Witzleben A, Goertler LT, Lennerz J, et al. **In chordoma, metastasis, recurrences, Ki-67 index, and a matrix-poor phenotype are associated with patients' shorter overall survival.** *Eur Spine J* 2016;25:4016–24 CrossRef Medline
- Tateishi U, Hasegawa T, Beppu Y, et al. **Prognostic significance of MRI findings in patients with myxoid-round cell liposarcoma.** *AJR Am J Roentgenol* 2004;182:725–31 CrossRef Medline
- Santamaria G, Velasco M, Bargallo X, et al. **Radiologic and pathologic findings in breast tumors with high signal intensity on T2-weighted MR images.** *Radiographics* 2010;30:533–48 CrossRef Medline
- Shih AR, Cote GM, Chebib I, et al. **Clinicopathologic characteristics of poorly differentiated chordoma.** *Mod Pathol* 2018;31:1237–45 CrossRef Medline
- Santos P, Peck KK, Arevalo-Perez J, et al. **T1-weighted dynamic contrast-enhanced MR perfusion imaging characterizes tumor response to radiation therapy in chordoma.** *AJNR Am J Neuroradiol* 2017;38:2210–16 CrossRef Medline
- Wei W, Wang K, Liu Z, et al. **Radiomic signature: a novel magnetic resonance imaging-based prognostic biomarker in patients with skull base chordoma.** *Radiother Oncol* 2019;141:239–46 CrossRef Medline
- Zhai Y, Bai J, Wang S, et al. **Aberrant expression of extracellular signal-regulated kinase and 15-hydroxyprostaglandin dehydrogenase indicates radiation resistance and poor prognosis for patients with clival chordomas.** *World Neurosurg* 2018;115:e146–51 CrossRef Medline
- Sasaki T, Moritani T, Belay A, et al. **Role of the apparent diffusion coefficient as a predictor of tumor progression in patients with chordoma.** *AJNR Am J Neuroradiol* 2018;39:1316–21 CrossRef Medline
- Buizza G, Molinelli S, D'Ippolito E, et al. **MRI-based tumour control probability in skull-base chordomas treated with carbon-ion therapy.** *Radiother Oncol* 2019;137:32–37 CrossRef Medline

Inter- and Intra-reader Agreement of NI-RADS in the Interpretation of Surveillance Contrast-Enhanced CT after Treatment of Oral Cavity and Oropharyngeal Squamous Cell Carcinoma

F.H.J. Elsholtz, S.-R. Ro, S. Shnayien, C. Erxleben, H.-C. Bauknecht, J. Lenk, L.-A. Schaafs, B. Hamm, and S.M. Niehues

ABSTRACT

BACKGROUND AND PURPOSE: The Neck Imaging Reporting and Data System was introduced to assess the probability of recurrence in surveillance imaging after treatment of head and neck cancer. This study investigated inter- and intra-reader agreement in interpreting contrast-enhanced CT after treatment of oral cavity and oropharyngeal squamous cell carcinoma.

MATERIALS AND METHODS: This retrospective study analyzed CT datasets of 101 patients. Four radiologists provided the Neck Imaging Reporting and Data System reports for the primary site and neck (cervical lymph nodes). The Kendall's coefficient of concordance (W), Fleiss κ (κ_F), the Kendall's rank correlation coefficient (τ_B), and weighted κ statistics (κ_w) were calculated to assess inter- and intra-reader agreement.

RESULTS: Overall, interreader agreement was strong or moderate for both the primary site ($W=0.74$, $\kappa_F=0.48$) and the neck ($W=0.80$, $\kappa_F=0.50$), depending on the statistics applied. Interreader agreement was higher in patients with proved recurrence at the primary site ($W=0.96$ versus 0.56 , $\kappa_F=0.65$ versus 0.30) or in the neck ($W=0.78$ versus 0.56 , $\kappa_F=0.41$ versus 0.29). Intra-reader agreement was moderate to strong or almost perfect at the primary site (range $\tau_B=0.67$ – 0.82 , $\kappa_w=0.85$ – 0.96) and strong or almost perfect in the neck (range $\tau_B=0.76$ – 0.86 , $\kappa_w=0.89$ – 0.95).

CONCLUSIONS: The Neck Imaging Reporting and Data System used for surveillance contrast-enhanced CT after treatment of oral cavity and oropharyngeal squamous cell carcinoma provides acceptable score reproducibility with limitations in patients with post-therapeutic changes but no cancer recurrence.

ABBREVIATIONS: BI = Breast Imaging; CECT = contrast-enhanced CT; LI = Liver Imaging; NI = Neck Imaging; OCSCC = oral cavity squamous cell carcinoma; OPSCC = oropharyngeal squamous cell carcinoma; PI = Prostate Imaging; RADS = Reporting and Data System

Oral cavity squamous cell carcinoma (OCSCC) is the most common malignancy of the head and neck but might soon be overtaken by oropharyngeal squamous cell carcinoma (OPSCC), whose incidence is rapidly rising, mainly because its occurrence is related to the human papillomavirus.¹⁻³ Smoking and alcohol use are outstanding risk factors with synergistic effects.⁴ While some authors use OCSCC for cancers in both locations, we think it is important to separate them. The oral cavity is separated from the oropharynx by the junction of the hard and soft palates above and the

circumvallate papillae located at the transition from the anterior two-thirds to the posterior third of the tongue below.⁵

After completion of curative treatment for OCSCC or OPSCC, patients are enrolled in a program of continuous surveillance imaging and clinical examinations. Surveillance imaging can be performed using CT, MR imaging, or PET/CT and PET/MR imaging.^{5,6} Radiologists interpreting posttherapeutic imaging studies in these patients typically focus on the detection of submucosal recurrence at the primary cancer site and the identification of suspicious lymph nodes in the neck. Mucosal recurrence might also be seen in surveillance imaging but is a domain of referring clinicians. Especially in patients who underwent high-dose radiation therapy, the best surveillance can be ensured with a combination of clinical examinations, high-resolution imaging, and possibly endoscopy.⁷

Interpretation of posttherapeutic neck imaging studies in these patients is often challenging for radiologists. In this setting, nonstandardized framing is the common way to rate the probability of cancer recurrence. Reporting and Data Systems (RADS) provide standardized terminology and guidance toward a final

Received August 21, 2019; accepted after revision March 8, 2020.

From the Institute of Radiology (F.H.J.E., S.-R.R., S.S., C.E., J.L., L.-A.S., B.H., S.M.N.), Charité-Universitätsmedizin Berlin, corporate member of Freie Universität Berlin, Humboldt-Universität zu Berlin, Campus Benjamin Franklin, Berlin, Germany; and Institute of Neuroradiology (H.-C.B.), Charité-Universitätsmedizin Berlin, corporate member of Freie Universität Berlin, Humboldt-Universität zu Berlin, Campus Virchow Klinikum, Berlin, Germany.

Please address correspondence to Fabian Henry Jürgen Elsholtz, MD, Charité-Universitätsmedizin Berlin, Institute of Radiology, Campus Benjamin Franklin, Hindenburgdamm 30, Berlin, Germany; e-mail: fabian.elsholtz@charite.de; @FabianElsholtz

<http://dx.doi.org/10.3174/ajnr.A6529>

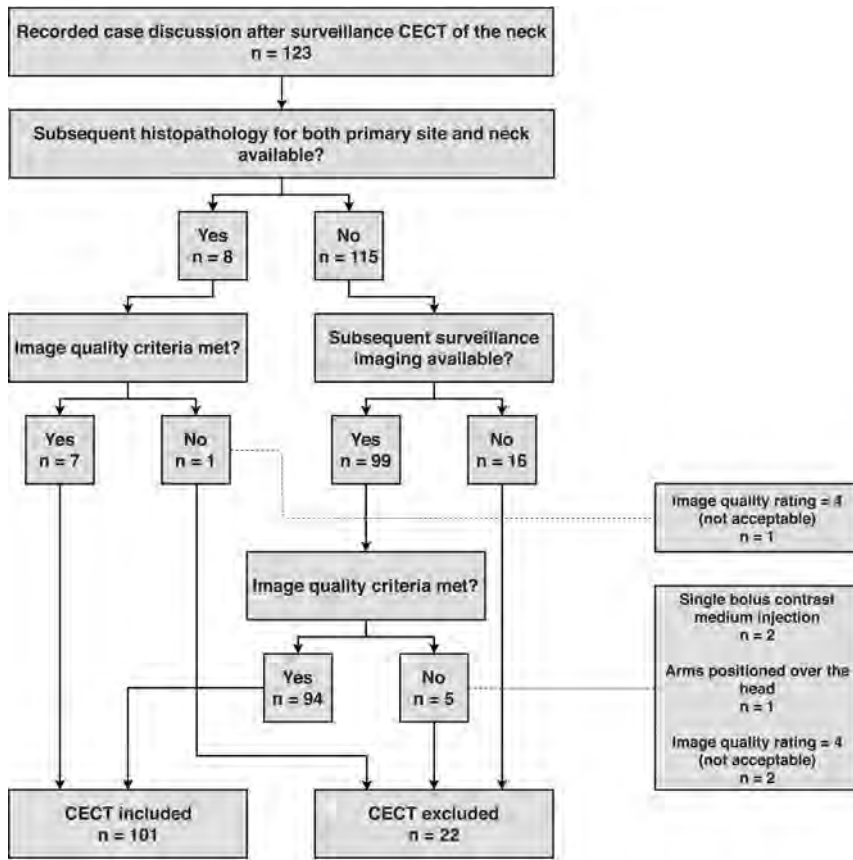


FIG 1. Flow chart of study participants.

score reflecting the probability of malignancy in patients enrolled in cancer surveillance programs. Following the introduction of such a system for breast imaging (BI-RADS) in 1997, several RADS for different organs and body regions (eg, PI-RADS for the prostate and LI-RADS for the liver) have been published and also become highly appreciated by referring clinicians, not in the least because they improve comparability and reproducibility.⁸⁻¹⁰

In 2016, the Neck Imaging Reporting and Data System (NI-RADS) was introduced by the American College of Radiology and has shown a promising initial performance.¹¹⁻¹³ Defined features and findings lead to a numeric value that reflects the probability of cancer recurrence and is directly linked to recommendations for measures to be taken for further patient management.

The major motivation to perform this study was to test NI-RADS for its reliability in interpreting contrast-enhanced CT (CECT), which is, by far, the most common technique used for the surveillance of patients with head and neck cancer in our institution, to obtain evidence to support its implementation as a reporting standard for imaging studies and discussion of findings with referring physicians from the department of oral and maxillofacial surgery.

MATERIALS AND METHODS

Patient Population

This retrospective study was approved by our institutional review board, and written informed consent was obtained from all

patients. In the records of our weekly interdisciplinary conferences (of radiologists and oral and maxillofacial surgeons) held between June 2017 and July 2019, we identified 123 consecutive patients for whom CECT studies performed at our department or by an external institution were available, and 101 patients (41 women, 60 men; median age, 64 years) were finally included in this study. A flow chart of participants is provided in Fig 1. A total of 202 target sites (primary cancer site and neck for each patient) were evaluated. Of the patients included, 72 had OSCC localized in the mouth floor ($n = 22$), the anterior two-thirds of the tongue ($n = 19$), the hard palate ($n = 3$), and the gingival, labial, or buccal mucosa ($n = 28$). Twenty-nine patients had OPSCC localized in the posterior third (base) of the tongue ($n = 13$), the soft palate ($n = 2$), the palatine tonsils ($n = 13$), and the posterior oropharyngeal wall ($n = 1$).

Imaging

Of the 101 CECT studies included, 72 were performed in our department, and 29, by an external institution. In our department, we perform neck CECT scans on an 80-section CT scanner (Aquilion PRIME; Canon Medical Systems, Otawara, Japan). Our standard protocol includes scout-based automated selection of tube voltages between 100 and 130 kV and tube current modulation between 60 and 600 mA, a tube rotation time of 0.75 seconds, collimated section thickness of 0.5 mm, and a pitch factor of 0.813. Seventy-five milliliters of contrast medium (iopamidol, Imeron 400; Bracco, Milan, Italy) is injected as a split bolus: the first bolus of 50 mL at a flow rate of 2.5 mL/s and the second bolus of 25 mL 55 seconds later at a flow rate of 3.5 mL/s, followed by a 40 mL saline chaser at a flow rate of 2.5 mL/s. The helical scan starts with a delay of 18 seconds after the start of the second bolus injection.

Image quality of the CECT datasets was rated on a 4-point scale (1, excellent; 2, good; 3, acceptable; 4, not acceptable) to ensure that the dataset allows adequate assessment of the primary site, which is often and primarily affected by metal artifacts. A rating of 4 means that the primary site cannot be evaluated for cancer recurrence.

Inclusion Criteria

- 1) Status posttreatment of OSCC or OPSCC and recorded case discussion in our weekly interdisciplinary conference (departments of radiology and of oral and maxillofacial surgery).
- 2) CECT within 3–12 months after treatment or prior surveillance imaging.
- 3) CECT imaging-quality requirements.

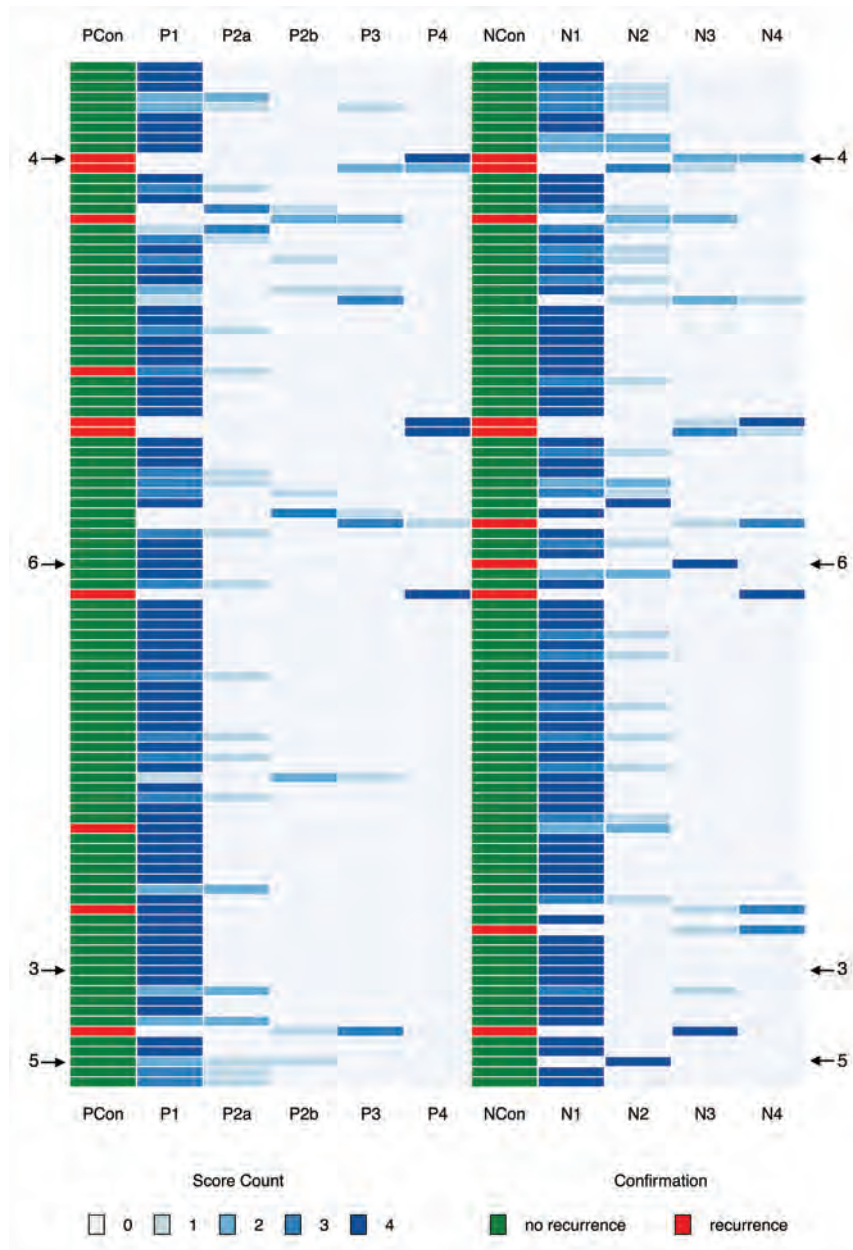


FIG 2. Score distribution chart for all 101 patients. Score counts are coded as shades of blue. Two columns (PCon and NCon) provide the result of the confirmation study. Arrows with numbers refer to figures providing CT images of respective patients. PCon and NCon indicate the results of the confirmation studies for the primary site and the neck; P1, P2a, P2b, P3, P4, NI-RADS categories for the primary site; N1, N2, N3, N4, NI-RADS categories for the neck.

- a) Split bolus injection of contrast medium resulting in a combined vascular and delayed phase in 1 acquisition.
- b) Arms positioned below the head and neck (next to the chest and abdomen).
- c) Image quality rating of 1 (excellent), 2 (good), or 3 (acceptable).
- 4) Confirmation study either as:
 - a) Subsequent surveillance imaging (CECT, MRI, PET) no earlier than 3 months after the CECT study included or
 - b) Histopathologic study.

Exclusion Criteria

- 1) Failure to meet CECT quality requirements:

- a) Single bolus injection of contrast medium resulting in a single delayed phase.
- b) Arms positioned over the head.
- c) Image quality rating of 4 (not acceptable).
- 2) No subsequent confirmation study.

Readers and Reporting Process

Four radiologists with different levels of experience (A, 3 years and ~300 prior reports of neck CECT; B, 4 years and ~300 reports of neck CECT; C, 7 years and ~700 reports of neck CECT; D, 15 years and ~3300 reports of neck CECT) reviewed the 101 cases included in our analysis. Radiologists A and B were grouped as less

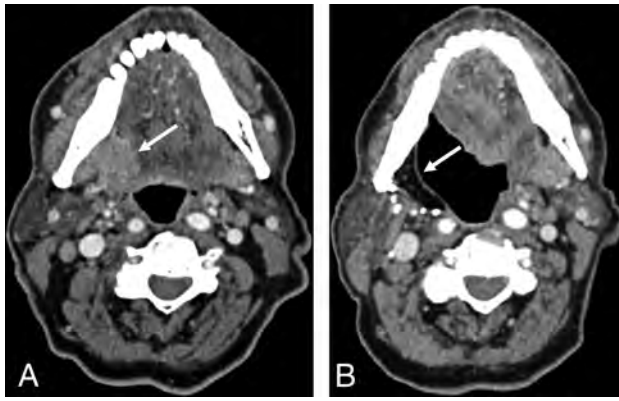


FIG 3. Pretreatment CT (A) of a patient with OCSCC located in the right glossopharyngeal sulcus. Posttreatment CT (B) of the same patient obtained 36 months after resection and neck dissection on the right side (B). A NI-RADS score of 1 was assigned in B for the primary site by all 4 readers. The white arrow indicates the cancer lesion in the primary site (A) and the fatty degenerated muscle flap after resection (B).

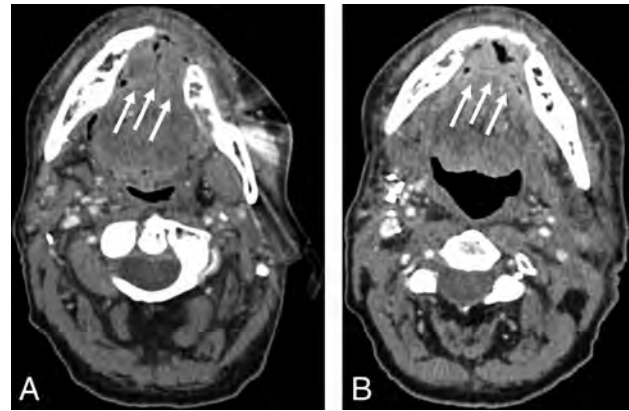


FIG 5. Posttreatment CTs of a patient with OCSCC located in the anterior mouth floor obtained 12 (A) and 24 (B) months after resection and bilateral neck dissection. The patient's position differed slightly between the 2 posttreatment CT scans. NI-RADS scores of 2a, 2b, 1, and 1 reflect inconsistent interpretation of the primary site (indicated by the white arrows) in B. Histopathology revealed no malignancy.

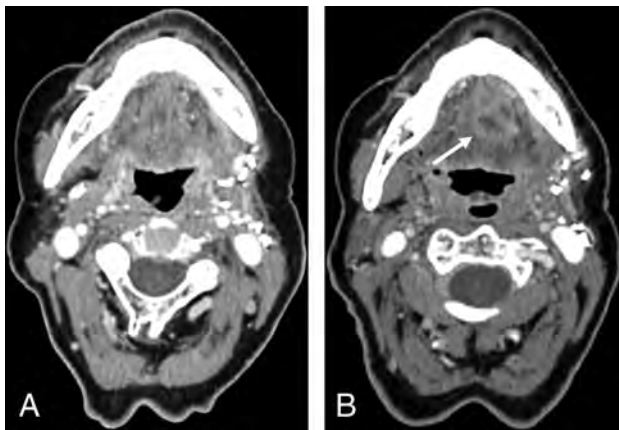


FIG 4. Posttreatment CTs of a patient with OPSCC located in the left mouth floor obtained 3 months (A) and 15 months (B) after resection and neck dissection on the left side. A NI-RADS score of 4 was assigned in B for the primary site by all 4 readers. Histopathology confirmed recurrence. The white arrow indicates a new enhancing mass in the mouth floor.

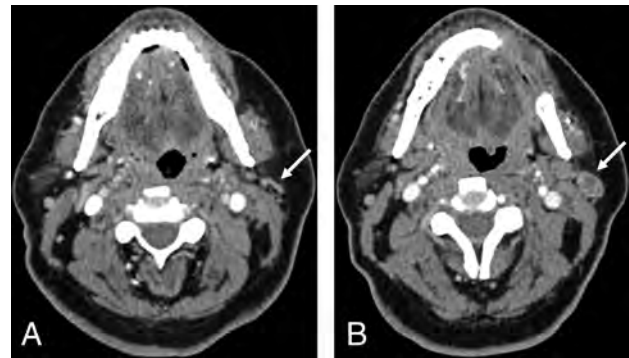


FIG 6. Pretreatment CT (A) of a patient with OCSCC located in the buccal mucosa in the upper left quadrant. Posttreatment CT (B) of the same patient 3 months after resection and neck dissection on the left side shows an enlarged and necrotic parotid lymph node on the left side as indicated by the white arrows. A NI-RADS score of 3 was assigned in B for the neck by all 4 readers, and histopathology confirmed malignancy.

experienced; C and D, as more experienced readers. Radiologist D is specialized in imaging of the head and neck. At no time were any of the 4 radiologists involved in the interdisciplinary conferences from which patients were included in this study. Anonymized patients were reordered using random numbers assigned by Excel (Version 16.16.10; Microsoft, Redmond, Washington). Readers had access to previous imaging studies (before and after treatment, if available), and they were aware of clinical information to simulate a real reporting situation. Subsequent imaging findings, diagnoses, or clinical examination reports were not available to the 4 readers. After 3 months, radiologists A, B, C, and D were asked again to report on the CECT datasets of the same 101 patients now presented in a newly randomized order. Each of the 2 serial rating sessions was performed in 4 rounds with 25, 25, 25, and 26 patients and a break of 1 week between each round. Another radiologist who was not part of the NI-RADS reader group (E, 6 years of

experience and ~400 CECT examinations of the neck) rated the image quality.

NI-RADS Scoring System

Reports of imaging findings were based on the NI-RADS White Paper published in 2018, which was well-studied and jointly discussed by our readers and the authors.¹¹ NI-RADS scores between 1 and 4, reflecting increasing probabilities of cancer recurrence, are assigned separately for the primary site and for cervical lymph nodes ("neck"). NI-RADS 0 is only used as a preliminary score in cases in which prior images have been obtained but are not available at the time of reading and therefore were not required in our study design. NI-RADS 1 is assigned for expected posttherapeutic changes like the typical superficial diffuse linear contrast enhancement in the primary site and absence of residual abnormal, new, or

Table 1: Interreader agreement

Group	Primary Site				Neck			
	W	τ_B	κ_F	κ_w	W	τ_B	κ_F	κ_w
Overall	0.74		0.48		0.80		0.50	
More experienced readers		0.50		0.80		0.60		0.76
Less experienced readers		0.82		0.96		0.96		0.99
No recurrence	0.56		0.30		0.56		0.29	
Recurrence	0.96		0.65		0.78		0.41	
NI-RADS 1 and 2 merged	0.51		0.23		0.56		0.26	
NI-RADS 3 and 4 merged	0.85		0.56		0.59		0.44	

Table 2: Intrareader agreement

Reader	Primary Site		Neck	
	τ_B	κ_w	τ_B	κ_w
A	0.73	0.85	0.86	0.93
B	0.67	0.90	0.86	0.95
C	0.82	0.96	0.86	0.94
D	0.76	0.92	0.76	0.89

enlarged lymph nodes in the neck. NI-RADS 2 for the primary site is subdivided into 2a for focal superficial enhancement and 2b for deep, ill-defined enhancement. NI-RADS 2 for the neck indicates residual abnormal or new, enlarged lymph nodes without new necrosis or extranodal extension. NI-RADS 3 is assigned for discrete masses in the primary site and new necrosis or extranodal extension of lymph node involvement in the neck. NI-RADS 4 indicates definitive primary site or nodal radiologically or even histopathologically proved recurrence.

Data Analysis

Statistical analysis was performed using R Studio (Version 1.1.383; <http://rstudio.org/download/desktop>) with the “irr” package installed. The heatmap (Fig 2) was generated using R Studio and the “gplots” package. The flowchart was issued using draw.io (Version 10.8.0; JGraph, Northampton, UK).

Subgroups were formed according to readers’ experience (more-versus-less experienced), the results of the confirmation studies (no recurrence versus recurrence), and the probability of cancer recurrence based on the NI-RADS scores of most readers (NI-RADS 1 and 2 versus NI-RADS 3 and 4).

The Kendall’s W (W) and Fleiss κ (κ_F) were calculated to test interreader agreement. Calculation of W included a correction factor for tied ranks, and its statistical significance was assessed using the χ^2 test. The Kendall’s rank correlation coefficient τ_B and the Cohen weighted κ (κ_w) were computed to quantify either interreader agreement between 2 readers or intrareader agreement. Calculation of κ_w provided weighted disagreements according to their squared distance from perfect agreement.

W and τ_B were interpreted on the basis of the guidelines of Schmidt,¹⁴ proposing a 5-step classification: 0.10–0.29, very weak agreement; 0.30–0.49, weak agreement; 0.50–0.69, moderate agreement; 0.70–0.89, strong agreement; 0.90–1.00, very strong agreement. Interpretation of κ_F and κ_w followed the recommendations of Landis and Koch:¹⁵ < 0.20, slight agreement; 0.21–0.40, fair agreement; 0.41–0.60, moderate agreement; 0.61–0.80, substantial agreement; 0.81–1.00, (almost) perfect agreement.

Recurrence rates were calculated from the NI-RADS scores of most readers. In case of tied scores, the score assigned by the most experienced reader D was decisive.

RESULTS

Figure 2 provides an overview of rating distributions for all 101 patients in the form of a heatmap. It also includes results of the confirmation studies with

arrows indicating exemplary cases with perfect or poor agreement among raters. Numbers next to the arrows indicate the figure in which the cases are presented (Figs 3–6).

Depending on the statistical tests used, overall interreader agreement (Table 1) was strong or moderate for both the primary site (W = 0.74, κ_F = 0.48) and the neck (W = 0.80, κ_F = 0.50). Less experienced readers showed higher interreader agreement for the primary site (τ_B = 0.82 versus 0.50, κ_w = 0.96 versus 0.80) and the neck (τ_B = 0.96 versus 0.60, κ_w = 0.99 versus 0.76). Other subgroups were formed according to the results of the confirmation studies. A total of 13 patients were diagnosed with cancer recurrence. Seven patients had simultaneous cancer recurrence at the primary site and in the neck, while 3 patients each had cancer recurrence at the primary site or in the neck. In patients without proved recurrence, interreader agreement was moderate or fair for the primary site (W = 0.56, κ_F = 0.30) and the neck (W = 0.56, κ_F = 0.29). By contrast, interreader agreement in patients with proved recurrence was very strong or substantial for the primary site (W = 0.96, κ_F = 0.65) and strong or moderate for the neck (W = 0.78, κ_F = 0.41). When forming merged NI-RADS categories according to high and low suspicion of cancer recurrence, we found higher interreader agreement for NI-RADS 3/4 than NI-RADS 1/2 for both the primary site (W = 0.85 versus 0.51, κ_F = 0.56 versus 0.23) and the neck (W = 0.59 versus 0.56, κ_F = 0.44 versus 0.26).

Intrareader agreement (Table 2) for the primary site ranged from moderate to strong (τ_B = 0.67–0.82) or almost perfect (κ_w = 0.85–0.96). Intrareader agreement for the neck was strong (τ_B = 0.76–0.86) or almost perfect (κ_w = 0.89–0.95).

All statistical analyses conducted to test inter- and intra-reader agreement showed statistical significance ($P < .05$).

Recurrence rates (Table 3) were between 3.57% (NI-RADS 1) and 100% (NI-RADS 4) for the primary site and 0% (NI-RADS 1) and 83.33% (NI-RADS 4) for lymph nodes (Table 3). Patients without histopathology for confirmation of their diagnosis were followed up for a median of 351 days (range, 159–772 days), defined by the date of their last surveillance imaging study.

DISCUSSION

Inter- and intrareader agreement is important for estimating the reliability of any diagnostic test. To the best of our knowledge, a study investigating inter- and intrareader agreement of NI-RADS scores has not been published. However, we can discuss our results for NI-RADS with those other investigators’ results obtained for the reliability of RADS in other organs. Published data give a very diverse picture. A study similar to ours in terms

Table 3: Score counts and recurrence rates for each category based on majority decision^a

NI-RADS Score	Score Count	Recurrence	No Recurrence	Recurrence Rate
Primary 1	84	3	81	3.57%
Primary 2a	6	0	6	0%
Primary 2b	3	1	2	33.33%
Primary 3	4	2	2	50%
Primary 4	4	4	0	100%
Node 1	83	0	83	0%
Node 2	7	1	6	14.29%
Node 3	5	4	1	80%
Node 4	6	5	1	83.33%

^aThe most experienced reader D was decisive in case of tied score counts.

of statistical methods and results was published by Irshad et al,¹⁶ who assessed consecutive versions of BI-RADS including 5 readers and 104 mammographic examinations. They found an overall interreader agreement of 0.65 and 0.57 (Fleiss κ), while overall intrareader agreement was 0.84 and 0.78 (Cohen weighted κ). A study by Smith et al¹⁷ determined the reliability of PI-RADS in the interpretation of multiparametric MR imaging of the prostate, including 4 readers and 102 examinations, again similar to our study design. However, by contrast, they reported an overall interreader agreement of 0.24 (Fleiss κ) and an overall intrareader agreement of 0.43–0.67 (Cohen κ).

When we compared the 2 studies with our results, the difference in overall interreader agreement stood out first. Our results obtained with NI-RADS ($\kappa_F = 0.48$ and 0.50) are much better than findings reported by other investigators for PI-RADS but inferior to results achieved with BI-RADS. NI-RADS showed a very high intrareader agreement ($\kappa_w = 0.85$ – 0.96 and $\kappa_w = 0.89$ – 0.95), especially against the poor values obtained in the PI-RADS study. Thus, our results are encouraging because they suggest that there is the potential for improving interreader agreement. Given that the NI-RADS lexicon and decision tree can only be used fully when interpreting PET/CT or PET/MR imaging, we expect that interreader agreement can be considerably improved using either of these modalities. Especially, NI-RADS categories 1 and 2 (2a and 2b) are defined more clearly when additional information on FDG uptake is available.

Apart from our findings regarding absolute overall agreement, our analysis also provides some interesting results regarding the subgroups formed. Unexpectedly, overall interreader agreement for both the primary site and the neck was higher between the 2 less experienced readers than between the 2 more experienced readers. Furthermore, interreader agreement for the absence of recurrence in lymph nodes was poorer than we expected. A possible explanation emerged from discussions with the readers after completion of the study: The definition for assigning a lymph node to NI-RADS 2 is “mildly enlarging without specific morphologically abnormal features such as new necrosis or extracapsular spread,” which was perceived as rather vague.¹¹ Some kind of measurable threshold might significantly increase agreement among raters. Other results of our study suggest adequate sensitivity of NI-RADS. Interreader agreement was significantly higher in cases of proved cancer recurrence compared with patients without recurrence.

Coincidentally low recurrence rates in the group classified as NI-RADS 1 as well as high recurrence rates in groups with NI-RADS scores of 3 and 4 suggest that NI-RADS is a powerful tool

for discrimination of patients with a low-versus-high risk of cancer recurrence. No patients assigned scores of 2a for the primary site had cancer recurrence, which might be attributable to the relatively small number of cases or greater variability in the interpretation of findings, as already discussed above. Recurrence rates calculated in our study are based on majority decision but align very well with initially published data.^{11,18,19}

While calculation of κ coefficients is by far the most common statistical test to quantify inter- and intrareader agreement,^{20,21} there are also more differentiated approaches addressing other aspects of inter- and intrareader agreement.²² Other investigators primarily recommend κ statistics for testing nominal scaled data.^{23,24} From our standpoint, NI-RADS scores should be regarded as ordinal data because rising values represent a rising probability of cancer recurrence. Therefore, the Kendall's coefficient of concordance (used to determine interreader agreement for >2 readers) and the Kendall's rank correlation coefficient (interreader agreement with 2 raters or intrareader agreement) should be most appropriate.²⁵ When we compared the result pairs of statistical methods in our study, it is apparent that values of W are always higher than those of κ_F but values of τ_B are always lower than those of κ_w , while their relationships stay basically constant. The intraclass correlation is also used to determine inter- and intrareader agreement; however, it should only be used for underlying continuous data. We therefore chose not to calculate intraclass correlation statistics for the discrete data provided by NI-RADS.

This study, although retrospective, was designed to put readers in a real-world clinical reporting situation. This means that the readers had access to information on OCSCC/OPSCC localization as defined by the multidisciplinary cancer conference, surgical and radiotherapeutic procedures, and pre-existing illnesses. This information is available to reporting radiologists in the clinical setting and is important for appropriately and comprehensively interpreting imaging findings and assessing the patient's condition. On the other hand, there were actions to reduce possible bias. Cases were presented in randomized order, and anonymization of patient data was performed to lower a possible detection bias. The 101 CECT datasets were split into 4 rating sessions (25, 25, 25, and 26) to minimize possible over- or underratings because of readers' raised awareness and altered perception of similarities and differences when comparing cases with others they have recently seen in the artificial reading situation.

Clinically suspected OCSCC or OPSCC and posttherapeutic surveillance are the most frequent indications for neck imaging in our institution, with CECT being much more commonly used than MR imaging. Future studies should investigate inter- and intrareader agreement of NI-RADS, not only for other malignancies (eg, larynx and salivary glands) but also for different imaging modalities (CECT, MR imaging, PET/CT and PET/MR imaging). The role of PET/CT and PET/MR imaging in up- or downgrading lesions seen on CECT or MR imaging without PET should also be of interest in studies, especially prospectively designed, studies.

Limitations

Four radiologists reported imaging findings in this study. While radiologists A and B were relatively close in terms of work experience (years and number of examinations), C and D were wider apart. Although C could easily be classified as more experienced than A and B, a work experience closer to D would have been desirable to ensure ideally balanced subgroups. Subdividing readers into 3 groups with an additional group of intermediate experience might also yield interesting additional results. Because we just started to integrate NI-RADS as a reporting system in our institution, future studies could address these limitations. As readers become more familiar with using NI-RADS and shared experience grows, common approaches might emerge and improve interreader agreement. Although all 4 radiologists were well-acquainted with the literature on NI-RADS, a joint discussion of exemplar cases from our department might have improved interreader and even intrareader agreement. Beyond that, in our opinion, more experience might also lead to higher rates of NI-RADS 2a/b scores being assigned because findings in this category are more difficult to express in prose reports because referring clinicians expect a clear decision between “suspected recurrence” versus “no suspected recurrence.” We determined recurrence rate as a secondary outcome. Although it attests to the good discriminatory power of NI-RADS, future studies investigating the validity of NI-RADS should define a longer follow-up period of at least 1 year.

CONCLUSIONS

NI-RADS used for interpreting CECT after treatment of OCSCC and OPSCC provides acceptable score reproducibility. A major strength of this standardized approach is the good interreader agreement in patients with proved cancer recurrence and overall intrareader agreement in general. At the same time, there are limitations in terms of interreader agreement in patients with post-therapeutic changes but no cancer recurrence. Although only determined as secondary outcomes, recurrence rates in our patients were similar to those in preliminary published data.

Disclosures: Stefan Markus Niehues—UNRELATED: Grants/Grants Pending: German Research Foundation grant*; Payment for Lectures Including Service on Speakers Bureaus: speakers honorarium for Canon, Guerbet, Bracco, Teleflex, Bernd Hamm—UNRELATED: Grants/Grants Pending: Abbott Laboratories, Actelion Pharmaceuticals, Bayer Schering Pharma, Bayer Vital, Bracco Group, Bristol-Myers Squibb, Charité Research Organization GmbH, Deutsche Krebshilfe, Deutsche Stiftung für Herzforschung, Essex Pharma, European Union Programs, FIBREX Medical Inc, Focused Ultrasound Surgery Foundation, Fraunhofer Gesellschaft, Guerbet, INC Research, InSightec Ltd, Ipsen Biopharmaceuticals, Kendle/MorphoSys AG, Lilly Deutschland GmbH, Lundbeck GmbH, MeVis Medical Solutions AG, Nexus Oncology, Novartis, Parexel CRO Service, Perceptive Innovations, Pfizer GmbH, Philipps Healthcare, Sanofi-Aventis SA, Siemens, Spectranetics GmbH, Terumo Medical Corporation, TNS Healthcare GmbH, Toshiba, UCB, Wyeth Pharmaceuticals, Zukunftsfond Berlin/TSB Medici.* Money paid to the institution.

REFERENCES

1. Chi AC, Day TA, Neville BW. **Oral cavity and oropharyngeal squamous cell carcinoma: an update.** *CA Cancer J Clin* 2015;65:401–21 CrossRef Medline
2. Chaturvedi AK, Engels EA, Pfeiffer RM, et al. **Human papillomavirus and rising oropharyngeal cancer incidence in the United States.** *J Clin Oncol* 2011;29:4294–301 CrossRef Medline
3. Bray F, Ferlay J, Soerjomataram I, et al. **Global cancer statistics 2018: GLOBOCAN estimates of incidence and mortality worldwide for 36 cancers in 185 countries.** *CA Cancer J Clin* 2018;68:394–424 CrossRef Medline
4. Rivera C. **Essentials of oral cancer.** *Int J Clin Exp Pathol* 2015;8:11884–94 Medline
5. Seeburg DP, Baer AH, Aygun N. **Imaging of patients with head and neck cancer: from staging to surveillance.** *Oral Maxillofac Surg Clin North Am* 2018;30:421–33 CrossRef Medline
6. Queiroz MA, Hullner M, Kuhn F, et al. **PET/MRI and PET/CT in follow-up of head and neck cancer patients.** *Eur J Nucl Med Mol Imaging* 2014;41:1066–75 CrossRef Medline
7. Pfister DG, Spencer S, Brizel DM, et al; National Comprehensive Cancer Network. **Head and neck cancers, Version 2.2014: clinical practice guidelines in oncology.** *J Natl Compr Canc Netw* 2014;12:1454–87 CrossRef Medline
8. D’Orsi CJ, Kopans DB. **Mammography interpretation: the BI-RADS method.** *Am Fam Physician* 1997;55:1548–50, 52 Medline
9. Barentsz JO, Richenberg J, Clements R, et al. **ESUR prostate MR guidelines 2012.** *Eur Radiol* 2012;22:746–57 CrossRef Medline
10. Puryso AS, Remer EM, Coppa CP, et al. **LI-RADS: a case-based review of the new categorization of liver findings in patients with end-stage liver disease.** *Radiographics* 2012;32:1977–95 CrossRef Medline
11. Aiken AH, Rath TJ, Anzai Y, et al. **ACR Neck Imaging Reporting and Data Systems (NI-RADS): A White Paper of the ACR NI-RADS Committee.** *J Am Coll Radiology* 2018;15:1097–108 CrossRef Medline
12. Krieger DA, Hudgins PA, Nayak GK, et al. **Initial performance of NI-RADS to predict residual or recurrent head and neck squamous cell carcinoma.** *AJNR Am J Neuroradiol* 2017;38:1193–99 CrossRef Medline
13. Aiken AH, Farley A, Bagnon KL, et al. **Implementation of a novel surveillance template for head and neck cancer: Neck Imaging Reporting and Data System (NI-RADS).** *J Am Coll Radiol* 2016;13:743–46.e1 CrossRef Medline
14. Schmidt RC. **Managing Delphi surveys using nonparametric statistical techniques.** *Decision Sciences* 1997;28:763–74 CrossRef
15. Landis JR, Koch GG. **The measurement of observer agreement for categorical data.** *Biometrics* 1977;33:159–74 CrossRef
16. Irshad A, Leddy R, Ackerman S, et al. **Effects of changes in BI-RADS Density Assessment Guidelines (fourth versus fifth edition) on breast density assessment: intra- and interreader agreements and density distribution.** *AJR Am J Roentgenol* 2016;207:1366–71 CrossRef Medline
17. Smith CP, Harmon SA, Barrett T, et al. **Intra- and interreader reproducibility of PI-RADSv2: a multireader study.** *J Magn Reson Imaging* 2019;49:1694–703 CrossRef Medline
18. Hsu D, Chokshi FH, Hudgins PA, et al. **Predictive value of first post-treatment imaging using standardized reporting in head and neck cancer.** *Otolaryngol Head Neck Surg* 2019;161:978–85 CrossRef Medline
19. Wangaryattawanich P, Branstetter BF, Hughes M, et al. **Negative predictive value of NI-category 2 in the first posttreatment FDG-PET/CT in head and neck squamous cell carcinoma.** *AJNR Am J Neuroradiol* 2018;39:1884–88 CrossRef Medline
20. Grimm LJ, Anderson AL, Baker JA, et al. **Interobserver variability between breast imagers using the fifth edition of the BI-RADS MRI lexicon.** *AJR Am J Roentgenol* 2015;204:1120–24 CrossRef Medline
21. Rosenkrantz AB, Ginocchio LA, Cornfeld D, et al. **Interobserver reproducibility of the PI-RADS Version 2 Lexicon: a multicenter study of six experienced prostate radiologists.** *Radiology* 2016;280:793–804 CrossRef Medline
22. Griessenauer CJ, Miller JH, Agee BS, et al. **Observer reliability of arteriovenous malformations grading scales using current imaging modalities.** *J Neurosurg* 2014;120:1179–87 CrossRef Medline
23. Hripscak G, Heitjan DF. **Measuring agreement in medical informatics reliability studies.** *J Biomed Inform* 2002;35:99–110 CrossRef
24. Zapf A, Castell S, Morawietz L, et al. **Measuring inter-rater reliability for nominal data - which coefficients and confidence intervals are appropriate?** *BMC Med Res Methodol* 2016;16:93 CrossRef Medline
25. Kendall MG, Babington Smith B. **The problem of m rankings.** *The Annals of Mathematical Statistics* 1939;10:275–87 CrossRef

Tumor Response Assessment in Diffuse Intrinsic Pontine Glioma: Comparison of Semiautomated Volumetric, Semiautomated Linear, and Manual Linear Tumor Measurement Strategies

L.A. Gilligan, M.D. DeWire-Schottmiller, M. Fouladi, P. DeBlank, and J.L. Leach

ABSTRACT

BACKGROUND AND PURPOSE: 2D measurements of diffuse intrinsic pontine gliomas are limited by variability, and volumetric response criteria are poorly defined. Semiautomated 2D measurements may improve consistency; however, the impact on tumor response assessments is unknown. The purpose of this study was to compare manual 2D, semiautomated 2D, and volumetric measurement strategies for diffuse intrinsic pontine gliomas.

MATERIALS AND METHODS: This study evaluated patients with diffuse intrinsic pontine gliomas through a Phase I/II trial (NCT02607124). Clinical 2D cross-product values were derived from manual linear measurements (cross-product = long axis × short axis). By means of dedicated software (mint Lesion), tumor margins were traced and maximum cross-product and tumor volume were automatically derived. Correlation and bias between methods were assessed, and response assessment per measurement strategy was reported.

RESULTS: Ten patients (median age, 7.6 years) underwent 58 MR imaging examinations. Correlation and mean bias (95% limits) of percentage change in tumor size from prior examinations were the following: clinical and semiautomated cross-product, $r = 0.36$, -1.5% (-59.9% , 56.8%); clinical cross-product and volume, $r = 0.61$, -2.1% (-52.0% , 47.8%); and semiautomated cross-product and volume, $r = 0.79$, 0.6% (-39.3% , 38.1%). Stable disease, progressive disease, and partial response rates per measurement strategy were the following: clinical cross-product, 82%, 18%, 0%; semiautomated cross-product, 54%, 42%, 4%; and volume, 50%, 46%, 4%, respectively.

CONCLUSIONS: Manual 2D cross-product measurements may underestimate tumor size and disease progression compared with semiautomated 2D and volumetric measurements.

ABBREVIATIONS: CP = cross-product; DIPG = diffuse intrinsic pontine glioma; PD = progressive disease; PR = partial response; SD = stable disease; TRC = tumor response criteria

Diffuse intrinsic pontine gliomas (DIPGs) comprise 80% of brain stem gliomas, which, in turn, account for 10%–20% of central nervous system tumors in children.^{1,2} DIPG carries a dismal prognosis, with a mean survival of 11 months and 1-, 2-, and 5-year overall survival rates of 42%, 10%, and 2%, respectively.³ Standard of care for DIPG consists of involved field radiation therapy, lengthening survival by an average of 3–4 months.^{3,4} Recently, it has been discovered that up to 80% of DIPGs have a pathognomonic point mutation in *histone H3.3* (*H3F3A*) (65% of tumors) or *histone H3.1* (*HIST1H3B*) (25%

of tumors), the latter conferring longer survival in most studies assessing this.³ Chemotherapeutic agents have failed to demonstrate efficacy, and no improvement in survival has been achieved in the past 4 decades.^{3,5-7} Currently, there are 69 interventional research studies for DIPG listed on ClinicalTrials.gov.

Additional support: The Cure Starts Now Foundation, Hope for Caroline Foundation, Julian Boivin Courage for Cures Foundation, Abbie's Army, Michael Mosier Defeat DIPG Foundation, Reflections of Grace Foundation, The Cure Starts Now Australia, Brooke Healey Foundation, Soar With Grace Foundation, Jeffrey Thomas Hayden Foundation, Cure Brain Cancer Foundation, The Jones Family Foundation, Musella Foundation, Pray, Hope, Believe Foundation, Smiles for Sophie Foundation, Benny's World, Love Chloe Foundation, Aiden's Avengers, A Cure from Caleb Society, The Operation Grace White Foundation, Ryan's Hope, Wayland Villars DIPG Foundation, American Childhood Cancer Organization, Juliana Rose Donnelly Trust, Sheila Jones and Friends, The Ellie Kavalieros DIPG Research Fund, Voices Against Brain Cancer, The DIPG Collaborative.

Please address correspondence to James L. Leach, MD, Department of Radiology, MLC 5031, Cincinnati Children's Hospital Medical Center, 3333 Burnet Ave, Cincinnati, OH 45229; e-mail: james.leach@cchmc.org
<http://dx.doi.org/10.3174/ajnr.A6555>

Received December 20, 2019; accepted after revision February 26, 2020.

From the Departments of Radiology (L.A.G., J.L.L.) and Cancer and Blood Diseases Institute (M.D.D.-S., M.F.), Cincinnati Children's Hospital Medical Center, Cincinnati, Ohio; Department of Graduate Medical Education (L.A.G., M.D.D.-S.), Mount Carmel Health System, Columbus, Ohio; and Departments of Pediatrics (M.F., P.D.) and Radiology (J.L.L.), University of Cincinnati College of Medicine, Cincinnati, Ohio.

This work was supported, in part, by Novartis Pharmaceuticals, A Phase I/II Study of Ribociclib, a CDK4/6 Inhibitor, Following Radiation Therapy. ClinicalTrials.gov Identifier: NCT02607124.

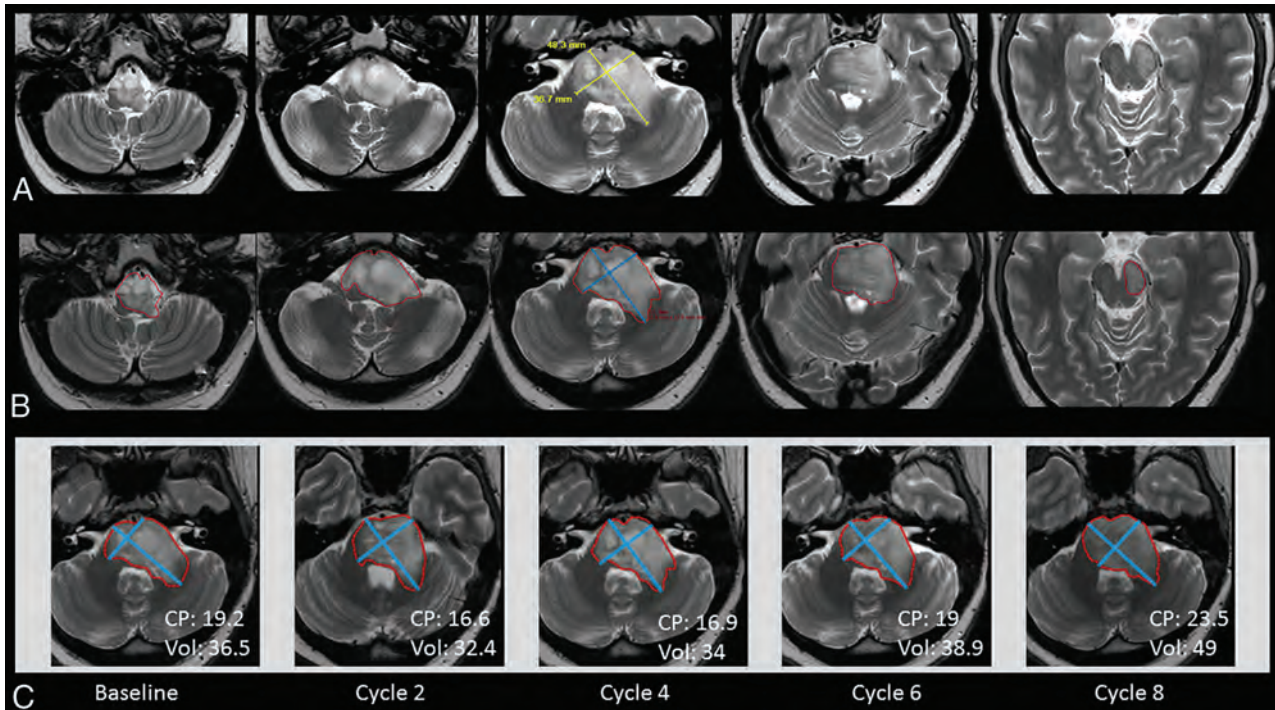


FIG 1. Sample case demonstrating measurement methods. *A*, Manual clinical transaxial (2D) measurements. Largest dimension identified on axial images and perpendicular short axis dimension performed and reported in the clinical radiology report and used for derivation of tumor response. *B*, Semiautomated 2D measurements. Tumor margins are traced (*red outline*) on each image, and automated 2D measurements (largest long axis dimension and perpendicular short axis dimension, *blue lines*) are automatically derived, along with tumor volume in the mint Lesion software package. *C*, Semiautomated 2D measurements and volumes performed during the treatment course. Imaging performed after cycles 2, 4, 6, and 8.

Most therapeutic trials for DIPG have assessed treatment response with Response Assessment in Neuro-Oncology, MacDonald, or World Health Organization criteria (or modifications), which use a 2D measurement of tumor size on MR imaging, allowing comparison with historical data.⁸⁻¹¹ While studies have demonstrated good correlation between 2D and volumetric measurements in high-grade gliomas, there is a lack of comparison data in tumor size measurement strategies in patients with brain stem gliomas.¹²⁻¹⁴ Furthermore, high interobserver variability among 2D measurements in DIPG has been observed.¹⁵ With increasing availability and capability of novel tumor segmentation software, semiautomated tumor volumetry is a potentially useful assessment tool that may be more sensitive to tumor response and enable earlier determination of treatment efficacy. However, research is needed to define therapeutic end point criteria before incorporation into clinical trials.

The purpose of this study was to compare methods of DIPG tumor measurement, including traditional manual 2D measurements and semiautomated, software-assisted 2D measurements and tumor volumes. A secondary aim was to explore the implications of using software-assisted 2D measurements and tumor volumes for response assessment, compared with the standard manual 2D method.

MATERIALS AND METHODS

The institutional review board at Cincinnati Children's Hospital Medical Center approved this study as part of a Phase I/II drug trial of ribociclib following radiation therapy in patients with newly diagnosed DIPG (NCT02607124). Patients between 1 and

30 years of age with nonbiopsied DIPG, retinoblastoma gene mutation–positive DIPG, or retinoblastoma gene mutation–positive high-grade glioma were prospectively recruited to undergo MR imaging before and following drug therapy between April 2016 and November 2017 as part of the treatment protocol.¹⁶ Written informed consent was obtained. MR imaging examinations were typically obtained before cycles 3, 5, 7, 9, and 11.

Imaging Protocol

Imaging examinations were performed on 3T scanners (Signa Architect, GE Healthcare). Imaging protocol included the following: volumetric T1WI and T2-FLAIR (1-mm isotropic, axial, and coronal reformations; FOV = 256 mm, matrix = 256 × 256, slice thickness = 1 mm), axial T2WI (FOV = 220, matrix = 512 × 224, slice thickness = 3 mm contiguous), DTI and SWI sequences. IV gadoterate meglumine (Dotarem; Guerbet) was injected (rate = 1 mL/s, dose = 0.1 mmol/kg). Postcontrast T1WI (volumetric, 1 mm) and axial T1-FLAIR (FOV = 220 mm, matrix = 320 × 288, slice thickness = 3 mm contiguous) sequences were obtained.

Tumor Measurements

For clinical purposes per the study protocol, 2D tumor measurements were made by 1 of 7 fellowship-trained, pediatric neuroradiologists at Cincinnati Children's Hospital Medical Center, including the largest diameter in the axial plane (long axis) and a measurement perpendicular to the long axis (short axis). Clinical cross-product (CP) was calculated by multiplying long and short axes (Fig 1).

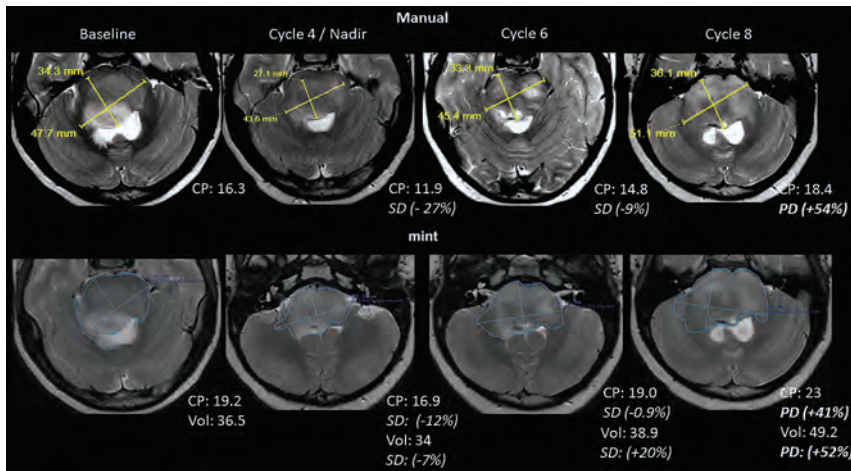


FIG 2. Sample case demonstrating clinical 2D measurements (clinical CP) and semiautomated 2D and volumetric measurements (semiautomated CP) during the treatment course. Note that in this case, although there were differences in orientation of the measurements with the semiautomated process, response classification was the same compared with manual clinical CP measurements.

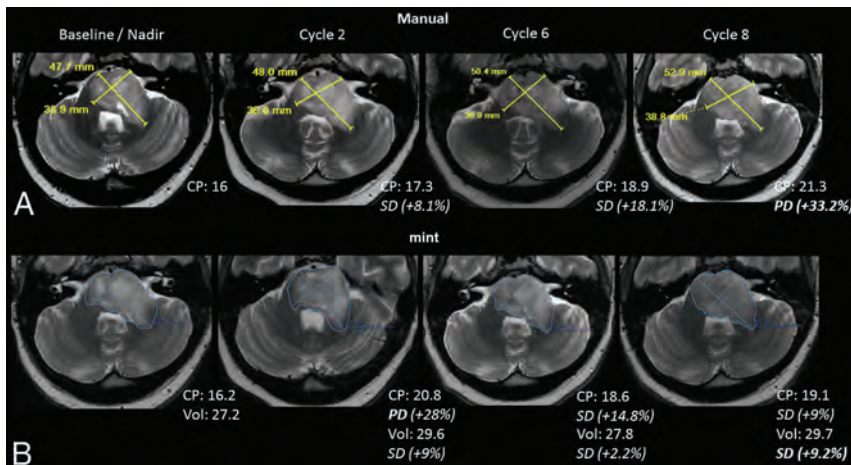


FIG 3. Sample case demonstrating clinical 2D measurements (clinical CP) and semiautomated 2D and volumetric measurements (semiautomated CP) during the treatment course. In this case, per protocol, imaging progression based on clinical CP (A) was called after cycle 8 (33.2% increase in CP). With semiautomated CP (B), progressive disease would have been called (based solely on imaging) after cycle 2 (28% increase). This is due to a different section choice as a maximum transaxial dimension and slightly different measurement orientation (B, cycle 2). Subsequently, however, on the basis of a protocol comparing with smallest CP during treatment (baseline), stable disease would have been called. Note that although the CP increased 28% (PD) after cycle 2, the tumor volume only increased 9% (SD). Such discrepancies were common when comparing treatment-response strategies.

For this study, a single reviewer (J.L.L.), a pediatric neuroradiologist with 25 years of experience, blinded to the clinical measurements, manually segmented each entire tumor by tracing tumor margins on axial T2WI and T2-FLAIR images using proprietary, clinically-available software (mint Lesion, Version 3.4.5; Mint Medical). From the outlined tumor, the largest axial diameter (long axis) and the measurement perpendicular to the long axis (short axis) were automatically derived. Semiautomated CP was calculated by multiplying the long and short axes. From the outlined tumor, tumor volume was also automatically derived (Fig 1).

Classification of Tumor Response

Per the study protocol, the following imaging-related tumor response criteria (TRC) were used to categorize each follow-up examination (in regard to tumor size): complete response, complete disappearance of all tumor and mass effect, maintained for 8+ weeks; partial response (PR), $\geq 50\%$ decrease from baseline; stable disease (SD), $< 50\%$ decrease from baseline size and $< 25\%$ increase from the prior lowest tumor size; and progressive disease (PD), $\geq 25\%$ increase from the prior lowest tumor size.^{11,17} These criteria were applied to 2D and volumetric data. Additionally, we applied another TRC to the volume data only, following previously published recommendations: PR, $\geq 65\%$ decrease from baseline; SD, $< 65\%$ decrease from baseline or $< 40\%$ increase from the prior lowest tumor size; and PD, $\geq 40\%$ increase from the prior lowest tumor size.^{18,19} These published TRC for volumetric measurements are extrapolated from linear values using a spheric tumor model. Currently, there are no published prospective studies regarding TRC for tumor volumes in pediatric brain tumors.¹⁸

Statistical Analysis

Continuous data were summarized as means and SDs or medians and ranges; categorical data were summarized as counts and percentages. Correlation coefficients were used to compare clinical and semiautomated CP measurements and the percentage change in tumor size (compared with a prior examination) among the 3 measurement strategies. Bland-Altman analyses were performed to assess bias among measurement strategies. Descriptive statistics were used to describe percentage change in tumor size per TRC classification and measurement strategy.

P values $< .05$ were considered statistically significant for inference testing. Correlation coefficients were classified by the following definitions: 0–0.19, very weak; 0.20–0.39, weak; 0.40–0.59, moderate; 0.60–0.79, strong; and 0.80–1.0, very strong.²⁰ Analyses were performed using MedCalc for Windows (MedCalc Software).

RESULTS

Ten patients were included, all with DIPGs. The median age at baseline MR imaging was 7.6 years (range, 3.9–20.1 years), and 6 patients (60%) were female. The median number of follow-up

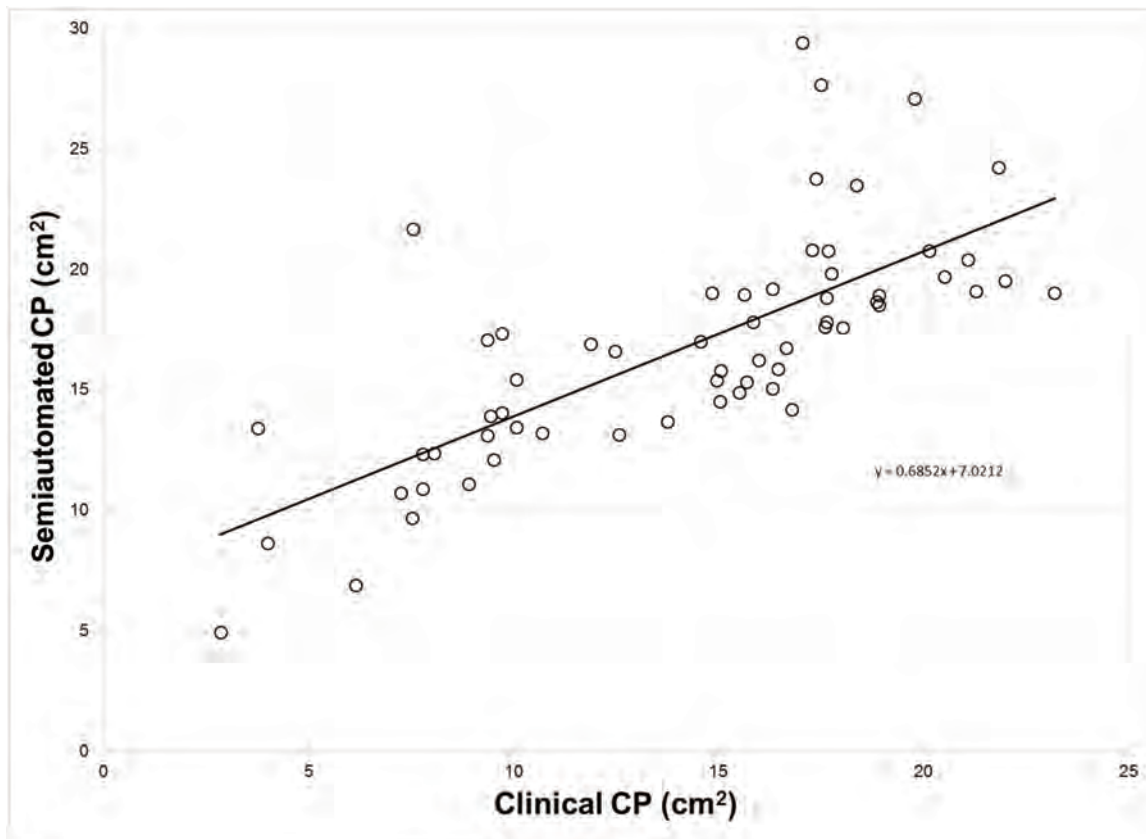


FIG 4. Clinically derived tumor CP versus semiautomated software–derived tumor CP for all time points with a linear trendline ($r = 0.74$, $P < .0001$).

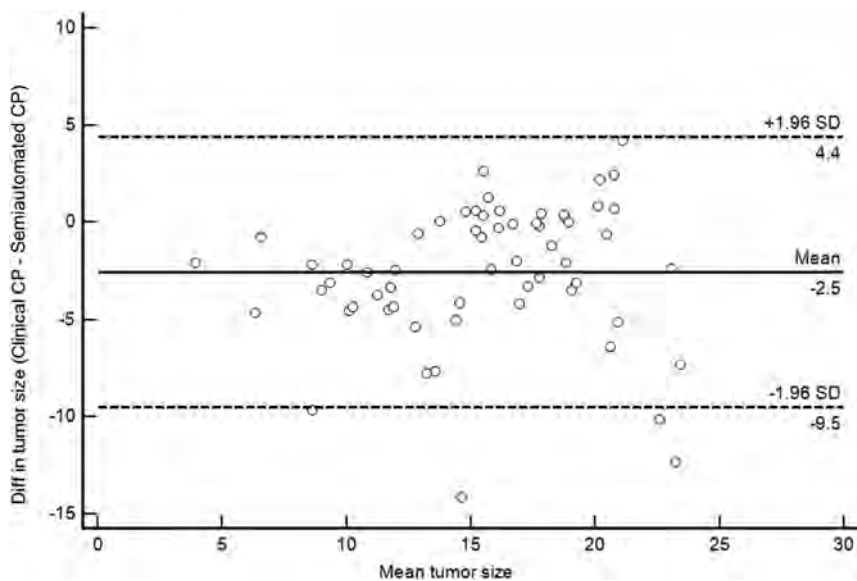


FIG 5. Bland-Altman plot demonstrating bias between clinical and semiautomated tumor CP for all time points. The *solid line* indicates a mean bias between techniques. *Dashed lines* indicate ± 2 SDs of the mean (95% limits of agreement). Overall, clinical CP measured less than semiautomated CP (mean bias, -2.5). Outliers (>1.96 SDs) were predominantly noted in larger tumors.

follow-up MR imaging of 177 ± 98 days (range, 56–411 days). One patient (with 2 follow-up MRIs) had 2 discrete tumors, each measured and analyzed separately. Case examples of tumor measurements over the study course are illustrated in Figs 2 and 3.

Correlation and Bias between Tumor Measurement Strategies

Clinical and semiautomated tumor CP measurements were strongly correlated ($r = 0.74$, $P < .001$), with a mean bias of -2.5 mm^2 (95% limits of agreement, -9.5 , $+4.4 \text{ mm}^2$) (Figs 4 and 5). There were strong, statistically significant correlations between the percentage change in tumor size between clinical CP and volume ($r = 0.61$, $P < .001$) and semiautomated CP and volume-measurement strategies ($r = 0.79$, $P < .001$). Correlation and mean bias of percentage change in tumor size between clinical and semiautomated CP measurement strategies

are depicted in Figs 6 and 7. There was a weak, statistically significant correlation ($r = 0.36$, $P = .011$) of percentage change from prior examinations comparing clinical and semiautomated

are depicted in Figs 6 and 7. There was a weak, statistically significant correlation ($r = 0.36$, $P = .011$) of percentage change from prior examinations comparing clinical and semiautomated

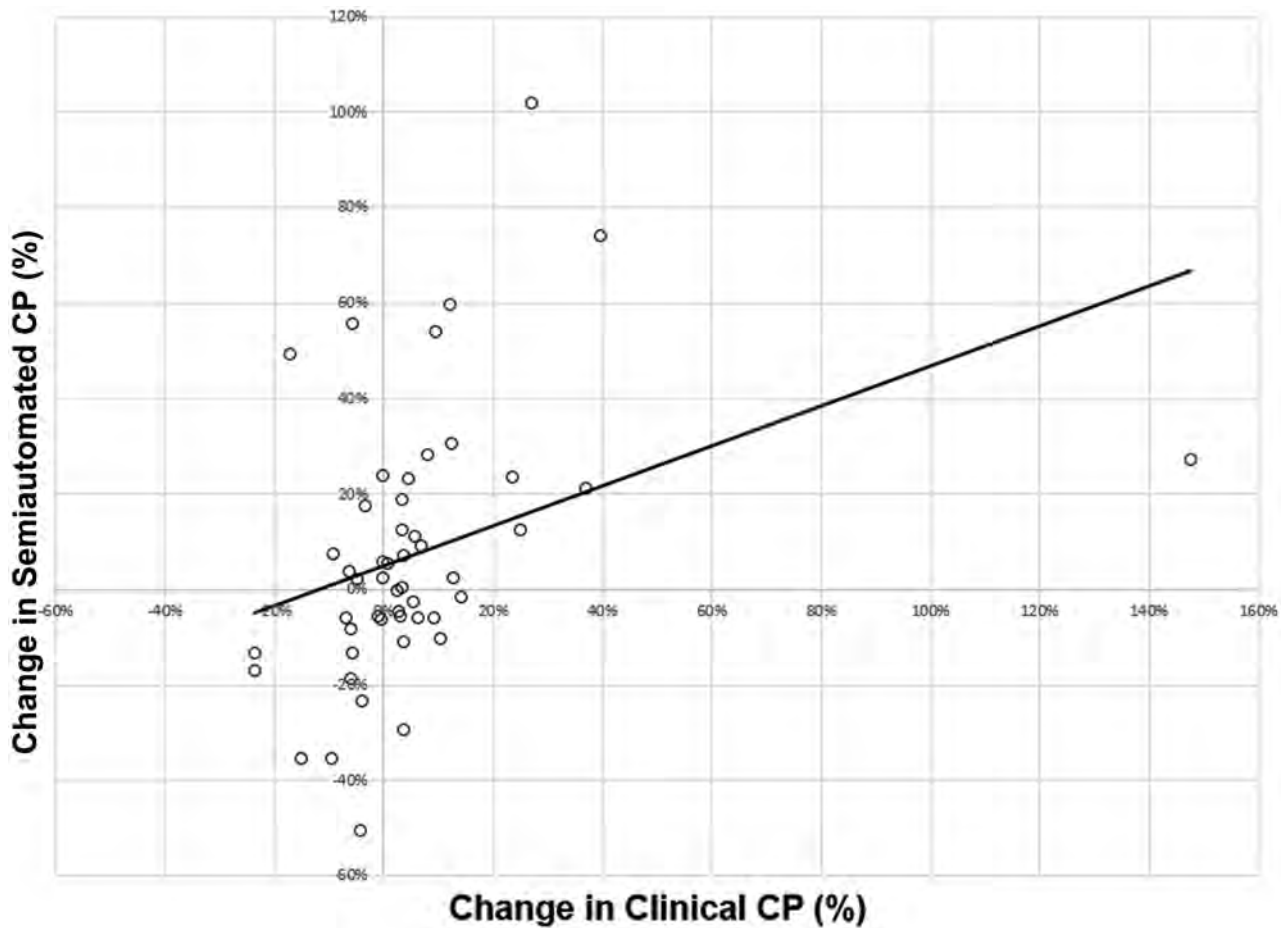


FIG 6. Correlation of percentage change from prior examination in clinical CP versus semiautomated CP ($r = 0.36$, $P = .011$).

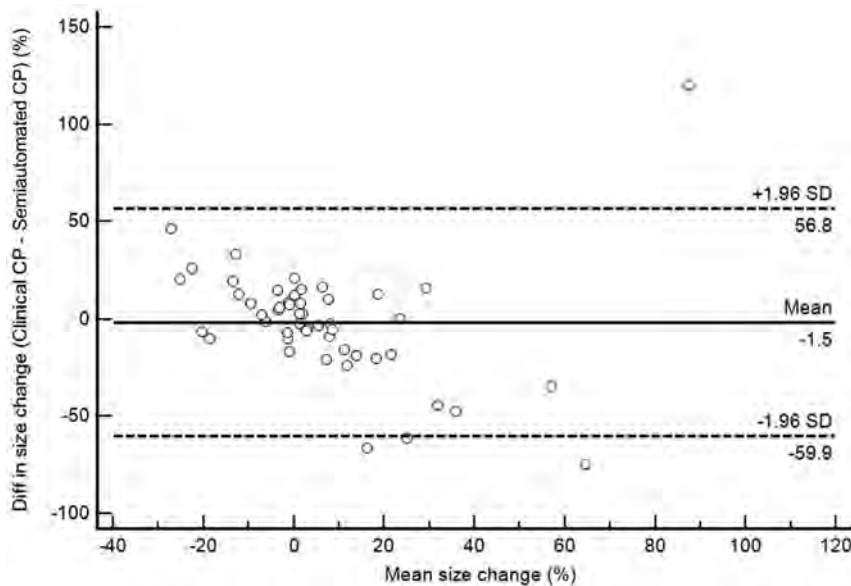


FIG 7. Bland-Altman plot demonstrating bias between the percentage change in clinical and semiautomated tumor CP from a prior examination. The *solid line* indicates mean bias between techniques. *Dashed lines* indicate ± 2 SDs of the mean (95% limits of agreement). Overall, percentage change in clinical CP was smaller than the percentage change in semiautomated CP (mean bias, -1.5% , 95% limits of agreement, -59.9 , $+56.8\%$) between time points.

CP measurements, with a mean bias of -1.5% (95% limits of agreement, -59.9 , $+56.8\%$).

Comparison of Treatment Response Assessment between Tumor Measurement Strategies

Classification of percentage change of tumor size from baseline or nadir examination, per the protocol TRC, yielded 25/50 (50%) cases that were classified concordantly across all 3 tumor measurement methods. Concordance was 32/50 (64%) between clinical and semiautomated CP, 30/50 (60%) between clinical CP and volume, and 38/50 (76%) between semiautomated CP and volume. Frequencies of SD, PD, and PR by tumor-measurement strategy are reported in Table 1. No examination or method demonstrated a complete response. Of note, 34% (14/41) of time points classified as SD by clinical CP were classified as PD by semiautomated

Table 1: Response assessment classifications of 50 MR imaging time points for 3 tumor-management strategies^a

	Clinical CP			Semiautomated CP			Volume (25/50)			Volume (40/65)		
	PR	SD	PD	PR	SD	PD	PR	SD	PD	PR	SD	PD
Clinical CP												
PR				0	0	0	0	0	0	0	0	0
SD				2	25	14	2	23	16	1	32	8
PD				0	2	7	0	2	7	0	3	6
Concordance				64%			60%			76%		
Semiautomated CP												
PR							2	0	0	1	1	0
SD							0	20	7	0	25	2
PD							0	5	16	0	9	12
Concordance							76%			76%		
Volume												
PR										1	1	0
SD										0	25	0
PD										0	9	14
Concordance										80%		

^a Two different tumor-response criteria were applied to the volume data (25/50 uses the same criteria as used for CP-response determinations, 40/65 denotes PR as >65% decrease from baseline and PD as >40% increase from the prior lowest tumor size). Unless otherwise noted, values represent the number of MR imaging time points.

Table 2: Descriptive statistics of the percentage change in tumor size from baseline or nadir to follow-up examination (assigned per clinical protocol) for each response assessment classification per tumor measurement strategy

TRC	Mean (%)				Standard Deviation (%)				Minimum (%)				Maximum (%)			
	CP _c	CP _{sa}	Vol ₁	Vol ₂	CP _c	CP _{sa}	Vol ₁	Vol ₂	CP _c	CP _{sa}	Vol ₁	Vol ₂	CP _c	CP _{sa}	Vol ₁	Vol ₂
PD	57	83	75	79	64	78	81	59	27	18	9	42	227	224	271	271
SD	6	14	16	8	13	28	32	20	-27	-68	-73	51	25	91	83	39

Note:—CP_c indicates clinical cross-product; CP_{sa}, semiautomated cross-product; Vol₁, volume (25/50% tumor response criteria); Vol₂, volume (40/65% tumor response criteria).

CP. The mean percentage change in tumor volume from follow-up examination to baseline or nadir per response category and tumor measurement strategy is reported in Table 2.

DISCUSSION

Recent research effort has aimed at improving and discovering imaging biomarkers of DIPG. Such work is relevant for the standardization of clinical trial end points and improved detection of treatment effect. Historically, DIPGs have been measured using MacDonald, World Health Organization, or Response Assessment in Neuro-Oncology criteria (or modifications). These criteria use a 2D measurement strategy in which 2 perpendicular measurements are made on the image with the largest observed cross-sectional area of tumor. However, these standard tumor measurements were not developed and may not be best-suited for DIPG, and there remains an overall lack of standardization in DIPG measurements.

2D and 3D DIPG tumor measurements have demonstrated poor interobserver agreement, possibly related to their infiltrative nature, indiscrete borders, and heterogeneous appearance.¹⁵ Furthermore, 1D, 2D, and 3D tumor measurements of DIPG have not correlated well with clinical outcomes.²¹⁻²⁴ Other surrogate imaging biomarkers of DIPG have been explored, including metabolic ratios by MR spectroscopy, tumor perfusion by dynamic susceptibility contrast MR imaging, and pontine size by conventional MR imaging.²⁴⁻²⁸ Recently, studies have investigated tumor volume measurement strategies (automated, semiautomated, or manual) and have shown them to be a promising tool with improved inter- and intraobserver agreement.^{18,29,30} It has been hypothesized that a volume measurement strategy

may be more appropriate for DIPG, given its often complex morphology.

In this study, we have demonstrated a strong correlation and relatively small bias between manual and semiautomated (from mint Lesion software) CP values. However, the correlation of percentage change in tumor size (the metric by which treatment response is assessed) between these 2 strategies was weak. In some cases, there was a large discrepancy between the percentage change in tumor size across the clinical CP, semiautomated CP, and volumetric measurement strategies. Generally, the mint Lesion-derived measurements (semiautomated CP, volume) tended to classify tumors as PD compared with the clinical CP strategy, which tended to classify tumors as SD.

There are several potential explanations for these discrepancies. DIPG can have variable, nonspheric morphology, and some shapes are not well-approximated by 1 CP measurement. In addition, tumor growth is constrained by anatomic boundaries to some degree and may be less constrained in certain directions. More pronounced growth along the cranial-caudal axis, for example, may not be captured by performing measurements only in the transverse plane. Furthermore, clinical CP measurements are likely biased toward the radiologist by using a section location and measurement orientation similar to those used on prior examinations. This bias may result in underestimation of tumor size if greater interval growth occurred at a different axial section or in a different orientation than the manual measurements. This bias is also supported by our results: mint Lesion automatically derives the largest CP, which explains why these measurements were, on average, 2.5 mm² larger than the clinical CP measurements. Our results have important implications for the use of

segmentation software in clinical practice. Further study is needed to determine which method is a better indicator of clinical outcome.

We found the strongest correlation in percentage change of tumor size between the 2 methods by using mint Lesion software (semiautomatic CP and volume). This is not surprising because the same segmented images (derived from 1 reviewer who traced tumor margins in all slices) were used for these 2 strategies. Although we found that the bias between these techniques was very low in magnitude (0.6%), the limits of agreement remained wide (−39%, +38%), which could be related to our small sample size. Furthermore, we did not have adequate power to define new cutoff values for tumor response–assessment classes using tumor volume measurements. If volumetric measurements of DIPG should be used for assessing tumor response, identifying relationships with linear measurements (to inform comparisons with prior studies and treatment trials) and clinical progression is critical to ensure maximum utility. Volumetric end points derived from spheric/elliptic mathematic models using cranial-caudal and transverse dimensions may not be applicable to tumors with nonspheric growth patterns.³⁰ Further research using larger groups of subjects and treatment time points is needed.

Correlations between true volumetric measurements and 2D measurements of brain tumors are few, particularly in children. One study of low-grade pediatric gliomas showed that 20% of MR imaging examinations demonstrated discordant response assessments between 2D and volumetric tumor measurement strategies.¹⁸ Shah et al,¹³ in a study of adult patients with glioblastomas, also demonstrated a 20% discordance rate in response assessments when comparing 2D and volumetric measurements. These discrepancy rates are quite similar to the 24% discrepancy rate between 2 techniques (clinical CP and volume) demonstrated in our study.

Our study was limited by several factors. First, we included a small sample size of patients with DIPG, inherent to the nature of this single-center study of a disease with low prevalence. Second, although the clinical trial protocol standardized the timing of MR imaging examinations, the actual timing and total number of MR imaging examinations varied across patients, often related to additional MR imaging examinations being performed when patients had a change in clinical status. Third, volumetric tumor measurements using the mint lesion software were made by only 1 reviewer; thus, we cannot draw conclusions regarding interobserver variability of the tumor measurements with this technique. Fourth, the software used for 2 of the measurement strategies in our study (semiautomatic CP, volume) may not be widely available, potentially limiting the application of our results. Finally, because the clinical outcome data for this trial remain unpublished, our study did not correlate tumor measurements or response assessment with clinical outcomes. This would be an important area of future investigation.

CONCLUSIONS

We have shown that correlation of change in DIPG tumor size among 3 measurement strategies is variable, with the strongest correlation observed between semiautomated 2D and volumetric strategies and the weakest correlation observed between clinical

2D and semiautomated 2D strategies. The conventional method of manual 2D (cross-product) tumor measurement likely underestimates tumor size and disease progression compared with semiautomated 2D measurements. Application of semiautomated 2D and volumetric measurements in therapeutic trials will alter response assessment compared with standard 2D measures in DIPG. Further research is needed to outline relationships among these methods, clinical signs of progression, and survival.

Disclosures: Mariko DeWire-Schottmiller—RELATED: Grant: The DIPG Collaborative and additional funding sources in the comments, Comments: The Cure Starts Now Foundation, Hope for Caroline Foundation, Julian Boivin Courage for Cures Foundation, Abbie's Army, Michael Mosier Defeat DIPG Foundation, Reflections of Grace Foundation, The Cure Starts Now Australia, Brooke Healey Foundation, Soar With Grace Foundation, Jeffrey Thomas Hayden Foundation, Cure Brain Cancer Foundation, The Jones Family Foundation, Musella Foundation, Pray, Hope, Believe Foundation, Smiles for Sophie Foundation, Benny's World, Love Chloe Foundation, Aiden's Avengers, A Cure from Caleb Society, The Operation Grace White Foundation, Ryan's Hope, Wayland Villars DIPG Foundation, American Childhood Cancer Organization, Juliana Rose Donnelly Trust, Sheila Jones and Friends, The Ellie Kavalieros DIPG Research Fund, Voices Against Brain Cancer, and The DIPG Collaborative*; Other: Novartis Pharmaceuticals.* Maryam Fouladi—RELATED: Grant: Cincinnati Children's Hospital Medical Center, Comments: Novartis-supported clinical trial.* *Money paid to the institution.

REFERENCES

1. Hassan H, Pinches A, Picton SV, et al. **Survival rates and prognostic predictors of high-grade brain stem gliomas in childhood: a systematic review and meta-analysis.** *J Neurooncol* 2017;135:13–20 CrossRef Medline
2. Jennings MT, Freeman ML, Murray MJ. **Strategies in the treatment of diffuse pontine gliomas: the therapeutic role of hyperfractionated radiotherapy and chemotherapy.** *J Neurooncol* 1996;28:207–22 CrossRef Medline
3. Hoffman LM, Veldhuijzen van Zanten SE, Colditz N, et al. **Clinical, radiologic, pathologic, and molecular characteristics of long-term survivors of diffuse intrinsic pontine glioma (DIPG): a Collaborative Report from the International and European Society for Pediatric Oncology DIPG Registries.** *J Clin Oncol* 2018;36:1963–72 CrossRef Medline
4. Haas-Kogan DA, Banerjee A, Poussaint TY, et al. **Phase II trial of tipifarnib and radiation in children with newly diagnosed diffuse intrinsic pontine gliomas.** *Neuro Oncol* 2011;13:298–306 CrossRef Medline
5. Gokce-Samar Z, Beuriat PA, Faure-Contier C, et al. **Pre-radiation chemotherapy improves survival in pediatric diffuse intrinsic pontine gliomas.** *Childs Nerv Syst* 2016;32:1415–23 CrossRef Medline
6. Jansen MH, Veldhuijzen van Zanten SE, Sanchez Aliaga E, et al. **Survival prediction model of children with diffuse intrinsic pontine glioma based on clinical and radiological criteria.** *Neuro Oncol* 2015;17:160–66 CrossRef Medline
7. Wagner S, Warmuth-Metz M, Emsler A, et al. **Treatment options in childhood pontine gliomas.** *J Neurooncol* 2006;79:281–87 CrossRef Medline
8. Eisenhauer EA, Therasse P, Bogaerts J, et al. **New response evaluation criteria in solid tumours: revised RECIST guideline (version 1.1).** *Eur J Cancer* 2009;45:228–47 CrossRef Medline
9. Macdonald DR, Cascino TL, Schold SC Jr, et al. **Response criteria for Phase II studies of supratentorial malignant glioma.** *J Clin Oncol* 1990;8:1277–80 CrossRef Medline
10. Sharma M, Juthani RG, Vogelbaum MA. **Updated response assessment criteria for high-grade glioma: beyond the MacDonald criteria.** *Chin Clin Oncol* 2017;6:37 CrossRef Medline
11. Wen PY, Macdonald DR, Reardon DA, et al. **Updated response assessment criteria for high-grade gliomas: Response Assessment in Neuro-Oncology Working Group.** *J Clin Oncol* 2010;28:1963–72 CrossRef Medline

12. Galanis E, Buckner JC, Maurer MJ, et al. **Validation of neuroradiologic response assessment in gliomas: measurement by RECIST, two-dimensional, computer-assisted tumor area, and computer-assisted tumor volume methods.** *Neuro Oncol* 2006;8:156–65 CrossRef Medline
13. Shah GD, Kesari S, Xu R, et al. **Comparison of linear and volumetric criteria in assessing tumor response in adult high-grade gliomas.** *Neuro Oncol* 2006;8:38–46 CrossRef Medline
14. Warren KE, Patronas N, Aikin AA, et al. **Comparison of one-, two-, and three-dimensional measurements of childhood brain tumors.** *J Natl Cancer Inst* 2001;93:1401–05 CrossRef Medline
15. Hayward RM, Patronas N, Baker EH, et al. **Inter-observer variability in the measurement of diffuse intrinsic pontine gliomas.** *J Neurooncol* 2008;90:57–61 CrossRef Medline
16. DeWire M, Fuller C, Hummel T, et al. **Dipg-27. Clec011xus17t (NCT 02607124): a Phase I/II study of ribociclib (Lee011) following radiation therapy in children with newly diagnosed non-biopsied diffuse pontine gliomas (DIPG) and Rb+ biopsied DIPG and high grade gliomas (HGG).** *Neuro Oncol* 2017;19(Suppl 4):iv10–10 CrossRef
17. Okada H, Weller M, Huang R, et al. **Immunotherapy response assessment in neuro-oncology: a report of the RANO working group.** *Lancet Oncol* 2015;16:e534–42 CrossRef Medline
18. D'Arco F, O'Hare P, Dashti F, et al. **Volumetric assessment of tumor size changes in pediatric low-grade gliomas: feasibility and comparison with linear measurements.** *Neuroradiology* 2018;60:427–36 CrossRef Medline
19. Henson JW, Ulmer S, Harris GJ. **Brain tumor imaging in clinical trials.** *AJNR Am J Neuroradiol* 2008;29:419–24 CrossRef Medline
20. Evans JD. *Straightforward Statistics for the Behavioral Sciences.* Brooks/Cole Pub. Co; 1996
21. Hargrave D, Chuang N, Bouffet E. **Conventional MRI cannot predict survival in childhood diffuse intrinsic pontine glioma.** *J Neurooncol* 2008;86:313–19 CrossRef Medline
22. Kornreich L, Schwarz M, Karmazyn B, et al. **Role of MRI in the management of children with diffuse pontine tumors: a study of 15 patients and review of the literature.** *Pediatr Radiol* 2005;35:872–79 CrossRef Medline
23. Liu AK, Brandon J, Foreman NK, et al. **Conventional MRI at presentation does not predict clinical response to radiation therapy in children with diffuse pontine glioma.** *Pediatr Radiol* 2009;39:1317–20 CrossRef Medline
24. Warren KE, Poussaint TY, Vezina G, et al. **Challenges with defining response to antitumor agents in pediatric neuro-oncology: a report from the Response Assessment in Pediatric Neuro-Oncology (RAPNO) Working Group.** *Pediatr Blood Cancer* 2013;60:1397–01 CrossRef Medline
25. Hipp SJ, Steffen-Smith E, Hammoud D, et al. **Predicting outcome of children with diffuse intrinsic pontine gliomas using multiparametric imaging.** *Neuro Oncol* 2011;13:904–09 CrossRef Medline
26. Steffen-Smith EA, Baker EH, Venzon D, et al. **Measurements of the pons as a biomarker of progression for pediatric DIPG.** *J Neurooncol* 2014;116:127–33 CrossRef Medline
27. Steffen-Smith EA, Shih JH, Hipp SJ, et al. **Proton magnetic resonance spectroscopy predicts survival in children with diffuse intrinsic pontine glioma.** *J Neurooncol* 2011;105:365–73 CrossRef Medline
28. Steffen-Smith EA, Venzon DJ, Bent RS, et al. **Single- and multivoxel proton spectroscopy in pediatric patients with diffuse intrinsic pontine glioma.** *Int J Radiat Oncol Biol Phys* 2012;84:774–79 CrossRef Medline
29. Riley GT, Armitage PA, Batty R, et al. **Diffuse intrinsic pontine glioma: is MRI surveillance improved by region of interest volumetry?** *Pediatr Radiol* 2015;45:203–10 CrossRef Medline
30. Singh R, Zhou Z, Tisnado J, et al. **A novel magnetic resonance imaging segmentation technique for determining diffuse intrinsic pontine glioma tumor volume.** *J Neurosurg Pediatr* 2016;18:565–72 CrossRef Medline

MR Imaging Correlates for Molecular and Mutational Analyses in Children with Diffuse Intrinsic Pontine Glioma

C. Jaimes, S. Vajapeyam, D. Brown, P.-C. Kao, C. Ma, L. Greenspan, N. Gupta, L. Goumnerova, P. Bandopahayay, F. Dubois, N.F. Greenwald, T. Zack, O. Shapira, R. Beroukhim, K.L. Ligon, S. Chi, M.W. Kieran, K.D. Wright, and T.Y. Poussaint



ABSTRACT

BACKGROUND AND PURPOSE: Recent advances in molecular techniques have characterized distinct subtypes of diffuse intrinsic pontine gliomas. Our aim was the identification of MR imaging correlates of these subtypes.

MATERIALS AND METHODS: Initial MRIs from subjects with diffuse intrinsic pontine gliomas recruited for a prospective clinical trial before treatment were analyzed. Retrospective imaging analyses included FLAIR/T2 tumor volume, tumor volume enhancing, the presence of cyst and/or necrosis, median, mean, mode, skewness, kurtosis of ADC tumor volume based on FLAIR, and enhancement at baseline. Molecular subgroups based on EGFR and MGMT mutations were established. Histone mutations were also determined (*H3F3A*, *HIST1H3B*, *HIST1H3C*). Univariate Cox proportional hazards regression was used to test the association of imaging predictors with overall and progression-free survival. Wilcoxon rank sum, Kruskal-Wallis, and Fisher exact tests were used to compare imaging measures among groups.

RESULTS: Fifty patients had biopsy and MR imaging. The median age at trial registration was 6 years (range, 3.3–17.5 years); 52% were female. On the basis of immunohistochemical results, 48 patients were assigned to 1 of 4 subgroups: 28 in MGMT–/epidermal growth factor receptor (EGFR)–, 14 in MGMT–/EGFR+, 3 in MGMT+/EGFR–, and 3 in MGMT+/EGFR+. Twenty-three patients had histone mutations in H3F3A, 8 in HIST1H3B, and 3 in HIST1H3C. Enhancing tumor volume was near-significantly different across molecular subgroups ($P = .04$), after accounting for the false discovery rate. Tumor volume enhancing, median, mode, skewness, and kurtosis ADC T2-FLAIR/T2 were significantly different ($P \leq .048$) between patients with H3F3A and HIST1H3B/C mutations.

CONCLUSIONS: MR imaging features including enhancement and ADC histogram parameters are correlated with molecular subgroups and mutations in children with diffuse intrinsic pontine gliomas.

ABBREVIATIONS: DIPG = diffuse intrinsic pontine glioma; EGFR = epidermal growth factor receptor; FDR = false discovery rate; PFS = progression-free survival; PG = postgadolinium; OS = overall survival

Diffuse intrinsic pontine glioma (DIPG) is a malignant brain tumor that accounts for 75%–80% of brain stem tumors in children.¹ Despite medical therapy, these tumors have a poor prognosis, with a median survival at 1, 2, and 3 years of 41%, 15.3%, and 7.2%, respectively.² The 2016 World Health Organization classification of

brain tumors introduced the term “diffuse midline glioma, H3 K27M mutant” to describe these neoplasms due to the high prevalence of unique histone protein mutations that differ from those of supratentorial (hemispheric) pediatric high-grade gliomas and adult high-grade gliomas. While H3 K27M is the most common variant detected, more recently, other distinct histone mutations have been identified in DIPG, which appear to correspond to subgroups with

Received November 30, 2019; accepted after revision March 16, 2020.

From the Departments of Radiology (C.J., S.V., T.Y.P.) and Pediatrics, Division of Oncology (P.-C.K., C.M., L.G., P.B., R.B., S.C., K.D.W.); Fetal-Neonatal Neuroimaging and Developmental Science Center (C.J.), Division of Newborn Medicine; Boston Children's Hospital, Boston, Massachusetts; Tumor Imaging Metrics Core (D.B.), Massachusetts General Hospital, Boston, Massachusetts; Dana Farber Cancer Institute (P.-C.K., C.M., L.G., P.B., F.D., O.S., R.B., K.L.L., S.C., K.D.W.), Boston, Massachusetts; Department of Pediatric Neurosurgery (N.G.), University of California San Francisco Benioff Children's Hospital, San Francisco, California; Clinical Trials Division (M.W.K.), Bristol-Myers-Squibb, New York, New York; Department of Pathology (K.L.L.), Brigham and Women's Hospital, Boston, Massachusetts; Harvard Medical School (C.J., S.V., C.M., P.B., F.D., R.B., K.L.L., S.C., K.D.W., T.Y.P.), Boston, Massachusetts; University of California San Francisco School of Medicine (N.G., T.Z.), San Francisco, California; Stanford University School of Medicine (N.F.G.), Palo Alto, California; and Broad Institute of Massachusetts Institute of Technology and Harvard University (O.S.), Cambridge, Massachusetts.

Paper previously presented at: Annual Meeting of the American Society of Neuroradiology, May 18–23, 2019, Boston, Massachusetts.

C. Jaimes was partially supported by the Schlaeger Fellowship for Neuroscience Research.

Please address correspondence to Tina Young Poussaint, MD, FACR, Boston Children's Hospital, Department of Radiology, 300 Longwood Ave, Boston, MA 02115; e-mail: Tinayoung.poussaint@childrens.harvard.edu; @TYPoussaintMD

 Indicates article with supplemental on-line tables.

 Indicates article with supplemental on-line photo.

<http://dx.doi.org/10.3174/ajnr.A6546>

Table 1: Baseline patient characteristics (n = 50)

Patient Characteristic	No. (%) or Median (Range)
No. of MR imaging studies	50 (100)
Sex	
Male	24 (48)
Female	26 (52)
Median age at registration (range) (yr)	6 (3.3–17.5)
Molecular subgroups	
MGMT–/EGFR–	28/48 (58)
MGMT–/EGFR+	14/48 (29)
MGMT +/EGFR–	3/48 (6)
MGMT +/EGFR+	3/48 (6)
Unassigned	2
Mutational status ^a	
Any histone mutation	34/49 (69)
Wild-type	15/49 (31)
Histone mutation (among patients with any histone mutations) ^a	
H3F3A	23/34 (68)
HIST1H3B	8/34 (24)
HISTH3C	3/34 (9)
Median follow-up time (range) (mo)	10.9 (0.4–33.4)

^a One patient with both H3F3A and HIST1H3B histone mutations was excluded.

different prognosis and pathologic phenotypes.³ Identification of these subgroups of tumors is important to appropriately counsel families and tailor treatment strategies.

Radiogenomic techniques are emerging as valuable tools to noninvasively characterize brain tumors and are increasingly important, given the evolving molecular landscape in pediatric neuro-oncology. Although most data available to date pertain to adult high-grade gliomas,^{4,5} radiogenomic techniques have been successfully implemented to characterize atypical teratoid/rhabdoid tumors⁶ and medulloblastomas.⁷ A challenge to molecular analysis of DIPGs is that historically, patients with these tumors did not routinely undergo biopsy due to a perceived high likelihood of morbidity associated with the procedure; consequently, most imaging-based studies do not have pathologic or molecular correlates.⁸ Despite this limitation, important imaging-based prognostic factors have been described for DIPG. Jansen et al⁹ and Hoffman et al¹⁰ reported that ring enhancement was associated with shorter survival. Chen et al¹¹ reported worse outcome in DIPGs with lower ADC values at baseline. Poussaint et al¹² reported that lower diffusion values on ADC histogram analysis, high skewness, and enhancement were associated with shorter survival. The association among these MR imaging features, the molecular subgroups, and various histone mutations has not been elucidated.

The purpose of this study was to investigate the relationship between the molecular subgroup and histone mutations of DIPGs and MR imaging features on anatomic sequences, and ADC histogram analysis, using the baseline MR imaging from a prospective clinical trial of children with newly diagnosed DIPG who underwent biopsy.¹³

MATERIALS AND METHODS

Subjects

Patients for this study were recruited as part of an institutional review board (Dana Farber Cancer Institute)–approved,

Health Insurance Portability and Accountability Act–compliant, multicenter clinical trial: Molecularly Determined Treatment of Diffuse Intrinsic Pontine Gliomas (DIPG) (NCT01182350). Prospective subjects had MR imaging that showed classic clinical-imaging criteria of nonmetastatic DIPG, including an expansile and infiltrative T1-isointense or -hypointense and T2-FLAIR and T2-hyperintense mass centered within the pons, encompassing at least 50% of the pons with no or little contrast enhancement, which could vary.¹⁴ Findings on clinical examination included multiple cranial nerve neuropathies, long tract signs, and ataxia.¹⁴ Detailed criteria for inclusion and exclusion are summarized in On-line Table 1. The patients enrolled in the trial underwent a biopsy before initiation of therapy; the biopsy target and approach were at the discretion of the neurosurgeon, with the goal of minimizing operative risk.¹³ All subjects received local radiation therapy (59.4 Gy) with adjuvant bevacizumab, as per the standard of care. Subsequently, patients were stratified into different treatment arms with erlotinib and/or temozolomide at the start of radiation therapy based on MGMT promoter methylation status and epidermal growth factor receptor (EGFR) expression in tumor tissue obtained from surgical biopsies.

Of 53 patients enrolled, 50 underwent biopsy and were included in the analytic cohort of this study. Subjects without biopsy were excluded from this analysis. We performed a retrospective review that included biopsy data (histone mutations, molecular groups), MR imaging features on baseline MR imaging, and clinical outcomes. The molecular analysis determined the MGMT methylation status and expression of EGFR; 4 categories were derived from molecular analysis: MGMT–/EGFR–, MGMT–/EGFR+, MGMT+/EGFR–, MGMT+/EGFR+. Three histone mutations were identified through whole-genome RNA sequencing: H3F3A, HIST1H3B, and HISTH3C.³ Clinical end points of the study were determined with longitudinal follow-up. Overall survival (OS) was measured from the time of registration to death or to last follow-up if censored. Progression-free survival (PFS) was measured from the time of registration to progression or death (whichever was first) or to the last follow-up if censored.

Image Analysis

The MR imaging of the brain used for analysis corresponded to the baseline examination obtained before treatment and biopsy. Images were obtained using 3T (n = 17) and 1.5T (n = 33) scanners. A standard clinical protocol was used, which included the following: sagittal T1, axial T2, precontrast axial T2-FLAIR, axial DTI (TR = 6500 ms, TE = 88 ms, section thickness = 2 mm, b-values = 0 and 1000 s/mm², 30 gradient directions), and postgadolinium (PG) 3D T1.

Volumetric data of various components of the tumor were obtained by generating 3D ROIs on a Vitrea workstation (Vital Images) on the anatomic sequences. Specifically, T2-FLAIR/T2 volume represents the volume of tissue (milliliter) with abnormal T2 hyperintense signal on a 2D TSE T2-FLAIR sequence; for cases in which T2-FLAIR was unavailable, this parameter was estimated using a 2D T2 TSE sequence. Tumor volume enhancing represents the volume (milliliter) of enhancement within the tumor estimated on the PG 3D T1 sequence.

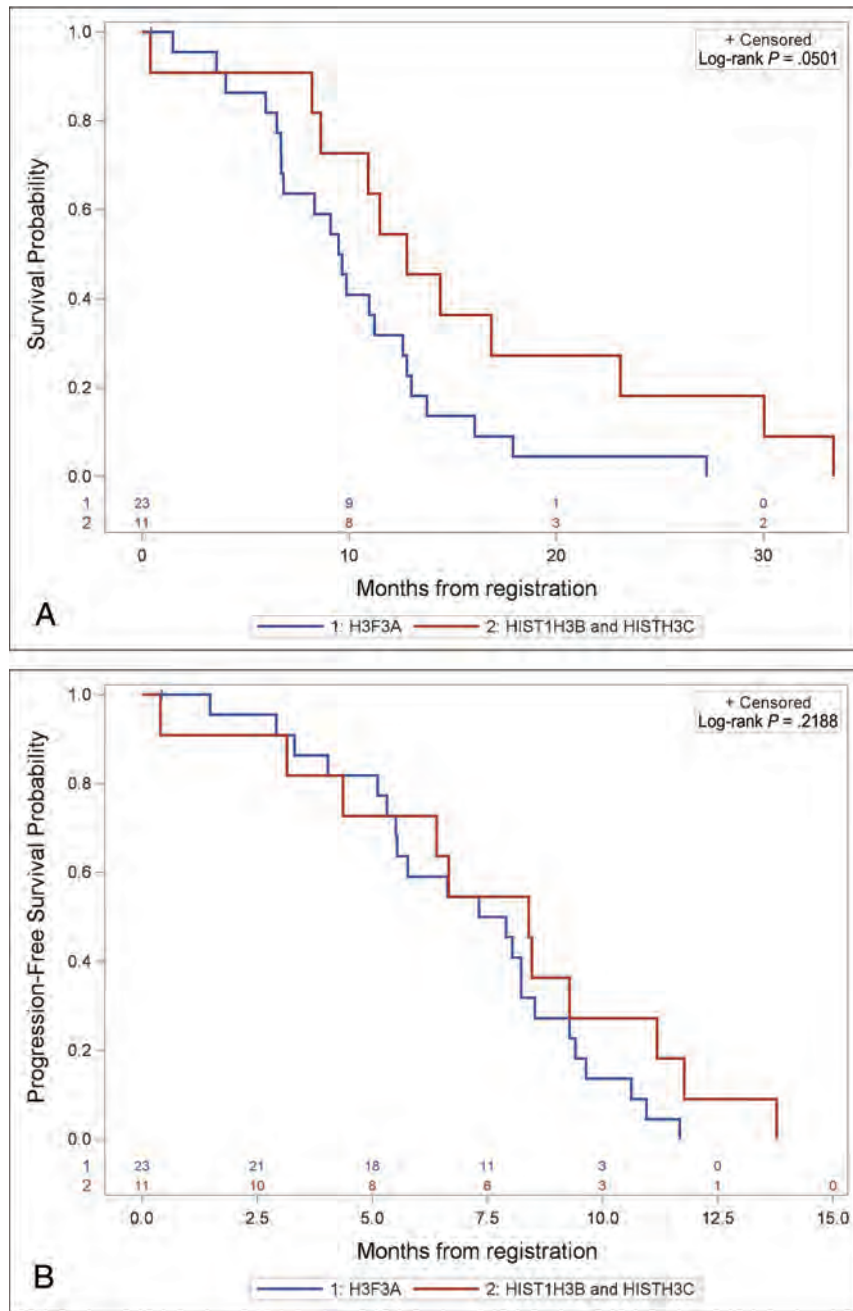


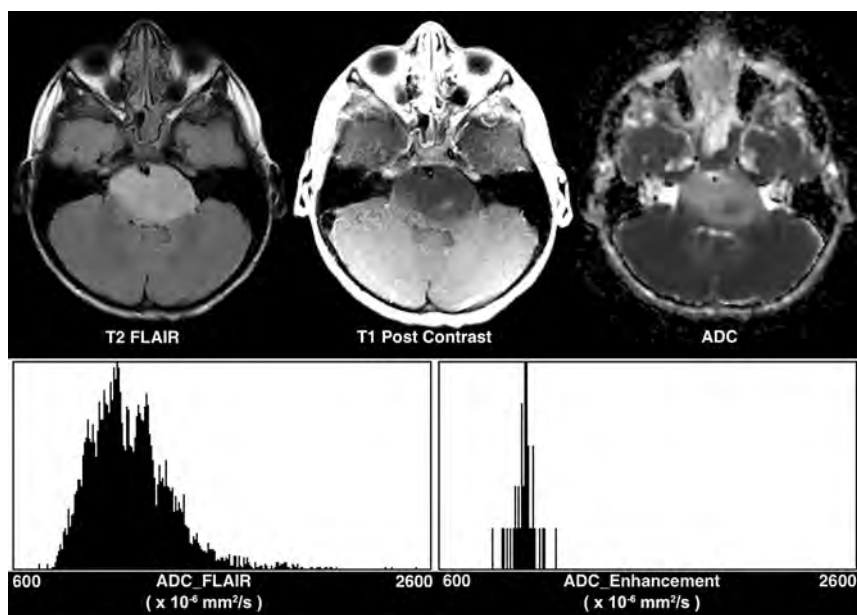
FIG 1. Prognostic differences in subjects with H3F3A ($n=23$) versus HIST1H3B/C ($n=11$) tumors. **A**, Kaplan-Meier curve shows a trend that approaches significance in OS between H3F3A versus HIST1H3B/C tumors. **B**, Kaplan-Meier curve shows no significant difference in PFS between H3F3A versus HIST1H3B/C tumors.

To perform ADC histogram analysis, we registered the ADC maps to the anatomic sequence of interest (T2-FLAIR/T2 and PG T1) using tools from the FSL library (<http://www.fmrib.ox.ac.uk/fsl>),¹⁵ as described by Poussaint et al.¹² Briefly, we transformed the $b=0$ (and subsequently the ADC map) into the space of the individual anatomic sequences. Subsequently, 3D ROIs were created using the thresholding feature in Fiji (<http://fiji.sc/>),¹⁶ an Open Source (<https://opensource.org/>) distribution of Java modules along with ImageJ software (National Institutes of Health); we then extracted the values from every pixel from the ADC map within the corresponding ROI.

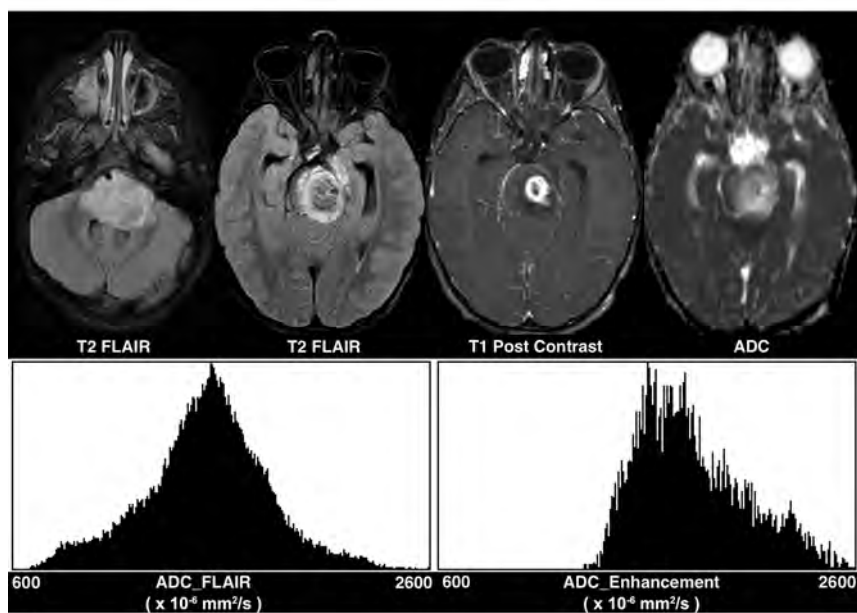
We applied a uniform threshold to the ADC maps, ranging from 600 to $2600 \times 10^{-6} \text{ mm}^2/\text{s}$ to differentiate solid tumor from cyst/necrosis. ADC histograms were then generated using a uniform bin width of $10 \text{ mm}^2/\text{s}$. Histogram metrics used for statistical analysis were mean, median, mode, skewness, and kurtosis of these histograms.

Statistical Analysis

Clinical and demographic variables were summarized using descriptive statistics. Continuous measures were summarized using medians and ranges, and categorical measures were summarized



A



B

FIG 2. Differences in tumor volume enhancing and ADC histogram parameters between histone mutations. A, H3F3A-mutated tumor shows lower tumor volume enhancing (0.08 mL), lower ADC_FLAIR mode ($1099 \times 10^{-6} \text{ mm}^2/\text{s}$), higher ADC_FLAIR skewness (1.41), and higher ADC_FLAIR kurtosis (4.39), relative to (B) a HIST1H3B-mutated tumor (tumor volume enhancing: 3.61 mL; FLAIR_ADC mode: $1558 \times 10^{-6} \text{ mm}^2/\text{s}$; FLAIR_ADC skewness: -0.039 ; and FLAIR_ADC kurtosis: 0.33).

using frequencies and proportions. Kaplan-Meier curves were used to summarize OS and PFS for all patients. Univariate Cox proportional hazards regression was used to test the association of imaging predictors with OS and PFS. The Wilcoxon rank sum and Kruskal-Wallis tests were used to compare continuous imaging features among groups. The Fisher exact test was used to compare categorical imaging features among groups. When applicable, the presence of enhancement (defined as patients with tumor volume enhancing $>0 \text{ mL}$) was recorded as a binary measure and used for

subanalyses. Due to the low number of H3.1 mutations (HIST1H3B=8, HIST1H3C=3), we grouped them into a single category and compared them with H3F3A mutations. For each outcome tested, we calculated the false discovery rate (FDR) using the Benjamini-Hochberg method to account for multiple hypothesis tests. Tests with a calculated FDR of $\leq 10\%$ were considered statistically significant after FDR adjustment.¹⁷ R version 3.5.0 (<http://www.r-project.org>) and SAS version 9.4 (SAS Institute) were used for statistical analyses.

RESULTS

Patients

Of the 50 patients who underwent biopsy, all had baseline MR imaging studies. The median age at time of enrollment was 6 years (range, 3.3–17.5 years). Twenty-six (52%) subjects were female, 48 (96%) were successfully assigned to a molecular subgroup (2 unassigned), and 34 (68%) patients had (single) identifiable histone mutations (Table 1). One subject was excluded from subsequent analysis due to the concurrent presence of 2 histone mutations.

Tumor Enhancement and Survival

The presence of enhancement (hazard ratio = 3.2; 95% CI, 1.5–7.0; $P = .003$) was associated with decreased OS after FDR adjustment (On-line Fig A and On-line Table 2). OS was not associated ($P \geq .07$) with T2-FLAIR/T2 volume, tumor volume cyst/necrosis, the presence of necrosis, tumor volume enhancing (subset of patients with enhancing tumor of $>0 \text{ mL}$), ADC_FLAIR histogram metrics, or PG ADC enhancement histogram metrics after FDR adjustment.

Higher tumor volume enhancing ($P = .02$) and the presence of enhancement ($P = .06$) showed a strong trend with decreased PFS but were not significant after FDR adjustment (On-line Fig B and On-line Table 2). T2-FLAIR/T2 tumor volume ($P = .07$) also showed a trend toward a significant association with decreased PFS.

Molecular Subgroup Analysis

There were differences in tumor volume enhancing across the 4 molecular subgroups within the subset of patients with tumor volume enhancing of $>0 \text{ mL}$, but the test was not significant

Table 2: Association of imaging predictors and variant histone mutation (H3F3A versus HIST1H3B/C) (n = 34)

Imaging Parameters (Median) (Range)	No.	Variant Histone Mutation		Wilcoxon P
		H3F3A (n = 23)	HIST1H3B and HIST1H3C (n = 11)	
FLAIR/T2 tumor volume	33	35.1 (10.7–70.9)	40.3 (11.6–63)	.4
Tumor volume cyst/necrosis (mL) in patients with cyst/necrosis	16	0.8 (0.07–8.1)	2.1 (0.09–4.1)	.8
Presence of necrosis (yes vs no) in patients with enhancing tumor volume >0	22	11/16 (69%)	5/6 (83%)	.6 ^a
Tumor volume enhancing (mL) in patients with enhancing tumor volume >0	22	2.5 (0.08–12.4)	6.3 (3.6–15.2)	.04 ^b
Presence of enhancement (yes vs no)	31	16/21 (76%)	6/10 (60%)	.4 ^a
Mean ADC_FLAIR × 10 ⁻⁶ mm ² /s	31	1306 (893.9–1915.2)	1411 (1168.8–2098.3)	.06
Median ADC_FLAIR × 10 ⁻⁶ mm ² /s	31	1260 (906.7–1913)	1370 (1189.4–2146.0)	.03 ^b
Mode ADC_FLAIR × 10 ⁻⁶ mm ² /s	31	1257 (895.5–1886.4)	1396 (1150.8–2214.4)	.02 ^b
Skewness ADC_FLAIR	29	1 (–0.6–2.0)	0.03 (–1.3–0.9)	.009 ^b
Kurtosis ADC_FLAIR	29	1.8 (–0.3–8.2)	0.3 (–1.1–2.4)	.03 ^a

^a Fisher exact test P value.

^b Test is significant after FDR adjustment <.1.

Table 3: Association of imaging predictors with mutational status (any histone mutation versus wild-type) (n = 49)

Imaging Parameters (Median) (Range)	No.	Any Histone Mutation (n = 34)	Wild-Type (n = 15)	Wilcoxon P
Mean ADC_T2-FLAIR/T2 × 10 ⁻⁶ mm ² /s	45	1360 (893.9–2098.3)	1327 (1040.4–1838.5)	.9
Median ADC_T2-FLAIR/T2 × 10 ⁻⁶ mm ² /s	45	1309 (906.7–2146.0)	1316 (952.0–1925.7)	.9
Mode ADC_T2-FLAIR/T2 × 10 ⁻⁶ mm ² /s	45	1311 (895.5–2214.4)	1342 (893.8–1965.4)	.99
Skewness ADC_T2-FLAIR/T2	42	0.5 (–1.3–2.0)	0.8 (–0.9–2.8)	.4
Kurtosis ADC_T2-FLAIR/T2	42	1.1 (–1.1–8.2)	2.0 (–0.1–9.0)	.1

after FDR adjustment ($P = .04$; $n = 30$) (On-line Table 3). All *MGMT+* tumors showed enhancement, most *MGMT-EGFR+* tumors (77%) showed enhancement, and 54% of *MGMT-EGFR-* tumors showed enhancement (On-line Table 3). The 3 *MGMT+/EGFR-* tumors had the highest tumor volume enhancing values, occasionally an order of magnitude higher than those of other molecular groups, including the *MGMT+/EGFR+* tumors. No other factor analyzed showed a significant association with molecular groups, including ADC histogram metrics.

Histone Mutation Analysis

Subjects with HIST1H3B/C tumors showed a trend toward improved OS that bordered on significance ($P = .0501$) compared with subjects with H3F3A tumors (Fig 1). There was no difference in PFS ($P = .22$) between subjects with H3F3A and HIST1H3B/C tumors.

Tumor volume enhancing (in a subset of patients with enhancing tumor volumes of >0 mL, $P = .048$), median ADC_FLAIR ($P = .03$), and mode ADC_FLAIR ($P = .02$) were significantly higher in tumors with HIST1H3B/C mutations. Skewness ADC_FLAIR ($P = .009$) and kurtosis ADC_FLAIR ($P = .03$) were significantly higher in tumors with H3F3A mutations. H3F3A mutations had lower ADC values compared with HIST1H3B tumors (Fig 2 and Table 2).

A comparison of ADC T2-FLAIR/T2 mean, median, and mode; skewness; and kurtosis did not show differences between wild-type tumors and grouped histone mutation (H3F3A and HIST1H3B/C) tumors (Table 3). Kaplan-Meier analysis also failed to demonstrate significant differences in OS or PFS between wild-type and grouped histone-mutated tumors (Fig 3).

DISCUSSION

Even though MR imaging has traditionally played a central role in the evaluation and monitoring of patients with DIPG, little is known regarding the biologic and molecular correlates of imaging features such as the presence of enhancement, low diffusivity, and findings on ADC histogram analysis.^{12,18} Recently, more centers are performing biopsies for DIPG, which has permitted identification of molecular subgroups with distinct clinical characteristics.^{3,19-21} This work demonstrates the feasibility of a radiogenomic approach to investigate differences among various tumor groups. Specifically, we identified significant differences in volume of enhancing tumor between molecular subgroups and differences in volume of enhancing tumor and ADC histogram parameters across tumors with different histone mutations. We followed a previously validated approach for patients with DIPG, thus, minimizing the risk of introducing methodologic bias in our analysis.¹²

Molecular characteristics of brain tumors are now widely accepted as important diagnostic criteria for many entities as well as independent prognostic markers.^{22,23} Castel et al³ investigated the molecular profile of DIPG in 91 children and identified 2 distinct subgroups with mutations in H3.3 (H3F3A) and H3.1 (HIST1H3B/C) histone variants. Tumors with H3F3A mutations had a worse prognosis, with a poor response to radiation therapy and earlier relapse compared with HIST1H3B/C mutated tumors.²⁰ Similar to the observations by Castel et al, we found a strong trend toward shorter OS in patients with H3F3A mutations relative to HIST1H3B/C, though this did not reach statistical significance, likely due to the smaller sample size in our study.

ADC histogram analysis revealed differences across histone mutations, with H3F3A-mutated tumors having lower ADC T2-FLAIR/T2, higher skewness, and higher kurtosis than HIST1H3B/C-mutated tumors. This finding suggests that histogram metrics

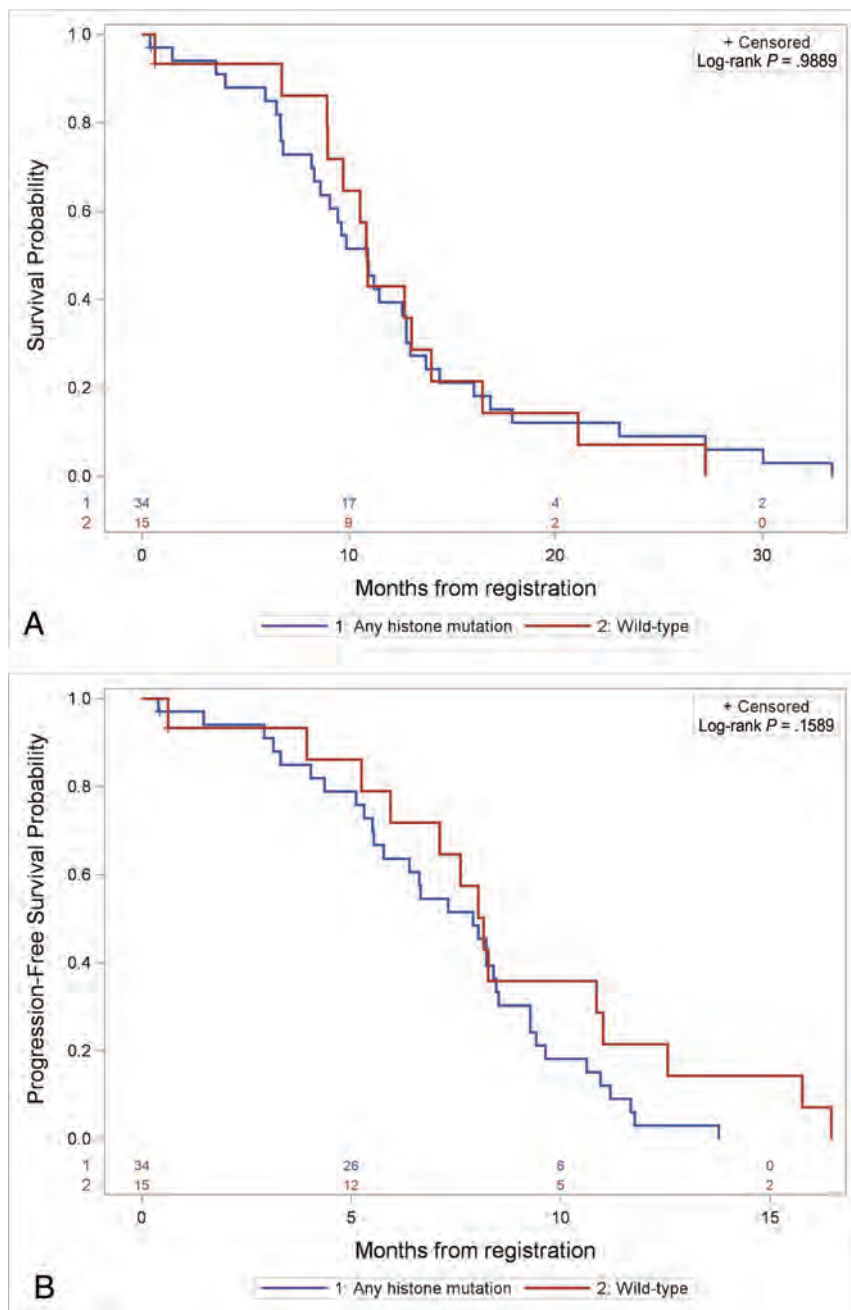


FIG 3. Prognostic differences in subjects with any histone mutation ($n=34$) versus wild-type ($n=15$) tumors. **A**, Kaplan-Meier curve shows no significant difference in OS between mutant versus wild-type tumors. **B**, Kaplan-Meier curve shows no significant difference in PFS between mutant versus wild-type tumors.

may help differentiate tumors that have the H3F3A mutation, which carries a worse prognosis, from those with HIST1H3B/C mutations.^{3,20,24,25} Poussaint et al¹² found that tumors with lower preradiotherapy mean, median, and mode ADC FLAIR (analogous to T2-FLAIR/T2 in our study) had shorter PFS and that tumors with higher skewness and kurtosis had shorter OS and PFS. Although that study did not include pathologic or molecular analysis of the tumors, the findings consistently indicated that ADC histogram metrics can identify tumors with more aggressive biology; it is therefore possible that some of the tumors with these ADC

histogram features in the study by Poussaint et al may have had H3F3A mutations.

The differences in ADC and ADC histogram parameters among histone-mutated tumors is likely multifactorial. As postulated by Poussaint et al,¹² Lober et al,²⁶ Zukotynski et al,²⁷ Chen et al,¹¹ and Lobel et al²⁸ on prior studies of DIPG, and by Nowosielski et al²⁹ on studies of adult high-grade gliomas, the lower diffusivity and increased kurtosis possibly reflect higher cellularity, which could be related to the more aggressive biology of H3F3A-mutated tumors. Additionally, Castel et al³ reported that the H3.1 tumors had an enrichment in genes associated with glioblastoma with edema, which correlated with exuberant extracellular edema in their histologic analysis; these factors may also contribute to overall higher ADC and lower skewness/kurtosis in H3.1-mutated tumors. A difference between the study by Poussaint et al¹² and the current study is that we did not find an association of ADC histogram metrics with PFS or OS, which could be related to a larger sample size in the former study, which analyzed approximately 3 times as many patients. However, the significant trends we observed showed an association of other adverse prognostic factors with the more aggressive (H3F3A) tumors.

We did not identify differences in mean, median, mode ADC histogram parameters, or survival between wild-type histone tumors and H3K27M-mutated tumors (collectively), consistent with the results from a study published by Aboian et al.³⁰ Similarly, the study by Castel et al³ did not identify differences in survival between wild-type tumors and histone-mutated tumors (collectively). Chen et al³¹

found lower ADC in the tumor and peritumoral regions of patients with H3K27M mutations compared with wild-type tumors; however, the patient population analyzed in that study is vastly different, possibly accounting for the discrepancy. For instance, the study by Chen et al included H3K27M tumors outside of the brain stem (spinal cord) and included substantially older subjects (most of subjects were older than 18 years of age).³¹

In our cohort, higher tumor volume enhancing had a significant association with shorter OS and PFS, as has been shown in

multiple prior studies.^{12,18} We also observed significant differences across molecular subgroups in tumor volume enhancing. Specifically, *MGMT*+ tumors (EGFR- and EGFR+) showed enhancement regardless of their EGFR status, most *MGMT*-/EGFR+ tumors showed enhancement, and slightly more than 50% of *MGMT*-/EGFR- tumors showed enhancement. These findings suggest that a radiogenomic approach could contribute to identifying specific mutations in tumors and could help individualize therapy to target the oncogenic pathways involved.^{19,21,32} Differences in tumor volume enhancing were also observed between tumors with H3F3A and HIST1H3B/C mutations, a finding that has not been previously reported in the literature.

Most interesting, higher tumor volume enhancing, which is thought to have a negative prognostic association, was higher in HIST1H3B/C tumors, which have a better prognosis compared with H3F3A tumors.³ We believe that this observation is likely related to the higher expression of genes responsible for angiogenesis in H3.1-mutated tumors, and these findings correlate with preliminary observations described by Castel et al³ in a subanalysis of their radiologic data. Our sample size was too small to perform a subgroup analysis between enhancing and nonenhancing tumors for each histone mutation; additional work is needed to further elucidate the implications of differences in enhancement in tumors with different histone mutations.²⁴ This complex landscape suggests that a multiparametric approach may be useful when evaluating DIPG, because multiple genetic pathways (including *MGMT*, EGFR, histone) probably account for the pleomorphic MR imaging appearance and clinical course of these tumors, and these factors likely interact with each other to determine the clinical course.³³

There are several limitations to this study. First, we conducted our analysis on a small sample size from a single prospective clinical trial. Consequently, our results are preliminary observations that need to be corroborated in a larger separate cohort. Due to the small sample size, we were unable to explore the prognostic implications of differences in enhancement and ADC histogram metrics within individual molecular subgroups and histone variants. Although we identified group differences in diffusion metrics, ADC histogram analysis, and enhancement, the exact biologic substrates for these were not explored. More detailed genetic analyses being performed on this cohort of patients may uncover biologic explanations for these differences. Finally, we analyzed only the baseline MR imaging and did not analyze the changes in any of the baseline parameters with treatment on subsequent MRIs. ADC histogram metrics and tumor enhancing volume could potentially serve as valuable markers of treatment response.

CONCLUSIONS

MR imaging features including enhancement and ADC histogram metrics are correlated with molecular subgroups and histone mutations in children with DIPG. Noninvasive markers that allow identification of molecular subgroups of DIPG could help prognosticate survival and guide therapy. Future studies in a larger cohort are required to verify these findings.

Disclosures: Sridhar Vajapeyam—RELATED: Consulting Fee or Honorarium: Dana Farber Cancer Institute, Comments: salary support for MRI data-processing and

analysis.* Nalin Gupta—UNRELATED: Grants/Grants Pending National Institutes of Health/National Institute of Neurological Disorders and Stroke, Chad Moser Foundation, Comments: Research grants funded by named entities*; Royalties: Millipore Corporation, Comments: Cell lines were submitted with named entity.* Liliana Goumnerova—UNRELATED: Payment for Lectures Including Service on Speakers Bureaus: Stanford University, Department of Neurosurgery, Comments: invited as a visiting professor in October 2019 and received an honorarium (\$500); Travel/Accommodations/Meeting Expenses Unrelated to Activities Listed: Stanford University, Department of Pediatric Neurosurgery, Comments: visiting professor (invited by them) October 2019, received transportation/accommodation and an honorarium. Pratiti Bandopahayay—RELATED: Grant: Novartis Institute of Biomedical Research, Comments: My lab receives grant funding for an unrelated project.* Rameen Beroukhim—UNRELATED: Grant: Novartis, Board Membership: Ampressa Therapeutics, Comments: member of scientific advisory board; Stock/Stock Options: Ampressa Therapeutics. Keith L. Ligon—UNRELATED: Consultancy: Bristol Myers Squibb for diffuse intrinsic pontine glioma trial design consulting. Susan Chi—RELATED: Grant: philanthropic and foundation, Comments: Zach Carson Fund, Ellie Kavalieros Diffuse Intrinsic Pontine Glioma Fund, Ryan Harvey Fund, Mikey Czech Diffuse Intrinsic Pontine Glioma Foundation, Caroline Cronk Fund, Prayers from Maria, Guglietti Diffuse Intrinsic Pontine Glioma Fund, Markoff Art in Giving Foundation, Brock Fleming Fund, Stop and Shop Pediatric Brain Tumor Program, the Diffuse Intrinsic Pontine Glioma Collaborative (which includes the Hope for Caroline Foundation, Reflections of Grace Foundation, Cure Starts Now Foundation, Soar with Grace Foundation, Abbie's Army Charity Trust, Julian Boivin Courage for Cures Foundation, Smiles for Sophie Forever, Caroline's Miracle Foundation, Love, Chloe Foundation, Benny's World Foundation, Pray Hope Believe Foundation, Jeffrey Thomas Hayden Foundation) and 5P30 CA006516*; UNRELATED: Consultancy: Epizyme Inc. Mark W. Kieran—UNRELATED: Consultancy: Novartis, Boehringer Ingelheim, Eli Lilly, Sanofi, Merck, Bristol Myers Squibb, Bayer Pharmaceuticals Company (Bayer), Takeda Pharmaceutical Company, Comments: Advisory Board; Travel/Accommodations/Meeting Expenses Unrelated to Activities Listed: Novartis, Comments: travel to Advisory Board. Karen D. Wright—RELATED: Grant: multiple grant funders, Comments: Zach Carson Fund, Ellie Kavalieros Diffuse Intrinsic Pontine Glioma Fund, Ryan Harvey Fund, Mikey Czech Diffuse Intrinsic Pontine Glioma Foundation, Caroline Cronk Fund, Prayers from Maria, Guglietti Diffuse Intrinsic Pontine Glioma Fund, Markoff Art in Giving Foundation, Brock Fleming Fund, Stop and Shop Pediatric Brain Tumor Program, the Diffuse Intrinsic Pontine Glioma Collaborative (which includes the Hope for Caroline Foundation, Reflections of Grace Foundation, Cure Starts Now Foundation, Soar with Grace Foundation, Abbie's Army Charity Trust, Julian Boivin Courage for Cures Foundation, Smiles for Sophie Forever, Caroline's Miracle Foundation, Love, Chloe Foundation, Benny's World Foundation, Pray Hope Believe Foundation, Jeffrey Thomas Hayden Foundation) and 5P30 CA006516*; Support for Travel to Meetings for the Study or Other Purposes: Diffuse Intrinsic Pontine Glioma Collaborative, Comments: fund travel to/from diffuse intrinsic pontine glioma meeting; specifically, Diffuse Intrinsic Pontine Glioma Collaborative paid for flights for attendees to a meeting in Sydney, Australia, August 2–4, 2019. This meeting, however, was not related to this work, only diffuse intrinsic pontine glioma in general and plans for future studies; UNRELATED: Board Membership: Canines-N-Kids, Comments: Scientific advisory board; Consultancy: Grand Rounds through association with Boston Children's Hospital, Boehringer Ingelheim, listed as consultant but have not done anything as of yet to warrant payment; Guidepoint Global Advisors, on list but have not participated in paid consult; Infinite MD, paid consultant for patients; Takeda Pharmaceutical Company, previously consulting because I was Principal Investigator/author for the trial they support with the drug TAK580, which has since been sold to Day One Biopharma; Grants/Grants Pending: 6314201, PLGA, \$300,000, 9619394; Team Jack Foundation gift funding, to be split between TAK580 and MEK162, \$600,000 (includes recent \$100,000 donation that is not intended for TAK580 but was deposited here as a placeholder); 6310103, Team Jack Foundation, \$300,000; Specialized Programs of Research Excellence in Human Cancers (SPORE) award fund I22249*; Patents (Planned, Pending or Issued): Dana Farber Cancer Institute (DFCI) case No. C2843 (participant is Karen Wright): Clinical Use of Day101 (formerly TAK580/MLN2840) for the treatment of low-grade glioma; and DFCI case No. C2844 (Participants are from DFCI, Day One Biopharmaceuticals, and Imaging Endpoints Core Lab): use of DWI/ADC as a biomarker of response specific to DAY101 (formerly TAK580/MLN2840). Tina Young Poussaint—UNRELATED: Grants/Grants Pending: Pediatric Brain Tumor Consortium neuroimaging center grant, National Institutes of Health*; Royalties: Springer. Frank Dubois—RELATED: Grant: German Research Foundation. *Money paid the institution.

REFERENCES

1. Ostrom QT, Gittleman H, Truitt G, et al. **CBTRUS Statistical Report: Primary Brain and Other Central Nervous System Tumors Diagnosed in the United States in 2011–2015.** *Neuro Oncol* 2018;20:iv1–86 CrossRef Medline

2. Hassan H, Pinches A, Picton SV, et al. **Survival rates and prognostic predictors of high-grade brain stem gliomas in childhood: a systematic review and meta-analysis.** *J Neurooncol* 2017;135:13–20 CrossRef Medline
3. Castel D, Philippe C, Calmon R, et al. **Histone H3F3A and HIST1H3B K27M mutations define two subgroups of diffuse intrinsic pontine gliomas with different prognosis and phenotypes.** *Acta Neuropathol* 2015;130:815–27 CrossRef Medline
4. Pope WB, Chen JH, Dong J, et al. **Relationship between gene expression and enhancement in glioblastoma multiforme: exploratory DNA microarray analysis.** *Radiology* 2008;249:268–77 CrossRef Medline
5. Gutman DA, Cooper LA, Hwang SN, et al. **MR imaging predictors of molecular profile and survival: multi-institutional study of the TCGA glioblastoma data set.** *Radiology* 2013;267:560–69 CrossRef Medline
6. Nowak J, Nemes K, Hohm A, et al. **Magnetic resonance imaging surrogates of molecular subgroups in atypical teratoid/rhabdoid tumor.** *Neuro Oncol* 2018;20:1672–79 CrossRef Medline
7. Perreault S, Ramaswamy V, Achrol AS, et al. **MRI surrogates for molecular subgroups of medulloblastoma.** *AJNR Am J Neuroradiol* 2014;35:1263–69 CrossRef Medline
8. Kieran MW, Goumnerova LC, Prados M, et al. **Biopsy for diffuse intrinsic pontine glioma: a reappraisal.** *J Neurosurg Pediatr* 2016;18:390–91 CrossRef Medline
9. Jansen MH, Veldhuijzen van Zanten SE, Sanchez Aliaga E, et al. **Survival prediction model of children with diffuse intrinsic pontine glioma based on clinical and radiological criteria.** *Neuro Oncol* 2015;17:160–66 CrossRef Medline
10. Hoffman LM, Veldhuijzen van Zanten SE, Colditz N, et al. **Clinical, radiologic, pathologic, and molecular characteristics of long-term survivors of diffuse intrinsic pontine glioma (DIPG): A Collaborative Report from the International and European Society for Pediatric Oncology DIPG Registries.** *J Clin Oncol* 2018;36:1963–72 CrossRef Medline
11. Chen HJ, Panigrahy A, Dhall G, et al. **Apparent diffusion and fractional anisotropy of diffuse intrinsic brain stem gliomas.** *AJNR Am J Neuroradiol* 2010;31:1879–85 CrossRef Medline
12. Poussaint TY, Vajapeyam S, Ricci KI, et al. **Apparent diffusion coefficient histogram metrics correlate with survival in diffuse intrinsic pontine glioma: a report from the Pediatric Brain Tumor Consortium.** *Neuro Oncol* 2016;18:725–34 CrossRef Medline
13. Gupta N, Goumnerova LC, Manley P, et al. **Prospective feasibility and safety assessment of surgical biopsy for patients with newly diagnosed diffuse intrinsic pontine glioma.** *Neuro Oncol* 2018;20:1547–55 CrossRef Medline
14. Fischbein NJ, Prados MD, Wara W, et al. **Radiologic classification of brain stem tumors: correlation of magnetic resonance imaging appearance with clinical outcome.** *Pediatr Neurosurg* 1996;24:9–23 CrossRef Medline
15. Jenkinson M, Beckmann CF, Behrens TE, et al. **FSL.** *Neuroimage* 2012;62:782–90 CrossRef Medline
16. Schindelin J, Arganda-Carreras I, Frise E, et al. **Fiji: an open-source platform for biological-image analysis.** *Nat Methods* 2012;9:676–82 CrossRef Medline
17. Benjamini Y, Hochberg Y. **Controlling the false discovery rate: a practical and powerful approach to multiple testing.** *Journal of the Royal Statistical Society, Series B (Methodological)* 1995;57:289–300 CrossRef
18. Poussaint TY, Kocak M, Vajapeyam S, et al. **MRI as a central component of clinical trials analysis in brainstem glioma: a report from the Pediatric Brain Tumor Consortium (PBTC).** *Neuro Oncol* 2011;13:417–27 CrossRef Medline
19. Infinger LK, Stevenson CB. **Re-examining the need for tissue diagnosis in pediatric diffuse intrinsic pontine gliomas: a review.** *Curr Neuropharmacol* 2017;15:129–33 CrossRef Medline
20. Khuong-Quang DA, Buczkowicz P, Rakopoulos P, et al. **K27M mutation in histone H3.3 defines clinically and biologically distinct subgroups of pediatric diffuse intrinsic pontine gliomas.** *Acta Neuropathol* 2012;124:439–47 CrossRef Medline
21. Buczkowicz P, Bartels U, Bouffet E, et al. **Histopathological spectrum of paediatric diffuse intrinsic pontine glioma: diagnostic and therapeutic implications.** *Acta Neuropathol* 2014;128:573–81 CrossRef Medline
22. Louis DN, Perry A, Reifenberger G, et al. **The 2016 World Health Organization Classification of Tumors of the Central Nervous System: a summary.** *Acta Neuropathol* 2016;131:803–20 CrossRef Medline
23. Yan H, Parsons DW, Jin G, et al. **IDH1 and IDH2 mutations in gliomas.** *N Engl J Med* 2009;360:765–73 CrossRef Medline
24. Goya-Outi JC, Orlhac R, Philippe F, et al. **Can structural MRI radiomics predict DIPG histone H3 mutation and patient overall survival at diagnosis time?** In: *Proceedings of the Institute of Electrical and Electronics Engineers Engineering in Medicine and Biology Society International Conference on Biomedical & Health Informatics (BHI'19)*, Chicago, Illinois. May 19–22, 2019: 1–4
25. Goya-Outi J, Orlhac F, Calmon R, et al. **Computation of reliable textural indices from multimodal brain MRI: suggestions based on a study of patients with diffuse intrinsic pontine glioma.** *Phys Med Biol* 2018;63:105003 CrossRef Medline
26. Lober RM, Cho YJ, Tang Y, et al. **Diffusion-weighted MRI derived apparent diffusion coefficient identifies prognostically distinct subgroups of pediatric diffuse intrinsic pontine glioma.** *J Neurooncol* 2014;117:175–82 CrossRef Medline
27. Zukotynski KA, Vajapeyam S, Fahey FH, et al. **Correlation of (18)F-FDG PET and MRI apparent diffusion coefficient histogram metrics with survival in diffuse intrinsic pontine glioma: a report from the Pediatric Brain Tumor Consortium.** *J Nucl Med* 2017;58:1264–69 CrossRef Medline
28. Lobel U, Sedlacik J, Reddick WE, et al. **Quantitative diffusion-weighted and dynamic susceptibility-weighted contrast-enhanced perfusion MR imaging analysis of T2 hypointense lesion components in pediatric diffuse intrinsic pontine glioma.** *AJNR Am J Neuroradiol* 2011;32:315–22 CrossRef Medline
29. Nowosielski M, Recheis W, Goebel G, et al. **ADC histograms predict response to anti-angiogenic therapy in patients with recurrent high-grade glioma.** *Neuroradiology* 2011;53:291–302 CrossRef Medline
30. Aboian MS, Tong E, Solomon DA, et al. **Diffusion characteristics of pediatric diffuse midline gliomas with histone H3-K27M mutation using apparent diffusion coefficient histogram analysis.** *AJNR Am J Neuroradiol* 2019;40:1804–10 CrossRef Medline
31. Chen H, Hu W, He H, et al. **Noninvasive assessment of H3 K27M mutational status in diffuse midline gliomas by using apparent diffusion coefficient measurements.** *Eur J Radiol* 2019;114:152–59 CrossRef Medline
32. Bailey S, Howman A, Wheatley K, et al. **Diffuse intrinsic pontine glioma treated with prolonged temozolomide and radiotherapy: results of a United Kingdom phase II trial (CNS 2007 04).** *Eur J Cancer* 2013;49:3856–62 CrossRef Medline
33. Aboian MS, Solomon DA, Felton E, et al. **Imaging characteristics of pediatric diffuse midline gliomas with histone H3 K27M mutation.** *AJNR Am J Neuroradiol* 2017;38:795–800 CrossRef Medline

Synthetic MRI of Preterm Infants at Term-Equivalent Age: Evaluation of Diagnostic Image Quality and Automated Brain Volume Segmentation

T. Vanderhasselt, M. Naeyaert, N. Watté, G.-J. Allemeersch, S. Raeymaeckers, J. Dudink, J. de Mey, and H. Raeymaekers



ABSTRACT

BACKGROUND AND PURPOSE: Neonatal MR imaging brain volume measurements can be used as biomarkers for long-term neurodevelopmental outcome, but quantitative volumetric MR imaging data are not usually available during routine radiologic evaluation. In the current study, the feasibility of automated quantitative brain volumetry and image reconstruction via synthetic MR imaging in very preterm infants was investigated.

MATERIALS AND METHODS: Conventional and synthetic T1WIs and T2WIs from 111 very preterm infants were acquired at term-equivalent age. Overall image quality and artifacts of the conventional and synthetic images were rated on a 4-point scale. Legibility of anatomic structures and lesion conspicuity were assessed on a binary scale. Synthetic MR volumetry was compared with that generated via MANTiS, which is a neonatal tissue segmentation toolbox based on T2WI.

RESULTS: Image quality was good or excellent for most conventional and synthetic images. The 2 methods did not differ significantly regarding image quality or diagnostic performance for focal and cystic WM lesions. Dice similarity coefficients had excellent overlap for intracranial volume (97.3%) and brain parenchymal volume (94.3%), and moderate overlap for CSF (75.6%). Bland-Altman plots demonstrated a small systematic bias in all cases (1.7%–5.9%)

CONCLUSIONS: Synthetic T1WI and T2WI sequences may complement or replace conventional images in neonatal imaging, and robust synthetic volumetric results are accessible from a clinical workstation in less than 1 minute. Via the above-described methods, volume assessments could be routinely used in daily clinical practice.

ABBREVIATIONS: BPV = brain parenchymal volume; SyMRI = synthetic MR imaging

Despite improvements in neonatal care, a high number of infants born very preterm develop sensorimotor, cognitive, and behavioral disabilities later in life.¹ Identifying children at risk is essential for adequate parental counseling and may also facilitate early intervention strategies.² Numerous studies have shown that structural MR imaging results at term-equivalent age are predictive of future motor and cognitive outcomes,^{3–5} and multiple volumetric MR imaging studies have identified associations between reduced

brain volume and impaired neurodevelopment.^{6–8} Notably however, quantifying brain volumes in neonates is challenging.

A neonate's head is only a quarter of the size of an adult's brain, and the relative signal intensity of the GM and WM is reversed due to the high amount of unmyelinated WM.⁹ Neonatal scans often demonstrate changes in the brain, such as moderate-to-severe dilation or distortion of the ventricles, hyperintensity or hypointensity zones, and cystic or hemorrhagic lesions; therefore, they require substantial adjustments to the segmentation approaches used in adults.¹⁰ Several studies have demonstrated the feasibility of neonatal MR volumetry with custom-made software.¹¹ These methods are often time-consuming and require specialized infrastructure, technical expertise, and powerful computing resources however and are thus not available in most centers.⁹ These difficulties hinder the use of this important biomarker in clinical practice.

Synthetic MR imaging (SyMRI; SyntheticMR, Linköping, Sweden) is an emerging imaging technique that simultaneously quantifies R1 and R2 relaxation rates, proton density, and B₁ field based on a fast, multidelay, multiecho acquisition.¹² Dedicated synthetic MR imaging (SyMRI) software (Synthetic MR, Linköping, Sweden) then facilitates the reconstruction of synthetic images with

Received December 23, 2019; accepted after revision March 16, 2020.

From the Department of Radiology (T.V., M.N., N.W., G.-J.A., S.R., J.d.M., H.R.), Vrije Universiteit Brussels, Universitair Ziekenhuis Brussels, Brussels, Belgium; Department of Neonatology (J.D.), Wilhelmina Children's Hospital/Utrecht University Medical Center, Utrecht, the Netherlands; and Rudolf Magnus Brain Center (J.D.), Utrecht University Medical Center, Utrecht, the Netherlands.

Please address correspondence to Tim Vanderhasselt, MD, Universitair Ziekenhuis Brussels, Department of Radiology, Laarbeeklaan 101, 1090 Brussels, Belgium; e-mail: tim.vanderhasselt@uzbrussel.be

Indicates article with supplemental on-line tables.

<http://dx.doi.org/10.3174/ajnr.A6533>

a combination of virtually any TE, TR, and TI. This may save time because multiple synthetic sequences can be reconstructed from the same multidelay, multiecho sequence even after the patient has left the scanner. SyMRI also provides fully automated volumetric analysis based on the expected quantitative values for different brain tissue types.¹³ The software is integrated into the radiology PACS system, and brain volume analysis is available in <1 minute.¹⁴

In 1 large, prospective, multicenter, multireader trial, the overall diagnostic quality of synthetic images in adults was reportedly similar to that of conventional imaging.¹⁵ Furthermore, synthetic MR imaging segmentation is reportedly rapid and robust and exhibits excellent repeatability.^{13,14,16-18} To date, only a few studies have examined the feasibility of synthetic MR imaging in children however, and there are very few data available on neonates.¹⁷⁻²² Notably, McAllister et al¹⁸ and Kim et al¹⁷ reported that in neonates, large parts of the brain parenchyma were incorrectly labeled as CSF by SyMRI.

In the current study, we used a prototype version of SyMRI (Version 11.1; <https://www.syntheticmr.com/>) that was adapted to perform fast and accurate volumetry in neonates. A neonate's brain is far more hydrated than an adult brain, which caused earlier versions of SyMRI to detect a CSF haze throughout the entire brain. In the new Version 11.1, the CSF contribution in the immature brain is suppressed. Because the WM definition remains at adult values, the erroneous CSF is converted nearly entirely to GM. Therefore, in the present study, total brain volume and intracranial volume were evaluated, but further distinction between GM and WM was not attempted.

The primary objective of the current study was to evaluate the image quality and diagnostic performance of synthetic MR imaging in a neonatal population compared with conventionally acquired images. A secondary objective was to assess the new and improved SyMRI algorithm for neonatal brain segmentation and its applicability in clinical practice. To validate these segmentations, the synthetic tissue volumes were compared with data derived from MANTiS (Morphologically Adaptive Neonatal Tissue Segmentation), (<http://developmentalimagingmcri.github.io/mantis>) a state-of-the-art research method for neonatal brain segmentation.¹⁰

MATERIALS AND METHODS

Study Population

A total of 111 very preterm infants (born at <32 weeks' gestation) were scanned at an average postmenstrual age of 40.0 ± 1.0 weeks at our institution (Universitair Ziekenhuis Brussels) as part of their routine clinical follow-up between February 2017 and June 2019. All patients who had both synthetic multidelay, multiecho, and conventional 2D or 3D MR imaging sequences were included in the study. Both 2D and 3D T2WI datasets were available for 59 neonates. Seventeen neonates had only the 2D T2WI dataset, while 32 neonates had only the 3D T2WI dataset.

Image quality and diagnostic performance were assessed on 76 subjects (mean gestational age at birth, 29.2 ± 2.6 weeks; 42 boys and 34 girls) who had both synthetic multidelay, multiecho, and conventional 3D T1WI and 2D T2WI TSE data available for comparison. Because evaluation of image artifacts and image quality was part of the experimental design, no subjects were excluded on this basis.

A conventional 3D T2WI dataset was required for segmentation using MANTiS. Ninety-one neonates (mean gestational age at birth, 29.4 ± 2.0 weeks; 49 boys and 42 girls) underwent both 3D T2WI TSE and multidelay, multiecho scanning and were included in the quantitative volumetric validation.

After visual quality control, 16 subjects were rejected due to the following: excessive movement during the multidelay, multiecho scan ($n = 5$), failed watershed skull-stripping by MANTiS ($n = 4$), segmentation error in MANTiS caused by a previously unreported bug ($n = 6$), or failed synthetic segmentation due to corrupted DICOM data ($n = 1$). The 75 remaining subjects included 40 boys and 35 girls with a mean gestational age at birth of 29.0 ± 2 weeks and a mean postmenstrual age at scanning of 40 ± 1 week.

MR Imaging Acquisition

All examinations were performed on a 3T Ingenia MR imaging scanner (Philips Healthcare, Best, the Netherlands) with a 16-channel head coil. The children were sedated using oral chloral hydrate (25–50 mg/kg) and placed in a MedVac vacuum immobilization device (CFI Medical Solutions, Fenton, Michigan) before scanning. Neonatal earmuffs (Minimuffs; Natus Medical, San Carlos, California) covered by headphones were used for ear protection. Informed parental consent was obtained before MR imaging and sedation.

First, conventional images were obtained in accordance with the standard dedicated neonatal MR imaging protocol used at our institution. This included, among other things, a 3D MPRAGE and a T2WI sequence (transversal T2WI TSE, 3D T2WI, or both when time allowed). A multidelay, multiecho acquisition covering the entire brain was then acquired to perform quantitative mapping of T1, T2, and proton density using synthetic MRI. Detailed imaging parameters are shown in On-line Table 1.

Synthetic T1WIs and T2WIs and their inversion recovery variants (T1 phase-sensitive inversion recovery and T2 STIR) were generated on the basis of R1, R2, and proton density maps by fitting the data to the analytic curves describing the signal intensity, using a least-squares approach. This method has been described in detail elsewhere.¹² TE, TR, and TI were chosen to maximize tissue contrast (On-line Table 2).

Image Quality and Diagnostic Performance

The image quality and diagnostic performance of conventional and synthetic images were assessed by a blinded senior pediatric neuroradiologist (T.V.), a neuroradiologist (S.R.), and a fellow in neuroradiology (G.-J.A.) with 12, 7, and 3 years of experience in neuroradiology, respectively. For each rater, the order of the datasets was randomized, and datasets were divided into 2 sessions with a mix of conventional and synthetic datasets in each session. Only the synthetic or the conventional images of a subject were presented in the same session. Both sessions were conducted at least 2 weeks apart to prevent recall bias.

The overall image quality for each series was assessed on a 4-point Likert scale, in which poor indicates severe image-quality issues precluding diagnosis; sufficient, moderate image-quality issues but acceptable for diagnosis; good, only minor image-quality issues; and excellent, no noticeable image-quality issues. Artifacts were scored on a similar 4-point scale (severe, moderate, minor, and

none). Lesion conspicuity and the legibility of different anatomic structures were evaluated for each conventional and synthetic dataset on a binary scale, as indicated in Table 1. Assessment of diagnostic performance included the detection of focal WM lesions and cystic degeneration. Conventional and synthetic datasets were compared with the original radiology report on the basis of all available MR images and knowledge of the clinical findings.

MR Volumetry Calculations

Synthetic tissue volumes were calculated from R1, R2, and proton density maps using the automated segmentation tool in SyMRI,

Version 11.1, optimized for segmenting neonatal brains. Segmentation was performed by comparing R1, R2, and proton density values of individual voxels with a lookup table.¹² This process enables rapid segmentation, capable of coping with partial volume effects and anatomic distortions such as hydrocephalus or cysts. Synthetic MR imaging brain segmentation was validated by comparing the results with those of MANTiS, a state-of-the-art toolbox based on SPM12 (<http://www.fil.ion.ucl.ac.uk/spm/software/spm12>) and ITK-SNAP 1.6 (www.itksnap.org) dedicated to segmentation of the neonatal brain.¹⁰ Brain extraction was performed before tissue segmentation using the watershed-based method provided in MANTiS.

Table 1: Image quality

Category	Assessment Scale
Overall image quality	Poor, sufficient, good, excellent
Artifacts	Severe, moderate, minor, none
Visualization of anatomic structures	Legible, illegible
Posterior cross-roads (T2/T2 STIR only)	
Central sulcus	
Lentiform nucleus	
Ventrolateral thalamus	
Dorsal pons	
Diagnostic performance	Present, absent
Focal WM lesions	
Cystic degeneration	

Statistics

Only good or excellent images are desirable in daily clinical practice; therefore, we chose to dichotomize image quality and artifact scores into poor-sufficient and good-excellent groups. Group differences for conventional and synthetic imaging sets were assessed with the McNemar test for all binary results, using SPSS Statistics 23 (IBM, Armonk, New York). Descriptive statistics were used to assess the legibility of anatomic structures.

Bland-Altman plots for brain parenchymal volume (BPV), brain parenchymal fraction, intracranial volume, and CSF were generated using Matlab 2016b (MathWorks, Natick, Massachusetts) to compare the measured volumes and identify systematic differences between the proposed synthetic method and MANTiS. The synthetic T2WIs were coregistered to

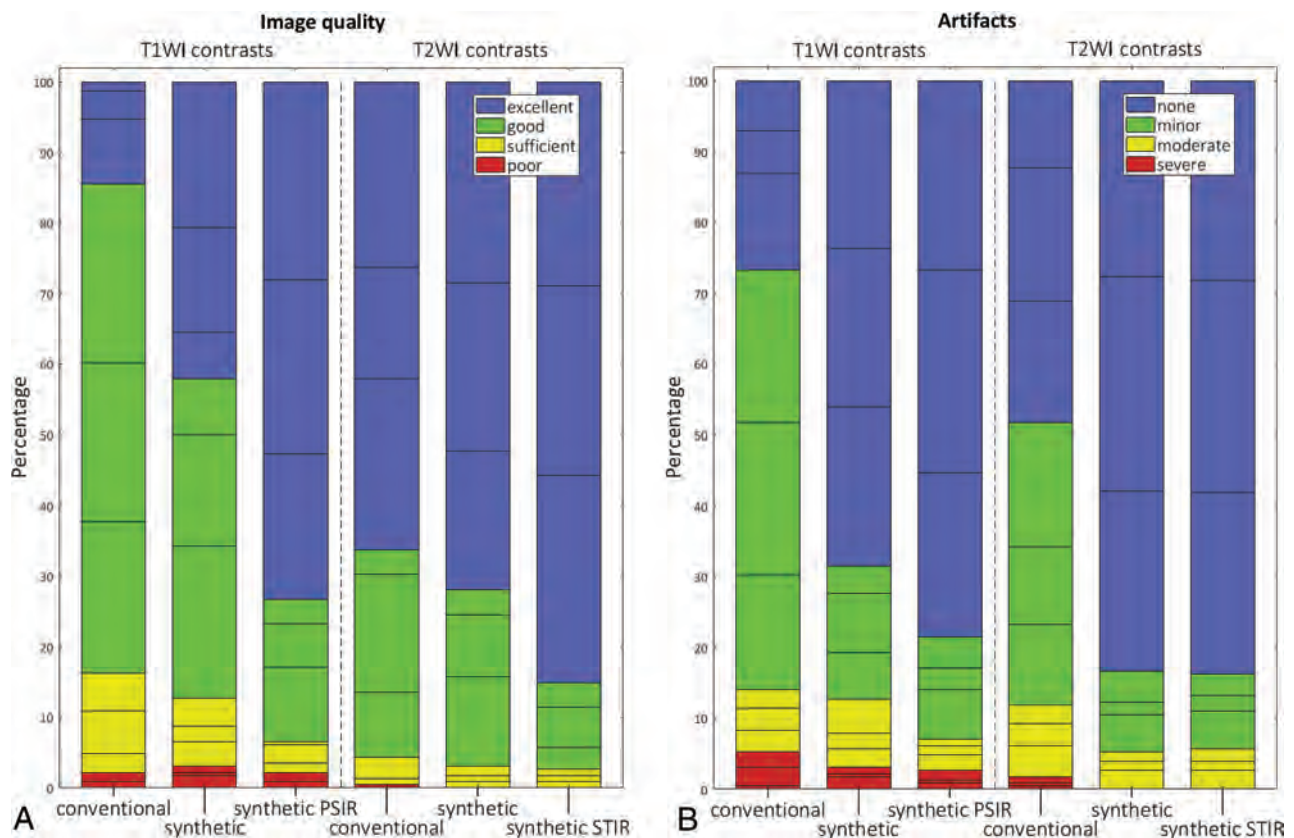


FIG 1. Qualitative comparison of T1WI and T2WI quality (A) and image artifacts (B). Horizontal lines within colored portions indicate scoring per rater. PSIR indicates phase-sensitive inversion recovery.

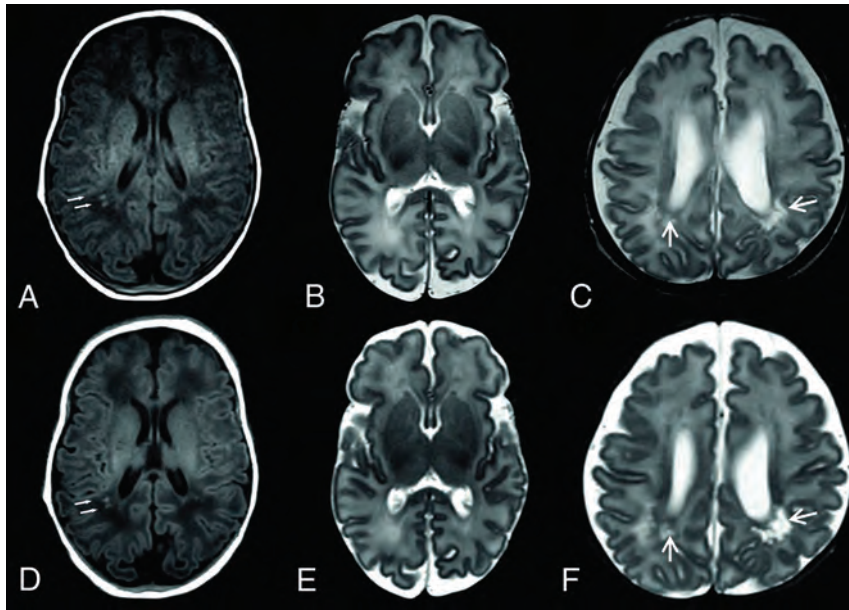


FIG 2. Upper row, Conventional T1WI (A) and T2WI (B and C). Lower row, Synthetic T1WI (D) and T2WIs (E and F). Focal WM lesions (small arrows) are clearly visible on both T1WIs. Cystic periventricular leukomalacia (arrows) is seen around the ventricles in both T2WIs.

Table 2: Lesion conspicuity

	Sensitivity	Specificity	Accuracy	P Value
WM lesions ($n = 23/76$)				
Conventional	91%	86%	89%	1.00
Synthetic	89%	77%	86%	
Cysts ($n = 7/76$)				
Conventional	96%	57%	92%	.29
Synthetic	100%	64%	95%	

the conventional dataset using SPM12 running on Matlab 2016b. The coregistration parameters were applied to the synthetic segmentation maps. A Dice similarity coefficient (DSC in the formula below) was then calculated in Matlab 2016b for CSF, BPV, and intracranial volume to investigate differences between the segmentation methods.²³ This score represents the overlap between 2 segments. For the component x , DSC_x is defined as

$$DSC_x = 2 \frac{|Synx \cap 3D_x|}{|Synx| + |3D_x|}$$

RESULTS

Image Quality and Artifacts

The results of the image-quality evaluation are presented in Fig 1. The number of scans rated as poor was negligible for both the conventional images and the synthetic images (0.0%–2.2%). The synthetic T1 phase-sensitive inversion recovery resulted in significantly more images of good or excellent quality (93.4%) than the conventional T1 (83.8%) ($P = .002$), but no other statistically significant differences were detected between synthetic and conventional images when they were dichotomized into a good or excellent group and a poor or sufficient group. A similar pattern was evident

regarding artifacts. The synthetic T1 phase-sensitive inversion recovery, synthetic T2W1, and synthetic T2 STIR produced significantly more images with minimal or minor artifacts ($P = .017$, $P = .008$, and $P = .016$, respectively) than the conventional images. The most marked difference, however, was the higher percentage of synthetic images with no or minimal artifacts ($P < .001$ for all comparisons).

Diagnostic Performance

A representative sample of conventional and synthetic images is shown in Fig 2. The anatomic structures outlined in Table 1 were identified in all the conventional and synthetic sequences. The accuracy of the detection of WM lesions was slightly better in the conventional image sets, whereas the detection of cysts was better in the synthetic images; but neither of these differences was statistically significant (Table 2).

Volumetric Validation

The results of the intracranial volume, BPV, parenchymal fraction, and CSF volume measurements are shown in the Bland-Altman plots in Fig 3. There was no correlation in the Bland-Altman plots between the mean metric under consideration and the relative difference. There was a small systematic bias

in all cases. SyMRI estimated the CSF volume to be 4.50% lower than in MANTiS, while intracranial volume, BPV, and parenchymal fraction were slightly larger (1.68% for parenchymal fraction, 4.19% for intracranial volume, and 5.87% for the BPV). Therefore, it is essential to consider which method is used for volumetry when interpreting the results. Except for the CSF measurement, the spread between both measures was small ($< 3.5\%$), indicating good agreement between the methods. For CSF, the spread was more substantial at 18%. This difference may be attributable to the smaller volume of CSF, for which minor differences in the segmentation threshold may have a greater impact. However, the spread of the relative CSF fraction (2.8%) was much lower.

Regarding overlap of segmentation maps, the average Dice similarity coefficients were 0.9731 ± 0.0004 for intracranial volume, 0.9428 ± 0.0007 for BPV, and 0.7566 ± 0.0055 for CSF. The very high scores for intracranial volume and BPV indicate substantial overlap. For the CSF maps, the overlap was moderate. Figure 4 shows a representative example of the overlap of 2 CSF segments.

DISCUSSION

A meticulous literature search suggests that this is the first dedicated study investigating the feasibility of synthetic MR imaging and brain volumetry in infants born very preterm, scanned at term-

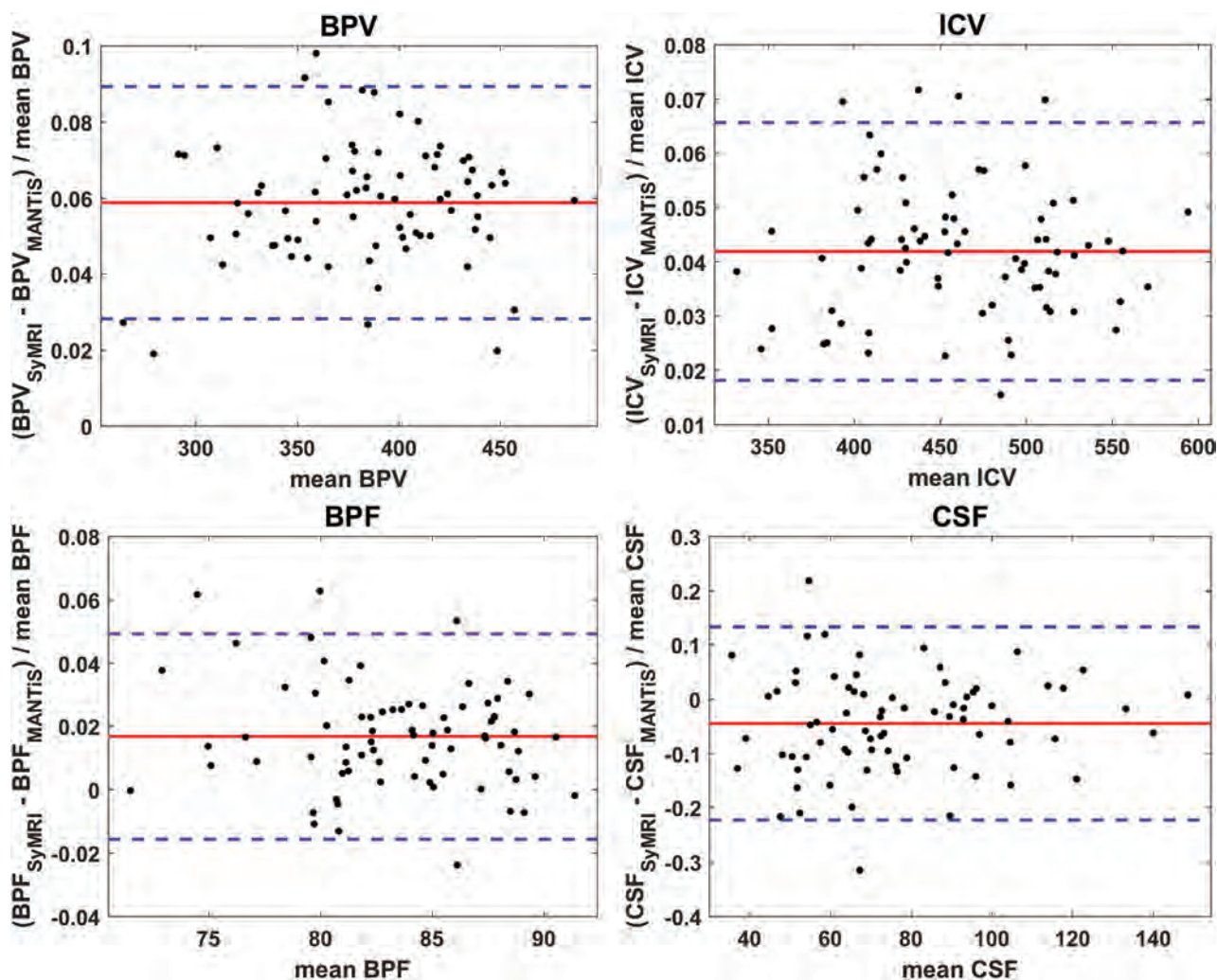


FIG 3. Bland-Altman plots comparing different volumetric metrics calculated with Synthetic MR imaging (labeled SyMRI) and MANTIS. The red line indicates the average relative difference, and the blue dashed lines indicate the average ± 1.96 .

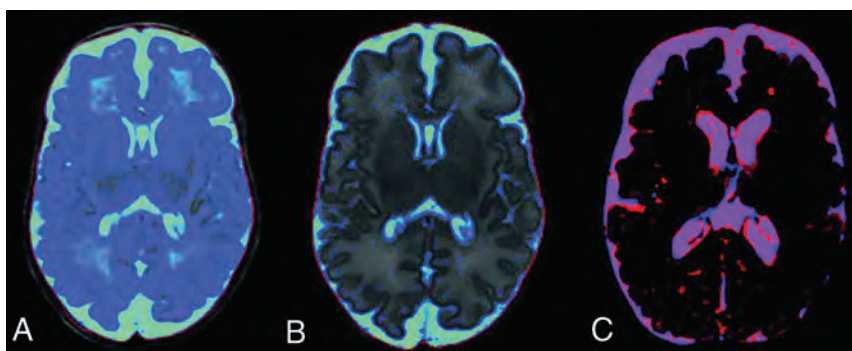


FIG 4. Synthetic CSF segmentation maps: SyMRI algorithm without optimization for the immature neonatal brain and CSF haze in the WM (blue) (A); improved SyMRI (Version 11.1) at the same level (B). Example of CSF overlap to calculate the Dice similarity coefficients (C). The synthetic CSF segment is red, and the MANTIS segment is blue. Regions where the segments overlap are purple. Voxels of the SyMRI CSF segment containing $< 20\%$ CSF are not shown.

equivalent age. The quality of the synthetic images did not differ significantly from that of conventional images when the images were dichotomized into a good or excellent group and a poor or

sufficient group. Both synthetic and conventional methods facilitated excellent visualization of normal brain structures. The accuracy of synthetic MR imaging for the detection of WM lesions was lower, but the difference was not significant ($P = 1.00$). Synthetic MR imaging sequences could therefore complement or possibly replace conventional T1WI and T2WI in neonatal imaging. Additionally, because the acquisition time remains approximately the same, contrasts that are currently omitted due to lack of time, such as single or double inverse recovery or proton density sequences, can be reconstructed without a time burden.

The inverted GM and WM contrast and the high amount of water in the neonatal brain render MR volumetrics in neonates challenging.¹¹ Previous versions of SyMRI often mislabeled WM as CSF in neonates, resulting in

inaccurate volumetric results.^{17,18} In the present study, a new version of SyMRI (Version 11.1) that features an optimized algorithm for neonatal brain segmentation was used.²⁴ The volumetric measurements of synthetic MR imaging with this optimized algorithm were generally concordant with those of MANTiS software analysis. The Dice similarity coefficients exhibited excellent overlap for intracranial volume and BPV and moderate overlap for CSF. The Bland-Altman tables also indicated minimal spread between the 2 methods for intracranial volume, BPV, and brain parenchymal fraction. The segmentation of SyMRI was more robust than that of MANTiS, with respective failure rates of 6.6% and 11.0%.

The added prognostic value of neonatal MR imaging volume-etry has been demonstrated in numerous studies.⁶⁻⁸ To the best of our knowledge, SyMRI is the first commercially available product capable of accurately measuring brain volume in neonates. The tool is integrated into the radiology PACS system, and volume measurements are available in <1 minute.

The current study had several strengths, such as the evaluation of both the image quality and the volumetric segmentation results of synthetic MR imaging. The multidelay, multiecho sequence was part of the standard MR imaging protocol for all neonates born very preterm, which makes it an excellent representation for this population. All MR images were obtained very close to the term-equivalent age (40 ± 1 week), which is considered optimal for the assessment of structural abnormalities that are related to long-term outcome.²⁵

The study also had some limitations. Because the children were scanned only once, it was not possible to evaluate the intramethod repeatability of volume segmentations. Second, although all the scans were carefully blinded for imaging method, the trained neuro-radiologists may have been able to discern the difference between synthetic and conventional images with the naked eye, and this may have introduced some bias. Third, even though MANTiS is state-of-the-art research software for neonatal brain segmentation, it cannot be regarded as a criterion standard like manual segmentation. In the present study, the correspondence between the 2 methods was excellent. The improved SyMRI segmentation algorithm performed well when segmenting the brain parenchyma and delineating the brain mask, but in contrast to MANTiS, it is still unable to differentiate between GM and WM in neonates.

CONCLUSIONS

The current study suggests that in neonates, synthetic MR imaging can complement or be an alternative to conventional T1WI and T2WI sequences because it had excellent image quality and diagnostic performance. Volumetric measurements can be obtained in <1 minute after processing and are comparable with measurements derived via current state-of-the-art research methods. Synthetic MR imaging may therefore facilitate the routine use of these biomarkers in daily clinical practice, bridging the existing gap between the past decade of research on volumetric measurements and long-term outcomes and clinical practice.

Disclosures: Tim Vanderhasselt—UNRELATED: Employment: Radiologist, Comments: Staff Member Radiology Department Universitair Ziekenhuis Brussels, Brussels, Belgium. Maarten Naeyaert—UNRELATED: Employment: paid PhD student at the Bio-Imaging lab, Universiteit Antwerpen, through the Interdisciplinary PhD grant BOF UA 2012. Nina Watté—UNRELATED: Employment: radiology resident. Jeroen

Dudink—UNRELATED: Grants/Grants Pending: European Union-Innovative Training Network grant, Comments: project called Infans. <https://www.tu-ilmenau.de/infans/>. * Hubert Raeymaekers—UNRELATED: Employment: Universitair Ziekenhuis Brussels. *Money paid to the institution.

REFERENCES

- Pascal A, Govaert P, Oostra A, et al. **Neurodevelopmental outcome in very preterm and very-low-birthweight infants born over the past decade: a meta-analytic review.** *Dev Med Child Neurol* 2018;60:342–55 CrossRef Medline
- Spittle A, Orton J, Anderson PJ, et al. **Early developmental intervention programmes provided post hospital discharge to prevent motor and cognitive impairment in preterm infants.** *Cochrane Database Syst Rev* 2015;24:CD005495 CrossRef Medline
- Woodward LJ, Anderson PJ, Austin NC, et al. **Neonatal MRI to predict neurodevelopmental outcomes in preterm infants.** *N Engl J Med* 2006;355:685–94 CrossRef Medline
- Alexander B, Murray AL, Loh WY, et al. **A new neonatal cortical and subcortical brain atlas: the Melbourne Children's Regional Infant Brain (M-CRIB) atlas.** *Neuroimage* 2017;147:841–51 CrossRef Medline
- Balakrishnan U, Amboiram P, Ninan B, et al. **MRI at term equivalent age for predicting long-term neurodevelopmental outcome in preterm infants: a cohort study.** *J Matern Fetal Neonatal Med* 2020;33:1867–73 CrossRef Medline
- Kidokoro H, Anderson PJ, Doyle LW, et al. **Brain injury and altered brain growth in preterm infants: predictors and prognosis.** *Pediatrics* 2014;134:e444–53 CrossRef Medline
- Keunen K, Išgum I, van Kooij BJ, et al. **Brain volumes at term-equivalent age in preterm infants: imaging biomarkers for neurodevelopmental outcome through early school age.** *J Pediatr* 2016;172:88–95 CrossRef Medline
- Gui L, Loukas S, Lazeyras F, et al. **Longitudinal study of neonatal brain tissue volumes in preterm infants and their ability to predict neurodevelopmental outcome.** *Neuroimage* 2019;185:728–41 CrossRef Medline
- Kelly CJ, Hughes EJ, Rutherford MA, et al. **Advances in neonatal MRI of the brain: from research to practice.** *Arch Dis Child Educ Pract Ed* 2019;104:106–10 CrossRef Medline
- Beare RJ, Chen J, Kelly CE, et al. **Neonatal brain tissue classification with morphological adaptation and unified segmentation.** *Front Neuroinform* 2016;10:12 CrossRef Medline
- Išgum I, Benders MJ, Avants B, et al. **Evaluation of automatic neonatal brain segmentation algorithms: the NeoBrainS12 challenge.** *Med Image Anal* 2015;20:135–51 CrossRef Medline
- Wartjes JB, Leinhard OD, West J, et al. **Rapid magnetic resonance quantification on the brain: optimization for clinical usage.** *Magn Reson Med* 2008;60:320–29 CrossRef Medline
- West J, Wartjes JB, Lundberg P. **Novel whole brain segmentation and volume estimation using quantitative MRI.** *Eur Radiol* 2012;22:998–1007 CrossRef
- Granberg T, Uppman M, Hashim F, et al. **Clinical feasibility of synthetic MRI in multiple sclerosis: a diagnostic and volumetric validation study.** *AJNR Am J Neuroradiol* 2016;37:1023–29 CrossRef Medline
- Tanenbaum LN, Tsiouris AJ, Johnson AN, et al. **Synthetic MRI for clinical neuroimaging: results of the magnetic resonance image compilation (MAGiC) prospective, multicenter, multireader trial.** *AJNR Am J Neuroradiol* 2017;38:1103–10 CrossRef Medline
- West J, Blystad I, Engström M, et al. **Application of quantitative MRI for brain tissue segmentation at 1.5 T and 3.0 T field strengths.** *PLoS One* 2013;8:e74795 CrossRef Medline
- Kim HG, Moon WJ, Han J, et al. **Quantification of myelin in children using multiparametric quantitative MRI: a pilot study.** *Neuroradiology* 2017;59:1043–51 CrossRef Medline
- McAllister A, Leach J, West H, et al. **Quantitative synthetic MRI in children: normative intracranial tissue segmentation values during development.** *AJNR Am J Neuroradiol* 2017;38:2364–72 CrossRef Medline
- Andica C, Hagiwara A, Nakazawa M, et al. **The advantage of synthetic MRI for the visualization of early white matter change in**

- an infant with Sturge-Weber syndrome. *Magn Reson Med Sci* 2016;15:347–48 CrossRef Medline
20. Betts AM, Leach JL, Jones BV, et al. **Brain imaging with synthetic MR in children: clinical quality assessment.** *Neuroradiology* 2016;58:1017–26 CrossRef Medline
21. West H, Leach JL, Jones BV, et al. **Clinical validation of synthetic brain MRI in children: initial experience.** *Neuroradiology* 2017;59:43–50 CrossRef Medline
22. Lee SM, Choi YH, Cheon JE, et al. **Image quality at synthetic brain magnetic resonance imaging in children.** *Pediatr Radiol* 2017;47:1638–47 CrossRef Medline
23. Dice LR. **Measures of the amount of ecologic association between species.** *Ecology* 1945;26:297–302 CrossRef
24. Naeyaert M, Vanderhasselt T, Warntjes M, et al. **Automatic brain segmentation in a neonatal population using a multi-delay multi-echo sequence.** In: *Proceedings of the Annual Meeting and Exhibition of the International Society for Magnetic Resonance in Medicine*, Paris France; June 16–21, 2018
25. Plaisier A, Govaert P, Lequin MH, et al. **Optimal timing of cerebral MRI in preterm infants to predict long-term neurodevelopmental outcome: a systematic review.** *AJNR Am J Neuroradiol* 2014;35:841–47 CrossRef Medline

Disrupted Functional and Structural Connectivity in Angelman Syndrome

H.M. Yoon, Y. Jo, W.H. Shim, J.S. Lee, T.S. Ko, J.H. Koo, and M.S. Yum



ABSTRACT

BACKGROUND AND PURPOSE: This work investigated alterations in functional connectivity (FC) and associated structures in patients with Angelman syndrome (AS) by using integrated quantitative imaging analysis and connectivity measures.

MATERIALS AND METHODS: We obtained 3T brain MR imaging, including resting-state functional MR imaging, diffusion tensor imaging, and 3D T1-weighted imaging from children with AS ($n = 14$) and age- and sex-matched controls ($n = 28$). The brains of patients with AS were analyzed by measuring FC, white matter microstructural analysis, cortical thickness, and brain volumes; these were compared with brains of controls.

RESULTS: Interregional FC analysis revealed significantly reduced intra- and interhemispheric FC, especially in the basal ganglia and thalamus, in patients with AS. Significant reductions in fractional anisotropy were found in the corpus callosum, cingulum, posterior limb of the internal capsules, and arcuate fasciculus in patients with AS. Quantitative structural analysis also showed gray matter volume loss of the basal ganglia and diffuse WM volume reduction in AS compared with the control group.

CONCLUSIONS: This integrated quantitative MR imaging analysis demonstrated poor functional and structural connectivity, as well as brain volume reduction, in children with AS, which may explain the motor and language dysfunction observed in this well-characterized neurobehavioral phenotype.

ABBREVIATIONS: AS = Angelman syndrome; BG = basal ganglia; FA = fractional anisotropy; FC = functional connectivity; FDR = false discovery rate; MI = primary motor area; MD = mean diffusivity; RD = radial diffusivity; rs-fMRI = resting-state functional MRI; SMA = supplementary motor area; TBSS = Tract-Based Spatial Statistics; UBE3A = ubiquitin protein ligase E3A; VBM = voxel-based morphometry; MNI = Montreal Neurological Institute; TCFE = threshold-free cluster enhancement

Angelman syndrome (AS) is a rare genetic disorder caused by the functional loss of ubiquitin protein ligase E3A (*UBE3A*), which arises from mutation of *UBE3A* or silencing of the maternal *UBE3A* allele. The distinctive clinical phenotypes of AS (ie, lack of expressive language development, frequent seizures, and gait abnormalities with ataxia) cause serious medical and social problems^{1,2}; moreover, approximately 10% of patients with AS never achieve self-ambulation.³ Despite their severe clinical features and well-known genetic causes, visual analysis of conventional brain MR imaging has revealed only nonspecific findings and minor abnormalities, such as mild cortical atrophy,

dysmyelination, focal white matter signal abnormalities, cerebral atrophy of frontotemporal areas, and callosal thinning.⁴⁻⁷

Recently, many functional MR imaging studies have investigated the abnormal neural connectivity in patients with speech disorders or ASD^{8,9} to identify the neural correlates of these functional deficits. However, there is no study to investigate an abnormal functional network in children with AS, which is a relatively homogeneous disease with a clear clinical and genetic delineation. Although WM pathway alteration and gray matter volume loss in patients with AS were previously reported by using diffusion tensor imaging and voxel-based morphometry

Received October 23, 2019; accepted after revision March 16, 2020.

From the Department of Radiology and Research Institute of Radiology (H.M.Y., W.H.S., J.S.L., J.H.K.), Asan Institute for Life Sciences (Y.J., W.H.S.), Asan Medical Center; and Department of Pediatrics (T.S.K., M.S.Y.), Asan Medical Center Children's Hospital, University of Ulsan College of Medicine, Seoul, Korea.

H.M. Yoon, Y. Jo, and W.H. Shim contributed equally to this study as the first author.

This research was supported by Basic Science Research Program through the National Research Foundation of Korea (NRF-2017RIDIA1B03030713) and Asan Institute for Life Sciences, Asan Medical Center (2018-551).

Please address correspondence to Mi-Sun Yum, Department of Pediatrics, Asan Medical Center Children's Hospital, University of Ulsan College of Medicine, 88 Olympic-ro 43-gil, Sonpa-gu, Seoul, Republic of Korea; e-mail: misun.yum@gmail.com

Indicates open access to non-subscribers at www.ajnr.org

Indicates article with supplemental on-line table.

Indicates article with supplemental on-line photos.

<http://dx.doi.org/10.3174/ajnr.A6531>

(VBM),¹⁰⁻¹³ it remains unclear whether alterations in functional connectivity (FC) are related to structural deformation in AS.

Based on previous studies,^{2,5} we hypothesized that the structural and FC of the fronto-striatal circuits, including language and sensorimotor domains, would be seriously compromised in patients with AS. Thus, we aimed to investigate the abnormal functional network in children with AS, which is associated with severe speech and motor deficits and to validate the key anatomic structures associated with functional loss of *UBE3A* by using multimodal quantitative MR imaging analysis.

METHODS

Participants

We enrolled patients who were clinically and genetically diagnosed with AS between July and November 2016. Eligibility criteria included (1) patients who were genetically confirmed with AS, (2) patients whose ages were less than 18 years old, and (3) patients who had no contraindications to brain MR imaging. Because most patients lack expressive language and have severe intellectual disability lower than 2 years of mental age, it was difficult to assess the patients' developmental status by using a standardized mean. The patients' motor and language functions were evaluated by an experienced pediatric neurologist (M.S.Y. with 15 years of clinical experience in pediatric neurology) at the time of their brain MR imaging. Patients were classified into 2 groups according to the severity of their verbal and motor functional status: 1) patients with no verbal output versus patients who can speak at least 1 word and 2) patients who are unable to walk unassisted versus patients who can walk unassisted.

Age- and sex-matched control subjects, with a patient to control ratio of 1:2, were retrieved from the retrospective database in our institution (Asan Medical Center) from May 2014 to July 2017. The institutional review board allowed the researchers to conduct the analysis of the MR data from this database without subject consent because the data were subject to anonymization. All patient data were anonymized when received before analysis. Children who were included in the control group were required to 1) have no alleged neurologic or psychiatric deficits, 2) be prescribed no regular medication, 3) have no abnormality on brain MR imaging, and 4) show clinically normal development. In total, 28 children (male:female = 14:14) were included, with a mean age of 7.7 ± 4.2 years (range, 1-16 years). They underwent brain MR imaging due to headache ($n = 15$), provoked seizures ($n = 7$), syncope ($n = 3$), dizziness ($n = 1$), tic disorder ($n = 1$), and minor head trauma ($n = 1$).

Written informed consent was obtained from the legal guardians of all patients. This study was performed in accordance with the ethical standards of the Declaration of Helsinki and was approved by the institutional review board of the Asan Medical Center (2016-0279, Seoul, Korea).

Imaging Protocol

All participants successfully underwent brain MR imaging by using a 3T MR imaging scanner (Achieva; Philips Healthcare, Best, The Netherlands) with an 8-channel, sensitivity-encoding head coil. 3D T1-weighted imaging sequences were acquired with the following image parameters: TR/TE, 9.9/4.6 ms; flip angle = 8°;

FOV = 224 mm, matrix = 224 × 224 mm, section thickness = 1 mm with no gap; and scan time, 4 min, 41 seconds. DTI was performed by using single-shot echo-planar imaging with the following parameters: TR/TE, 5615/70 ms; section thickness, 3 mm; diffusion directions, 32; b-value, 1000 seconds/mm²; number of excitations, 1; matrix, 112 × 112; FOV, 224 mm; acquired voxel size, 2 × 2 × 3 mm; and scan time, 3 min, 17 seconds. Blood oxygen level-dependent contrast functional images at rest (resting-state functional MR imaging [rs-fMRI]) were acquired by using single-shot gradient-echo/EPI with the following parameters: TR/TE, 3000/30 ms; flip angle, 90°; FOV, 224 mm; matrix, 112 × 112; section thickness, 6 mm with no gap; number of slices, 17; number of dynamics, 150; and acquisition time, 7 min, 42 seconds. Sedation during MR imaging examination was performed by trained anesthesiologists in accordance with our standard institutional protocol. All participants in the AS group were sedated by using intravenous administration of propofol, and children in the control group were sedated by using intravenous administration of propofol or oral chloral hydrate. Ten children in the control group did not require sedation during MR imaging examination.

Seed-Based Resting-State Functional MR Analysis

Before statistical analysis, rs-fMRI data were preprocessed by using the Analysis of Functional Neuro Images (AFNI; <http://afni.nimh.nih.gov/afni>) basic ANATICOR program to remove artifacts and normalize the image data.¹⁴ In brief, we removed the first 3 EPIs to control for error, aligned the EPIs, corrected for section-time acquisition, realigned for motion correction, co-registered the EPI to anatomical T1WI, and bandpass filtered from 0.01 to 0.1 Hz.

Anatomic segmentations of 42 subjects were created by using FreeSurfer and were used to mask the following regions for FC analysis: thalami, basal ganglia (BG), primary motor area (M1), supplementary motor area (SMA), sensory area, Broca area (Brodmann area 44 and 45), and Wernicke area (superior temporal gyrus) in the left and right hemispheres. Previous studies with patients with AS^{2,5,11} indicated severe speech impairment and difficulty in motor controls as well as volume reduction of the BG. The associated anatomic areas were selected as seed regions based on these clinical phenotypes of patients with AS.

Pearson correlation coefficients were calculated by using the Matlab (Matlab 8.2.0.701; MathWorks, Natick, Massachusetts) corr function between the hypothesis-derived, selectively masked regions to indicate the strength of FC between the 2 regions, producing a 14-by-14 matrix for each subject. Individual subjects' correlation matrices were then grouped into control and patient groups, and the patient group's FC was compared with that of the control group by using 2-sample t-tests after testing for equal variance (false discovery rate [FDR] corrected; $P < .05$).

Tract-Based Spatial Statistics

The DTI original time-series data were corrected for head movement and eddy current distortions by using the "eddy_correct" function within the FMRIB Diffusion Toolbox (<http://fsl.fmrib.ox.ac.uk/fsl/fslwiki/FDT>). The FMRIB DTIFit module (http://fsl.fmrib.ox.ac.uk/fsl/fsl-4.1.9/fdt/fdt_dtifit.html) was used to independently fit the diffusion tensors to each voxel, creating an output of voxelwise maps of fractional anisotropy (FA) for each

Table 1: Clinical characteristics of children with Angelman syndrome in this study

Characteristic	Angelman Syndrome (n = 14)	
Age (months)	95.9 ± 57.8 (range, 3–18 years)	
Sex (male:female)	7:7	
Genetic mutation	UBE3A (15q11-q13 deletions)	13
	Paternal UPD	1
Seizure	10 (71.4%)	
Use of at least 1 meaningful word	5 (35.7%)	
Walking alone	11 (78.6%)	
Ataxia or tremor	10 (71.4%)	
Strabismus	5 (35.7%)	
Ataxia and unable to walk alone	3 (21.4%)	
Ataxia but walking alone	7 (50.0%)	
No ataxia (walking alone)	4 (28.6%)	

Note: UPD indicates uniparental disomy.

subject. To limit the result to be strictly pertinent to the subject's brain, we obtained a binary brain mask from each participant's B0 image with the FSL Brain Extraction Tool's (<http://fsl.fmrib.ox.ac.uk/fsl/fslwiki/BET>) bet2 function and applied the brain mask to mask-out structures external to the subject's FA map.

Diffusion MR imaging data were analyzed by using FMRIB's Diffusion Toolbox Tract-Based Spatial Statistics (TBSS; v1.2; <https://fsl.fmrib.ox.ac.uk/fsl/fslwiki/TBSS>) module, which used the FA, mean diffusivity (MD), and radial diffusivity (RD) maps of each participant.¹⁵ All FA images were preprocessed using TBSS's `tbss_1_preproc` command to further clean the FA images. Next, all FA images were registered to the MNI space by using nonlinear registration (`tbss_2_reg`), and the group mean FA image and WM skeleton were created by averaging all FA images (`tbss_3_postreg -S`), which represents the center of all WM tracts common to the group. For each individual, the local FA maxima were found along the perpendicular direction of the mean FA image and then projected onto the mean FA skeleton using a FA threshold of 0.2 (`tbss_4_prestats 0.2`). With the randomization function in the FMRIB Diffusion Toolbox, the skeletonized FA images were subjected to voxelwise, cross-subject statistical analysis. MD and RD maps were measured by running the FSL tool `tbssds_non_FA` script. Here, the mean skeletons of the control and AS groups were compared using voxelwise 2-sample unpaired t-tests with nonparametric permutation with threshold-free cluster enhancement (TFCE) corrections by using the T2 option and cluster-based thresholding at 0.95 ($P < .05$) in the randomize function (5000 permutations/design, TFCE-corrected $P < .05$ for significance).

Cortical Thickness and Volume Measurements

Entire cortex analyses were computed to explore local cortical thicknesses and cortical volumes in the AS and control groups. Statistical maps were generated with the Query, Design, Estimate, Contrast interface within FreeSurfer (version 5.3.1) used to perform group averaging and inference on cortical morphometric data. For each hemisphere, a general linear model was computed vertex by vertex for analysis of cortical thickness and cortical volume, respectively, and for regression to exclude the covariate of age. Cortical maps were smoothed with a 10-mm full width at half maximum Gaussian filter and multiple comparisons were corrected by FDR with a P value set at $<.05$. Comparisons of

segmented brain volumes between subgroups in the AS group were analyzed using Mann-Whitney U tests in commercial statistical software (SPSS, version 21; SPSS; IBM, Armonk, New York). A P value less than 0.05 was considered statistically significant.

Voxel-Based Morphometry

VBM analysis in SPM8 software (<http://www.fil.ion.ucl.ac.uk/spm/>) was performed with the VBM technique by adhering to the standard VBM processing routine. Images of each subject were normalized and regis-

tered to MNI space; the resulting images were modulated (without the affine component) and smoothed with a full width at half maximum of 10 mm. Measurements for the transformed GM and WM images were then clustered with a threshold over 20 voxels. The final processed images were used for statistical inference; age as a covariate measure was excluded by regression with the GLM. Statistical nonparametric mapping with 5000 permutations, without variance smoothing, was used to compare voxelwise differences in GM volumes between the AS and control groups. The level of significance in SPM was considered a P value $<.001$, and multiple comparisons were corrected with family-wise error rate.

RESULTS

Patient Characteristics

A total of 14 patients (male:female = 7:7) were enrolled in this study. The mean age of the patient group was 7.6 ± 4.7 years (range, 3–18 years). All patients were genetically confirmed with AS; microdeletion within chromosome 15q11-q13 in 13 patients and paternal uniparental disomy in 1 patient. Most patients initially presented with developmental delay and hypotonia. Clinical phenotypes of the enrolled patients are shown in Table 1. Among 10 patients who had seizures, 2 had histories of myoclonic status in nonprogressive encephalopathies or intractable epilepsy.

Interregional Functional Connectivity between Language, Motor, and Subcortical Areas

Fourteen seeds were placed in bilateral thalami, BG, M1, SMA, sensory, Broca, and Wernicke areas. General reduction of interregional FC was found in the AS group compared with the control group (Fig 1). In terms of interhemispheric FC, interregional FC between the left thalamus and all seeds of the right hemisphere, as well as FC between the left BG and all seeds of right hemisphere except for the right sensory area, was significantly reduced in patients with AS compared with the control group. In addition, significant reduction of interhemispheric FC between the right thalamus and left M1, sensory, and Broca areas and of FC between the right BG and left Broca area were observed in patients with AS. Regarding intrahemispheric FC of the right hemisphere, interregional FC of thalamocortical networks (thalamus and M1, Broca, Wernicke), BG and cortical networks (M1, SMA, Broca,

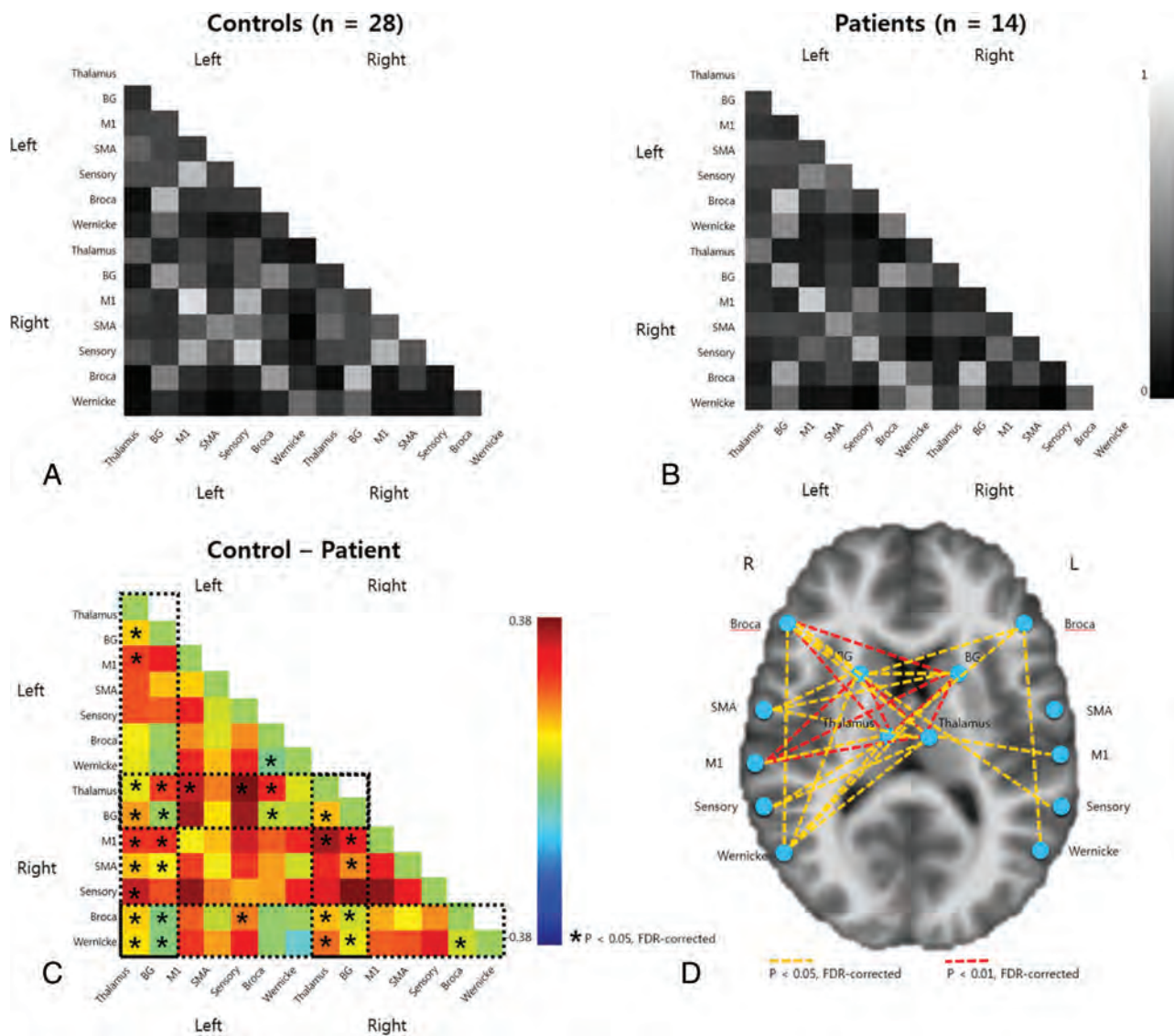


FIG 1. Correlation matrices representing functional connectivity between seed regions; (A) control group, (B) AS group, (C) subtraction map of A – B with asterisks identifying significantly different connections between A and B (FDR-corrected, $P < .05$), and (D) significantly reduced functional connections marked as an asterisk placed on an MNI template for visualization (blue circle: seed region; yellow dotted line: FDR-corrected, $P < .05$; red dotted line: FDR-corrected, $P < .01$).

Wernicke), and the language network (Broca and Wernicke areas) was significantly decreased in patients with AS. Among left intrahemispheric interregional FC, there were significant FC reductions between thalamus and BG, between thalamus and M1, and between Broca and Wernicke areas in patients with AS (all $P < .05$, FDR-corrected).

To test the effect of sedation during rs-fMRI, the Pearson correlation coefficients between patients with AS (all sedated) and sedated controls patients and the Pearson's correlation coefficients between sedated controls and nonsedated controls were compared (On-line Fig 1). Using unpaired 2-sample t-tests, we found no significant FC differences between the sedated and nonsedated controls, and the FC reduction in patients with AS showed similar results when compared with all controls (age and sex matched; $n = 28$; Fig 1; FDR-corrected, $P < .05$) or sedated controls (younger, age 3–13 years; sex matched; $n = 10$) (On-line Fig 1; FDR-corrected, $P < .05$).

Tract-Based Spatial Statistics

TBSS showed a significant FA decrease in the medial superior corpus callosum, cingulum, bilateral posterior limb of the internal capsules, corticospinal tract, cerebral peduncle, and arcuate fasciculus in the patient group compared with the control group (threshold $P < .005$ TFCE corrected, obtained using the FMRIB Software Library tool `tbss_fill`; Fig 2). The anatomic locales with the reduced FA were identified by using AFNI's `whereami` function with matching MNI coordinates, of which the MNI atlas was used for image registration. MD and RD were also analyzed in the bilateral anterior corpus callosum, posterior limb of the internal capsules, and arcuate fasciculus and posterior corpus callosum (On-line Table). All but the mean MD in bilateral posterior limb of internal capsule and posterior corpus callosum showed significant increases in the AS group.

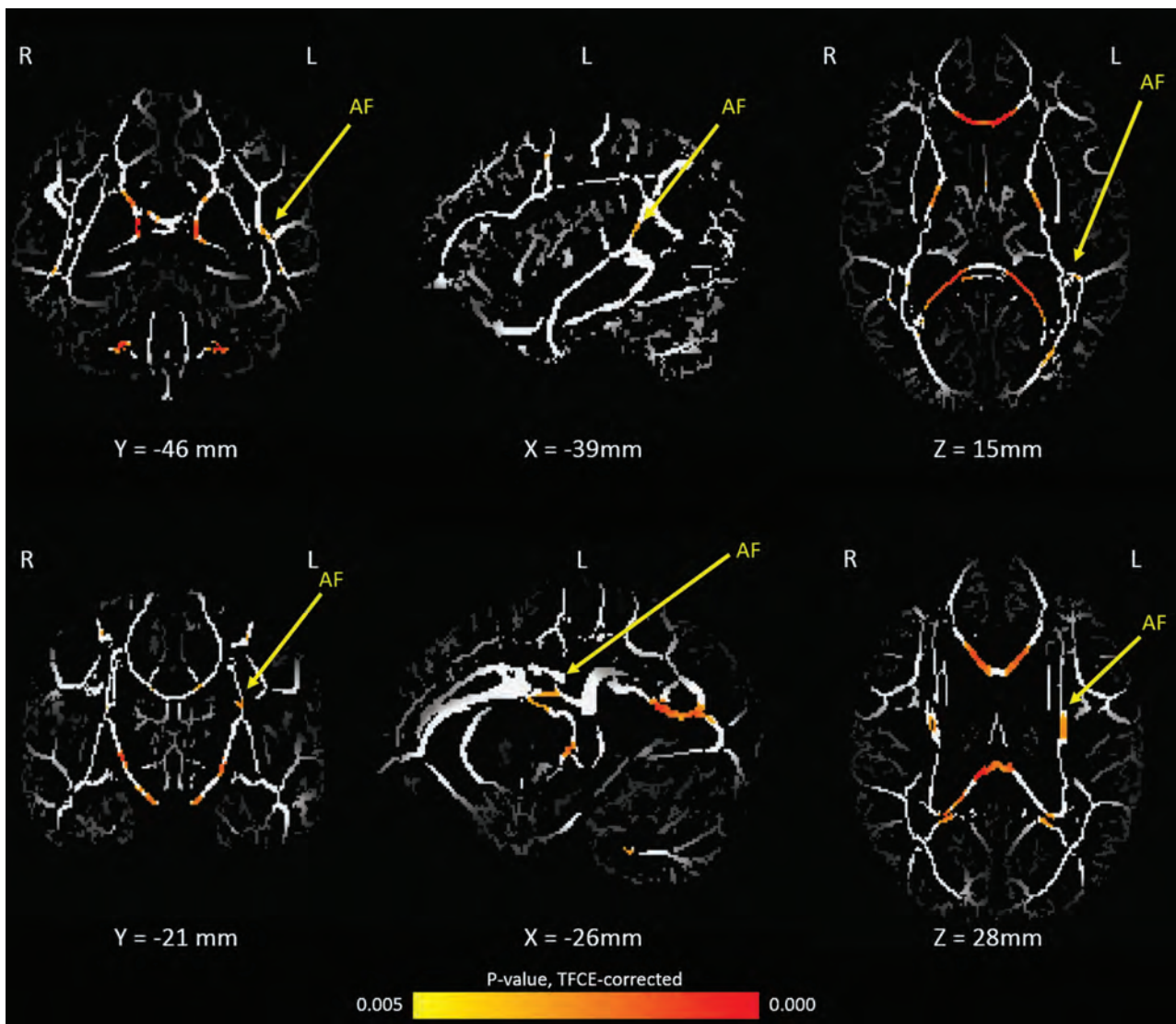


FIG 2. Regions with reduced FA in patients with AS compared with age-matched controls, determined by whole brain TBSS. The results show regions that are significantly different with the threshold of TFCE corrected, $P < .005$. The FA values of corpus callosum and arcuate fasciculus (yellow arrows) are significantly reduced in patients with AS.

Table 2: Cortical thicknesses of children with Angelman syndrome compared with the control group

Area Label	Brodmann Area	Size (mm ²)	Stereotactic Coordinates (Talairach Space)			T (-Log ₁₀ P)
			x	y	z	
Left hemisphere						
Transverse temporal	22	154.89	-51.1	-16.4	4.4	-4.9827
Postcentral	4	77.17	-60.1	-6.7	10.8	-4.7438
Superior temporal	21	86.13	-50.7	-14.6	-11.9	-4.2409
Right hemisphere						
Superior temporal	10	39.51	55.8	2.8	-12.3	-4.1946
Postcentral	1	9.20	63.6	-8.9	12.6	-3.8439
Supramarginal	40	37.79	48.0	-23.9	20.5	-3.8319
Superior frontal	8	13.04	11.3	21.6	37.7	-3.8079

Cortical Thickness and Volume Alteration

Altered Cortical Thickness in Patients with Angelman Syndrome. Compared with the control group, the AS group showed significantly smaller cortical thickness in bilateral superior temporal,

bilateral postcentral, left transverse temporal, right supramarginal, and right superior frontal gyrus when using Mann-Whitney U tests (Table 2; FDR-corrected, $P < .05$).

Altered Brain Volume in Patients with Angelman Syndrome. In patients with AS, the global GM volume (mean \pm SD of patients with AS versus control group, $600,625.8 \pm 62,103.7$ mm³ versus $723,046.5 \pm 53,590.5$ mm³; t , -4.83; df , 40; $P < .0001$), cerebral WM volume ($306,694.5 \pm 45,254.5$ mm³ versus $390,684.4 \pm 60,945.5$ mm³; t ,

-4.05; df , 40; $P < .0001$), brain segmentation volume ($941,639.3 \pm 94,951.1$ mm³ versus $1,155,856.0 \pm 103,920.5$ mm³; t , -5.08; df , 40; $P < .0001$), total intracranial volume ($1,212,398.8 \pm 132,858.0$

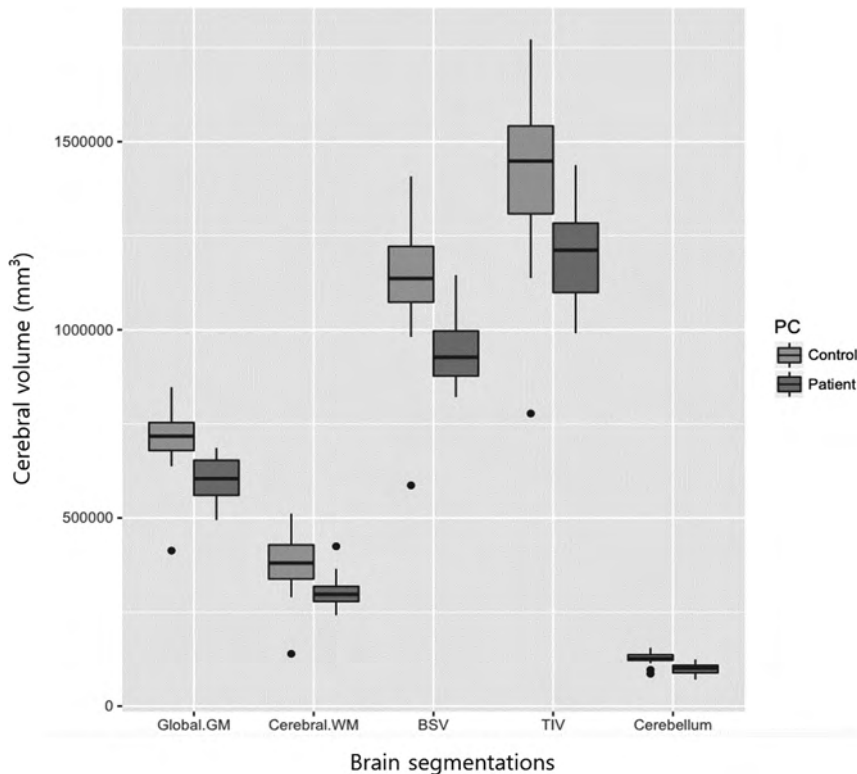


FIG 3. Boxplot for segmented volume (mm^3) of the global GM, cerebral WM, brain segmentation volume (BSV), total intracranial volume (TIV), and cerebellum. The AS group (*dark gray box*) shows significantly reduced volume of the global GM, cerebral WM, BSV, TIV, and cerebellum compared with the age-matched control group (*light gray box*). y-axis = mm^3 ; black dots = outliers.

mm^3 versus $1,442,983.0 \pm 174,949.8 \text{ mm}^3$; $t, -3.90$; $df, 40$; $P < .0001$) and cerebellar volume ($99,621.8 \pm 15,085.7 \text{ mm}^3$ versus $127,993.0 \pm 12806.0 \text{ mm}^3$; $t, -5.69$; $df, 40$; $P < .0001$) decreased significantly compared with those of the control group. No significant difference was found in the global CSF volume between the 2 groups ($14,668.07 \pm 5,554.20 \text{ mm}^3$ versus $15,084.69 \pm 5,661.31 \text{ mm}^3$; $t, -0.22$; $df, 40$; $P = .821$) (Fig 3). In subgroup analysis, volumes of cerebral WM and corpus callosum were smaller in patients with no verbal output compared with patients who can speak at least 1 word (Fig 4, upper 5 boxplots). In addition, patients who are unable to walk unassisted showed smaller volumes of total GM, cortex, central portion of corpus callosum, right cerebellar cortex, and left amygdala compared with patients who can walk unassisted (Fig 4, lower five boxplots).

Voxel-Based Morphometry

Gray Matter Volume Loss in Patients with Angelman Syndrome. Regional GM volume loss was found in the AS group compared with the control group (Table 3, On-line Fig 1). Using statistical nonparametric mapping with age regressed out as a covariate measure using the general linear model (5000 permutations; $P < .001$ corrected for family-wise error rate), we found regional volumes of the bilateral putamen, globus pallidus, caudate nucleus, rectus gyrus, left hippocampus, and left cerebellar cortex were significantly reduced in the AS group compared with the control group.

White Matter Volume Loss in Patients with Angelman Syndrome. In the AS cohort, we found significant WM volume loss in the pons, anterior commissure, splenium of the corpus callosum, bilateral subinsular WM, right frontal subcortical WM, and bilateral parietal periventricular WM (On-line Fig 2) compared with the control group. These results were also found by using statistical nonparametric mapping with 5000 permutations and age excluded as a covariate measure by using the general linear model ($P < .001$, corrected for family-wise error rate).

DISCUSSION

This study used a multimodal imaging approach to study patients with AS with severe speech impairment and motor deficits. With combined use of rs-fMRI and quantitative structural imaging analysis, we attempted to define functional brain network changes in AS and compare these functional changes with the structural changes observed in these children. Children with AS exhibited significantly decreased FC in multiple intra- and interhemispheric networks; this

altered FC substantially correlated with specific volume deficits in patients with AS.

In rs-fMRI analysis, children with AS showed a general decrease in interregional FC when we focused the seeds in areas associated with primary motor and language systems. Especially, intra- and interhemispheric FC associated with the thalamus and BG of patient with AS were significantly decreased compared with controls. Considering the role of the BG and the thalamus network in motor control and balance,^{16,17} altered FC mainly involving thalamus and BG might be related to the impaired motor function in patients with AS. Furthermore, BG volume was smaller in the AS group than the control group in VBM analysis. In a murine AS model, *ube3a* reinstatement could alleviate the AS-relevant phenotypes.¹⁸ However, cerebellum-specific reinstatement of *ube3a* in AS mice alone could not rescue the locomotor deficits, which suggests the role of other structures, such as the BG, in locomotor dysfunctions of AS.¹⁹

Regarding the language network, interregional FC between the Broca and Wernicke areas in each hemisphere was significantly reduced in the AS group. In TBSS analysis, the AS group also showed significant reductions in FA in the arcuate fasciculus, which connects the Broca and Wernicke areas; this was consistent with previous reports.¹² This association between functional and structural alteration in the language network may be associated with impairment of language function in patients with AS. In addition, the language network demonstrated decreased interregional FC with the thalamus and BG, intra- and

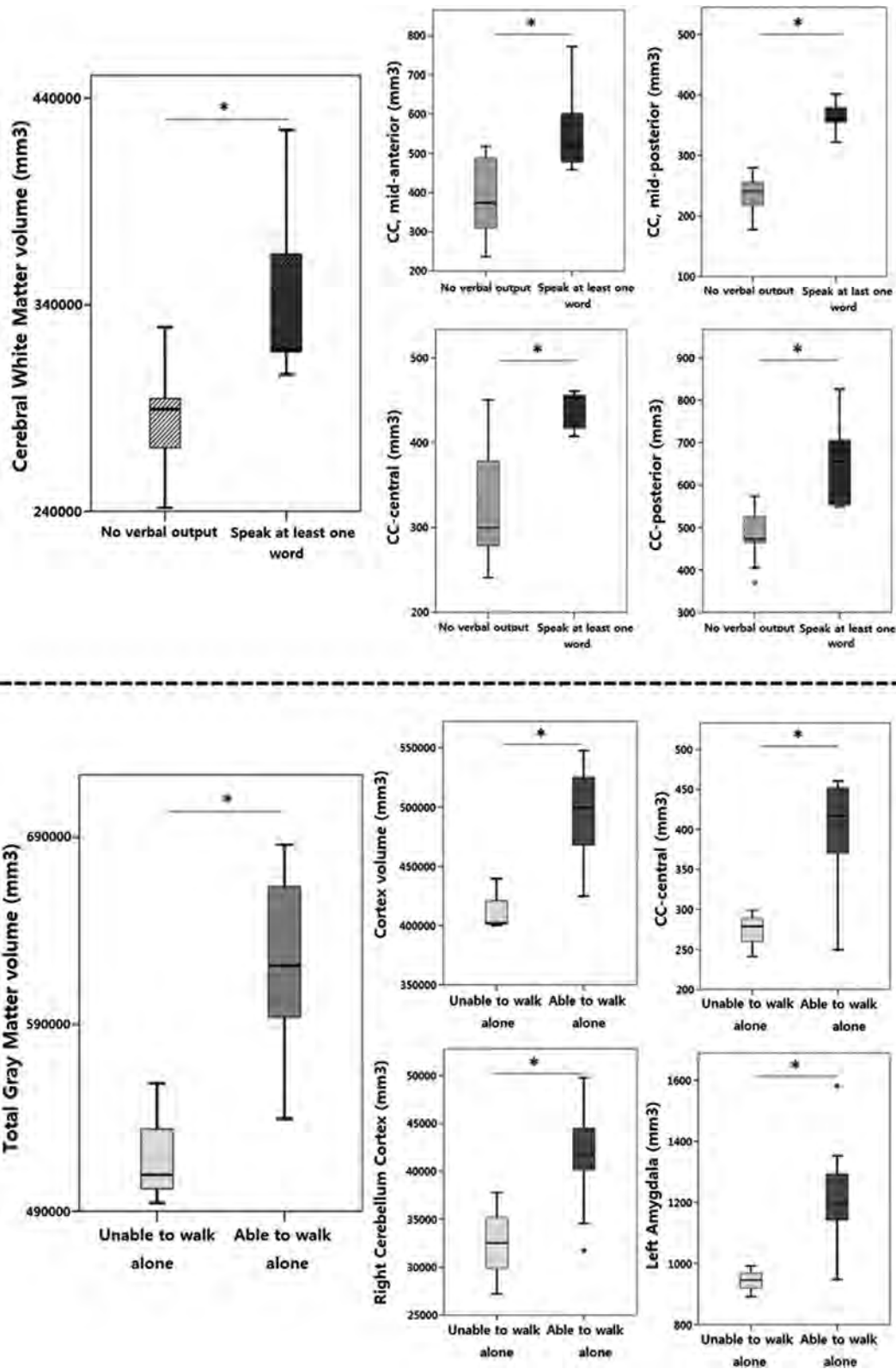


FIG 4. Upper 5 plots: boxplots for segmented volume (mm^3) of the cerebral white matter and segments of the corpus callosum. Patients with no verbal output (gray box) show significantly reduced volume of aforementioned areas compared with patients who can speak at least a word (black box). Lower 5 plots: boxplots for segmented volume (mm^3) of the total gray matter, cortex, corpus callosum (central), right cerebellum cortex, and left amygdala. Patients who were unable to walk alone (light gray box) have significantly reduced volume of aforementioned areas compared with patients who can walk alone (gray box). Asterisks indicate significant difference ($P < .05$). y-axis = mm^3 .

Table 3: Regional gray matter volume reductions in patients with Angelman syndrome compared with controls based on voxel-based morphometry analysis^a

Anatomic Region	Number of Voxels in Each Cluster	Peak Z Score	Coordinates of Voxel of Maximal Statistical Significance (MNI Space)
Left putamen, pallidum, caudate nucleus	18,317	7.73	-21, 2, 12
Right caudate nucleus		7.68	9, 11, 15
Right putamen, pallidum		7.66	21, 5, 12
Right rectal gyrus	469	6.16	9, 34, -26
Right superior orbital gyrus			
Left rectal gyrus			
Left hippocampus	159	5.96	-20, -34, -0
Left thalamus			
Left parahippocampal gyrus			
Left lingual gyrus			
Left cerebellum (Crus 1, 2)	156	5.95	-51, -48, -36
Left cerebellum (VII, VIII, crus 2)	47	5.67	-46, -43, -50
Left rectal gyrus	28	5.58	-6, 36, -30
Right rectal gyrus			
Left superior orbital gyrus			

^aWhole-brain analysis (FWE-corrected at $P < .001$; cluster threshold >20 voxels).

interhemispherically; these changes were more prominent in the right hemisphere. The BG, including dorsal striatum, is involved in language processing²⁰; however, the role of the thalamus in language function remains controversial.²¹ Altered FC in the language network and BG or thalamus may be associated with impairment of language function in patients with AS.

TBSS analysis also showed significant overall reductions in FA in the corpus callosum, arcuate fasciculus, and corticospinal tracts, as in a previous report.¹² Additional analysis of other metrics of DTI showed significant increased MD and RD in these areas (On-line Table). Furthermore, consistent with broad structural connectivity abnormalities of patients with AS, VBM analysis in this study showed diffuse WM volume reduction in patients with AS, including the pons, anterior commissure, splenium of the corpus callosum, bilateral subinsular, and parietal periventricular areas. These WM volume reductions, as well as the reduced WM microstructural connectivity, can mirror behavioral phenotypes in AS. Similarly, research involving the murine model of AS showed that dysfunctional *ube3a* causes alteration in the intrinsic properties of membranes and axons²² and the disproportional loss of WM volumes and lowered integrity, as well as smaller axon caliber.²³

Together with this global reduction of functional and structural connectivity, as well as WM volume reduction in AS, VBM analysis also showed consistent cerebral and cerebellar volume reductions in patients with AS. In the human cortex, *UBE3A* is expressed in both glutamatergic, GABAergic neurons and glial cells,²⁴ which suggests that *UBE3A* dysregulation might affect the whole neuronal circuit. Considering the symptoms of AS (ie, severe speech impairment, unique puppet-like movement, autistic features), the global reduction of brain volume as well as the abnormal FC is deemed reasonable. When we divided the patients into subgroups according to motor and language function to test whether anatomic change can be used as an imaging biomarker for these neurobehaviors, patients with poor language or motor function showed smaller cortical WM or GM volumes. These subgroups consisted of a smaller

number of subjects, and further investigation is required. However, these findings provide further evidence that quantitative brain MR imaging may demonstrate functional deficits in AS.

When compared with the age- and sex-matched children with normal development, patients with AS exhibited cortical thinning of the superior temporal and transverse temporal gyri, the area of primary auditory cortex involved in auditory processing, including language sense and social cognition.²⁵ The thinning of the right superior frontal gyrus, which mediates the inhibitory control of impulsive behavior,²⁶ and the supramarginal gyrus, a part of the somatosensory association cortex with a mirror neuron system,^{27,28} were also observed by cortical thickness analysis.

Nonetheless, this study has several limitations. First, the number of patients was small. This syndrome is quite rare; furthermore, recruitment of patients for MR imaging examination is difficult because many parents or guardians of the patients tend to be reluctant to make their children undergo MR imaging because of sleep and behavioral problems, which are closely associated with each other. After sedation, sleep disturbances in patients with AS can be exacerbated by sleep cycle changes, which can lead to behavioral deterioration. Second, different sedation protocols were applied in the control and AS groups. It has been shown that the FC of several brain networks can be influenced by sedative drugs used for MR imaging.^{29,30} Sedation was inevitable for all patients with AS because of severe communication difficulties; older children in the control group did not need sedation during MR imaging. However, it is unethical to make normal children undergo brain MR imaging under sedation. These heterogeneities in sedation protocol may affect our results, especially rs-fMRI data. Although the pattern of FC difference was similar when we excluded the nonsedated patients, the effect of age, sex, and sedation should be carefully considered. Last, the control group in this study had minor neurologic symptoms, such as headache or febrile seizures, which might also affect our results. Further studies with a homogeneous sedation protocol and control group without any neurologic symptoms are required to confirm our preliminary results.

CONCLUSIONS

We found reduced brain connectivity with associated anatomic structural changes in children with AS. Functional and structural underconnectivity, as well as diffuse brain volume reduction, shown by MR imaging may provide striking imaging evidence for the impairment of motor and speech ability seen in individuals with AS.

ACKNOWLEDGMENTS

We thank all of the patients and families involved in this study and the biomedical computing core facility at the ConveRgence

mEDiCine research cenTer (CREDIT), Asan Medical Center for support and instrumentation.

Disclosures: Woo-Hyun Shim—*RELATED: Grant:* This research was supported by Basic Science Research Foundation of Korea (NRF) funded by the Ministry of Education (2017RID1A1B0303713). Mi-Sun Yum—*RELATED: Grant:* This research was supported by Asan Institute for Life Sciences, Asan Medical Center (2018-551). *Money paid to institution.

REFERENCES

1. Lalonde M, Calciano MA. **Molecular epigenetics of Angelman syndrome.** *Cell Mol Life Sci* 2007;64:947–60 CrossRef
2. Williams CA. **The behavioral phenotype of the Angelman syndrome.** *Am J Med Genet C Genet* 2010;154C:432–37 CrossRef
3. Buiting K, Williams C, Horsthemke B. **Angelman syndrome—insights into a rare neurogenetic disorder.** *Nat Rev Neurol* 2016;12:584–93 CrossRef
4. Clayton-Smith J. **Clinical research on Angelman syndrome in the United Kingdom: observations on 82 affected individuals.** *Am J Med Genet* 1993;46:12–15 CrossRef
5. Leyser M, Gonsalvez MCD, Vianna PES, et al. **Scrutinizing brain magnetic resonance imaging patterns in Angelman syndrome.** *Neurol India* 2016;64:228–32 CrossRef
6. Castro-Gago M, Gomez-Lado C, Eiris-Punal J, et al. **Abnormal myelination in Angelman syndrome.** *Eur J Paediatr Neurol* 2010;14:292 CrossRef
7. Harting I, Seitz A, Rating D, et al. **Abnormal myelination in Angelman syndrome.** *Eur J Paediatr Neurol* 2009;13:271–76 CrossRef
8. Rashid B, Blanken LME, Muetzel RL, et al. **Connectivity dynamics in typical development and its relationship to autistic traits and autism spectrum disorder.** *Hum Brain Mapp* 2018;39:3127–42 CrossRef
9. Morgan A, Bonthron A, Liegeois FJ. **Brain basis of childhood speech and language disorders: are we closer to clinically meaningful MRI markers?** *Curr Opin Pediatr* 2016;28:725–30 CrossRef
10. Peters SU, Kaufmann WE, Bacino CA, et al. **Alterations in white matter pathways in Angelman syndrome.** *Dev Med Child Neurol* 2011;53:361–67 CrossRef
11. Aghakhanyan G, Bonanni P, Randazzo G, et al. **From cortical and subcortical grey matter abnormalities to neurobehavioral phenotype of Angelman syndrome: a voxel-based morphometry study.** *PLoS One* 2016;11:e0162817 CrossRef
12. Tiwari VN, Jeong JW, Wilson BJ, et al. **Relationship between aberrant brain connectivity and clinical features in Angelman syndrome: a new method using tract based spatial statistics of DTI color-coded orientation maps.** *Neuroimage* 2012;59:349–55 CrossRef
13. Wilson BJ, Sundaram SK, Huq AH, et al. **Abnormal language pathway in children with Angelman syndrome.** *Pediatr Neurol* 2011;44:350–56 CrossRef
14. Jo HJ, Saad ZS, Simmons WK, et al. **Mapping sources of correlation in resting state FMRI, with artifact detection and removal.** *Neuroimage* 2010;52:571–82 CrossRef
15. Smith SM, Jenkinson M, Johansen-Berg H, et al. **Tract-based spatial statistics: voxelwise analysis of multi-subject diffusion data.** *Neuroimage* 2006;31:1487–505 CrossRef
16. Mestres-Misse A, Turner R, Friederici AD. **An anterior-posterior gradient of cognitive control within the dorsomedial striatum.** *Neuroimage* 2012;62:41–47 CrossRef
17. Patel N, Jankovic J, Hallett M. **Sensory aspects of movement disorders.** *Lancet Neurol* 2014;13:100–12 CrossRef
18. Silva-Santos S, van Woerden GM, Bruinsma CF, et al. **Ube3a reinstatement identifies distinct developmental windows in a murine Angelman syndrome model.** *J Clin Invest* 2015;125:2069–76 CrossRef
19. Bruinsma CF, Schonewille M, Gao Z, et al. **Dissociation of locomotor and cerebellar deficits in a murine Angelman syndrome model.** *J Clin Invest* 2015;125:4305–15 CrossRef
20. Klostermann F, Krugel LK, Ehlen F. **Functional roles of the thalamus for language capacities.** *Front Syst Neurosci* 2013;7:32 CrossRef
21. Llano DA. **Functional imaging of the thalamus in language.** *Brain Lang* 2013;126:62–72 CrossRef
22. Kaphzan H, Buffington SA, Jung JI, et al. **Alterations in intrinsic membrane properties and the axon initial segment in a mouse model of Angelman syndrome.** *J Neurosci* 2011;31:17637–48 CrossRef
23. Judson MC, Burette AC, Thaxton CL, et al. **Decreased axon caliber underlies loss of fiber tract integrity, disproportional reductions in white matter volume, and microcephaly in Angelman syndrome model mice.** *J Neurosci* 2017;37:7347–61 CrossRef
24. Burette AC, Judson MC, Li AN, et al. **Subcellular organization of UBE3A in human cerebral cortex.** *Mol Autism* 2018;9:54 CrossRef
25. Bigler ED, Mortensen S, Neeley ES, et al. **Superior temporal gyrus, language function, and autism.** *Dev Neuropsychol* 2007;31:217–38 CrossRef
26. Hu S, Ide JS, Zhang S, et al. **The right superior frontal gyrus and individual variation in proactive control of impulsive response.** *J Neurosci* 2016;36:12688–96 CrossRef
27. Woo YJ, Wang T, Guadalupe T, et al. **A common cyfip1 variant at the 15q11.2 disease locus is associated with structural variation at the language-related left supramarginal gyrus.** *PLoS One* 2016;11:e0158036 CrossRef
28. Hoffmann F, Koehne S, Steinbeis N, et al. **Preserved self-other distinction during empathy in autism is linked to network integrity of right supramarginal gyrus.** *J Autism Dev Disord* 2016;46:637–48 CrossRef
29. Liu X, Lauer KK, Ward BD, et al. **Differential effects of deep sedation with propofol on the specific and nonspecific thalamocortical systems.** *Anesthesiology* 2013;118:59–69 CrossRef
30. Hashmi JA, Loggia ML, Khan S, et al. **Dexmedetomidine disrupts the local and global efficiencies of large-scale brain networks.** *Anesthesiology* 2017;126:419–30

Balanced Steady-State Free Precession Techniques Improve Detection of Residual Germ Cell Tumor for Treatment Planning

W.A. Mehan, Jr., K. Buch, M.F. Brasz, F.F.J. Simonis, S. MacDonald, S. Rincon, J.E. Kirsch, and P. Caruso

ABSTRACT

BACKGROUND AND PURPOSE: Identification of a partial/complete chemotherapy response in pediatric patients with intracranial germ cell tumors is clinically important for radiation treatment and management. Partial/complete response is conventionally determined on postcontrast MR imaging sequences. The purpose of this study was to assess the diagnostic utility of a balanced steady-state free precession sequence as an adjunct to standard MR imaging sequences for the detection of residual tumor in pediatric patients on postchemoreduction pre-radiation planning MR imaging.

MATERIALS AND METHODS: This was a retrospective study of pediatric patients with intracranial germ cell tumors undergoing postchemotherapy, preradiotherapy MR imaging. Patients underwent 1.5T or 3T MR imaging with pre- and postcontrast T1WIs, T2WIs, and a balanced steady-state free precession sequence. Two neuroradiologists independently reviewed standard MR imaging sequences without the balanced steady-state free precession sequence, then with the balanced steady-state free precession sequence 1 week later. Assessment for partial/complete response was determined using Response Assessment in Neuro-Oncology criteria. A 5-point Likert scale scored the diagnostic confidence of the neuroradiologist rating each study without/with the balanced steady-state free precession sequence. Rates of residual disease concordance and diagnostic confidence levels without/with the balanced steady-state free precession sequence were calculated.

RESULTS: Thirty-nine patients were included with 31 males and 8 females (mean age, 14.15 ± 4.26 years). Thirty-one patients had single-site disease; 8 patients had multisynchronous disease (47 sites in total). Compared to review of the standard MR sequences alone, the addition of the balanced steady state free precession sequence resulted in higher rates of tumor partial response categorization and greater diagnostic confidence levels ($P < .001$, $P < .001$).

CONCLUSIONS: The balanced steady-state free precession sequence improves detection of residual chemotherapy-reduced intracranial germ cell tumors and increases diagnostic confidence of the neuroradiologist. The balanced steady-state free precession sequence may be an important adjunct to the standard MR imaging protocol for radiation planning.

ABBREVIATIONS: BRAVO = axial MRI 3D brain volume; bSSFP = balanced steady-state free precession; CR = complete response; GCT = germ cell tumor; PR = partial response; SPGR = spoiled gradient echo

Standard of care treatment for CNS germ cell tumors (GCTs) is chemotherapy followed by radiation therapy.¹ Treatment is based on the amount of residual tumor after chemotherapy. Patients with a complete response (CR) are defined by response assessment in neuro-oncology (RANO) criteria as having a complete radiographic disappearance of all tumor, whereas those with

a partial response (PR) are defined as having a $\geq 50\%$ decrease (compared with baseline) in the sum of the products of the perpendicular diameters of the tumor.^{1,2} MR imaging is considered the standard of care for assessment of residual tumor and thus is used to determine CR versus PR.

The balanced steady-state free precession (bSSFP) technique is a heavily water-weighted 3D sequence used with isotropic or near-isotropic spatial encoding, which has been shown to be useful in neuro-oncologic imaging, given its high signal-to-noise ratio and superior discrimination of soft tissue from CSF within the ventricular system or cisterns.³⁻⁸ Recent consensus recommendations on MR imaging for the pediatric brain include axial T2-weighted images, axial diffusion-weighted images, and 3D T1 pre- and post-contrast sequences but do not specifically include bSSFP sequences.²

Received December 12, 2019; accepted after revision March 16, 2020.

From the Departments of Radiology (W.A.M., Jr., K.B., S.R., J.E.K., P.C.) and Radiation Oncology (S.M.), Massachusetts General Hospital and Harvard Medical School, Boston, Massachusetts; and Magnetic Detection and Imaging (M.F.B., F.F.J.S.), TechMed Centre, University of Twente, Enschede, the Netherlands.

Please address correspondence to William A. Mehan, Jr, MD, MBA, Massachusetts General Hospital, 55 Fruit St, Gray 2-273A, Boston, MA 02114; e-mail: mehan.william@mgh.harvard.edu
<http://dx.doi.org/10.3174/ajnr.A6540>

The assessment of CR versus PR is clinically relevant for the management and treatment of these patients. In patients with either CR or PR with residual disease of <1 cm, radiation therapy protocols typically include 18 Gy to the whole ventricles with a boost of 12 Gy to the primary tumor site. In patients with PR but with residual disease measuring between 1 and 1.5 cm, a higher whole-ventricular radiation dose to 24 Gy with a 12-Gy boost is delivered. Furthermore, if patients with a PR have residual disease measuring >1.5 cm, a second-look surgery is considered to assess for the presence of residual GCT such as mature teratoma versus scar.⁹⁻¹²

The purpose of our study was to evaluate whether the bSSFP sequence improves the detection of residual chemoreduced germ cell tumor over the standard neuro-oncologic MR imaging sequences.

MATERIALS AND METHODS

Study Design

This retrospective, institutional review board–approved study included pediatric patients who presented to Massachusetts General Hospital between 2010 and 2019 with an intracranial GCT. Patients were identified through a search of the institutional radiology information system and an in-house clinical neuro-oncology data base. Inclusion criteria for this study were patients 21 years of age or younger; a clinical diagnosis of intracranial GCT based on biopsy or CSF; and paired prechemotherapy MR imaging examinations and postchemotherapy, preradiation MR imaging examinations. Standard sequences included pre- and postcontrast T1WI, diffusion-weighted sequences, and T2WI as well as a bSSFP sequence. Patients with prior radiation treatment and nondiagnostic MRIs related to technical factors and motion artifacts were excluded.

Clinical Data

The electronic medical record for each patient was reviewed for the following: 1) demographic information, including age and sex; 2) tumor histology (eg, germinoma, yolk sac tumor, mature teratoma, or embryonal carcinoma); 3) tumor site (pineal, suprasellar, multiple midline, posterior fossa, purely intraventricular); and 4) treatment history, including a prior operation (date and biopsy versus debulking), chemotherapy (date and type), and radiation planning dose.

Scanner Hardware and Sequence Parameters

Imaging was performed on either a 1.5T (Signa Excite HDx, GE Healthcare; Avanto, Siemens) or 3T scanner (Discovery MR750, GE Healthcare; Tim Trio and Skyra, Siemens). The scans were obtained with an 8-channel brain array coil or a 16-channel head, neck, and spine coil for the Signa Excite HDx; a 20-channel head coil for the Avanto; a 16-channel head, neck, and spine coil for the Discovery MR750; and a 32-channel head coil for the Tim Trio.

Imaging Protocol

General anesthesia, child life specialists, and video goggles were used when deemed appropriate and based on our institutional protocols.

The standard acquired sequences obtained included a pregadolinium 3D T1WI, axial diffusion-weighted imaging, and axial T2WI. Following an intravenous bolus injection of gadoterate meglumine at 0.2 mL/kg (Dotarem; Guerbet), a postcontrast 3D T1WI was performed. Scan parameters such as TE, TR, and flip angle were optimized per patient.

The scan parameters for the 1.5T Avanto scanner for the T1WI (MPRAGE) pre- and postgadolinium were TR/TE = 2140/4.75 to 2200/4.76 ms, NEX = 1, matrix = 256 × 256, flip angle = 15°, FOV = 250 × 250 to 256 × 256 mm, section thickness = 1 mm, gap = 0 mm, with an acquisition time of approximately 5 minutes, 30 seconds. For T2WI, the parameters were TR/TE = 3000/104 to 5510/114 ms, NEX = 2, matrix = 256 × 256 to 448 × 448, flip angle = 180°, FOV = 160 × 160 to 175 × 220 mm, section thickness = 3 mm, gap = 3 mm, with an acquisition time of approximately 4 minutes, 30 seconds.

The scan parameters for the GE 1.5T Signa Excite HDx scanners for the T1WI (axial MRI 3D brain volume [BRAVO; GE Healthcare] and echo-spoiled gradient echo [SPGR]; GE Healthcare) pre- and postgadolinium were TR/TE = 14.66/6.36 ms to 15.59/6.64 ms for BRAVO and 32/8 ms for SPGR, NEX = 1, matrix = 260 × 260 for BRAVO and 256 × 192 for SPGR, flip angle = 13° for BRAVO and 25° for SPGR, FOV = 260 × 260 mm for BRAVO and 220–340 mm for SPGR, section thickness = 1 mm for BRAVO and 1.5 mm for SPGR, gap = 1 mm for BRAVO and 1.5 mm for SPGR, with an acquisition time of approximately 3 minutes, 30 seconds for BRAVO and 5.9–7.5 minutes for SPGR. For the T2WI, the parameters were TR/TE = 4150/95.5 to 6700/97.2 ms, NEX = 2, matrix = 320 × 256, flip angle = 90°, FOV = 220 × 220 to 240 × 240 mm, section thickness = 3 mm, gap = 3 mm, with an acquisition time of approximately 3–5 minutes, 30 seconds.

The scan parameters for the 3T Siemens Tim Trio scanner and the 3T Skyra scanner for the T1WI (MPRAGE) pre- and postgadolinium were TR/TE = 2530/7.22 ms, NEX = 1, matrix = 256 × 256, flip angle = 7°, FOV = 256 × 256 mm, section thickness = 1 mm, gap = 0 mm, with an acquisition time of approximately 4–6 minutes, 18 seconds. For the T2WI, they were TR/TE = 3890/97 to 8760/97 ms, NEX = 2, matrix = 512 × 294 to 512 × 336, flip angle = 150°, FOV = 256 × 256 mm, section thickness = 3 mm, gap = 3 mm, with an acquisition time of 3 minutes, 6 seconds–4 minutes, 30 seconds.

The scan parameters for the 3T Discovery MR750 scanner for the T1WI (SPGR) pre- and postgadolinium were TR/TE = 8.219/3.22 ms, NEX = 1, matrix = 256 × 256, flip angle = 20°, FOV = 240 × 240 mm, section thickness = 1.2 mm, gap = 1.2 mm, with an acquisition time of approximately 2 minutes, 12 seconds. For the T2WI, they were TR/TE = 4747/84.8 ms, NEX = 2, matrix = 384 × 288, flip angle = 111°, FOV = 220 × 220 mm, section thickness = 3 mm, gap = 3 mm, with an acquisition time of approximately 1 minute, 48 seconds.

The bSSFP sequence on the 3T Tim Trio and Skyra scanners (CISS) was performed using the following parameters: TR/TE = 11.26/5.85 to 12.55/6.28 ms, NEX = 1, matrix = 448 × 269, flip angle = 50°, FOV = 160 × 160 to 199 × 199 mm, section thickness = 0.8 mm, gap = 0 mm, with an acquisition time of approximately 8 minutes.

Table 1: Difference between the recordings with and without the bSSFP sequence for all cases and separately for different locations^a

	Reader 1		Reader 2	
	Without bSSFP	With bSSFP	Without bSSFP	With bSSFP
All cases (47)				
28 CR (60%)		4 CR (9%)	22 CR (47%)	2 CR (4%)
19 PR (40%)		43 PR (91%)	25 PR (53%)	45 PR (96%)
Pineal location (27)				
15 CR (56%)		3 CR (11%)	10 CR (37%)	1 CR (4%)
12 PR (44%)		24 PR (89%)	17 PR (63%)	26 PR (96%)
Suprasellar location (17)				
12 CR (71%)		1 CR (6%)	11 CR (65%)	1 CR (6%)
5 PR (29%)		16 PR (94%)	6 PR (35%)	16 PR (94%)
Other location (3)				
2 CR (67%)		0 CR	2 CR (67%)	0 CR
1 PR (33%)		3 PR (100%)	1 PR (33%)	3 PR (100%)

^aThe recordings of the intraventricular and posterior fossa locations are described with the label "other location."

The bSSFP sequence on the 3T Discovery MR750 scanners (FIESTA) was performed using the following parameters: TR/TE = 6.878/2.78 ms, NEX = 1, matrix = 320 × 256, flip angle = 65°, FOV = 160 × 160 mm, section thickness = 1 mm, gap = 1 mm, with an acquisition time of approximately 4 minutes, 6 seconds.

The bSSFP sequence on the 1.5T Avanto scanner (CISS) was performed using the following parameters: TR/TE = 5.72/2.4–11.94/5.97 ms, NEX = 1, matrix = 320 × 224, flip angle = 70–80°, FOV 160 × 160 to 170 × 170 mm, slice thickness = 0.7–0.8 mm, gap = 0 mm, with an acquisition time of approximately 5 minutes, 24 seconds.

The bSSFP sequence on the 1.5T Signa Excite HDx scanner (FIESTA) was performed using the following parameters: TR/TE = 6.048/2.33 to 12.47/2.43 ms, NEX = 1–6, matrix = 448 × 256, flip angle = 65°, FOV = 180 × 180 to 220 × 220 mm, section thickness = 0.8–1 mm, gap = 0.4–0.5 mm, with an acquisition time of approximately 2 minutes, 54 seconds–8 minutes, 54 seconds.

Image Analysis

The presentation, pretreatment MRIs and the postchemotherapy, preradiation MRIs were reviewed by 2 neuroradiologists (W.A.M. with >5 years' postfellowship experience and P.C. with >15 years' postfellowship experience), independently, at 2 separate sessions. During the first session, informed only of the location of the tumor, the 2 neuroradiologists reviewed the cases with standard neuro-oncologic sequences that included axial T2WI and postgadolinium SPGR/MPRAGE/BRAVO sequences, but without the bSSFP sequence. During the second session, at least 1 week later, the same 2 neuroradiologists independently reviewed all sequences, but this time with the addition of the bSSFP sequence. An interval of at least 1 week was chosen between the first and second readout sessions to avoid memory bias.

At both the first and second readout sessions, the 2 neuroradiologists evaluated the primary treatment bed as per Kretschmar et al for CR, defined as no radiographic evidence of disease at the site of the original tumor; PR, defined as ≥50% decrease in the sum of the products of perpendicular diameters of the lesion

compared with the presentation MR imaging; stable disease, defined as no appreciable change in tumor volume; and progressive disease, defined as ≥25% increase in the sum of the products of perpendicular diameters.¹

Cubic tumor volumes (anteroposterior × transverse × superoinferior) were measured on all prechemotherapy, pre-radiation therapy MRIs on the volumetric T1 postgadolinium and bSSFP sequences and on all postchemotherapy, pre-radiation therapy MRIs for which a PR was recorded. Cubic tumor volumes were calculated for all cases on both the volumetric T1 postgadolinium and bSSFP sequences.

A 5-point Likert scale confidence score (1 = not confident at all, 2 = slightly confident, 3 = somewhat confident, 4 = fairly confident, 5 = completely confident) was recorded for each neuroradiologist's assessment of CR versus PR during both review sessions without-versus-with the inclusion of the bSSFP sequence.¹²

Statistical Analysis

A 2-sample test of proportions and a Fisher exact test were performed to analyze differences in confidence scores and assessment of CR versus PR in the bSSFP and non-bSSFP groups. The κ score was used to assess the level of interrater agreement between the 2 radiologists with SPSS statistics 25 (IBM).

RESULTS

Cohort Description

A total of 74 patients were considered for this study. Thirty-five patients were excluded, with 31 due to lack of a bSSFP sequence, 2 due to prior radiation therapy, and 2 due to motion artifacts. In this cohort, a total of 39 pediatric patients were included, 31 males and 8 females, ranging from 4 to 21 years of age (mean, 14.15 ± 4.26 years). Twenty-four patients were diagnosed with a pure germinoma, and 15 patients were diagnosed with a nongerminomatous germ cell tumor. All patients had documented negative serum and CSF tumor markers before evaluation for radiation therapy. The nongerminomatous germ cell tumor group contained 1 yolk sac tumor, 1 mature teratoma, 1 embryonal carcinoma, and 12 mixed tumors with germ cell and mature/immature or yolk sac components. Of the 39 patients, 19 had pineal tumor location only, 9 had suprasellar tumor location only, 2 had intraventricular location only, 1 had posterior fossa location only and 8 patients had multiple midline germ cell tumors, including the suprasellar and pineal regions. There were 47 tumor locations in total: Twenty-seven tumors were pineal, 17 tumors were suprasellar, 2 tumors were intraventricular, and 1 tumor was located in the posterior fossa.

Imaging Protocol

Twenty-seven patients were scanned on a 1.5T scanner, and 12 patients were scanned on a 3T scanner.

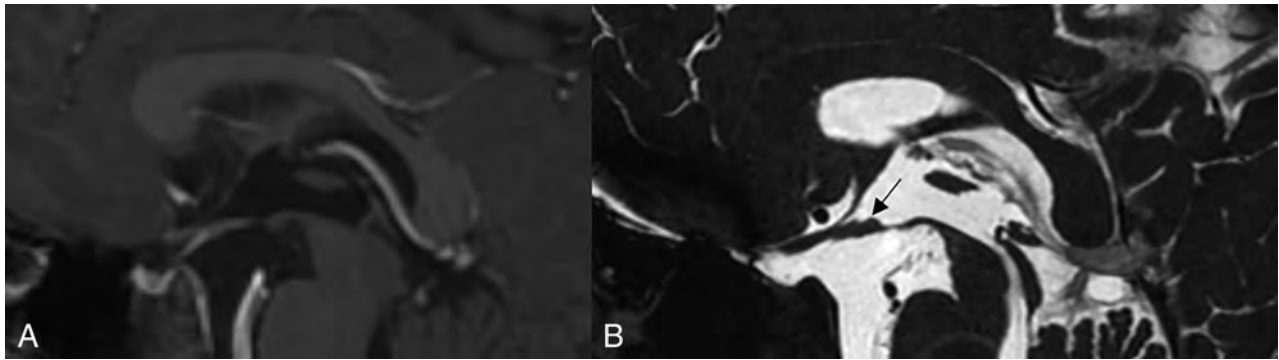


FIG 1. A 10-year-old boy with a history of chemotherapy-treated suprasellar germ cell tumor. Sagittal 3D T1 postcontrast SPGR image through the sella (A), interpreted as complete response in the first readout session without the bSSFP sequence. Sagittal FIESTA image through the sella (B) from the same patient interpreted as partial response during the second readout session with small nodules identified along the floor of the third ventricle (arrow).

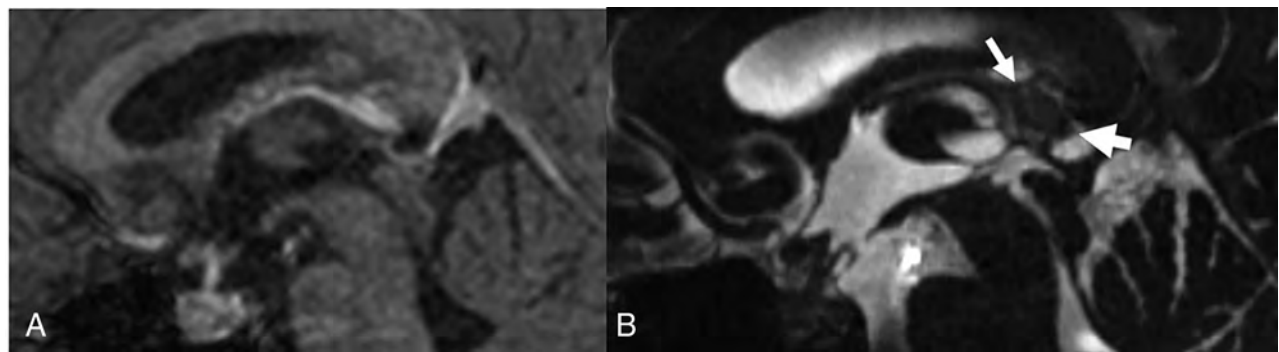


FIG 2. A 19-year-old woman with a history of chemotherapy-treated pineal germ cell tumor. Sagittal 3D T1 postcontrast MPRAGE image through the pineal region (A) interpreted as complete response in the first readout session without the bSSFP sequence. Sagittal CISS image through the pineal region (B) from the same patient interpreted as partial response during the second readout session with a >1-cm nodule identified within the pineal gland (arrows).

Evaluation of CR and PR

Evaluation of Response during First Review (without the bSSFP). Reader 1 detected 28 instances of CR, 19 PR, 0 stable disease, and 0 progressive disease during the first review in all cases, and reader 2 recorded 22 CR, 25 PR, 0 stable disease, and 0 progressive disease.

Evaluation of Response during Second Review (with the bSSFP). During the second review, with the addition of the bSSFP sequence, reader 1 recorded 4 CR, 43 PR, 0 stable disease, and 0 progressive disease in all cases. Reader 2 recorded 2 CR, 45 PR, 0 stable disease, and 0 progressive disease.

Table 1 shows the difference between the recordings with and without the bSSFP sequence for all cases and separately for different locations.

There were 24 cases (reader 1) and 20 cases (reader 2) that were initially interpreted as CR during the first session of the evaluation and were recategorized as PR during the second review with the addition of the bSSFP sequence (Figs 1 and 2). There was a significant difference between the number of CR and PR evaluations between the recordings with and without the bSSFP sequence ($P < .001$, Fisher exact test performed for both readers).

Tumor Size and Volume Measurements

For the presentation MRIs, the mean cubic tumor volume on the volumetric postcontrast T1WI was $8.88 \pm 12.85 \text{ cm}^3$ (range, 0.06–68.94 cm^3). The mean cubic tumor volume for all PR evaluations on the volumetric postcontrast T1WI was $0.97 \pm 1.67 \text{ cm}^3$ (range, 0.004–7.54 cm^3). The mean cubic tumor volume for the PR evaluations on the bSSFP sequence was $1.31 \pm 1.88 \text{ cm}^3$ (range, 0.016–8.09 cm^3). Although the mean cubic tumor volume on the postchemotherapy preradiation planning MRIs was slightly higher on the bSSFP sequence compared with the postcontrast T1WI, the difference was not significant ($P = .33$).

Of the cases recategorized from CR to PR after review of the bSSFP sequence, the mean tumor volume was $0.24 \pm 0.55 \text{ cm}^3$ (range, 0.002–2.84 cm^3), and 1 of these cases had a volume of $>1 \text{ cm}^3$.

Of the cases recategorized from CR to PR after review of the bSSFP sequence, 6 tumors had a single plane measurement of $\geq 1 \text{ cm}$ (average single plane measurement, $1.4 \pm 3.2 \text{ cm}$).

Confidence Scores

The confidence scores of both sessions and the difference between the interval per location are shown in Table 2. Reader 1 noted a confidence interval of 2–5 (mean, 4.17 ± 0.82) for all cases during

Table 2: Confidence scores recorded by the 2 readers for all cases and for individual locations on the bSSFP sequence compared with postcontrast T1WI^a

	Reader 1	Reader 2
All cases (47)		
TIWI	4.17 ± 0.82 (2–5)	4.36 ± 0.61 (3–5)
bSSFP	4.77 ± 0.43 (4–5)	4.55 ± 0.58 (3–5)
Pineal location (27)		
Without bSSFP	4.07 ± 0.96 (2–5)	4.41 ± 0.67 (3–5)
With bSSFP	4.74 ± 0.45 (4–5)	4.63 ± 0.56 (3–5)
Suprasellar location (17)		
Without bSSFP	4.35 ± 0.61 (3–5)	4.29 ± 0.69 (3–5)
With bSSFP	4.94 ± 0.24 (4–5)	4.47 ± 0.28 (3–5)
Other location (3)		
Without bSSFP	4 ± 0.00 (4)	4.3 ± 0.58 (4–5)
With bSSFP	4 ± 0.00 (4)	4.3 ± 0.58 (4–5)

^aData are mean and range.

the first recording. Reader 2 noted a confidence interval of 3–5 (mean, 4.36 ± 0.61).

During the second review session, with the bSSFP sequence, the mean confidence score for both readers was higher. Reader 1 showed a confidence interval of 4–5 (mean, 4.77 ± 0.43) for all cases. Reader 2 noted a confidence interval of 3–5 (mean, 4.55 ± 0.58).

There was a statistically significant difference between the confidence scores between the reviews performed with the bSSFP sequence compared with reviews performed without bSSFP sequence ($P < .001$, 2-tailed t test).

Interrater Reliability

The number of discrepant cases between readers 1 and 2 during the first review, without the bSSFP sequence, was 12. The number of discrepancies between readers 1 and 2 during the second review, with the bSSFP sequence, was 4. For the first review session, without the bSSFP, the calculated κ score between reader 1 and reader 2 was 0.128. For the second review session, with the bSSFP, the calculated κ score between reader 1 and 2 was 0.872.

DISCUSSION

Our study demonstrates that the addition of a bSSFP technique to a neuro-oncology MR imaging protocol increases the detection of residual germ cell tumor and improves the interpreting neuroradiologist's confidence in reporting the presence of residual disease.

Compared with the neuroimaging standard of T1-weighted postcontrast imaging for assessing tumor response, the bSSFP sequence adds value through improved contrast and higher spatial resolution, which facilitates the detection of nonenhancing or minimally enhancing tumor components. These features allow improved residual germ cell tumor detection, particularly in the typical locations in the suprasellar and pineal regions, which are surrounded by CSF, thus allowing superior contrast resolution between hypointense tumor and hyperintense CSF.

The sensitivity of bSSFP sequences for the detection of small volumes of residual tumor is exemplified by the 24 (reader 1) and 20 (reader 2) cases reclassified from CR to PR by the addition of bSSFP sequences. The residual tumor volumes were, on average, 0.25 cm³, which are small and could be potentially overlooked on standard T1 postcontrast and T2/FLAIR sequences. A total of 6

cases had tumors that demonstrated a residual maximal single-plane measurement of ≥ 1 cm, which, based on the Children's Oncology Group ACNS1123 protocol, would have stratified 4 patients for a radiation boost and 2 patients for second-look surgery.^{9–12} Another important finding is that the addition of a bSSFP sequence improves reader confidence in detecting residual tumor and determining PR-versus-CR status. The average confidence score for the 2 neuroradiologists was 4.17 with the standard MR images and 4.77 with the addition of the bSSFP sequence ($P < .001$). The number of discrepant interpretations decreased from 12 with the standard MR images to 4 with the inclusion of the bSSFP sequence. Furthermore, interrater agreement also improved from poor (0.128) to excellent (0.872) with the bSSFP sequence.

Both the improved sensitivity for residual tumor and higher reader confidence with the bSSFP sequence when interpreting post-chemotherapy-induction MR imaging studies are of paramount importance for therapeutic decision-making. Recategorizing patients from CR to PR is clinically relevant and may influence radiation therapy dosing and treated tumor volumes as well as help determine whether a second-look surgery may be necessary.^{1,2,9–12}

Our findings are similar to those in other previous studies that have demonstrated the benefits of adding bSSFP sequences to standard neuroimaging protocols for CNS tumor detection, including high accuracy for vestibular schwannoma detection and spinal drop metastases.^{4,13–16}

Although the inclusion of a bSSFP sequence increased the total scan length by 6 minutes on average, we found that the improved sensitivity and confidence in the interpretation justify the additional imaging time. Furthermore, there is diagnostic synergy between the bSSFP and the standard MR images when interpreted in conjunction. At our institution, for several years now, we have routinely performed a bSSFP sequence as part of the neuro-oncology MR imaging protocol, given that the pediatric neuroradiologists prefer this sequence for its high spatial resolution, isotropic images, and ability to characterize cystic tumoral components. One pitfall of bSSFP, however, is a banding artifact caused by destructive interference between the 2 primary coherent signal pathways in off-resonance regions of B₀ inhomogeneities. This generates dark lines on the images that may at times obscure anatomic structures and lesions.¹⁷ CISS is a 2-pass bSSFP technique that attempts to minimize these artifacts. Nevertheless, in 1 case in our sample, there were a large amount of banding artifacts obscuring the pineal region on the bSSFP sequence; this issue was surmounted by simultaneously correlating with the postcontrast T1-weighted images.

This study has several limitations. The sample size was relatively small. Also, patients were imaged on different MR imaging scanners, which introduced heterogeneity between magnet field strengths (1.5T versus 3T) as well as between the vendor-specific bSSFP sequences (CISS for Siemens versus FIESTA for GE Healthcare). However, each patient's standard MR images and bSSFP sequence were performed on the same scanner. In no case was a comparison made in the same patient between MR images obtained at different magnetic field strengths or between different vendors. The increased rate of detection of tissue nodularity at the primary tumor site with the addition of the bSSFP sequence may not be clinically important in all patients, particularly given

that most residual tumors detected were <1 cm. Given the investigational nature of our current study, additional studies are needed to determine whether these areas of presumed residual tumor identified on bSSFP imaging impact patient management and outcomes. Furthermore, there was a lack of histopathologic confirmation in most cases. Postsurgical and postchemotherapy scar tissue may have been misinterpreted as residual tumor, thus resulting in false-positives. However, histopathologic confirmation is not standard of care.

CONCLUSIONS

Adding a bSSFP sequence to the standard neuro-oncology MR imaging protocol improves the neuroradiologist's detection of presumed residual chemotherapy-reduced CNS germ cell tumor and increases confidence in distinguishing partial response from complete response disease status. This distinction could have important therapeutic consequences for the patient with regard to determining the radiation dose or the need for an additional operation; however, further investigations are required.

Disclosures: William A. Mehan—UNRELATED: Consultancy; Kura Oncology. Comments: reviewer of radiologic studies for a clinical trial dealing with head and neck cancer; Expert Testimony; CRICO and other medical insurance companies. Comments: expert review for malpractice cases involving neuroimaging.

REFERENCES

- Kretschmar C, Kleinberg L, Greenberg M, et al. **Pre-radiation chemotherapy with response-based radiation therapy in children with central nervous system germ cell tumors: a report from the Children's Oncology Group.** *Pediatr Blood Cancer* 2007;48:285–91 CrossRef Medline
- Warren KE, Vezina G, Poussaint TY, et al. **Response assessment in medulloblastoma and leptomeningeal seeding tumors: recommendations from the Response Assessment in Pediatric Neuro-Oncology committee.** *Neuro Oncol* 2018;20:13–23 CrossRef Medline
- Hingwala D, Chatterjee S, Kesavadas C, et al. **Applications of 3D CISS sequence for problem solving in neuroimaging.** *Indian J Radiol Imaging* 2011;21:90–97 CrossRef Medline
- Buch K, Caruso P, Ebb D, et al. **Balanced steady-state free precession sequence (CISS/FIESTA/3D driven equilibrium radiofrequency reset pulse) increases the diagnostic yield for spinal drop metastases in children with brain tumors.** *AJNR Am J Neuroradiol* 2018;39:1355–61 CrossRef Medline
- Gloor M, Scheffler F, Bieri O. **Quantitative magnetization transfer imaging using balanced SSFP.** *Magn Reson Med* 2008;60:691–700 CrossRef Medline
- Sheth S, Branstetter BF 4th, Escott EJ. **Appearance of normal cranial nerves on steady-state free precession MR images.** *Radiographics* 2009;29:1045–55 CrossRef Medline
- Algin O, Hakyemez B, Gokalp G, et al. **The contribution of 3D-CISS and contrast-enhanced MR cisternography in detecting cerebrospinal fluid leak in patients with rhinorrhea.** *Br J Radiol* 2010;83:225–32 CrossRef Medline
- Algin O, Hakyemez B, Parlak M. **Phase-contrast MRI and 3D-CISS versus contrast-enhanced MR cisternography on the evaluation of the aqueductal stenosis.** *Neuroradiology* 2010;52:99–108 CrossRef Medline
- Children's Oncology Group. **ACNS1123: Phase 2 trial of response-based radiation therapy for patients with localized central nervous system germ cell tumor.** <https://childrensoncologygroup.org/index.php/acns1123>. Accessed February 20, 2020
- Khatua S, Fangusaro J, Dhall G, et al. **GC-17: the Children's Oncology Group (COG) current treatment approach for children with newly diagnosed central nervous system (CNS) localized germinoma (ACNS1123 STRATUM 2).** *Neuro Oncol* 2016;18(Suppl 3):iii45.4–46 CrossRef
- Osorio DS, Allen JC. **Management of CNS germinoma.** *CNS Oncol* 2015;4:273–79 CrossRef Medline
- Murphy ES, Fangusaro J, Dhall G, et al. **ACNS1123: Phase 2 trial of response-based radiation therapy for patients with localized central nervous system germ cell tumor (CNS GCT)—a Children's Oncology Group (COG) study. Patterns of failure and radiation dosimetry for nongerminomatous germ cell tumors.** *International Journal of Radiation Oncology Biology Physics* 2018;102:S49–50 CrossRef
- Abele TA, Besachio DA, Quigley EP, et al. **Diagnostic accuracy of screening MR imaging using unenhanced axial CISS and coronal T2WI for detection of small internal auditory canal lesions.** *AJNR Am J Neuroradiol* 2014;35:2366–70 CrossRef Medline
- Stuckey SL, Harris AJ, Mannolini SM. **Detection of acoustic schwannoma: use of constructive interference in the steady state three-dimensional MR.** *AJNR Am J Neuroradiol* 1996;17:1219–25 Medline
- Hermans R, Van der Goten A, De Foer B, et al. **MRI screening for acoustic neuroma without gadolinium: value of 3DFT-CISS sequence.** *Neuroradiology* 1997;39:593–98 CrossRef Medline
- Buch K, Juliano A, Stankovic KM, et al. **Noncontrast vestibular schwannoma surveillance imaging including an MR cisternographic sequence: is there a need for postcontrast imaging?** *J Neurosurg* 2018;131:549–54 CrossRef Medline
- Bangerter NK, Hargreaves BA, Vasanawala SS, et al. **Analysis of multiple-acquisition SSFP.** *Magn Reson Med* 2004;51:1038–47 CrossRef Medline

Neuroimaging Findings in Children with Constitutional Mismatch Repair Deficiency Syndrome

A. Kerpel, M. Yalon, M. Soudack, J. Chiang, A. Gajjar, K.E. Nichols, Z. Patay, S. Shrot, and C. Hoffmann



ABSTRACT

BACKGROUND AND PURPOSE: Constitutional mismatch repair deficiency is a hereditary childhood cancer predisposition syndrome characterized by brain tumors and colorectal and hematologic malignancies. Our objective was to describe the neuroimaging findings in patients with constitutional mismatch repair deficiency.

MATERIALS AND METHODS: This retrospective study included 14 children with genetically confirmed constitutional mismatch repair deficiency who were referred to 2 tertiary pediatric oncology centers.

RESULTS: Fourteen patients from 11 different families had diagnosed constitutional mismatch repair deficiency. The mean age at presentation was 9.3 years (range, 5–14 years). The most common clinical presentation was brain malignancy, diagnosed in 13 of the 14 patients. The most common brain tumors were glioblastoma ($n = 7$ patients), anaplastic astrocytoma ($n = 3$ patients), and diffuse astrocytoma ($n = 3$ patients). Nonspecific subcortical white matter T2 hyperintensities were noted in 10 patients (71%). Subcortical hyperintensities transformed into overt brain tumors on follow-up imaging in 3 patients. Additional non-neoplastic brain MR imaging findings included developmental venous anomalies in 12 patients (85%) and nontherapy-induced cavernous hemangiomas in 3 patients (21%).

CONCLUSIONS: On brain MR imaging, these patients have both highly characteristic intra-axial tumors (typically multifocal high-grade gliomas) and nonspecific findings, some of which might represent early stages of neoplastic transformation. The incidence of developmental venous anomalies is high in these patients for unclear reasons. Awareness of these imaging findings, especially in combination, is important to raise the suspicion of constitutional mismatch repair deficiency in routine diagnostic imaging evaluation or surveillance imaging studies of asymptomatic carriers because early identification of the phenotypic “gestalt” might improve outcomes.

ABBREVIATIONS: CMMRD = constitutional mismatch repair deficiency; DVA = developmental venous anomaly; WHO = World Health Organization

DNA replication is a highly controlled process during cell division. The DNA mismatch repair system primarily functions to correct errors arising during DNA replication. Hence, mutations in mismatch repair genes and their dysfunctional protein products lead to accumulation of other “unrepaired” mutations in each cell division, which could cause neoplastic (malignancies, premalignancies, and benign tumors) or non-neoplastic phenotypic features to develop. In humans, germline

mutations in the mismatch repair genes result in distinct cancer predisposition syndromes.^{1–3} Heterozygous germline mutations in 1 of the 4 mismatch repair genes (*mutL homolog 1* [*MLH1*], *PMS1 homolog 2*, *mismatch repair system component* [*PMS2*], *mutS homolog 2* [*MSH2*], or *mutS homolog 6* [*MSH6*]) result in Lynch syndrome, which is the most frequent form of inherited colorectal cancer.⁴ Lynch syndrome manifests in early adulthood and is characterized by an increased incidence of endometrial and genitourinary cancer.^{4,5} Biallelic germline mutations in the mismatch repair genes result in a distinct phenotypically

Received December 4, 2019; accepted after revision February 26, 2020.

From the Department of Radiology (A.K., M.S., S.S., C.H.), Sheba Medical Center, Tel Hashomer, Ramat Gan, Israel; Pediatric Hemato-Oncology (M.Y.), Edmond and Lilly Safra Children's Hospital and Cancer Research Center, Sheba Medical Center, Tel Hashomer, Ramat Gan, Israel; Sackler School of Medicine (A.K., M.Y., M.S., S.S., C.H.), Tel Aviv University, Tel Aviv, Israel; and Department of Pathology (J.C.), Divisions of Neuro-Oncology (A.G.), and Cancer Predisposition (K.E.N.), and Department of Oncology and Section of Neuroimaging, Department of Diagnostic Imaging (Z.P.), St. Jude Children's Research Hospital, Memphis, Tennessee.

A. Kerpel and M. Yalon contributed equally to this article. S. Shrot and C. Hoffmann contributed equally to this article.

This work was supported, in part, by the American Lebanese Syrian Associated Charities.

Please address correspondence to Ariel Kerpel, MD, Sheba Medical Center, Tel Hashomer, Emek HaEla St 1, Ramat Gan 52621, Israel; e-mail: arikerp@gmail.com

Indicates article with supplemental on-line table.

<http://dx.doi.org/10.3174/ajnr.A6512>

Table 1: Indication criteria for CMMRD testing in patients with cancer^a

Criteria	
Indication for CMMRD testing	≥3 Points
Malignancies/premalignancies: 1 is mandatory; if >1 is present in the patient, add the points	
Carcinoma from the LS spectrum ^b at younger than 25 years of age	3 points
Multiple bowel adenomas at younger than 25 years of age and absence of <i>APC/MUTYH</i> mutations or a single high-grade dysplasia adenoma at younger than 25 years of age	3 points
WHO grade III or IV glioma at younger than 25 years of age	2 points
NHL of T-cell lineage or sPNET at younger than 18 years of age	2 points
Any malignancy at younger than 18 years of age	1 point
Additional features: optional; if >1 of the following is present, add the points	
Clinical sign of NF1 and/or ≥2 hyperpigmented and/or hypopigmented skin alterations Ø > 1 cm in the patient	2 points
Diagnosis of LS in a first-degree or second-degree relative	2 points
Carcinoma from LS spectrum ^b before 60 years of age in first-degree, second-degree, and third-degree relatives	1 point
A sibling with carcinoma from the LS spectrum, ^b high-grade glioma, sPNET, or NHL	2 points
A sibling with any type of childhood malignancy	1 point
Multiple pilomatricomas in the patient	2 points
One pilomatricoma in the patient	1 point
Agenesis of the corpus callosum or nontherapy-induced cavernoma in the patient	1 point
Consanguineous parents	1 point
Deficiency/reduced levels of immunoglobulin (Ig)G2/4 and/or IgA	1 point

Note:—LS indicates Lynch syndrome; NHL, non-Hodgkin lymphoma; sPNET, supratentorial primitive neuroectodermal tumor; NF1, neurofibromatosis type 1.

^a Reprinted with permission from Wimmer et al.⁵

^b Colorectal, endometrial, small bowel, ureter, renal pelvis, biliary tract, stomach, bladder carcinoma.

defined constitutional mismatch repair deficiency syndrome (CMMRD).^{2,6-8} Individuals with biallelic mismatch repair gene mutations are at risk of developing a vast spectrum of malignancies carrying a dismal prognosis during childhood. Typical malignancies include brain tumors, digestive tract tumors, hematologic malignancies, and Lynch syndrome-associated tumors other than in the digestive tract.^{2,5,6,9} Synchronous and metachronous cancers are common.^{10,11} A proposed scoring system based on clinical features was developed by the European Consortium “Care for CMMRD”⁵ (Table 1), indicating which patients should be further tested for CMMRD.

Early diagnosis of CMMRD could have considerable clinical importance, not only for surveillance of the index patient but also for screening in the entire pedigree.⁵ CMMRD should be considered in children with multiple malignancies and café au lait spots without the genetic diagnosis of neurofibromatosis type 1.¹² Remarkably, in children with CMMRD, both parents almost always have Lynch syndrome. Because genetic testing has considerably improved in recent years, our ability to confidently diagnose CMMRD has increased. Surveillance guidelines are also emerging (eg, European Consortium “Care for CMMRD,”⁶ US Multi-Society Task Force on Colorectal Cancer,⁴ and American Association of Cancer Research).⁸ Recently, a remarkable response to immune checkpoint inhibitors has been reported in patients with CMMRD with glioblastoma.¹¹ Hence, early detection of brain tumors and precancerous conditions might offer opportunities to improve outcomes.^{5,7,13}

Our objective is to describe neuroimaging findings in children with both CMMRD and brain tumors, thus increasing neuroradiologists’ awareness of this newly discovered cancer predisposition syndrome.

MATERIALS AND METHODS

Study Design and Patient Eligibility

Children with CMMRD diagnosed in Sheba Medical Center, Tel Hashomer, Ramat Gan, Israel and St. Jude Children’s Research

Hospital, Memphis, Tennessee between 2014 and 2019 were included in this retrospective study. Review of the patients’ medical records provided demographic, clinical, and genetic data. Brain MR imaging studies were reviewed by board-certified neuroradiologists in each participating institution. This retrospective study was approved by the institutional review boards in both hospitals.

Imaging Studies

MR imaging was performed on the following platforms: 1.5T (Magnetom Avanto or Magnetom Essenza, Siemens; Optima MR450w, GE Healthcare) or 3T (Ingenia, Philips Healthcare; Signa, GE Healthcare; Magnetom Prisma or Skyra, Siemens). Routine brain imaging protocols were different at each institution but always included multiplanar nonenhanced T1-weighted images, T2-weighted images, diffusion-weighted images, and postcontrast T1-weighted sequences, which were occasionally and inconsistently complemented by precontrast T2-FLAIR, SWI/T2*, and postcontrast T2-FLAIR sequences. Acquisition parameters differed according to the specific MR imaging vendors.

Statistical Analysis

Descriptive statistics were used to analyze data. Continuous variables are presented as mean and range.

RESULTS

Clinical Data and Tumor Types

Fourteen patients from 11 families with diagnosed CMMRD were included in this retrospective case series (5 boys and 9 girls). A summary of the patients’ clinical and genetic features is presented in the On-line Table. Twelve patients (86%) had *MSH6* mutations and 2 (14%) had *PMS2* mutations. Consanguinity was found in 4 of the 11 families. The mean age at diagnosis was 9.3 years (range, 5–14 years). Multiple synchronous and metachronous malignancies were common. Eighteen brain tumors were found in 13 of 14 patients (93%). Colorectal adenocarcinoma was diagnosed in 4

patients (29%), and 2 patients had multiple colorectal polyps with no high-grade features. Hematologic malignancies were diagnosed in 3 of 14 patients (21%), 2 with non-Hodgkin lymphomas of the T-cell lineage and 1 with B-cell acute lymphoblastic leukemia. Café au lait spots were observed on physical examination on all patients in our cohort. The mean surveillance period was 4.6 years (range, 1–9 years).

Neoplastic Neuroimaging Findings

Glioblastoma (World Health Organization [WHO] IV) was the most common brain malignancy in our cohort and was diagnosed in 7 patients (50%). All these tumors were supratentorial. On MR imaging, the lesions were irregular, poorly margined,

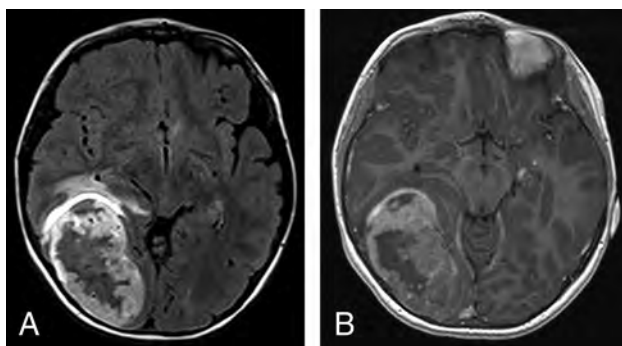


FIG 1. MR imaging of an 8-year-old girl with CMMRD (patient 6). Axial T2-FLAIR (A) and postcontrast T1 (B) show a right occipitotemporal heterogeneously enhancing mass with regional mass effect. Pathology results indicated glioblastoma.

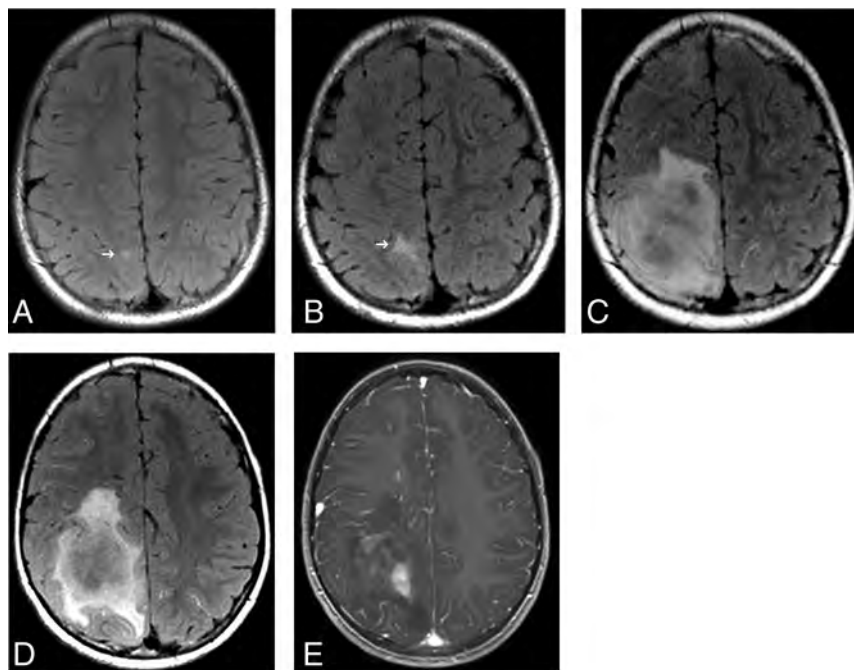


FIG 2. MR images of a boy with CMMRD (patient 3). Routine surveillance imaging at 8 years of age shows subtle right parietal subcortical T2-FLAIR hyperintensity (arrow in A). This subcortical T2-FLAIR hyperintensity increased in size a year later (arrow in B). Two years later, a large heterogeneously enhancing mass is evident on T2-FLAIR (C and D) and postcontrast T1WI (E). The histopathologic diagnosis is glioblastoma (WHO IV).

and resulted in marked mass effect. Typically, these tumors showed low-T1 and heterogeneous high-T2 or T2-FLAIR signal, with thick irregular peripheral enhancement surrounding central necrosis (Fig 1). The enhancing margins showed some degree of diffusion restriction. In 1 patient, glioblastoma showed irregular patchy areas of enhancement without characteristic central necrosis (Fig 2). Prominent T2 flow voids (ie, prominent feeding vessels) were also noted.

Supratentorial diffuse astrocytoma (WHO II) was diagnosed in 3 patients. On imaging, infiltration and expansion of the overlying cortex were noted. No contrast enhancement or restricted diffusion was identified in these cases. Supratentorial anaplastic astrocytoma (WHO III) was diagnosed in another 3 patients. One tumor of the latter group was partly intraventricular. Diffuse brain stem tumors were found in 2 patients (1 with diffuse intrinsic pontine glioma and 1 with glioblastoma). Pleomorphic xanthoastrocytoma (WHO II) involving the temporal lobe was diagnosed in 1 patient. *Sonic hedgehog* (*SHH*)-activated medulloblastoma (WHO IV) was diagnosed in 1 patient.

Spinal imaging, performed routinely as part of the surveillance protocol, did not show any structural or neoplastic spinal cord lesions.

Nonspecific, Subcortical T2/T2-FLAIR Hyperintensities

In our cohort, 10 of 14 patients (71%) had single or multiple nonspecific patchy subcortical white matter T2-FLAIR hyperintensities, most commonly in the frontal and parietal lobes, but occasionally in the cerebellum and/or the brain stem (Table 2). No mass effect, enhancement, or restricted diffusion were noted in these lesions (Figs 1 to 3). Most of the lesions were stable or showed very modest

changes during the surveillance period (Fig 4). In 3 patients, a gradual transformation toward overt brain tumors was observed on surveillance studies (2 with glioblastomas and 1 with diffuse astrocytoma; Figs 2 and 3, respectively). Occasionally, additional new lesions emerged during the follow-up period, too.

Vascular Abnormalities and Focal Areas of Signal Intensity

Developmental Venous Anomaly. Twelve of the 14 patients (86%) presented with a network of prominent medullary veins converging into a single draining vein (caput medusae), meeting the conventional MR imaging criteria of developmental venous anomaly (DVA). These DVAs drained into the dural sinuses or ependymal veins. The average number of DVAs in patients who had them was 2.5 (range, 1–5). These DVAs were already present at the initial diagnostic imaging evaluation. DVAs were either supra- (mostly frontoparietal) or infratentorial (cere-

Table 2: Nonmalignant neuroradiologic findings

Patient	T2-FLAIR Subcortical Hyperintensities	Focal Areas of T2-FLAIR Hyperintense Signal Intensity (Basal Ganglia, Thalamus, Pons, or Cerebellum)	Developmental Venous Anomalies	Cavernous Hemangioma
1	Parietal	—	Cerebellum	Frontal periventricular
2	—	—	Frontal, cerebellum	—
3	Frontal	—	Frontal, cerebellum	Pons
4	—	—	—	—
5	Frontal, parietal	+	Frontoparietal	—
6	Frontal, parietal, occipital	—	Insula	Temporal
7	—	—	Pons	—
8	Frontal, temporal	—	Frontal	—
9	—	—	Frontal, temporal	—
10	Frontal, parietal, temporal, occipital	+	Frontal, parietal	—
11	Temporal, cerebellar peduncle	+	Frontal, temporal, cerebellum	—
12	Cerebellum, cerebellar peduncle, frontal brain stem	+	—	—
13	Frontal, temporal	—	Frontal, temporal	—
14	Frontal	—	Frontal	—

Note:— indicates absent; +, present.

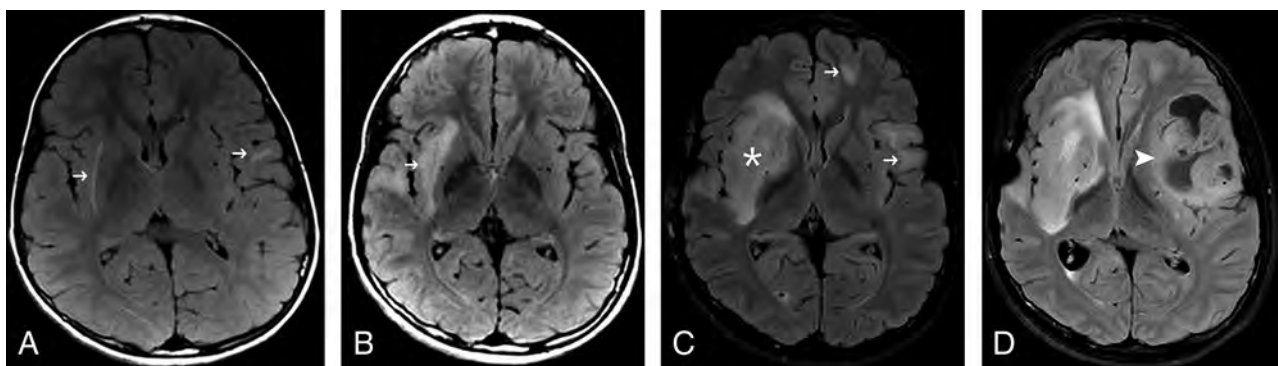


FIG 3. Surveillance brain MR imaging studies of a boy with CMMRD (patient 2). Serial T2-FLAIR imaging shows nonspecific subcortical hyperintensities (arrows) slowly increasing in size (10 years of age, A; 15 years of age, B). At 18 years of age (C), there is an infiltrative lesion involving the right insula (asterisk) and base of the right frontal lobe. Biopsy results indicated diffuse astrocytoma (WHO II). Three months later (D), marked increase in the left frontotemporal lesion was obvious along with central necrosis (arrowhead). This lesion was resected, and pathologic testing indicated glioblastoma.

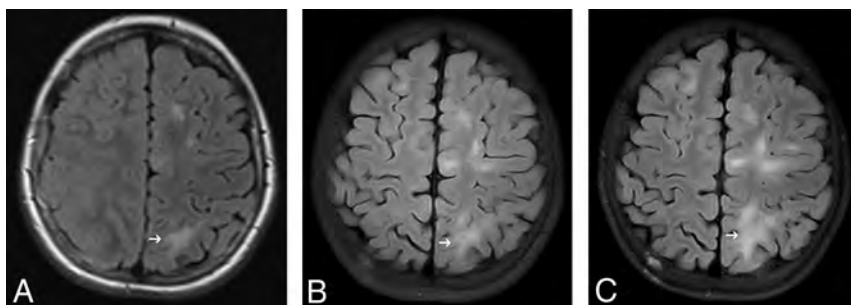


FIG 4. MR images of a girl with CMMRD (patient 6) and glioblastoma (not shown). A gradual increase in frontoparietal subcortical T2-FLAIR hyperintensities (arrows) is noted during 2 years of surveillance (7 years of age, A; 8 years of age, B; and 9 years of age, C).

bellum and pons) or in both locations. No spatial association was found between DVAs and other parenchymal abnormalities (overt brain tumors, subcortical T2/T2-FLAIR hyperintensities) (Fig 5).

these were not considered to be primary cavernous hemangiomas. Not all patients had T2* or SWI sequences included in the MR imaging protocol.

These findings were seen on initial imaging with no new DVAs identified during follow-up.

Non-Therapy-Related Cavernous Hemangioma. Popcorn-like nonenhancing lesions with prominent T2*/SWI blooming artifacts suggestive of cavernous hemangiomas were identified in 3 of 14 patients (21%). These findings were seen on initial imaging with no new nontherapy-induced cavernomas identified during follow-up. After radiation therapy, several patients showed multiple foci of microhemorrhage, yet

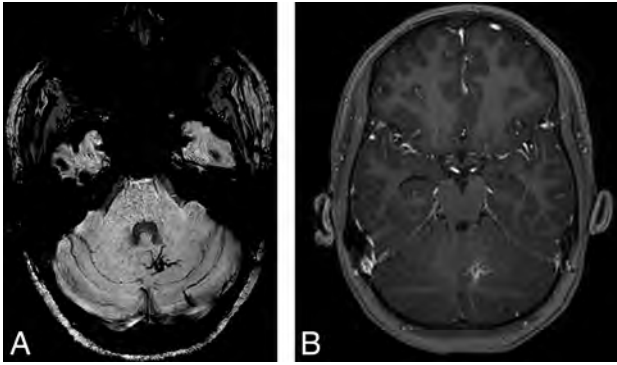


FIG 5. Left cerebellar developmental venous anomaly seen in patient 1, as shown by axial SWI (A) and postcontrast T1 imaging (B).

Focal Areas of Signal Intensity. Four patients showed nonenhancing T2/T2-FLAIR hyperintense white matter lesions within the supratentorial deep gray matter nuclei (globus pallidus and thalamus), similar to patchy T2/T2-FLAIR hyperintensities commonly seen in neurofibromatosis type 1 (Fig 6). All 4 patients were younger than 15 years of age. All lesions persisted during follow-up.

DISCUSSION

Here, we report the neuroimaging findings in a series of patients with CMMRD. As previously published, brain tumors, particularly high-grade gliomas, are common in patients with CMMRD.¹⁴ In children, high-grade gliomas are usually primary, rarely originating from pre-existing low-grade tumors.¹⁵ Recent data based on molecular abnormalities found in patients with cancer predisposition syndromes suggest that high-grade gliomas in that setting might be secondary (ie, following malignant transformation of low-grade gliomas),¹⁶ as seen typically in young adult patients. Subcortical T2/T2-FLAIR hyperintensities described in patients with CMMRD in our study might support these findings because some of the high-grade gliomas eventually emerged from these lesions, possibly as a result of the relentlessly increasing mutation burden during the disease course. Therefore, we hypothesize that accumulation of somatic mutations in patients with CMMRD leads to these low-grade/precancerous lesions, similar to low-grade and dysplastic polyps found on gastrointestinal endoscopy in patients with CMMRD, which may evolve to malignancies. Unfortunately, histopathologic analysis of these ill-defined subcortical lesions is lacking because no biopsies of those lesions were performed in our patients.

High-grade glioma was the most prevalent brain tumor in our patients with CMMRD, as in previous reports.¹⁴ Nevertheless, low-grade gliomas were not uncommon (found in 21% of our patient cohort). Supratentorial embryonal tumors, which have been reported previously¹⁷ in patients with CMMRD, were not found in our series. The median age of our patients at diagnosis of brain tumors was 9.3 years (range, 5–14 years of age), as has been previously reported.¹⁷ The imaging characteristics of various brain tumors in our series resembled those in brain tumors in patients without CMMRD. Nevertheless, recent genetic evaluation of pediatric brain tumors shows that in patients with CMMRD, mutations in mismatch repair genes may lead to

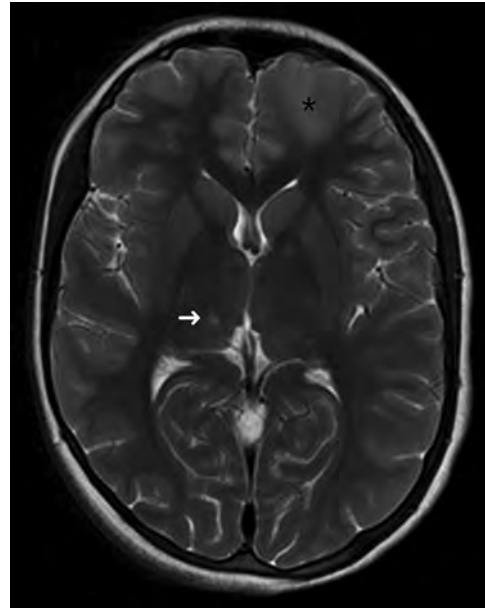


FIG 6. T2-weighted image of a diffuse astrocytoma in the left frontal lobe (asterisk) of a 14-year-old girl (patient 5). Ovoid nonenhancing hyperintense foci are noted in the right thalamus (arrow) and left globus pallidus, similar to focal areas of signal intensities commonly seen in patients with neurofibromatosis type 1.

accumulation of multiple somatic mutations, resulting in considerably higher tumoral mutation burden than that in non-CMMRD childhood gliomas.¹⁸

In humans, most CMMRD cases are due to *MSH6* or *PMS2* mutation. Similarly, in our cohort, 12 patients had *MSH6* mutations (86%) and 2 (14%) had *PMS2* mutations. Individuals with these mutations in the context of Lynch syndrome exhibit low penetrance, which might partially explain the negative family history in our cohort.^{4,12} Additionally, patients with *PMS2* and *MSH6* mutations have a higher reported prevalence of brain tumors than do those with other mismatch repair mutations, and these patients are more likely to survive their first tumor and develop a metachronous tumor.²

Individuals with CMMRD frequently display neurofibromatosis type 1 stigmata, such as café au lait spots. All the patients in our cohort presented with café au lait spots. Brain lesions similar to the focal areas of signal intensity, commonly seen in prepubertal patients with neurofibromatosis type 1, were identified in 4 of our patients. All 4 showed lesions before 15 years of age, in a timeline similar to that of neurofibromatosis type 1,¹⁹ yet all persisted during the available follow-up. The associations between CMMRD and neurofibromatosis type 1 have been described by Wimmer et al,³ and a presumed explanation is that common somatic mutations in the *neurofibromin 1* (*NF1*) gene are acquired as a consequence of the mismatch repair malfunction.

Structural brain abnormalities were reported by Baas et al²⁰ in a case series of 4 patients with CMMRD with agenesis of the corpus callosum and gray matter heterotopia. Such malformative abnormalities were not found in our cohort.

Additional non-neoplastic brain MR imaging findings in CMMRD include DVAs and nontherapy-induced cavernous hemangiomas, as have been recently reported.^{20,21} Remarkably, 12 of

our 14 patients had DVAs (typically multiple DVAs), indicating a considerably higher prevalence than that reported in healthy populations (6%–7%).²² Because DVAs are considered a normal variant, under-reporting is probably common. However, patients with primary brain tumors have a higher prevalence of DVAs than the healthy population (10.2% versus 5.3%, respectively).²³ In our series of children with brain tumors and CMMRD, there was no apparent association between the tumor location and the location of the DVA. DVAs have a well-recognized association with cavernomas,²⁴ which was also noted in some of our patients. The pathogenesis of these vascular anomalies is not clearly understood. DVAs might arise as a response to compromise of the normal venous drainage by stenosis, thrombosis, or maldevelopment. Cavernomas might occur in both sporadic and familial forms. Patients with familial cavernomas typically have multiple malformations. Familial cavernomas have been linked to 3 specific cerebral cavernous malformation genes KRIT1/CCM1 (Krev interaction trapped 1), MGC4607/CCM2 (cerebral cavernous malformation 2), or PDCD10/CCM3 (programmed cell death protein 10). Almost 80% of patients with the hereditary form have a heterozygous germline mutation in 1 of these 3 genes. Development of sporadic cavernomas is thought to be secondary to microhemorrhages and angiogenic growth factor activation in a cause-and-effect relationship with adjacent DVA.^{23,25,26} Recognizing vascular abnormalities in the brain, particularly DVAs, is important; hence, they seem to contribute to a potentially suggestive “imaging gestalt” in children with CMMRD.

CMMRD should be clinically suspected in children with brain tumors who have café au lait spots, a family history of Lynch syndrome, or a sibling with childhood cancer manifesting as brain tumors or lymphoproliferative malignancies. Because high-grade gliomas are uncommon in neurofibromatosis type 1, any child with a clinical suspicion of this syndrome and a high-grade tumor should also be evaluated for CMMRD.¹⁷ Because it is an autosomal recessive syndrome, consanguinity is a common feature, as seen in 3 of the families included in our study. The final confirmation of the diagnosis of CMMRD should come from the determination of the causative biallelic mutations of the patient.

Because penetrance is high, reaching >90% at 20 years of age and almost all patients develop cancer as children, surveillance is crucial. Consensus surveillance protocols were recently published, which advocate brain MR imaging every 6 months following diagnosis.⁸ In addition to screening for brain tumors, close attention to nonspecific subcortical T2/T2-FLAIR hyperintensities is important, as shown in the current study, because those lesions have the potential for malignant neoplastic transformation with time. Nuclear medicine studies including ¹¹C-methionine PET and ¹⁸F-fluoroethyl-L-tyrosine PET have increased sensitivity to detect insidiously developing brain tumors.²⁷ This was also demonstrated in another hereditary cancer predisposition syndrome, L-2-hydroxyglutaric aciduria;²⁸ hence, it could be a useful adjunct to any MR imaging study, raising the possibility of neoplastic transformation of the subcortical T2 hyperintensities. Additional surveillance imaging studies include annual whole-body MR imaging beginning at 6 years of age (this should not replace a dedicated brain MR imaging protocol), annual abdominal sonography beginning at

1 year of age, and annual transvaginal sonography beginning at 20 years of age.⁸

The principal limitation of this study is the relatively small number of patients in our cohort. However, the frequency of the cardinal MR imaging findings, such as cerebral neoplasms, nonspecific subcortical T2 hyperintensities, DVAs, cavernous angiomas, and focal areas of signal intensity, is quite compelling. Further assessment of larger patient cohorts is needed to define and describe the full spectrum of neuroimaging phenotypic features of CMMRD. Additionally, advanced imaging techniques (diffusion- and perfusion-weighted imaging, spectroscopy, and so forth) and/or nuclear medicine (PET) studies are needed to improve our understanding of the natural course of potentially precancerous nonspecific subcortical white matter signal abnormalities for further characterization. Likewise, another limitation is the lack of histopathologic correlation of the nonspecific subcortical T2/T2-FLAIR hyperintensities.

CONCLUSIONS

On brain imaging, patients with CMMRD present with overt tumors and several nonspecific findings, some of which might be precancerous; however, others, including non-neoplastic vascular anomalies, may also contribute to a suggestive imaging “gestalt.” Awareness of these imaging findings is important at both the initial diagnostic imaging evaluation of children with suspected brain tumors and at that of those known to carry the genetic predisposition and requiring regular surveillance studies because early detection of brain neoplasms may improve clinical outcomes.

Disclosures: Amar Gajjar—UNRELATED: Consultancy: Roche Pharmaceuticals. Kim E. Nichols—UNRELATED: Grants/Grants Pending: Incyte, Comments: small research grant to support work ongoing in basic laboratory.

REFERENCES

- Jiricny J. **The multifaceted mismatch-repair system.** *Nat Rev Mol Cell Biol* 2006;7:335–46 CrossRef Medline
- Wimmer K, Kratz CP. **Constitutional mismatch repair-deficiency syndrome.** *Haematologica* 2010;95:699–701 CrossRef Medline
- Wimmer K, Rosenbaum T, Messiaen L. **Connections between constitutional mismatch repair deficiency syndrome and neurofibromatosis type 1.** *Clin Genet* 2017;91:507–19 CrossRef Medline
- Durno C, Boland CR, Cohen S, et al. **Recommendations on Surveillance and Management of Biallelic Mismatch Repair Deficiency (BMMRD) Syndrome: A Consensus Statement by the US Multi-Society Task Force on Colorectal Cancer.** *Gastroenterology* 2017;152:1605–14 CrossRef Medline
- Wimmer K, Kratz CP, Vasen HF, et al; EU-Consortium Care for CMMRD (C4CMMRD). **Diagnostic criteria for constitutional mismatch repair deficiency syndrome: suggestions of the European Consortium “Care for CMMRD” (C4CMMRD).** *J Med Genet* 2014; 51:355–65 CrossRef Medline
- Vasen HF, Ghorbanoghi Z, Bourdeaut F, et al; EU-Consortium Care for CMMRD-D (C4CMMRD-D). **Guidelines for surveillance of individuals with constitutional mismatch repair-deficiency proposed by the European Consortium “Care for CMMRD-D” (C4CMMRD-D).** *J Med Genet* 2014;51:283–93 CrossRef Medline
- Johannesma PC, van der Klift HM, van Grieken NC, et al. **Childhood brain tumours due to germline bi-allelic mismatch repair gene mutations.** *Clin Genet* 2011;80:243–55 CrossRef Medline
- Tabori U, Hansford JR, Achatz MI, et al. **Clinical management and tumor surveillance recommendations of inherited mismatch**

- repair deficiency in childhood. *Clin Cancer Res* 2017;23:e32–37 CrossRef Medline
9. Aronson M, Gallinger S, Cohen Z, et al. **Gastrointestinal findings in the largest series of patients with hereditary biallelic mismatch repair deficiency syndrome: report from the international consortium.** *Am J Gastroenterol* 2016;111:275–84 CrossRef Medline
 10. Kim B, Tabori U, Hawkins C. **An update on the CNS manifestations of brain tumor polyposis syndromes.** *Acta Neuropathol* 2020 Jan 22. [Epub ahead of print] CrossRef Medline
 11. Bouffet E, Larouche V, Campbell BB, et al. **Immune checkpoint inhibition for hypermutant glioblastoma multiforme resulting from germline biallelic mismatch repair deficiency.** *J Clin Oncol* 2016;34:2206–01 CrossRef Medline
 12. Q Rana H, Syngal S. **Biallelic mismatch repair deficiency: management and prevention of a devastating manifestation of the Lynch syndrome.** *Gastroenterology* 2017;152:1254–57 CrossRef Medline
 13. Shinagare AB, Giardino AA, Jagannathan JP, et al. **Hereditary cancer syndromes: a radiologist's perspective.** *AJR Am J Roentgenol* 2011; 197:W1001–07 CrossRef Medline
 14. Bakry D, Aronson M, Durno C, et al. **Genetic and clinical determinants of constitutional mismatch repair deficiency syndrome: report from the Constitutional Mismatch Repair Deficiency Consortium.** *Eur J Cancer* 2014;50:987–96 CrossRef Medline
 15. Broniscer A, Baker SJ, West AN, et al. **Clinical and molecular characteristics of malignant transformation of low-grade glioma in children.** *J Clin Oncol* 2007;25:682–89 CrossRef Medline
 16. Paugh BS, Qu C, Jones C, et al. **Integrated molecular genetic profiling of pediatric high-grade gliomas reveals key differences with the adult disease.** *J Clin Oncol* 2010;28:3061–68 CrossRef Medline
 17. Michaeli O, Tabori U. **Pediatric high-grade gliomas in the context of cancer predisposition syndromes.** *J Korean Neurosurg Soc* 2018;61:319–332. CrossRef Medline
 18. Shlien A, Campbell BB, de Borja R, et al; Biallelic Mismatch Repair Deficiency Consortium. **Combined hereditary and somatic mutations of replication error repair genes result in rapid onset of ultra-hypermutated cancers.** *Nat Genet* 2015;47:257–62 CrossRef Medline
 19. Itoh T, Magnaldi S, White RM, et al. **Neurofibromatosis type 1: the evolution of deep gray and white matter MR abnormalities.** *AJNR Am J Neuroradiol* 1994;15:1513–19 Medline
 20. Baas AF, Gabbett M, Rimac M, et al. **Agenesis of the corpus callosum and gray matter heterotopia in three patients with constitutional mismatch repair deficiency syndrome.** *Eur J Hum Genet* 2013;21:55–61 CrossRef Medline
 21. Shiran SI, Ben-Sira L, Elhasid R, et al. **Multiple brain developmental venous anomalies as a marker for constitutional mismatch repair deficiency syndrome.** *AJNR Am J Neuroradiol* 2018;39:1943–46 CrossRef Medline
 22. Gökçe E, Acu B, Beyhan M, et al. **Magnetic resonance imaging findings of developmental venous anomalies.** *Clin Neuroradiol* 2014;24:135–43 CrossRef Medline
 23. Jones BV, Linscott L, Koberlein G, et al. **Increased prevalence of developmental venous anomalies in children with intracranial neoplasms.** *AJNR Am J Neuroradiol* 2015;36:1782–85 CrossRef Medline
 24. Meng G, Bai C, Yu T, et al. **The association between cerebral developmental venous anomaly and concomitant cavernous malformation: an observational study using magnetic resonance imaging.** *BMC Neurol* 2014;14:50 CrossRef Medline
 25. Riant F, Bergametti F, Ayrignac X, et al. **Recent insights into cerebral cavernous malformations: the molecular genetics of CCM.** *FEBS J* 2010;277:1070–75 CrossRef Medline
 26. Linscott LL, Leach JL, Jones BV, et al. **Developmental venous anomalies of the brain in children – imaging spectrum and update.** *Pediatr Radiology* 2016;46:394–406, quiz 391–93 CrossRef Medline
 27. Treglia G, Muoio B, Trevisi G, et al. **Diagnostic performance and prognostic value of PET/CT with different tracers for brain tumors: a systematic review of published meta-analyses.** *Int J Mol Sci* 2019;20 CrossRef Medline
 28. Patay Z, Orr BA, Shulkin BL, et al. **Successive distinct high-grade gliomas in L-2-hydroxyglutaric aciduria.** *J Inherit Metab Dis* 2015;38:273–77 CrossRef Medline

Utility of Pre-Hematopoietic Cell Transplantation Sinus CT Screening in Children and Adolescents

J.H. Harreld, R.A. Kaufman, G. Kang, G. Maron, W. Mitchell, J.W. Thompson, and A. Srinivasan



ABSTRACT

BACKGROUND AND PURPOSE: The clinical benefit of pre-hematopoietic cell transplantation sinus CT screening remains uncertain, while the risks of CT radiation and anesthesia are increasingly evident. We sought to re-assess the impact of screening sinus CT on pretransplantation patient management and prediction of posttransplantation invasive fungal rhinosinusitis.

MATERIALS AND METHODS: Pretransplantation noncontrast screening sinus CTs for 100 consecutive patients (mean age, 11.9 ± 5.5 years) were graded for mucosal thickening (Lund-Mackay score) and for signs of noninvasive or invasive fungal rhinosinusitis (sinus calcification, hyperattenuation, bone destruction, extrasinus inflammation, and nasal mucosal ulceration). Posttransplantation sinus CTs performed for sinus-related symptoms were similarly graded. Associations of Lund-Mackay scores, clinical assessments, changes in pretransplantation clinical management (additional antibiotic or fungal therapy, sinonasal surgery, delayed transplantation), and subsequent development of sinus-related symptoms or invasive fungal rhinosinusitis were tested (exact Wilcoxon rank sums, Fisher exact test, significance $P < .05$).

RESULTS: Mean pretransplantation screening Lund-Mackay scores ($n = 100$) were greater in patients with clinical symptoms (8.07 ± 6.00 versus 2.48 ± 3.51 , $P < .001$) but were not associated with pretransplantation management changes and did not predict posttransplantation sinus symptoms ($n = 21$, $P = .47$) or invasive fungal rhinosinusitis symptoms ($n = 2$, $P = .59$).

CONCLUSIONS: Pre-hematopoietic cell transplantation sinus CT does not meaningfully contribute to pretransplantation patient management or prediction of posttransplantation sinus disease, including invasive fungal rhinosinusitis, in children. The risks associated with CT radiation and possible anesthesia are not warranted in this setting.

ABBREVIATIONS: ENT = ear, nose, and throat; GVHD = graft versus host disease; HCT = hematopoietic cell transplantation; IFRS = invasive fungal rhinosinusitis

Due to prolonged immunosuppression, children undergoing hematopoietic cell transplantation (HCT) are at increased risk of opportunistic infections, including potentially lethal invasive fungal rhinosinusitis (IFRS).¹⁻⁵ Children at St. Jude Children's Research Hospital, therefore, undergo rigorous pretransplantation evaluation, including ear, nose, and throat

(ENT) examination, infectious disease risk assessment, fungal serologies, and noncontrast sinus CT.

However, the clinical utility of screening sinus CT remains unclear, and the practice is not universal. According to the American Academy of Pediatrics and the American College of Radiology, uncomplicated sinusitis should be a clinical diagnosis,^{6,7} and several large studies ($n \geq 100$) have failed to identify pre-HCT imaging features predictive of post-HCT sinusitis.⁸⁻¹⁰ Fewer studies have evaluated the contribution of pretransplantation CT to patient management or prediction of posttransplantation IFRS. A small study in adults found that screening sinus CT did not contribute to a pretransplantation diagnosis or management or predict posttransplantation sinusitis or IFRS, but it was limited by a small sample size.¹¹ A study of 187 children reported an association between pre-HCT sinus CT findings and management changes, but while 119 (64%) had abnormal sinus CT findings, only 29 had symptoms and were treated, suggesting symptoms, not imaging, drove treatment.¹²

Received June 3, 2019; accepted after revision March 3, 2020.

From the Departments of Diagnostic Imaging (J.H.H., R.A.K.), Biostatistics (G.K.), Infectious Diseases (G.M.), Bone Marrow Transplantation and Cellular Therapy (W.M., A.S.), and Surgery (J.W.T.), St. Jude Children's Research Hospital, Memphis, Tennessee; and Department of Otolaryngology (J.W.T.), University of Tennessee Health Sciences Center, Memphis, Tennessee.

This work was supported, in part, by grant No. CA21765 from the National Cancer Institute and by the American Lebanese and Syrian Associated Charities.

Please address correspondence to Julie H. Harreld, MD, Department of Diagnostic Imaging, St. Jude Children's Research Hospital, 262 Danny Thomas Place, MS 220, Memphis, TN 38105; e-mail: Julie.harreld@stjude.org

Indicates open access to non-subscribers at www.ajnr.org

<http://dx.doi.org/10.3174/ajnr.A6509>

While the benefits of pre-HCT sinus CT remain unclear, the risks associated with sinus CT are well-established and include a low-but-real risk of radiation-induced cancers^{13,14} and early cataract formation.¹⁵ Evidence is also emerging that anesthesia, required by some children to complete CT, may negatively impact cognitive development.^{16,17} On the other hand, advances in fungal prophylaxis have significantly reduced the incidence of invasive fungal infections in immunocompromised children.¹⁸

Given these potential shifts in the risk-benefit ratio, we sought to re-evaluate the clinical utility of pre-HCT screening sinus CT for IFRS risk assessment and its role in pre-HCT management of pediatric patients.

MATERIALS AND METHODS

With institutional review board approval and waiver of consent, imaging, clinical, ENT risk assessment, and laboratory data were prospectively recorded for 100 sequential participants who had pre-HCT screening sinus CT at our institution between June 2015 and April 2017. A sample size of 100 was chosen to detect at least 1 case of IFRS, which has an incidence of approximately 2% in patients with hematologic disorders.² The patients' medical records were reviewed for microbiologic diagnosis of IFRS for at least 100 days posttransplantation. With additional institutional review board approval and waiver of consent, medical records were retrospectively reviewed for subsequent clinical, imaging, and laboratory data until the patient's death or November 2017.

Clinic and Laboratory

Recorded data included primary diagnosis; transplant donor type; absolute neutrophil count at imaging; pretransplantation imaging indication; development of posttransplantation graft versus host disease (GVHD) grades II–IV (moderate-to-life-threatening); pretransplantation galactomannan (*Aspergillus* antigen); sinonasal symptoms (rhinorrhea, congestion, nasal/facial pain, swelling, visible nasal lesion), or fever at pretransplantation evaluation; and changes to pretransplantation management (changes in fungal prophylaxis regimen, addition of antibiotics, sinonasal operation, or delay of HCT) attributable to screening sinus CT.

ENT pretransplantation risk assessment included visualization of the nasal septum, palate, and back of throat under magnification and complete allergy and sinusitis histories. These findings were summarized as “at-risk” or “not at-risk” for IFRS.

For patients requiring post-HCT sinus imaging for symptoms, we recorded symptoms, galactomannan serologies, endoscopy findings, fungal organism (if applicable), and consecutive days of neutropenia (absolute neutrophil count < 500/mm³) immediately preceding imaging. The date of acquisition of tissue positive for IFRS by microbiologic/pathologic examination was considered the date of diagnosis.

Imaging

CTs were axially acquired with a section thickness of ≤ 2.5 mm on a LightSpeed VCT or Revolution CT scanner (GE Healthcare) with bone and soft-tissue reconstructions. The average effective dose for all ages was ~ 0.8 mSv; the eye/lens dose was 0.7–1.2 mGy.

Images were reviewed in consensus by a board-certified pediatric radiologist with 40 years' experience (R.A.K.) and a board-certified neuroradiologist with 10 years' experience (J.H.H.) for the presence or absence of bone destruction, extrasinus inflammation, and nasal mucosal ulceration, associated with IFRS.^{4,19–22} Because noninvasive fungal disease could theoretically predispose to IFRS with pre-HCT conditioning/immunodepletion, the presence of calcifications and sinus hyperdensity was also noted.²³

Each anterior and posterior ethmoid, maxillary, frontal, and sphenoid sinus was graded as clear = 0, partially opacified = 1, or completely opacified = 2; each ostiomeatal unit was graded as clear = 0 or occluded = 2; and the numbers were added per Lund and Mackay.²⁴ To account for age-related differences in sinus development, we calculated an adjusted Lund-Mackay score as²⁵

Adjusted Lund Score =

$$\text{Raw score} \times \frac{24}{\text{Maximum Lund for No. Pneumatized Sinuses}}$$

Statistical Analysis

Sinus CT scores, laboratory values, symptoms, changes in management, and ENT risk were compared using the Fisher exact test or the Pearson χ^2 test for categorical variables and a 2-sample *t* test or (exact) Wilcoxon rank sum test for continuous variables, based on the normality assumption. The Lund-Mackay scores between pre- and posttransplantation were compared using a 1-sample *t* test or Wilcoxon signed rank test, depending on the normality assumption. All *P* values are 2-sided and were considered statistically significant if $< .05$. Statistical analyses were performed with R-3.6.1 (R statistical and computing software; <http://www.r-project.org/>).

RESULTS

One hundred participants (60 males, 40 females; 8 months to 24 years of age; mean, 11.9 ± 5.5 years; males, 11.6 ± 5.7 years; females, 12.5 ± 5.2 years) had screening sinus CT an average of 24.6 ± 9.6 days before transplantation for IFRS risk assessment. Patient characteristics, imaging, and clinical findings are summarized in Table 1.

Follow-up for survivors ($n = 82$) ranged from 189 to 889 days post-HCT. During the follow-up period, 9 patients died of relapsed disease from 28 to 519 days post-HCT. Nine died of complications between 23 and 557 days post-HCT, none related to sinus disease.

Clinical Symptoms and Provided Imaging Indications

At the time of the screening sinus CT, 18 patients had sinonasal symptoms documented in the medical record: Thirteen had rhinorrhea, 2 had nasal congestion, and 3 had both. No patients had overt signs or symptoms of IFRS or complicated rhinosinusitis—localized facial pain or inflammation, nasal ulcer/eschar, fever, or altered mental status—documented in the medical record at the time of CT.

The provided indication for 98/100 screening sinus CTs was “pretransplantation evaluation.” Symptoms mentioned for 2 patients did not match the medical record, possibly being erroneous or outdated. One request indicated fever without localizing symptoms, though the clinical examination documented congestion and rhinorrhea without fever. The other request indicated possible periorbital edema, which was not present on CT or the physical examination. On examination, the patient had clear rhinorrhea and nasal wash positive for enterovirus/rhinovirus and was determined eligible for transplantation the same day.

Pretransplantation Screening and Management

Mucosal thickening was present (Lund-Mackay score of ≥ 1) at screening in 66/100 patients, including 48/82 (58.5%) asymptomatic patients and all 18 symptomatic patients. No asymptomatic patients received antibiotics based on sinus CT.

The Lund-Mackay score was higher for patients with symptoms documented in the medical record ($P < .0001$, Table 2). Patients with clinical symptoms were more likely to be treated

with antibiotics (5/18 with symptoms versus 0/82 asymptomatic, $P = .0001$). The Lund-Mackay scores were greater for symptomatic patients who received antibiotics ($n = 5$, 12.8 ± 5.72) compared with those who did not ($n = 13$, 6.25 ± 5.25), but this finding did not reach statistical significance ($P = .058$) (Table 2).

All 5 patients treated with pretransplantation antibiotics had clinical sinusitis. Nasal wash was positive for enterovirus/rhinovirus in 3/5 (60%). Two received antibiotics primarily for pneumonia and secondary coverage of possible bacterial sinusitis. None developed IFRS before or after transplantation.

One patient had a smooth nasal septal perforation, which was negative for IFRS at screening endoscopy. Two others had sinus calcifications. All 3 were asymptomatic, and none developed IFRS or symptoms posttransplantation. No patients (0/100) had sinus hyperdensity, nasal ulceration, extrasinus inflammation, or bone destruction at screening.

No patients underwent a pretransplantation sinus operation, received new antifungal therapy, or had HCT delayed as a result of screening sinus CT.

Table 1: Patient characteristics

Characteristics	
No.	100
Male	60
Female	40
Age (mean) (yr)	11.9 \pm 5.5
Primary diagnosis (No.) (%)	
Hematologic malignancy	65, 65%
Acute myeloid leukemia	34, 34%
Acute lymphoblastic leukemia	17, 17%
Hodgkin lymphoma	8, 8%
Myelodysplastic syndrome	5, 5%
Anaplastic large-cell lymphoma	1, 1%
Hematologic disorder	5, 5%
Severe aplastic anemia	3, 3%
Sickle cell disease	2, 2%
Solid tumor	28, 28%
Neuroblastoma	15, 15%
Ewing sarcoma	9, 9%
Germ cell tumor	3, 3%
Desmoplastic small round cell tumor	1, 1%
Immune disorder	2, 2%
Severe combined immunodeficiency	1, 1%
Wiskott-Aldrich syndrome	1, 1%
Transplant donor (No.) (%)	
Allogenic	66, 66%
Autologous	34, 34%
Disease status at transplantation (No.) (%)	
Complete remission	82, 82%
Active disease	18, 18%
T-cell depletion (No.) (%)	2, 2%
GVHD II–IV (No.) (%)	15, 15%

Table 2: Pretransplantation sinus CT Lund-Mackay scores, sinonasal symptoms, and management

	No. (Frequency)	Pre-HCT Lund-Mackay Score (Mean)	P Value
All at screening	100 (100%)	3.48 \pm 4.58	
No symptoms at screening	82 (82%)	2.48 \pm 3.51	<.001
Symptoms at screening	18 (18%)	8.07 \pm 6.00	
With symptoms, received antibiotics	5 (28%)	12.80 \pm 5.72	.058
With symptoms, no antibiotics	13 (72%)	6.25 \pm 5.25	

Posttransplantation Imaging

Symptoms prompted posttransplantation evaluation of 21 patients whose Lund-Mackay scores had increased (7.43 ± 6.36) from baseline screening CT (3.87 ± 4.99 ; $P = .007$).

Two of the 21 (9.5%) symptomatic patients or 2% (2/100) of the entire cohort developed IFRS, 615 days (*Bipolaris* spp) and 248 days (*Fusarium* spp) posttransplantation. Pretransplantation, neither had symptoms. These 2 patients had lower Lund-Mackay scores (4.5 ± 3.54) than symptomatic patients without IFRS ($n = 19$, 7.74 ± 6.57), but this finding was not statistically significant ($P = .59$).

Prediction of Posttransplantation Sinus Disease

The degree of mucosal thickening (Lund-Mackay score) on pretransplantation CT did not predict posttransplantation symptoms ($P = .47$) or posttransplantation IFRS ($P = .58$) (Table 3).

The pretransplantation test for galactomannan was negative in all patients at screening. The mean absolute neutrophil count at screening was 2510 ± 5568 (range, 0–50,200). There was no association between screening absolute neutrophil count and pre-HCT symptoms, post-HCT symptoms, or post-HCT IFRS. Disease status, transplant donor, T-cell depletion, and posttransplantation GVHD grades II–IV did not predict development of IFRS ($P = 1$ for all; Table 4).

Of 96 participants evaluated by ENT, 29 were considered at risk for IFRS. ENT risk assessment did not predict development of IFRS ($P = .61$). There was no association between the Lund-Mackay score and the ENT risk stratum ($P = .99$).

The presence of symptoms before transplantation ($n = 18$) did not predict posttransplantation symptoms ($n = 21$); only 3 patients were symptomatic both before and after transplantation ($P = .62$).

DISCUSSION

In this study, we found no association between pre-HCT screening sinus CT and changes in pretransplantation

Table 3: Pre-HCT Lund-Mackay scores versus posttransplantation sinus outcomes

	No. (Frequency)	Pre-HCT Lund-Mackay Score (Mean)	P Value
All at screening	100 (100%)	3.48 ± 4.58	
No post-HCT symptoms	79 (79%)	3.38 ± 4.49	.47
Post-HCT symptoms	21 (21%)	3.86 ± 5.00	
Post-HCT symptoms, IFRS	2 (9.5%)	4.00 ± 4.24	.58
Post-HCT symptoms, no IFRS	19 (90.5%)	3.84 ± 5.17	

Table 4: Clinical findings at screening for patients who did and did not develop IFRS after transplantation

	All at Pre-HCT Screen	No Post-HCT IFRS	Post-HCT IFRS	P Value
No.	100	98	2	
ENT risk estimate (No.) (frequency)				
At risk	29 (29%)	28 (29%)	1 (50%)	.61
Low risk	67 (67%)	62 (63%)	1 (50%)	
Not evaluated	4 (4%)	8 (8%)	0	
ANC at imaging (mean)	2510 ± 5568	2524 ± 5622	1800 ± 1697	.86
Transplant donor (No.) (frequency)				
Allogenic	66 (66%)	65 (66%)	1 (50%)	1
Autologous	34 (34%)	33 (34%)	1 (50%)	
Disease status at transplantation (No.) (frequency)				
Complete remission	82 (82%)	80 (80%)	2 (100%)	1
Active disease	18 (18%)	18 (18%)		
T-cell depletion (No.) (frequency)	2 (2%)	2 (2%)	0	1
GVHD II–IV (No.) (frequency)	15 (15%)	15 (15%)	0	1

Note:—ANC indicates absolute neutrophil count.

patient management, including the addition of antibiotics or changes to the antifungal prophylaxis regimen or transplantation schedule. Like other authors,^{9,10} we found no association between pretransplantation Lund-Mackay scores and the development of posttransplantation sinus symptoms or IFRS. Unlike Won et al,⁹ we did not find pre-HCT symptoms predictive of post-HCT symptoms. In our study, clinical and laboratory features, including pretransplantation ENT evaluation, also failed to predict posttransplantation sinusitis and IFRS. Our findings are in agreement with adult studies by Thompson et al⁸ ($n = 100$) and Moeller et al¹¹ ($n = 71$), which found no benefit at all for pre-HCT sinus screening. A similar study of 1589 adult patients with kidney transplants found no increase in the prevalence of rhinosinusitis posttransplantation, concluding that routine pretransplantation sinonasal evaluation is not warranted.²⁶

The origins and evidence supporting pre-HCT screening sinus CT are unclear. In a 1995 study, Shibuya et al²⁷ recommended screening CT on the basis of 33/107 pretransplantation patients with clinical sinusitis and imaging abnormalities, despite imaging only symptomatic patients. At our institution, the practice may date back to a 1982 article by Bartley et al,²⁸ prompting routine screening abdominal CT for detection of hepatosplenic fungal abscesses, to which chest and sinus CT were subsequently added. Subsequent work by Kasow et al¹² found no utility in routine chest or abdominal CT in asymptomatic patients but suggested that sinus CT drove changes in management. However, supporting data were sparse, and the number of treated and symptomatic patients precisely matched ($n = 29/187$, 15.5%), suggesting a clinical basis for treatment. In a small ($n = 51$) study

in 2000, Billings et al²⁹ found that children with severe sinus disease on pre-bone marrow transplantation CT were more likely to have sinusitis after bone marrow transplantation and reported a trend toward decreased survival in these children, but these findings were not statistically significant ($P = .750$). In a study of 252 adults, Won et al⁹ found that asymptomatic radiographic sinus abnormalities did not increase the risk of post-HCT sinusitis, but they also reported a trend toward reduction of post-HCT sinusitis with the treatment of asymptomatic abnormalities, which did not reach statistical significance ($P = .057$). To our knowledge, no investigators have identified pretransplantation imaging predictors of IFRS.

It has been suggested that CT might be a surrogate for inflammatory symptoms in immunocompromised patients, who may not be able to mount an inflammatory response.^{27,30} However, evidence shows that clinical sinusitis and imaging severity go hand in hand, even in immunocompromised children.^{10,29,30} This was also true in our study, in which Lund-Mackay scores were greater in the presence of symptoms. The American Academy of Pediatrics and American College of Radiology guidelines dictate that diagnosis and treatment of acute sinusitis should be clinical, with imaging reserved for suspicion of orbital or CNS complications.^{6,7} IFRS typically presents with a combination of fever, facial pain, nasal congestion, headache, eye symptoms, and/or facial swelling, which should also prompt imaging, and likely endoscopy.^{3-5,31} On pretransplantation physical examination, none of the 100 patients in our series had findings suggestive of orbital, CNS, or fungal involvement warranting imaging evaluation.

On the other hand, isolated radiographic abnormalities, common in asymptomatic children,³² may be confusing or lead to overtreatment.³³ In our series, 58.8% of 82 asymptomatic children had mucosal thickening on pre-HCT CT. As suggested by other authors,^{9,30} a thorough sinus history and examination are likely to be more meaningful than CT, without the associated risk of radiation-induced cancers and cataracts.^{13-15,34}

Our findings suggest that there is insufficient benefit to justify the risks of radiation exposure, and potentially of anesthesia, associated with pre-HCT screening CT.^{13,15-17} To reduce the risk of radiation-induced cancers, to which children are particularly susceptible,³⁴ the As Low As Reasonably Achievable principle dictates the use of the lowest possible radiation dose necessary for diagnosis.³⁴ Most pediatric imaging centers, like ours, use targeted protocols with dose-reduction techniques like iterative reconstruction and low tube voltage wherever possible.³⁵

However, the best way to reduce the pediatric radiation dose is to eliminate imaging that does not meaningfully contribute to diagnosis or management.¹⁴ The preponderance of the evidence, including ours, suggests that pre-HCT screening sinus CT falls into this category and that the practice should be discontinued.

This study had several weaknesses. Clinical evaluation was rarely performed on the same day as screening sinus CT, and symptoms were recorded from the medical record because they were frequently omitted from the imaging requisitions. These features could result in a mismatch between symptoms and imaging manifestations. Although a trend toward greater Lund-Mackay scores in symptomatic patients receiving antibiotics was not statistically significant, the sample size was small. It is possible that the degree of mucosal thickening on sinus CT unduly influenced the decision to treat with antibiotics, which should be based on history and examination.^{6,7} Mucosal thickening on CT does not differentiate between bacterial and viral pathogens, and 3 of 5 patients receiving antibiotics in this study had nasal washes positive for viral pathogens. Next, only patients undergoing imaging work-up were considered symptomatic post-HCT. It is possible that some patients were treated on the basis of clinical symptoms with no imaging, though observation of our current clinical practice suggests that this is unlikely. Similar to other studies,^{2,4} only 2% (2/100) of this study population ultimately developed IFRS, limiting statistical evaluation. However, neither had clinical or imaging findings suspicious for IFRS pretransplantation. Although a single-institution sample size of 100 children undergoing HCT may be considered large, given the rarity of the condition, it was nonetheless insufficient to identify clinical or imaging features associated with IFRS. A retrospective case-control study would be more practical for such analysis.

CONCLUSIONS

Pre-HCT sinus CT does not meaningfully contribute to pretransplantation patient management or prediction of posttransplantation sinus disease, including IFRS, in children. The risks associated with CT radiation and possible anesthesia are not warranted in this setting.

ACKNOWLEDGMENTS

The authors wish to thank Edwina Anderson and Cindy Morris for assistance with data collection.

Disclosures: Julie H. Harreld—*RELATED: Grant:* National Cancer Institute, *Comments:* Grant No. CA21765 supports the St. Jude Cancer Center*; *Other:* American Lebanese and Syrian Associated Charities, *Comments:* The American Lebanese and Syrian Associated Charities is the fundraising arm of St. Jude.* Gabriela Maron—*UNRELATED: Other:* Astellas Pharma Inc, *Comments:* local Principal Investigator for pharmaceutical research protocols.* Jerome W. Thompson—*UNRELATED: Employment:* University of Tennessee Faculty. *Money paid to the institution.

REFERENCES

1. Deo SS, Gottlieb DJ. **Adoptive T-cell therapy for fungal infections in haematology patients.** *Clin Transl Immunology* 2015;4:e40 CrossRef Medline
2. Chen CY, Sheng WH, Cheng A, et al. **Invasive fungal sinusitis in patients with hematological malignancy: 15 years' experience in a single university hospital in Taiwan.** *BMC Infect Dis* 2011;11:250 CrossRef Medline
3. Gillespie MB, O'Malley BW, Francis HW. **An approach to fulminant invasive fungal rhinosinusitis in the immunocompromised host.** *Arch Otolaryngol Head Neck Surg* 1998;124:520–26 CrossRef Medline
4. Park AH, Muntz HR, Smith ME, et al. **Pediatric invasive fungal rhinosinusitis in immunocompromised children with cancer.** *Otolaryngol Head Neck Surg* 2005;133:411–16 CrossRef Medline
5. Smith A, Thimmappa V, Shepherd B, et al. **Invasive fungal sinusitis in the pediatric population: systematic review with quantitative synthesis of the literature.** *Int J Pediatr Otorhinolaryngol* 2016;90:231–35 CrossRef Medline
6. Kirsch CF, Bykowski J, Aulino JM, et al; Expert Panel on Neurologic Imaging. **ACR Appropriateness Criteria Sinonasal Disease.** *J Am Coll Radiology* 2017;14:S550–59 CrossRef Medline
7. Wald ER, Applegate KE, Bordley C, et al; American Academy of Pediatrics. **Clinical practice guideline for the diagnosis and management of acute bacterial sinusitis in children aged 1 to 18 years.** *Pediatrics* 2013;132:e262–80 CrossRef Medline
8. Thompson AM, Couch M, Zahurak ML, et al. **Risk factors for post-stem cell transplant sinusitis.** *Bone Marrow Transplant* 2002;29:257–61 CrossRef Medline
9. Won YW, Yi SY, Jang JH, et al. **Retrospective analysis of paranasal sinusitis in patients receiving hematopoietic stem cell transplantation.** *Int J Hematol* 2011;93:383–88 CrossRef Medline
10. Zamora CA, Oppenheimer AG, Dave H, et al. **The role of screening sinus computed tomography in pediatric hematopoietic stem cell transplant patients.** *J Comput Assist Tomogr* 2015;39:228–31 CrossRef Medline
11. Moeller CW, Martin J, Welch KC. **Sinonasal evaluation preceding hematopoietic transplantation.** *Otolaryngol Head Neck Surg* 2011;144:796–801 CrossRef Medline
12. Kasow KA, Krueger J, Srivastava DK, et al. **Clinical utility of computed tomography screening of chest, abdomen, and sinuses before hematopoietic stem cell transplantation: the St. Jude experience.** *Biol Blood Marrow Transplant* 2009;15:490–95 CrossRef Medline
13. Miglioretti DL, Johnson E, Williams A, et al. **The use of computed tomography in pediatrics and the associated radiation exposure and estimated cancer risk.** *JAMA Pediatr* 2013;167:700–07 CrossRef Medline
14. Donnelly LF. **Reducing radiation dose associated with pediatric CT by decreasing unnecessary examinations.** *AJR Am J Roentgenol* 2005;184:655–57 CrossRef Medline
15. Fish DE, Kim A, Ornelas C, et al. **The risk of radiation exposure to the eyes of the interventional pain physician.** *Radiology Res Pract* 2011;2011:609537 CrossRef Medline
16. Banerjee P, Rossi MG, Angheliescu DL, et al. **Association between anesthesia exposure and neurocognitive and neuroimaging outcomes in long-term survivors of childhood acute lymphoblastic leukemia.** *JAMA Oncol* 2019 Jun 20. [Epub ahead of print] CrossRef Medline
17. Lei S, Ko R, Sun LS. **Neurocognitive impact of anesthesia in children.** *Adv Anesth* 2018;36:125–37 CrossRef Medline
18. Maron GM, Hayden RT, Rodriguez A, et al. **Voriconazole prophylaxis in children with cancer: changing outcomes and epidemiology of fungal infections.** *Pediatr Infect Dis J* 2013;32:e451–55 CrossRef Medline
19. DelGaudio JM, Swain RE Jr, Kingdom TT, et al. **Computed tomographic findings in patients with invasive fungal sinusitis.** *Arch Otolaryngol Head Neck Surg* 2003;129:236–40 CrossRef Medline
20. Groppo ER, El-Sayed IH, Aiken AH, et al. **Computed tomography and magnetic resonance imaging characteristics of acute invasive fungal sinusitis.** *Arch Otolaryngol Head Neck Surg* 2011;137:1005–10 CrossRef Medline
21. Ni Mhurchu E, Ospina J, Janjua AS, et al. **Fungal rhinosinusitis: a radiological review with intraoperative correlation.** *Can Assoc Radiology J* 2017;68:178–86 CrossRef Medline

22. Middlebrooks EH, Frost CJ, De Jesus RO, et al. **Acute invasive fungal rhinosinusitis: a comprehensive update of CT findings and design of an effective diagnostic imaging model.** *AJNR Am J Neuroradiol* 2015;36:1529–35 CrossRef Medline
23. Aribandi M, McCoy VA, Bazan C 3rd. **Imaging features of invasive and noninvasive fungal sinusitis: a review.** *Radiographics* 2007;27:1283–96 CrossRef Medline
24. Lund VJ, Kennedy DW. **Staging for rhinosinusitis.** *Otolaryngol Head Neck Surg* 1997;117:S35–40 CrossRef
25. Hill M, Bhattacharyya N, Hall TR, et al. **Incidental paranasal sinus imaging abnormalities and the normal Lund score in children.** *Otolaryngol Head Neck Surg* 2004;130:171–75 CrossRef Medline
26. Ryu G, Seo MY, Lee KE, et al. **Clinical course of rhinosinusitis and efficacy of sinonasal evaluation in kidney transplant recipients: review of 1589 patients.** *Eur Arch Otorhinolaryngol* 2018;275:1183–88 CrossRef Medline
27. Shibuya T, Momin F, Abella E, et al. **Jerome W. Thompson—UNRELATED: Employment: Sinus disease in the bone marrow transplant population: incidence, risk factors, and complications.** *Otolaryngol Head Neck Surg* 1995;113:705–11 CrossRef Medline
28. Bartley DL, Hughes WT, Parvey LS, et al. **Computed tomography of hepatic and splenic fungal abscesses in leukemic children.** *Pediatr Infect Dis* 1982;1:317–21 CrossRef Medline
29. Billings KR, Lowe LH, Aquino VM, et al. **Screening sinus CT scans in pediatric bone marrow transplant patients.** *Int J Pediatr Otorhinolaryngol* 2000;52:253–60 CrossRef Medline
30. Arulrajah S, Symons H, Cahoon EK, et al. **Relationship between clinical sinusitis symptoms and sinus CT severity in pediatric post bone marrow transplant and immunocompetent patients.** *Eur J Pediatr* 2012;171:375–81 CrossRef Medline
31. Kasapoglu F, Coskun H, Ozmen OA, et al. **Acute invasive fungal rhinosinusitis: evaluation of 26 patients treated with endonasal or open surgical procedures.** *Otolaryngol Head Neck Surg* 2010;143:614–20 CrossRef Medline
32. von Kalle T, Fabig-Moritz C, Heumann H, et al. **Incidental findings in paranasal sinuses and mastoid cells: a cross-sectional magnetic resonance imaging (MRI) study in a pediatric radiology department.** *Rofo* 2012;118:629–34 CrossRef Medline
33. Tomazic P, Neuschitzer A, Koele W, et al. **Feasibility of routine paranasal sinus CT-scans in preoperative transplant patients.** *Ann Transplant* 2011;16:31–35 CrossRef Medline
34. Brody AS, Frush DP, Huda W, et al; American Academy of Pediatrics Section on Radiology. **Radiation risk to children from computed tomography.** *Pediatrics* 2007;120:677–82 CrossRef Medline
35. Nagayama Y, Oda S, Nakaura T, et al. **Radiation dose reduction at pediatric CT: use of low tube voltage and iterative reconstruction.** *Radiographics* 2018;38:1421–40 CrossRef Medline

The Perirolandic Sign: A Unique Imaging Finding Observed in Association with Polymerase γ -Related Disorders

F.G. Gonçalves, B. Hill, Y. Guo, C.C. Muraresku, E. McCormick, C.A.P.F. Alves, S.R. Teixeira, J.S. Martin-Saavedra, Z. Zolkipli-Cunningham, M.J. Falk, A. Vossough, A. Goldstein, and G. Zuccoli



ABSTRACT

SUMMARY: Pathogenic variants in the *polymerase γ gene (POLG)* cause a diverse group of pathologies known as *POLG*-related disorders. In this report, we describe brain MR imaging findings and electroencephalogram correlates of 13 children with *POLG*-related disorders at diagnosis and follow-up. At diagnosis, all patients had seizures and 12 had abnormal MR imaging findings. The most common imaging findings were unilateral or bilateral perirolandic (54%) and unilateral or bilateral thalamic signal changes (77%). Association of epilepsy partialis continua with perirolandic and thalamic signal changes was present in 86% and 70% of the patients, respectively. The occipital lobe was affected in 2 patients. On follow-up, 92% of the patients had disease progression or fatal outcome. Rapid volume loss was seen in 77% of the patients. The occipital lobe (61%) and thalamus (61%) were the most affected brain regions. Perirolandic signal changes and seizures may represent a brain imaging biomarker of early-onset pediatric *POLG*-related disorders.

ABBREVIATIONS: ASL = arterial spin-labeling; EEG = electroencephalogram; EPC = epilepsy partialis continua; MELAS = mitochondrial encephalomyopathy with lactic acidosis and stroke-like episodes; mtDNA = mitochondrial DNA; Pol γ = polymerase γ ; *POLG*-RD = DNA polymerase γ -related disorder

Polymerase γ (Pol γ) is the only DNA polymerase active during human mitochondrial DNA (mtDNA) genome replication.¹ Pathogenic variants in the Pol γ gene (*DNA polymerase γ [POLG]*) cause a group of clinical syndromes known as *POLG*-related disorders (*POLG*-RDs).¹ Patients with *POLG*-RDs fall into a heterogeneous clinical spectrum. At the least severe end of the spectrum, patients present in adulthood with ptosis and ophthalmoplegia, whereas those most severely affected present with progressive and severe neurologic impairment and liver involvement in early childhood.²

Pathogenic variants of *POLG* are the most frequently detected genetic forms of mitochondrial epilepsy.³ Seizures are described as

the first clinical manifestation in up to 50% of patients. Seizure types include myoclonus, focal motor seizures, generalized seizures, status epilepticus, refractory febrile seizures, and epilepsy partialis continua (EPC).⁴

Neuroimaging findings in *POLG*-RDs have been described primarily in the later stages of the disease,⁵ with the occipital lobe being the most commonly involved region.⁴ Brain MR imaging findings in the early onset of pediatric *POLG*-RDs are not well-known. The primary goal of this study was to describe the early brain MR imaging findings in children, including the “perirolandic sign,” defined as signal changes in the brain parenchyma surrounding the central sulcus of *POLG*-RDs, and to correlate them with electroencephalogram (EEG) findings. Our secondary goal was to describe the evolution of brain MR imaging findings on follow-up imaging.

Case Series

This retrospective institutional review board–approved study was conducted in a single academic pediatric hospital, Children’s Hospital of Philadelphia. Medical records were searched for primary mitochondrial disorders from January 2001 to July 2018. Patients with brain MR imaging and a confirmed molecular diagnosis of *POLG*-RDs (confirmed biparental inheritance for autosomal recessive disease when possible) were included. Exclusion criteria consisted of the unavailability of brain MR imaging or confirmed molecular diagnosis.

Received December 18, 2019; accepted after revision February 27, 2020.

From the Departments of Radiology and Division of Neuroradiology (F.G.G., B.H., C.A.P.F.A., S.R.T., J.S.M.-S., A.V., G.Z.); Mitochondrial Medicine Frontier Program, Division of Human Genetics (C.C.M., E.M., Z.Z.-C., M.J.F., A.G.), Children’s Hospital of Philadelphia, Philadelphia, Pennsylvania; Departments of Pediatrics (Y.G., Z.Z.-C., M.J.F., A.G.); Radiology (A.V.), University of Pennsylvania Perelman School of Medicine, Philadelphia, Pennsylvania; and The Program for the Study of Neurodevelopment in Rare Disorders (NDRD) (G.Z.), Children’s Hospital of Pittsburgh of UPMC.

G.Z. is the Principal Investigator (P.I.).

This work was funded, in part, by the Mitochondrial Medicine Frontier Program at Children’s Hospital of Philadelphia.

Please address correspondence to Fabricio Guimarães Gonçalves, MD, Department of Radiology and Division of Neuroradiology, Children’s Hospital of Philadelphia, 3401 Civic Center Blvd, Philadelphia, PA 19104; e-mail: goncalves.neuroradio@gmail.com; @Fab_Neuroradio



Indicates article with supplemental on-line tables.

<http://dx.doi.org/10.3174/ajnr.A6514>

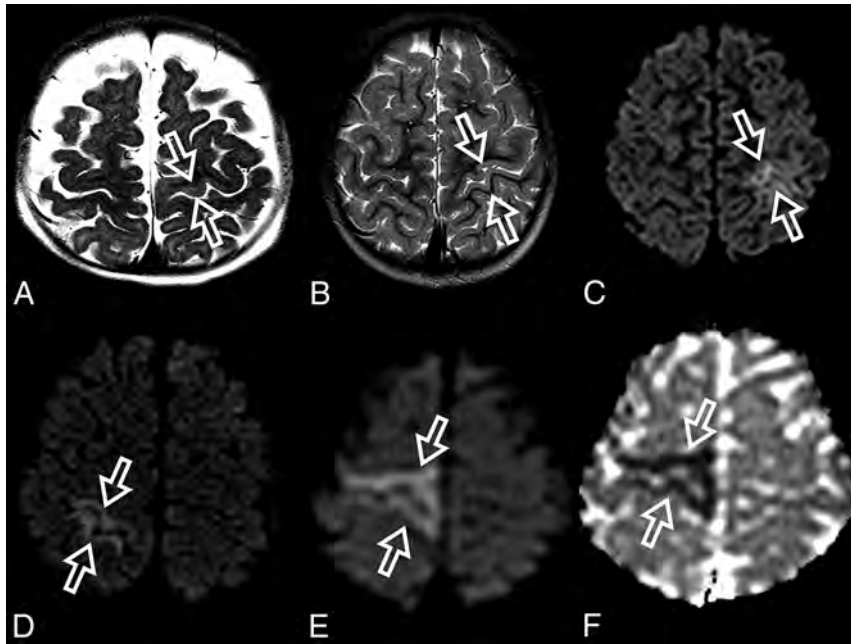


FIG 1. Perirolandic sign in 4 different patients with *POLG*-related disorders (A, An 8-month-old female), (B and C, A 3 year-old-male), (D, An 1-year-old male) and (E and F, A 9-month-old female). Signal changes around the central sulcus were variable with varying degrees of conspicuity. A, T2WI. Signal changes are subtle and focal, evident only in the left precentral gyrus (open arrows). B, T2WI. Signal changes are subtle and focal, evident in the left pre- and postcentral gyrus (open arrows), but more conspicuous in the DWI (open arrows, C). D, DWI. Linear signal changes involving mainly the cortex surrounding the right central sulcus (open arrows). E and F, DWI and ADC map, respectively. Marked signal changes in both right pre- and postcentral gyri.

Demographic data, clinical history, brain MR imaging at diagnosis, and the EEG most contemporaneous with the MR imaging at diagnosis were reviewed. On the basis of prior observation of an index case (which was included in the analysis), we also explicitly assessed the presence of MR imaging signal changes around the central sulcus involving the pre- or postcentral gyri perirolandic sign. Brain MR imaging was reviewed (at diagnosis and follow-up) by 3 pediatric neuroradiologists in consensus (F.G.G., A. V., and G.Z.). T1 and T2 imaging and DWI were available in at least 1 plane in all examinations. T2* and SWI, MR spectroscopy, and arterial spin-labeling (ASL) were partially available across the studies. When obtained, MR spectroscopy was acquired with the point resolved spectroscopy protocol, using at least a voxel in the right basal ganglia with the following parameters: TR/TE=1700/20 ms.

From a cohort of 117 patients with primary mitochondrial disorders, 13 met the criteria for a *POLG*-RD. Demographic information, age at onset, brief relevant history at presentation, EEG findings, elapsed time between the first brain MR imaging and the most contemporaneous EEG, and pathogenic variants of each patient's pathogenic variants are shown in On-line Table 1. The presence of the perirolandic sign involving either the pre- or postcentral gyri, MR imaging signal changes in the thalami, additional brain MR imaging findings, and the specific sequences in which the signal changes were depicted in each patient are shown in On-line Table 2. All patients had follow-up imaging, which varied significantly in number among patients. Thus, instead of being mentioned individually, their follow-up

findings were pooled and summarized in 1 single column in On-line Table 2, called "Pooled Follow-Up Imaging."

Most patients were female ($n=9$, 69%). The median age was 3 years (interquartile range, 0.7–7.5 years). All patients presented clinically with seizures ($n=13$, 100%). Other common associated symptomatology included regression, developmental delay, hypotonia, vomiting, and signs of liver damage. All patients had an EEG available around the time of their first brain MR imaging ($n=13$, 100%); all the scans had abnormal findings. Clinical or EEG evidence of EPC was detected in most patients ($n=8$, 61%). The mean elapsed time between the most contemporaneous EEG and brain MR imaging at diagnosis was 6 days. The most common pathogenic variant found from each parent with another variant was $c.1399G>A:p.A467T$ ($n=7$, 54%), which is consistent with findings in previous literature.⁶

At diagnosis, brain MR imaging findings were abnormal in most patients ($n=12$, 92%). The most common brain MR imaging findings were unilateral or bilateral perirolandic signal changes ($n=7$, 54%) (Fig 1) and unilateral or bilateral thalamic signal changes ($n=10$, 77%) (Fig 2). Perirolandic signal abnormalities were unilateral in most cases ($n=5$, 71%) and were more frequently seen only affecting the precentral or both the pre- and postcentral gyri. Half of the thalamic changes were unilateral ($n=5$, 50%). Simultaneous perirolandic and thalamic signal changes occurred in 6 patients ($n=6$, 46%). An association of EPC (clinically/EEG) and perirolandic signal changes was present in 6 patients ($n=6$, 75%), and an association of EPC (clinically/EEG) and thalamic signal changes, in 7 patients ($n=7$, 87.5%). Two patients with EPC (clinically/EEG) did not present with perirolandic signal abnormalities. The findings positive for lesions overall were on the DWI of 10 patients ($n=10$, 83%), on the T2WI of 9 patients ($n=9$, 75%), and on FLAIR of 7 patients ($n=7$, 58%). In 4 patients, DWI was the only sequence with abnormal findings. The occipital lobe was affected in the early brain MR imaging in 2 patients ($n=2$, 15%). Signal changes in other brain regions were found in 5 patients ($n=5$, 42%), involving multiple regions, namely the cerebral white matter, insula, putamen, caudate nucleus, fornix, cerebellar vermis, and also the frontal and occipital lobes. One patient did not present with either perirolandic or thalamic changes but instead presented with a diffuse pattern similar to that of leukoencephalopathy, with restricted diffusion in the white matter and white matter tracts (Fig 3). Three patients had an abnormally high lactate peak on MR spectroscopy. None of our patients had ASL or other perfusion-weighted imaging at the time

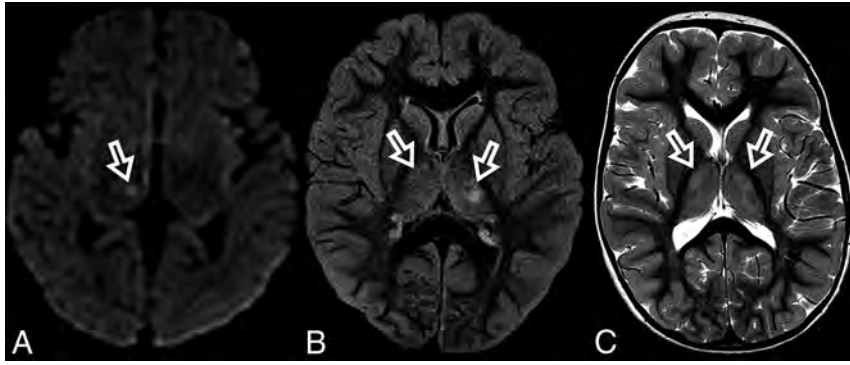


FIG 2. MR imaging thalamic signal changes in 3 different patients with *POLG*-related disorders (A, A 9-month-old female), (B, A 3-year-old female), and (C, A 3-year-old male). Thalamic signal changes were also variable with varying degrees of conspicuity. A, DWI. Signal changes were subtle and focal with restricted diffusion in the right thalamus (open arrow). B, FLAIR. Signal changes involved both thalami, more conspicuous on the left side (open arrows). C, T2WI. Signal changes were bilateral and symmetric involving both thalami (open arrows).

of diagnosis. T1 and T2* imaging and SWI had negative findings at the time of diagnosis.

All patients had at least 1 follow-up brain MR imaging. Most patients had imaging findings suggesting disease progression ($n = 12$, 92%) or a fatal outcome. On follow-up imaging, most demonstrated volume loss ($n = 10$, 77%), which was typically very rapid, in a matter of a few weeks in most patients. On the follow-up brain MR imaging, the perirolandic and thalamic signal changes had various evolutions, with resolution, stability, contralateral involvement (unilateral \rightarrow bilateral), or progression with time. The most affected brain regions at follow-up were the occipital lobe ($n = 8$, 61%) and thalamus ($n = 8$, 61%). The perirolandic sign was detected in 3 patients who did not have any evidence of perirolandic involvement at diagnosis. Other affected brain regions included the hippocampus, brain stem, dentate nucleus, cerebellar vermis, cerebellar hemispheres, other regions of the frontal and parietal lobes, and the occipital (Fig 4) and temporal lobes. ASL perfusion was obtained in only some of the patients at follow-up imaging. Regions more commonly found with increased ASL perfusion included the thalamus, the perirolandic region, and the occipital and parietal lobes. The areas with increased ASL perfusion also had signal changes visible on T2WI, FLAIR, or DWI. An increased lactate peak was seen in all patients in whom MR spectroscopy was performed on follow-up. Diffuse brain edema was noted in 1 patient, who died shortly thereafter. One patient had unremarkable brain MR imaging on follow-up with resolution of findings.

DISCUSSION

Pol γ is the only human DNA polymerase active during mtDNA replication.¹ *POLG* is a nuclear gene that encodes for Pol γ , and pathogenic variants lead to errors in mtDNA replication, resulting in multiple small mtDNA deletions, an overall reduction in the number of mtDNA genome copies (mtDNA depletion), and decreased adenosine triphosphate production leading to chronic loss of cellular energy.²

Patients with *POLG*-RD have been grouped into multiple distinct clinically-defined syndromes, which were later attributed to different subtypes of pathogenic variants. The

prototypical clinical phenotypes associated with *POLG* pathogenic variants are the following: 1) Alpers-Huttenlocher syndrome; 2) myocerebrohepatopathy spectrum; 3) myoclonic epilepsy myopathy sensory ataxia; 4) ataxia neuropathy spectrum, which includes mitochondrial recessive ataxia syndrome, spinocerebellar ataxia with epilepsy, and sensory ataxia neuropathy dysarthria and ophthalmoplegia; 5) autosomal recessive progressive external ophthalmoplegia; and 6) autosomal dominant progressive external ophthalmoplegia.¹² Nevertheless, it is increasingly recognized that there is a broad clinical spectrum across these clinical syndromes, in which a

patient with *POLG*-RD may present with clinical features that may not fit within a single classically described syndrome.⁷

POLG pathogenic variants are the most common cause of mitochondrial epilepsy.⁸ Seizures are reported as the first clinical presentation in 50% of all patients with *POLG*-RDs.⁴ The most critical factor that triggers epileptic activity is the loss of mtDNA (mtDNA depletion). mtDNA depletion causes loss of the respiratory chain components, which restricts normal energy metabolism, causing a continued neurodegenerative process that interferes with neuronal function. This causes a vicious cycle that ultimately leads to neuronal death and parenchymal necrosis.⁸

EPC is a distinct type of focal motor seizure, first described in 1894.⁹ EPC characteristically involves repetitive, sometimes rhythmic, unilateral focal motor twitching of the limbs and/or face, with preservation of consciousness, suggesting an underlying brain lesion.¹⁰ EPC presentation is variable, occurring as single or multiple episodes, and it may be chronic, progressive, or nonprogressive.¹¹ Several neurologic entities are associated with EPC, such as tuberous sclerosis, Sturge-Weber syndrome, and cortical dysplasia. Metabolic abnormalities such as hyponatremia; hypoglycemia; hyperglycemia; hyperuricemia; uremia; brain tumors such as oligodendroglioma, meningioma, and high-grade glioma; autoimmune processes; and infections. Rasmussen encephalitis also has a well-known association with EPC.^{11,12}

A comprehensive literature review of 136 patients with epilepsy with *POLG*-RDs has shown that stroke-like changes were the most common imaging findings. The lesions were more commonly located in the occipital lobes. Other structures involved were the parietal, temporal, and frontal lobes; thalamus; basal ganglia; and cerebellum.⁴ The age of the patients in this study varied from younger than 30 days to 64 years, with a median of 2 years (first quartile = 0.75 and third quartile = 13.50).⁴ Before our study, reports of perirolandic MR imaging signal changes in *POLG*-RDs have only been mentioned in a few isolated case reports, including a 10-month-old child with Alpers-Huttenlocher syndrome who showed multifocal diffusion restriction areas in the left insula, deep gray matter, and

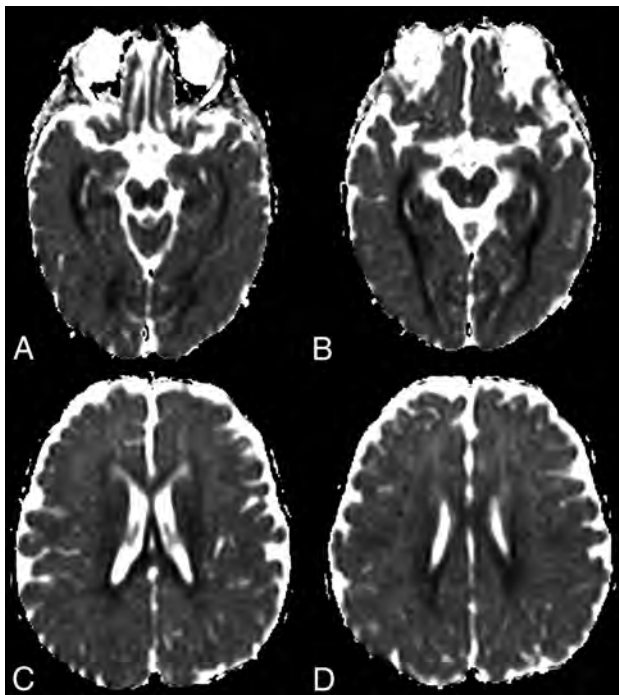


FIG 3. ADC map images of a 7-month-year old male with *POLG*-related disorder, demonstrating a diffuse pattern of leukoencephalopathy with restricted diffusion of the periventricular white matter of the bilateral temporal lobes in A, the occipital lobes in B, and also of the bilateral fornix in C and corpus callosum in D.

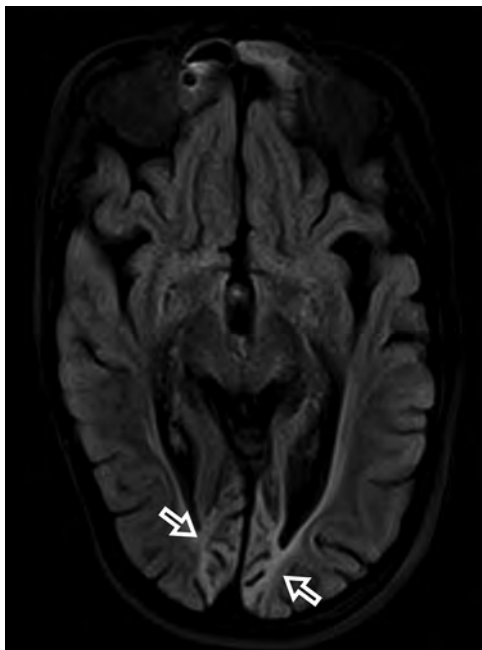


FIG 4. Bilateral occipital volume loss, gliosis, and encephalomalacia in a 16-year-old female patient with *POLG*-related disorder (open arrows).

bilateral perirolandic area, which were initially related to a nonspecific metabolic process.¹³ Right pre- and post-central gyri T2 and DWI signal abnormalities were also detected in a 7-month-old girl with *POLG*-RD who developed focal clonic status

epilepticus, mainly of her left arm and occasionally also involving the left leg.¹⁴ Additional case reports described subtle signal changes on FLAIR in a 15-year-old girl with EPC¹⁵ and a 13-month-old child with bilateral perirolandic restricted diffusion with a history of hypotonia, mild motor delay, and EPC.¹⁶

In this current study of children with *POLG*-RDs, all patients presented initially with seizures. Most initial brain MR imaging findings were abnormal. A temporal association between seizures and brain MR imaging abnormalities was found, suggesting lesion-related seizures. The primary brain MR imaging abnormalities included unilateral or bilateral signal changes in the perirolandic region, unilateral or bilateral signal changes in the thalamus, or a combination of the 2 in most of our patients. At diagnosis, the perirolandic region or the thalamus was spared in only 2 patients in our cohort, one with unremarkable brain MR imaging findings and the other in whom diffuse white matter with restricted diffusion was noted (Fig 3).

The perirolandic sign was common and present in most patients at diagnosis. Moreover, the sign was seen in most patients during the course of the disease because half of the patients who did not have the sign initially presented with the sign later. The presence of perirolandic signal changes would reflect neuronal death following acute energy failure in a metabolically demanding region (primary motor and sensory cortex) within the dominant hemisphere. Further studies are needed to confirm this hypothesis.

The MR imaging appearance of the perirolandic sign was varied. Signal changes involved both the pre- and postcentral gyri, more commonly in the precentral gyri. The conspicuity of the perirolandic sign was also variable (Fig 1). In the more notable cases, signal changes were ribbon-like following the course of the gyri, which were readily detectable as T2 hyperintensities and restricted diffusion. DWI was the most sensitive MR imaging sequence to detect signal changes and, therefore, should always be included in the protocol and carefully evaluated when a case of *POLG*-RD is suspected.

Thalamic signal changes were also frequent at the time of diagnosis and on follow-up imaging. Unilateral or bilateral thalamic involvement was identified in most patients during the onset of their disease. In our cohort, there was no new thalamic involvement at follow-up. On follow-up imaging, thalamic changes had different outcomes: complete resolution, progression from unilateral to bilateral involvement, progression accompanied by volume loss, and fluctuation with periods of an almost-complete resolution and frank progression. Thalamic signal changes were variably detected on DWI, T2WI, FLAIR, or ASL.

Volume loss was detected almost always on follow-up imaging. Volume loss varied from mild to severe, showing rapid evolution in most cases. Most important, volume loss showed no lobar predominance in most patients. However, in severe cases, the occipital lobes were affected asymmetrically and with encephalomalacic changes. Signal changes were detected virtually in any part of the brain, except the medulla. The spinal cord was not part of the scope of this study.

The occipital lobe was rarely affected at diagnosis, though frequently involved on follow-up imaging. Advanced MR imaging sequences such as MR spectroscopy and ASL, albeit not

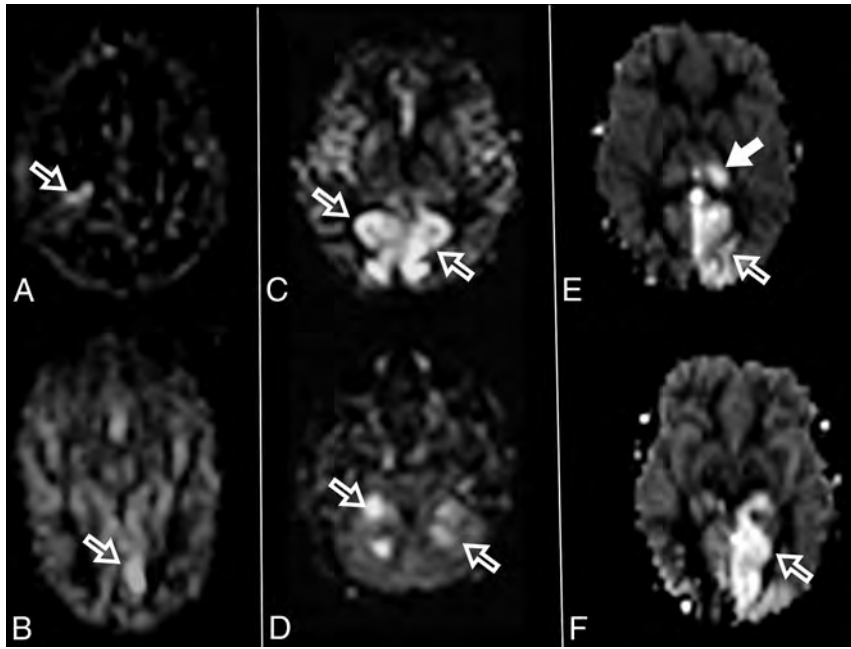


FIG 5. Increased ASL perfusion in 3 different patients with *POLG*-related disorders (A and B), (C and D), and (E and F). Increased perfusion regions are seen in the right perirolandic region in A (open arrow) and in the left occipital lobe in B (open arrow). Bilateral parietal and occipital increased perfusion is seen in C (open arrows) and in the bilateral cerebellar hemispheres (open arrows) in D. Increased ASL perfusion is seen in the left thalamus in E (solid arrow) and in the left parietal and occipital lobes in E and F (open arrows).

being acquired in all the patients, were useful to demonstrate increased lactate peaks and areas of localized hyperperfusion, respectively. An increased lactate peak is an expected finding in primary mitochondrial disorders and has already been described in patients with *POLG*-RDs, reflecting mitochondrial dysfunction.⁸ ASL perfusion has mostly been described in patients with mitochondrial encephalomyopathy with lactic acidosis and stroke-like episodes (MELAS), but rarely in *POLG*-RDs. Increased ASL perfusion in MELAS preceded signal changes on conventional MR imaging in 3 patients, indicating that ASL imaging has the potential for predicting the emergence of stroke-like lesions.¹⁷ In our cohort, increased ASL perfusion was coincident with either T2WI, FLAIR, or DWI signal changes and may have been related to seizure activity. ASL, however, was useful to indicate areas that would undergo further volume loss in some of our patients (Fig 5). The complete role of ASL perfusion in patients with *POLG*-RDs needs further investigation.

Valproic acid is an effective antiepileptic drug to manage epilepsy. However, it is strictly contraindicated to treat seizures in patients with *POLG*-RD due to its potential to cause fulminant hepatotoxicity.⁵ The best diagnostic test to prevent valproic acid-induced liver toxicity is *POLG* gene testing before the use of this medication.¹⁸ The presence of a unilateral or bilateral perirolandic sign, unilateral or bilateral thalamic MR imaging signal changes, or a combination of both in a child with seizures/EPC may be a *POLG*-RD biomarker, which can also be useful for early suspicion of this diagnosis and to prevent the use of valproic acid in these children.

MR imaging findings in our cohort are not pathognomonic for *POLG*-RD, and the differential diagnosis includes postictal changes and stroke-like episodes similar to MELAS. At this time, we can only speculate about their nature, and further laboratory, genetic, and imaging correlation are necessary to establish their pathogenesis. Bilateral perirolandic cortical involvement can also be seen in patients with hypoxic-ischemic injury,¹⁹ urea-cycle disorders,²⁰ and Wernicke encephalopathy,²¹ though these patients often have a different clinical context. Perirolandic white matter involvement can be seen in cases of hypoxic-ischemic injury¹⁹ and maple syrup urine disease.²² Unilateral cortical perirolandic involvement can be seen in vascular infarcts, focal cortical dysplasia, and primary and metastatic tumors.²³ Unilateral or bilateral thalamic signal changes can be seen in multiple entities such as arterial infarction, hypoxic-ischemic injuries, several metabolic diseases, infection, inflammatory processes, neoplasms, and veno-occlusive syndromes.^{24,25}

Limitations of our study include the small number of patients with this rare disorder and the fact that this was a retrospective analysis. However, this study is about the first and largest cohort, describing the very early brain MR imaging findings in pediatric patients with confirmed *POLG*-RD. EPC, in association with perirolandic signal abnormalities, may serve as an early sign and a potential biomarker of *POLG*-RD. This clinical presentation should increase awareness and prompt testing for *POLG* pathogenic variants because the discovery of *POLG*-RD has relevant implications for acute clinical management and long-term prognosis.

Disclosures: Zarazuela Zolkipli-Cunningham—UNRELATED: Employment: Children's Hospital of Philadelphia. Marni J. Falk—UNRELATED: Board Membership: United Mitochondrial Disease Foundation, Comments: travel reimbursement for serving on scientific and medical advisory boards and board of trustees of the United Mitochondrial Disease Foundation; Consultancy: several pharma companies, Comments: paid consultant for Mitobridge/Astellas, NeuroVive, Cycleric Therapeutics, Reneo Pharmaceuticals, Mission Therapeutics, Stealth BioTherapeutics, and Imel Therapeutics; Grants/Grants Pending: several pharma companies and foundations, Comments: grants from Mitobridge/Astellas, NeuroVive, Cycleric Therapeutics, Mission Therapeutics (pending), Stealth BioTherapeutics, Minovia Therapeutics (pending)*; Patents (Planned, Pending or Issued): several, Comments: several patents (no current value) at home institution in mitochondrial disease diagnostic and therapeutic development*; Royalties: Elsevier, Comments: editor of book now in press at Elsevier, *Mitochondrial Disease Genes Compendium: Stock/Stock Options*: Mitocureia, Comments: co-founder and scientific advisory board co-Chair of Mitocureia; Travel/Accommodations/Meeting Expenses Unrelated to Activities Listed: education travel, Comments: reimbursed for travel to speak at meetings on mitochondrial diagnostics and therapeutics including at CardiInfantil, Bogota, Columbia; Pediatric Neurology Society, Mexico; American College of Medical Genetics; Emory/Atlanta Children's Hospital; New York University; Cornell University; Washington University in St Louis; Seattle Children's Hospital; scientific

and family meetings hosted by United Mitochondrial Disease Foundation; European Society of Human Genetics; Society for the Study of Inborn Errors of Metabolism; Society of Inherited Metabolic Disease; Hebrew University; Asian Society Of Inborn Errors of Metabolism; Wellcome Genome Campus; Cold Spring Harbor Laboratory. Amy Goldstein—UNRELATED: Board Membership; United Mitochondrial Disease Foundation, Comments: Scientific and Medical Advisory Board. *Money paid to the institution.

REFERENCES

- Copeland WC. **The mitochondrial DNA polymerase in health and disease.** *Subcell Biochem* 2010;50:211–22 CrossRef Medline
- Stumpf JD, Saneto RP, Copeland WC. **Clinical and molecular features of POLG-related mitochondrial disease.** *Cold Spring Harb Perspect Biol* 2013;5:a011395 CrossRef Medline
- Zsurka G, Kunz WS. **Mitochondrial dysfunction and seizures: the neuronal energy crisis.** *Lancet Neurol* 2015;14:956–96 CrossRef Medline
- Anagnostou ME, Ng YS, Taylor RW, et al. **Epilepsy due to mutations in the mitochondrial polymerase gamma (POLG) gene: a clinical and molecular genetic review.** *Epilepsia* 2016;57:1531–45 CrossRef Medline
- Rahman S, Copeland WC. **POLG-related disorders and their neurological manifestations.** *Nat Rev Neurol* 2019;15:40–52 CrossRef Medline
- Nurminen A, Farnum GA, Kaguni LS. **Pathogenicity in POLG syndromes: DNA polymerase gamma pathogenicity prediction server and database.** *BBA Clin* 2017;7:147–56 CrossRef Medline
- Cohen BH, Chinnery PF, Copeland WC. POLG-related disorders. In: Adam MR, Ardinger HH, Pagon RA. eds. *GeneReviews*. University of Washington; 2018
- Hikmat O, Eichele T, Tzoulis C, et al. **Understanding the epilepsy in POLG related disease.** *Int J Mol Sci* 2017;18 CrossRef Medline
- Vein AA, van Emde Boas W. **Kozhevnikov epilepsy: the disease and its eponym.** *Epilepsia* 2011;52:212–18 CrossRef Medline
- Thomas JE, Reagan TJ, Klass DW. **Epilepsia partialis continua: a review of 32 cases.** *Arch Neurol* 1977;34:266–75 CrossRef Medline
- Mameniškienė R, Wolf P. **Epilepsia partialis continua: a review.** *Seizure* 2017;44:74–80 CrossRef Medline
- Bien CG, Widman G, Urbach H, et al. **The natural history of Rasmussen's encephalitis.** *Brain* 2002;125:1751–59 CrossRef Medline
- Park S, Kang HC, Lee JS, et al. **Alpers-Huttenlocher syndrome first presented with hepatic failure: can liver transplantation be considered as treatment option?** *Pediatr Gastroenterol Hepatol Nutr* 2017;20:259–62 CrossRef Medline
- Wolf NI, Rahman S, Schmitt B, et al. **Status epilepticus in children with Alpers' disease caused by POLG1 mutations: EEG and MRI features.** *Epilepsia* 2009;50:1596–1607 CrossRef Medline
- Lagan NC, Gorman KM, Shahwan A, et al. **Teaching Video Neuro: epilepsy partialis continua in an adolescent with preexisting focal epilepsy.** *Neurology* 2017;89:e274–75 CrossRef Medline
- Papandreou A, Rahman S, Fratter C, et al. **Spectrum of movement disorders and neurotransmitter abnormalities in paediatric POLG disease.** *J Inherit Metab Dis* 2018;41:1275–83 CrossRef Medline
- Ikawa M, Yoneda M, Muramatsu T, et al. **Detection of preclinically latent hyperperfusion due to stroke-like episodes by arterial spin-labeling perfusion MRI in MELAS patients.** *Mitochondrion* 2013;13:676–80 CrossRef Medline
- Saneto RP, Lee I-C, Koenig MK, et al. **POLG DNA testing as an emerging standard of care before instituting valproic acid therapy for pediatric seizure disorders.** *Seizure* 2010;19:140–46 CrossRef Medline
- White ML, Zhang Y, Helvey JT, et al. **Anatomical patterns and correlated MRI findings of non-perinatal hypoxic-ischaemic encephalopathy.** *Br J Radiol* 2013;86:20120464 CrossRef Medline
- Takanashi JI, Barkovich AJ, Cheng SF, et al. **Brain MR imaging in neonatal hyperammonemic encephalopathy resulting from proximal urea cycle disorders.** *AJNR Am J Neuroradiol* 2003;24:1184–87 Medline
- Zuccoli GE, Siddiqui N, Bailey A, et al. **Neuroimaging findings in pediatric Wernicke encephalopathy: a review.** *Neuroradiology* 2010;52:523–29 CrossRef Medline
- Shah T, Purohit S, Raval M. **Imaging in maple syrup urine disease.** *Indian J Pediatr* 2018;85:927–28 CrossRef Medline
- Magill ST, Han SJ, Li J, et al. **Resection of primary motor cortex tumors: feasibility and surgical outcomes.** *J Neurosurg* 2018;129:961–72 CrossRef Medline
- Smith AB, Smirniotopoulos JG, Rushing EJ, et al. **Bilateral thalamic lesions.** *AJR Am J Roentgenol* 2009;192:W53–62 CrossRef Medline
- Tuttle C, Boto J, Martin S, et al. **Neuroimaging of acute and chronic unilateral and bilateral thalamic lesions.** *Insights Imaging* 2019;10:24 CrossRef Medline

Cerebellar Watershed Injury in Children

J.N. Wright, D.W.W. Shaw, G. Ishak, D. Doherty, and F. Perez



ABSTRACT

BACKGROUND AND PURPOSE: Focal signal abnormalities at the depth of the cerebellar fissures in children have recently been reported to represent a novel pattern of bottom-of-fissure dysplasia. We describe a series of patients with a similar distribution and appearance of cerebellar signal abnormality attributable to watershed injury.

MATERIALS AND METHODS: Twenty-three children with MR imaging findings of focal T2 prolongation in the cerebellar gray matter and immediate subjacent white matter at the depth of the fissures were included. MR imaging examinations were qualitatively analyzed for the characteristics and distribution of signal abnormality within posterior fossa structures, the presence and distribution of volume loss, the presence of abnormal contrast enhancement, and the presence and pattern of supratentorial injury.

RESULTS: T2 prolongation was observed at the depths of the cerebellar fissures bilaterally in all 23 patients, centered at the expected location of the deep cerebellar vascular borderzone. Diffusion restriction was associated with MR imaging performed during acute injury in 13/16 patients. Five of 23 patients had prior imaging, all demonstrating a normal cerebellum. The etiology of injury was hypoxic-ischemic injury in 17/23 patients, posterior reversible encephalopathy syndrome in 3/23 patients, and indeterminate in 3/23 patients. Twenty of 23 patients demonstrated an associated classic parasagittal watershed pattern of supratentorial cortical injury. Injury in the chronic phase was associated with relatively preserved gray matter volume in 8/15 patients, closely matching the published appearance of bottom-of-fissure dysplasia.

CONCLUSIONS: In a series of patients with findings similar in appearance to the recently described bottom-of-fissure dysplasia, we have demonstrated a stereotyped pattern of injury attributable to cerebellar watershed injury.

ABBREVIATIONS: HII = hypoxic-ischemic injury; PRES = posterior reversible encephalopathy syndrome; SCA = superior cerebellar artery

Focal signal abnormalities at the depth of the cerebellar fissures in children have recently been reported and have been hypothesized to represent a novel pattern of bottom-of-fissure dysplasia.¹ On the basis of our observation of a similar imaging pattern in patients—including some with initially normal scan findings—who displayed a depth of cerebellar fissure abnormality attributable to ischemic injury, we sought to review our institutional experience. We report a series of 23 patients with a similar distribution and appearance of cerebellar signal abnormality attributable to watershed injury.

MATERIALS AND METHODS

The study was approved by our institutional review board, and on the basis of minimal risk, the need for written informed consent

was waived. Twenty-three patients with MR imaging findings of focal T2 prolongation in the cerebellar gray matter at the depth of the fissures were identified by querying our local radiology data base for the past 15 years and are included in this review. Retrospective analysis of the MR imaging studies was performed by 2 subspecialty board-certified pediatric neuroradiologists with 8 (J.N.W.) and 7 (F.P.) years of experience. Imaging datasets were qualitatively analyzed for the characteristics and distribution of signal abnormality within posterior fossa structures, the presence and distribution of volume loss, the presence of abnormal contrast enhancement, and the presence and pattern of supratentorial injury. Patient demographics, clinical histories, and ultimate clinical radiologic diagnoses were determined by chart review.

RESULTS

Patients

Twenty-three patients with characteristic abnormal cerebellar signal were included in our retrospective analysis, of which 16 were males and 7 females (1 proportion *Z*-test; $z = 1.877$; $P = .06$). Age

Received December 17, 2019; accepted after revision March 16, 2020.

From the Departments of Radiology (J.N.W., D.W.W.S., G.I., F.P.) and Pediatrics (D.D.), Divisions of Developmental and Genetic Medicine, University of Washington and Seattle Children's Hospital, Seattle, Washington.

Please address correspondence to Jason N. Wright, MD, M/S MA.7.220, Seattle Children's Hospital, PO Box 5371, Seattle, WA, 98105; e-mail: jnixon@uw.edu

<http://dx.doi.org/10.3174/ajnr.A6532>

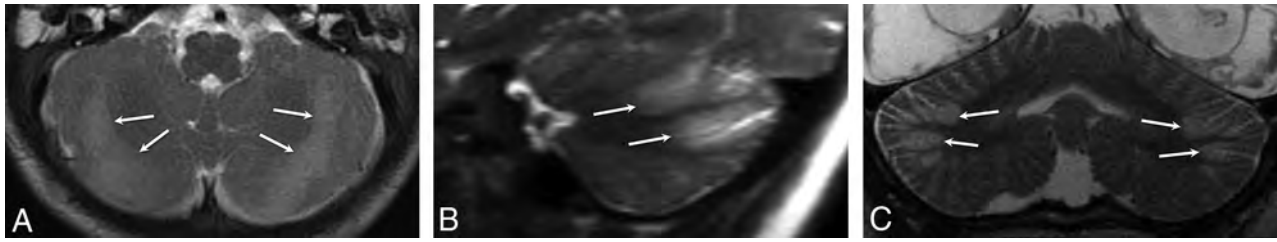


FIG 1. Axial T2WI from patient 2 (A), parasagittal T2WI from patient 8 (B), and a coronal T2WI from patient 6 (C) demonstrate the characteristic appearance and location of cerebellar watershed injury. There is T2 prolongation greatest in the gray matter at the depths of the cerebellar fissures (white arrows) within the deep cerebellar watershed territory.

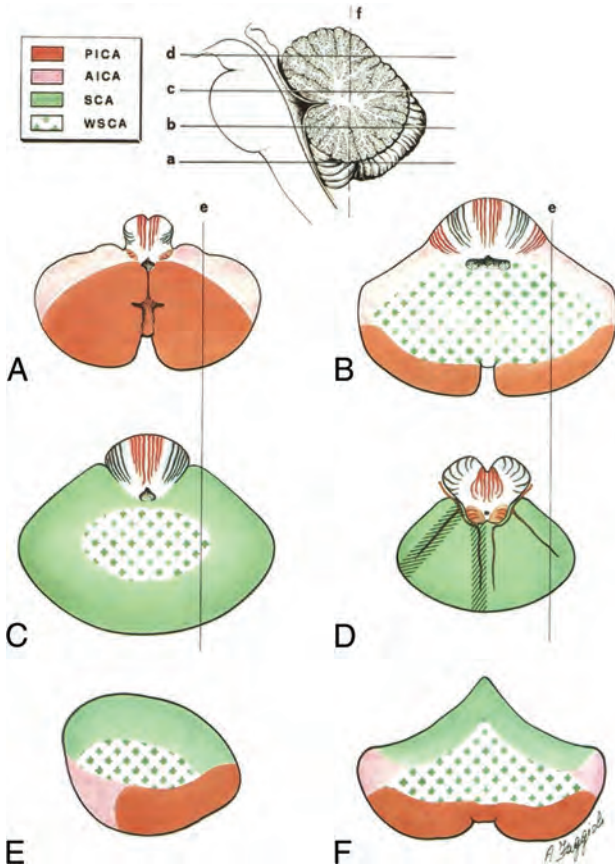


FIG 2. Schematic drawing of the vascular territories of the cerebellum. Note the central distribution of the cerebellar watershed areas (WSCA) at the junction of PICA, AICA, and SCA. The distribution of MR imaging signal abnormality in our case series corresponds to cerebellar watershed regions, best demonstrated by comparing the axial (B), parasagittal (E), and coronal (F) schematic images with multiplanar MR images in Fig 1. Modified from Savoiaro et al.⁷

at the first MR imaging examination demonstrating cerebellar signal abnormality ranged from 2 months to 18 years, with a mean of 4.4 years and a median of 1.2 years. The mean age for patients with acute-phase imaging ($n = 16$) was 3.2 years; and for acute-phase imaging excluding posterior reversible encephalopathy syndrome (PRES) ($n = 13$), it was 0.7 years. Final clinicoradiologic determination of the etiology of brain injury was hypoxic-ischemic injury (HII) in 17 patients, PRES in 3 patients, and indeterminate in 3 patients. Among patients with HII, 5 cases

were secondary to abusive head trauma; 4, to cardiorespiratory arrest; 3, to perinatal birth injury; 2, to profound septic shock; 2, to perioperative hypotension; and 1, to accidental asphyxiation. Ten patients had follow-up imaging at least 1 year after the initial MR imaging demonstrating cerebellar abnormality, with a median follow-up of 64 months (range, 15–142 months). Five patients had past MR imaging studies available, obtained before the first MR imaging that demonstrated the cerebellar abnormality.

Infratentorial Imaging Findings

The key imaging feature was T2 and FLAIR hyperintensity and T1 hypointensity confined to the gray matter and immediate subjacent white matter at the depths of the cerebellar fissures (Fig 1). The findings were best seen on coronal and parasagittal fluid-sensitive sequences. In all patients, bilateral hemispheric involvement was present, with injury typically involving multiple fissures centered at the expected location of the borderzone between the superior cerebellar artery (SCA), AICA, and PICA (Fig 2). The cerebellar tonsils were injured in 39% (9/23) of cases. The cerebellar vermis was spared in 91% (21/23) of patients. Five of the 23 patients had prior imaging studies, all of which demonstrated a normal cerebellar cortex (Fig 3).

Imaging was available for 16/23 patients during the acute phase of injury, defined as <7 days from the suspected clinical event. All patients demonstrated normal thickness or a mildly thickened cerebellar cortex (Figs 3 and 4). Eighty-one percent (13/16) of patients demonstrated acute diffusion restriction (12 with an eventual clinical diagnosis of HII, 1 of unknown etiology) (Fig 4A–C), while 19% (3/16) of patients demonstrated no diffusion abnormality (all with an eventual clinical diagnosis of PRES) (Fig 4D–F). The 3 patients with PRES were imaged in the acute phase only, with no imaging follow-up available.

Imaging was available for 7/23 patients in the subacute phase of injury, defined as 7–30 days from the suspected clinical event. Three of 7 patients (patients 4, 18, and 22) demonstrated intrinsic T1 signal hyperintensity at the depths of the cerebellar fissures (Fig 5A). In 1 case, this was demonstrated to have resolved on a follow-up study performed 1 month later (patient 22) (Fig 5B). One patient who underwent contrast-enhanced MR imaging in the subacute phase demonstrated focal contrast enhancement in the areas of cerebellar injury (patient 18).

Imaging was available for 15/23 patients in the chronic phase of injury, defined as >30 days from the suspected clinical event. All had variable thicknesses of T2 prolongation without diffusion restriction in the cerebellar cortex and the immediate subcortical

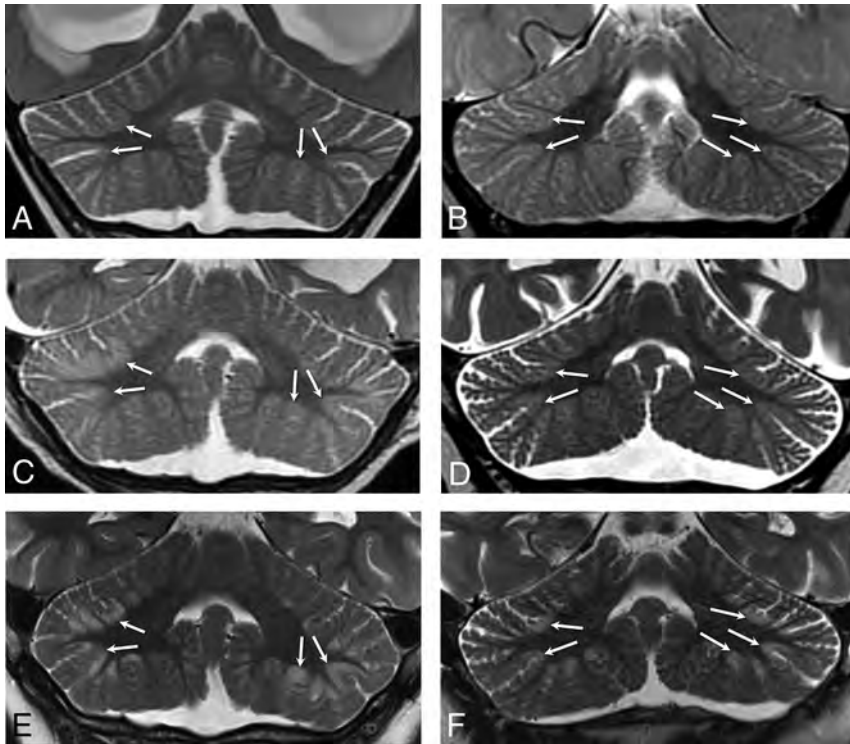


FIG 3. Coronal T2WI from patient 4 (A, C, and E) and patient 11 (B, D, and F) demonstrates the appearance of newly developed acute (C and D) and subsequent chronic (E and F) phase injury in previously normal cerebella (A and B). *White arrows* highlight multiple sites demonstrating progressive development of typical watershed injury in previously normal gray matter.

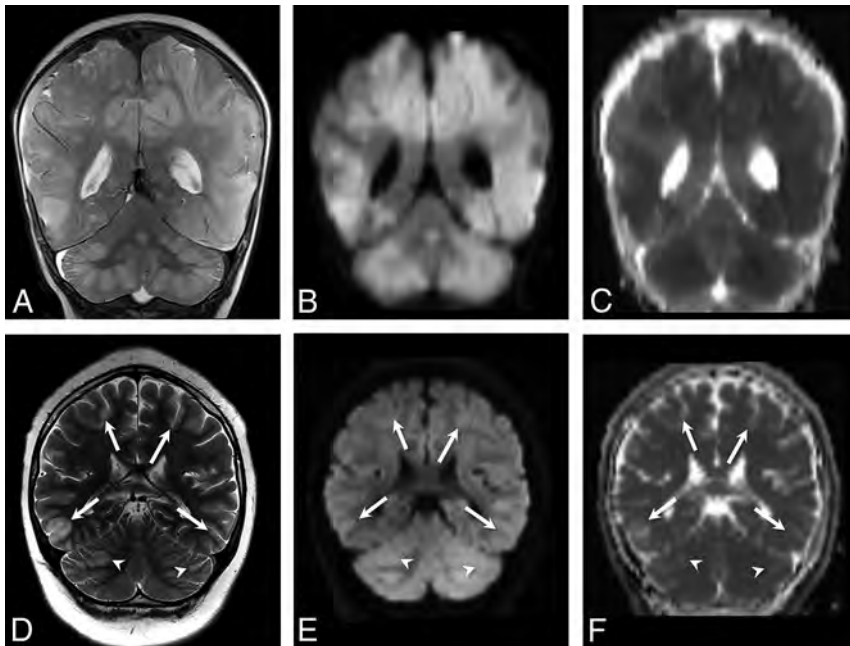


FIG 4. Coronal T2WI (A), coronal DWI (B), and coronal ADC map (C) from patient 18 demonstrate acute cerebellar and supratentorial injury with T2 prolongation and restricted diffusion in the setting of HII. Coronal T2WI (D), coronal DWI (E), and coronal ADC map (F) from patient 9 demonstrate acute cerebellar (*white arrowheads*) and supratentorial (*white arrows*) injury without diffusion restriction in the setting of PRES.

white matter (Fig 6). Seven of 15 patients had marked cortical volume loss with minimal residual T2 hyperintensity (Fig 6A, -B), while the remaining 8 demonstrated a relatively thick layer of T2 hypersignal involving the foliar cortex without substantial volume loss (Fig 6C, -D). Subtle fissural prominence and mild foliar volume loss were identified in 14/15 patients. Ten patients had follow-up for >1 year after the initial MR imaging demonstrating cerebellar signal abnormality, with a median follow-up interval of 5.3 years (range, 1.3–11.8 years). Cerebellar signal abnormality persisted in all cases and for up to 11.8 years in the case with the longest follow-up (patient 1). There were no discernable group differences in terms of the presence of supratentorial injury, overall injury extent or severity, the presence of acute-phase diffusion restriction, underlying etiology, or mean length of follow-up between patients with thick or thin T2 foliar hyperintensity in the chronic phase.

Supratentorial Imaging Findings

In the supratentorial brain, 87% (20/23) of patients demonstrated a classic parasagittal watershed pattern of cortical injury (Fig 7), with 11 with additional evidence of associated basal ganglia injury. Seventeen patients had watershed infarctions and a concordant clinical history of HII. The remaining 3 patients demonstrated a watershed pattern of injury typical of PRES. In all cases, the apparent timing of the supratentorial injury was consistent with the estimated timing relative to the suspected clinical event.

Three of 23 patients demonstrated no evidence of supratentorial watershed cortical injury. One (patient 11) demonstrated diffuse progressive cortical atrophy and a deep pattern of watershed injury in the supratentorial white matter, in the context of underlying drug-resistant chronic epileptic encephalopathy. The remaining 2 patients had no demonstrable supratentorial cortical injury. The first of these had a history of remote aortic stenosis and coarctation repair, and the second had end-stage renal disease

complicated by chronic hypotension and respiratory failure, both of which may have predisposed to recurrent hypoperfusion events that were clinically unsuspected. Of the 3 patients without supratentorial cortical watershed injury, 2 had prior imaging demonstrating normal cerebella (patients 10 and 11).

DISCUSSION

We hypothesize that the pathologic basis for the stereotyped depth-of-cerebellar-fissure MR imaging findings in our case series is cerebellar watershed injury for the following reasons: 1) location at the deep borderzone between the cerebellar artery vascular territories, 2) association with a classic watershed pattern of supratentorial cortical injury, 3) frequent acute-phase diffusion restriction with expected evolution across time, and 4) frequent late foliar volume loss with fissural prominence. Furthermore, among patients with MR imaging performed before the suspected clinical insult, the cerebellar abnormalities were not previously present, indicating an acquired insult rather than a congenital malformation. Diaschisis

secondary to the supratentorial injury was considered an unlikely contributor to the observed infratentorial injury pattern, due to the simultaneous evolution of brain injury in both locations and the multifocal rather than diffuse nature of the cerebellar findings.

Two distinct etiologies of watershed injury were observed in our case series, including PRES and watershed infarctions in the setting of HII. The cortical injury in PRES is poorly characterized at the cellular level but is presumed secondary to abnormal perfusion in the setting of disturbed autoregulation. As is typical of this entity, acute-phase imaging demonstrated T2 prolongation associated with facilitated diffusion. PRES has a strong and well-described predilection for vascular borderzones in the supratentorial brain. While cerebellar involvement has been reported, its distribution has not been well-characterized.²

A classic parasagittal distribution of supratentorial watershed infarctions is well-recognized, with preferential involvement of the end-arterial borderzones between the anterior, middle, and posterior cerebral artery vascular territories. Cerebellar watershed infarcts remain less well-described, with scattered case reports and case series describing predominantly embolic watershed infarcts in adults.³⁻⁶ A few authors have emphasized the distinction between superficial cerebellar borderzone embolic infarcts and deep cerebellar watershed infarcts, the latter related to hypoperfusion and centered at the interface between the penetrating arteries of the cerebellar arteries.⁷⁻¹⁰

Although some authors have asserted that deep watershed infarcts predominantly affect the deep cerebellar white matter, several lines of evidence suggest that focal injury to the gray matter at the depth of the cerebellar fissures is, in fact, the expected pattern. In a primate model of induced cerebral hypoperfusion,^{11,12} cerebellar injury in the watershed between the SCA and PICA was noted in 7/15 adult rhesus monkeys, in conjunction with classic supratentorial watershed injury. The injury predominantly affected cortical gray matter at the depths of the cerebellar fissures. Depth of fissure gray matter injury was also noted on

gross and histopathologic evaluations of human brains after hypoxic injury,¹³ in a pattern exactly corresponding to the distribution of injury in our case series. This distribution may reflect the unique angioarchitecture of the penetrating arteries in the cerebellum, analogous to the propensity for depth-of-sulcus cortical injury in neonates with HII reported by Takashima et al.¹⁴

Sparing of the cerebellar vermis was a notable feature in our patients, possibly because the arterial supply to the vermis is almost entirely derived from the SCA, with relatively minor contributions from the inferior cerebellar arteries.¹⁵ In contrast, cerebellar tonsillar injury was observed in more than one-third of patients in our series, likely reflecting its location at the borderzone between the AICA and PICA territories.¹⁵

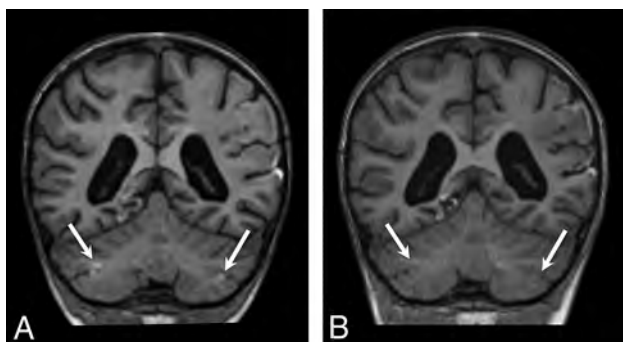


FIG 5. Coronal T1WI from patient 22 in the subacute (A) and chronic (B) phases demonstrates focal T1 hyperintensity in the bilateral cerebellar watershed (white arrows in A), consistent with laminar necrosis and resolved within 1 month on follow-up (white arrows in B).

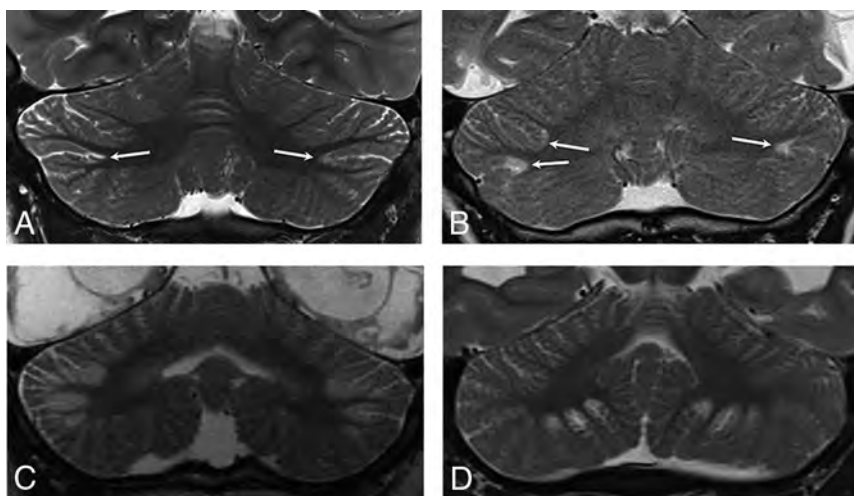


FIG 6. Coronal T2WI from patients during the chronic phase. Patients 1 (A) and 2 (B) demonstrate T2 prolongation with relatively marked gray matter volume loss at the sites of prior injury (white arrows). Patients 7 (C) and 10 (D) demonstrate a thick lamina of gray matter T2 prolongation centered at the depths of the cerebellar fissures in an arterial watershed distribution. See also Figs 1C, 3E, and 3F for additional examples.

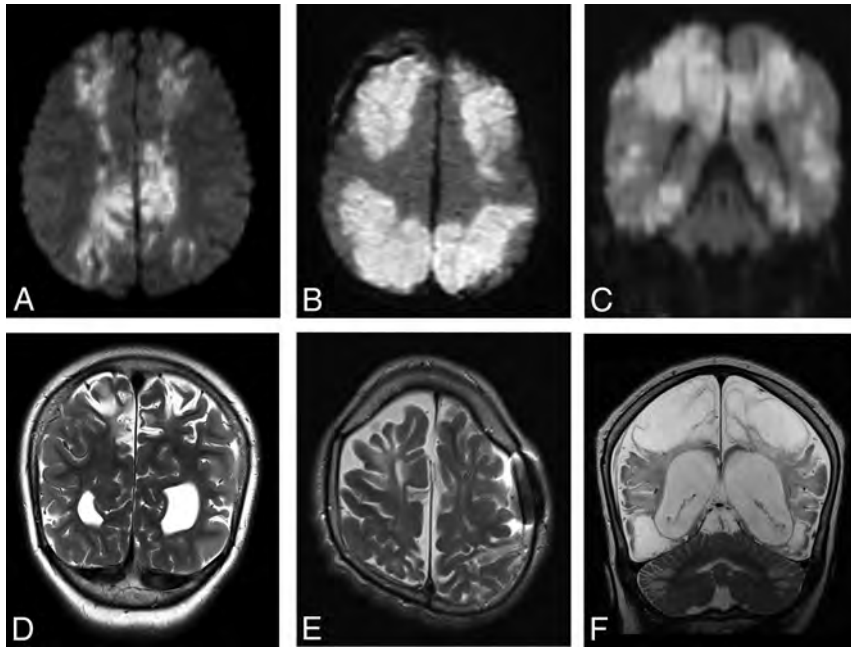


FIG 7. Findings of both acute and remote supratentorial watershed injury in patients 1–6 (A–F, respectively). Acute watershed infarcts with signal abnormality on axial (A and B) and coronal (C) DWI in a characteristic parasagittal distribution. Subacute or remote watershed infarcts with hyperintensity and parenchymal volume loss on coronal (D and F) and axial (E) T2.

Our patient series comprised a disproportionate number of male patients, though this finding did not reach statistical significance regarding variance from an expected population proportion of 50% male. This may, in part, be related to the number of cases of HII secondary to abusive head trauma in our series, which is known to disproportionately affect male patients.¹⁶ Haas-Lude et al¹⁷ recently reported a strikingly similar pattern of cerebellar injury in 2 patients with abusive head trauma, both with a supratentorial watershed pattern of HII. It would be interesting to investigate the prevalence of this finding in a larger cohort of patients with suspected abusive head trauma to better understand its predictive value above and beyond the presence of HII more generally.

Our case series is among the first to describe the characteristic appearance of cerebellar watershed injury in children. Recognition of this pattern of injury is important for identifying patients with HII or PRES and for avoiding misdiagnosis. For example, 1 of our patients was originally misdiagnosed with cerebellitis based on abnormal cerebellar T2 hyperintensity (patient 10), delaying definitive diagnosis. Similarly, Mills et al¹⁸ reported a case of “severe cerebellitis” in a child with supratentorial watershed infarcts following methadone poisoning. The imaging findings in that case are strikingly similar to those in our case series, raising the possibility of watershed cerebellar injury rather than cerebellitis.

A second patient in our case series was initially diagnosed with bottom-of-fissure dysplasia; however, a prior MR imaging subsequently became available demonstrating a normal cerebellum, indicating an acquired rather-than-congenital lesion. The similarity between our reported imaging findings and those of Poretti et al¹ suggests that unrecognized watershed injury may have been

present in some or all of their cases, or that cerebellar watershed injury and bottom-of-fissure dysplasia share a common imaging appearance. Although they considered the possibility of cerebellar watershed injury as the etiology of the imaging findings in Poretti et al,¹ they ultimately concluded that lack of substantial white matter involvement, variability of distribution of involved fissures, and stability with time all argued against this possibility. It is clear from our patient series—corroborated by the available experimental neurophysiology and neuropathology literature—that the foliar gray matter at the depths of the fissures is an expected location of cerebellar watershed injury, with minimal or absent white matter involvement.^{11–13} Variable fissural involvement is expected because it reflects the relatively variable vascular territories and shifting borderzones of the cerebellar arteries.¹⁵ Furthermore, stability with time in the chronic phase, often with unexpectedly subtle volume loss, was the norm in our series.

There are several limitations to our analysis, primarily reflecting the small sample size and retrospective design. We were unable to assess the clinical implications of cerebellar watershed injury in our case series because of the small and heterogeneous sample. Our study does not permit an analysis of the prevalence of cerebellar imaging findings among children with supratentorial watershed injury. It is also possible that a subset of our cases may represent a dysplastic process as suggested by Poretti et al,¹ particularly those without corroborative supratentorial findings. However, 5 of our patients had a prior MR imaging study demonstrating a normal cerebellum, including 2 of the 3 patients without clear supratentorial cortical watershed injury, arguing against the likelihood of a developmental abnormality.

CONCLUSIONS

We have demonstrated a stereotyped pattern of injury that is most plausibly attributable to cerebellar watershed injury. This report extends the reported imaging findings in watershed cortical injury related to HII and PRES, which are an important diagnostic consideration when cerebellar dysplasia and inflammatory pathologies such as cerebellitis are being entertained.

REFERENCES

1. Poretti A, Capone A, Hackenberg A, et al. **Cerebellar bottom-of-fissure dysplasia: a novel cerebellar gray matter neuroimaging pattern.** *Cerebellum* 2016;15:705–09 CrossRef Medline
2. Bartynski WS, Boardman JF. **Distinct imaging patterns and lesion distribution in posterior reversible encephalopathy syndrome.** *AJNR Am J Neuroradiol* 2007;28:1320–27 CrossRef Medline

3. Amarenco P, Kase CS, Rosengart A, et al. **Very small (border zone) cerebellar infarcts: distribution, causes, mechanisms and clinical features.** *Brain* 1993;116:161–86 CrossRef Medline
4. Yin WM, Nagata K, Satoh Y, et al. **Infratentorial infarction: correlation of MR findings with neurological and angiographical features.** *Neurol Res* 1994;16:154–58 CrossRef Medline
5. Benjumea V, Vélez A, Hernández O, et al. **Infartos limitrofes cerebrales y cerebelosos asociados a compromiso hemodinámico: reporte de caso y revisión de la literature.** *Acta Neurol Colomb* 2014;30:342–45. <http://www.scielo.org.co/pdf/anco/v30n4/v30n4a16.pdf>. Accessed April 6, 2020
6. Zheng M, Sun AP, Sun QL, et al. **Clinical and imaging analysis of a cerebellar watershed infarction.** *Chinese Medicine* 2015;06:54–60 CrossRef
7. Savoirdo M, Bracchi M, Passerini A, et al. **The vascular territories in the cerebellum and brainstem: CT and MR study.** *AJNR Am J Neuroradiol* 1987;8:199–209 Medline
8. Cormier PJ, Long ER, Russell EJ. **MR imaging of posterior fossa infarctions: vascular territories and clinical correlates.** *Radiographics* 1992;12:1079–96 CrossRef Medline
9. Amarenco P. **Cerebellar infarctions and their mechanisms.** *Rev Neurol (Paris)* 1993;149:728–48 Medline
10. Caplan LR. **Cerebellar infarcts: key features.** *Rev Neurol Dis* 2005;2:51–60 Medline
11. Brierley JB, Excell BJ. **The effects of profound systemic hypotension upon the brain of M. rhesus.** *Brain* 1966;89:269–98 CrossRef Medline
12. Brierley JB, Brown AW, Excell J, et al. **Brain damage in the rhesus monkey resulting from profound arterial hypotension, I: its nature, distribution and general physiological correlates.** *Brain Res* 1969;13:68–100 CrossRef Medline
13. Graham DI. **Pathology of hypoxic brain damage in man.** *J Clin Pathol Suppl (R Coll Pathol)* 1977;11:170–80 CrossRef Medline
14. Takashima S, Armstrong DL, Becker LE. **Subcortical leukomalacia: relationship to development of the cerebral sulcus and its vascular supply.** *Arch Neurol* 1978;35:470–72 CrossRef Medline
15. Icardo JM, Ojeda JL, Garcia-Porrero JA, et al. **The cerebellar arteries: cortical patterns and vascularization of the cerebellar nuclei.** *Acta Anat (Basel)* 1982;113:108–16 CrossRef Medline
16. Selassie AW, Borg K, Busch C, et al. **Abusive head trauma in young children: a population-based study.** *Pediatr Emerg Care* 2013;29:283–91 CrossRef Medline
17. Haas-Lude K, Roulet-Perez E, Döbler-Neumann M, et al. **Cerebellar lesions in pediatric abusive head trauma.** *Eur J Paediatr Neurol* 2019;23:604–08 CrossRef Medline
18. Mills F, MacLennan SC, Devile CJ, et al. **Severe cerebellitis following methadone poisoning.** *Pediatr Radiol* 2008;38:227–29 CrossRef Medline

Sensitivity of the Inhomogeneous Magnetization Transfer Imaging Technique to Spinal Cord Damage in Multiple Sclerosis

H. Rasoanandrianina, S. Demortière, A. Trabelsi, J.P. Ranjeva, O. Girard, G. Duhamel, M. Guye, J. Pelletier, B. Audoin, and V. Callot



ABSTRACT

BACKGROUND AND PURPOSE: The inhomogeneous magnetization transfer technique has demonstrated high specificity for myelin, and has shown sensitivity to multiple sclerosis-related impairment in brain tissue. Our aim was to investigate its sensitivity to spinal cord impairment in MS relative to more established MR imaging techniques (volumetry, magnetization transfer, DTI).

MATERIALS AND METHODS: Anatomic images covering the cervical spinal cord from the C1 to C6 levels and DTI, magnetization transfer/inhomogeneous magnetization transfer images at the C2/C5 levels were acquired in 19 patients with MS and 19 paired healthy controls. Anatomic images were segmented in spinal cord GM and WM, both manually and using the AMU₄₀ atlases. MS lesions were manually delineated. MR metrics were analyzed within normal-appearing and lesion regions in anterolateral and posterolateral WM and compared using Wilcoxon rank tests and z scores. Correlations between MR metrics and clinical scores in patients with MS were evaluated using the Spearman rank correlation.

RESULTS: AMU₄₀-based C1-to-C6 GM/WM automatic segmentations in patients with MS were evaluated relative to manual delineation. Mean Dice coefficients were 0.75/0.89, respectively. All MR metrics (WM/GM cross-sectional areas, normal-appearing and lesion diffusivities, and magnetization transfer/inhomogeneous magnetization transfer ratios) were observed altered in patients compared with controls ($P < .05$). Additionally, the absolute inhomogeneous magnetization transfer ratio z scores were significantly higher than those of the other MR metrics ($P < .0001$), suggesting a higher inhomogeneous magnetization transfer sensitivity toward spinal cord impairment in MS. Significant correlations with the Expanded Disability Status Scale ($\rho = -0.73/P = .02$, $\rho = -0.81/P = .004$) and the total Medical Research Council scale ($\rho = 0.80/P = .009$, $\rho = -0.74/P = .02$) were observed for inhomogeneous magnetization transfer and magnetization transfer ratio z scores, respectively, in normal-appearing WM regions, while weaker and nonsignificant correlations were obtained for DTI metrics.

CONCLUSIONS: With inhomogeneous magnetization transfer being highly sensitive to spinal cord damage in MS compared with conventional magnetization transfer and DTI, it could generate great clinical interest for longitudinal follow-up and potential remyelinating clinical trials. In line with other advanced myelin techniques with which it could be compared, it opens perspectives for multicentric investigations.

ABBREVIATIONS: AMU = Aix-Marseille University; CSA = cross-sectional areas; EDSS = Expanded Disability Status Scale; FA = fractional anisotropy; HC = healthy controls; ihMT = inhomogeneous magnetization transfer; ihMTR = inhomogeneous magnetization transfer ratio; $\lambda_{//}$ = axial diffusivity; λ_{\perp} = radial diffusivity; MRC = Medical Research Council; MT = magnetization transfer; MTR = magnetization transfer ratio; NA = normal-appearing; SC = spinal cord; TWT = Timed 25-Foot Walk Test; SCT = Spinal Cord Toolbox

MS is a chronic autoimmune disease of the CNS affecting the brain and the spinal cord (SC), characterized by multifocal

demyelination and inflammation, edema, axonal loss, and gliosis, whose diagnosis is based on anatomic MR imaging.¹ Although

Received June 20, 2019; accepted after revision March 12, 2020.

From the Center for Magnetic Resonance in Biology and Medicine (H.R., S.D., A.T., J.P.R., O.G., G.D., M.G., J.P., B.A., V.C.), Centre National de la Recherche Scientifique, Aix-Marseille Université, Marseille, France; Centre d'Exploration Métabolique par Résonance Magnétique (H.R., S.D., A.T., J.P.R., O.G., G.D., M.G., J.P., B.A., V.C.), Assistance Publique-Hopitaux de Marseille, Hôpital Universitaire Timone, Marseille, France; Laboratoire de Biomécanique Appliquée, Institut Français des Sciences et Technologies des Transports, de l'Aménagement et des Réseaux, Aix-Marseille Université; iLab-Spine International Associated Laboratory (H.R., J.P.R., V.C.), Marseille-Montreal, France-Canada; and Department of Neurology (S.D., J.P., B.A.), Centre Hospitalier Universitaire Timone, Assistance Publique-Hopitaux de Marseille, Marseille, France.

Henitsoa Rasoanandrianina and Sarah Demortière contributed equally to this article.

This work was performed by a laboratory member of France Life Imaging network (grant ANR-II-INBS-0006) and supported by the French Centre National de la Recherche Scientifique, the French Ministère de l'Enseignement Supérieur et de la Recherche, and the Fondation pour l'Aide à la Recherche sur la Sclérose En Plaques.

Please address correspondence to Virginie Callot, PhD, CRMBM-CEMEREM, UMR 7339, CNRS, Aix-Marseille Université, Faculté de Médecine, 27, bd Jean Moulin, 13385 Marseille Cedex 5, France; e-mail: virginie.callot@univ-amu.fr

Indicates open access to non-subscribers at www.ajnr.org

Indicates article with supplemental on-line tables.

Indicates article with supplemental on-line photo.

<http://dx.doi.org/10.3174/ajnr.A6554>

extensive investigations including demonstration of multicentric capabilities and scan time reduction are still necessary to bridge the gap to clinical practice, quantitative MR imaging techniques now have the potential to help improve disease diagnosis and monitoring,² as well as treatment evaluation.

Given the clinical relevance and the risk of long-term disability in spinal MS,³ a better characterization of pathologic mechanisms underlying SC tissue impairment, including myelin damage, is therefore essential.

Unfortunately, SC MR imaging lags behind brain MR imaging, mainly due to technical challenges related to the small size, CSF pulsatility, respiratory motion, and susceptibility artifacts of the spinal cord due to surrounding bony structures.⁴ Nonetheless, due to recent methodologic improvements, a growing number of SC MR imaging studies in MS have been reported, mostly using DTI⁵ and conventional magnetization transfer (MT)⁶ imaging, highlighting SC microstructural changes with significant correlations to physical disability.^{7,8}

Although highly sensitive to MS-related tissue changes, both DTI and MT metrics are not specific to myelin damage because they could also be affected by inflammation and/or axonal loss.⁹ Tremendous effort has thus recently been made toward the development of more myelin-specific MR imaging techniques.^{10,11} These particularly include myelin-water imaging,¹² which gives access to the myelin water fraction¹³ or water protons associated with myelin trapped between the finely spaced lipid bilayers of the myelin sheaths, as well as quantitative MT,^{14,15} which gives a robust estimate of the macromolecular-to-free pool size ratio, which has been shown to strongly correlate with white matter myelin density,¹⁶ or the recently described inhomogeneous MT (ihMT) technique.¹⁷⁻¹⁹ This latter allows selectively isolating the contribution of dipolar order within the broad MT signal and hence appears particularly sensitive to myelinated structures due to their relatively long dipolar relaxation times.¹⁷ Applied in a preliminary clinical MS study, ihMT was found to be highly sensitive to cerebral microstructural changes with strong correlation to the Expanded Disability Status Scale (EDSS).²⁰ Furthermore, embedded within a protocol optimized for the SC,¹⁸ it has also already demonstrated high sensitivity to SC tissue changes in both aging healthy subjects²¹ and patients with amyotrophic lateral sclerosis.²²

In line with these studies, the main purpose of this work was to assess the sensitivity of the ihMT technique to SC impairment in MS relative to more conventional MR imaging markers, including atrophy, MT, and DTI measures and to demonstrate its potential in clinical monitoring. To do so, we applied a multiparametric MR imaging protocol, including high-resolution anatomic and quantitative DTI and MT/ihMT imaging techniques, together with a SC template-based approach to quantify data collected in patients with MS and age-matched healthy controls (HC) in different ROIs.

MATERIALS AND METHODS

Subjects

This retrospective study was approved by our institutional ethics committee (CCP Sud Méditerranée 1), and written informed

Table 1: Demographic and clinical features of the study population including HC and patients with MS^a

Demographics	HC	MS
Count (female/male)	19 (11/8)	19 (11/8)
Age (years)	52 (22–74)	46 (26–70)
Disease duration (months)	–	117 (48–372)
EDSS	–	2.5 (1–7)
Total MRC ^b (/120)	–	118 (103–120)
NHPT ^c (sec)	–	24.1 (17.8–73.4)
TWT (sec)	–	5.5 (3.4–73)
Handgrip ^d (kPa)	–	82.5 (25.5–122.5)
No. of SC lesions	–	4 (2–7)
Volume of brain lesions (mm ³)	–	3261 (726–38,013)

Note:—NHPT indicates Nine-Hole Peg Test; –, not applicable measurements.

^aReported values are medians (minimum–maximum). Lesion burden in the cervical SC and brain of patients with MS is also reported.

^bMedical Research Council scale: normal value per muscle, 5; range, 0–5, for upper (7 muscles on each side) and lower limbs (5 muscles on each side), with a total maximum score of 120.

^cThe Nine-Hole Peg Test for each hand and TWTs were performed twice for each patient, and the best performance was preserved.

^dHandgrip measurements for each patient were repeated thrice for each hand and then averaged to get 1 value per limb.

consent was obtained from all subjects. Nineteen patients with MS (13 relapsing-remitting and 6 secondary-progressive forms) and 19 sex- and age-matched HC were included during 2 years. Inclusion criteria for patients were a diagnosis of MS according to the revised McDonald criteria²³ and clinical symptoms suggesting SC involvement. Clinical symptoms were evaluated >3 months after steroid infusion. Exclusion criteria were any neurologic disease other than MS and chronic psychiatric diseases. Neurologic examinations were performed right after the MR imaging acquisitions. They included a specific MS global disability rating scale with EDSS scoring. A muscle strength grading with the Medical Research Council scale (MRC)²⁴ for the 4 limbs was also performed. Specific assessment of the upper limbs was performed with a handgrip strength test²⁵ and the Nine-Hole Peg Test, currently used in MS to assess manual dexterity. For lower limb evaluation, a Timed 25-Foot Walk Test (TWT)²⁶ was performed. Additional details are found in Table 1.

Image Acquisition

MR imaging was performed on a 3T scanner (Magnetom Verio; Siemens) using the body coil for transmission and standard 12-channel head, 4-channel neck, and 24-channel spine matrix array coils for reception. The subjects were positioned with the neck in a neutral position using a cervical collar to reduce subject motion.

The MR imaging protocol (summarized in On-line Table 1) was optimized to last approximately 50 minutes. It included a 3D-T2WI sequence for vertebral level identification and cervical lesion depiction (see postprocessing in Fig 1), a 2D multisection multiangle T2*WI multiecho gradient-echo sequence (7 slices, 1 per cervical level from C1 to C7), providing a good contrast to delineate GM and WM, as well as 2-level DTI and ihMT acquisitions (single-section) centered at mid-C2 and mid-C5 cervical levels, placed strictly perpendicular to the cord axis. Patients also underwent, during the same session, conventional brain and SC acquisitions at the cervical level (T1WI, T2WI, FLAIR, STIR, and postgadolinium T1) for lesion burden evaluation.

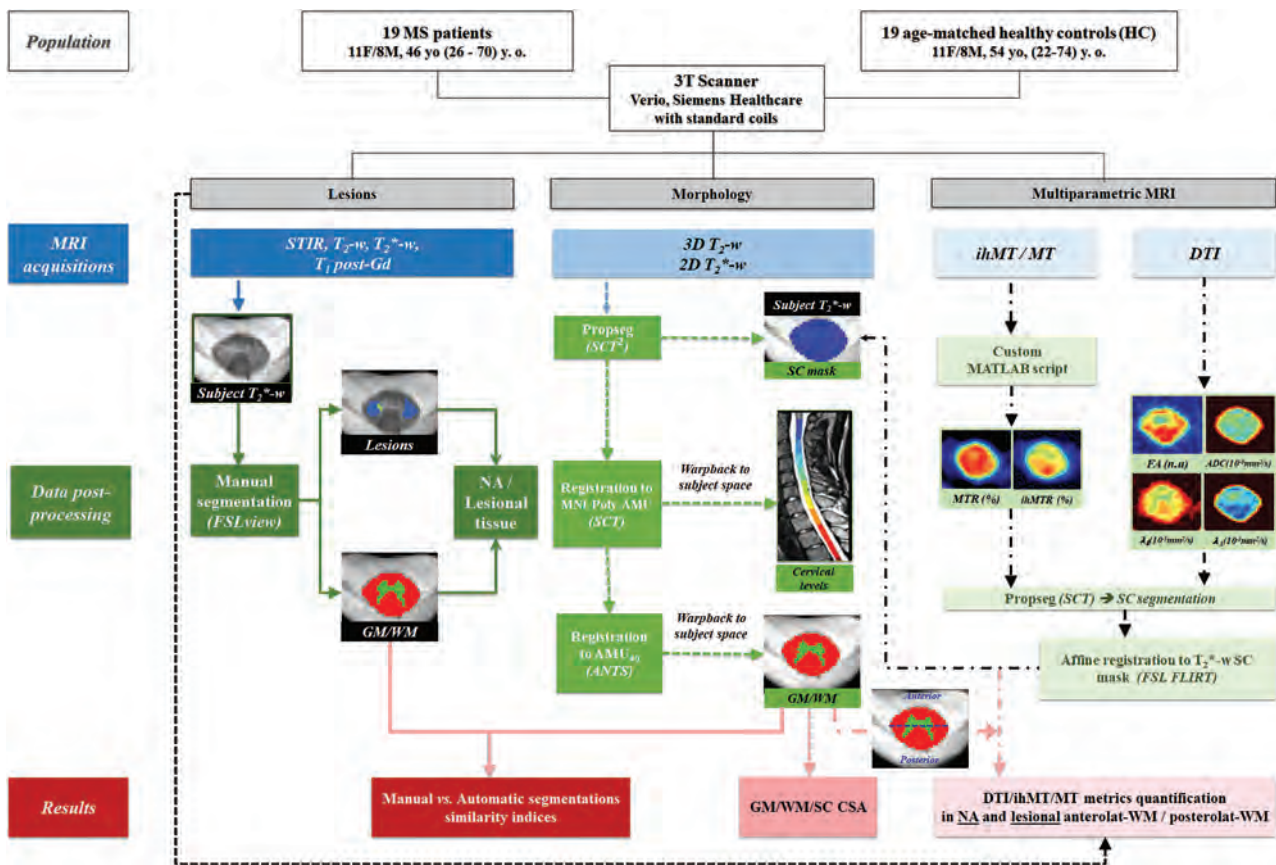


FIG 1. Design of the study. Acquisition and postprocessing pipeline for MR imaging data shown for the C2 cervical level in a patient with MS, including the following: manual SC, GM/WM, and lesional/NA tissue segmentations on T2*WI and registration of the 3D-T2WI to the MNI-Poly-AMU template to automatically identify the cervical levels from C1 to C7 (warped back into the subject's space; this step allows cord volume per level measurements, not reported in this study); SC segmentation on T2*WI and T2WI by the SCT PropSeg³¹ function; T2WI registration to the MNI-Poly-AMU template²⁸ to obtain cervical levels; T2*WI registration to the AMU₄₀ template²⁹ to obtain GM/WM segmentations, warped back into the subject's space followed by CSA (square millimeters) extraction and intrasubject multiparametric data normalization, taking into account the presence of lesions, allowing metrics extraction from lesional and NA anterolateral WM and posterolateral WM, derived from the WM tracts atlas and defined as delimited by the *blue horizontal line*. Masks were eroded (2D surface) before quantification. y.o. indicates years of age; Gd, gadolinium; anterolat, anterolateral; posterolat, posterolateral; FSL view refers to the FSL viewer software;³⁰ ANTs, Advanced Normalization Tools (<http://stnava.github.io/ANTs/>); FLIRT, FMRIB is the FSL Linear Image Registration Tool (<http://www.fmrib.ox.ac.uk/fsl/fslwiki/FLIRT>);⁵¹ WM tracts atlas (<https://sourceforge.net/p/spinalcordtoolbox/wiki/White%20Matter%20atlas/>);³²

Data Analysis

The entire postprocessing pipeline, detailed in Fig 1, was performed off-line using a custom Matlab script (Matlab R2014a; MathWorks), relying on the Spinal Cord Toolbox (SCT; <https://sourceforge.net/projects/spinalcordtoolbox/>)²⁷ functions and dedicated SC templates and atlases (MNI-Poly-AMU; <https://sourceforge.net/p/spinalcordtoolbox/wiki/MNI-Poly-AMU/>)²⁸ and AMU₄₀²⁹), allowing automatic delineation of the GM and WM.

To evaluate the efficacy of the AMU₄₀-based automated GM/WM segmentation applied for the first time in MS, 2 independent experts (S.D., an in-training neurologist, and H.R., a 3-year MR imaging expert) manually outlined the SC and GM using FSLview software (Version 5.0.10; <http://fsl.fmrib.ox.ac.uk/fsl/fslwiki/fslview/>)³⁰ on all T2*WI images. The WM region was subsequently obtained by subtracting SC and GM masks. Agreement between the 2 raters and between manual and automatic segmentations was evaluated by computing 3 conventional parameters:³¹ the Dice similarity coefficient (range, 0–1, with 1 indicating

perfect similarity), the Hausdorff distance (in millimeters), and the maximum median distance between skeletonized segmentations (in millimeters), using the SCT.²⁷ For each subject, a comparison of the 3 WM/GM metrics between the 2 raters was performed; then, the average value per structure was calculated. All automatic segmentations presenting manual/automatic Dice coefficients of <0.8 (considered imperfect) were manually corrected under strict consensus between the 2 experts and subsequently used for multiparametric metrics quantification.

Morphologic measurements were then performed on all subjects by extracting the cross-sectional areas (CSA, in square millimeters) from automatic GM/WM segmentations (manually corrected if necessary) at each cervical level from C1 to C6 (C7 was discarded due to subject motion in 7/19 subjects [37%]).

Cervical SC lesions (characterized by signal hyperintensities) were finally depicted and counted from both STIR and T2WI. Then, for quantitative analyses, manual segmentation of lesions was performed on the T2*WI by expert 1 (S.D.) using both STIR and T2WI series as additional references to improve the accuracy

of the lesion location. All the segmented lesions were visible on all 3 images. Normal-appearing (NA) regions were subsequently differentiated from lesion regions for metrics quantification.

For quantitative analysis, 4 DTI metrics (fractional anisotropy [FA], ADC, axial diffusivity [$\lambda_{//}$], and radial diffusivity [λ_{\perp}], along with MT and ihMT ratios [MTR/ihMTR]) were derived afterward and quantified within the anterolateral WM and posterolateral WM at C2 and C5. The GM was not considered. These regions were chosen to comply with current ihMT HASTE limitations in terms of partial volume effect and the loss of spatial resolution (see Discussion). To match ihMT single-section quantification, only the middle section was considered for the DTI metrics. At the end of the postprocessing pipeline, the quantitative dataset for each subject included SC, GM, and WM CSA at each level from C1 to C6, as well as mean \pm SD values of FA, ADC, λ_{\perp} , $\lambda_{//}$, ihMTR, and MTR from anterolateral and posterolateral WM regions free from or having MS lesions (NA/lesional regions). For each metric, values from C2 and C5 were averaged to obtain a single value per ROI per subject for statistical purposes.

Last, brain lesions were manually segmented on T2 and FLAIR images to estimate their volume.

Statistical Analysis

Statistical analyses were performed using JMP9 (SAS Institute), considering $P < .05$ for statistical significance.

Comparison of MR Imaging Data between Patients with MS and Healthy Controls

For MS-related morphologic change evaluation, GM, WM, and SC CSA at each level were compared between patients with MS and HC, using nonparametric Wilcoxon rank tests corrected for multiple comparisons ($n = 6$ cervical levels) with the Holm-Bonferroni method.

Considering multiparametric data, we used the nonparametric Steel-Dwass all-pairs tests corrected for multiple comparisons to assess DTI/MT/ihMT metrics differences between patients and HC.

Sensitivity of ihMT to MS-Related Changes

DTI, MT, and ihMT metrics z scores were computed for NA and lesional anterolateral WM, posterolateral WM, and total WM for each patient with MS relative to mean values of HC. CSA z scores, all cervical levels considered, were calculated for global GM, WM, and SC.

Z scores of ihMTR were then compared with z scores of all metrics using nonparametric Wilcoxon rank tests to assess the sensitivity of ihMT to MS-related changes compared with the more conventional atrophy (CSA), DTI, and MT measures. Henceforth, the term “metric variation” will be used to refer to a change in the absolute z score value of the metrics.

Correlations with Clinical Scores. Correlations among brain lesion volume, SC lesion number, SC/GM/WM CSA, and DTI/MT/ihMT metrics variations (ie, z scores) in lesion and NA WM regions and each clinical score (disease duration, total MRC, hand-grip, TWT, Nine-Hole Peg Test, and EDSS) were evaluated using the statistical nonparametric Spearman rank test. The resulting

significant correlations were then corrected to control for multiple comparisons using the false discovery rate procedure.

RESULTS

Patient Characteristics

Demographic information and clinical features of patients with MS are summarized in Table 1. The median EDSS score and disease duration of the patients at the time of MR imaging were 2.5 and 117 months, respectively.

Reliability of the Automated AMU₄₀ GM/WM Segmentation

On-line Table 2 summarizes the similarity indices (Dice coefficient, Hausdorff, and skeletonized mean distances) with regard to manual GM/WM segmentations. The reader is referred to the On-line Figure for illustrations of representative AMU₄₀-based GM segmentations from patients with MS with/without the presence of lesions. In the HC group, AMU₄₀-based segmentations were found to be highly reliable with mean Dice coefficients of 0.85 ± 0.05 and 0.92 ± 0.02 for GM and WM, respectively. In patients with MS, 8/114 slices were discarded due to visually observed poor contrast in the images, mostly due to breathing motion of the patients. When applied to the remaining 106 slices, indices from WM (Dice, 0.89 ± 0.04) were close to those found in HC, whereas the values from GM segmentations (0.75 ± 0.14) were found to be lower, with higher SDs. Worse GM indices were found in slices with lesions (0.73 ± 0.12) compared with slices without lesions (0.79 ± 0.09), whereas WM indices were similar whether or not lesions were present in the slices. Afterward, 29% (31/106 slices) of the AMU₄₀-based segmentations (with Dice, <0.8) were manually corrected for measurements of CSA and multiparametric analysis.

Comparison of MR Imaging Data between Patients with MS and Healthy Controls

Boxplots of GM and WM CSA from HC and patients with MS along with the corresponding z scores and percentages of variation are presented in Fig 2. A significant decrease in CSA for the SC ($P < .001$, data not shown) and WM ($P < .003$) across all cervical levels was found in patients with MS compared with HC. Decrease trends were additionally found for GM areas, significant at C6 ($P = .003$).

Figure 3 shows representative multiparametric datasets of 2 patients with MS (MS_1: 64 years of age, EDSS score, 2; MS_2: 60 years of age, EDSS score, 6) and a healthy control (65 years of age). Overall, in patients with MS, the DTI, ihMTR, and MTR values were all found altered in both NA and lesional WM regions (Table 2 and Fig 4) compared with the healthy control. λ_{\perp} and ADC showed trends toward an increase, albeit not significant, whereas ihMTR and MTR significantly decreased in both regions, with higher metric variations found in regions with lesions compared with NA tissue.

Sensitivity of ihMT to MS-Related Changes

Among all DTI, MT, and ihMT metrics, ihMTR showed the most important metrics variations (ie, higher absolute z score values) as illustrated in Fig 4. Results of Wilcoxon rank tests showed significant differences between these ihMTR variations and z scores

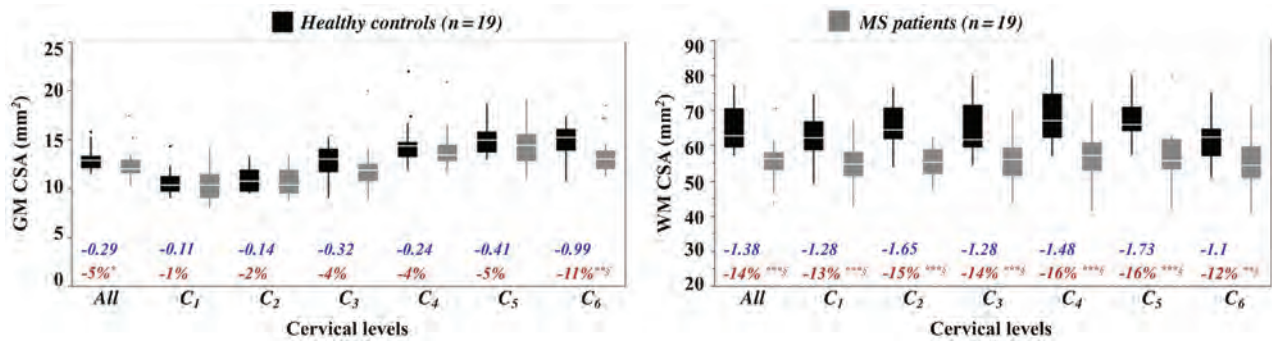


FIG 2. CSAs (square millimeters) in HC and patients with MS. Mean values were extracted from AMU₄₀-based GM and WM segmentations for each cervical level (C1 to C6). *Boxplots* of subjects' mean CSA values across all cervical levels are also presented in the first column of each graph. The *boxplots* represent the minimum, first quartile (25%), the median, the third quartile (75%) and the maximum from upper to lower, respectively. Significant decreases in CSA in patients with MS relative to HC, assessed using Wilcoxon rank tests are reported as * $P < .05$, ** $P < .001$, *** $P < .0001$. The section symbol indicates statistical differences that survive the Holm-Bonferroni correction for multiple comparisons. The percentage difference of CSA between MS and HC groups (in red) and the average z scores (no unit, in blue) in patients with MS relative to HC at each level are also reported; a negative value indicates a decrease in CSA in patients.

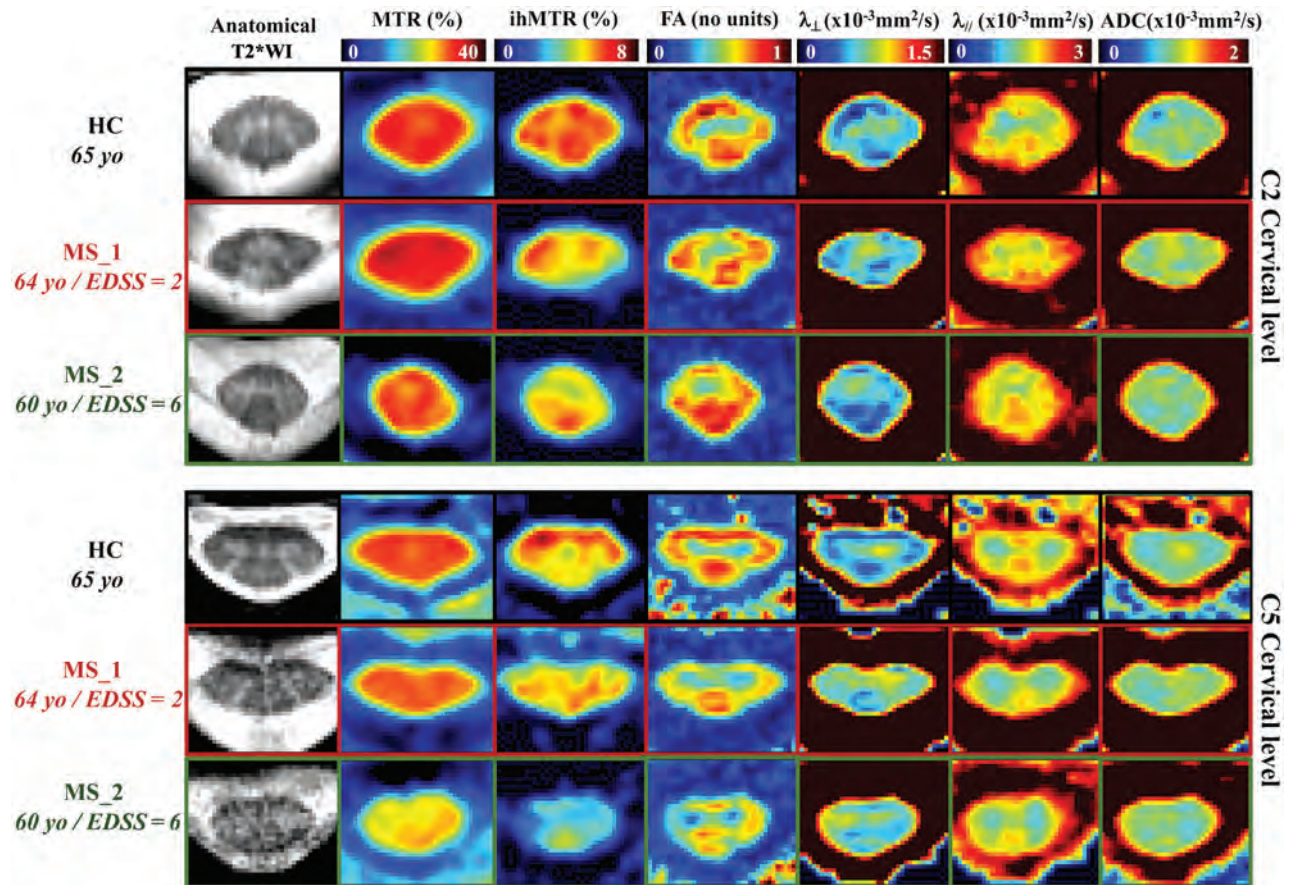


FIG 3. Representative multiparametric maps extracted from a patient with relapsing-remitting MS (MS_1, 64 years of age and EDSS score, 2) and a patient with secondary-progressive MS (MS_2, 60 years of age and EDSS score, 6) along with maps from an age-matched HC (65 years of age) for illustration. yo, years of age.

of DTI and MT metrics ($P < .0001$), in both NA and lesional regions.

Correlations with Clinical Scores

Significant correlations were found between ihMTR z scores in NA whole-WM and total MRC scores ($\rho = 0.80$, $P = .009$)

as well as EDSS scores ($\rho = -0.73$, $P = .02$). MTR z scores were also found correlated with total MRC scores ($\rho = 0.74$, $P = .02$) and EDSS scores ($\rho = -0.81$, $P = .004$). On the other hand, weaker and nonsignificant correlation trends were found for DTI metrics variations, such as between FA z scores and MRC scores ($\rho = 0.64$, $P = .06$), for example.

Brain lesion volume was also significantly correlated with the TWT ($\rho = 0.66$, $P = .008$). Because correlations with the TWT were mostly related to data from a patient with important clinical disabilities (TWT = 73 seconds), they were not considered afterward. No other significant correlations were found.

DISCUSSION

This study provides 3 main findings: 1) AMU₄₀-based SC WM/GM segmentation is feasible in patients with MS; 2) ihMTR shows higher sensitivity to MS-related SC pathophysiologic changes compared with more conventional approaches; and 3) ihMTR might be useful in a clinical context.

MR templates and atlases are very useful tools for automated postprocessing pipelines. Across the years, effort has been directed toward construction^{28,29,32,33} and application of such templates in the SC.^{29,34} To our knowledge, only 2 studies^{35,36} applied and evaluated automated SC GM segmentation in MS: the work of Prados et al³⁵ based on WM/GM segmentation using the Similarity and Truth Estimate for Propagated Segmentations algorithm and the work of Datta et al,³⁶ based on active contour segmentation, with both studies mostly focusing on the C2/C3 cervical levels. Our work is the first to apply the AMU₄₀ template in SC MS and investigate WM/GM segmentation capability from C1 to C6 cervical levels in such cases. The AMU₄₀-based segmentation was previously validated in healthy subjects²¹ (with Dice coefficients of ~0.90/0.83 for WM/GM, respectively) and was used in patients with amyotrophic lateral sclerosis.²² In this study, WM/GM segmentation in MS seemed less efficient than in HC, mostly due to the presence of lesions extending on

Table 2: Multiparametric values for anterolateral/posterolateral/total WM in HC and normal-appearing and lesional regions in patients with MS^a

ROI/MRI Metrics	HC (n = 19)	MS (n = 19)	
		NA	Lesions
Anterolateral WM			
ADC (10 ⁻³ mm ² /s)	1.04 ± 0.08	1.08 ± 0.14	1.11 ± 0.17
FA (n.u)	0.65 ± 0.04	0.62 ± 0.07	0.61 ± 0.06
$\lambda_{//}$ (10 ⁻³ mm ² /s)	1.90 ± 0.08	1.92 ± 0.15	1.96 ± 0.19
λ_{\perp} (10 ⁻³ mm ² /s)	0.60 ± 0.10	0.66 ± 0.15	0.69 ± 0.20
ihMTR (%)	5.88 ± 0.40	5.03 ± 0.62 ^{b,c}	4.30 ± 0.4 ^{c,d,e}
MTR (%)	32.04 ± 1.87	30.65 ± 2.25	29.69 ± 2.89 ^f
Posterolateral WM			
ADC (10 ⁻³ mm ² /s)	1.00 ± 0.08	1.00 ± 0.10	1.09 ± 0.18
FA (n.u)	0.69 ± 0.03	0.67 ± 0.08	0.65 ± 0.06 ^f
$\lambda_{//}$ (10 ⁻³ mm ² /s)	1.95 ± 0.07	1.90 ± 0.11	2.05 ± 0.17 ^e
λ_{\perp} (10 ⁻³ mm ² /s)	0.53 ± 0.10	0.56 ± 0.14	0.63 ± 0.20
ihMTR (%)	5.82 ± 0.39	5.11 ± 0.49 ^{b,c}	4.18 ± 0.70 ^{c,d,f}
MTR (%)	31.42 ± 1.23	30.12 ± 1.45	28.99 ± 2.57 ^b
Total WM			
ADC (10 ⁻³ mm ² /s)	1.01 ± 0.08	1.04 ± 0.10	1.09 ± 0.16
FA (n.u)	0.68 ± 0.03	0.66 ± 0.07	0.64 ± 0.05 ^f
$\lambda_{//}$ (10 ⁻³ mm ² /s)	1.94 ± 0.07	1.93 ± 0.10	2.02 ± 0.16
λ_{\perp} (10 ⁻³ mm ² /s)	0.55 ± 0.10	0.59 ± 0.13	0.64 ± 0.19
ihMTR (%)	5.84 ± 0.40	4.95 ± 0.55 ^f	4.27 ± 0.6 ^{c,d}
MTR (%)	31.58 ± 1.53	29.85 ± 1.56 ^f	29.32 ± 2.48 ^f

Note:—(n.u) indicates no unit.

^a Values are reported as group mean ± SD. Significant differences between metrics from control subjects and NA tissue in patients with MS as well as between HC and lesional tissue were assessed with Steel-Dwass tests and are indicated with the *P* values below.

^b *P* < .001.

^c Differences that survived the Holm-Bonferroni correction for multiple comparisons.

^d *P* < .0001.

^e The only significant metric difference between NA and lesions in patients with MS (*P* = .003).

^f *P* < .05.

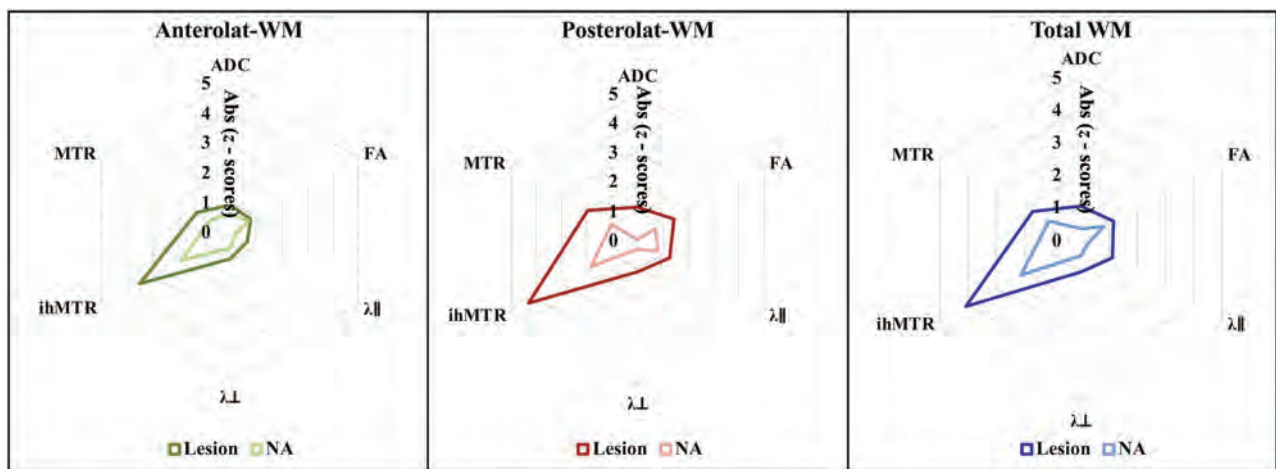


FIG 4. Spider graphs showing mean absolute z scores of each quantitative MR metric in patients with MS relative to HC computed for NA and lesional anterolateral WM (left graph), posterolateral WM (middle graph), and total WM (right graph). Wilcoxon tests for paired values performed between ihMTR absolute z scores and each of the other metrics to assess the sensitivity of the ihMT technique to microstructural changes in MS compared with DTI and MT show significant differences of all tested pairs, with *P* < .0001. Absolute (Abs) z scores are used for visualization purposes and statistical comparison.

both GM and WM, mitigating the difference of contrasts between these structures. The template, nonetheless, demonstrated fairly good compliance with manual segmentations, with Dice coefficients (0.76 ± 0.09 at C2/C3) in line with the 2 previously mentioned MS studies, including patients with visible lesions (GM Dice coefficients: 0.80 ± 0.07 and 0.88 ± 0.03 , respectively, at C₂₋₃).^{35,36} The AMU₄₀ template is not available for whole-spinal cord coverage or for 3D data; however, a former version of it (AMU₁₅) could be found in the recently proposed PAM50³³ template (formerly the MNI-Poly-AMU template; <https://sourceforge.net/p/spinalcordtoolbox/wiki/MNI-Poly-AMU/>), which presents the advantages of being compatible with larger spatial coverage, 3D acquisitions, and acquisition with different contrasts, while also proposing segmentation approaches based on machine learning. Comparison with this template version was beyond the scope of the study but would be interesting.

MS-related morphologic changes have been largely reported with evidence of cervical SC and GM atrophy in patients with MS relative to HC, with a strong correlation with clinical disability.³⁷⁻³⁹ In our study, SC, WM, and GM semiautomated measurements of CSA were performed along the cervical cord from C1 to C6 and results suggested atrophy of both SC GM and WM in patients with MS (5%/14% decrease on average, respectively), consistent with the literature, with more important and more significant atrophy in WM.

DTI and MT imaging have already been largely used to evaluate MS-related SC microstructural changes, with reports of higher ADC and λ_{\perp} and lower FA and MTR in patients with MS relative to HC.^{7,40,41} In this study, DTI and MT metrics in patients with MS demonstrated overall similar variations, with higher variations in lesions compared with NA tissue, suggesting MS-related microstructural changes in the cervical SC as described in previous reports. However, both DTI and conventional MT techniques have been proved to lack specificity toward any pathophysiologic mechanism, due to confounding factors linked to inflammation, demyelination, edema, or axonal degeneration,⁹ making the use of more myelin-specific or sensitive methods interesting.

This work focused on ihMT. Previously published studies reported a supposedly higher ihMT specificity to myelinated structures compared with conventional MT as well as higher sensitivity of associated microstructural changes, in both healthy²¹ and pathologic SC (amyotrophic lateral sclerosis²²), and in the pathologic (MS) brain.²⁰ In the present SC study, among all the considered MR metrics (CSA, DTI, ihMTR, and MTR), ihMTR had the most important and significant variations (absolute value decreases compared with HC and highest z scores), particularly in lesions. Although less important than in lesions, an ihMTR decrease in NA tissue of patients with MS was also found highly significant, suggesting tissue changes occurring away from a lesion or before lesion occurrence, currently not visible on conventional MR imaging. Better detection of such subtle changes could improve disease monitoring, particularly for future treatment based on neuroprotection. Of interest and though not assessed in the current MS work, the ihMT technique was previously demonstrated to be highly reproducible, with a small scan-rescan ihMTR variability (2.9%).²¹

Finally, despite a readout module inducing severe blurring and precluding quantification within specific WM tracts or GM areas, ihMTR z scores measured in total NA WM regions were significantly associated with MRC and EDSS scores, whereas correlations between MTR and DTI with most clinical scores were not significant. These results could advocate for clinical and trial applications of the ihMT technique. They also support the higher sensitivity of the ihMT to MS-related deficits compared with DTI or MT. Further investigations related to the ihMT myelin specificity should now be performed, in conjunction with other myelin imaging techniques that have been successfully applied to SC imaging in recent years, such as quantitative MT imaging¹⁵ or myelin water fraction, which have already demonstrated great interest for SC MS investigations.^{15,42} Future studies should also focus on the ability to detect subtle and early changes.

Indeed, from the clinical point of view, in addition to the small number of patients, the main limitations were the cohort heterogeneity (especially regarding phenotypes, combining relapsing-remitting and secondary-progressive) and the disease duration. It would be relevant to include early forms of MS for longitudinal monitoring of ihMTR variation at different times to judge its utility to better characterize myelin-related processes. From the methodologic point of view, the readout module used for the ihMT measurements induced severe resolution loss and tissue blurring (~ 6 voxels for a T2 of 75 ms) in the phase-encoding direction (right-left), hence only allowing investigating anterolateral and posterolateral regions free from lesions or presenting lesions. Further acquisition strategies, such as recently presented,^{43,44} should help in achieving refined tissue separation. These latter strategies should also permit investigating multiple SC levels and hence characterize the diffuse pattern of cervical SC tissue alteration in MS (DTI/MT/ihMT acquisitions were limited here to C2 and C5 levels to keep the protocol duration to <1 hour). Optimized excitation pulse schemes and translation to higher fields (eg, 7T^{45,46}) should also be considered to increase spatial resolution, SNR, and sensitivity.⁴⁷ Finally, lesions were manually delineated; further studies should evaluate the use of the recently proposed automated MS lesion segmentation algorithms using convolutional neural networks^{48,49} or lesion-prediction algorithms.

Nevertheless, despite these limitations, the MR imaging acquisition and template-based postprocessing strategies used in the current study led to promising results supporting higher ihMT sensitivity toward cervical SC pathologic changes in MS, thereby inspiring future work to use this technique for MR imaging monitoring and as a tool in remyelination therapeutic strategies. Meanwhile, further investigations should be directed toward confirming this higher sensitivity in different cohorts and further evaluation of the specificity of ihMT to these myelin-related pathologic changes.

CONCLUSIONS

The use of a multiparametric MR imaging protocol combined with an automatic template-based GM/WM segmentation approach in the current study outlined a higher sensitivity of the ihMT technique toward SC pathophysiologic changes in MS compared with atrophy measurements, DTI, and conventional MT, presumably

due to its supposed higher specificity to myelin-content variations. The clinical correlations between ihMTR and functional impairment observed in patients with MS also argue for its potential clinical relevance, paving the way for future longitudinal multicentric clinical trials in MS.

ACKNOWLEDGMENTS

The authors thank V. Gimenez and L. Pini for study logistics, A. Rico for patient recruitment, and S. Gherib for brain lesion segmentation.

Disclosures: Jean Pelletier—UNRELATED: Board Membership: Biogen, Teva Pharmaceutical Industries, Novartis, Merck, MedDay Pharma, Roche; Grants/Grants Pending: Roche, Merck; Travel/Accommodations/Meeting Expenses Unrelated to Activities Listed: Biogen, Roche, Teva Pharmaceutical Industries, Merck, MedDay. Virginie Callot—RELATED: Grant: Fondation pour l'Aide à la Recherche sur la Sclérose En Plaques, Comments: The money helped for MR imaging exploration.* *Money paid to the institution.

REFERENCES

- Thompson AJ, Banwell BL, Barkhof F, et al. **Diagnosis of multiple sclerosis: 2017 revisions of the McDonald criteria.** *Lancet Neurol* 2018;17:162–73 CrossRef Medline
- Gass A, Rocca MA, Agosta F, et al; MAGNIMS Study Group. **MRI monitoring of pathological changes in the spinal cord in patients with multiple sclerosis.** *Lancet Neurol* 2015;14:443–54 CrossRef Medline
- Kearney H. **Clinical monitoring of multiple sclerosis should routinely include spinal cord imaging: No.** *Mult Scler* 2018;24:1537–39 CrossRef Medline
- Stroman PW, Wheeler-Kingshott C, Bacon M, et al. **The current state-of-the-art of spinal cord imaging: methods.** *Neuroimage* 2014;84:1070–81 CrossRef Medline
- Basser PJ, Mattiello J, LeBihan D. **MR diffusion tensor spectroscopy and imaging.** *Biophys J* 1994;66:259–67 CrossRef Medline
- Wolff SD, Balaban RS. **Magnetization transfer contrast (MTC) and tissue water proton relaxation in vivo.** *Magn Reson Med* 1989;10:135–44 CrossRef Medline
- Zackowski KM, Smith SA, Reich DS, et al. **Sensorimotor dysfunction in multiple sclerosis and column-specific magnetization transfer-imaging abnormalities in the spinal cord.** *Brain* 2009;132:1200–09 CrossRef Medline
- Oh J, Cybulsky K, Chen M, et al. **Longitudinal changes in quantitative spinal cord MRI in multiple sclerosis patients: results of a 5-year study (S47.001).** *Neurology* Apr 2018, 90:(15 Supplement) S47.001. https://n.neurology.org/content/90/15_Supplement/S47.001. Accessed May 10, 2019
- Mottershead JP, Schmierer K, Clemence M, et al. **High field MRI correlates of myelin content and axonal density in multiple sclerosis.** *J Neurol* 2003;250:1293–1301 CrossRef Medline
- O'Muircheartaigh J, Vavasour I, Ljungberg E, et al. **Quantitative neuroimaging measures of myelin in the healthy brain and in multiple sclerosis.** *Hum Brain Mapp* 2019;40:2104–16 CrossRef Medline
- Heath F, Hurley SA, Johansen-Berg H, et al. **Advances in noninvasive myelin imaging.** *Dev Neurobiol* 2018;78:136–51 CrossRef Medline
- Mackay A, Whittall K, Adler J, et al. **In vivo visualization of myelin water in brain by magnetic resonance.** *Magn Reson Med* 1994;31:673–77 CrossRef Medline
- Alonso-Ortiz E, Levesque IR, Pike GB. **MRI-based myelin water imaging: a technical review.** *Magn Reson Med* 2015;73:70–81 CrossRef Medline
- Sled JG, Pike GB. **Quantitative imaging of magnetization transfer exchange and relaxation properties in vivo using MRI.** *Magn Reson Med* 2001;46:923–31 CrossRef Medline
- Smith AK, Dortch RD, Dethrage LM, et al. **Rapid, high-resolution quantitative magnetization transfer MRI of the human spinal cord.** *Neuroimage* 2014;95:106–16 CrossRef Medline
- Schmierer K, Tozer DJ, Scaravilli F, et al. **Quantitative magnetization transfer imaging in postmortem multiple sclerosis brain.** *J Magn Reson Imaging* 2007;26:41–51 CrossRef Medline
- Varma G, Girard OM, Prevost VH, et al. **In vivo measurement of a new source of contrast, the dipolar relaxation time, T_{1D}, using a modified inhomogeneous magnetization transfer (ihMT) sequence.** *Magn Reson Med* 2017;78:1362–72 CrossRef Medline
- Girard OM, Callot V, Prevost VH, et al. **Magnetization transfer from inhomogeneously broadened lines (ihMT): improved imaging strategy for spinal cord applications.** *Magn Reson Med* 2017;77:581–91 CrossRef Medline
- Varma G, Duhamel G, Bazelaire C, et al. **Magnetization transfer from inhomogeneously broadened lines: a potential marker for myelin.** *Magn Reson Med* 2015;73:614–22 CrossRef Medline
- Van Obberghen E, Mchinda S, Le Troter A, et al. **Evaluation of the sensitivity of inhomogeneous magnetization transfer (ihMT) MRI for multiple sclerosis.** *AJNR Am J Neuroradiol* 2018;39:634–41 CrossRef Medline
- Taso M, Girard OM, Duhamel G, et al. **Tract-specific and age-related variations of the spinal cord microstructure: a multi-parametric MRI study using diffusion tensor imaging (DTI) and inhomogeneous magnetization transfer (ihMT).** *NMR Biomed* 2016;29:817–32 CrossRef Medline
- Rasoanandrianina H, Grapperon AM, Taso M, et al. **Region-specific impairment of the cervical spinal cord (SC) in amyotrophic lateral sclerosis: a preliminary study using SC templates and quantitative MRI (diffusion tensor imaging/inhomogeneous magnetization transfer).** *NMR Biomed* 2017;30:e3801 CrossRef Medline
- Polman CH, Reingold SC, Banwell B, et al. **Diagnostic criteria for multiple sclerosis: 2010 revisions to the McDonald criteria.** *Ann Neurol* 2011;69:292–302 CrossRef Medline
- Compston A. **Aids to the investigation of peripheral nerve injuries: Medical Research Council—Nerve Injuries Research Committee. His Majesty's Stationery Office: 1942; pp. 48 (iii) and 74 figures and 7 diagrams; with aids to the examination of the peripheral nervous system. By Michael O'Brien for the Guarantors of Brain. Saunders Elsevier: 2010; pp. [8] 64 and 94 figures.** *Brain* 2010; 133:2838–44 CrossRef Medline
- Allgöwer K, Kern C, Hermsdörfer J. **Predictive and reactive grip force responses to rapid load increases in people with multiple sclerosis.** *Arch Phys Med Rehabil* 2017;98:525–33 CrossRef Medline
- Cutter GR, Baier ML, Rudick RA, et al. **Development of a multiple sclerosis functional composite as a clinical trial outcome measure.** *Brain* 1999;122:871–82 CrossRef Medline
- De Leener B, Lévy S, Dupont SM, et al. **SCT: Spinal Cord Toolbox, an open-source software for processing spinal cord MRI data.** *NeuroImage* 2017;145:24–43 CrossRef Medline
- Fonov VS, Le Troter A, Taso M, et al. **Framework for integrated MRI average of the spinal cord white and gray matter: the MNI-Poly-AMU template.** *Neuroimage* 2014;102(Pt 2):817–87 CrossRef Medline
- Taso M, Le Troter A, Sdika M, et al. **A reliable spatially normalized template of the human spinal cord: applications to automated white matter/gray matter segmentation and tensor-based morphometry (TB1000) mapping of gray matter alterations occurring with age.** *Neuroimage* 2015;117:20–28 CrossRef Medline
- Jenkinson M, Beckmann CF, Behrens TE, et al. **FSL.** *Neuroimage* 2012;62:782–90 CrossRef Medline
- De Leener B, Kadoury S, Cohen-Adad J. **Robust, accurate and fast automatic segmentation of the spinal cord.** *Neuroimage* 2014;98:528–36 CrossRef Medline
- Lévy S, Benhamou M, Naaman C, et al. **White matter atlas of the human spinal cord with estimation of partial volume effect.** *Neuroimage* 2015;119:262–71 CrossRef Medline

33. De Leener B, Fonov VS, Collins DL, et al. **PAM50: unbiased multi-modal template of the brainstem and spinal cord aligned with the ICBM152 space.** *Neuroimage* 2018;165:170–79 CrossRef Medline
34. Kearney H, Schneider T, Yiannakas MC, et al. **Spinal cord grey matter abnormalities are associated with secondary progression and physical disability in multiple sclerosis.** *J Neurol Neurosurg Psychiatry* 2015;86:608–14 CrossRef Medline
35. Prados F, Cardoso MJ, Yiannakas MC, et al. **Fully automated grey and white matter spinal cord segmentation.** *Sci Rep* 2016;6:36151 CrossRef Medline
36. Datta E, Papinutto N, Schlaeger R, et al. **Gray matter segmentation of the spinal cord with active contours in MR images.** *Neuroimage* 2017;147:788–99 CrossRef Medline
37. Schlaeger R, Papinutto N, Panara V, et al. **Spinal cord gray matter atrophy correlates with multiple sclerosis disability.** *Ann Neurol* 2014;76:568–80 CrossRef Medline
38. Zeydan B, Gu X, Atkinson EJ, et al. **Cervical spinal cord atrophy: an early marker of progressive MS onset.** *Neurol Neuroimmunol Neuroinflamm* 2018;5:e435 CrossRef Medline
39. Valsasina P, Aboulwafa M, Preziosa P, et al. **Cervical cord T1-weighted hypointense lesions at MR imaging in multiple sclerosis: relationship to cord atrophy and disability.** *Radiology* 2018;288:234–44 CrossRef Medline
40. Oh J, Zackowski K, Chen M, et al. **Multiparametric MRI correlates of sensorimotor function in the spinal cord in multiple sclerosis.** *Mult Scler J* 2013;19:427–35 CrossRef Medline
41. Filippi M, Agosta F. **Magnetization transfer MRI in multiple sclerosis.** *J Neuroimaging* 2007;17(Suppl 1):22S–26S CrossRef Medline
42. Dvorak AV, Ljungberg E, Vavasour IM, et al. **Rapid myelin water imaging for the assessment of cervical spinal cord myelin damage.** *Neuroimage Clin* 2019;23:101896 CrossRef Medline
43. Rasoanandrianina H, Duhamel G, Massire A, et al. **A new rapid and high-resolution multi-slice inhomogeneous magnetization transfer protocol to evaluate diffuse and regional cervical cord myelination at 3T.** In: *Proceedings of the Annual Meeting of the International Society of Magnetic Resonance in Medicine*, Paris, France; June 16–21, 2018; 1855
44. Troalen T, Callot V, Varma G, et al. **Cervical spine inhomogeneous magnetization transfer (ihMT) imaging using ECG-triggered 3D rapid acquisition gradient-echo (ihMT-RAGE).** In: *Proceedings of the Annual Meeting of the International Society for Magnetic Resonance in Medicine*, Montreal, Canada; May 11–16, 2019; 0300
45. Dula AN, Pawate S, Dortch RD, et al. **Magnetic resonance imaging of the cervical spinal cord in multiple sclerosis at 7T.** *Mult Scler* 2016;22:320–28 CrossRef Medline
46. Massire A, Taso M, Besson P, et al. **High-resolution multi-parametric quantitative magnetic resonance imaging of the human cervical spinal cord at 7T.** *Neuroimage* 2016;143:58–69 CrossRef Medline
47. Mchinda S, Varma G, Prevost VH, et al. **Whole brain inhomogeneous magnetization transfer (ihMT) imaging: sensitivity enhancement within a steady-state gradient echo sequence.** *Magn Reson Med* 2018;79:2607–19 CrossRef Medline
48. Gros C, De Leener B, Badji A, et al. **Automatic segmentation of the spinal cord and intramedullary multiple sclerosis lesions with convolutional neural networks.** *Neuroimage* 2019;184:901–15 CrossRef Medline
49. Eden D, Gros C, Badji A, et al. **Spatial distribution of multiple sclerosis lesions in the cervical spinal cord.** *Brain* 2019;142:633–46 CrossRef Medline
50. Feiweier T, Huwer S, Kim TH, Porter DA, et al. **Method and magnetic resonance system to reduce distortions in diffusion imaging.** Siemens Aktiengesellschaft, assignee. United States patent 20110187367. 2011 04.08.2011. <http://www.google.com/patents/US8508226>. Accessed June 11, 2016
51. Jenkinson M, Bannister P, Brady M, et al. **Improved optimization for the robust and accurate linear registration and motion correction of brain images.** *Neuroimage* 2002;17:825–41 CrossRef Medline

MR Myelography for the Detection of CSF-Venous Fistulas

J.L. Chazen, M.S. Robbins, S.B. Strauss, A.D. Schweitzer, and J.P. Greenfield



ABSTRACT

SUMMARY: CSF-venous fistula is an important treatable cause of spontaneous intracranial hypotension that is often difficult to detect using traditional imaging techniques. Herein, we describe the technical aspects and diagnostic performance of MR myelography when used for identifying CSF-venous fistulas. We report 3 cases in which the CSF-venous fistula was occult on CT myelography but readily detected using MR myelography.

ABBREVIATIONS: CVF = CSF-venous fistula; SIH = spontaneous intracranial hypotension; VIBE = volumetric interpolated brain examination

CSF-venous fistula (CVF) is an important cause of spontaneous intracranial hypotension (SIH) and a critical diagnosis because treatment can result in a clinical cure.¹⁻⁵ The fistulous connection is typically associated with a nerve root sleeve diverticulum; therefore, a detectable epidural fluid collection is often absent. Some authors advocate decubitus CT myelography to improve CVF detection,^{1,2,6} while others suggest that digital subtraction myelography may increase rates of fistula identification.^{7,8} We report surgically confirmed cases of CVF that were identified using MR myelography following the intrathecal administration of gadolinium.

MR Myelography Technique

Intrathecal gadolinium was instilled in the subarachnoid space via CT-guided lumbar puncture using a Gertie Marx Whitacre-style spinal needle (IMD). The opening pressure was measured and recorded, and 0.5 mL of gadobutrol (Gadavist; Bayer Schering Pharma) mixed with 4.5 mL of iohexol (Omnipaque 180; GE Healthcare) was intrathecally administered. After a 1-mL test injection, CT imaging confirmed intrathecal contrast, and 5 mL was instilled before the needle was removed with

the stylet in place. The patient was positioned in a decubitus Trendelenberg position and rolled multiple times to disperse contrast throughout the subarachnoid space. The patient was then transferred to the MR imaging suite where MR myelography was performed on a 3T Biograph mMR scanner (Siemens) using multiplanar fat-suppressed T1 sequences (On-line Table). Imaging was reviewed in real time, and delayed thin-section axial sequences were acquired as needed. MR imaging was completed approximately 1 hour after intrathecal gadolinium administration.

Cases

Case 1. A 26-year-old woman with a 3-year history of orthostatic headaches after a spontaneous onset had brain MR imaging findings characteristic of SIH, including sagging, pituitary enlargement, venous distention, small subdural collections, and pachymeningeal enhancement. A CT myelogram was unrevealing for CSF leak, and 3 epidural blood patches were unsuccessful. She subsequently developed upper extremity pain and paresthesias, leading to the discovery of a large cervicothoracic syrinx on cervical spine MR imaging (Fig 1). She was treated with a posterior fossa decompression to improve craniocervical CSF flow but obtained neither symptom nor imaging improvement. Eventually, she underwent MR myelography with an opening pressure of <4 cm H₂O and was discovered to have a prominent left T7-T8 spinal meningeal diverticulum fistulizing to a left paraspinous vein draining into the azygous system. She also had early contrast opacification of her renal collecting system on the MR myelography completed approximately 1 hour after intrathecal contrast injection (Fig 2). The patient was offered and accepted surgical CVF ligation at T7-T8. The diverticulum was identified with dilated draining veins, and the entire nerve root complex with the CVF was interrupted with

Received December 25, 2019; accepted after revision February 29, 2020.

From the Departments of Radiology (J.L.C., S.B.S., A.D.S.), Neurology (M.S.R.), and Neurological Surgery (J.P.G.), Weill Cornell Medicine, New York-Presbyterian Hospital, New York, New York.

Please address correspondence to J. Levi Chazen, MD, Weill Cornell Medicine, New York-Presbyterian Hospital, Department of Radiology, 520 E. 70th St. Starr 631 New York, NY 10065; e-mail: jlc2008@med.cornell.edu; @LeviChazen

 Indicates article with supplemental on-line table.

 Indicates article with supplemental on-line photos.

<http://dx.doi.org/10.3174/ajnr.A6521>

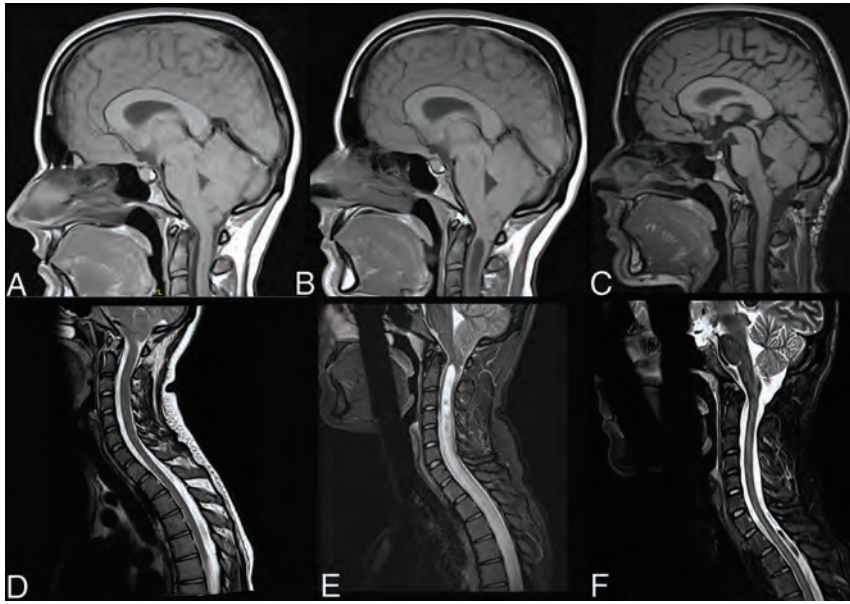


FIG 1. Sagittal T1 brain (A–C) and sagittal T2-weighted cervical spine (D–F) imaging. Initial MR imaging from June 2016 (A and D) shows classic intracranial findings of SIH with low-lying cerebellar tonsils, effacement of the prepontine cistern, enlarged pituitary, and brain stem sagging. Spine imaging findings are normal. Follow-up MRIs from June 2018 (B and E) show similar brain findings with interval development of a large cervicothoracic syrinx. Postoperative MRIs from June 2019 (C and F) reveal complete resolution of intracranial SIH sequelae, with a normal position of the cerebellar tonsils and resolution of spinal syrinx.



FIG 2. MR myelogram axial T1 VIBE (A) demonstrates early contrast opacification of the renal collecting system (*dashed circles*). CT myelogram (B) demonstrates an irregular left T7–T8 perineural cyst without evidence of an opacifying paraspinal vein. No renal contrast excretion was identified on CT myelography. MR myelogram axial T1 VIBE (C) shows a spinal meningeal diverticulum with an opacifying paraspinal vein (*arrows*) draining into the azygous system, consistent with a CSF-venous fistula.

an aneurysm clip and silk suture (On-line Fig 1). The patient experienced an immediate improvement in symptoms followed by a transient new headache and sixth-nerve palsy 3 days following the operation. This was presumed to be secondary to transient rebound intracranial hypertension, and her symptoms slowly resolved. Eight months postoperatively, she is without headaches, and follow-up MR imaging revealed both a dramatic resolution of brain sagging and near-complete resolution of the spinal cord syrinx (Fig 1).

Case 2. A 64-year-old man presented with a 9-month history of orthostatic headache, distorted hearing, and tinnitus with onset during Valsalva exacerbated by severe constipation. Brain imaging demonstrated a venous distention sign without other intracranial sequelae of SIH. Standard CT myelography could not identify a CSF leak, and multiple epidural blood patches were unsuccessful. An MR myelogram with an opening pressure of 9 cm H₂O revealed a left T8–T9 spinal meningeal diverticulum and adjacent opacification of a paraspinous vein (Fig 3).

Small-volume contrast was also seen in the renal collecting systems. The patient was offered and accepted surgical CVF ligation at T8–T9. The diverticulum was identified with dilated draining veins, and the entire nerve root complex with the CVF was interrupted with an aneurysm clip and silk suture. The patient experienced marked symptomatic improvement with resolution of headache and tinnitus, sustained at the most recent 4-month follow-up visit.

Case 3. A 53-year-old woman presented with a 2-year history of spontaneous-onset orthostatic headache and neck pressure. Brain imaging findings were suspicious for SIH with sagging, pituitary enlargement, venous distention, small subdural collections, and pachymeningeal enhancement. A CT myelogram revealed multiple spinal meningeal diverticula and Tarlov cysts without evidence of spinal fluid leak, and the patient received multiple epidural blood patches with only transient improvement of symptoms. An MR myelogram with an opening pressure of <4 cm H₂O revealed a left T9–T10 spinal meningeal diverticulum and an opacified left paraspinous vein (On-line Fig 2). The patient was offered and accepted surgical CVF ligation at T9–T10. The diverticulum was identified with dilated draining veins, and the entire nerve root complex with the CVF was interrupted with an aneurysm clip and silk suture. The patient reported an immediate improvement in symptoms with return to baseline and resolution of headache, sustained for 7 months at the most recent follow-up visit.

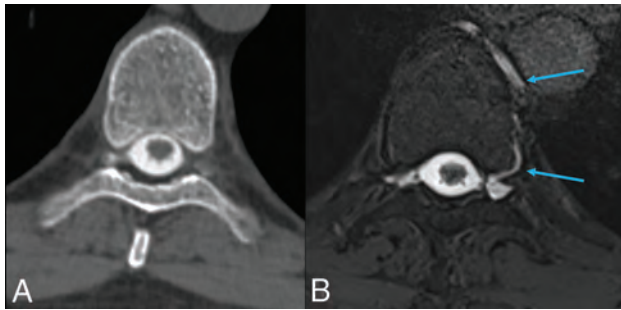


FIG 3. CT and MR myelogram images from case 2. *A*, CT myelogram reveals perineural cysts at T8–T9 without opacification of the left-sided cyst. *B*, MR myelogram axial T1 VIBE demonstrates opacification of the left-sided spinal meningeal diverticulum and left paraspinous vein draining into the azygous system (arrows), consistent with a CSF-venous fistula.

DISCUSSION

CSF-venous fistulas are an under-recognized cause of SIH. Improved detection using advanced imaging techniques may increase our sensitivity in detecting CSF leaks. CT myelography may detect CVF, and the technique can be augmented with decubitus positioning and provocative maneuvers to increase CSF pressure.^{5,9} Digital subtraction myelography has also been used to identify CSF-venous fistulas. However, both of these techniques require substantial ionizing radiation exposure to the patient, and the digital subtraction myelography technique is operator-dependent with different techniques described in the literature.^{7,8} Intrathecal administration of gadolinium is an off-label use in the United States but is well-tolerated and frequently used for clinical and research applications.^{10,11} However, while no long-term harmful effects from intrathecal gadolinium are known, this has not been extensively studied. Only a macrocyclic gadolinium agent (gadobutrol) was used in this study, which has a weaker association with deposition compared with linear gadolinium agents.¹² MR myelography eliminates the ionizing radiation exposure aside from any used for lumbar puncture. Additionally, multiple imaging sequences can be repeated as necessary to confirm a suspected fistula. Furthermore, while the attenuation of intrathecal CT contrast fades rapidly within an hour of intrathecal administration, intrathecal gadolinium maintains robust T1-shortening MR imaging signal for hours after administration. We found the axial T1 fat-suppressed volumetric interpolated brain examination (VIBE) imaging sequences to be particularly helpful. These may help highlight a fistula on MR myelography that may be less apparent on other imaging modalities. The technique is further bolstered by the improved soft-tissue contrast of MR imaging and the prominent signal intensity of gadolinium on fat suppressed T1-weighted images. MR myelography has been shown previously to detect leaking gadolinium from perineural cysts.¹³

Outstanding questions remain regarding the diagnostic performance of MR myelography and other myelographic techniques in the detection of CVF because no known criterion standard is

available. We report 3 patients who had unrevealing CT myelograms in whom CVF was detected on MR myelography, all of whom experienced marked clinical improvement following ligation of the suspected fistula. This report raises important questions for further study regarding the optimal technique for imaging patients with suspected CSF leak.

In conclusion, MR myelography with intrathecal gadolinium may identify CSF-venous fistulas in patients without readily apparent fistulas on CT myelography. Further study is needed to confirm these promising findings.

Disclosures: Dr. Chazen—RELATED: Grant: Insightec, Inc., Alzheimer's Drug Discovery Foundation.

REFERENCES

1. Kranz PG, Gray L, Amrhein TJ. Decubitus CT myelography for detecting subtle CSF leaks in spontaneous intracranial hypotension. *AJNR Am J Neuroradiol* 2019;40:754–56 CrossRef Medline
2. Kranz PG, Amrhein TJ, Gray L. CSF venous fistulas in spontaneous intracranial hypotension: imaging characteristics on dynamic and CT myelography. *AJR Am J Roentgenol* 2017;209:1360–66 CrossRef Medline
3. Kumar N, Diehn FE, Carr CM, et al. Spinal CSF venous fistula: a treatable etiology for CSF leaks in craniocervical hypovolemia. *Neurology* 2016;86:2310–12 CrossRef Medline
4. Schievink WI, Moser FG, Maya MM. CSF-venous fistula in spontaneous intracranial hypotension. *Neurology* 2014;83:472–73 CrossRef Medline
5. Duvall JR, Robertson CE, Cutsforth-Gregory JK, et al. Headache due to spontaneous spinal cerebrospinal fluid leak secondary to cerebrospinal fluid-venous fistula: case series. *Cephalalgia* 2019;39:1847–54 CrossRef Medline
6. Kranz PG, Amrhein TJ, Schievink WI, et al. The “hyperdense paraspinous vein” sign: a marker of CSF-venous fistula. *AJNR Am J Neuroradiol* 2016;37:1379–81 CrossRef Medline
7. Schievink WI, Maya MM, Moser FG, et al. Lateral decubitus digital subtraction myelography to identify spinal CSF-venous fistulas in spontaneous intracranial hypotension. *J Neurosurg Spine* 2019 Sep 1–4. [Epub ahead of print] CrossRef Medline
8. Farb RI, Nicholson PJ, Peng PW, et al. Spontaneous intracranial hypotension: a systematic imaging approach for CSF leak localization and management based on MRI and digital subtraction myelography. *AJNR Am J Neuroradiol* 2019;40:745–53 CrossRef Medline
9. Griffin AS, Lu L, Peacock S, et al. CSF volume provocation maneuvers during lumbar puncture as a possible predictive tool for diagnosing spontaneous intracranial hypotension. *Clin Neurol Neurosurg* 2019;186:105552 CrossRef Medline
10. Dillon WP. Intrathecal gadolinium: its time has come? *AJNR Am J Neuroradiol* 2008;29:3–4 CrossRef Medline
11. Akbar JJ, Luetmer PH, Schwartz KM, et al. The role of MR myelography with intrathecal gadolinium in localization of spinal CSF leaks in patients with spontaneous intracranial hypotension. *AJNR Am J Neuroradiol* 2012;33:535–40 CrossRef Medline
12. Rowe SK, Rodriguez D, Cohen E, et al. Switching from linear to macrocyclic gadolinium-based contrast agents halts the relative T1-weighted signal increase in deep gray matter of children with brain tumors: a retrospective study. *J Magn Reson Imaging* 2020;51:288–95 CrossRef Medline
13. Chazen JL, Talbott JF, Lantos JE, et al. MR myelography for identification of spinal CSF leak in spontaneous intracranial hypotension. *AJNR Am J Neuroradiol* 2014;35:2007–12 CrossRef Medline

Celebrating 35 Years of the AJNR

May 1985 edition

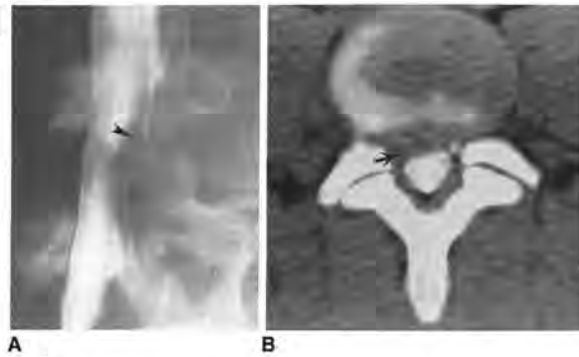
Chymopapain Chemonucleolysis: Correlation of Diagnostic Radiographic Factors and Clinical Outcome

Lindell R. Gentry^{1,2}
Charles M. Strother¹
Patrick A. Turski¹
Marucher J. Javik²
Joseph F. Sackett¹

The therapeutic response to treatment of lumbar disk herniation with chymopapain chemonucleolysis is significantly influenced by the criteria used for patient selection. Although careful clinical selection of patients reduces the frequency of treatment failure, some patients do not achieve satisfactory relief of pain with chemonucleolysis. In an attempt to identify objective pretreatment radiographic findings that might refine selection criteria and further reduce the failure rate of chemonucleolysis, a retrospective correlation of pretreatment radiographic and clinical responses was made of 200 consecutive chemonucleolysis patients. Marked improvement in sciatica occurred in 79.5% and 79.2% of patients at early and late follow-up, respectively. There was a significantly higher response rate, however, in patients who had definite radiographic evidence of focal disk herniation and in those patients with definite radiographic evidence of nerve-root compression (marked nerve-root deviation, nerve-root flattening or edema, root-sleeve angulation) by disk material. Those patients with a protrusion disk height greater than the mean had a slightly better response rate (81.1%) than those whose disk height was smaller than the mean (80.2%). Most cases of treatment failure could be attributed to an incorrect radiographic diagnosis, treatment of patients with equivocal diagnostic studies, the presence of "free" disk fragments, and causes of nerve-root compression unresponsive to chymopapain.

Chymopapain, a proteolytic enzyme derived from papaya latex, catalyzes the rapid hydrolysis of the chondromucoprotein part of the nucleus pulposus of the intervertebral disk. In 1964, Smith [1] first demonstrated the possibility of using chymopapain to enzymatically treat lumbar disk herniations (chymopapain chemonucleolysis). Clinical trials designed to establish the safety and efficacy of this procedure quickly followed.

By 1975, over 17,000 people had been treated with chymopapain chemonucleolysis in 75 centers [2, 3]. Wide variations were reported in the frequency of successful results, ranging from 50% to 85%, and controversy concerning its



This article appears in the May/June 1985 issue of AJNR and the August 1985 issue of AJNR. Received December 27, 1983; accepted after revision May 3, 1984.

Presented in part at the annual meeting of the American Society of Neuroradiology, San Francisco, June 1983.

¹ Department of Radiology, University of Wisconsin Hospital and Clinics, Madison, WI 53792.

² Present address: Department of Radiology, University of Iowa Hospitals and Clinics, 2006 Carroll, Iowa City, IA 52242. Address reprint requests to L. R. Gentry.

³ Division of Neurosurgery, University of Wisconsin Hospital and Clinics, Madison, WI 53792.

AJNR 6:511-520, May/June 1985
0195-4646/85/0605-0511
© American Roentgen Ray Society

Computed Tomographic Changes of Hypertensive Encephalopathy

Karen L. Weingarten¹
Robert D. Zimmerman¹
Richard S. Finkel¹
Margaret A. Whelan¹

Computed tomographic (CT) scans of hypertensive encephalopathy. Hypertensive encephalopathy is associated with a severe rise in blood pressure, associated mental status, and focal neurologic deficits. The systemic blood pressure is usually greater than 170 mm Hg. The most common CT finding affecting the supratentorial compartment is right. These changes resolved after treatment. Permanent abnormalities are common. These abnormalities are common.

Hypertensive encephalopathy is an acute condition associated with convulsions, stupor, and coma [1-4]. It is usually associated with a severe rise in blood pressure, associated mental status, and focal neurologic deficits, and rapid improvement after control of blood pressure. The range of systolic blood pressure was 200-280 mm Hg (mean, 250 mm Hg); the range of diastolic pressure was 130-170 mm Hg (mean, 150 mm Hg).

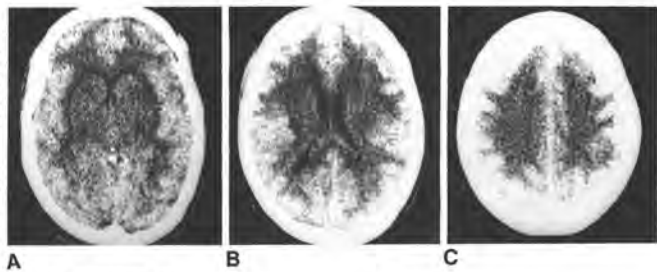
Materials and Methods

The hospital records and CT scans of 11 patients with hypertensive encephalopathy from Montefiore Medical Center and New York University Medical Center were reviewed. In all cases, CT scans were obtained during the acute phase of blood pressure elevation. Six patients had follow-up CT scans.

The six male and five female patients were 10-59 years old (mean, 46). The diagnosis of hypertensive encephalopathy was made by the clinical criteria of an acute, severe rise in blood pressure associated with headache, nausea, vomiting, altered mental status, and focal neurologic deficits, and rapid improvement after control of blood pressure. The range of systolic blood pressure was 200-280 mm Hg (mean, 250 mm Hg); the range of diastolic pressure was 130-170 mm Hg (mean, 150 mm Hg).

Results

The CT findings in hypertensive encephalopathy can be divided into supratentorial and infratentorial abnormalities. All cases demonstrated supratentorial abnormalities in the acute stage of hypertensive encephalopathy, characterized by edema and expansion of the white matter, compression of the ventricles, and obliteration of sulci and cisternal spaces (figs. 1-5). This diffuse white-matter edema resolved after the blood pressure was lowered in all patients in whom follow-up scans were obtained (figs. 2-5). Other supratentorial abnormalities observed during the acute phase of the disease were ganglionic edema in two patients (fig. 1), bilateral



Received May 30, 1984; accepted after revision September 20, 1984.

Presented at the annual meeting of the American Society of Neuroradiology, San Francisco, June 1983.

¹ Department of Radiology, New York University Medical Center, 580 First Ave., New York, NY 10016. Address reprint requests to K. L. Weingarten.

² Department of Radiology, New York University Medical Center, 580 First Ave., New York, NY 10016.

AJNR 6:240-268, May/June 1985
0195-4646/85/0505-0240
© American Roentgen Ray Society

Identification of Vortex Cores in Cerebral Aneurysms on 4D Flow MRI

We read with interest the study by Futami et al,¹ "Identification of Vortex Cores in Cerebral Aneurysms on 4D Flow MRI." They described the visualization, complexity, and stability of vortex cores on 4D flow MR imaging in a series of 40 cerebral aneurysms. Discriminating single, stable, vortex cores from complex flow patterns with temporarily unstable vortices, they found an association between a complex vortical flow pattern and complex aneurysm morphology. Thus, they concluded that the identification of vortex core flow patterns on 4D flow MR imaging may help to stratify aneurysm rupture risk. Moreover, they explained the mathematic definition of a vortex core line and referred to other previous research using computational fluid dynamics simulation data models that describe the phenomenon of vortex cores with cerebral aneurysm models.^{2,3}

We agree with Futami et al¹ that vortex core identification is a promising new tool for aneurysm assessment, which is in line with our findings published more than 10 years ago.⁴ Our group first described normal intracranial artery hemodynamics with a helical flow phenomenon in the carotid siphon using in vivo 4D flow MR imaging.⁵ Moreover, we were the first to describe intra-aneurysmal hemodynamics, including the visualization of intra-aneurysmal vortex cores.⁴ In these studies, we performed postprocessing and visualization of aneurysm flow using a commercially available 3D visualization software package (EnSight; Computational Engineering International, Apex, North Carolina). Besides 3D streamlines, 2D vector graphs, and time-resolved particle traces, a dedicated integrated algorithm of this software was applied to segment and illustrate vortex core patterns from 3D vector fields. Thus, the core of the vortical is represented by colored bars indicating the location and magnitude of the vortical flow.

We were also able to analyze the temporal and spatial stability of vortex cores inside the aneurysm during the whole cardiac cycle (Fig 3 from our original work⁴). Likewise in the work by Futami et al,¹ a link between the stability and complexity of intra-aneurysmal vortex core patterns and aneurysm geometry, including the aspect ratio, was disclosed in a series of 5 cerebral aneurysms. In 2 of these aneurysms with a smooth surface and low aspect ratio, temporally stable, single vortex cores were identified, whereas in the other aneurysms with a lobulated surface and/or high aspect ratio, vortex cores showed spatio-temporal and magnitude alterations during the cardiac cycle.

We acknowledge the authors' work studying vortex core patterns in a higher number of aneurysms and support their conclusions drawn from their cohort, though mostly ruptured cases were included. However, we would like to stress that correct reference to the existing body of literature should be given relative to the original description of in vivo visualization of aneurysmal vortex core flow.

Disclosures: Michael Markl—UNRELATED: Consultancy: Circle Cardiovascular Imaging; Grants/Grants Pending: research support: Siemens; research grant, Circle Cardiovascular Imaging; research grant, Cryolife.* *Money paid to the institution.

REFERENCES

1. Futami K, Uno T, Misaki K, et al. **Identification of vortex cores in cerebral aneurysms on 4D flow MRI.** *AJNR Am J Neuroradiol* 2019;40:2111–16 CrossRef Medline
2. Le TB, Troolin DR, Amatya D, et al. **Vortex phenomena in sidewall aneurysm hemodynamics: experiment and numerical simulation.** *Ann Biomed Eng* 2013;41:2157–70 CrossRef Medline
3. Oeltze-Jafra S, Cebra J, Janiga G, et al. **Cluster analysis of vortical flow in simulations of cerebral aneurysm hemodynamics.** *IEEE Trans Vis Comput Graph* 2016;22:757–66 CrossRef Medline
4. Meckel S, Stalder AF, Santini F, et al. **In vivo visualization and analysis of 3-D hemodynamics in cerebral aneurysms with flow sensitized 4-D MR imaging at 3 T.** *Neuroradiology* 2008;50:473–84 CrossRef Medline
5. Wetzel S, Meckel S, Frydrychowicz A, et al. **In vivo assessment and visualization of intracranial arterial hemodynamics with flow-sensitized 4D MR imaging at 3T.** *AJNR Am J Neuroradiol* 2007;28:433–38 Medline Medline

© S. Meckel

Department of Neuroradiology
Faculty of Medicine
Medical Center, University of Freiburg
Freiburg, Germany

© M. Markl

Departments of Radiology and Biomedical Engineering
Feinberg School of Medicine and McCormick School of Engineering
Northwestern University
Chicago, Illinois

© S. Wetzel

Institute of Neuroradiology
Hirslanden Clinic Zurich
Zurich, Switzerland

REPLY:

We applaud the advanced and multidirectional studies performed by Wetzel et al¹ and Meckel et al.² We agree with Meckel et al,² who showed that aneurysms with an irregular shape or a high aspect ratio may have complex and unstable flow.

In our study,³ we differentiated vortex core lines from vortex cores. We identified vortex cores as thin streamline bundles with minimum velocities by progressively decreasing a threshold to visualize flow streamlines with velocities under the threshold in aneurysms. In extremely low velocity thresholds, a vortex core was exhibited as a line. In our study, we did not include such lines into vortex cores, because we could not definitely discriminate the lines from irregular streamlines which were usually visualized in aneurysms via 4D flow MR imaging. In our study,³ the velocity-encoding (VENC) for 4D flow MR imaging was set to 40–60 cm/s to correctly extract low-velocity vectors in aneurysms. We verified that the thin streamline bundle was a vortex core by showing that the bundle passed through the center of vortical flow vectors in the aneurysmal dome.³

Meckel et al² showed a vortex core line using an algorithm to identify the points on the face where reduced velocity is zero and to connect these distinct points.⁴ However, the locations of vortex core lines can vary between algorithms.³ In 4 of 5 aneurysms examined in their study, the VENC for 4D flow MR imaging was 90 cm/s to detect high-velocity flow components.² This VENC value can lead to errors in the extraction of flow vectors with low

velocities in aneurysms, which may cause mislocations of the zero velocity points. Therefore, we suggest that it should be verified that their vortex core lines are located in the center of vortex flows in aneurysms. This verification would guarantee the usefulness of the tool integrating the algorithm to automatically identify vortex core lines in aneurysms and to avoid the interobserver differences. We hope that the tool helps to clarify the role of the vortical flow pattern in aneurysm behavior in future studies.

REFERENCES

1. Wetzel S, Meckel S, Frydrychowicz A, et al. **In vivo assessment and visualization of intracranial arterial hemodynamics with flow-sensitized 4D MR imaging at 3T.** *AJNR Am J Neuroradiol* 2007;28:433–38 Medline
2. Meckel S, Stalder AF, Santini F, et al. **In vivo visualization and analysis of 3-D hemodynamics in cerebral aneurysms with flow sensitized 4-D MR imaging at 3 T.** *Neuroradiology* 2008;50:473–84 CrossRef Medline
3. Futami K, Uno T, Misaki K, et al. **Identification of vortex cores in cerebral aneurysms on 4D flow MRI.** *AJNR Am J Neuroradiol* 2019;40:2111–16 CrossRef Medline
4. Sujudi D, Haimes R. **Identification of swirling flow in 3-D vector fields.** In: *Proceedings of the 12th Computational Fluid Dynamics Conference*, San Diego, California; June 19–22, 1995; <https://doi.org/10.2514/6.1995-1715> CrossRef

 **K. Futami**

Department of Neurosurgery
Hokuriku Central Hospital
Toyama, Japan

 **K. Misaki**

 **M. Nakada**

Department of Neurosurgery
Kanazawa University School of Medicine
Ishikawa, Japan

<http://dx.doi.org/10.3174/ajnr.A6474>

ASPECTS Distorts Infarct Volume Measurement

Sundaram et al¹ reported lucidly on agreements and correlations of ASPECTS for NCCT (manual, automatic) and CTP-CBV (manual). But why use ASPECTS, not volume?

Invented as a volume surrogate, ASPECTS takes the form of “content analysis”—a research method to quantify texts and symbols,² wherein ASPECTS *unitizes* the MCA territory by defining 10 regions and *categorizes* each unit as having either no or any acute infarction. Measurement is degraded by the unitization’s vague definitions and diverse volumes, the binary categorization of so few units, and the bias of “any.” ASPECTS promotes interobserver disagreement (masked by “auto-”) and scatters markedly away from true volume. It is not excused for individual patient use by mere population correlation. Moreover, ASPECTS tends to advance infarcts by sometimes large margins of error beyond a supposed threshold of risk or futility, denying thrombectomy. A detailed explanation of ASPECTS and its flaws and a quick remediation by manual volumetry using the diameter formula *ABC/2* (or a PACS-friendly refinement called *2Sh/3*) are available.³

<http://dx.doi.org/10.3174/ajnr.A6485>

Besides the well-documented *ABC/2* and *2Sh/3*, the software behind any auto-ASPECTS can, in principle, report infarct volumes. If these and other authors skip ASPECTS and use volume, their agreements and correlations might be stronger and their plots less scattered.

Disclosures: Marco C. Pinho—UNRELATED: Consultancy: ABC Medical Education, Comments: On-line educational activities related to MRI.

REFERENCES

1. Sundaram VK, Goldstein J, Wheelwright D, et al. **Automated ASPECTS in acute ischemic stroke: a comparative analysis with CT perfusion.** *AJNR Am J Neuroradiol* 2019;40:2033–38 CrossRef Medline
2. Krippendorff K. *Content Analysis: An Introduction to its Methodology*, 4th ed. Los Angeles: Sage Publications; 2019
3. Suss RA. **ASPECTS, the mismeasure of stroke: a metrological investigation.** *OSF Preprints* 2019 <https://doi.org/10.31219/osf.io/c4tkp>. Accessed December 31, 2019

 R.A. Suss
 M.C. Pinho

Department of Radiology
University of Texas Southwestern Medical Center
Dallas, Texas

REPLY:

We thank Drs Suss and Pinho for their interest in reading our article and sharing their opinion on the use of ASPECTS in patients with acute ischemic stroke. Several valid points have been raised about the limitations of ASPECTS, with which we agree.

Regardless of its limitations, ASPECTS is currently being used for treatment decision-making in patients with acute stroke who present <6 hours from symptom onset. This use is supported by a strong level of evidence that has emerged from randomized clinical trials and is included in the latest American Heart Association guidelines.¹

Volume (of ischemic core) measurements if accurate and reliable can improve the screening process of patients with acute ischemic stroke and avoid several shortcomings of ASPECTS, including variability and ambiguity associated with the binary nature of ASPECTS.

While we have seen the successful use of ischemic core volume estimation obtained from CT perfusion or MR imaging to treat patients with stroke presenting beyond 6 hours from onset,²

current data on volumetric estimates of ischemic core via NCCT alone are limited. It is plausible that with a future successful large, prospective study, volumetric assessment of ischemic core on NCCT could potentially replace ASPECTS. This scenario may be not too far ahead, in particular considering the emergence of deep learning techniques with the potential for making this process even more reliable and effortless.³

REFERENCES

1. Powers WJ, Rabinstein AA, Ackerson T, et al; American Heart Association Stroke Council. **2018 Guidelines for the Early Management of Patients with Acute Ischemic Stroke: A Guideline for Healthcare Professionals From the American Heart Association/American Stroke Association.** *Stroke* 2018;49:e46–110 CrossRef Medline
2. Albers GW, Marks MP, Kemp S, et al; DEFUSE 3 Investigators. **Thrombectomy for stroke at 6 to 16 hours with selection by perfusion imaging.** *N Engl J Med* 2018;378:708–18 CrossRef Medline
3. Nael K. **Detection of acute infarction on non-contrast-enhanced CT: closing the gap with MRI via machine learning.** *Radiology* 2020;294:645–46 CrossRef Medline

 **K. Nael**

Department of Radiological Sciences
David Geffen School of Medicine at UCLA
Los Angeles, California

<http://dx.doi.org/10.3174/ajnr.A6504>

How Far Can We Take Vessel Wall MRI for Intracranial Atherosclerosis? The Tissue is Still the Issue



We read with great interest the recent article by Zwartbol et al¹, and the accompanying commentary by Dr Chan.² While the data from the SMART-MR cohort add to the body of research on intracranial vessel wall MR imaging (vwMRI) studies, we have concerns with the interpretation of the results, specifically that the findings do not support “a different etiology” between intracranial (ICAD) and extracranial (ECAD) atherosclerosis. While vwMRI allows us to visualize disease in the vessel walls themselves, this provides only a snapshot of a dynamic process (atherogenesis) that is years-to-decades in the making. We are far from being able to see underlying processes at a molecular and tissue level that lead to these vwMRI findings.

Since the Virchow era, it has been understood that the distribution of atherosclerosis is not uniform; plaques occur primarily at bifurcations, in curved segments, and in coronary arteries. Intracranial and extracranial arterial systems are derived from different germ cell layers, ectoderm and mesoderm, respectively, and have distinct structural elements and physiologic flow characteristics.³ Accordingly, the risk factors for the development of ECAD and ICAD differ with respect to systemic processes like hyperlipidemia, hyperglycemia, or hypertension. Furthermore, atherosclerosis causes symptoms through different mechanisms and recurrence rates by site. As providers who are often frustrated by suboptimal treatment options for ICAD, we can confirm what has been known for decades, that atherosclerosis responds to treatment differently depending on location. Indeed, Dr Chan cites a seminal manuscript from 1964.⁴ Pathophysiologic mechanisms must be taken into account when considering what is seen on imaging.

The association between ICAD and general vascular risk factors examined in Zwartbol et al¹ has previously been identified. A major limitation of these factors is over-reliance on stenosis. Prior work suggests that high-grade stenosis in ICAD is a feature of late-stage disease, and algorithms relying on stenosis measurement alone can ignore nonstenotic-but-clinically-active disease. A major benefit of vwMRI is the ability to identify plaque features

like remodeling pattern, enhancement, fibrous cap thickness, proximity to perforator ostia, intraplaque hemorrhage, or lipid-rich necrotic core volume. Using vwMRI to merely identify the presence of ICAD misses an opportunity to better characterize the disease.

Another limitation of the methodology in Zwartbol et al¹ is identification of ICAD burden regardless of symptomatology. The prevalence of ICAD is rather high, but most lesions prove harmless. The advantage of the granularity of vwMRI is that it could potentially distinguish the multiple ways ICAD can cause ischemic strokes and possibly predict which ICAD plaques are most likely to cause stroke, regardless of level of stenosis. This study also evaluates ICAD and ECAD cross-sectionally, without any clarification of the temporal relationship of disease development in each vascular bed. In addition, there is no indication of ethnicities within the study cohort of 130 patients; certain ethnic populations preferentially develop atherosclerosis in different vascular beds.

This critique is not meant to disparage the work of Zwartbol et al¹ or the fine research conducted by the UCC-SMART study group. However, this must be viewed as an opportunity to refocus on the need for tissue validation of vwMRI for the investigation of ICAD, a feat that will prove difficult and likely rely on animal models. The burden of proof lies in such validation, and the value of vwMRI lies in its potential to identify processes that mediate disease rather than assuming there is a common pathophysiologic driver of atherosclerosis in all vascular beds.

Disclosures: Adam de Havenon—RELATED: Grant: National Institutes of Health—National Institute of Neurological Disorders and Stroke, Comments: supported by the National Institutes of Health—National Institute of Neurological Disorders and Stroke K23NS105924.* Joseph Scott McNally—RELATED: Grant: American Heart Association, National Institutes of Health, Comments: support from the following grants: 1) American Heart Association Scientist Development Grant (Principal Investigator) 17SDG33460420; 2) American Cancer Society, Huntsman Cancer Institute grant (Principal Investigator) 129785IRG161900IIRG; 3) National Institutes of Health (Co-Investigator under D. Dennis Parker, Principal Investigator) 1R01 HL127582-01A1.* *Money paid to the Institution.

REFERENCES

1. Zwartbol MH, Geerlings MI, Ghaznawi R, et al. **Intracranial atherosclerotic burden on 7T MRI is associated with markers of**

Indicates open access to non-subscribers at www.ajnr.org

<http://dx.doi.org/10.3174/ajnr.A6501>

- extracranial atherosclerosis: the SMART-MR study.** *AJNR Am J Neuroradiol* 2019;40:2016–22 CrossRef Medline
2. Chan LL. **Intracranial and extracranial atherosclerosis: more similar than different?** *AJNR Am J Neuroradiol* 2019;40:2023–24 CrossRef Medline
 3. Lasjaunias PL, ter Brugge KG, Berenstein A, et al. *Clinical and Interventional Aspects in Children: With 102 Tables*. 2nd ed. Heidelberg: Springer-Verlag; 2006
 4. Resch JA, Baker AB. **Etiologic mechanisms in cerebral atherosclerosis: preliminary study of 3,839 cases.** *Arch Neurol* 1964;10:617–28 CrossRef Medline

 **M.D. Alexander**

Departments of Radiology and Imaging Sciences and Neurosurgery

 **A. de Havenon**

Department of Neurology
University of Utah
Salt Lake City, Utah

 **M. Mossa-Basha**

Department of Radiology
University of Washington
Seattle, Washington

 **J.S. McNally**

Departments of Radiology and Imaging Sciences
University of Utah
Salt Lake City, Utah

REPLY:

We thank Dr Alexander and colleagues for their interest in our work and appreciate the opportunity to respond to their concerns.¹

A concern is raised regarding the interpretation of our results, which led us to conclude that our findings do not support “a different etiology” between extracranial atherosclerosis (ECAS) and intracranial atherosclerosis (ICAS). We agree with the data used to substantiate their concern, including data on histopathology and etiology, but do not share their opinion that our findings are contradictory. As described in our article—and noted by Alexander et al—there are several limitations to our study design, which is why we tried to carefully word our conclusion to avoid overinterpretation of our results. We showed that there is a relationship between ICAS and several clinical markers of ECAS, suggesting a similar etiology; or in other words (used in the article), our (limited) results do not support a different etiology. However, there are indeed differences in etiology and pathophysiology, which we do not claim to contradict. Apparently, we were not able to successfully convey this subtle difference to all readers.

As carefully described by Alexander et al, ICAS is a complex disease with many facets, and intracranial vessel wall MR imaging (vwMRI) facilitates our attempts to elucidate parts of this disease process. We agree that vwMRI can provide us with information not only on the presence or absence of atherosclerotic plaques but also on plaque components and the (from extracranial atherosclerosis) well-known “vulnerable plaque.” However, most vessel wall lesions encountered in our populations, Caucasian subjects, which Alexander et al justly noted were not specifically mentioned in our article, are too small to accurately measure, let alone characterize,

apart from the presence or absence of enhancement.² It would indeed also have been of interest to correlate vessel wall lesion locations with cerebrovascular symptoms, but this would necessitate a different study population—with more (cerebrovascular) symptomatic patients—to reach any statistically significant results.

Finally, we would like to provide our whole-hearted support for the suggestion of Alexander et al to “refocus the need for tissue validation of vwMRI.” The ease of characterizing extracranial carotid atherosclerotic plaques is in stark contrast with the difficulty of performing the same analyses in intracranial plaques, which is mainly caused by the lack of methods to compare in vivo–acquired vwMRI with ex vivo histopathology. Nonetheless, sequence validation is essential for our conception of how we should interpret vessel wall lesions on vwMRI and how we should incorporate intracranial vwMRI in clinical practice. We would like to thank Alexander and colleagues for their critical review and compliment them on highlighting the possibilities of vwMRI and opportunities for further research.

REFERENCES

1. Zwartbol MHT, Geerlings MI, Ghaznawi R, et al. **Intracranial atherosclerotic burden on 7T MRI is associated with markers of extracranial atherosclerosis: the SMART-MR study.** *AJNR Am J Neuroradiol* 2019;40:2016–22 CrossRef Medline
2. van Hespem KM, Zwanenburg JJM, Hartevelde AA, et al. **Intracranial vessel wall magnetic resonance imaging does not allow for accurate and precise wall thickness measurements.** *Stroke* 2019;50:e283–84 CrossRef Medline

© **M.H.T. Zwartbol**
© **A.G. van der Kolk**
Department of Radiology
© **M.I. Geerlings**

Julius Center for Health Sciences and Primary Care
University Medical Center Utrecht and UtrechtUniversity
Utrecht, the Netherlands

<http://dx.doi.org/10.3174/ajnr.A6516>

Time to Discontinue Use of the Term Stroke in Neuroradiology

We read with interest the editorial of Aftab and Salman¹ about discontinuing the use of the term “hemorrhagic stroke.” The word “stroke” was coined in medicine to define an acute focal deficit event of the central nervous system of vascular origin² and has been very useful in clinical practice. The division into ischemic and hemorrhagic has served to make a rapid classification of acute cerebrovascular events.

The term “stroke” is unique in the medical literature in English and is not used in other languages. Older words such as “apoplexy” that have their equivalent in other languages have long since ceased to be used, and it is preferred to use “cerebrovascular attack,” “event,” or “accident.” With the advances in the images of the central nervous system and with the globalization of medical knowledge, it is no longer justified to use the term “stroke” in neuroradiology to define lesions of vascular origin. Terms such as “infarct,” “hypoperfusion,” or “focal ischemia” are more precise and better explain the pathophysiology of the neurologic deficit.

Finally, the editorial says that ischemic events are caused by hypoperfusion of a region of the brain secondary to vascular

occlusion or hypoxia. It seems controversial to say that hypoxia causes cerebral hypoperfusion; usually, the opposite is true.³

REFERENCES

1. Aftab M, Salman M. **Time to discontinue use of the term “hemorrhagic stroke.”** *AJNR Am J Neuroradiol* 2019;40:1893 CrossRef Medline
2. Sacco RL, Kasner SE, Broderick JP, et al; Council on Nutrition, Physical Activity and Metabolism. **An updated definition of stroke for the 21st century: a statement for healthcare professionals from the American Heart Association/American Stroke Association.** *Stroke* 2013;44:2064–89 CrossRef Medline
3. Xing C, Arai K, Lo EH, et al. **Pathophysiologic cascades in ischemic stroke.** *Int J Stroke* 2012;7:378–85 CrossRef Medline

 **D.A.L. Ortega**

Fundación Santa Fé de Bogotá
Universidad El Bosque
Bogotá, Colombia

 **A.J. Morillo**

Fundación Santa Fé de Bogotá
Bogotá, Colombia

 **S. González-Gómez**

Fundación Santa Fé de Bogotá
Universidad El Bosque
Bogotá, Colombia

<http://dx.doi.org/10.3174/ajnr.A6479>

REPLY:

I agree with Ortega et al that the term “stroke” is vague and more precise terms such as infarct or ischemia should be used in radiology reporting. Unfortunately, the term stroke is a ubiquitous part of the general (nonradiologic) medical lexicon and national guidelines, particularly given the new emphasis on timely stroke therapy. In this context, what is being referred to is ischemic stroke.

What used to be classified as hemorrhagic stroke is now best classified as simply “intracranial hemorrhage,” which, as was pointed out in the original editorial, carries a different set of etiologies, symptoms, and therapies than ischemic stroke.

To ease the confusion on this terminology, it is being suggested that the term stroke be reserved for what used to be called

ischemic stroke, supplanting the ancient definition of the term stroke.

Finally, examples of hypoxia causing ischemia would include etiologies of hypoxic-ischemic injury such as carbon monoxide poisoning. In these cases, vascular perfusion may be preserved but the perfusing blood may lack adequate oxygen, resulting in ischemia. Perhaps a comma may have helped, “Ischemic events are caused by hypoperfusion of a region of the brain secondary to vascular occlusion, or hypoxia.”

 **M.A. Aftab**

Department of Neuroradiology
Michigan State University
East Lansing, Michigan
Central Michigan University
Saginaw, Michigan
A.T. Still University of Health Sciences
Kirksville, Missouri

<http://dx.doi.org/10.3174/ajnr.A6528>